Exclusive reactions with light mesons: From low to high energies

Piotr Lebiedowicz

The Henryk Niewodniczański
Institute of Nuclear Physics
Polish Academy of Sciences
Kraków, Poland

Thesis submitted for the Degree of Doctor of Philosophy in Physics
prepared under the supervision of Prof. Antoni Szczurek

Kraków, 2014

Abstract

In this Thesis, a theoretical analysis of exclusive production of mesons for various reactions in nucleon-nucleon collisions is presented. Detailed studies of the central exclusive production of the resonance states and the light dimeson pairs ($\pi^+\pi^-$, K^+K^-) within the Regge-based framework as well as the exclusive production of forward neutral particles has been performed in a broad range of collision energy. Different aspects of production mechanism for the considered processes have been discussed, such as the model of soft pomeron, the absorption corrections, the off-shell effects of exchanged mesons. The cross section and many differential distributions were calculated and compared with existing experimental data wherever possible. Predictions for experiments at PANDA, RHIC, Tevatron and LHC energies have been presented. In addition, diffractive and electromagnetic production of the diboson pairs ($\gamma\gamma$, W^+W^-, ZZ) at high energies has been considered in the framework of k_t-factorization approach with the formalism of unintegrated gluon distribution functions. The production of technipions in dominant photon-photon channel as complementary possibility of search of particles beyond the Standard Model at the LHC has been studied.

Streszczenie

W niniejszej pracy przedstawiono teoretyczną analizę ekskluzywnej produkcji mezonów w różnych reakcjach w zderzeniach nukleon-nukleon. Przeanalizowano mechanizm centralnej ekskluzywnej produkcji stanów rezonansowych i par lekkich mezonów ($\pi^+\pi^-$, K^+K^-) w ramach formalizmu Reggego, jak również mechanizmy ekskluzywnej produkcji neutralnych cząstek produkowanych "do przodu", w szerokim zakresie energii zderzeń. Omówiono różne aspekty mechanizmu produkcji rozważanych procesów, takie jak model "miękkiego" pomeronu, poprawki absorpcyjne, efekty pozapowłokowe wymienianych mezonów. Policzono przekroje czynne i wyznaczono szereg różniczkowych rozkładów dla rozważanych reakcji. Wyniki obliczeń zostały porównane z istniejącymi danymi eksperymentalnymi. Przedstawiono przewidywania dla eksperymentów PANDA, RHIC, Tevatron i LHC. Rozważono także dyfrakcyjną i elektromagnetyczną produkcję par bozonów ($\gamma\gamma$, W^+W^-, ZZ) przy wysokich energiach. Dyfrakcyjne procesy policzono w formalizmie k_t-faktoryzacji z uwzględnieniem funkcji nieprzecałkowanych rozkładów gluonów. Jako uzupełnienie przebadano produkcję technipionów w dominującym kanale foton-foton, jako przykład poszukiwania cząstek poza Modelem Standardowym w eksperymentach przy LHC.

Acknowledgments

First and foremost, I would like to thank my supervisor Professor Antoni Szczurek who has introduced me into the field of Particle Physics and has been supporting my efforts through all the years during the PhD studies. I have been very fortunate to work under his supervision, and I thank him sincerely for his invaluable help, guidance and unlimited patience.

I have been lucky to work in a research group that has helped me a lot and made this period really very pleasant. My thanks to Anna Cisek, Mariola Kłusek-Gawenda, Gabriela Kubasiak, Marta Łuszczak and Rafał Maciuła for creating a stimulating atmosphere. I thank the members of the Department of Strong Interactions and Mechanisms of Nuclear Reactions (NZ21), particularly Wolfgang Schäfer, for their help and very useful suggestions and discussions. I gratefully acknowledge discussions and co-operation with Robert Kamiński, Roman Pasechnik, Rafał Staszewski and Maciej Trzebiński.

Last but not least I most heartily thank my family and friends, without whose support, patience and encouragement I could not have achieved so much.

Research was partially supported by the Polish National Science Centre on the basis of decisions DEC-2011/01/N/ST2/04116 and DEC-2013/08/T/ST2/00165.

Contents

Preface

The main goal of the Thesis is a theoretical investigation of various exclusive reactions and careful discussion of unique and novel associated phenomena from low to high energies. The processes, when we measure all particles in the final state are called exclusive processes. The mechanism of exclusive production of particles in nucleon-nucleon collisions both at low and high energies became recently a very active field of research. This study provides an unique tool to deepen our insight into the properties of strong and electromagnetic interactions. Various exclusive production mechanism involving in the final state some light unflavoured mesons, but also strange mesons and charmonium states, dimeson pairs, single photon as well as gauge dibosons and technipion resonance are considered and discussed. We analyse the interplay of different mechanisms both in two-body, three-body, and in a quite rich four-body phase space. The fully differential studies of exclusive cross sections are executed and the influence of various kinematical cuts on some distributions is investigated.

The outline of this Thesis is as follows:

In **Chapter 1** we describe the pion-pion rescattering mechanism to the $NN \to NN\pi^+\pi^-$ reactions and discuss some of their characteristics. We compare our results with the close-to-threshold experimental data. The pion-pion rescattering contribution is found there to be negligible. The predictions for future experiments with PANDA detector at High Energy Storage Ring (HESR) in GSI Darmstadt are presented. It is discussed how to cut off the dominant Roper resonance and double-Δ excitation mechanisms leading to the $p\bar{p}\pi^+\pi^-$ channel in final state. Differential distributions in momentum transfers, transverse momentum, two-pion invariant mass, relative azimuthal angle between outgoing pions, and pion rapidities are presented.

In the second part, we evaluate differential distributions for exclusive scalar $f_0(1500)$ meson (glueball candidate) production for proton-antiproton (FAIR@GSI) and proton-proton (J-PARC@Tokai) collisions. Both the QCD diffractive, the pion-pion meson exchange current (MEC) components as well as the nonperturbative central diffractive mechanism with the intermediate pionic loop are calculated. The pion-pion MEC component, which can be reliably calculated, dominates close to the threshold while the diffractive component (only an upper limit can be obtained) may take over only for larger energies. The perturbative QCD calculations for production of $f_0(1500)$ meson has no region of validity at the PANDA energy. The QCD diffractive component is calculated based on two-gluon impact factors as well as in the k_t-factorization framework of Khoze-Martin-Ryskin approach with unintegrated gluon distribution functions (UGDFs) for the proton. Rather large cross sections due to pion-pion fusion are predicted for PANDA energies, where the gluonic mechanism is shown to be negligible. The production of $f_0(1500)$ close to threshold could limit the so-called πNN form factor in the region of larger pion virtualities. Furthermore, we discuss in detail the two-pion background to the production of the $f_0(1500)$ meson. We include a new mechanism relevant at lower energies (FAIR, J-PARC) relying on the exchange of two pion. Cross section for non-resonant background is large and some cuts are needed to extract the $f_0(1500)$ signal.

In **Chapter 2** we evaluate differential distributions for the four-body $NN \to NNM\bar{M}$ ($M\bar{M} = \pi^+\pi^-$ or K^+K^-) reactions. These processes constitute an irreducible background to the three-body processes $pp \to ppR$, where R are a broad resonances, and provide a valuable tool to investigate in detail the properties of resonance states. We consider central diffractive contribution mediated by pomeron and reggeon exchanges as well as the pion-pion rescattering contribution. The first process dominates at higher energies and small pion-pion invariant masses while the second becomes important at lower energies and higher pion-pion invariant masses. The amplitudes are calculated in the Regge approach. We include absorption effects due to proton-proton interaction and meson-meson rescattering. We compare our results with measured cross sections for the FNAL at Fermilab and the ISR at CERN experiments. We make

predictions for experiments at RHIC, Tevatron and LHC energies. Two-dimensional distribution in the $(y_M, y_{\bar{M}})$ meson rapidities space is particularly interesting. For the central diffractive mechanism, the higher the incident energy the higher preference for the same-hemisphere emission of mesons. The processes considered here constitute a sizeable contribution to the total proton-proton cross section as well as to pion/kaon inclusive cross section. Furthermore, for the K^+K^- production we consider completely new mechanism of emission of kaons directly from proton lines and we find that the kaons are produced rather forward and backward but the corresponding cross section is rather small at the LHC. We discuss the relationships between the various cuts and how the cross section depends on them. We also make predictions for observable quantities such as the transverse momentum of meson and two-meson invariant mass distributions, which can directly reveal important features of the production mechanism. The soft hadronic models required to calculate the absorption effects. We present how future experiments may further test some aspects of diffractive mechanisms calculate in the Regge-based approach.

Next, we consider a measurement of exclusive production of scalar $\chi_c(0^{++})$ meson via $\chi_{c0} \to \pi^+\pi^-$ and K^+K^- decays in the proton-proton collisions at RHIC and LHC and in the proton-antiproton collisions at the Tevatron. The corresponding amplitude for exclusive central diffractive χ_{c0} ($c\bar{c}$) meson production is calculated within the k_t-factorization approach (in heavy quark approximation) and the corresponding cross section is calculated with unintegrated gluon distribution functions (UGDFs). We calculate several differential distributions for $pp(\bar{p}) \to pp(\bar{p})\chi_{c0}$ process including the absorptive corrections. Predictions for signal-to-background ratio are shown and a proposal of kinematical cuts for experimental studies is presented.

After that, we focus on the possibility of measurement of the $pp \to pp\pi^+\pi^-$ reaction, during the special low luminosity LHC runs, with the help of the ATLAS central detector for measuring pions and the ALFA stations for tagging the scattered protons. A visible cross section is estimated to be 21 μb for $\sqrt{s} = 7$ TeV. Differential distributions in pion pseudorapidities, pion and proton transverse momenta as well as $\pi^+\pi^-$ invariant mass are shown and discussed.

In **Chapter 3** the exclusive diffractive production of scalar ($f_0(980)$, $f_0(1370)$, $f_0(1500)$) and pseudoscalar (η, $\eta'(958)$) mesons in proton-proton collisions is discussed. As an interesting extension of the standard Donnachie-Landshoff pomeron, a new model of soft pomeron with an effective spin 2 exchange is discussed. A model of soft high-energy scattering is formulated in terms of effective propagators and vertices for the exchanged pomeron and reggeons. Different pomeron-pomeron-meson tensorial coupling structures are possible in general. In most cases two lowest orbital angular momentum - spin couplings are necessary to describe experimental differential distributions. For $f_0(980)$ and η production reggeon-pomeron, pomeron-reggeon, and reggeon-reggeon exchanges are included in addition, which seems to be necessary at relatively low energies. The theoretical results are compared with the WA102 experimental data in order to determine the model parameters. Correlations in azimuthal angle between outgoing protons, distributions in rapidities and transverse momenta of outgoing protons and mesons, in a special "glueball filter variable", as well as some two-dimensional distributions are presented. We discuss differences between results of the "vectorial pomeron" and "tensorial pomeron" models. We show that high-energy central production, in particular of pseudoscalar mesons, could provide crucial information on the spin structure of the soft pomeron.

Chapter 4 describes the $NN \to NNX$ processes at high energies, where X is a very forward system $X = \pi^0, \gamma, \omega$ or neutron. Because at high energies the pomeron exchange is the driving mechanism of bremsstrahlung it is logical to call these mechanisms as diffractive bremsstrahlung to distinguish from the low-energy bremsstrahlung driven by meson exchanges. For the $pp \to pp\pi^0$ process the diffractive bremsstrahlung (the Drell-Hiida-Deck–type model), photon-photon and photon-omega exchange mechanisms are included. Large cross sections of the order of mb are predicted. The corresponding differential cross sections in rapidities and transverse momenta of outgoing protons and pions as well as relative azimuthal angle between outgoing protons are calculated for RHIC and LHC energies. The hadronic bremsstrahlung con-

tributions dominate at large (forward, backward) pion rapidities. The diffractive nonresonant background contributes at small $\pi^0 p$ invariant mass and could be therefore misinterpreted as the Roper resonance. We predict strong dependence of the slope in t (squared four-momentum transfer between ingoing and outgoing proton) on the mass of the supplementary excited $\pi^0 p$ system. At high energies and midrapidities, the photon-photon contribution dominates over the diffractive components, however, the corresponding cross section is rather small. The photon-odderon and odderon-photon contributions are included in addition and first estimates (upper limits) of their contributions to rapidity and transverse momentum distribution of neutral pions are presented. We suggest a search for the odderon contribution at midrapidity and $p_{\perp,\pi^0} \simeq 0.5$ GeV at the LHC. The bremsstrahlung mechanisms discussed here contribute also to the $pp \to p(n\pi^+)$ reaction. Both channels give a sizable contribution to the low-mass single diffractive cross section and must be included in extrapolating the measured experimental single diffractive cross section.

Next, we discuss differential distributions for the $pp \to pp\omega$ reaction at RHIC, Tevatron and LHC energies. First we calculate cross section for the $\gamma p \to \omega p$ reaction from the threshold to very large energies. At low energies the pion exchange is the dominant mechanism. At large energies the experimental cross section can be well described within the k_t-factorization approach by adjusting light-quark constituent mass. We consider photon-pomeron (pomeron-photon), photon-pion (pion-photon) as well as diffractive hadronic bremsstrahlung mechanisms. The latter are included in the meson/reggeon exchange picture with parameters fixed from the known phenomenology. Absorptions effects are included and discussed. Interesting rapidity distributions are predicted. The hadronic bremsstrahlung contributions dominate at large (forward, backward) rapidities. Our predictions are ready for verification at RHIC and LHC. At small energies the photon-pomeron contribution is negligible compared to the bremsstrahlung contributions. It could be, however, easily identified at LHC energies at the ω-meson midrapidity.

For the $pp \to pp\gamma$ reaction at the LHC energy $\sqrt{s} = 14$ TeV we consider the diffractive bremsstrahlung mechanisms including effects of non point-like nature of protons. In addition, we take into account (vector meson)-pomeron, photon-pion as well as photon-pomeron exchange processes for the first time in the literature. Predictions for the total cross section and several observables related to these processes e.g. differential distributions in pseudorapidities and transverse momenta of photons or protons are shown and discussed. The integrated diffractive bremsstrahlung cross section ($E_\gamma > 100$ GeV) is only of the order of μb. We try to identify regions of the phase space where one of the mechanisms dominates. The γ-bremsstrahlung dominates at large forward/backward photon pseudorapidities, close to the pseudorapidities of scattered protons. In contrast, the photon-pomeron (pomeron-photon) mechanism dominates at midrapidities but the related cross section is rather small. In comparison the virtual-omega–rescattering mechanism contributes at smaller angles of photons (larger photon rapidities). Photons in the forward/backward region can be measured by the Zero Degree Calorimeters (ZDCs) installed in experiments at the LHC while the midrapidity photons are difficult to measure (small cross section, small photon transverse momenta). Protons could be measured by the ALFA+ATLAS detector or the TOTEM+CMS detector. The exclusivity could be checked with the help of main central detectors.

Finally, we evaluate differential distributions for the four-body $pp \to nn\pi^+\pi^+$ reaction. The amplitude for the process is calculated in the phenomenological Regge approach including many diagrams. We make predictions for possible future experiments at RHIC and LHC energies. Very large cross sections are found which is partially due to interference of a few mechanisms. Presence of several interfering mechanisms precludes extraction of the elastic $\pi^+\pi^+$ scattering cross section. Absorption effects are estimated. Differential distributions in pseudorapidity, rapidity, invariant two-pion mass, transverse-momentum and energy distributions of neutrons are presented for proton-proton collisions at $\sqrt{s} = 500$ GeV (RHIC) and $\sqrt{s}$ = 0.9, 2.36 and 7 TeV (LHC). Cross sections with experimental cuts are presented.

Chapter 5 presents results of the evaluation of diffractive mechanism of central exclusive production of W^+W^- pairs in proton-proton collisions at the LHC. We include diagrams with intermediate virtual Higgs boson as well as quark box diagrams. Several observables related to this process are calculated. Predictions for the total cross section and differential distributions in W-boson rapidity and transverse momentum as well as WW invariant mass are presented. We also show results for different polarization states of the final $W^{\pm}$ bosons. We compare the contribution of the $\gamma\gamma \to W^+W^-$ mechanism considered in the literature with the contribution of the diffractive mechanism through the $gg \to W^+W^-$ subprocess for the different observables. The phase space integrated diffractive contribution when separated is only a small fraction of fb compared to 115.4 fb of the $\gamma\gamma$-initiated contribution without absorption. The latter contribution dominates at small four-momentum transfers in the proton lines and in a broad range of W^+W^- invariant masses. This offers a possibility of efficient searches for anomalous triple-boson (γWW) and quartic-boson ($\gamma\gamma WW$) couplings and testing models beyond the Standard Model. We discuss shortly also the $pp \to pp\gamma\gamma$ process, where the box contribution is very similar to that for $gg \to W^+W^-$ reaction and compare our results with recent CDF data. Nice agreement has been achieved without additional free parameters. Several tests of the applicability of many models of unintegrated gluon distribution functions are done by direct comparison of the theoretical predictions with experimental data.

We focus also on exclusive production of neutral technipion π_T^0 in pp collisions at the LHC, i.e. on the $pp \to pp\pi_T^0$ reaction. The dependence of the cross section on parameters of recently proposed vector-like Technicolor model is studied. Characteristic features of the differential distributions are discussed. For not too large technipion masses the diphoton decay channel has the dominant branching fraction. This is also the main reason for an enhanced production of neutral technipions in $\gamma\gamma$-fusion reaction. We discuss backgrounds of the QCD and QED origin to the $pp \to pp(\pi_T^0 \to \gamma\gamma)$ process at large invariant $\gamma\gamma$ masses. We conclude that compared to inclusive case the signal-to-background ratio in the considered exclusive reaction is vary favorable which thereby could serve as a good probe for Technicolor dynamics searches at the LHC.

The Summary and Outlook close the Thesis. It also discussed possible extensions of the exclusive reactions in view of future phenomenological and experimental studies. In four Appendices we have collected some useful formulae concerning details of the calculations.

The results discussed in this thesis were published in the following papers:

[1]. A. Szczurek and P. Lebiedowicz,
Exclusive scalar $f_0(1500)$ meson production for energy ranges available at GSI Facility for Antiproton and Ion Research (GSI-FAIR) and at the Japan Proton Accelerator Research Complex (J-PARC),
Nucl. Phys. **A826** (2009) 101, arXiv:0906.0286 [nucl-th].

[2]. P. Lebiedowicz, A. Szczurek, and R. Kamiński,
Low-energy pion-pion scattering in the $pp \to pp\pi^+\pi^-$ and $p\bar{p} \to p\bar{p}\pi^+\pi^-$ reactions,
Phys. Lett. **B680** (2009) 459, arXiv:0904.3872 [nucl-th].

[3]. P. Lebiedowicz and A. Szczurek,
Exclusive $pp \to pp\pi^+\pi^-$ reaction: From the threshold to LHC,
Phys. Rev. **D81** (2010) 036003, arXiv:0912.0190 [hep-ph].

[4]. P. Lebiedowicz and A. Szczurek,
Exclusive $pp \to nn\pi^+\pi^+$ reaction at LHC and RHIC,
Phys. Rev. **D83** (2011) 076002, arXiv:1005.2309 [hep-ph].

[5]. A Cisek, P. Lebiedowicz, W. Schäfer, and A. Szczurek,
Exclusive production of ω meson in proton-proton collisions at high energies,
Phys. Rev. **D83** (2011) 114004, arXiv:1101.4874 [hep-ph].

[6]. P. Lebiedowicz, R. Pasechnik, and A. Szczurek,
Measurement of exclusive production of scalar χ_{c0} meson in proton-(anti)proton collisions via $\chi_{c0} \to \pi^+\pi^-$ decay,
Phys. Lett. **B701** (2011) 434, arXiv:1103.5642 [hep-ph].

[7]. R. Staszewski, P. Lebiedowicz, M. Trzebiński, J. Chwastowski, and A. Szczurek,
Exclusive $\pi^+\pi^-$ Production at the LHC with Forward Proton Tagging,
Acta Phys. Polon. **B42** (2011) 1861, arXiv:1104.3568 [hep-ex].

[8]. P. Lebiedowicz and A. Szczurek,
$pp \to ppK^+K^-$ reaction at high energies,
Phys. Rev. **D85** (2012) 014026, arXiv:1110.4787 [hep-ph].

[9]. P. Lebiedowicz and A. Szczurek,
Exclusive $pp \to pp\pi^0$ reaction at high energies,
Phys. Rev. **D87** (2013) 074037, arXiv:1303.2882 [hep-ph].

[10]. P. Lebiedowicz and A. Szczurek,
Exclusive diffractive photon bremsstrahlung at the LHC,
Phys. Rev. **D87** (2013) 114013, arXiv:1302.4346 [hep-ph].

[11]. P. Lebiedowicz, R. Pasechnik, and A. Szczurek,
QCD diffractive mechanism of exclusive W^+W^- pair production at high energies,
Nucl. Phys. **B867** (2013) 61, arXiv:1203.1832 [hep-ph].

[12]. P. Lebiedowicz, R. Pasechnik, and A. Szczurek,
Search for technipions in exclusive production of diphotons with large invariant masses at the LHC,
Nucl. Phys. **B881** (2014) 288, arXiv:1309.7300 [hep-ph].

[13]. P. Lebiedowicz, O. Nachtmann, and A. Szczurek,
Exclusive central diffractive production of scalar and pseudoscalar mesons; tensorial vs. vectorial pomeron,
Annals Phys. **344** (2014) 301, arXiv:1309.3913 [hep-ph].

They were also presented during international conferences including [14–22]:

1. **P. Lebiedowicz** and A. Szczurek,
Exclusive scalar $f_0(1500)$ meson production,
PoS (EPS-HEP 2009) **457**, arXiv:1206.2065 [hep-ph].
2009 Europhysics Conference on High Energy Physics (EPS-HEP 2009), 16-22 Jul 2009, Cracow, Poland.
2. **P. Lebiedowicz** and A. Szczurek,
Exclusive production of $\pi^+\pi^-$ pairs in proton-proton and proton-antiproton collisions,
Int. J. Mod. Phys. **A26** (2011) 748, arXiv:1008.4469 [hep-ph].
11th International Workshop on Meson Production, Properties and Interaction (MESON 10), 10-15 Jun 2010, Cracow, Poland.
3. **P. Lebiedowicz**, R. Pasechnik, and A. Szczurek,
Exclusive production of $\chi_c(0^+)$ meson and its measurement in the $\pi^+\pi^-$ channel,
Nucl. Phys. **B219** (Proc. Suppl.) (2011) 284, arXiv:1108.2522 [hep-ph].
5th Joint International Hadron Structure'11 Conference (HS 11), 27 Jun - 1 Jul 2011, Tatranská Ŝtrba, Slovakia.
4. **P. Lebiedowicz**,
Exclusive open strangeness production in the $pp \to ppK^+K^-$ reaction at high energies and a measurement of scalar χ_{c0} meson,
Acta Phys. Polon. **B5** - Proceedings Supplement (2012) 393, arXiv:1112.1022 [hep-ph].
International Conference on Strangeness in Quark Matter (SQM 2011), 18-24 Sep 2011, Cracow, Poland.
5. **P. Lebiedowicz**, R. Pasechnik, and A. Szczurek,
Diffractive pQCD mechanism of exclusive production of W^+W^- pairs in proton-proton collisions,
PoS (QNP 2012) **143**, arXiv:1206.2754 [hep-ph].
6th International Conference on Quarks and Nuclear Physics (QNP 2012), 16-20 Apr 2012, Palaiseau, France.
6. **P. Lebiedowicz** and A. Szczurek,
Exclusive meson pair production in proton-proton collisions,
EPJ Web Conf. **37** (2012) 06001, arXiv:1208.4288 [hep-ph].
12th International Workshop on Meson Production, Properties and Interaction (MESON 12), 31 May - 5 Jun 2012, Cracow, Poland.
7. **P. Lebiedowicz** and A. Szczurek,
Exclusive production of meson pairs and resonances in proton-proton collisions,
AIP Conf. Proc. **1523** (2012) 132, arXiv:1212.0166 [hep-ph].
7th International Workshop on Diffraction in High Energy Physics (Diffraction 2012), 10-15 Sep 2012, Puerto del Carmen, Lanzarote, Canary Islands, Spain.
8. **P. Lebiedowicz** and A. Szczurek,
Diffractive mechanisms in $pp \to pp\pi^0$ reaction at high energies,
PoS (DIS 2013) **305**, arXiv:1306.6823 [hep-ph].
21st International Workshop on Deep-Inelastic Scattering and Related Subjects (DIS 2013), 22-26 Apr 2013, Marseilles, France.
9. P. Lebiedowicz and **A. Szczurek**,
Exclusive diffractive photon bremsstrahlung at high energies,
PoS (DIS 2013) **086**, arXiv:1306.6819 [hep-ph].
21st International Workshop on Deep-Inelastic Scattering and Related Subjects (DIS 2013), 22-26 Apr 2013, Marseilles, France.

Chapter 1

Exclusive Production of Meson Pairs at Low Energies

1.1 The two-pion rescattering in $pp \to pp\pi^+\pi^-$ and $p\bar{p} \to p\bar{p}\pi^+\pi^-$ reactions

The light mesons production in nucleon-nucleon collisions is one of the sources of information on the nucleon-nucleon interaction and the resonance properties. The exclusive $NN \to NN\pi^+\pi^-$ reaction, which is one of the reactions with four charged particles in the final state, can be easily measured. The Roper resonance $N^*(1440)$ and $\Delta(1232)$ are the first excited states of the nucleon. They play an important role for pion production at nucleon-nucleon c.m. energies near threshold value $s_{thr} = (2m_p + 2m_\pi)^2$. The two-pion production mechanism close to threshold is dominated by the excitation of one of the nucleons into the Roper resonance $N^*(1440)$ and its subsequent decay into nucleon and two pions $N^* \to p(\pi\pi)_{l=I=0}$. At intermediate energies the other decay channel $N^* \to \Delta\pi$ is the main contribution. At higher energies the simultaneous $\Delta(1232)$ excitation of both nucleons (produced via π, ρ t-channel exchanges) constitutes the dominant reaction mechanism [23–26]. This is understandable, because more energy is needed to excite both Δ than is needed for one $N^*(1440)$. It is the aim of this Section to evaluate the pion-pion rescattering contribution shown in Fig.1.1 for the measured close-to-threshold region of the $pp \to pp\pi^+\pi^-$ reaction as well as to make predictions for the future experiments with the PANDA detector at HESR in GSI Darmstadt [27] for the $p\bar{p} \to p\bar{p}\pi^+\pi^-$ reaction.

On the other hand a significant progress in studying pion-pion scattering at low-energy has been recently achieved due to works based on dispersive analyses of experimental data [28–33]. These works, led to precise determination of the $\pi\pi$ scattering amplitudes consistent with analyticity, unitarity and crossing symmetry. Strong theoretical constraints from forward dispersion relations and sum rules allowed to test several, sometimes conflicting sets of data [32]. The twice subtracted dispersion relations (Roy's equations) used in [28, 29] allowed to calculate very precisely sigma pole position and S-wave scattering lengths a_0 and a_2. In other works, also using the Roy's equations, [30–33] these results were even improved. In Ref. [31] the sigma position was determined from first principles with unprecedented precision. Recent works on once subtracted dispersion relations give results with similar precision [34, 35]. Application of Roy's equations in another dispersive analysis of experimental data allowed to eliminate the long standing "up-down" ambiguity below 1 GeV in $S0$ wave [1] [36]. The simple and model independent amplitudes of the $S0$, P, $S2$, $D0$, $D2$, F and G waves presented in series of works [32–35] seem to be efficient and easy to use in analyses of $\pi\pi$ interactions. Amplitudes presented in [33] have been applied in this analysis to parametrise the final state interactions $\pi^0\pi^0 \to \pi^+\pi^-$; see also [37], where the description of pion-pion scattering data have been improved.

[1] Here we use following notation to denote the $\pi\pi$ partial wave by $lI = S0, P, S2, D0, D2$, etc., where l is angular momentum between pions and I is the total isospin of the pion pair.

The study of the $\pi\pi$ system also bears on current issues in the spectroscopy of conventional $q\bar{q}$ mesons and non-$q\bar{q}$ mesons such as glueballs or mesonic molecules. In particular, the isoscalar scalar and tensor sectors have more states than can be accommodated within the conventional quark model. A recent review of light meson spectroscopy [38–40] includes a summary of the current both theoretical and experimental situation in these sectors. Non-$q\bar{q}$ candidates include the poorly understood $f_0(980)$ and the scalar glueball candidates $f_0(1500)$ and $f_0(1710)$, all of which couple to the $\pi\pi$ system. Information about the masses, widths, and decay modes of these states, along with knowledge of their production mechanisms, as revealed by their $|t|$ dependences, will help in unraveling their substructure [41]. It is worth to mention that the $\pi\pi$ partial wave analysis have been obtained e.g. from the charge exchange $\pi^- p \to \pi^0\pi^0 n$ reaction at incident π^- momentum $P_{lab} = 18.3$ GeV/c by the E853 experiment at BNL [42] and at $P_{lab} = 100$ GeV/c ($\sqrt{s} = 13.729$ GeV) by the GAMS Collaboration at CERN [43]. A bump-dip structure of the S-wave at low momentum transfer is shown in Ref. [43]. The combined analysis in the $\pi^+\pi^-$, $\pi^0\pi^0$, K^+K^-, $\eta\eta$, $\eta\eta'$, etc. systems can be used to provide information on how cross sections of produced states and relative ratios of partial wave contributions depend on center-of-mass energy. In Ref. [44] the authors stressed that the number of observables provided by such experiment is much smaller then the number of real parameters needed to describe the partial waves. Consequently, a special physical assumptions (generally connected with ignoring of the role of nucleon spin) were made in most studies of the $\pi\pi$ systems. The knowledge of the $\pi\pi \to \pi\pi$ reaction can almost directly be used in our $pp \to pp\pi\pi$ reaction ($2 \to 4$ reaction [2]).

1.1.1 The two-pion rescattering amplitude

Before we go to the four-body pion-pion rescattering mechanism shown in Fig.1.1 let us focus first on the $\pi^0\pi^0 \to \pi^+\pi^-$ scattering. This reaction contains both isospin $I = 0$ and $I = 2$ states. We illustrate how the $\pi\pi$ isospin amplitude for a given angular momentum l arise. For the scattering process $1 + 2 \to 3 + 4$ both the initial and final states can be expressed in terms of isospin states $|I, I_z\rangle$ and the scattering amplitude may be decomposed as

$$\left\langle \pi^+\pi^- \left| \mathcal{A}^l \right| \pi^0\pi^0 \right\rangle = \sum_I \langle I_3, I_4, I_{3z}, I_{4z} \,|\, I, I_z\rangle^* \, \langle I_1, I_2, I_{1z}, I_{2z} \,|\, I, I_z\rangle \, \mathcal{A}^{l,I} \,, \tag{1.1}$$

where $\langle I_1, I_2, I_{1z}, I_{2z} \,|\, I, I_z\rangle$, $\langle I_3, I_4, I_{3z}, I_{4z} \,|\, I, I_z\rangle$ are the isospin Clebsch-Gordan coefficients and $\mathcal{A}^{l,I}$ is independent of I_z. In terms of isospin states we can write

$$\begin{aligned} \left|\pi^0\pi^0\right\rangle &= -\frac{1}{\sqrt{3}} \left|0,0\right\rangle + \sqrt{\frac{2}{3}} \left|2,0\right\rangle \,, \\ \left|\pi^+\pi^-\right\rangle &= \frac{1}{\sqrt{3}} \left|0,0\right\rangle + \frac{1}{\sqrt{2}} \left|1,0\right\rangle + \frac{1}{\sqrt{6}} \left|2,0\right\rangle \,, \end{aligned} \tag{1.2}$$

so we have

$$\left\langle \pi^+\pi^- \left| \mathcal{A}^l \right| \pi^0\pi^0 \right\rangle = \mathcal{A}^l(\pi^0\pi^0 \leftrightarrow \pi^+\pi^-) = -\frac{1}{3}\mathcal{A}^{l,I=0} + \frac{1}{3}\mathcal{A}^{l,I=2} \,. \tag{1.3}$$

Let us notice that the isospin $I = 1$ amplitude will not contribute to the $\pi^0\pi^0 \to \pi^+\pi^-$ reaction.

The on-shell amplitude can be expanded into partial-wave amplitudes $f_l^I(s)$ with angular momentum l and isospin I:

$$\mathcal{M}(s,z) = 16\pi \sum_I \sum_l (2l+1) P_l(z) f_l^I(s) \,, \tag{1.4}$$

where the scattering angle $cos\theta = z$ and $P_l(z)$ is a Legendre polynomial containing the angular dependence. The differential cross-section for spinless particles is

$$\frac{d\sigma}{dz} = \frac{1}{32\pi s} |\mathcal{M}(s,z)|^2 \,. \tag{1.5}$$

[2] $2 \to 4$ reaction denotes a type of the reaction with two initial and four final particles.

In our calculation $f_l^I(s)$ can be parametrised in terms of the pion-pion phase shifts $\delta_l^I(s)$ and the inelasticities $\eta_l^I(s)$ taken from [33]

$$f_l^I(s) = \sqrt{\frac{s}{s-4m_\pi^2}}\frac{\eta_l^I(s)e^{2i\delta_l^I(s)}-1}{2i}\,, \tag{1.6}$$

where the inelasticity (absorption) coefficients obey $0 \leqslant \eta_l^I(s) \leqslant 1$. Clearly, $\eta_l^I(s) = 1$ for elastic scattering. Below the inelastic threshold (when only the elastic channel is open) the scattering amplitude is completely specified by

$$f_l^I(s) = \sqrt{\frac{s}{s-4m_\pi^2}}e^{i\delta_l^I(s)}\sin\delta_l^I(s) = \sqrt{\frac{s}{s-4m_\pi^2}}\frac{1}{\cot\delta_l^I(s)-i}\,. \tag{1.7}$$

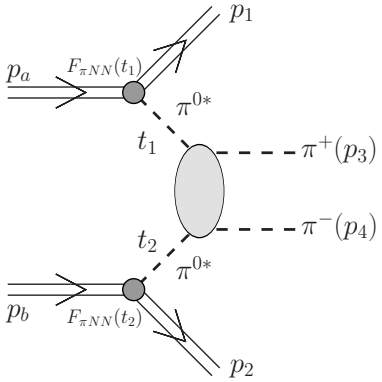

Figure 1.1: The pion-pion rescattering mechanisms of exclusive production of π^+ and π^- in proton-proton and proton-antiproton collisions. Some kinematical variables are shown explicitly. The stars attached to π^0 mesons denote the fact that they are off-mass-shell.

It is straightforward to evaluate the pion-pion rescattering mechanism shown in Fig.1.1. If we assume the $i\gamma_5$ type coupling of the pion to the nucleon then the Born amplitude according to the Feynman rules can be written

$$\begin{aligned}\mathcal{M}^{2\to4}_{\lambda_a\lambda_b\to\lambda_1\lambda_2\pi\pi} &= \bar{u}(p_1,\lambda_1)i\gamma_5 u(p_a,\lambda_a)\\ &\times g_{\pi NN}\sqrt{T_k}\,S_\pi(t_1)\,F_{\pi NN}(t_1)\;\mathcal{M}^{2\to2}_{\pi^*\pi^*\to\pi\pi}\;g_{\pi NN}\sqrt{T_k}\,S_\pi(t_2)\,F_{\pi NN}(t_2)\\ &\times\bar{u}(p_2,\lambda_2)i\gamma_5 u(p_b,\lambda_b)\,,\end{aligned} \tag{1.8}$$

where $u(p,\lambda)$, $\bar{u}(p',\lambda') = u^\dagger(p',\lambda')\gamma^0$ are the Dirac spinors of the incident and outgoing protons with the four-momentum p and the helicities λ; normalized as $\bar{u}(p')u(p) = 2m_p$. The factor $g_{\pi NN}$ is the familiar pion nucleon coupling constant and is relatively well known [45] ($g^2_{\pi NN}/(4\pi) = 13.5-14.6$). In our calculations the coupling constants was fixed to $g^2_{\pi NN}/4\pi = 13.5$. The isospin factor T_k equals 1 for the $\pi^0\pi^0$ fusion and equals 2 for the $\pi^+\pi^-$ fusion. In the case of proton-antiproton collisions both $N\bar{N}\pi^+\pi^-$ and $N\bar{N}\pi^0\pi^0$ final state channels are possible (where N denotes p or n), i.e. both $\pi^0\pi^0$ and $\pi^+\pi^-$ exchanges are allowed. In the case of $\pi^+\pi^-$ scattering, isospin 0 and 1 are allowed in the s-channel, so for example it contains the ρ, f_0 and f_2 resonances, but in $\pi^0\pi^0$ scattering the ρ meson is excluded. The four-momentum transfers along the pion line defined in Fig.1.1 are $t_{1,2} = q^2_{1,2} = (p_{a,b} - p_{1,2})^2$. In the following for brevity we shall use notation $t_{1,2}$ which means t_1 or t_2. The propagator of the off-shell pion is

$$S_\pi(t_{1,2}) = \frac{i}{t_{1,2}-m_\pi^2}\,. \tag{1.9}$$

The off-shell amplitude for the subsystem $\mathcal{M}^{2\to2}_{\pi^*\pi^*\to\pi\pi}$ is discussed below (1.12).

Explicitly, we obtain the $2 \to 4$ amplitude squared averaged over initial and summed over final spin polarization of nucleons as

$$\begin{aligned}
\overline{|\mathcal{M}|^2} &= (E_a + m_p)\,(E_1 + m_p)\left(\frac{\mathbf{p}_a^2}{(E_a+m_p)^2} + \frac{\mathbf{p}_1^2}{(E_1+m_p)^2} - \frac{2\mathbf{p}_a\cdot\mathbf{p}_1}{(E_a+m_p)(E_1+m_p)}\right) \\
&\times \frac{g^2_{\pi NN}T_k}{(t_1-m_\pi^2)^2}F^2_{\pi NN}(t_1)\,|\mathcal{M}_{\pi^{0*}\pi^{0*}\to\pi^+\pi^-}(s_{34},\cos\theta^*,t_1,t_2)|^2\,\frac{g^2_{\pi NN}T_k}{(t_2-m_\pi^2)^2}F^2_{\pi NN}(t_2) \\
&\times (E_b + m_p)\,(E_2 + m_p)\left(\frac{\mathbf{p}_b^2}{(E_2+m_p)^2} + \frac{\mathbf{p}_2^2}{(E_2+m_p)^2} - \frac{2\mathbf{p}_b\cdot\mathbf{p}_2}{(E_b+m_p)(E_2+m_p)}\right),
\end{aligned} \tag{1.10}$$

where m_π and m_p is the mass of the nucleon and the pion, respectively; E_a, E_b and E_1, E_2 are the energies of initial and outgoing nucleons, $\mathbf{p}_a, \mathbf{p}_b$ and $\mathbf{p}_1, \mathbf{p}_2$ are the corresponding three-momenta.

In the case of central production of pion pairs not far from the threshold region rather large transferred four-momenta squared t_1 and t_2 are involved and one has to include non-point-like and off-shellness nature of the particles involved in corresponding vertices. This is incorporated via the $F_{\pi NN}(t_1)$ or $F_{\pi NN}(t_2)$ vertex form factors. In the meson exchange approach [46] they are parametrised in the monopole form as

$$F_{\pi NN}(t) = \frac{\Lambda^2 - m_\pi^2}{\Lambda^2 - t} \tag{1.11}$$

normalised to 1 at the on-shell point $F_{\pi NN}(m_\pi^2)$. Typical values of the form factor parameters are $\Lambda = 1.2 - 1.4\,\mathrm{GeV}$ [46,47], however the Gottfried Sum Rule violation prefers smaller $\Lambda \approx 0.8\,\mathrm{GeV}$ [48–50]. We shall discuss how the uncertainties of the form factors influence our final results.

The amplitude of the subprocess $\pi^{0*}\pi^{0*} \to \pi^+\pi^-$ with virtual initial pions is written in terms of the amplitude for real initial pions and the correction factors as:

$$\mathcal{M}_{\pi^{0*}\pi^{0*}\to\pi^+\pi^-}(s_{34},\cos\theta^*,t_1,t_2) = \mathcal{M}_{\pi^0\pi^0\to\pi^+\pi^-}(s_{34},\cos\theta^*)F_{\pi^{0*}}(t_1)F_{\pi^{0*}}(t_2)\,, \tag{1.12}$$

where we use exponential form factors of the type

$$F_{\pi^{0*}}(t) = \exp\left(\frac{t-m_\pi^2}{\Lambda_{off}^2}\right), \tag{1.13}$$

i.e. normalized to unity on the pion-mass-shell $F_{\pi^{0*}}(m_\pi^2) = 1$. In general, the parameter Λ_{off} is not known but in principle could be fitted to the experimental data providing that our mechanism is the dominant mechanism which can be true only in a limited corner of the phase space. From our general experience in hadronic physics we expect Λ_{off} to be of the order 1 GeV.

The $\cos\theta^*$ in Eq. (1.12) requires a separate discussion. In the on-shell and spinless particles case the $\cos\theta$ can be expressed in terms of the two-body Mandelstam invariants $\hat{t}$ and $\hat{u}$ in two equivalent ways:

$$\cos\theta_{\hat{t}} = 1 + \frac{2\hat{t}}{s_{34} - 4m_\pi^2}, \qquad \cos\theta_{\hat{u}} = -1 - \frac{2\hat{u}}{s_{34} - 4m_\pi^2}\,. \tag{1.14}$$

This can be generalized to the case of off-shell initial pions as:

$$\cos\theta^*_{\hat{t}} = 1 + \frac{2\hat{t}}{s_{34} - m_\pi^2 - m_\pi^2 - t_1 - t_2}, \qquad \cos\theta^*_{\hat{u}} = -1 - \frac{2\hat{u}}{s_{34} - m_\pi^2 - m_\pi^2 - t_1 - t_2}\,. \tag{1.15}$$

In our case of the $2 \to 4$ reaction we have to deal with off-shell initial pions and an analytical continuation of formula (1.15) is required. In the following we use the most straightforward prescription:

$$\cos\theta^* = \frac{1}{2}(\cos\theta^*_{\hat{t}} + \cos\theta^*_{\hat{u}}) = \frac{\hat{t} - \hat{u}}{s_{34} - m_\pi^2 - m_\pi^2 - t_1 - t_2}\,. \tag{1.16}$$

The formula above reproduces the on-shell formula (1.14) when $t_1 \to m_\pi^2$ and $t_2 \to m_\pi^2$, is symmetric with respect to $\hat{t}$ and $\hat{u}$ and fulfils the requirement $-1 < \cos\theta^* < 1$.

1.1.2 Reactions via Roper resonance excitation and its decay

Close to the two-pion production threshold the dominant mechanism for the reaction $pp \to pp\pi^+\pi^-$ is the Roper resonance excitation and its subsequent three-body decay [23, 51]. As was shown in Ref. [25] below $T_p = 1$ GeV the $N^*(1440) \to N\sigma$ term is the largest while the $N^*(1440) \to \Delta\pi$ term is the next in size. Of these two terms the σ-meson exchange gives much bigger contribution than the π-meson exchange and this shows the importance of the isoscalar excitation of the Roper resonance. This mechanism constitutes an "unwanted background" to our pion-pion rescattering. At low energy the sigma and pion exchanges are the dominant mechanisms of Roper resonance excitation (see [52]). Here we show how to approximately estimate the phase-space integrated contribution of the mechanism shown in Fig.1.2 not very close to the threshold [3].

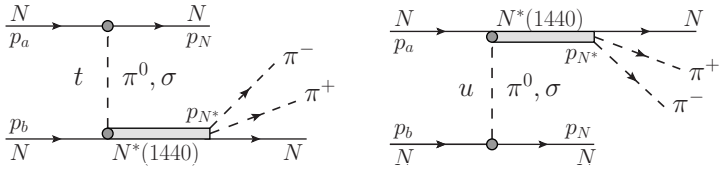

Figure 1.2: The dominant mechanisms of Roper resonance production via π, σ-meson exchanges at low energy proton-proton scattering.

The amplitudes for the Roper resonance $N^*(1440)$ excitation via π, σ-meson exchanges can be written as

$$\begin{aligned}
\mathcal{M}^{\sigma-exch.}_{\lambda_a\lambda_b\to\lambda_N\lambda_{N^*}}(k^2) &= g_{\sigma NN}F_{\sigma NN}(k^2)\,\bar{u}(p_N,\lambda_N)u(p_a,\lambda_a)\,\frac{i}{k^2-m_\sigma^2} \\
&\quad\times g_{\sigma NN^*}F_{\sigma NN^*}(k^2)\,\bar{u}(p_{N^*},\lambda_{N^*})u(p_b,\lambda_b)\,, \qquad (1.17)\\
\mathcal{M}^{\pi-exch.}_{\lambda_a\lambda_b\to\lambda_N\lambda_{N^*}}(k^2) &= g_{\pi NN}F_{\pi NN}(k^2)\,\bar{u}(p_N,\lambda_N)i\gamma_5 u(p_a,\lambda_a)\,\frac{i}{k^2-m_\pi^2} \\
&\quad\times g_{\pi NN^*}F_{\pi NN^*}(k^2)\,\bar{u}(p_{N^*},\lambda_{N^*})i\gamma_5 u(p_b,\lambda_b)\,, \qquad (1.18)
\end{aligned}$$

where $k^2 = t$ or u are the four-momentum transfers and m_π and m_σ are the mass of the pion and sigma mesons; $u(p_a,\lambda_a)$, $u(p_b,\lambda_b)$, $u(p_N,\lambda_N)$, $u(p_{N^*},\lambda_{N^*})$ are the spinors of the proton and Roper resonance.

In our calculations the coupling constants are taken as $g^2_{\pi NN}/(4\pi) = 13.5$ [45], $g^2_{\sigma NN}/(4\pi) = 5.69$ [46], $g^2_{\pi NN^*}/(4\pi) = 2$ and $g^2_{\sigma NN^*}/(4\pi) = 2$. Because numerically the σ-exchange is the dominant mechanism and the π-exchange is only a small correction [4], in practice the latter can be neglected. The coupling constant $g_{\sigma NN^*}$ is in fact an unknown parameter which in principle should be determined from the experimental data. Different values have been used in the literature [46, 53]. Our number is an average value of those found in the literature.

We parametrise the form factors $F_{MNN}(k^2)$ (where M denotes π or σ) either in the monopole form with cut-off parameter Λ_M as traditionally used for low energy processes:

$$F_{MNN}(k^2) = \frac{\Lambda_M^2 - m_M^2}{\Lambda_M^2 - k^2}\,, \qquad (1.19)$$

or in the exponential form often used at high energies with cut-off parameter Λ_E:

$$F_{MNN}(k^2) = \exp\left(\frac{k^2 - m_M^2}{\Lambda_E^2}\right)\,. \qquad (1.20)$$

[3] Very close to the threshold the reaction must be treated as genuine four-body reaction due to the presence of nucleon-nucleon interaction effects that should be properly taken into account, especially the NN final state interactions (FSI), which could be strong close to threshold (see [23, 24]).

[4] The difference is due to scalar coupling for σ-meson exchange or pseudoscalar $i\gamma_5$ coupling for pion exchange.

The angular distribution for single Roper resonance excitation can be calculated from the amplitude above as

$$\frac{d\sigma_{pp\to pN^*(1440)}}{d\Omega} = \frac{1}{64\pi^2 s}\left(\frac{q_f}{q_i}\right)\frac{1}{4}\sum_{\lambda_a\lambda_b\lambda_N\lambda_{N^*}} |\mathcal{M}^{(t)}_{\lambda_a\lambda_b\to\lambda_N\lambda_{N^*}}(z) - \mathcal{M}^{(u)}_{\lambda_a\lambda_b\to\lambda_N\lambda_{N^*}}(z)|^2 , \qquad (1.21)$$

where s is a square of the proton-proton center-of-mass energy; q_i and q_f are center-of-mass momenta in the initial pp or the final pN^* systems, respectively and $z = \cos\theta$, where θ is the center-of-mass angle between the outgoing and initial nucleon. The factor $\frac{1}{4}$ and $\sum_{\lambda_a\lambda_b\lambda_N\lambda_{N^*}}$ emerge for the simple reason that the polarization of initial and final particles is not considered. In general, one should calculate the cross section for $2 \to 4$ reaction based on diagrams shown in Fig. 1.2 with the Roper resonance in the intermediate state (in general off-shell particle). However, for sufficiently high energies the total cross section for the $pp\pi^+\pi^-$ final state can be written approximately as a cross section for the Roper resonance excitation and a probability for the $N^*(1440) \to p\pi^+\pi^-$ decay (on-shell approximation):

$$\sigma_{pp\to pp\pi^+\pi^-}(\sqrt{s}) \approx \sigma_{pp\to pN^*}(\sqrt{s})\,\mathcal{BR}(N^*(1440) \to p\pi^+\pi^-)\,. \qquad (1.22)$$

This formula will be used to calculate the total cross section for the Roper resonance mechanism to show as a reference for the discussed above two-pion rescattering contribution. The branching ratio into the $p\pi^+\pi^-$ channel is not very well known and the mechanism of the Roper resonance decay can be complicated. Particle Data Book contains only branching fraction for all $N\pi\pi$ states. Our decay channel ($p\pi^+\pi^-$) is only one out of three possible ($p\pi^0\pi^0$, $p\pi^+\pi^-$, $n\pi^+\pi^0$). We take $\mathcal{BR}(N^*(1440) \to p\pi^+\pi^-) = 0.1$.

In principle, all processes (pion rescattering, Roper resonance production and decay, etc.) add coherently and can interfere. At low energy, where the phase space is very limited the interference seems unavoidable. Some distance from the threshold (of our main interest) they may occupy different regions of the phase space. This automatically means small interference effects. In our preliminary calculation we have estimated the Roper resonance contribution in a simplified way (in terms of the two-body reaction amplitude and a probability of the 3-body decay). In order to address numerically the interference effects with pion rescattering the Roper resonance must be treated as a genuine four-body processes. This requires a modelling of the 3-body Roper resonance decay (not necessarily simple as different sequential processes are possible). To avoid the rather complicated problem of the interference we proposed instead imposing extra kinematical cuts which is possible at sufficiently large energies. In the next section we shall show our predictions for several differential distributions in different variables.

1.2 Results

Before we go to our four-body reaction let us stay for a moment with the $\pi^0\pi^0 \to \pi^+\pi^-$ on-shell scattering. In Fig.1.3 we show the total (angle-integrated) cross section for the $\pi^0\pi^0 \to \pi^+\pi^-$ process which constitutes the subprocess in the $NN \to NN\pi^+\pi^-$ reactions. Here the partial wave expansion (1.4) with δ_l^I and η_l^I parametrisations from Ref. [33] were used. In the present work we have limited to the pion-pion c.m. energies $W_{\pi\pi} < 1.45$ GeV. We show also individual contributions of different partial waves $(l, I) = (0, 0)$, $(0, 2)$, $(2, 0)$ and $(2, 2)$. Because of identity of particles in the initial state only partial waves with even l contribute. The sum of the individual contributions is not equal to the cross section calculated with the sum of the partial wave amplitudes because of relatively strong interference effects. One can see characteristic bumps related to the famous scalar-isoscalar σ-meson at $W_{\pi\pi} \approx 0.5 - 0.6$ GeV and the tensor-isoscalar $f_2(1270)$. The dip at $W_{\pi\pi} = 980$ MeV is due to interference of the σ meson with another scalar-isoscalar narrow $f_0(980)$ meson and a broad background. Generally the contributions of partial waves with $I = 2$ are much smaller than those for $I = 0$.

In Fig.1.4 we present angular distributions $d\sigma/dz$, $z = \cos\theta$, at the pion-pion collision energies $W_{\pi\pi} = 0.6$, 1, and 1.275 GeV. As explained in the figure caption we show results for the

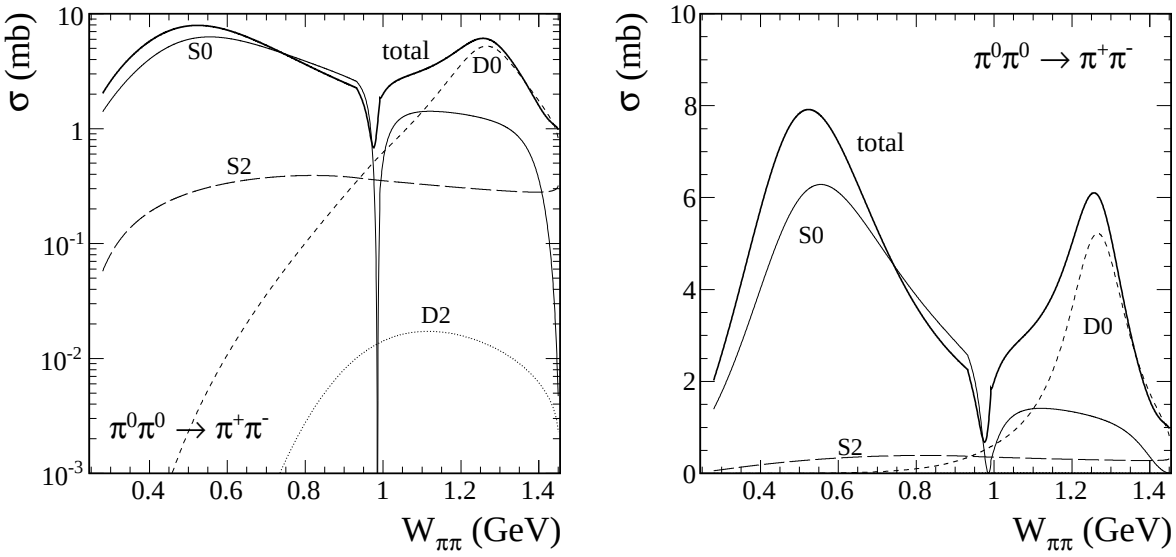

Figure 1.3: The angle-integrated cross section for the $\pi^0\pi^0 \to \pi^+\pi^-$ reaction in logarithmic (left panel) and linear (right panel) scale as a function of pion-pion c.m. energy. The thick solid line represents the coherent sum of all partial waves. The contributions for individual partial waves $S0$, $S2$, $D0$ and $D2$ are shown for comparison.

coherent sum of all partial waves as well as the individual contributions. By comparing panels at different $W_{\pi\pi}$ we infer that the interference effects are rather large.

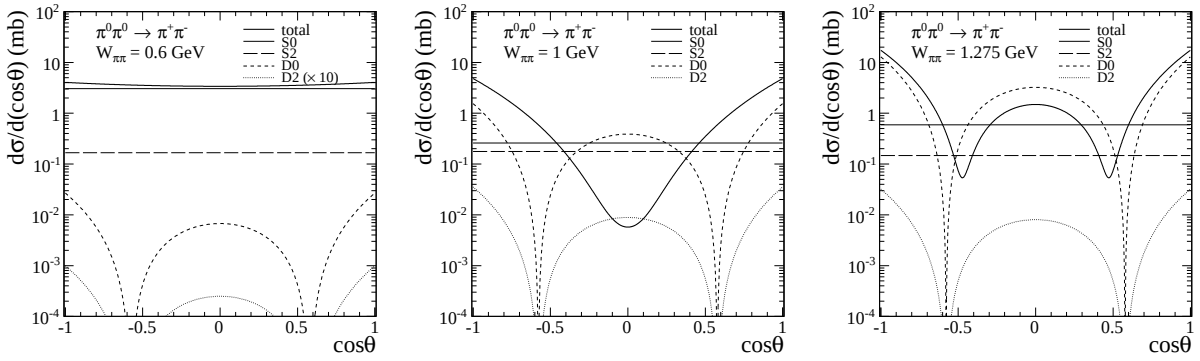

Figure 1.4: Differential cross section for the process $\pi^0\pi^0 \to \pi^+\pi^-$. The thick solid line represents the coherent sum of all partial waves. The individual contributions to the cross section for partial waves $S0$, $S2$, $D0$ and $D2$ are shown for comparison.

In Fig. 1.5 we show the proton energy excitation function of the integral cross section for the $pp \to pp\pi^+\pi^-$ reaction. The differential cross sections for the $2 \to 4$ reaction are calculated using the general formula given by Eq. (A.32), see Appendix A. The beam energy $T_p = 1.4$ GeV corresponds to a center-of-mass energy of $\sqrt{s} = 2.48$ GeV. We compare our results with the experimental data for the $pp \to pp\pi^+\pi^-$ reaction (from Refs. [54–62]). and for the $p\bar{p} \to p\bar{p}\pi^+\pi^-$ one (only data from the JETSET (PS202) experiment at LEAR [63]). We present previous data (open symbols) with low statistics coming mainly from bubble-chamber measurements on hydrogen or on deuterium from Refs. [54,56,57] as well as one datum point from an inclusive spectrometer measurement at 800 MeV [55]. The newer data taken from Refs. [58–63] (full symbols) are much closer to the threshold of the reaction, where the final state interactions between protons (FSI) may be important [5], and are an order of magnitude smaller. We show how the uncertainties of

[5]In Refs. [23, 24] the FSI is found to cause a strong enhancement of the cross section (up to a factor 10 close to

the form factor parameters Λ affect our final results. For the pion-pion rescattering we modify the cut-off parameter Λ in Eq. (1.11) ($\Lambda \in (0.8, 1.4)$ GeV) and the cut-off parameter Λ_{off} in Eq. (1.13) ($\Lambda_{off} \in (0.5, 2)$ GeV). The thick solid line show theoretical predictions from the model calculations with $\Lambda = 0.8$ GeV and $\Lambda_{off} = 1$ GeV. We see that at low energies the pion-pion rescattering contribution gives a negligible contribution to the cross section.

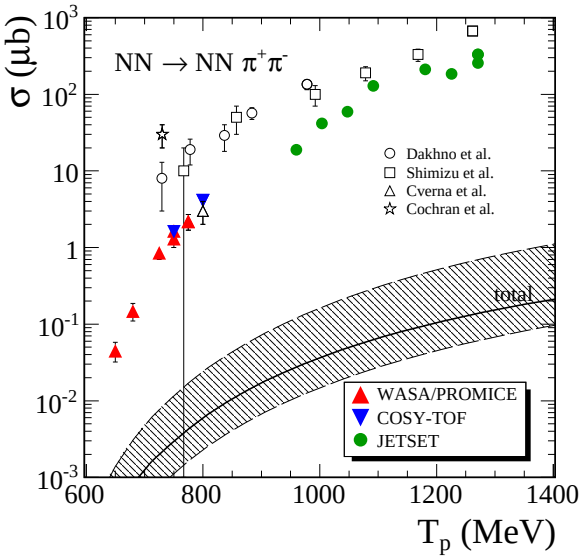

Figure 1.5: The phase-space integrated cross section for the $pp \to pp\pi^+\pi^-$ and $p\bar{p} \to p\bar{p}\pi^+\pi^-$ reactions as a function of the incoming proton kinetic energy in the laboratory frame T_p together with the experimental data from Refs. [54–63]. The thick solid line corresponds to the pion-pion rescattering contribution as explained in the text. The uncertainties band is also shown. In all cases a coherent sum of all partial waves is taken.

As discussed in Section 1.1.1, the two-pion rescattering amplitude used for the $\pi^0\pi^0 \to \pi^+\pi^-$ reaction can, after a small "correction" for the virtualities of both initial π^0's, be used for the four-body process of our main interest. In Fig.1.6 (left panel) we show the total cross section (integrated over the whole phase space with the restriction $M_{\pi\pi} < 1.45$ GeV) for the four-body reaction as a function of the overall center-of-mass energy $\sqrt{s}$. We show the coherent sum of partial waves for different angular momentum (l) and isospin (I) as well as individual contributions. The maximum of the cross section occurs at $\sqrt{s} \approx 5$ GeV, i.e. at the highest energy planned for the FAIR HESR. There, the $S0$ $(l, I) = (0, 0)$ partial wave has the dominant contribution.

In the right panel of Fig. 1.6 we compare the pion-pion rescattering contribution and the contribution of Roper resonance excitation through σ-meson exchange. In both cases we have estimated the uncertainties of the contributions. For the pion-pion rescattering we modify Λ in Eq.(1.11) ($\Lambda \in (0.8, 1.4)$ GeV) and Λ_{off} in Eq.(1.13) ($\Lambda_{off} \in (0.5, 2)$ GeV). The bottom dashed line was obtained with $\Lambda = 0.8$ GeV and $\Lambda_{off} = 0.5$ GeV while the top dashed line with $\Lambda = 1.4$ GeV and $\Lambda_{off} = 2$ GeV. For the contribution of the Roper resonance excitation through σ-meson exchange we modify $\Lambda_M \in (1.5, 2)$ GeV (band with vertical lines) in the monopole parametrisation and $\Lambda_E \in (1, 1.5)$ GeV (band with horizontal lines) in the exponential parametrisation.

Because at low energies the Roper resonance excitation and double-Δ excitation play the dominant role [25, 26] it is not obvious how to extract the pion-pion rescattering contributions.

threshold and about a factor 2 at $T_p \sim 900$ MeV). This increase is concentrated at low pp invariant masses, since the FSI is stronger when the protons move in the same direction. This effect is not taken into account in our model calculation. Although the ISI and FSI (the initial and final state interaction, respectively) could be taken into account by some approaches [64–67], there is still some model dependence. Since, we mainly investigate the relative importance of $\pi\pi$-rescattering contribution, we have not included complicated treatments of ISI and FSI which are not expected to influence our main conclusions.

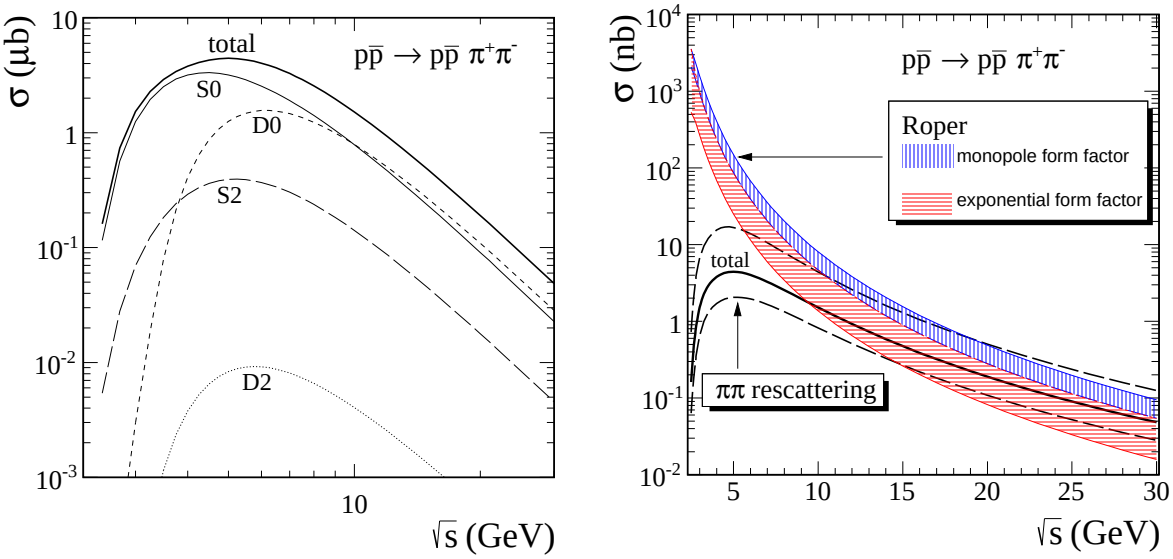

Figure 1.6: The phase-space integrated cross section for the reaction $p\bar{p} \to p\bar{p}\pi^+\pi^-$ as a function of center of mass energy $\sqrt{s}$. In the left panel the thick solid line represents the coherent sum of all partial waves. The contributions for individual partial waves $S0$, $S2$, $D0$ and $D2$ are shown. The pions are restricted to lie in the region $M_{\pi\pi} < 1.45$ GeV. In the right panel we compare the pion-pion rescattering contribution and the Roper resonance contribution (only σ-meson exchange included). The uncertainty bands for both contributions are also shown. The area of uncertainties for the pion-pion rescattering contribution is indicated by the dashed lines.

To cut off the Roper resonance excitation contribution we eliminate from the phase space those cases when

$$(M_{N^*} - \Delta M_{N^*} < M_{134} < M_{N^*} + \Delta M_{N^*}) \text{ or } (M_{N^*} - \Delta M_{N^*} < M_{234} < M_{N^*} + \Delta M_{N^*}) \,. \quad (1.23)$$

The $p\bar{p} \to p\bar{p}\pi^+\pi^-$ reaction is interesting because its double-Δ contribution mainly comes from the simultaneous $\bar{\Delta}^{--}$ and Δ^{++} excitation; see Ref. [26]. To suppress the double-Δ excitation we eliminate from the phase space those cases when

$$\begin{aligned}&(M_\Delta - \Delta M_\Delta < M_{13} < M_\Delta + \Delta M_\Delta \text{ and } M_\Delta - \Delta M_\Delta < M_{24} < M_\Delta + \Delta M_\Delta) \text{ or} \\ &(M_\Delta - \Delta M_\Delta < M_{14} < M_\Delta + \Delta M_\Delta \text{ and } M_\Delta - \Delta M_\Delta < M_{23} < M_\Delta + \Delta M_\Delta) \,. \end{aligned} \quad (1.24)$$

Above M_{ijk} and M_{ik} represent effective mass of the $p\pi\pi$ and $p\pi$ systems, respectively; ΔM_{N^*} and ΔM_Δ are cut-off parameters. We take $M_{N^*} = 1.44$ GeV, $\Delta M_{N^*} = 0.4$ GeV, and $M_\Delta = 1.22$ GeV, $\Delta M_\Delta = 0.2$ GeV which are considerably bigger than the decay width.

In Fig.1.7 we present differential cross section as a function of the (anti)proton transverse momentum, the pion transverse momentum, the transferred four-momentum squared between the initial and final nucleons (t) as well as the $p_{\perp,sum} = |\vec{p}_{\perp,sum}| = |\vec{p}_{\perp,34}| = |\vec{p}_{3\perp}(\pi^+) + \vec{p}_{4\perp}(\pi^-)|$ for pion-pion rescattering only. The shape of the $|t| = |t_1| = |t_2|$ distribution reflects tensorial structure of the πNN vertices (see Eq. (1.10)) and t_1 or t_2 dependence of vertex form factor (see Eq. (1.11)). This plot illustrates how virtual are "initial" pions. In principle, measuring such distributions would allow to limit, or even extract, the πNN form factor in relatively broad range of t_1 or t_2. This is not possible in elastic nucleon-nucleon scattering where many different exchange processes contribute. For collinear (parallel to the parent nucleons) initial pions the $d\sigma/dp_{\perp,sum}$ distribution would be proportional to the Dirac $\delta(p_{\perp,sum})$. The deviation from $\delta(p_{\perp,sum})$ is therefore a measure of non-collinearity and is strongly related to virtualities of "initial" pions (see panel (c)).

The two-pion invariant mass distribution given by the differential cross section $d\sigma/dM_{\pi\pi}$ is particularly interesting, see Fig. 1.8. In the left panel we show the coherent sum and the individual contributions of different partial waves $(l, I) = (0,0)$, $(0,2)$, $(2,0)$ and $(2,2)$. Here one

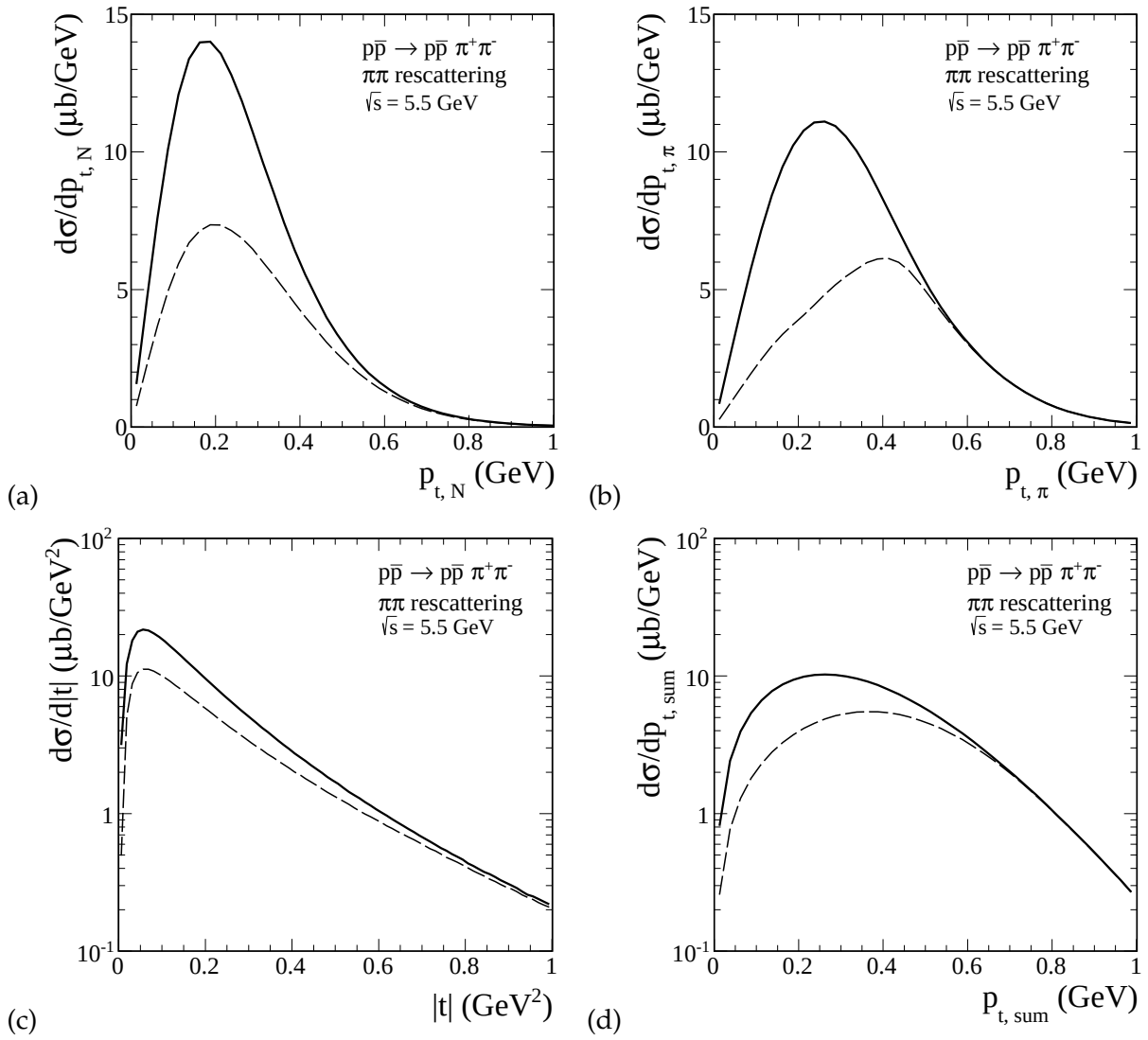

Figure 1.7: Differential cross section $d\sigma/dp_{\perp,N}$ (panel(a)), $d\sigma/dp_{\perp,\pi}$ (panel(b)), $d\sigma/d|t|$ (panel(c)), and $d\sigma/dp_{\perp,sum}$ (panel(d)), integrated over all other variables, for the $p\bar{p} \to p\bar{p}\pi^+\pi^-$ reaction at $\sqrt{s} = 5.5$ GeV. The pions are restricted to lie in the region $M_{\pi\pi} < 1.45$ GeV. The solid line is the cross section without additional cuts, the long-dashed line includes cuts to remove regions of Roper resonance and double-Δ excitations.

can see two characteristic bumps corresponding to the broad scalar σ meson and tensor $f_2(1270)$ meson as well as the dip from the interference with $f_0(980)$ and σ as in elastic $\pi\pi$ scattering (see Fig 1.3). However, here a size of bumps corresponding to scalar mesons are in contrast to elastic $\pi\pi$ scattering. In the right panel we can see how the cuts applied to remove regions of Roper resonance (1.23) and double-Δ excitation (1.24) modify the spectral shapes. The cuts to remove regions of Roper resonance decrease the cross section only in the region $M_{\pi\pi} < 0.85$ GeV while the cuts to remove regions of double-Δ excitation modify the whole region of two-pion invariant mass. In Fig. 1.9 we present distributions in the $N\pi$ and $N\pi\pi$ systems.

In Fig.1.10 (top panels) we show two-dimensional distributions in $(t, M_{\pi\pi})$ when all partial waves (left panel) and $S0$ wave (central panel) and $D0$ wave (right panel) only contributed to the cross section. In the bottom two panels we show the $\pi\pi$ invariant mass distribution with restrictions on both four-momentum transfers t_1 and t_2: $|t| < t_0$ (short-dashed line) and $|t| > t_0$ (long-dashed line), where $t_0 = 0.1$ GeV^2 and 0.2 GeV^2 in the panel (a) and (b), respectively. If we impose a $|t| < 0.1$ GeV^2 cut, we can see in the panel (a) that the $D0$ wave contribution is strongly reduced.

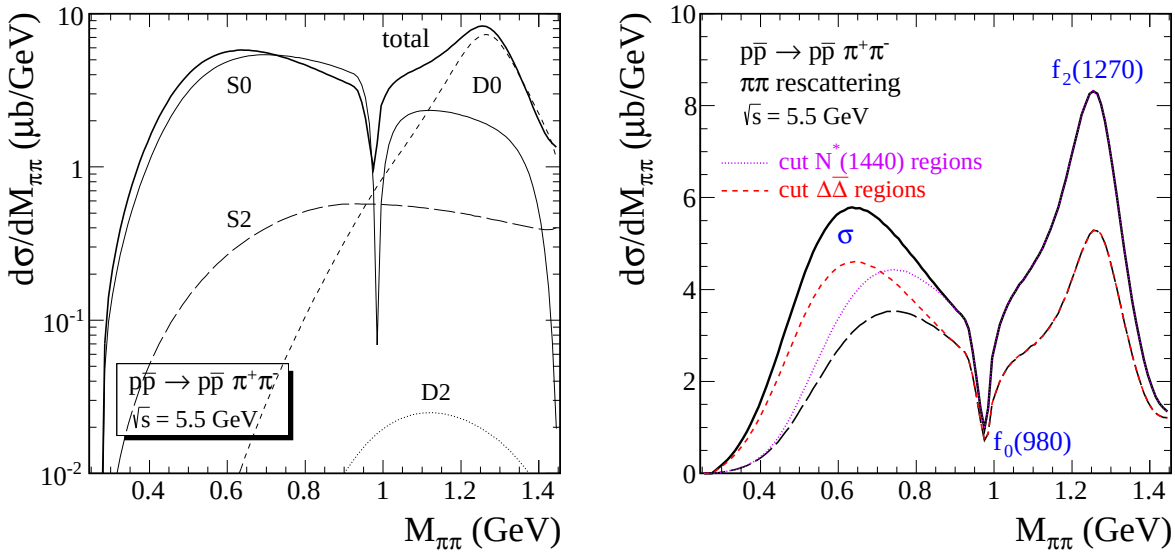

Figure 1.8: Differential cross section $d\sigma/dM_{\pi\pi}$ for the $p\bar{p} \to p\bar{p}\pi^+\pi^-$ reaction at $\sqrt{s} = 5.5$ GeV. The thick solid line represents the coherent sum of all partial waves. In the left panel the contributions for individual partial waves $S0$, $S2$, $D0$ and $D2$ are shown. In the right panel we show the cross section with additional cuts. The long-dashed line includes cuts to remove both regions of $N^*(1440)$ resonance and double-Δ excitations. The violet dotted line corresponds to cut on Roper resonance regions and the red short-dashed line correspondsto cut on double-Δ excitation regions, separately).

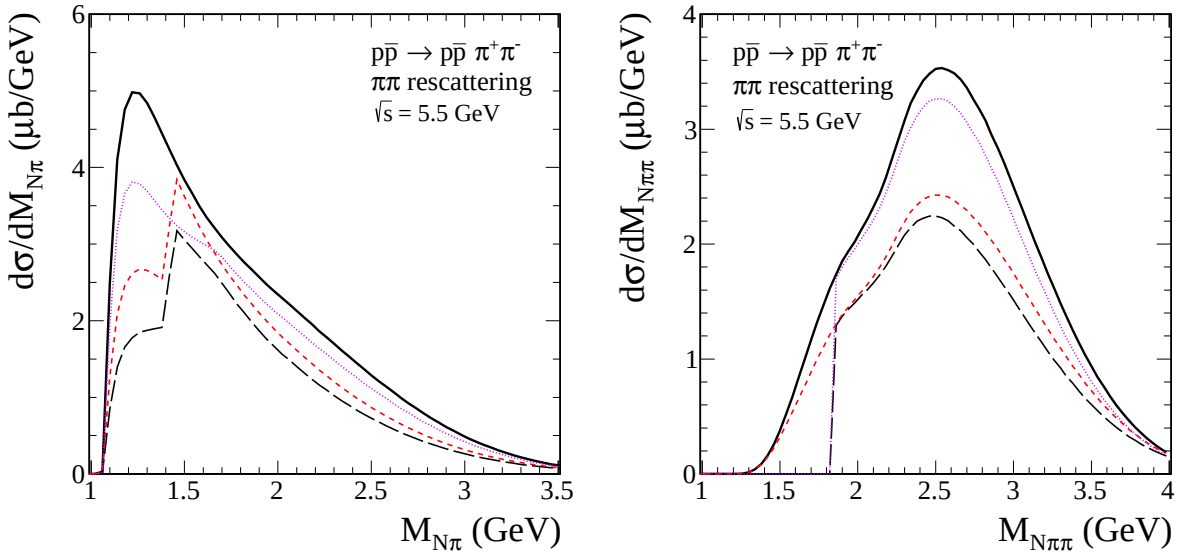

Figure 1.9: Differential cross section $d\sigma/dM_{p\pi}$ (left panel) and $d\sigma/dM_{p\pi\pi}$ (right panel) for the $p\bar{p} \to p\bar{p}\pi^+\pi^-$ reaction at $\sqrt{s} = 5.5$ GeV. The pions are restricted to lie in the region $M_{\pi\pi} < 1.45$ GeV. The solid line is the cross section without additional cuts, the long-dashed line includes cuts to remove both regions of $N^*(1440)$ resonance and double-Δ excitations (the violet dotted line corresponds to cut on Roper resonance regions, the red short-dashed line to cut on Δ and $\bar{\Delta}$ excitation regions, separately).

In Fig.1.11 we show two-dimensional distributions in $(\cos\theta^*, M_{\pi\pi})$ (left panel) and in $(p_{\perp,\pi}, M_{\pi\pi})$ (right panel). It is apparent that the bulk of $f_2(1270)$ meson is emitted at $\cos\theta^* = \pm 1$. The kinematic variable $\cos\theta^*$ is given by Eq. (1.16).

The PANDA detector is supposed to be a 4π solid angle detector with good particle identification for charged particles and photons. This opens a possibility to study several correlation observables for outgoing particles. One of them is azimuthal angle correlation between charged outgoing pions $\phi_{\pi\pi} = \phi_{34}$. In Fig.1.12 we present differential cross sections $d\sigma/d\phi_{p\bar{p}}$ and

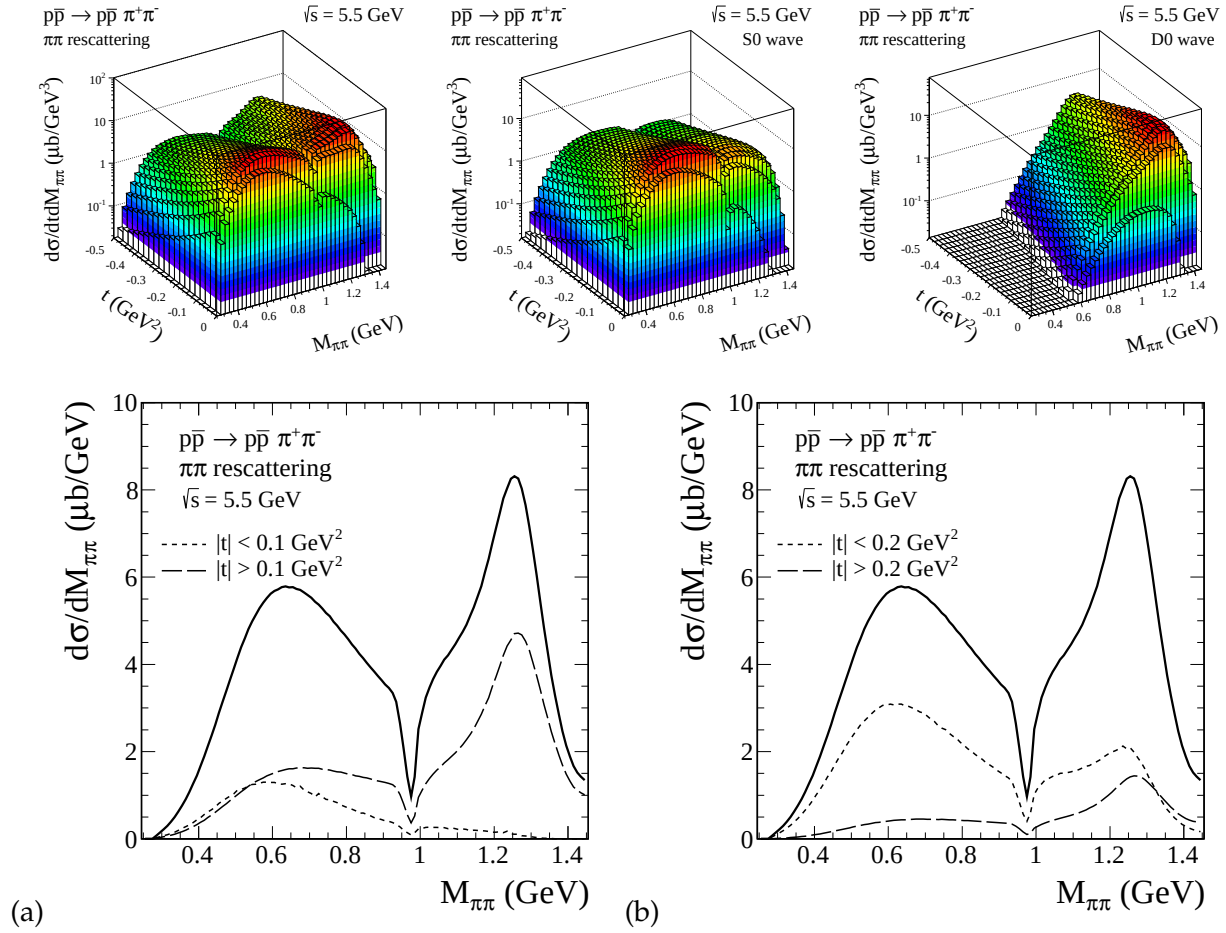

Figure 1.10: Distributions in $(t, M_{\pi\pi})$ for the $p\bar{p} \to p\bar{p}\pi^+\pi^-$ reaction at $\sqrt{s} = 5.5$ GeV. The bottom panels (a) and (b) show two-pion invariant mass distribution for different cuts on both four-momentum transfers $|t_1|$ and $|t_2|$.

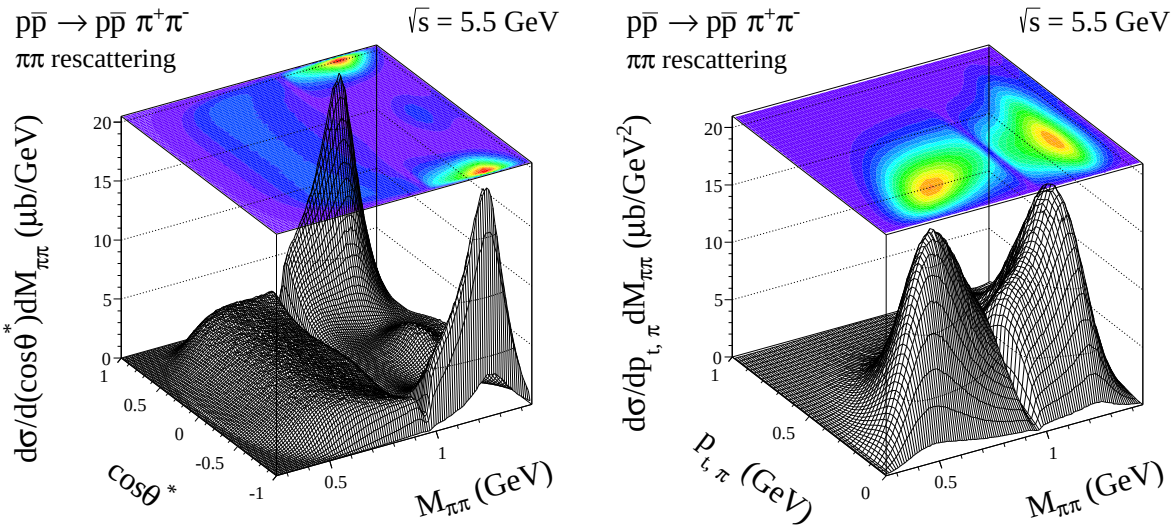

Figure 1.11: Two-dimensional distributions in $(\cos\theta^*, M_{\pi\pi})$ (left panel) and $(p_{\perp,\pi}, M_{\pi\pi})$ (right panel) for the $p\bar{p} \to p\bar{p}\pi^+\pi^-$ reaction at $\sqrt{s} = 5.5$ GeV.

$d\sigma/d\phi_{\pi\pi}$. Clearly a preference of back-to-back emissions can be seen. Imposing cuts on the Roper resonance and double-Δ excitation lowers the cross section and strongly modifies the shape in

$\phi_{p\bar{p}}$ distribution but only mildly in $\phi_{\pi\pi}$ distribution. Because the shape of the azimuthal angle correlations strongly depends on the reaction mechanism, measuring such correlation would provide then very valuable information.

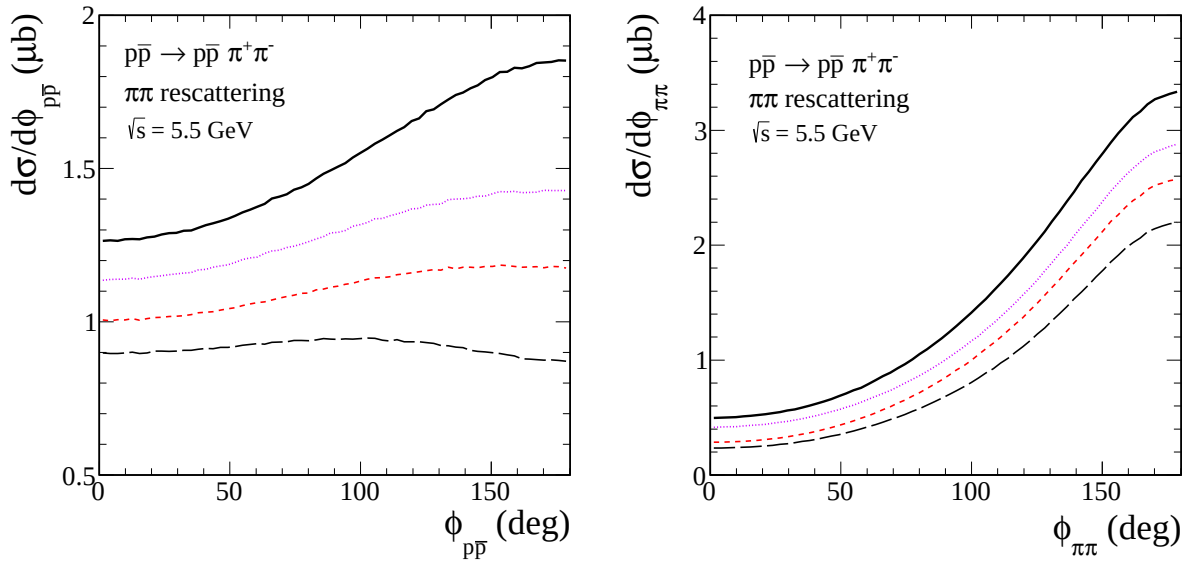

Figure 1.12: The distributions in azimuthal angle between outgoing nucleons (left panel) and outgoing pions (right panel) for the $p\bar{p} \to p\bar{p}\pi^+\pi^-$ reaction at $\sqrt{s} = 5.5$ GeV. In both cases the pions are restricted to lie in the region $M_{\pi\pi} < 1.45$ GeV. The solid line is the cross section without additional cuts, the long-dashed line includes cuts to remove both regions of $N^*(1440)$ resonance and double-Δ excitations (the violet dotted line corresponds to cut on Roper resonance region, the red short-dashed line to cut on Δ and $\bar{\Delta}$ excitation regions, separately).

In Fig. 1.13 we present the Feynman-x distribution. We see that the $x_{F,\pi}$ distribution for the π^+ meson (or equivalently π^- meson) peaks at $x_F = 0$ (A.16) and the scattered nucleons at $x_F \approx \pm 0.75$.

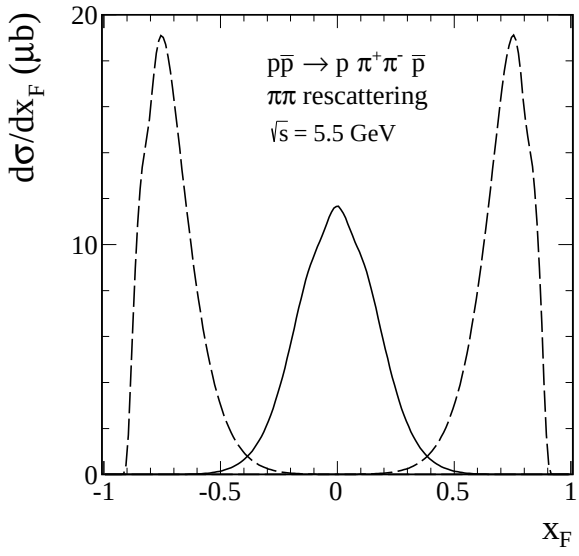

Figure 1.13: The x_F distribution of pions (at $x_F = 0$) and the nucleons (at $x_F \to \pm 0.75$) for the $p\bar{p} \to p\bar{p}\pi^+\pi^-$ reaction at $\sqrt{s} = 5.5$ GeV. The pions are restricted to lie in the region $M_{\pi\pi} < 1.45$ GeV. We have included the additional cuts to remove regions of Roper resonance and double-Δ excitations.

Finally, in Fig.1.14 we show differential cross section $d\sigma/dy_3dy_4$ in the two-dimensional space (y_3, y_4) when extra cuts to remove regions of Roper resonance (1.23) (left panel) or double-

Δ excitation (1.24) (right panel) are imposed. These cuts do not much affect the region of pion midrapidities $y_3, y_4 \approx 0$. In practice, the cuts on the Roper resonance region almost not at all modify the distribution. The cuts on Roper resonance act for ($y_3 < 0$ and $y_4 < 0$) or ($y_3 > 0$ and $y_4 > 0$), i.e. in the rapidity region where the two-pion rescattering contribution is very small. The cuts on double-Δ excitation act for ($y_3 < 0$ and $y_4 > 0$) or ($y_3 > 0$ and $y_4 < 0$), i.e. in the region where the two-pion rescattering contribution is sizeable. This shows that the double-Δ excitation is more critical than the Roper resonance excitation in the context of extracting the pion-pion rescattering contribution.

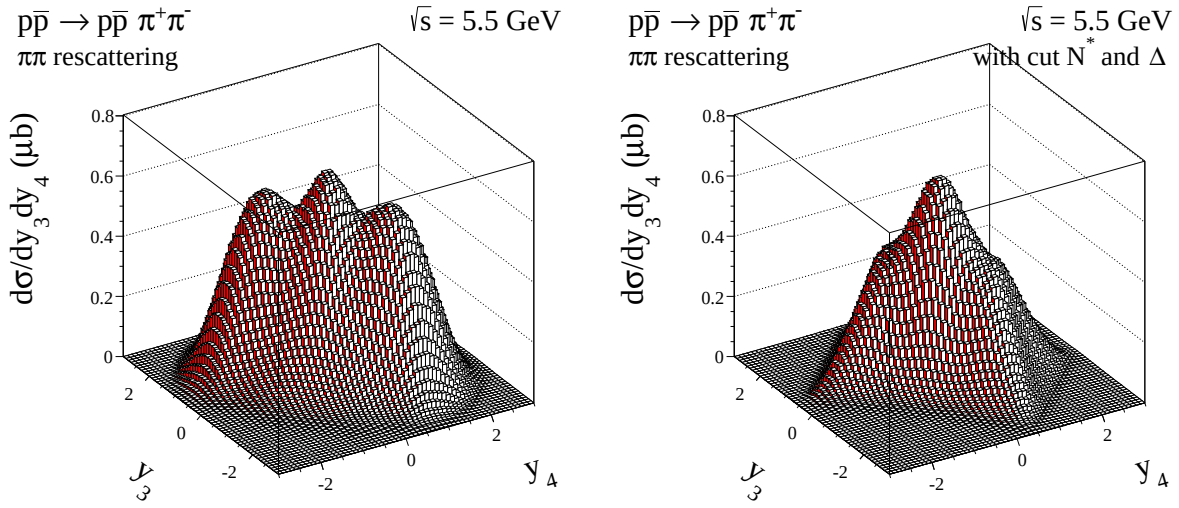

Figure 1.14: Two-dimensional differential cross section $d\sigma/dy_3dy_4$ in $(y_3(\pi^+), y_4(\pi^-))$ for the $p\bar{p} \to p\bar{p}\pi^+\pi^-$ reaction at $\sqrt{s} = 5.5$ GeV (left panel). The pions are restricted to lie in the region $M_{\pi\pi} < 1.45$ GeV. In the right panel we have included in addition cuts to remove regions of Roper resonance and double-Δ excitations.

1.3 Conclusions

We have calculated both differential and total cross sections for the $pp \to pp\pi^+\pi^-$ and $p\bar{p} \to p\bar{p}\pi^+\pi^-$ reactions close to threshold and for future PANDA experiments. Our results have been compared with very close to threshold data measured by the WASA Collaboration. We have shown that very close to threshold the pion-pion rescattering mechanism gives much smaller contribution than the excitation of the Roper resonance via σ-exchange and its subsequent decay $N^*(1440) \to N(\pi\pi)^{S-\text{wave}}_{I=0}$ as well as the double-Δ excitation and subsequent decays studied in the past [23, 24]. At low energies all these mechanisms overlap and it is not possible to extract the pion-pion rescattering contributions and therefore not possible to study the $\pi^0\pi^0 \to \pi^+\pi^-$ process.

Going to higher energies allows to find regions of the final state phase space where the pion-pion rescattering process dominates over the Roper resonance and double-Δ excitation mechanisms. We stress that the PANDA (anti-Proton ANnihilation at DArmstadt) experiment [27] at GSI-FAIR (Facility of Antiproton and Ion Research) could play an important role in understanding of the baryon spectrum, provide an excellent place for studying the properties of relevant barionic resonances and open a possibility to study the pion-pion rescattering processes. At present it is not clear how precisely the pion-pion rescattering can be studied experimentally as the PANDA detector is in the exploratory phase and its detailed final design is still an open issue. We expect that the minimal scenario would be to verify models like the one discussed here. If the phase shift analysis is possible requires extra Monte Carlo studied including efficiencies of

the PANDA detector. We hope that the cross section for exclusive production and the line shape (position and width) of the Roper resonance can be studied with the PANDA detector. Such exclusive production of pion pairs can be useful in planning of experiments at GSI-FAIR which is the only possible place where the exclusive $p\bar{p} \to p\bar{p}(\pi^0\pi^0 \to \pi^+\pi^-)$ reaction can be studied at sufficiently large energy. The channels of $p\bar{p} \to p\bar{n}\pi^0\pi^-$, $p\bar{p} \to n\bar{p}\pi^+\pi^0$, $p\bar{p} \to n\bar{n}\pi^+\pi^-$, can also be measured by the PANDA experiment. A simultaneous study of these reactions may help to pin down contributions from various meson exchanges. At the Tevatron the pion rescattering cross section is completely negligible and other mechanisms become important.

We have presented several distributions which could be measured in the future with the PANDA detector at the GSI HESR. Particularly interesting is the distribution in two-pion invariant mass, see Fig. 1.8, where one should observe bumps related to the famous scalar-isoscalar σ-meson and to tensor-isoscalar $f_2(1270)$ meson as well as a dip from the interference with $f_0(980)$ and σ mesons. This distribution is slightly different compared to the dependence of the total $\pi^0\pi^0 \to \pi^+\pi^-$ cross section on $W_{\pi\pi}$, see Fig. 1.3. This is caused mainly by the four-body phase space modifications.

The pions from the pion-pion rescattering are produced preferentially in opposite hemispheres, i.e. if one pion is produced at positive center-of-mass rapidities the second pion is produced at negative ones. This is similar to the double-Δ excitation mechanism. Imposing cuts on double-Δ excitation leaves untouched the region of midrapidities. Also the region of large $p_{\perp,sum}$ stays unmodified by the cuts on double-Δ excitations. A direct comparison of our theoretical results with the measured total cross sections and invariant-mass distributions will certainly provide useful information about the mechanisms governing this process.

1.4 Exclusive scalar $f_0(1500)$ meson production

Many theoretical calculations, including lattice QCD, predicted existence of non-$q\bar{q}$ scalar objects, such as glueballs, that is, the particles dominantly made of gluons with masses $M(G) >$ 1.5 GeV. No one of them was up to now unambiguously identified. The nature of scalar mesons below 2 GeV is also not well understood. Lattice QCD approach with quenched quarks find a scalar gluonium (glueball) at approximately 1.6 GeV [68–70] [6]. Also the analyses in the framework of chiral Lagrangians [72–74] indicate that $f_0(1500)$ meson is dominantly gluonium state. The QCD Sum Rules [75–82] suggest that the states at approximately 1 GeV and $1.5 - 1.6$ GeV are admixtures of gluonium and $q\bar{q}$ states. A recent analysis in the framework of Gaussian QCD Sum Rules [83], which is well suited to $q\bar{q}$ - gluonium mixing, find that the states at about 1 GeV ($f_0(980)$ meson) and at about 1.4 GeV are strongly mixed with the preference of the higher-mass state to have slightly larger gluonium admixture. Summarizing this discussion, it may be very difficult to find a clear signal of gluonium. Further studies of the scalar meson production in several processes may shed more light on the quite complicated problem.

The lowest mass meson considered as a glueball candidate is a scalar $f_0(1500)$ [84, 85] discovered by the Crystall Barrel Collaboration in proton-antiproton annihilation [86–88]. The branching fractions are consistent with the dominant glueball component [89]. It was next observed by the WA102 Collaboration in central production in charged two-pion and two-kaon [90] as well four-pion [91] decay channels at $\sqrt{s} \approx 30$ GeV in proton-proton collisions. Close and Kirk [92, 93] proposed a phenomenological model of central exclusive $f_0(1500)$ production. In their language the pomerons (transverse and longitudinal) are the effective (phenomenological) degrees of freedom [94, 95]. The Close-Kirk amplitude was parametrised as

$$\mathcal{M}(t_1, t_2, \phi') = a_T \exp\left(\frac{b_T}{2}(t_1 + t_2)\right) + a_L \exp\left(\frac{b_L}{2}(t_1 + t_2)\right) \frac{\sqrt{t_1 t_2}}{\mu^2} \cos\phi' \,, \tag{1.25}$$

where the ϕ' dependence applies in the meson rest frame (current-current c.m.). In their ap-

[6] The approaches with dynamical quarks find relatively large mixing with $q\bar{q}$ states [71].

proach there is no explicit $f_0(1500)$-rapidity dependence of the corresponding amplitude. Since the parameters were rather fitted to the not-normalized WA102 experimental data [90] no absolute normalization can be obtained within this approach. Furthermore the parametrisation is not giving energy dependence of the cross section, so predictions for other (not-measured) energies are not possible. In this Section we will investigate rather a QCD-inspired approach. It provides absolute normalization [7], energy dependence and dependence on meson rapidity (or equivalently on Feynman-x of the meson).

In the present analysis we shall concentrate on central exclusive production of scalar $f_0(1500)$ in the following reactions:

$$\begin{aligned} p + p &\to p + f_0(1500) + p\,, \\ p + \bar{p} &\to p + f_0(1500) + \bar{p}\,, \\ p + \bar{p} &\to n + f_0(1500) + \bar{n}\,. \end{aligned} \tag{1.26}$$

While the first process can be measured at J-PARC, the latter two reactions could be measured by the PANDA Collaboration at the new complex FAIR at GSI Darmstadt. The combination of these processes could shed more light on the mechanism of $f_0(1500)$ meson production as well as on its nature. Our aim here is to explore a possibility of studying exclusive $f_0(1500)$ meson production in the FAIR and J-PARC energy range and explore the potential of these facilities.

Since the two-pion channel is one of the dominant decay channels of $f_0(1500)$ (34.9 $\pm$ 2.3) % [96] one may expect the two-pion fusion (see Fig.1.15) to be one of the dominant mechanisms of exclusive $f_0(1500)$ production at the FAIR energies. The two-pion fusion can be also relative reliably calculated in the framework of meson exchange theory. The pion coupling to the nucleon is well known [97]. The πNN form factor for larger pion virtualities is somewhat less known. This may limit our predictions close to the threshold, where rather large virtualities are involved due to specific kinematics. At largest HESR (antiproton ring) energy, as will be discussed in this Section, this is no longer a limiting factor as average pion virtualities are rather small.

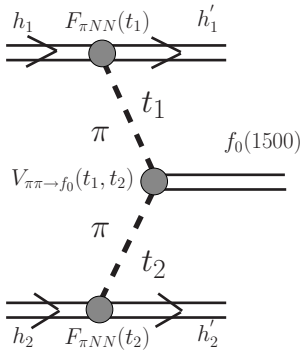

Figure 1.15: The sketch of the pion-pion MEC mechanism for production of the $f_0(1500)$ meson in proton-(anti)proton collisions. Form factors appearing in different vertices and kinematical variables are shown explicitly.

If the $f_0(1500)$ meson is a scalar glueball (or has a strong glueball component [98]) then the mechanism shown in Fig. 1.16 (a) may be important, at least in the high-energy regime. This mechanism is often considered as the dominant mechanism of exclusive Higgs boson [99–103] and $\chi_c(0^+)$ meson [104] production at high energies. At intermediate energies the same mechanism is, however, not able to explain large cross section for exclusive η' production [105] as measured by the WA102 Collaboration.

While there are some ideas about the reaction mechanism at higher energies, the mechanism at lower energies was never studied. We shall investigate new mechanisms of pion-pion

[7] As will be discussed later it is rather upper limit which can be easily obtained.

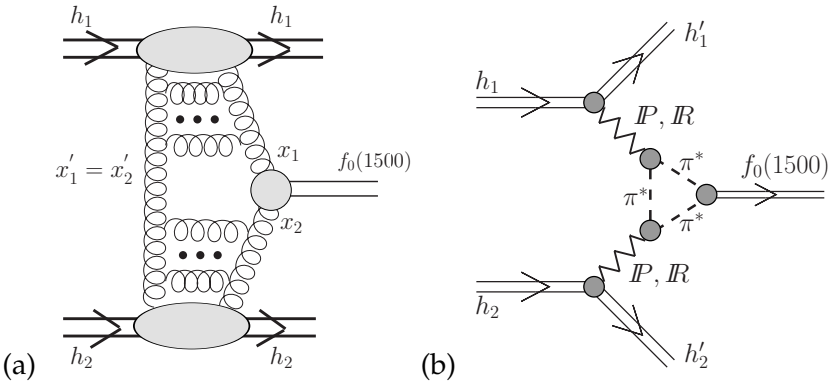

Figure 1.16: The sketch of the "bare" perturbative QCD mechanism (panel (a)) and the "bare" non-perturbative mechanism with the intermediate pionic triangle (panel (b)) for diffractive central exclusive production of the $f_0(1500)$ meson (glueball candidate). The kinematical variables are shown in addition. In panel (b) the stars attached to π mesons denote the fact that they are off-mass-shell.

fusion shown in Fig.1.15, the QCD mechanism shown in Fig.1.16 (a) and the non-perturbative mechanism with the intermediate pionic loop shown in Fig.1.16 (b). The QCD mechanism is typical for high energies but here we wish to investigate its role at intermediate energies and in particular its vanishing at low energies and the interplay with the pion-pion fusion mechanism.

1.4.1 Pion-pion MEC amplitude

It is straightforward to evaluate the pion-pion meson exchange current (MEC) contribution shown in Fig.1.15. The Born amplitude is similar as (1.8) with $\mathcal{M}^{\pi^{0*}\pi^{0*}\to\pi^+\pi^-}(s_{34},t_1,t_2)$ replaced by off-shell vertex function

$$\Gamma^{\pi^*\pi^*\to f_0(1500)}(t_1,t_2) = g_{f_0(1500)\pi\pi}\, V_{\pi\pi\to f_0(1500)}(t_1,t_2)\,, \tag{1.27}$$

where the coupling constant $g_{f_0(1500)\pi\pi}$ (the normalization constant $|C_{f_0\to\pi\pi}|$ in the formula below) can be calculated from the partial decay width as

$$\Gamma_{f_0\to\pi\pi} = \frac{3}{32\pi m_{f_0}}|C_{f_0\to\pi\pi}|^2\left(1-\frac{4m_\pi^2}{m_{f_0}^2}\right)^{1/2}\,, \tag{1.28}$$

where

$$\begin{aligned}\Gamma_{f_0\to\pi\pi} &= \Gamma_{f_0\to\pi^0\pi^0}+\Gamma_{f_0\to\pi^+\pi^-}\,,\\ \Gamma_{f_0\to\pi\pi} &= 3\Gamma_{f_0\to\pi^0\pi^0} = \frac{3}{2}\Gamma_{f_0\to\pi^+\pi^-}\,.\end{aligned} \tag{1.29}$$

From [96] we have $\Gamma_{f_0\to\pi\pi}$ as

$$\Gamma_{f_0(1500)\to\pi\pi} = \Gamma_{f_0(1500),tot}\,\mathcal{BR}(f_0(1500)\to\pi\pi)\,, \tag{1.30}$$

where $\Gamma_{f_0(1500),tot} = 0.109\pm0.007$ GeV is the average value of $f_0(1500)$ width and $\mathcal{BR} = 0.349\pm0.023$ is the branching ratio $f_0(1500)\to\pi\pi$ mode.

Limiting to nucleons in the final state, in the case of proton-proton collisions only $ppf_0(1500)$ final state channel is possible and therefore the $\pi^0\pi^0$ fusion is allowed while in the case of proton-antiproton collisions both $p\bar{p}f_0(1500)$ and $n\bar{n}f_0(1500)$ final state channels are possible, i.e. both $\pi^0\pi^0$ and $\pi^+\pi^-$ MEC are allowed. In the hadronic vertices we have to take into account form factors (1.11) since the hadrons are extended objects. The influence of the t-dependence of the form factors will be discussed in the result section.

The off-shellness of pions is also included for the $\pi\pi \to f_0(1500)$ transition through the extra $V_{\pi\pi\to f_0(1500)}(t_1,t_2)$ form factor which we take in the factorized form

$$V_{\pi\pi\to f_0(1500)}(t_1,t_2) = F_M(t_1)F_M(t_2) = \frac{\Lambda^2_{\pi\pi f_0} - m^2_\pi}{\Lambda^2_{\pi\pi f_0} - t_1}\,\frac{\Lambda^2_{\pi\pi f_0} - m^2_\pi}{\Lambda^2_{\pi\pi f_0} - t_2}\,. \tag{1.31}$$

It is normalized to unity when both pions are on mass shell $F(t_1 = m^2_\pi, t_2 = m^2_\pi) = 1$. In the present calculation we shall take $\Lambda_{\pi\pi f_0} = 1$ GeV.

1.4.2 Diffractive QCD amplitude

According to Khoze-Martin-Ryskin approach (KMR) [99–103], the amplitude of exclusive double diffractive colour singlet production $pp \to ppf_0(1500)$ can be written as

$$\mathcal{M}^{g^*g^*} = \frac{s}{2}\pi^2\frac{1}{2}\frac{\delta_{c_1c_2}}{N_c^2-1}\,\mathrm{Im}\int d^2q_{0\perp}V_J^{c_1c_2}\frac{f^{off}_{g,1}(x_1,x_1',q^2_{0\perp},q^2_{1\perp},t_1)f^{off}_{g,2}(x_2,x_2',q^2_{0\perp},q^2_{2\perp},t_2)}{q^2_{0\perp}\,q^2_{1\perp}\,q^2_{2\perp}}. \tag{1.32}$$

The normalization of this amplitude differs from the KMR one [99–103] by the factor $s/2$ and coincides with the normalization in a previous work on exclusive η'-production [105]. The amplitude is averaged over the colour indices and over two transverse polarisations of the incoming gluons [99–103]. The bare amplitude above is subjected to absorption corrections which depend on collision energy (the bigger the energy, the bigger the absorption corrections). We shall discuss this issue shortly when presenting our results.

The vertex factor $V_J^{c_1c_2} = V_J^{c_1c_2}(q^2_{1\perp},q^2_{2\perp},P^2_{M\perp})$ in expression (1.32) describes the coupling of two virtual gluons to $f_0(1500)$ meson. Recently the vertex was obtained for off-shell values of $q_{1\perp}$ and $q_{2\perp}$ in the case of $\chi_c(0)$ exclusive production [104]. An almost alternative way to describe the vertex is to express it via partial decay width $\Gamma(M\to gg)$. [8] The latter (approximate) method can be used also for the $f_0(1500)$ meson production.

In the original Khoze-Martin-Ryskin (KMR) approach [99–103] the amplitude is written as

$$\mathcal{M} = N\int\frac{d^2q_{0\perp}P[f_0(1500)]}{q^2_{0\perp}q^2_{1\perp}q^2_{2\perp}}f_g^{KMR}(x_1,x_1',Q^2_{1\perp},\mu^2;t_1)f_g^{KMR}(x_2,x_2',Q^2_{2\perp},\mu^2;t_2)\,, \tag{1.33}$$

where only one transverse momentum is taken into account somewhat arbitrarily as

$$Q^2_{1\perp} = \min\{q^2_{0\perp},q^2_{1\perp}\}\,,\qquad Q^2_{2\perp} = \min\{q^2_{0\perp},q^2_{2\perp}\}\,, \tag{1.34}$$

and the normalization factor N can be written in terms of the $f_0(1500)\to gg$ decay width. Other prescriptions are also possible [104, 106]. In the KMR approach the large meson mass approximation $M \gg |\mathbf{q}_{1\perp}|$, $|\mathbf{q}_{2\perp}|$ is adopted, so the gluon virtualities are neglected in the vertex factor

$$P[f_0(1500)] \simeq (q_{1\perp}q_{2\perp}) = (q_{0\perp}+p_{1\perp})(q_{0\perp}-p_{2\perp})\,. \tag{1.35}$$

The KMR UGDFs are written in the factorized form:

$$f_g^{KMR}(x,x',Q^2_\perp,\mu^2;t) = f_g^{KMR}(x,x',Q^2_\perp,\mu^2)\exp(b_0t) \tag{1.36}$$

with $b_0 = 2$ GeV^{-2} [99–103]. In our approach we use somewhat different parametrisation of the t-dependent isoscalar form factors [9]. The KMR skewed distributions are given in terms of

[8] The last value is not so well known. We shall take $\Gamma(M\to gg) = \Gamma_{f_0(1500),tot}$. This will give us an upper estimate. As a consequence this will allow us to show that the gluonic component is negligible for future experiments with the PANDA detector.

[9] Please note that the KMR and our (general) skewed UGDFs have different number of arguments. In the KMR approach there is only one effective gluon transverse momentum (see Eq. (1.34)) compared to two independent transverse momenta in general case (1.41).

conventional integrated densities $g(x, Q_\perp^2)$ and the so-called Sudakov form factor T_g (5.19) (see discussion in Section 5.1) as follows

$$f_g^{KMR}(x, x', Q_\perp^2, \mu^2) = R_g \frac{\partial}{\partial \ln Q_\perp^2} \left[\sqrt{T_g(Q_\perp^2, \mu^2)} x g(x, Q_\perp^2) \right] . \tag{1.37}$$

The square root here was taken using arguments that only survival probability for hard gluons is relevant. It is not so-obvious if this approximation is reliable for light meson production. The factor R_g in the KMR approach approximately accounts for the single $\log Q^2$ skewed effect [99–103]. Usually this factor is estimated to be $1.3 - 1.5$. In our evaluations here we take it to be equal 1 to avoid further uncertainties. Please note also that in contrast to our approach the skewed KMR UGDFs does not explicitly depend on x' (assuming $x' \ll x \ll 1$). Following the KMR notations we write the total amplitude (1.32) (averaged over colour and polarisation states of incoming gluons) in the limit $M \gg q_{1,t},\, q_{2,t}$ as

$$\mathcal{M} = C_{f_0(1500)\to gg}\, \pi^2\, \frac{s}{2} \int d^2 q_{0\perp} P[f_0(1500)] \frac{f_{g,1}^{off}(x_1, x_1', q_{0\perp}^2, q_{1\perp}^2, t_1) f_{g,2}^{off}(x_2, x_2', q_{0\perp}^2, q_{2\perp}^2, t_2)}{q_{0\perp}^2\, q_{1\perp}^2\, q_{2\perp}^2} , \tag{1.38}$$

where the normalization constant obtained from the decay of $f_0(1500)$ into two soft gluons is

$$|C_{f_0(1500)\to gg}|^2 = \frac{64\pi}{(N_c^2 - 1) m_{f_0}^3}\, \Gamma_{f_0(1500)\to gg} . \tag{1.39}$$

Of course the partial decay width is limited from above:

$$\Gamma_{f_0(1500)\to gg} < \Gamma_{tot} . \tag{1.40}$$

In addition to the standard KMR approach we could use other off-diagonal gluon distributions (for details and a discussion see Ref. [104,105]). In the present work we shall use a few sets of unintegrated gluon distributions which aim at the description of phenomena where small gluon transverse momenta are involved. Some details concerning the distributions can be found in Ref. [107]. We shall follow the notation there.

In the general case we do not know off-diagonal UGDFs very well. In [104, 105] a prescription how to calculate the off-diagonal UGDFs was proposed:

$$\begin{aligned} f_{g,1}^{off} &= \sqrt{f_g^{(1)}(x_1', q_{0\perp}^2, \mu_0^2)\, f_g^{(1)}(x_1, q_{1\perp}^2, \mu^2)}\, F_1(t_1) , \\ f_{g,2}^{off} &= \sqrt{f_g^{(2)}(x_2', q_{0\perp}^2, \mu_0^2)\, f_g^{(2)}(x_2, q_{2\perp}^2, \mu^2)}\, F_1(t_2) , \end{aligned} \tag{1.41}$$

where $F_1(t_1)$ and $F_1(t_2)$ are isoscalar nucleon form factors. They can be parametrised as (B.2), where t_1 and t_2 are total four-momentum transfers in the first and second proton line, respectively. While in the emission line the choice of the scale is rather natural, there is no so-clear situation for the second screening-gluon exchange [105].

Even at intermediate energies ($\sqrt{s} = 10 - 50$ GeV) typical $x_1' = x_2'$ are relatively small (~ 0.01). However, characteristic $x_1, x_2 \sim m_{f_0}/\sqrt{s}$ are not too small (typically > 0.1). Therefore here we cannot use the small-x models of UGDFs. In the latter case a Gaussian smearing of the collinear distribution seems a reasonable solution:

$$f_g^{Gauss}(x, k_\perp^2, \mu_F^2) = x g^{coll}(x, \mu_F^2)\, F_{Gauss}(k_\perp^2; \sigma_0) , \tag{1.42}$$

where $g^{coll}(x, \mu_F^2)$ are standard collinear (integrated) gluon distribution and $F_{Gauss}(k_\perp^2; \sigma_0)$ is a Gaussian two-dimensional function

$$F_{Gauss}(k_\perp^2, \sigma_0) = \frac{1}{2\pi\sigma_0^2} \exp\left(-k_\perp^2/2\sigma_0^2\right)/\pi , \tag{1.43}$$

where σ_0 is a free parameter which one can expect to be of the order of 1 GeV. We expect strong sensitivity to the actual value of the parameter σ_0; see [105]. Summarizing, a following prescription for the off-diagonal UGDF seems reasonable:

$$f(x,x',k_\perp^2,k_\perp'^2,t) = \sqrt{f_{small-x}(x',k_\perp'^2)\, f_g^{Gauss}(x,k_\perp^2,\mu_F^2)}\, F(t)\ , \tag{1.44}$$

where $f_{small-x}(x',k_\perp'^2)$ is one of the typical small-x UGDFs (see e.g. [107]). So exemplary combinations are: KL⊗Gauss, BFKL⊗Gauss, GBW⊗Gauss (for notation see [107]). The natural choice of the scale is $\mu_F^2 = m_{f_0}^2$. This relatively low scale is possible with the GRV-type of PDF parametrisation [108]. We shall call (1.44) a "mixed prescription" for brevity.

The smaller energies $\sqrt{s}$ the larger values of x_1 and x_2 are involved. Many of unintegrated gluon distributions in the literature are formulated in the region of very small x. Extrapolation of the method down to small energies automatically means going to the region of large x. In Fig.1.17 we wish to demonstrate this fact. We show the ratio of the cross sections

$$\text{Ratio} = \frac{\sigma(\sqrt{s}; x_1 < x_0, x_2 < x_0)}{\sigma(\sqrt{s})}\,, \tag{1.45}$$

as a function of center-of-mass energy. Above x_0 was introduced to define the region of small/large x. The solid line corresponds to $x_0 = 0.1$ and the dashed line to $x_0 = 0.2$. At the largest HESR energies one stays in the region of $x_1, x_2 < 0.2$.

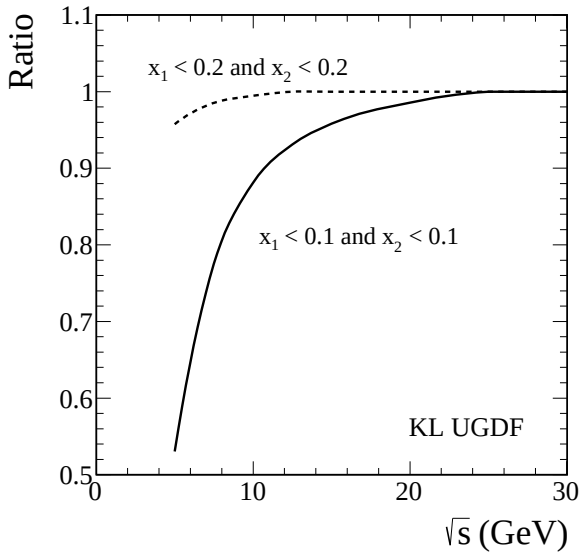

Figure 1.17: The ratio of the cross sections (see Eq. (1.45)) as a function of center-of-mass energy. The solid line corresponds to $x_0 = 0.1$ and the dashed line to $x_0 = 0.2$.

1.4.3 Two-gluon impact factor approach for subasymptotic energies

The amplitude in the previous section, written in terms of off-diagonal UGDFs, was constructed for rather large energies. The smaller the energy the shorter the QCD ladder. It is not obvious how to extrapolate the diffractive amplitude down to lower (close-to-threshold) energies. Here we present slightly different method which seems more adequate at lower energies.

At not too large energies the amplitude of elastic scattering can be written as amplitude for two-gluon exchange [109–111]

$$\mathcal{M}_{pp\to pp}(s,t) = is\frac{N_c^2-1}{N_c^2}\int d^2k_\perp\ \alpha_s(k_{1\perp}^2)\alpha_s(k_{2\perp}^2)\frac{3F(\mathbf{k}_{1\perp},\mathbf{k}_{2\perp})3F(\mathbf{k}_{1\perp},\mathbf{k}_{2\perp})}{(k_{1\perp}^2+\mu_g^2)(k_{2\perp}^2+\mu_g^2)}\,. \tag{1.46}$$

In analogy to dipole-dipole or pion-pion scattering (see e.g. [111]) the impact factor can be parametrised as:

$$F(\mathbf{k}_{1\perp},\mathbf{k}_{2\perp}) = \frac{\Lambda^2}{\Lambda^2+(\mathbf{k}_{1\perp}+\mathbf{k}_{2\perp})^2} - \frac{\Lambda^2}{\Lambda^2+(\mathbf{k}_{1\perp}-\mathbf{k}_{2\perp})^2}\,. \tag{1.47}$$

At high energy the net four-momentum transfer: $t = -(\mathbf{k}_{1\perp}+\mathbf{k}_{2\perp})^2$. Λ in Eq.(1.47) is a free parameter which can be adjusted to elastic scattering. For our rough estimate we take $\Lambda = m_\rho$.

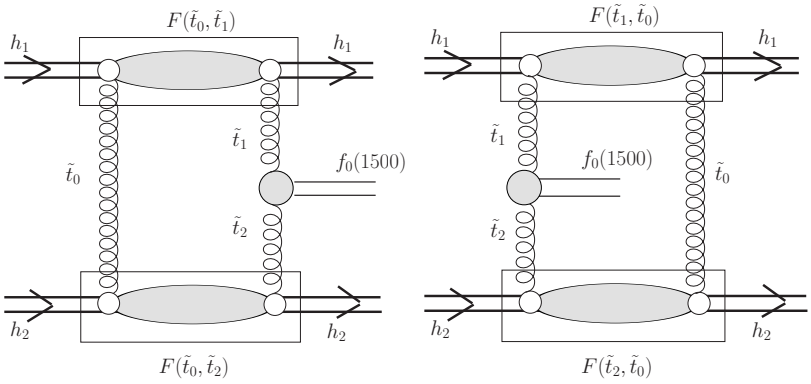

Figure 1.18: The sketch of the two-gluon impact factor approach. Some kinematical variables are shown explicitly.

Generalizing, the amplitude for exclusive $f_0(1500)$ production can be written as the amplitude for three-gluon exchange shown in Fig.1.18:

$$\begin{aligned}\mathcal{M}_{pp\to ppf_0(1500)}(s,y,t_1,t_2,\phi) &= is\frac{N_c^2-1}{N_c^2}\int d^2k_{0\perp}\ \left(\alpha_s(k_{0\perp}^2)\alpha_s(k_{1\perp}^2)\right)^{1/2}\left(\alpha_s(k_{0\perp}^2)\alpha_s(k_{2\perp}^2)\right)^{1/2}\\ &\times\frac{3F(\mathbf{k}_{0\perp},\mathbf{k}_{1\perp})3F(\mathbf{k}_{0\perp},\mathbf{k}_{2\perp})}{(k_{0\perp}^2+\mu_g^2)(k_{1\perp}^2+\mu_g^2)(k_{2\perp}^2+\mu_g^2)}\ V_{gg\to f_0(1500)}(\mathbf{k}_{1\perp},\mathbf{k}_{2\perp})\,.\end{aligned} \tag{1.48}$$

At high energy and $y \approx 0$ the four-momentum transfers can be calculated as:
$t_1 = -(\mathbf{k}_{0\perp}+\mathbf{k}_{1\perp})^2$, $t_2 = -(\mathbf{k}_{0\perp}-\mathbf{k}_{2\perp})^2$.
At low energy and/or $y \neq 0$ the kinematics is slightly more complicated. Let us define effective four-vector transfers:

$$\begin{aligned} q_1 &= (p_1'-p_1) = (q_{10},q_{1x},q_{1y},q_{1z})\,,\\ q_2 &= (p_2'-p_2) = (q_{20},q_{2x},q_{2y},q_{2z})\,. \end{aligned} \tag{1.49}$$

Then $t_1 \equiv q_1^2 = q_{1\|}^2 + q_{1\perp}^2$ and $t_2 \equiv q_2^2 = q_{2\|}^2 + q_{2\perp}^2$. Close to threshold the longitudinal components $q_{1\|}^2 = q_{10}^2 - q_{1z}^2 \ll 0$ and $q_{2\|}^2 = q_{20}^2 - q_{2z}^2 \ll 0$. Then the amplitude (1.48) must be corrected. Then also four-vectors of exchanged gluons (k_0, k_1 and k_2) cannot be purely transverse and longitudinal components must be included as well. To estimate the effect we use formula (1.48) [10] but modify the transferred four momenta of gluons entering the $g^*g^* \to f_0(1500)$ production vertex:

$$\begin{aligned} k_1 &= (0,\mathbf{k}_{1\perp},0) \to (q_{10},\mathbf{k}_{1\perp},q_{1z})\,,\\ k_2 &= (0,\mathbf{k}_{2\perp},0) \to (q_{20},\mathbf{k}_{2\perp},q_{2z}) \end{aligned} \tag{1.50}$$

and leave k_0 purely transverse. This procedure is a bit arbitrary but comparing results obtained with formula (1.48) with that from the formula with modified four-momenta would allow to estimate related uncertainties.

[10] It would be more appropriate to calculate in this case a four-dimensional integral instead of the two-dimensional one.

We write the vertex function $gg \to f_0(1500)$ in the following tensorial form [11]:

$$V(k_1,k_2) = C_{f_0(1500)\to gg}\, g_{\mu\nu} k_1^\mu k_2^\nu \,. \tag{1.51}$$

The normalization factor is obtained from the decay of $f_0(1500)$ into two soft gluons; see (1.39).

The amplitudes discussed here involve transverse momenta in the infra-red region. Then a prescription how to extend the perturbative $\alpha_s(k_\perp^2)$ dependence to a nonperturbative region of small gluon virtualities is unavoidable. In the following $\alpha_s(k_\perp^2)$ is obtained from an analytic freezing proposed by Shirkov and Solovtsov [112].

1.4.4 Central diffractive mechanism with intermediate pionic triangle

The $f_0(1500) \to \pi\pi$ is the second most probable decay channel [96]. As a consequence the mechanism with an intermediate pionic triangle shown in Fig.1.19 may play important role in the exclusive production of $f_0(1500)$. It is relatively easy to estimate the contribution of this mechanism at high energies. Here we shall make an estimate of the corresponding cross section not far from the threshold, where the situation is slightly more complicated.

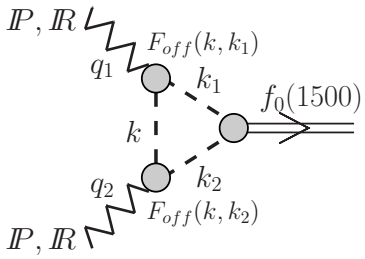

Figure 1.19: A sketch of the central diffractive mechanism with pionic loop for exclusive production of the glueball candidate $f_0(1500)$ meson. Some kinematical variables are shown explicitly.

The amplitude of the process $pp \to ppf_0(1500)$ sketched in Fig.1.16 (b) can be written in a simplified form as

$$\begin{aligned}\mathcal{M}_{\lambda_a\lambda_b\to\lambda_1\lambda_2 M}(y,p_{1\perp},p_{2\perp},\phi_{12}) \;&\approx\; \tilde{T}_{\boldsymbol{P}\boldsymbol{P}M}(q_1,q_2,p_M)\, M(s_{1,eff},t_1)\, M(s_{2,eff},t_2)\, \delta_{\lambda_1\lambda_a}\delta_{\lambda_2\lambda_b} \\ &\quad \times F_{cont}(s_{1,eff})\, F_{cont}(s_{2,eff})\,,\end{aligned} \tag{1.52}$$

where the Regge (sub)amplitudes

$$\begin{aligned}M(s_{i,eff},t_i) \;&=\; i\, s_{i,eff}\, C_{\boldsymbol{P}}^{\pi p} \left(\frac{s_{i,eff}}{s_0}\right)^{\alpha_{I\!P}(t_i)-1} \exp\left(\frac{B_{\boldsymbol{P}}^{\pi N}}{2} t_i\right) \\ &\quad + \eta_{\boldsymbol{R}}\, s_{i,eff}\, C_{\boldsymbol{R}}^{\pi p} \left(\frac{s_{i,eff}}{s_0}\right)^{\alpha_{I\!R}(t_i)-1} \exp\left(\frac{B_{\boldsymbol{R}}^{\pi N}}{2} t_i\right).\end{aligned} \tag{1.53}$$

The delta functions are related to helicity conservation in hadronic processes. While the pomeron (sub)amplitudes are dominantly imaginary, the reggeon (sub)amplitudes have both real and imaginary parts ($\eta_{\boldsymbol{R}} \approx i-1$). In the formula above we use the parameters (see [113, 114]) of the Regge trajectories (2.12). The strength parameters for the πN scattering fitted to the corresponding total cross sections [113]: $C_{\boldsymbol{P}}^{\pi p} = 13.63$ mb and $C_{\boldsymbol{R}}^{\pi p} = (27.56+36.02)/2$ mb [12]. At not too high

[11] In general, another tensorial forms are also possible. This may depend on the structure of the considered meson. In principle, the details depend on the form of the vertex. To avoid uncertainties in the k_t-factorization approach we work in the on-shell approximation. In the on-shell approximation (or infinitely heavy meson approximation) the vertex is expressed through decay width and all vertices should be equivalent. Even if the off-shell effects are included we do not expect very different energy dependence of the cross section for different tensorial forms as due to kinematics only small virtualities of gluons enter into game.

[12] We take average value for the $\pi^+ p$ and $\pi^- p$ scattering.

energies the slope parameter $B_{\boldsymbol{P}}^{\pi N} = B_{\boldsymbol{R}}^{\pi N} \approx 6\,\mathrm{GeV}^{-2}$. The subchannel Mandelstam variable $s_{1,eff}$ and $s_{2,eff}$ are related to center-of-mass energies of relevant πN subsystem. In principle, they are functions of pion-four momenta in the triangle: $s_{1,eff} = s_{1,eff}(k, k_1, p_1)$ and $s_{2,eff} = s_{2,eff}(k, k_2, p_2)$ and in general should be put inside of the triangle function $\tilde{T}_{\boldsymbol{P}\boldsymbol{P}f_0}(q_1, q_2, p_M)$ which depend on the three-body kinematics, i.e. on four-momenta of the two exchanged pomerons (in general the pomeron-reggeon, the reggeon-pomeron or the reggeon-reggeon). In order to simplify the calculation we take instead average values as

$$s_{1,eff} = (p_1 + p_M/2)^2\,, \qquad s_{2,eff} = (p_2 + p_M/2)^2\,. \tag{1.54}$$

The factors F_{cont} in (1.52) are added to cut off the low-energy region of relevant πN subsystem, where the naive Regge parametrisation does not apply. We parametrise them in terms of purely phenomenological smooth cut-off correction factor (2.20); see Section 2.2. Here we take $W_0 = 2$ GeV and $a_0 = 0.1$ GeV. The parameter W_0 gives the position of the cut and parameter a_0 describes how sharp is the cut off. However, the latter parameter can have significant influence on the numerics.

The effective Regge parametrisations of πN interactions [113] are for both colliding particles being on-mass-shell. In our case the triangle pions are off-mass-shell. We "correct" the Regge strength parameters by multiplying by two vertex form factors $F_{off}(k, k_i)$ (see Fig.1.19). We take them in the following factorized form:

$$F_{off}(k, k_i) = \exp\left(-|k^2 - m_\pi^2|/\Lambda_{off}^2\right) \exp\left(-|k_i^2 - m_\pi^2|/\Lambda_{off}^2\right)\,, \tag{1.55}$$

where Λ_{off} is in principle a free parameter. In the calculation shown in the result section we shall take $\Lambda_{off} = 1$ GeV. The dependence on triangle four-momenta forces us to merge the form factors inside the triangle integration which leads to a modified pion-triangle function:

$$\tilde{T}_{\boldsymbol{P}\boldsymbol{P}M}(q_1, q_2, p_M) = \int \frac{d^4k}{(2\pi)^4} \hat{T}(k; q_1, q_2, p_M) F_{off}(k, k_1) F_{off}(k, k_2)\,, \tag{1.56}$$

where standard triangle integrand $\hat{T}(k; q_1, q_2, p_M)$ reads

$$\hat{T}(k; q_1, q_2, p_M) = \frac{F(q_1, k_1, k)}{(q_1 - k)^2 - m_\pi^2 + i\epsilon} \frac{F(q_2, k_2, k)}{(q_2 + k)^2 - m_\pi^2 + i\epsilon} \frac{g_{\pi\pi M}\, F(k_1, k_2, p_M)}{k^2 - m_\pi^2 + i\epsilon}\,. \tag{1.57}$$

In addition to three pion propagators we have written three vertex form factors which are functions of four momenta of corresponding legs. In principle, these functions are relatively well known for space-like pions. We parametrise the triangle-vertex form factors in the following factorized exponential form

$$\begin{aligned} F(q_1, k_1, k) &= \exp\left(-|k_1^2 - m_\pi^2|/\Lambda_\pi^2\right) \exp\left(-|k^2 - m_\pi^2|/\Lambda_\pi^2\right)\,, \\ F(q_2, k_2, k) &= \exp\left(-|k_2^2 - m_\pi^2|/\Lambda_\pi^2\right) \exp\left(-|k^2 - m_\pi^2|/\Lambda_\pi^2\right)\,, \\ F(k_1, k_2, p_M) &= \exp\left(-|k_1^2 - m_\pi^2|/\Lambda_\pi^2\right) \exp\left(-|k_2^2 - m_\pi^2|/\Lambda_\pi^2\right)\,. \end{aligned} \tag{1.58}$$

In this factorized form each exponent is associated with individual leg in the vertex. Such form factors (exponents) are normalized to unity when pions in the loop are on-mass shell. Please note that we symmetrically (modulus in (1.58)) damp configurations above and below pion-mass shell. Λ_π is related to the size of the pions in the triangle. It is natural to expect: $\Lambda_\pi < \Lambda_{off}$. In the calculation presented here we shall take $\Lambda_\pi = 0.5$ GeV. Since the configurations close to the mass shells give the biggest contributions the sensitivity to the actual value of the form factor F (see Eqs.(1.57) and (1.58)) is not substantial. The $g_{\pi\pi M}$ coupling constant can be calculated from the corresponding partial decay width; see (1.28).

Calculating the triangle function for running kinematics of the $p_a p_b \to p_1 p_2 f_0(1500)$ process (each point of the phase space) is in practice impossible. We calculate numerically the triangle function for:

$$\begin{aligned} q_1 &\to \left(\langle q_{10} \rangle_{y=0}, 0, 0, \langle q_{1z} \rangle_{y=0} \right) , \\ q_2 &\to \left(\langle q_{20} \rangle_{y=0}, 0, 0, \langle q_{2z} \rangle_{y=0} \right) . \end{aligned} \tag{1.59}$$

Transverse components are on average small and are neglected in the present approximation. Close to threshold $|\langle q_{10} \rangle_{y=0}| \neq |\langle q_{1z} \rangle_{y=0}|$ and $|\langle q_{20} \rangle_{y=0}| \neq |\langle q_{2z} \rangle_{y=0}|$.

1.5 Results

1.5.1 Gluonic QCD mechanism

Let us start with the QCD mechanism relevant at higher energies. We wish to present differential distributions in x_F, t_1 or t_2 and relative azimuthal angle ϕ between outgoing nucleons. In the following we shall assume:

$$\Gamma_{f_0(1500) \to gg} = \Gamma_{f_0(1500), tot} , \tag{1.60}$$

where $\Gamma_{f_0(1500), tot} = 0.109$ GeV [96]. This assumption means that our differential distributions mean upper limit of the cross section. If the fractional branching ratio is known, our results should be multiplied by its value. There are almost no absolutely normalized experimental data on exclusive $f_0(1500)$ production in the literature, except of Ref. [115]. The absolutely normalized data of the ABCDHW Collaboration [116] put emphasis rather on $f_2(1270)$ meson production. In principle, some (model-dependent) information on glueball wave function could be obtained from radiative decays $J/\psi \to \gamma f_0(1500)$ and $\Upsilon \to \gamma f_0(1500)$ [117]. The present data are not good enough to provide a detailed information on coupling of gluons to $f_0(1500)$ meson.

In Fig.1.20 we show as example distribution in Feynman $x_{F,M}$ for the Kharzeev-Levin UGDF (the solid lines) and the mixed distribution KL$\otimes$Gaussian (the dashed lines) for several values of collision energy in the interval $\sqrt{s} = 10 - 50$ GeV and 100 GeV. In general, the higher collision energy the larger cross section. With the rise of the initial energy the cross section becomes peaked more and more at $x_{F,M} \sim 0$. The mixed UGDF produces slightly broader distribution in $x_{F,M}$.

In Fig.1.21 we present corresponding distributions in $|t| = |t_1|, |t_2|$. The slope depends on UGDF used, but for a given UGDF is almost energy independent.

In Fig. 1.22 we present corresponding distributions in relative azimuthal angle between outgoing protons or proton and antiproton [13]. These distributions have maximum when outgoing nucleons are back-to-back ($\phi_{pp} = \pi$) and the shape seems to be only weekly energy dependent.

Finally, in Fig. 1.23 we present different differential observables (in y_M meson rapidity, $p_{1\perp}$ proton transverse momenta as well as in ϕ_{pp} relative azimuthal angle between outgoing protons) for the central exclusive production of $f_0(1500)$ meson in the two-gluon impact factor approach at several center-of-mass energies $\sqrt{s}$. As explained in the figure caption we show results for both transverse and longitudinal components as well as the distributions for transverse components only in the $g^* g^* \to f_0(1500)$ vertex (1.51). As can be seen from the left panel distributions for both transverse and longitudinal components are placed at midrapidity region $y_M \approx 0$. The distributions for transverse components only are placed at larger region of y_M. These distributions have maximum when outgoing nucleons are back-to-back. Again the shape seems to be only weekly energy dependent.

[13] The QCD gluonic mechanism is of course charge independent.

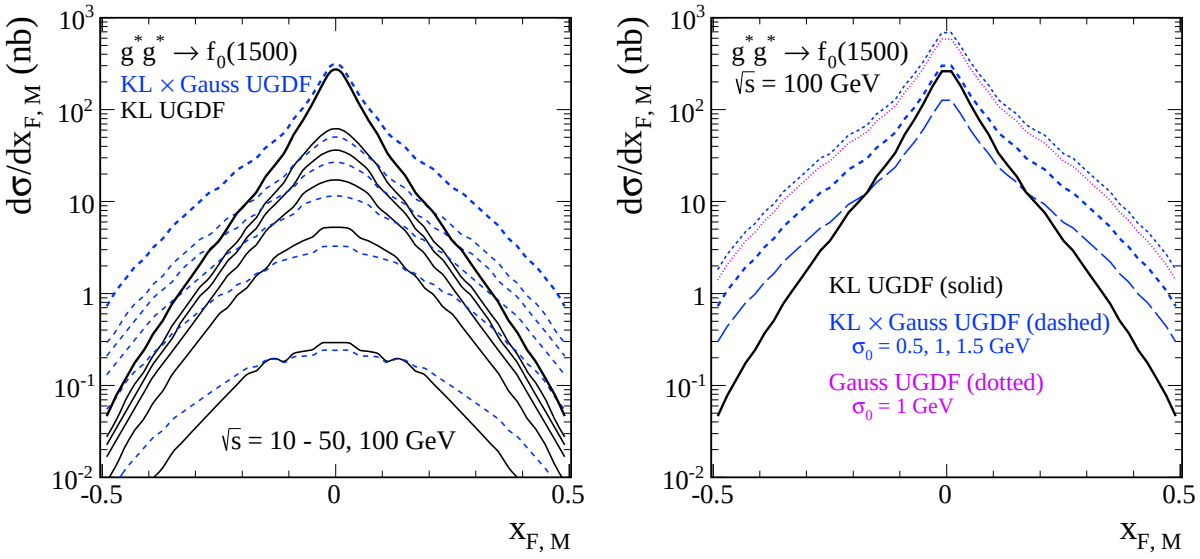

Figure 1.20: The distribution in Feynman $x_{F,M}$ for the central exclusive $f_0(1500)$ meson production at $\sqrt{s}$ = 10, 20, 30, 40, 50 and 100 GeV (from bottom to top). In the calculation the Kharzeev-Levin UGDF (the black solid lines) and the mixed distribution KL⊗Gauss with the parameter $\sigma_0 = 1$ GeV (the blue dashed lines) were used. In the right panel we compare the KL⊗Gauss (the short dashed, dashed and long-dashed curves correspond to calculations with $\sigma_0 = 0.5, 1$ and 1.5 GeV) and the Gauss UGDFs (the dotted line, $\sigma_0 = 1$ GeV) with the KL UGDF at $\sqrt{s} = 100$ GeV.

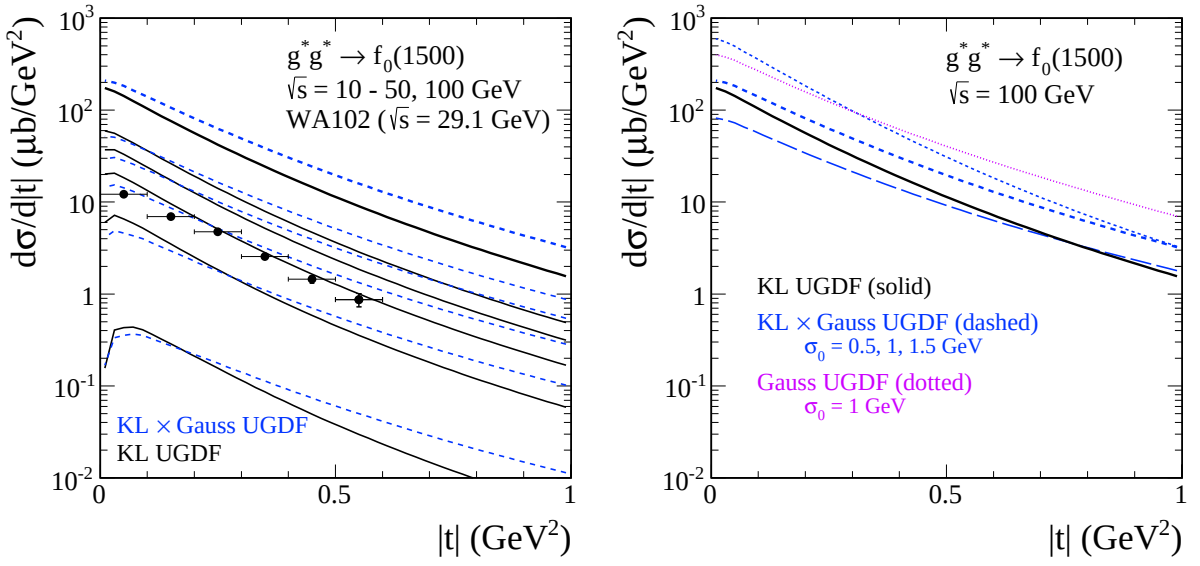

Figure 1.21: The $|t|$ distributions for $f_0(1500)$ meson production at $\sqrt{s}$ = 10, 20, 30, 40, 50 and 100 GeV (from bottom to top) for the Kharzeev-Levin UGDF (the black solid lines) and the mixed distribution KL⊗Gauss (the blue dashed lines). In the right panel we compare the KL⊗Gauss and Gauss UGDFs obtained for different σ_0 parameters with the KL UGDF at $\sqrt{s} = 100$ GeV. The notation here is the same as in Fig. 1.20. The WA102 experimental data points from [90] have been normalized to the mean value of the total cross section given in Table 3.2 as obtained from [115].

1.5.2 Diffractive versus pion-pion mechanism

What about the pion-pion fusion mechanism? Can it dominate over the gluonic mechanism discussed in the previous subsection? In Fig.1.24 we show the integrated cross section for the exclusive $f_0(1500)$ elastic production ($p\bar{p} \to pf_0(1500)\bar{p}$) and for double charge exchange reaction ($p\bar{p} \to nf_0(1500)\bar{n}$).

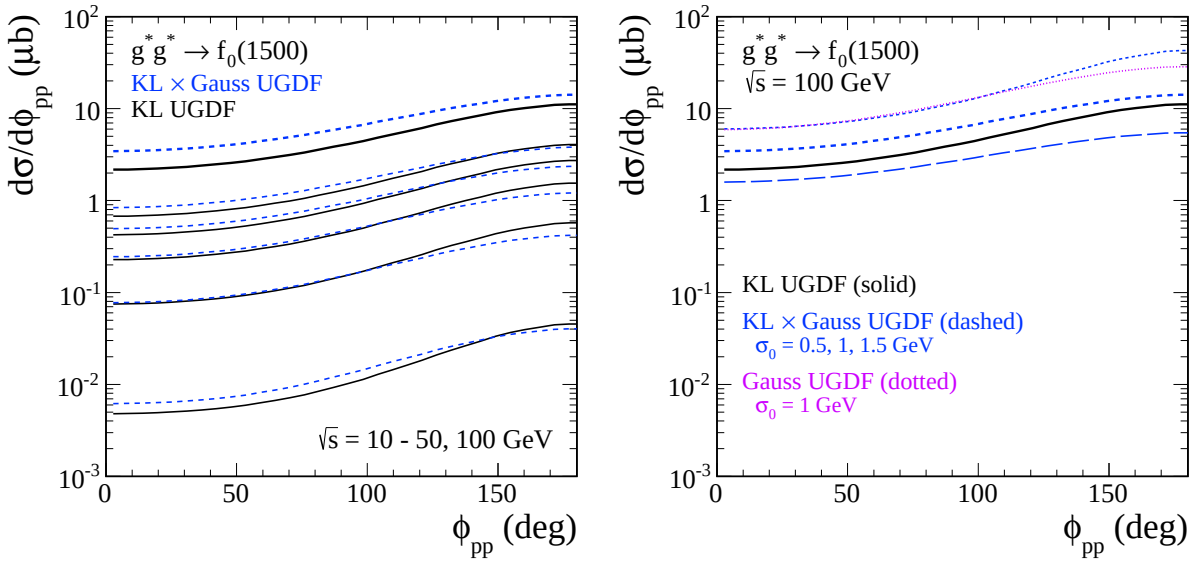

Figure 1.22: Distribution in relative azimuthal angle between outgoing nucleons at $\sqrt{s}$ = 10, 20, 30, 40, 50 and 100 GeV (from bottom to top) for the Kharzeev-Levin UGDF (the black solid lines) and the mixed distribution KL⊗Gauss (the blue dashed lines). In the right panel we compare the KL⊗Gauss and Gauss UGDFs obtained for different σ_0 parameters with the KL UGDF at $\sqrt{s} = 100$ GeV. The notation here is the same as in Fig.1.20.

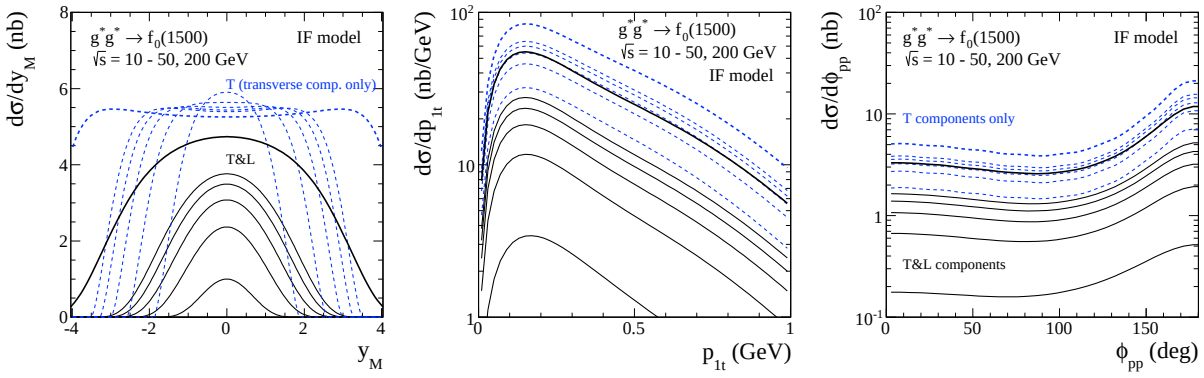

Figure 1.23: The differential observables for the central exclusive production of $f_0(1500)$ meson by two-gluon impact factor approach at $\sqrt{s}$ = 10, 20, 30, 40, 50 and 200 GeV (from bottom to top). We show the distributions to the cross sections with transverse components only (the upper blue dashed lines) and with both transverse and longitudinal components (the lower black solid lines).

The thick solid line represents the pion-pion component calculated with monopole vertex form factors (1.11) with $\Lambda = 0.8$ GeV (lower) and $\Lambda = 1.2$ GeV (upper). The difference between the lower and upper curves represents uncertainties on the pion-pion component. The pion-pion contribution grows quickly from the threshold, takes maximum at $\sqrt{s} \approx 6 - 7$ GeV and then slowly drops with increasing energy. The gluonic contribution calculated with unintegrated gluon distributions drops with decreasing energy towards the kinematical threshold and seems to be about order of magnitude smaller than the pion-pion component at $\sqrt{s} = 10$ GeV. We show the result with the Kharzeev-Levin UGDF (dashed line) which includes gluon saturation effects relevant for small-x, the Khoze-Martin-Ryskin UGDF (dotted line) used for the exclusive production of the Higgs boson and the result with the "mixed prescription" (KL⊗Gaussian) for different values of the σ_0 parameter: 0.5 GeV (the upper thin solid line), 1 GeV (the lower thin solid line). In the latter case results rather strongly depend on the value of the smearing parameter. The experimental data point of the WA102 Collaboration from Ref. [115] which lies between the results obtained with "KL" and "mixed" off-diagonal UGDFs. For comparison, the

(violet) thick long-dashed line corresponds to the second diffractive mechanism with pionic triangle contribution which is above the WA102 experimental data point. This is probably because of absorption effects not included in the present calculation. This contribution stays below the pion-pion fusion contribution at the GSI HESR energies.

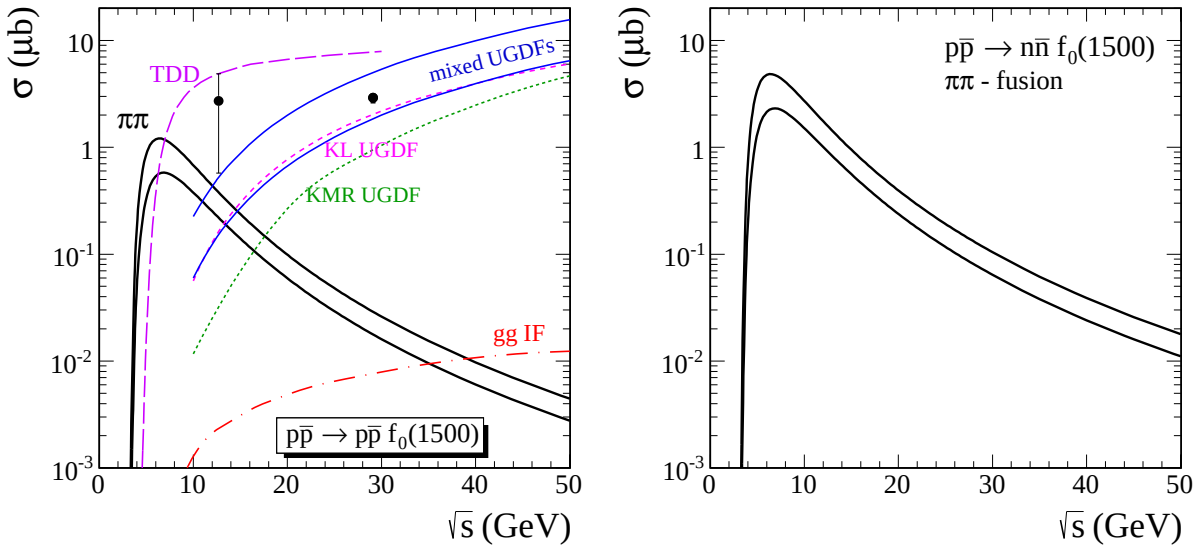

Figure 1.24: The integrated cross section as a function of the center of mass energy for $p\bar{p} \to p\bar{p}f_0(1500)$ (left panel) and $p\bar{p} \to n\bar{n}f_0(1500)$ (right panel) reactions. The thick solid lines are for pion-pion MEC contribution ($\Lambda = 0.8, 1.2$ GeV - the lower and upper curves, respectively), the dashed line is for QCD diffractive contribution obtained with the Kharzeev-Levin UGDF, the dotted line for the KMR approach and the (blue) thin solid lines are for "mixed" UGDF (KL⊗Gaussian) with $\sigma_0 = 0.5, 1$ GeV (the upper and lower curves, respectively). The dash-dotted line represents the two-gluon impact factor result. The thick long-dashed line corresponds to the second diffractive mechanism with intermediate pionic triangle. The experimental data point at $\sqrt{s} = 29.1$ GeV is from Ref. [115] and the experimental point at $\sqrt{s} = 12.7$ GeV has been obtained from ratio of the cross section; see Table 3.1.

We calculate the gluonic contribution down to $\sqrt{s} = 10$ GeV. Extrapolating the gluonic component to even lower energies in terms of UGDFs seems rather unsure. At lower energies the two-gluon impact factor approach seems more relevant. The two-gluon impact factor approach result is even order of magnitude smaller than that calculated in the KMR approach (see the (red) lowest dash-dotted line in Fig. 1.24), so it seems that the diffractive contribution is completely negligible at the FAIR energies. Our calculation suggests that quite different energy dependence of the cross section may be expected in elastic and charge-exchange channels. Experimental studies at FAIR and J-PARC could shed more light on the glueball production mechanism.

1.5.3 Predictions for PANDA at HESR

Let us concentrate now on $p\bar{p}$ collisions at energies relevant for future experiments at HESR at the FAIR facility in GSI [27]. Here the pion-pion MEC (see Fig.1.15) seems to be the dominant mechanism, especially for the charge exchange reaction $p\bar{p} \to n\bar{n}f_0(1500)$. As discussed in the previous section the gluonic component can be there safely neglected.

Below we shall present cross sections for the $p\bar{p} \to n\bar{n}f_0(1500)$ reaction. The cross section for the $p\bar{p} \to p\bar{p}f_0(1500)$ reaction can be obtained by rescaling by the factor of $1/4$. In Fig.1.25 we show average values of t_1 (or t_2) for the two-pion MEC as a function of the center of mass energy. Close to threshold $\sqrt{s} = 2m_N + m_{f_0(1500)}$ the transferred four-momenta squared are the biggest, of the order of about 1.5 GeV^2. The bigger energy the smaller the transferred four-momenta squared. Therefore experiments close to threshold open a unique possibility to study physics of large transferred four-momenta squared at relatively small energies. This is a

quite new region, which was not studied so far in the literature.

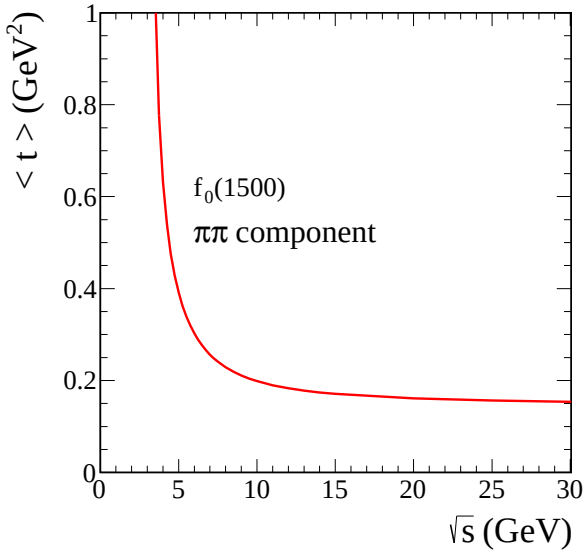

Figure 1.25: Average value of $< t_1 >=< t_2 >$ as a function of the center-of-mass collision energy for the two-pion exchange mechanism. In this calculation $\Lambda = 0.8$ GeV.

The maximal energy planned for the HESR is $\sqrt{s} = 5.5$ GeV. At this energy the phase space is still very limited. In Fig.1.26 (left panel) we show rapidity distribution of $f_0(1500)$ calculated including pion-pion fusion only. For comparison the rapidity of incoming antiproton and proton is 1.74 and -1.74, respectively. This means that in the center-of-mass system the $f_0(1500)$ - glueball is produced at midrapidities, on average between rapidities of outgoing nucleons. In the right panel we present distribution in the meson transverse momentum.

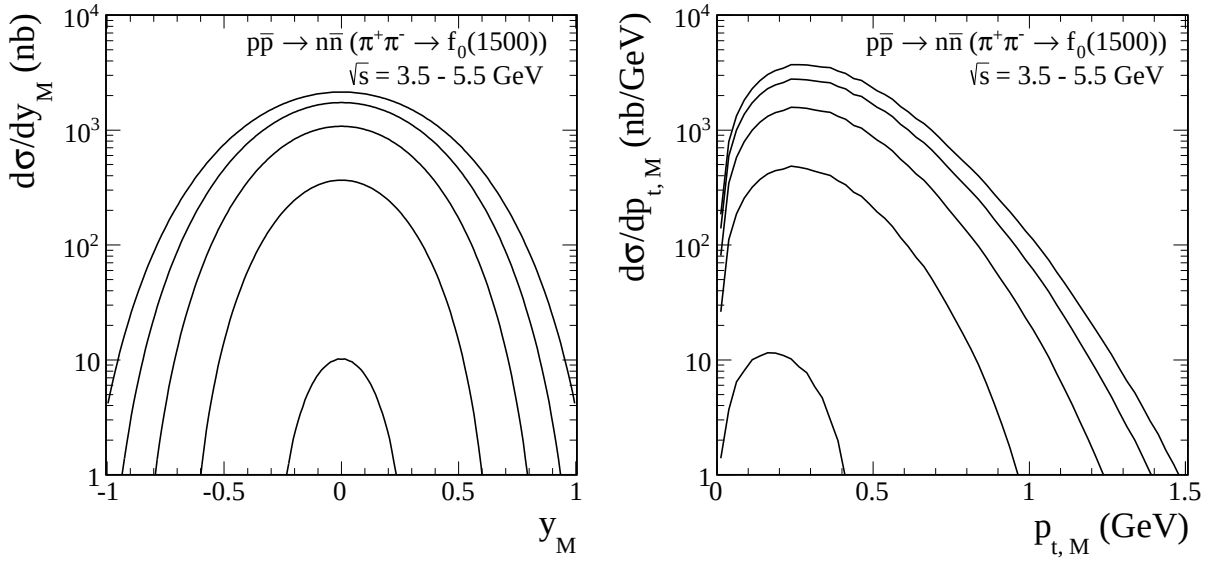

Figure 1.26: Rapidity y_M and transverse momentum $p_{\perp,M}$ distributions of $f_0(1500)$ meson produced in the reaction $p\bar{p} \to n\bar{n}f_0(1500)$ ($\pi^+\pi^-$ fusion only) at $\sqrt{s}$ = 3.5, 4.0, 4.5, 5.0, 5.5 GeV (from bottom to top). In this calculation $\Lambda = 1$ GeV.

In Fig.1.27 we show the transverse momentum distribution of neutrons or antineutrons (left panel) and the azimuthal angle correlation between outgoing hadrons (right panel) produced in the reaction $p\bar{p} \to n\bar{n}f_0(1500)$. The $p_\perp$ distribution depends on the πNN form factors $F_{\pi NN}(t_1)$ and $F_{\pi NN}(t_2)$. The preference for back-to-back configurations is caused merely by the

limitations of the phase space close to the threshold (the matrix element for pion-pion fusion is ϕ-independent). This correlation vanishes in the limit of infinite energy. At high energy, where the phase space limitations are small, the distributions are isotropic, there is no dependence on azimuthal angle. In practice far from the threshold the distribution becomes almost constant in azimuth. This has to be contrasted with similar distributions for pomeron-pomeron fusion shown in Fig.1.22 which are clearly peaked for the back-to-back configurations. Therefore a deviation from the constant distribution in relative azimuthal angle for the highest HESR energy of $\sqrt{s}$ = 5.5 GeV for $p\bar{p} \to p f_0(1500)\bar{p}$ can be a signal of the gluon induced processes and/or the presence of subleading reggeon exchanges, e.g. $\rho\rho$. It is not well understood what happens with the gluon induced diffractive processes when going down to intermediate ($\sqrt{s}$ = 5-10 GeV) energies. Our calculations shows, however, that the diffractive component is negligible compared to the pion-pion fusion at $\sqrt{s} < 10$ GeV. Possible future experiments performed at J-PARC could bring some new insights into this issue by studying distortions (probably very small) from the pion-pion fusion mechanism. In Fig.1.28 we show we show the distributions in transferred four-momentum squared (t) between the initial and final nucleons at $\sqrt{s}$ = 3.5, 4.0, 4.5, 5.0, 5.5 GeV as well as two-dimensional distribution in (t_1, t_2) at $\sqrt{s} = 5.5$ GeV.

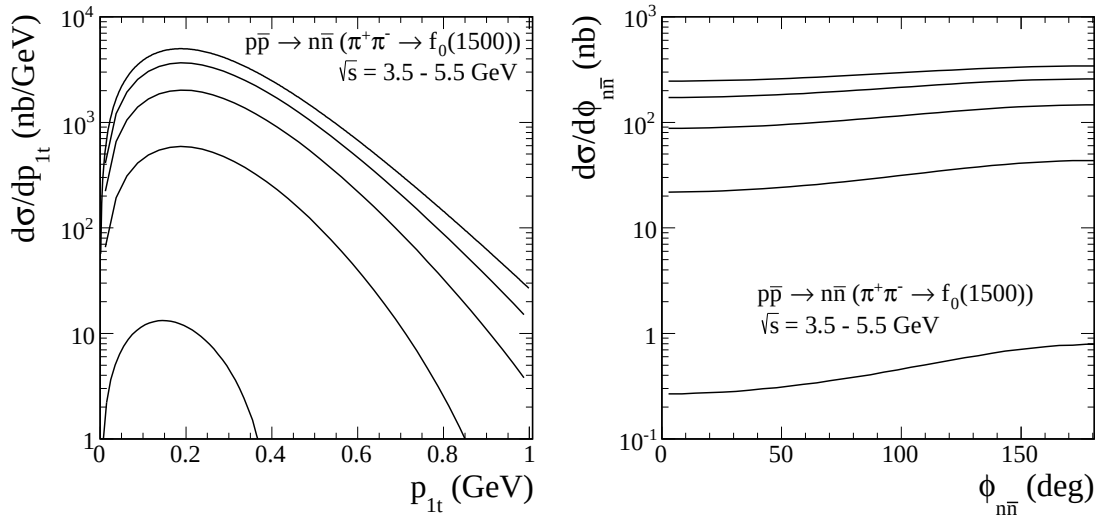

Figure 1.27: Transverse momentum distribution of neutrons or antineutrons (left panel) and azimuthal angle correlations between outgoing nucleons (right panel) produced in the reaction $p\bar{p} \to n\bar{n}f_0(1500)$ ($\pi^+\pi^-$ fusion only) at $\sqrt{s}$ = 3.5, 4.0, 4.5, 5.0, 5.5 GeV (from bottom to top). In this calculation $\Lambda = 1$ GeV.

Up to now we have neglected interference between pion-pion and pomeron-pomeron contributions (for the same final channel). This effect may be potentially important when both components are of the same order of magnitude. At J-PARC energies there could be, in principle, some small interference effect [14] While the pomeron-pomeron contribution is dominantly nucleon helicity preserving the situation for pion-pion fusion is more complicated. In the latter case we define 4 classes of contributions with respect to the nucleon helicities: cc (both helicities conserved), cf (first conserved, second flipped), fc (first flipped, second conserved) and ff (both helicities flipped). The corresponding ratios of individual contributions to the sum of all contributions are shown in Fig.1.29. In practice, only the cc $\pi\pi$ contribution may potentially interfere with the gluonic one. From the figure one can conclude that this can happen only when both transverse momenta of the final nucleons are small. We shall leave numerical studies of the interference effect for future investigations, when experimental details of such measurements will be better known; but already now one can expect them to be rather small.

Now we wish to show the size of the central diffractive mechanism with intermediate pionic triangle (TDD) component at the GSI HESR energy range. In Fig.1.30 we compare it with

[14] At the PANDA energies the problem is rather academic as the diffractive component can be neglected.

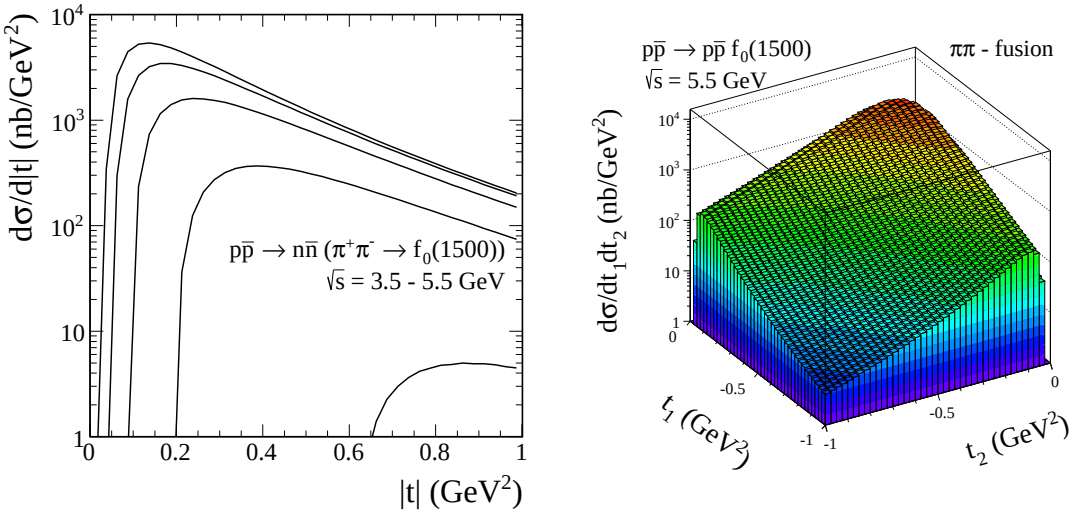

Figure 1.28: The t distributions for $f_0(1500)$ meson production in the reaction $p\bar{p} \to n\bar{n}f_0(1500)$ ($\pi^+\pi^-$ fusion) at $\sqrt{s}$ = 3.5, 4.0, 4.5, 5.0, 5.5 GeV (from bottom to top). In the right panel we show two-dimensional distribution in (t_1, t_2) space at $\sqrt{s} = 5.5$ GeV. In this calculation $\Lambda = 1$ GeV.

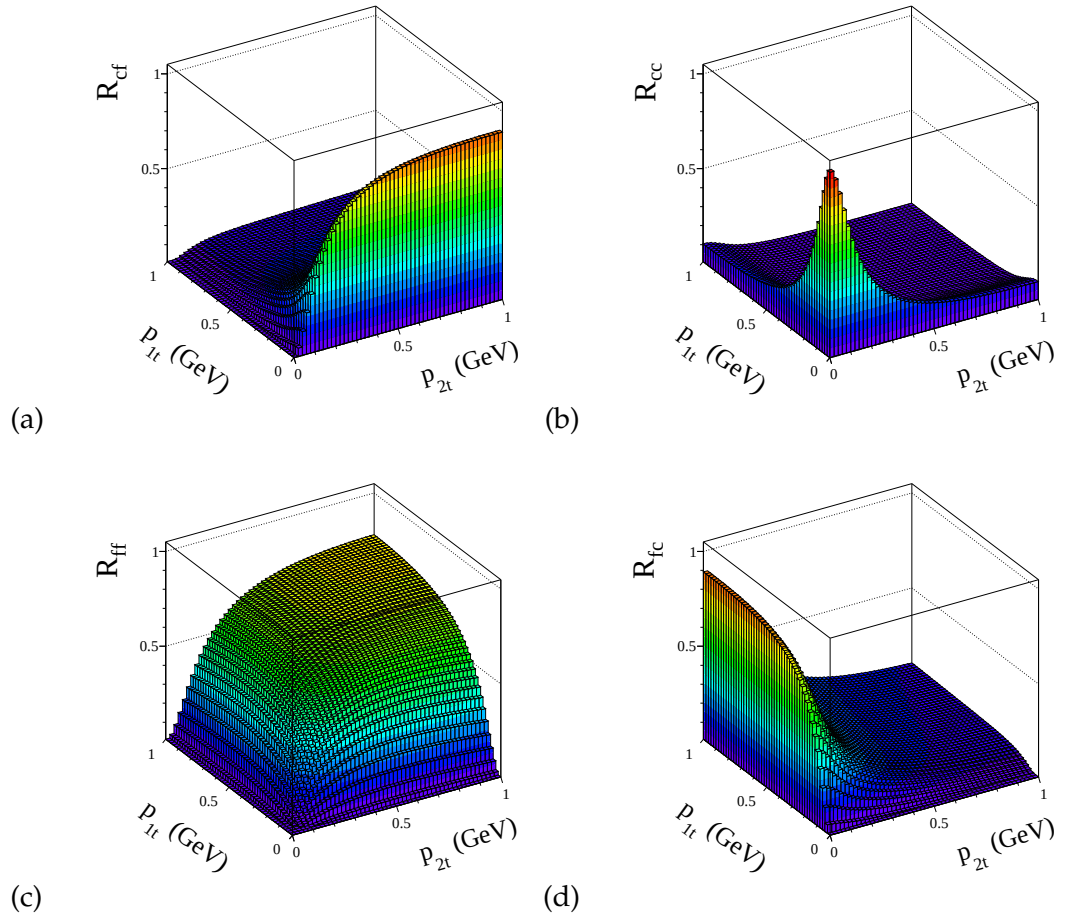

Figure 1.29: Helicity decomposition of the cross section on the (p_{1t}, p_{2t}) plane at $\sqrt{s} = 10$ GeV. The corresponding ratios of individual contributions to the sum of all contributions are shown: R_{cf} (panel (a)), R_{cc} (panel (b)), R_{ff} (panel (c)), R_{fc} (panel (d)).

the pion-pion fusion component. The TDD component vanishes quickly with decreasing energy and stays below the pion-pion fusion component for the HESR energy range. The quick decrease

of the cross section is caused mainly by the $F_{cont}(s_{1,eff})$ and $F_{cont}(s_{2,eff})$ factors (2.20) in Eq.(1.52) and reflects smallness of πN subchannel energies.

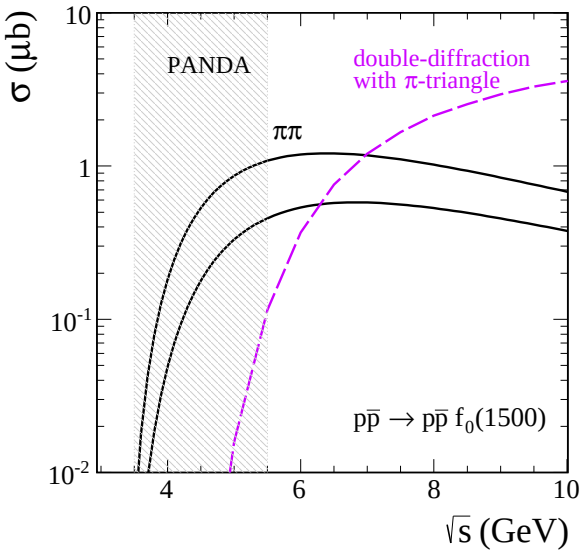

Figure 1.30: Comparison of the pion-pion fusion component (the lower and upper curves for $\Lambda = 0.8$ GeV and 1.2 GeV, respectively) and the central diffractive one with the intermediate pionic triangle (dashed line). The details concerning the central diffractive component (the violet long-dashed line) are explained in Section 1.4.4. The vertical gray band shows the range of the center-of-mass energy available by the PANDA experiment at the FAIR in Darmstadt.

1.6 Measurement of $f_0(1500)$ meson via $f_0(1500) \to \pi^+\pi^-$ decay

In the previous subsection we have shown that in the PANDA energy range the pion-pion fusion is the dominant reaction mechanism for the production of the glueball candidate $f_0(1500)$. Up to now we have calculated the cross section for production of $f_0(1500)$ meson – a process with three particles (p, $\bar{p}$ and $f_0(1500)$) in the final state. In practice one must select a given decay channel of $f_0(1500)$ meson. There are a few options:

- $\pi\pi$ decay ($\pi^+\pi^-$ or $\pi^0\pi^0$) – Is attractive due to its simplicity but may have a large background. The branching ratio $f_0(1500) \to \pi\pi$ mode is $\mathcal{BR}(f_0(1500) \to \pi\pi) = (34.9 \pm 2.3)\%$ [96].

- $\pi\pi\pi\pi$ decay ($4\pi^0$, $2\pi^+2\pi^-$, $\rho\rho$, $\pi(1300)\pi$, $a_1(1260)\pi$) – Requires more complicated analysis but may have smaller background. All investigations agree that the 4π decay mode represents about half of the $f_0(1500)$ decay width $\mathcal{BR}(f_0(1500) \to 4\pi) = (49.5 \pm 3.3)\%$ [96]. The $p\bar{p}$, $p\bar{n}/n\bar{p}$ measurements show a single enhancement in the invariant 4π mass spectra, which is resolved into $f_0(1370)$ and $f_0(1500)$ mesons [118, 119]. The data on 4π from central production [120] require both resonances, but disagree on the relative content of $\rho\rho$ and $\sigma\sigma$ in 4π. The $p\bar{p} \to p\bar{p}\pi\pi\pi\pi$ reaction may be more favourable as far as the signal-to-background ratio is considered. Unfortunately theoretical calculation of background are not feasible in this case. It is not clear to us at present if the 6-body channel can be measured by the PANDA detector at FAIR.

- $K\bar{K}$ decay – The relevant branching fraction $\mathcal{BR}(f_0(1500) \to K\bar{K}) = (8.6 \pm 0.1)\%$ is smaller by a factor of about 4 than for the two-pion channel [96]. On the other hand the contribution from nucleon resonances is probably considerably smaller. There is, however, unreduceable contribution from the K^* exchange in the $\pi^0\pi^0 \to K^+K^-$ subprocess. The parameters for the latter reaction are less known than those for the $\pi^0\pi^0 \to \pi^+\pi^-$ subprocess.

- $\eta\eta$ or $\eta\eta'(958)$ decays – The relevant branching fractions $\mathcal{BR}(f_0(1500) \to \eta\eta) = (5.1 \pm 0.9)\%$ and $\mathcal{BR}(f_0(1500) \to \eta\eta') = (1.9 \pm 0.8)\%$ [96] are small but not negligible. These channels are considered to be promising places to look for glueballs since it is thought likely that glueballs will decay with the emission of η and η'; see [121].

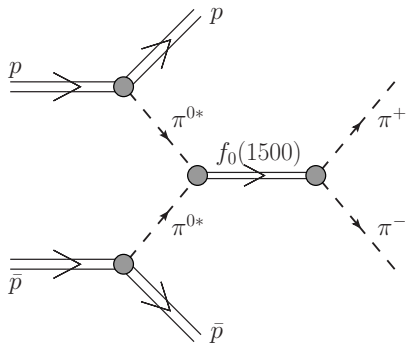

Figure 1.31: Representative diagram for the $2 \to 4$ reaction through the $f_0(1500)$ meson (scalar glueball candidate) in proton-(anti)proton collisions. The stars attached to π^0 mesons denote the fact that they are off-mass-shell.

We can write the Born amplitude as (1.8) with $\mathcal{M}^{\pi^{0*}\pi^{0*}\to\pi^+\pi^-}$ replaced by

$$\begin{aligned}\mathcal{M}^{\pi^{0*}\pi^{0*}\to f_0(1500)\to\pi^+\pi^-}(s_{34},t_1,t_2) &= g_{\pi\pi f_0}\frac{F_{f_0}(s_{34})F_{f_0}(s_{34})}{s_{34}-m^2_{f_0}+im_{f_0}\Gamma_{f_0(1500),tot}}\,g_{f_0\pi\pi} \\ &\times V_{\pi\pi\to f_0(1500)}(t_1,t_2)\,, \end{aligned} \tag{1.61}$$

where the off-shell $\Gamma^{\pi^*\pi^*\to f_0(1500)}$ vertex given in Section 1.4.1 is used and the $g_{\pi\pi M} = g_{M\pi\pi}$ coupling constant can be calculated from the corresponding partial decay width; see (1.28). We take the $V_{\pi\pi\to f_0(1500)}(t_1,t_2)$ vertex form factor (1.31). We have added an extra $F_{f_0}(s_{34})$ form factor taking into account that a variation of the $f_0\pi\pi$ coupling with off-shellness of the $f_0(1500)$ meson must be expected. A convenient parametrisation of such a form factor is the exponential form

$$F_{f_0}(s_{34}) = \exp\left(-\frac{(s_{34}-m^2_{f_0})^2}{\Lambda^4_{f_0}}\right) \tag{1.62}$$

or alternatively, we can use the form

$$F_{f_0}(s_{34}) = \frac{\Lambda^4_{f_0}}{(s_{34}-m^2_{f_0})^2+\Lambda^4_{f_0}} \tag{1.63}$$

with $\Lambda_{f_0} = 1$ GeV. Here the normalization condition $F_M(m^2_M)$ is clearly satisfied.

Let us consider now an estimate of the background to the $p\bar{p} \to p\bar{p}\pi^+\pi^-$ reaction. In Fig.1.31 we present our reaction of interest – the reaction which proceeds through the scalar resonance $f_0(1500)$. This reaction is viewed now as a process with four particles $(p, \bar{p}, \pi^+, \pi^-)$ in the final state. Unavoidably there exists a nonreduceable background to this reaction sketched in Fig. 1.32. We shall call the two first complex diagrams (a) as ρ-meson(reggeon) exchanges or $\pi\pi$-induced background for brevity and the diagrams (b) as the central diffractive exchanges. The underlying mechanism was proposed at high energies long ago in Ref. [122]. The central diffractive (reggeon and pomeron exchanges) mechanism as the two-pion continuum will be discussed in more details in Chapter 2.

The region of $W_{\pi\pi} \sim 1.5$ GeV is slightly above the region of application of the standard meson-exchange formalism and slightly below the region of application of high-energy Regge

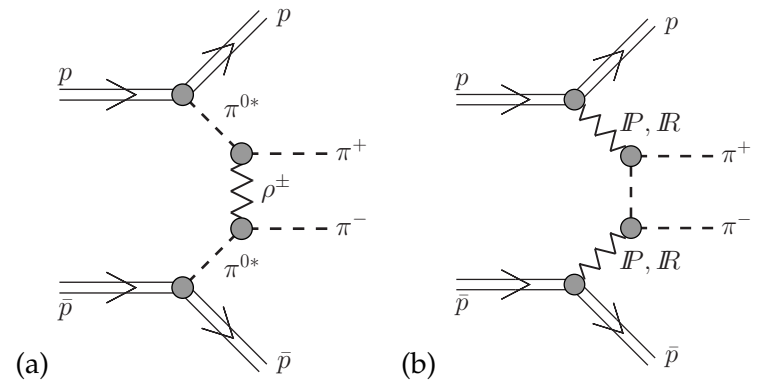

Figure 1.32: A sketch of the $2 \to 4$ amplitudes for the non-perturbative exclusive production of the $\pi^+\pi^-$ pair as an example of the background for the $f_0(1500)$ meson production. Diagram (a) represents the intermediate t-channel off-shell ρ-meson (reggeon) exchange mechanism and diagram (b) the central diffractive mechanism with an intermediate off-shell pion. In the latter mechanism both the leading pomeron ($I\!P$) and subleading reggeon ($I\!R$) exchanges are possible. At the highest PANDA center-of-mass energy $\sqrt{s} = 5.5$ GeV the two f_2-reggeon ($f_{2I\!R}$) exchanges is the dominant contribution.

approach. In principle, one should consider both approaches. In the ρ-meson exchange formalism the reduced amplitude for the $\pi^0\pi^0 \to \pi^+\pi^-$ process can be written as:

$$\begin{aligned}\mathcal{M}^{\rho-exchange}_{\pi^0\pi^0\to\pi^+\pi^-} &= g_{\pi\pi\rho}F_{\pi\pi\rho}(\hat{t})\frac{(q_1^\mu + p_3^\mu)P_{\mu\nu}(k_t)(q_2^\nu + p_4^\nu)}{\hat{t} - m_\rho^2 + im_\rho\Gamma_{\rho,tot}}g_{\pi\pi\rho}F_{\pi\pi\rho}(\hat{t}) \\ &+ g_{\pi\pi\rho}F_{\pi\pi\rho}(\hat{u})\frac{(q_1^\mu + p_4^\mu)P_{\mu\nu}(k_u)(q_2^\nu + p_3^\nu)}{\hat{u} - m_\rho^2 + im_\rho\Gamma_{\rho,tot}}g_{\pi\pi\rho}F_{\pi\pi\rho}(\hat{u})\,, \qquad (1.64)\end{aligned}$$

where $\hat{t} = k_t^2$, $\hat{u} = k_u^2$ and $P_{\mu\nu}(k) = -g_{\mu\nu} + k_\mu k_\nu / m_\rho^2$. The quantities $F_{\pi\pi\rho}(k^2)$ in (1.64) describe couplings of extended objects: pions and the exchanged ρ-meson. We parametrise them in the exponential form

$$F_{\pi\pi\rho}(k^2) = \exp\left(\frac{k^2 - m_\rho^2}{\Lambda^2}\right) = \exp\left(\frac{B_\rho^{\pi\pi}}{4}(k^2 - m_\rho^2)\right)\,. \qquad (1.65)$$

Consistent with the definition of the coupling constant the form factors are normalized to unity when ρ meson is on-mass-shell. We take $g^2_{\pi\pi\rho}/(4\pi) = 2.6$, which reproduces the ρ-meson decay width [96], and $\Lambda = 1$ GeV ($B_\rho^{\pi\pi} = 4\,\text{GeV}^{-2}$).

At larger pion-pion c.m. energies, $W_{\pi\pi} \gg W_{thr}$, one should use reggeons rather than mesons. The "reggeization" of the amplitude given in Eq. (1.64) is included here only approximately by a factor assuring asymptotically correct high energy dependence

$$\mathcal{F}(s_{34}, k^2) = \left(\frac{s_{34}}{s_{thr}}\right)^{\frac{2}{\pi}\arctan[(s_{34}-s_{thr})/\Lambda^2_{thr}](\alpha_{I\!R}(k^2)-1)}\,, \qquad (1.66)$$

where $\Lambda_{thr} = 4$ GeV and $\alpha_{I\!R}(0) = 0.5$ and $\alpha'_{I\!R} = 0.9\,\text{GeV}^{-2}$.

In the case of ρ-reggeon ($\rho_{I\!R}$) exchange the pion-pion scattering amplitude of the subprocess $\pi^0\pi^0 \to \pi^+\pi^-$ can be written as

$$\begin{aligned}\mathcal{M}^{\rho_{I\!R}-exchange}_{\pi^0\pi^0\to\pi^+\pi^-}(s_{34}, \hat{t}, \hat{u}) &= s_{34}\eta_{\rho_{I\!R}}C^{\pi\pi}_{\rho_{I\!R}}\left(\frac{s_{34}}{s_0}\right)^{\alpha_{I\!R}(\hat{t})-1}\exp\left(\frac{B^{\pi\pi}_{\rho_{I\!R}}}{2}\hat{t}\right) \\ &+ s_{34}\eta_{\rho_{I\!R}}C^{\pi\pi}_{\rho_{I\!R}}\left(\frac{s_{34}}{s_0}\right)^{\alpha_{I\!R}(\hat{u})-1}\exp\left(\frac{B^{\pi\pi}_{\rho_{I\!R}}}{2}\hat{u}\right)\,, \qquad (1.67)\end{aligned}$$

where the signature factor is $\eta_{\rho_{I\!R}} \approx i + 1$. We parametrised the vertex form factors in the exponential form used conveniently in the Regge phenomenology with the slope parameter

$B^{\pi\pi}_{\rho_{I\!R}} = 4 - 6$ GeV^{-2}. The reggeon trajectory parameters (2.12) we take from the phenomenology [113]. The strength parameter $C^{\pi\pi}_{\rho_{I\!R}}$ can be obtained assuming Regge factorization (see e.g. [111])

$$C^{\pi\pi}_{\rho_{I\!R}} = \frac{(C^{\pi N}_{\rho_{I\!R}})^2}{C^{NN}_{\rho_{I\!R}}} \tag{1.68}$$

and using the known strength parameters for the NN and πN scattering fitted to the corresponding total cross sections [113]. The corresponding value of strength parameters are collected in Table 2.1. In our case of pion-pion scattering energies of $W_{\pi\pi} = \sqrt{s_{34}} \sim 1.5$ GeV are of interest. Here a small modification of the Regge formula (1.67) may be in order. Consistent with meson-exchange formalism (spin-1 exchange) one may expect saturation of the $\pi^0\pi^0 \to \pi^+\pi^-$ cross section at lower energies. The following freezing of the energy factor in (1.67) seems a reasonable correction:

$$\left(\frac{s_{\pi\pi}}{s_0}\right)^{\alpha_\rho} \to \left(\frac{s_{freez}}{s_0}\right)^{\alpha_\rho}, \tag{1.69}$$

where $s_{freez} = W^2_{freez}$. One may expect $W_{freez} = 1.5 - 2$ GeV. The compatibility of the Regge formalism with low-energy approaches for pion-pion scattering was discussed in Ref. [123].

The $2 \to 2$ amplitudes (1.64) and (1.67) may be inserted into the $2 \to 4$ amplitude of Fig.1.32(a). When doing so we include in addition the correction factors due to off-shellness of incoming pions as was done for the $f_0(1500)$ meson using exponential form factors $F_{\pi^*}(t_{1,2})$ of the type (1.13). Now we can perform a genuine $2 \to 4$ calculation including four-body phase space; see Appendix A.

Before we go to our four-body reaction let us focus for a moment on $\pi^0\pi^0 \to \pi^+\pi^-$ on-shell scattering. In Fig.1.33 (left panel) we show the total (angle-integrated) cross section for the $\pi^0\pi^0 \to \pi^+\pi^-$ process. We include both the pion-pion rescattering contribution obtained from partial wave analysis (Section 1.1) as well as contribution from the Regge phenomenology relevant at higher energies. The parameters of the Regge amplitude for the $\pi\pi \to \pi\pi$ scattering were obtained from different isospin combinations of nucleon-(anti)nucleon, and pion-nucleon scattering assuming Regge factorization (1.68). For our case of $\pi^0\pi^0 \to \pi^+\pi^-$ reaction only the ρ-reggeon exchange is relevant. We show predictions for the Regge contribution for corrected ($W_0 = 1.5, 2$ GeV and $a_0 = 0.2$ GeV in Eq.(2.20)) extrapolations to low energies and for two values of the slope parameter: $B^{\pi\pi}_{\rho_{I\!R}} = 4$ GeV^{-2} (the long dashed lines) and $B^{\pi\pi}_{\rho_{I\!R}} = 6$ GeV^{-2} (the solid lines). A relatively good matching is achieved without extra fitting the model parameters. In the right panel we show angular dependence for corresponding contributions at $W_{\pi\pi} = 1.5$ GeV.

Now we discuss the results for the two-pion involved $\rho_{I\!R}$ (ρ-reggeon) exchange and the central diffractive exchanges contribution at $\sqrt{s} = 5.5$ GeV. We have checked that the ρ-meson exchange mechanism provides approximately the same results at $W_{\pi\pi} < 1.2$ GeV as the modified $\rho_{I\!R}$ exchange with $W_{freez} = 1.5 - 2$ GeV (see formula (1.69)). Therefore the modified reggeon-exchange calculation provides a realistic predictions in the broad range of pion-pion energies, both above and below the $f_0(1500)$ resonance. In Fig.1.34 we show the two-pion invariant mass distribution (left panel) and the distribution in pion rapidity (right panel). We show results of the central diffractive background calculating with the smooth cut-off formula (2.20) ($W_0 = 2$ GeV, $a_0 = 0.2$ GeV) and with the pion off-shell form factors ($\Lambda^2_{off,E} = 1.6$ GeV^2) as well as we use usual (mesonic) propagator of the off-shell pion. In this calculation the integration over whole phase space was done. We show the cross section for all ingredients in the amplitude included and for some exchanges separately. At low energies all individual cross sections when isolated are comparable, see also Table 2.2. The $I\!P I\!P$ and $f_{2R} f_{2R}$ components peak at midrapidities of pions, while the $I\!P f_{2R}$ and $f_{2R} I\!P$ components at backward and forward pion rapidities, respectively. They strongly interfere leading to increase of the cross section.

In Fig.1.35 we show two-pion invariant mass distribution. In this calculation the integration over whole phase space was done. The red solid line corresponds to our resonance contribution calculated without (the dotted line) and with (the solid (1.62) and long-dashed (1.63)

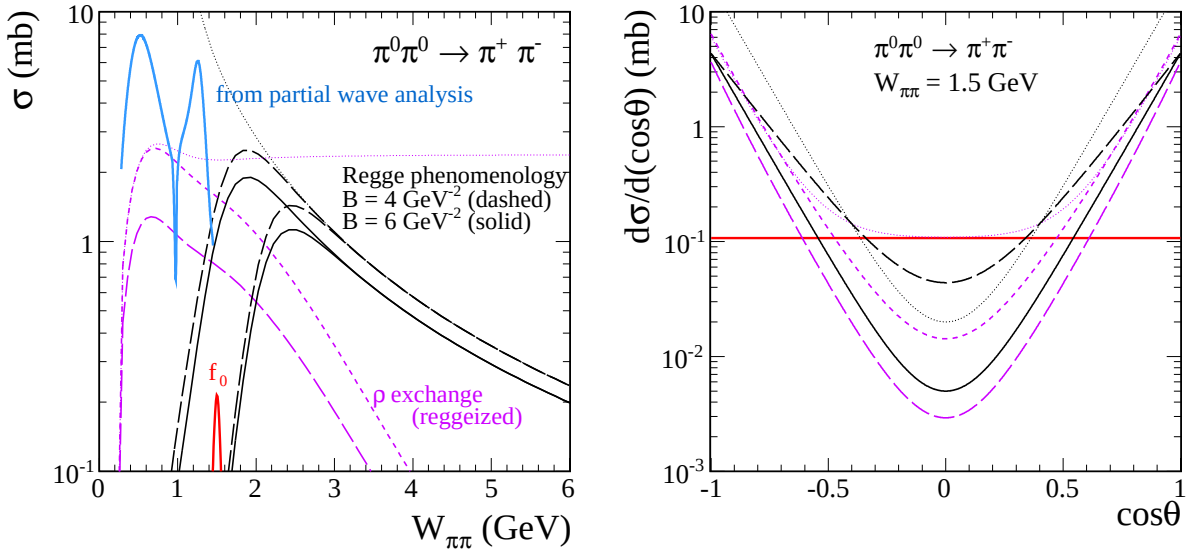

Figure 1.33: In the left panel we show the angle-integrated cross section as a function of pion-pion c.m. energy $W_{\pi\pi}$ and in the right panel we show the angular dependence at $W_{\pi\pi} = 1.5$ GeV for the $\pi^0\pi^0 \to \pi^+\pi^-$ reaction. The blue solid line present a contribution obtained from the partial wave analysis [2]. The black lines present the ρ-reggeon contribution from the Regge phenomenology [111] for a naive (the dotted line) and corrected ($W_0 = 1.5, 2$ GeV and $a_0 = 0.2$ GeV in Eq.(2.20)) extrapolations to low energies. The violet lines present the ρ-meson contribution for a naive (the dotted line) and reggeized approaches (for the cut-off parameter $\Lambda = 1$ GeV and 0.9 GeV in (1.65) correspond to the short-dashed line and long-dashed line, respectively). For comparison, the red solid line presents the $f_0(1500)$ meson contribution.

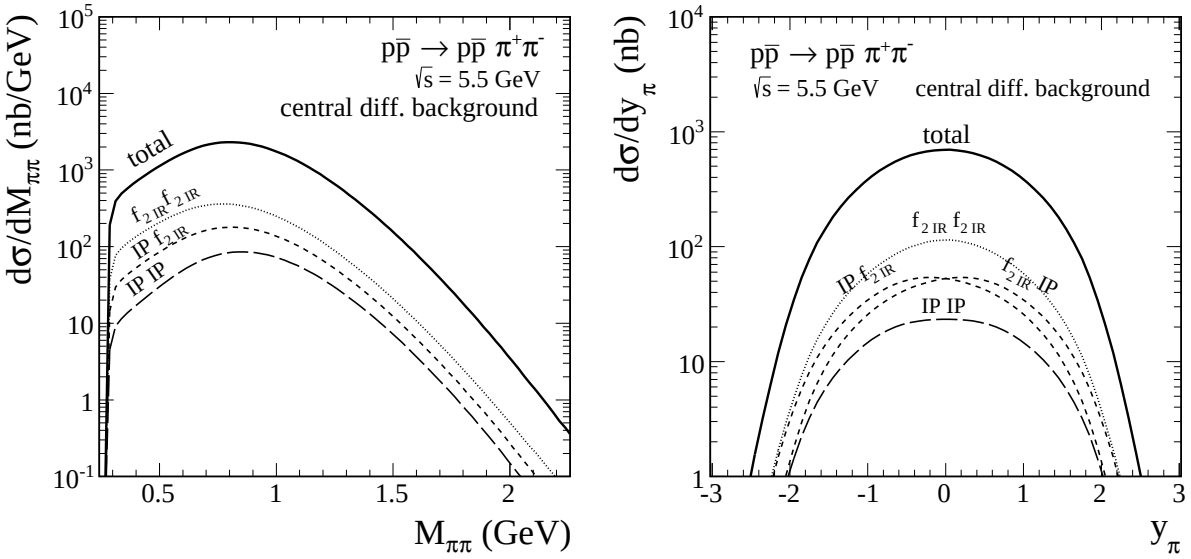

Figure 1.34: Two-pion invariant mass (left panel) and π^+ rapidity (right panel) distributions in the $p\bar{p} \to p\bar{p}\pi^+\pi^-$ reaction at $\sqrt{s} = 5.5$ GeV. In the calculations of central diffractive contribution we use the exponential form factors (2.29) for $\Lambda^2_{off,E} = 1.6\,\text{GeV}^2$ and we include the smooth cut-off formula (2.20) ($W_0 = 2$ GeV and $a_0 = 0.2$ GeV). The black solid line corresponds to the upper (blue) long-dashed line in Fig. 1.35. We show the individual Regge contributions to the cross section and their coherent sum (total, denoted by the thick solid line). The double-pomeron exchange ($I\!P I\!P$) is plotted by the long-dashed line, the pomeron-f_2 reggeon ($I\!P f_{2R}$) and the f_2 reggeon-pomeron ($f_{2R} I\!P$) exchanges by the short-dashed line, and the double-reggeon exchange ($f_{2R} f_{2R}$) by the dotted line. In the calculations we use usual (mesonic) propagator of the off-shell pion.

lines) off-shell form factors and the black dashed lines correspond to the background contribution. In the left panel we can see that the signal contribution is much lower than the ρ_R-exchange background. As explained in the figure caption we show results with different values of W_{freez} parameter (1.69). In the right panel we show the distribution of the central diffractive background together with the $f_0(1500)$ signal. In our calculation we include both pomeron and reggeon exchanges, see Section 2.3. The strength parameters were found from fitting the total πN cross sections to the world experimental data [96, 124], see Table 2.1. The difference between the lower and upper curves of the same type represent the uncertainties from the exponential pion off-shell form factors for the parameter $\Lambda^2_{off,E} = 1$ GeV^2 and 1.6 GeV^2, respectively. In order to exclude barionic resonance regions we multiply the amplitude by the smooth cut-off correction factor (2.20). The two top curves correspond to the parameters $W_0 = 1.5$ GeV and $a_0 = 0.2$ GeV, while two bottom curves correspond to $W_0 = 2.0$ GeV and $a_0 = 0.2$ GeV. For these two set of parameters and $\Lambda^2_{off,E} = 1$ GeV^2 we obtained the total cross section $\sigma_{tot} = 60$ μb and 0.6 μb, respectively. The results suggest that the central diffractive background, that is, without regions of baryon resonances, should not disturb in the observation of the $f_0(1500)$ signal at the highest PANDA experiment energy.

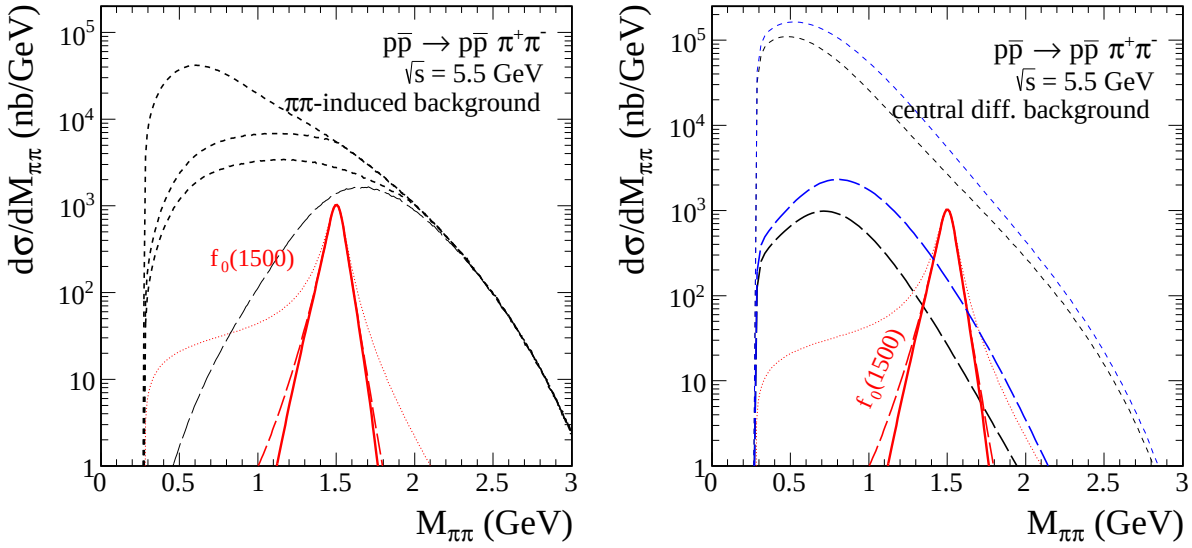

Figure 1.35: Two-pion invariant mass distribution in the $p\bar{p} \to p\bar{p}\pi^+\pi^-$ reaction at the highest PANDA center-of-mass energy $\sqrt{s} = 5.5$ GeV. Here the full phase space has been included. In the figures the red lines show the contribution of $f_0(1500)$ meson obtained without (the dotted line) and with extra form factors given by Eq.(1.62) and Eq.(1.63) (the solid and long-dashed line, respectively). In the calculations of signal ($f_0(1500)$ meson) contribution we use off-shell form factors for the cut-off parameter $\Lambda = 1$ GeV. The black lines correspond to the background contribution obtained by the fusion of two neutral pions (the ρ_R exchange) (left panel) and the contribution initiated by the fusion of two reggeon/pomeron exchanges (right panel). The $\pi\pi$-induced background was calculated with the pion off-shell monopole form factors (1.11) for $\Lambda_{off,M} = 1$ GeV and $B^{\pi\pi}_{\rho_R} = 4$ GeV^{-2} in (1.65). We show the results for naive (the upper line) and corrected (two lower lines with $W_{freez} = 1.5, 2$ GeV) extrapolations to low energies. For comparison, the black long-dashed line corresponds to calculations with with the smooth cut-off function given by Eq. (2.20) ($W_0 = 1.5$ GeV and $a_0 = 0.2$ GeV). In the right panel we show the central diffractive background for the smooth cut-off function (2.20) (the short-dashed lines for $W_0 = 1.5$ GeV and $a_0 = 0.2$ GeV and the long-dashed lines for $W_0 = 2$ GeV and $a_0 = 0.2$ GeV). The difference between the lower black and the upper blue curves of the same type represent the uncertainties from the pion off-shell form factors taken in the exponential form (2.29) for $\Lambda^2_{off,E} = 1$ GeV^2 and 1.6 GeV^2, respectively.

In Fig.1.36 (top panels) we show corresponding distributions in pion rapidity. In order to better see the overlap of the signal and background for the ρ_R exchange (see left panel) we impose in addition 1.4 GeV $< M_{\pi\pi} <$ 1.6 GeV (the region of the $f_0(1500)$ resonance). Limiting to very small pion rapidities one can further improve the signal-to-background ratio. In the right

panel we show the contribution for the central diffractive background. In this case, unlike for the intermediate ρ_R exchange, imposing cuts on pion rapidities would not be helpful as the central diffractive contribution is concentrated at midrapidities, i.e for both outgoing pions $|y_\pi| \to 0$. At lower HESR energies the situation is better, the central diffractive background is relatively smaller. In the bottom panels we show two-pion invariant mass distribution with extra cuts $-0.5 < y_{\pi^+}, y_{\pi^-} < 0.5$. While the $f_0(1500)$ contribution is only slightly modified, the $\pi\pi$-induced background contribution is reduced by more than order of magnitude. One can clearly see the signal over background in this case. Especially the high-energy side of the $f_0(1500)$ meson is now free of the ρ/ρ_R-exchange background. A better separation can be done by using pion-pion partial wave analysis.

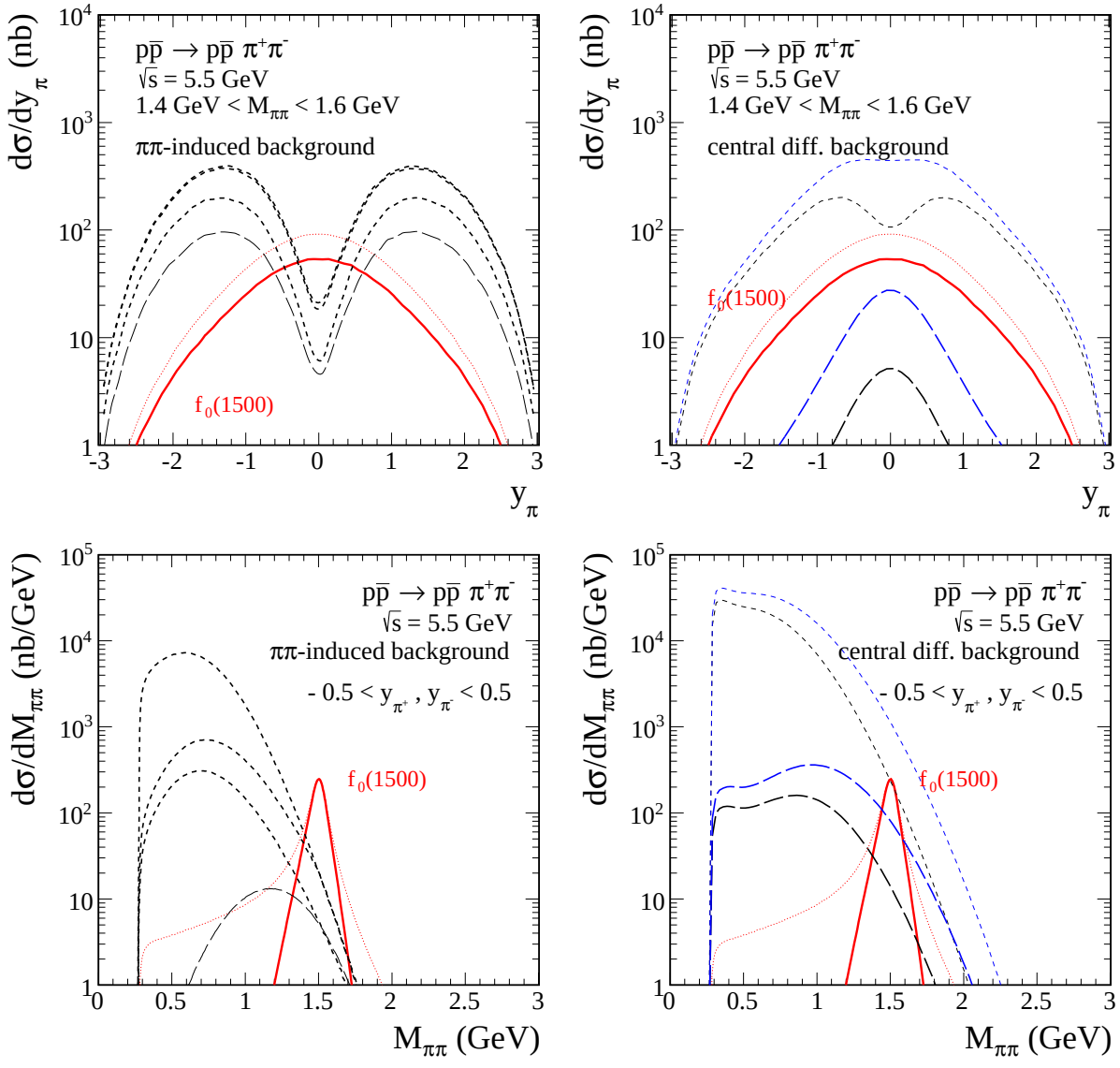

Figure 1.36: In the top panels we show rapidity distribution of pions from the decay of the glueball candidate $f_0(1500)$ (the red solid line) and from the $\pi\pi$-induced background (left panel) for naive (upper line) and corrected (two lower lines) extrapolations to low energies as well as from the central diffractive background (right panel) for the smooth cut-off function in the πN systems (2.20). The curves are explained in the caption of Fig. 1.35. The calculation was performed at $\sqrt{s} = 5.5$ GeV and we impose in addition 1.4 GeV $< M_{\pi\pi} <$ 1.6 GeV on both the signal and background contributions. In the bottom panels we show two-pion invariant mass distribution for the $f_0(1500)$ meson (solid line) and the background (dashed lines) with an additional condition on center-of-mass rapidities $-0.5 < y_{\pi^+}, y_{\pi^-} < 0.5$.

In Fig. 1.37 we show differential cross section for angular distributions ($\cos\theta^*$ is defined as (1.16)) obtained from our signal and background models. The $\pi\pi$-induced background contribution is dominantly produces at $cos\theta^* \approx \pm 0.95$ while the central diffractive background contribution may interplay with the signal contribution at $cos\theta^* \approx 0$.

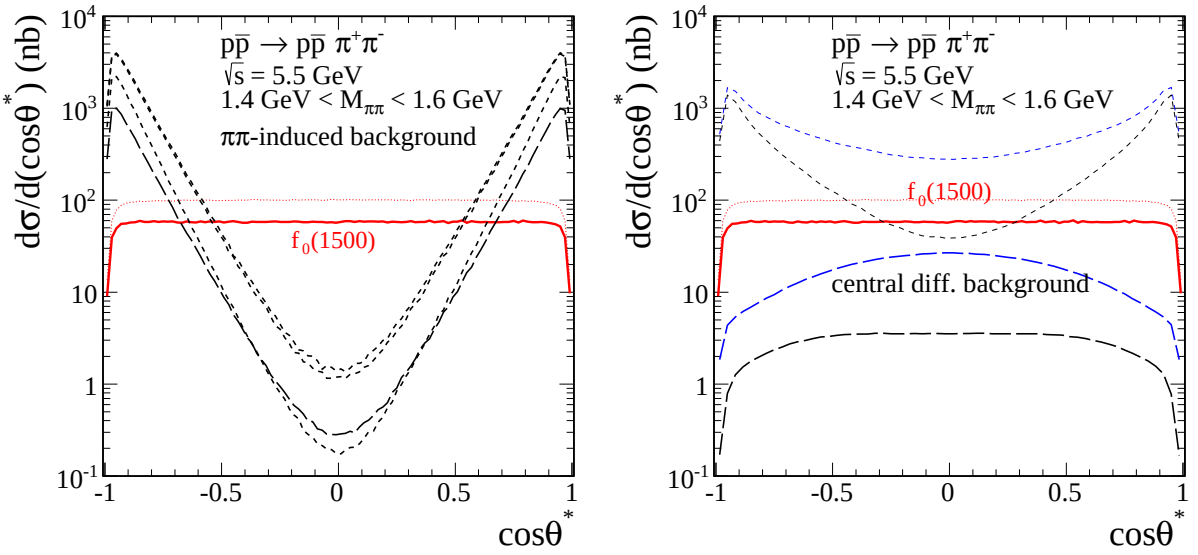

Figure 1.37: Differential cross section for the polar angle in the $\pi\pi$ subsystem for the $f_0(1500)$ meson (solid line) and the background (dashed lines) contributions with an additional condition on two-pion invariant mass 1.4 GeV $< M_{\pi\pi} <$ 1.6 GeV. The calculation was performed at $\sqrt{s} = 5.5$ GeV. The curves are explained in the caption of Fig. 1.35.

Finally, in Fig. 1.38 we show two-pion invariant mass distribution (left panel) and distribution in pion rapidity with condition 1.4 GeV $< M_{\pi\pi} <$ 1.6 GeV (right panel). Both in the signal and background calculations we include the "sharp" cut-off for $M_{\pi N} = W_{\pi N}$ subsystems: $W_{\pi N,min} = 1.8, 1.9$ and 2 GeV corresponding to the dotted, short-dashed and long-dashed lines, respectively.

Close to the two-pions production threshold the Roper resonance excitation and its subsequent decay ($N^*(1440) \to N\pi\pi$) is known to give the dominant contribution to the $pp \to pp\pi^+\pi^-$ reaction [23]. The same may be expected also for the $p\bar{p} \to p\bar{p}\pi^+\pi^-$ reaction. The Roper resonance produces the two-pions in dominantly the $l = 0$ and $I = 0$ state [15] (the tail of the σ meson), i.e. the strength is concentrated at $M_{\pi\pi}$ much lower than $f_0(1500)$ meson. The kinematical constraint gives $M_{\pi\pi} < M_{N^*(1440)} - M_N \approx 0.5$ GeV. In addition, this contribution could be eliminated by extra cuts on invariant masses $M(p\pi^+\pi^-)$ and $M(\bar{p}\pi^+\pi^-)$ (1.23). The same method can, at least in principle, be used to eliminate the Δ and $\bar{\Delta}$ excitations followed by their decays $\Delta^{++} \to \pi^+ p$ and $\bar{\Delta}^{--} \to \pi^-\bar{p}$ [16]. In this sense the last two contributions (the Roper resonance and the double isobar excitations) are reduceable. To which extend precision of the real apparatus will allow such a reduction is a matter of further investigations. Certainly complete analysis requires including more processes and an analysis of the role of cuts in improving the signal-to-background ratio.

[15] Here l is the angular momentum between pions and I indicates the total isospin of the $\pi\pi$ system.

[16] We have checked that eliminating the region of double-Δ excitation (1.24) at the highest PANDA energy $\sqrt{s} =$ 5.5 GeV with an additional condition on two-pion invariant mass 1.4 GeV $< M_{\pi\pi} <$ 1.6 GeV reduces the signal by less than about 10%.

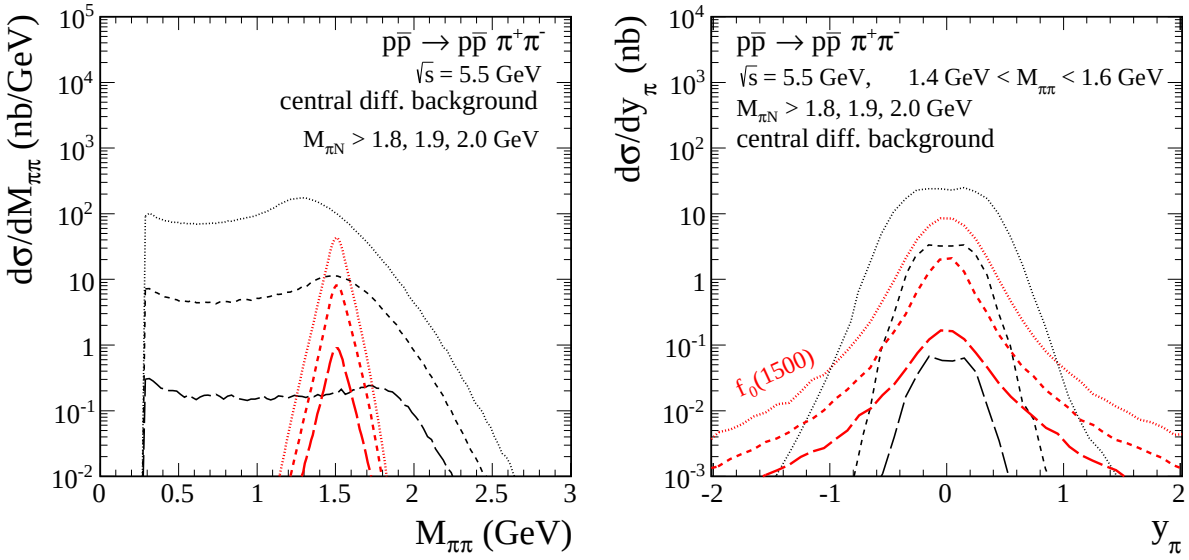

Figure 1.38: Differential distributions of the two-pion invariant mass (left panel) and pion rapidity (right panel) imposing cuts on πN subsystem on both signal and background contributions. The dotted, short-dashed and long-dashed lines correspond to "sharp" cut-off values on πN invariant mass: $M_{\pi N} > 1.8, 1.9$ and 2 GeV, respectively, and for the pion off-shell form factors for $\Lambda_{off,E} = 1$ GeV. The calculation was performed at $\sqrt{s} = 5.5$ GeV. The curves are explained in the caption of Fig. 1.35.

1.7 Conclusions

We have estimated the cross section for exclusive $f_0(1500)$ meson (glueball candidate) production not far from the threshold. We have included both the gluon-induced diffractive and the pionic-triangle diffractive mechanisms as well as the pion-pion exchange contributions.

The QCD diffractive component was obtained by extrapolating down the cross section in the Khoze-Martin-Ryskin approach with unintegrated gluon distributions from the literature as well as using two-gluon impact factor approach. A rather large uncertainties are associated with the QCD diffractive component. At present only upper limit can be obtained for the diffractive component as the $f_0(1500) \to gg$ decay coupling constant remains unknown. The coupling constant could be extracted only in high-energy exclusive production of $f_0(1500)$ meson where other mechanisms are negligible. We have found rather large contribution of pionic-triangle diffractive component at higher energies ($\sqrt{s} > 10$ GeV). However, at the GSI HESR energies this contribution is strongly damped because of the phase space limitations on the πN subchannel energies. Future experimental data at high energies could contribute to shed some light on the competition of the both diffractive mechanisms.

The calculation of the MEC contribution requires introducing extra vertex form factors. At largest PANDA energies they are relatively well known and the pion-pion fusion can be reliably calculated. The situation becomes more complicated very close to the threshold where rather large $|t_1|$ and $|t_2|$ are involved. The cross section for energies close to the threshold is very sensitive to the functional form and parameters of vertex form factor. Therefore a measurement of $f_0(1500)$ close to its production threshold could limit the so-called πNN form factors in the region of exchanged four-momenta never tested before.

We predict the dominance of the pion-pion contribution close to the threshold. Our calculation shows that the diffractive components (in fact its upper limit for the QCD mechanism) are by more than order of magnitude smaller than the pion-pion fusion component in the energy region of future PANDA experiment. The diffractive components may dominate over the pion-pion component only for center-of-mass energies $\sqrt{s} > 15$ GeV.

Disentangling the mechanism of the exclusive $f_0(1500)$ production not far from the meson production threshold would require study of the $p\bar{p} \to p\bar{p}f_0(1500)$, $p\bar{p} \to n\bar{n}f_0(1500)$

processes with the PANDA detector at FAIR and $pp \to pp f_0(1500)$ reaction at J-PARC. In the case the pion exchange mechanism is the dominant process one expects $\sigma(p\bar{p} \to n\bar{n} f_0(1500)) = 4 \times \sigma(p\bar{p} \to p\bar{p} f_0(1500))$. At high energies the gluon-induced or the intermediate pionic-triangle diffractive components dominate over MEC components $\sigma(p\bar{p} \to p\bar{p} f_0(1500)) > \sigma(p\bar{p} \to n\bar{n} f_0(1500))$.

At intermediate energies one cannot exclude a priori subleading reggeon exchanges like $\rho\rho$ for instance. However, we do not know how to reliably calculate them from first principles. We believe that the distortions from the pion-pion at low energies and/or distortions from the QCD gluonic mechanism at high energy may tell us more and allow for a phenomenological analysis taking into account the $\rho\rho$ component explicitly.

Only a careful studies of different final channels in the broad range of energies could help to shed light on coupling of (nonperturbative) gluons to $f_0(1500)$ and therefore would give a new hint on its nature. The experimental studies of exclusive production of $f_0(1500)$ are not easy at all as in the $\pi\pi$ decay channel one expects a large continuum. We have performed an involved calculation of the four-body $p\bar{p}\pi^+\pi^-$ background. Our calculation shows that imposing extra cuts should allow to extract the signal of the glueball $f_0(1500)$ candidate at the highest PANDA energy. A partial wave $\pi\pi$ analysis should be helpful in this context. Scalar resonances are difficult to resolve because some of them have large decay widths which cause a strong overlap between resonances and background. A smaller continuum may be expected in the $K\bar{K}$ or four-pion of $f_0(1500)$ decay channels. This requires, however, a good geometrical (full solid angle) coverage and high registration efficiencies. The PANDA detector seems to fulfill these requirements, but planning real experiment requires a dedicated Monte Carlo simulation of the apparatus.

It is a central problem of our field if $f_0(1500)$ state is a $q\bar{q}$ or glueball type. Unfortunately, our analysis does not allow to give a definite answer to this important question. Some information on baryon-baryon correlation may be helpful but certainly not decisive. New large-scale devices being completed (J-PARC at Tokai, COMPASS at CERN) or being constructed (FAIR at GSI) may open a new possibility to study the production of scalar mesons and an exotic states in more details.

If the cross section at high energies (where the contribution of subleading reggeon exchanges may be neglected) is much smaller than predicted based on the KMR method it means that gluons only weakly couple to $f_0(1500)$ meson. This could provide some indirect information on the $f_0(1500)$ structure. A direct comparison of the shape of differential distributions at high energies may provide a valuable test of the KMR method originally proposed for exclusive Higgs production. A possible disagreement with the prediction for exclusive $f_0(1500)$ production at high energies could put into question the KMR approach, at present state of art in the field. Experiments at high energies (RHIC, LHC) could be useful in this context and could shed light on the nonperturbative coupling of gluons to $f_0(1500)$ state.

Chapter 2

Exclusive Production of Meson Pairs at High Energies

Diffractive processes although very difficult from the point of view of perturbative QCD are very attractive from the general point of view of the reaction mechanism. There are several classes of soft diffractive-type processes in high-energy nucleon-nucleon collisions such as: (1) elastic scattering; (2) single-diffractive excitation of one of the nucleons; (3) central diffractive excitation of both participating nucleons; (4) central diffractive production of a simple final state. The energy dependence of the first three types of the reaction was measured and can be nicely described [125, 126] in a somewhat academic two-state (but fulfilling unitarity) the Good-Walker model [127]. Diffractive reaction channels contribute about 30% to the total hadronic cross section at the energies of the Large Hadron Collider LHC at CERN. A good understanding of hadronic diffraction is therefore necessary for a comprehensive understanding of proton-proton collisions. The last case was almost not studied in much detail both experimentally and theoretically. Therefore, the processes of central exclusive production became recently a very active field of research (for recent reviews see [128] and references therein). Although the attention is paid mainly to high-$p_\perp$ processes that can be used for new physics searches (exclusive Higgs boson, $\gamma\gamma$ interactions, etc.), measurements of low-$p_\perp$ signals are also very important as they can help to constrain models of the backgrounds for the former ones.

Recently there is a growing interest in understanding exclusive three-body reactions $NN \to NNR$ (3.1) at high energies, where the meson (resonance) R is produced in the central rapidity region, that is, separated by rapidity gaps from both nucleons. Many of these resonances decay into $\pi\pi$ and/or KK channels. The representative examples are: $R = \sigma$, ρ^0, $f_0(980)$, ϕ, $f_2(1270)$, $f_0(1500)$, χ_{c0}. Various decay channels can be studied. It is clear that these resonances are seen (or will be seen) "on" the background of $\pi\pi$ or KK continuum [1], see Section 1.6 and Ref. [1]. The aim of this Section is to discuss mechanisms of exclusive $\pi^+\pi^-$ and K^+K^- production in hadron-hadron collisions at high energies. Similar analysis can be done for $\pi^0\pi^0$ exclusive production [2].

2.1 Regge phenomenology

In this Section we provide a very basic introduction to the Regge theory concepts to hadronic reactions. For a detailed treatment of Regge theory we refer instead to Refs. [114, 130, 131]. The Regge theory is based on the unitarity, analyticity and crossing symmetry of the scat-

[1] In general, the resonance and continuum contributions may interfere. This may produce even a dip. A good example is the $f_0(980)$ production (see e.g. Ref. [2, 129])

[2] We recall that the $\pi^0\pi^0$ central exclusive production is approximately 1/2 of the $\pi^+\pi^-$ cross section due to the identity of particles in the final state.

tering matrix. The Regge phenomenology was developed originally to describe the behaviour of total hadronic cross sections and diffractive/elastic scattering at high energies. It is very successful in describing the cross section behaviour in the high energy limit. With the advent of quantum chromodynamics (QCD) the emphasis shifted to the investigation of scattering processes at short distances (at large momentum transfer) for which the strong coupling is small and perturbative methods can be applicable. However, for low momentum transfers, in the long-range regime, the QCD has not yet given accurate predictions. This regime of soft interactions is dominated by phenomenological or QCD-inspired models constrained by the asymptotic theorems. Since, the soft diffraction and elastic scattering processes cannot be described by perturbative QCD (pQCD), and Regge theory remains an important tool.

The Regge approach establishes a connection between the high energy scattering and a spectrum of particles and resonances. The reggeon/pomeron t-channel exchanges are dual to the low energy s-channel resonances/non-resonance background. This is two-component duality; see e.g. Section 4.3 of [114]. The theory uses a concept of the complex angular momentum to describe the scattering amplitude. In its relativistic formulation a high energy behaviour of the amplitude is related to the singularities in the complex momentum plane of the partial waves in crossed channel. It makes use of the crossing symmetry which relates the two-body scattering processes $ab \to cd$ and $a\bar{c} \to \bar{b}d$. In the former the centre-of-mass energy is $s = (p_a + p_b)^2$ and the four-momentum transfer $t = (p_a - p_c)^2$ defines the scattering angle. In the latter reaction the role of the two variables is interchanged. The crossing symmetry implies that the two processes are described by the same amplitude since the objects exchanged there has the same quantum numbers. The simplest singularities are the Regge poles the exchange of which is a generalisation of an exchange of a particle with spin J to complex values of J. The Regge theory describes the interaction by including exchanges with all possible J-values (with the same quantum numbers) fulfilling the Froissart-Martin bound [132,133] for the asymptotic behaviour of total cross sections which implies that $\sigma_{ab}^{tot}(s)$ cannot grow faster than $C^{ab} \log^2(s/s_0)$ with C^{ab} and s_0 constants.

A plot of the exchanged particles spin J versus its squared mass m_J^2 shows that all possible exchanges form trajectories called the Regge trajectories or reggeons ($\mathbb{R}$). In Fig. 2.1 we show the so called Chew-Frautschi plots [134]. To good approximation the two $C = +1$ (f_2, a_2) trajectories and the two $C = -1$ (ω, ρ) trajectories are all degenerate with intercept $\alpha(0) \approx 0.5$, so they all contribute terms that behave approximately like $1/\sqrt{s}$. However, the measurements show that the cross section after the initial decrease starts to increase slowly with energy. This cannot be explained by $\alpha(t = 0) < 1$ trajectories. To generate a non-falling total cross section a new trajectory (Pomeranchuk trajectory) with the leading pole called the pomeron ($\mathbb{P}$) was postulated. It has $\alpha(t = 0)$ slightly above 1 and the isospin zero and even charge parity, $C = +1$, i.e. it has the quantum numbers of the vacuum. In the Regge theory the t-channel Regge exchanges ($\mathbb{R}$) correspond to a sum of ordinary mesons (ρ^0, ω, etc.) with the same quantum numbers. In QCD, the pomeron exchange is described in terms of multi-gluon exchange and a point-like coupling to quarks and gluons. A color singlet two-gluon exchange with $C = +1$ corresponds to the pomeron exchange while the color singlet three-gluon exchange with $C = -1$ describes the so called odderon exchange.

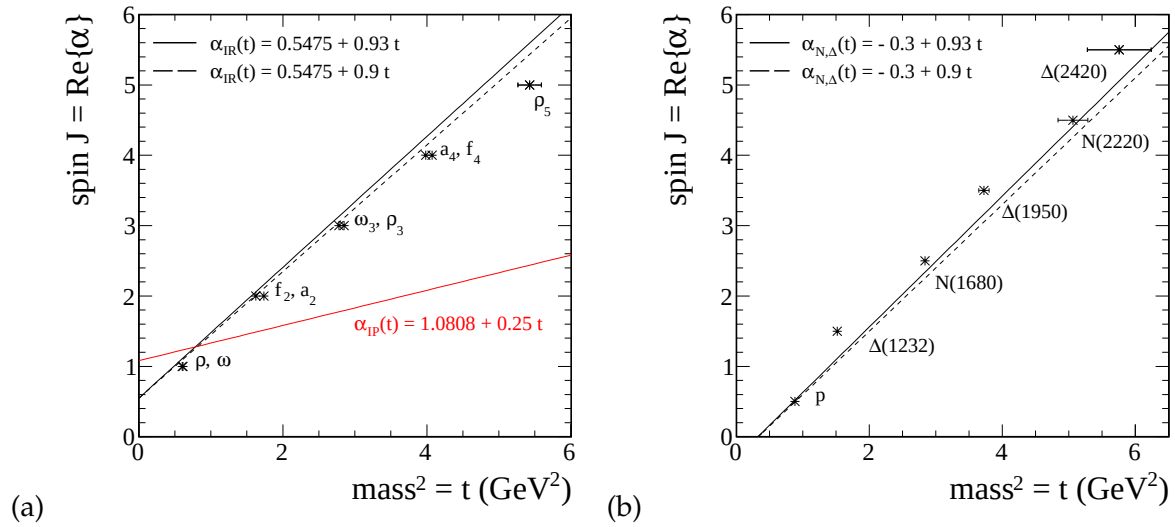

Figure 2.1: Chew-Frautschi plots of the particle spin versus their squared masses $t = m_J^2$. The meson (panel (a)) and baryon (panel (b)) states lie on approximately linear, parallel, exchange-degenerate Regge trajectories $\alpha(t) = \alpha(0) + \alpha' t$. The linearity of the Regge trajectories allows a simple extrapolation from t-channel physical region $t > 4m_\pi^2$ to the s-channel scattering region $t < 0$. Left panel shows the "leading trajectory" contains four near degenerate meson trajectories $(f_2(1270), f_4(2050), ...)$, $(a_2(1320), a_4(2040), ...)$, $(\omega(780), \omega_3(1670), ...)$, and $(\rho(770), \rho_3(1690), ...)$. The pomeron trajectory has a small slope but an intercept $\alpha_{I\!P}(0)$ slightly above 1. All the well established mesons and less well verified ρ_5 state are listed in the data tables [96]. Right panel shows two baryon (N and Δ) trajectories. The proton trajectory, also called N^+ trajectory, contains the baryons with corresponding J^P: $p\,1/2^+$, $N(1680)\,5/2^+$, and $N(2220)\,9/2^+$ and $N(2700)\,13/2^+$. The slope α'_N is comparable to that for the meson trajectories. Apart from the well established proton trajectory, there is a prominent resonance $I = 1/2, J^P = 1/2^+$ with mass 1440 MeV, known as the Roper resonance. The Roper resonance may appear on the daughter trajectory of N^* states treated above, although its status is still disputable.

2.2 Total cross sections and elastic scattering

In order to fix parameters in our central diffractive model we analyse various experimental data of the elastic $ab \to ab$ scattering. The forward amplitudes $M_{ab\to ab}(s, t = 0)$ of the few elastic reactions can be written in terms of the Regge exchanges $A_i(s, t = 0)$, as

$$
\begin{aligned}
M_{\pi^\pm p\to\pi^\pm p}(s) &= A_{I\!P}(s) + A_{f_{2R}}(s) \mp A_{\rho_R}(s)\,, && (2.1)\\
M_{K^\pm p\to K^\pm p}(s) &= A_{I\!P}(s) + A_{f_{2R}}(s) + A_{a_{2R}}(s) \mp A_{\omega_R}(s) \mp A_{\rho_R}(s)\,, && (2.2)\\
M_{K^\pm n\to K^\pm n}(s) &= A_{I\!P}(s) + A_{f_{2R}}(s) - A_{a_{2R}}(s) \mp A_{\omega_R}(s) \pm A_{\rho_R}(s)\,, && (2.3)\\
M_{pp\to pp}(s) &= A_{I\!P}(s) + A_{f_{2R}}(s) + A_{a_{2R}}(s) - A_{\omega_R}(s) - A_{\rho_R}(s)\,, && (2.4)\\
M_{\bar{p}p\to\bar{p}p}(s) &= A_{I\!P}(s) + A_{f_{2R}}(s) + A_{a_{2R}}(s) + A_{\omega_R}(s) + A_{\rho_R}(s), && (2.5)\\
M_{pn\to pn}(s) &= A_{I\!P}(s) + A_{f_{2R}}(s) - A_{a_{2R}}(s) - A_{\omega_R}(s) + A_{\rho_R}(s)\,, && (2.6)\\
M_{\bar{p}n\to\bar{p}n}(s) &= A_{I\!P}(s) + A_{f_{2R}}(s) - A_{a_{2R}}(s) + A_{\omega_R}(s) - A_{\rho_R}(s)\,. && (2.7)
\end{aligned}
$$

Under $p \leftrightarrow n$ odd-isospin ρ_R and a_{2R} change sign of contribution. Under particle $\leftrightarrow$ anti-particle the odd-C ρ_R and ω_R change sign.

The optical theorem relates the total cross section $\sigma_{tot}(s)$ for the scattering of a pair of hadrons a and b to the amplitude $M_{ab\to ab}(s, t = 0)$ for elastic ab scattering. When the centre-of-mass energy $\sqrt{s}$ is large, the theorem reads

$$\sigma_{tot}(s) \sim s^{-1}\,\mathrm{Im} M_{ab\to ab}(s, t = 0) \qquad (2.8)$$

and a Regge trajectory $\alpha(t)$ contributes a term to $\sigma_{tot}(s)$ that behaves as $C_i s^{\alpha(0)-1}$. The total cross section tests, via optical theorem (2.8), only imaginary part of the scattering amplitude. In writ-

Table 2.1: The strength parameters of pomeron and reggeon exchanges determined from the elastic and the total cross sections used in the present calculations.

Regge exchange, i	C_i^{NN} (mb)	$C_i^{\pi N}$ (mb)	C_i^{KN} (mb)	$C_i^{\pi\pi}$ (mb)	C_i^{KK} (mb)
$I\!P$	21.7	13.63	11.82	$\simeq 8.56$	$\simeq 6.44$
f_{2R}	75.4875	31.79	15.67	$\simeq 13.39$	$\simeq 3.25$
ρ_R	1.0925	4.23	2.05	$\simeq 16.38$	$\simeq 3.85$
a_{2R}	1.7475	–	1.585	–	$\simeq 1.44$
ω_R	20.0625	–	7.055	–	$\simeq 2.48$

ing the above amplitudes we have omitted indices related to helicities as we have assumed helicity conservation. At low energies, the total cross sections for $\pi^+ p$ and $\pi^- p$ show a significant energy-dependent asymmetry defined as $|\sigma_{tot}^{\pi^+ p}(s) - \sigma_{tot}^{\pi^- p}(s)|/(\sigma_{tot}^{\pi^+ p}(s) + \sigma_{tot}^{\pi^- p}(s))$. In contrast to the total cross section the $\pi^{\pm} p$ elastic scattering cross sections show at low energies rather small asymmetry.

The elastic ab scattering amplitude $M_{ab\to ab}(s,t)$ is a sum of Regge terms

$$A_i(s,t) = \eta_i\, s\, C_i^{ab} \left(\frac{s}{s_0}\right)^{\alpha_i(t)-1} \exp\left(\frac{B_i^{ab}}{2} t\right), \quad \text{where } i = I\!P, f_{2R}, \rho_R, a_{2R}, \omega_R \tag{2.9}$$

and the slope of the elastic ab scattering is

$$B(s) = B_i^{ab} + 2\alpha_i' \ln\left(\frac{s}{s_0}\right), \tag{2.10}$$

where the energy scale s_0 is fixed at $s_0 = 1\ \text{GeV}^2$ and only the B_i^{ab} parameters must be fitted to the existing experimental data of the elastic ab scattering. We can see, that the Regge exchange with linear trajectory predicts an exponential fall-off of the t-distribution with the slope parameter which increases with increasing energy. This means that small scattering angles become more preferable or in other words the forward scattering peak becomes sharper or "shrinks" with increasing energy. The values of strength parameters C_i^{ab}, are obtained from the Donnachie-Landshoff analysis of the total cross section in several hadronic reactions [113] and are listed in Table 2.1. This means that our effective phenomenological model describes the available total cross sections. The reggeons and pomeron trajectories, $\alpha_R(t)$ and $\alpha_{I\!P}(t)$, respectively, are assumed to be of standard form, see for instance [114], that is, linear in t:

$$\alpha_{I\!P}(t) = \alpha_{I\!P}(0) + \alpha_{I\!P}'\, t, \qquad \alpha_{I\!P}(0) = 1.0808, \quad \alpha_{I\!P}' = 0.25\ \text{GeV}^{-2}, \tag{2.11}$$

$$\alpha_R(t) = \alpha_R(0) + \alpha_R'\, t, \qquad \alpha_R(0) = 0.5475, \quad \alpha_R' = 0.93\ \text{GeV}^{-2}. \tag{2.12}$$

The factors η_i in Eq.(2.9) are the signature factors [3]. If the energy variation is parametrised as an effective power $s^{\alpha(t)}$, the phase $e^{i\phi(\alpha(t))}$ depends on the C-parity of the dominant exchange

$$\eta_i^+ = \frac{-(1+\exp(-i\pi\alpha_i))}{sin(\pi\alpha_i)} = i - cot\left(\frac{\pi\alpha_i}{2}\right) = \frac{-\exp\left(-i\frac{\pi}{2}\alpha_i\right)}{sin\left(\frac{\pi}{2}\alpha_i\right)}, \tag{2.14}$$

$$\eta_i^- = \frac{-(1-\exp(-i\pi\alpha_i))}{sin(\pi\alpha_i)} = -i - tan\left(\frac{\pi\alpha_i}{2}\right) = \frac{-i\exp\left(-i\frac{\pi}{2}\alpha_i\right)}{cos\left(\frac{\pi}{2}\alpha_i\right)}. \tag{2.15}$$

[3] If $\alpha_i = 0.5$ then we can use a simple form

$$\eta_i^+ = -\sqrt{2}\exp\left(-i\frac{\pi}{2}\alpha_i\right), \quad \eta_i^- = -\sqrt{2}\exp\left(-i\frac{\pi}{2}(\alpha_i - 1)\right). \tag{2.13}$$

As an example, the amplitude for the elastic scattering of pions on nucleons can be explicitly written in the Regge-like form as

$$\begin{aligned}\mathcal{M}_{\pi^{\pm}p\to\pi^{\pm}p}(s,t) &= i\,s\,C_{\boldsymbol{P}}^{\pi p}\left(\frac{s}{s_0}\right)^{\alpha_{\mathbb{P}}(t)-1}\exp\left(\frac{B_{\boldsymbol{P}}^{\pi N}}{2}t\right)\\ &+\eta_{f_{2\mathbb{R}}}\,s\,C_{f_{2\mathbb{R}}}^{\pi p}\left(\frac{s}{s_0}\right)^{\alpha_{\mathbb{R}}(t)-1}\exp\left(\frac{B_{\boldsymbol{R}}^{\pi N}}{2}t\right)\\ &\pm\eta_{\rho_{\mathbb{R}}}\,s\,C_{\rho_{\mathbb{R}}}^{\pi p}\left(\frac{s}{s_0}\right)^{\alpha_{\mathbb{R}}(t)-1}\exp\left(\frac{B_{\boldsymbol{R}}^{\pi N}}{2}t\right),\end{aligned} \tag{2.16}$$

where $\eta_{f_{2\mathbb{R}}} = -0.860895 + i$ and $\eta_{\rho_{\mathbb{R}}} = -1.16158 - i$. The first term describes the leading trajectory (the pomeron exchange) while the next terms describe the subleading reggeon exchanges. Above, the $B^{\pi N}$ slope parameters are only free parameters and must be adjusted to the elastic scattering data.

The differential elastic cross section is expressed with the help of the elastic scattering amplitude as usually

$$\frac{d\sigma_{el}}{dt} = \frac{1}{16\pi s^2}|M_{el}(s,t)|^2\,. \tag{2.17}$$

The differential distributions $d\sigma_{el}/dt$ for three representative incident-beam momenta of $P_{lab} =$ 5 GeV, $P_{lab} = 50$ GeV, and $P_{lab} = 200$ GeV for both $\pi^{\pm}p$ and $K^{\pm}p$ elastic scattering are shown in Figs 2.4 and 2.5, respectively. We can see that with the slope parameters for Regge exchanges

$$B_{\boldsymbol{P}}^{\pi N} = B_{\boldsymbol{P}}^{KN} = 5.5\ \text{GeV}^{-2}\,,\quad B_{\boldsymbol{R}}^{\pi N} = B_{\boldsymbol{R}}^{KN} = 4\ \text{GeV}^{-2} \tag{2.18}$$

a rather good description of experimental $d\sigma_{el}/dt$ is achieved. The exception is the low energy K^+p scattering. There the Λ baryon exchange (with the strangeness q.n. $S = -1$) is a possible mechanism in addition to the pomeron and reggeon exchanges. Under a detailed inspection one can observe that the local slope parameter

$$B_{eff}(t) \equiv \frac{d}{dt}\ln\left(\frac{d\sigma_{el}}{dt}\right) \tag{2.19}$$

is t-dependent and is slightly larger for π^-p than for π^+p. The local slope decreases with increasing t. Such an effect was observed experimentally in Ref. [135–139]. [4].

The integrated cross sections for πN and KN total and elastic scattering versus center-of-mass energy $\sqrt{s}$ are presented in Figs. 2.2 and 2.3, respectively. We can see, that the high energy cross section is dominated by the pomeron exchange while the reggeon exchanges play the crucial role in the nucleon resonance region. While the total cross section is just a sum of the pomeron and reggeon terms, the elastic cross section have the interference term. We describe the existing experimental data of the elastic scattering for $\sqrt{s} > 3$ GeV, but in the case of the $K^+p \to K^+p$ process only for $\sqrt{s} > 7$ GeV. For instance, the K^+p and K^-p scattering have the same t-channel quantum numbers but very different s-channel quantum numbers. At sufficiently high energy, when pomeron exchange dominates, the two cross sections come together. However at lower energies they are very different.

The Donnachie-Landshoff parametrisation can be used only above resonance regions for the energy $\sqrt{s_{ab}} = W_{ab} > 2.5$ GeV. The region below contains nucleon resonances and is therefore very difficult for modelling. In principle, their contribution could and should be included explicitly. In order to exclude resonance region we shall "correct" the Regge parametrisation (Eq. (2.9)) multiplying it by a purely phenomenological smooth cut-off correction factor

$$f_{cont}^{ab}(W_{ab}) = \left(\exp\left(\frac{W_{ab}-W_0}{a_0}\right)\right) / \left(1+\exp\left(\frac{W_{ab}-W_0}{a_0}\right)\right), \tag{2.20}$$

[4]The effective slope observed in t-distributions is of course much larger ($B(s) = 7 - 10$ GeV^{-2} for $P_{lab} = 3 -$ 200 GeV [135–139]).

where the parameter $W_0 = 2$ GeV gives the position of the cut and the parameter $a_0 = 0.2$ GeV describes how "sharp" the cut-off is. For large energies $f^{ab}_{cont}(W_{ab}) \approx 1$ and close to kinematical threshold $f^{ab}_{cont}(W_{ab} \simeq m_a + m_b) \approx 0$. As will be discussed in the Results Section, the small meson-nucleon energies in four-body processes, where we fail to describe the experimental data, are important only at large meson (pseudo)rapidities, where a measurement is practically impossible.

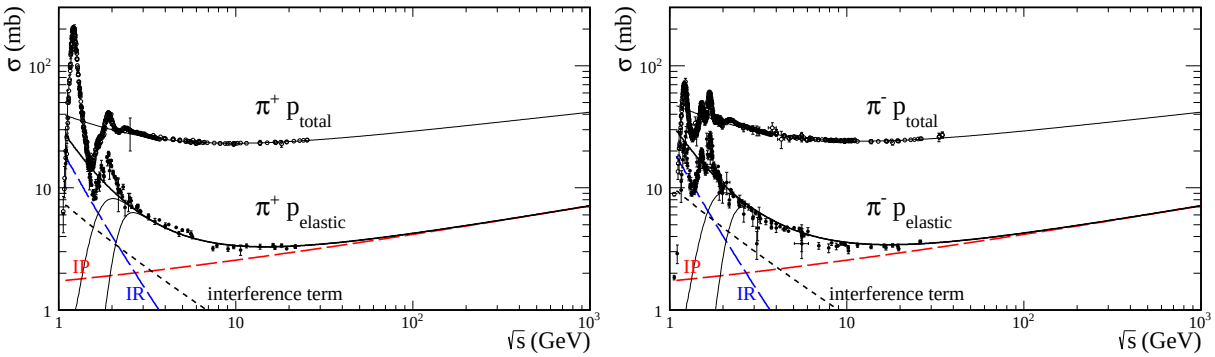

Figure 2.2: Integrated cross section for πN total and elastic scattering as a function of center-of-mass energy compared with the experimental data from PDG (Particle Data Group) [96, 124]. The high energy cross section is dominated by the pomeron exchange while at smaller energies, secondary, non-leading trajectories contribute as well, see the red and blue long-dashed line, respectively. The black short-dashed line corresponds to the interference term. We exclude resonance regions multiplying the Regge parametrisation (Eq. (2.9)) by a purely phenomenological smooth cut-off correction factor (2.20) with parameters $W_0 = 1.5$ GeV, $a_0 = 0.2$ GeV and $W_0 = 2$ GeV, $a_0 = 0.2$ GeV, see the black solid lines, respectively.

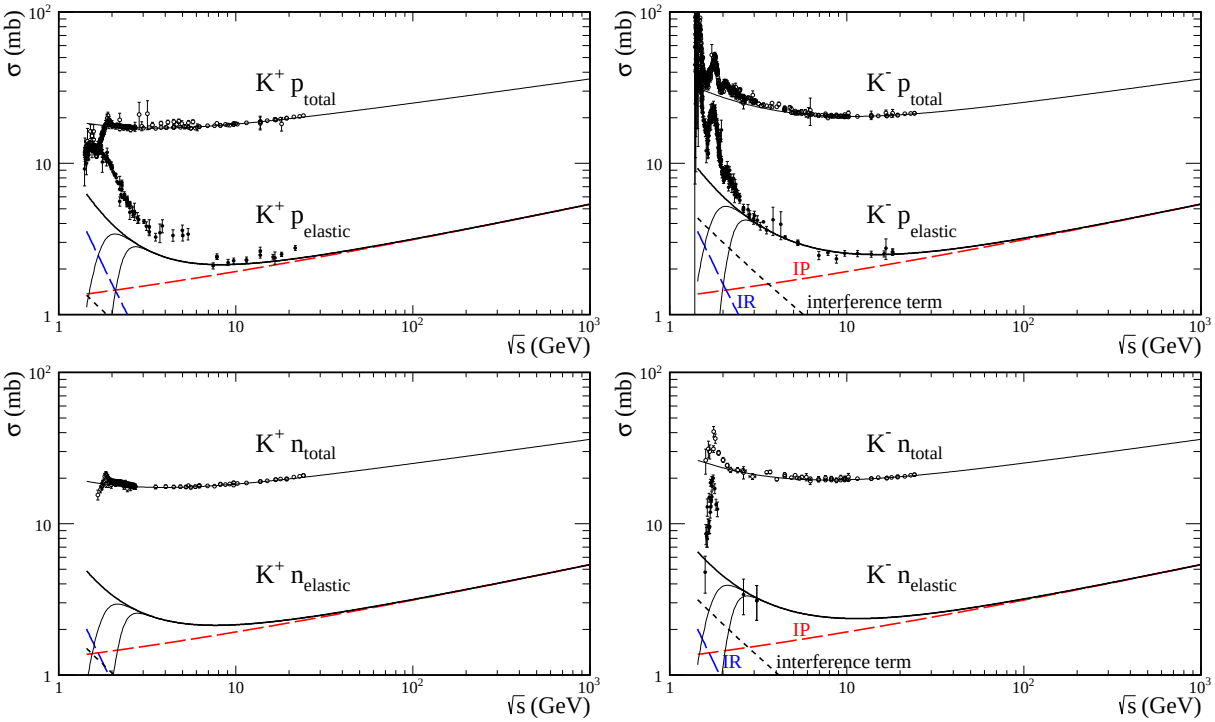

Figure 2.3: Integrated cross section for the KN total and elastic scattering. The experimental data are taken from PDG [96, 124]. The lines are explained in the main text and in Fig.2.2.

In Fig.2.6 we nicely describe the existing experimental data for elastic nucleon-nucleon scattering with the slope parameters fixed as

$$B_P^{NN} = 9 \text{ GeV}^{-2}, \quad B_R^{NN} = 6 \text{ GeV}^{-2}. \tag{2.21}$$

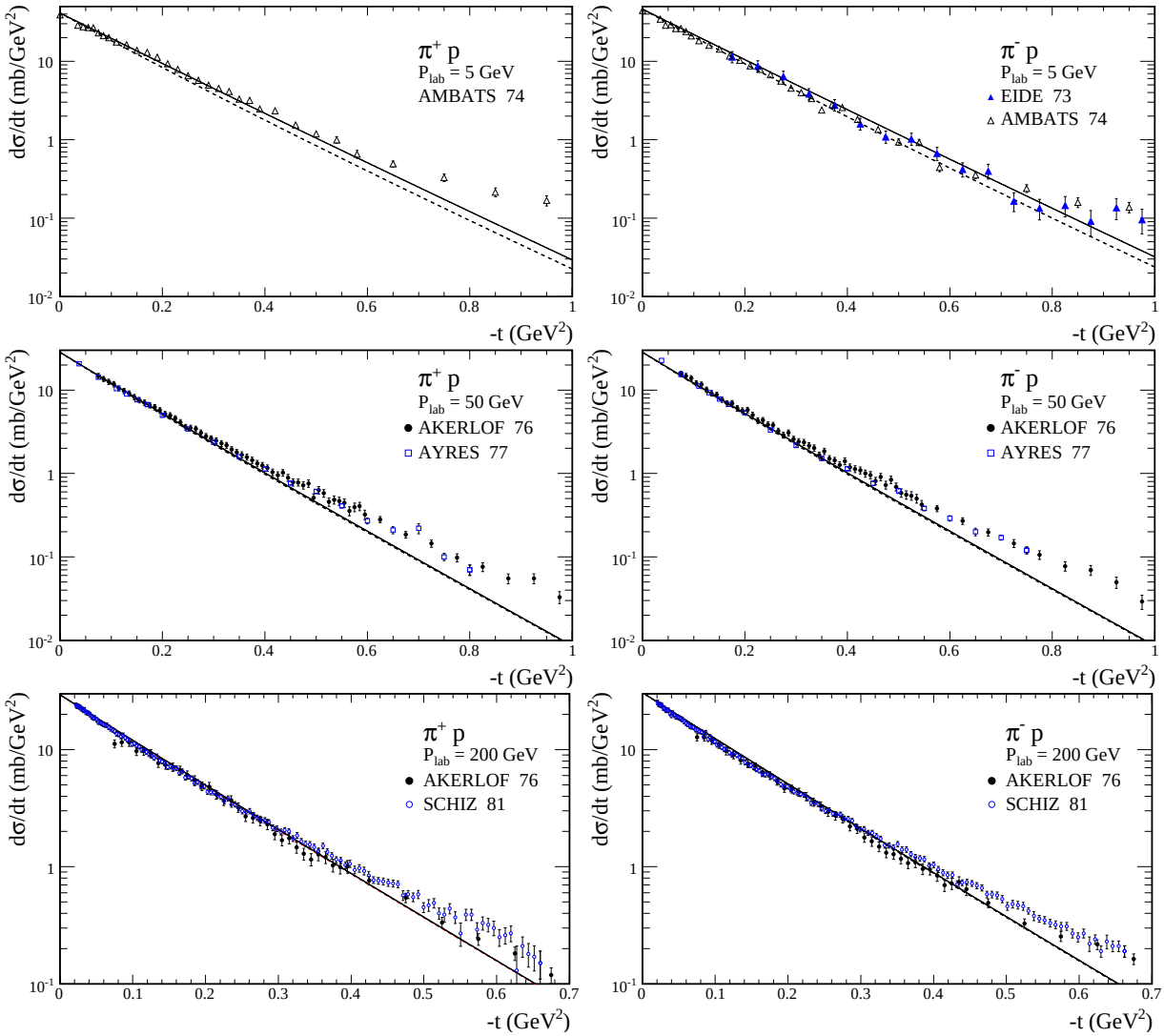

Figure 2.4: Differential distributions for $\pi^+ p$ (left) and $\pi^- p$ (right) elastic scattering for three incident-beam momenta of $P_{lab} = 5, 50$, and 200 GeV. A fit calculated with the amplitude (2.16) and parameters as given in the text to the world πN elastic scattering data, taken from Ref. [135–139], suggest that the pomeron and reggeon slopes may be slightly different. The solid lines show results with $B_{\boldsymbol{P}}^{\pi N} = 5.5\,\mathrm{GeV}^{-2}$ and $B_{\boldsymbol{R}}^{\pi N} = 4\ \mathrm{GeV}^{-2}$ while the dashed lines results with the same value of slope parameter for the pomeron and reggeons $B_{\boldsymbol{P}}^{\pi N} = B_{\boldsymbol{R}}^{\pi N} = 5.5\,\mathrm{GeV}^{-2}$.

Similarly as in meson-nucleon elastic scattering, there is a region of energies where the interference term dominates, see the black long-dashed lines. The high energy cross section is dominated by pomeron exchange while the low energies by the reggeon exchanges, see the red and blue long-dashed line, respectively. The high energy experiments deliver also possibility to test another asymptotic prediction, i.e. the pp and $p\bar{p}$ cross section difference vanishes at asymptotic energies. The data on hadronic interactions seem to support this view. It is worth stressing that due to slow increase of the cross section its high energy behaviour can only be tested with precise high energy data.

The differential distribution $d\sigma_{el}/dt$ for pp elastic scattering at $\sqrt{s} = 7$ TeV is shown in Fig.2.7. A rather good description of experimental $d\sigma_{el}/dt$ data is achieved, where t is not large. The experimental cross section $d\sigma_{el}^{pp\to pp}/dt\ |_{t=0} = 506.4 \pm 22.98$ mb [140] fitted at $t = 0$ is a slightly larger in comparison to 420.7 mb from our phenomenological analysis. Reproducing a dip requires the simultaneous near-vanishing of both the real and imaginary parts of the amplitude. In Ref. [141] has been reported some ideas how to doing this. The energies at which the dip is seen are quite large, so the contributions from reggeon exchanges are too small, and to cancel

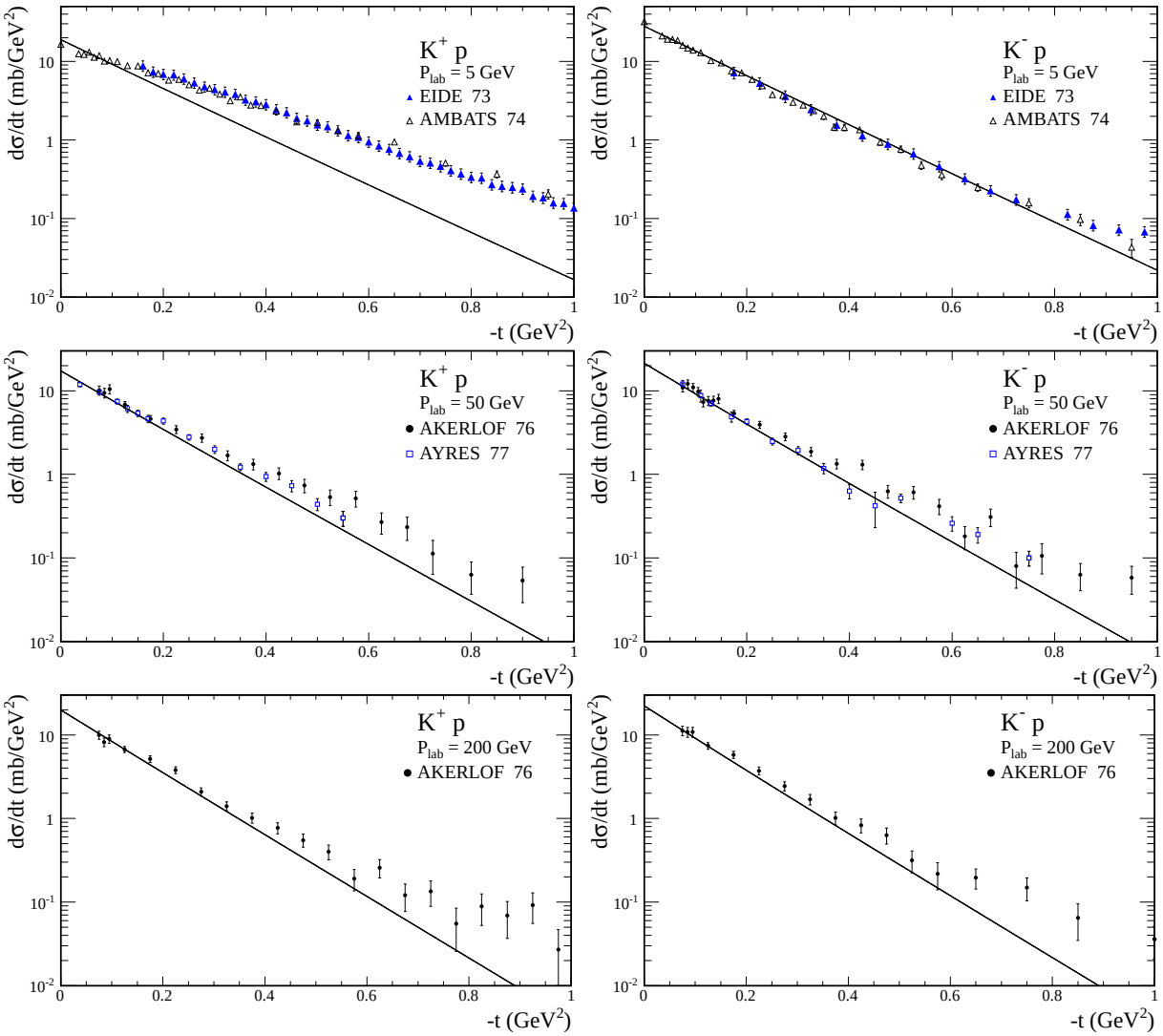

Figure 2.5: Differential distributions for K^+p (left panels) and K^-p (right panels) elastic scattering for different energies. The experimental data are taken from Refs. [135–139].

the imaginary part of single pomeron exchange is needed also $I\!P I\!P$ exchange. We do not have the theoretical knowledge correctly to calculate any of the $I\!P$ terms beyond single exchange, though we do have some knowledge of their general properties, which enables one to make models. To cancel the real part they bring in triple-gluon exchange, since this appears to dominate the elastic amplitude at large values of t, giving it an energy-independent behaviour t^{-4}, see [141].

Summarizing, a model presented here sufficiently well describes the elastic scattering data at not to small (> 0.01 GeV^2) and not to large four-momentum transfer $|t|$ and includes absorption effects due to meson-nucleon rescatterings in an effective way. This has advantage for an applications to the four-body soft processes, where the meson-nucleon absorption effects do not need to be included explicitly. This considerably simplifies the calculation for the $2 \to 4$ reaction and actually this makes it feasible. Having fixed the parameters we can proceed to the four-body $pp\pi^+\pi^-$ and ppK^+K^- final states.

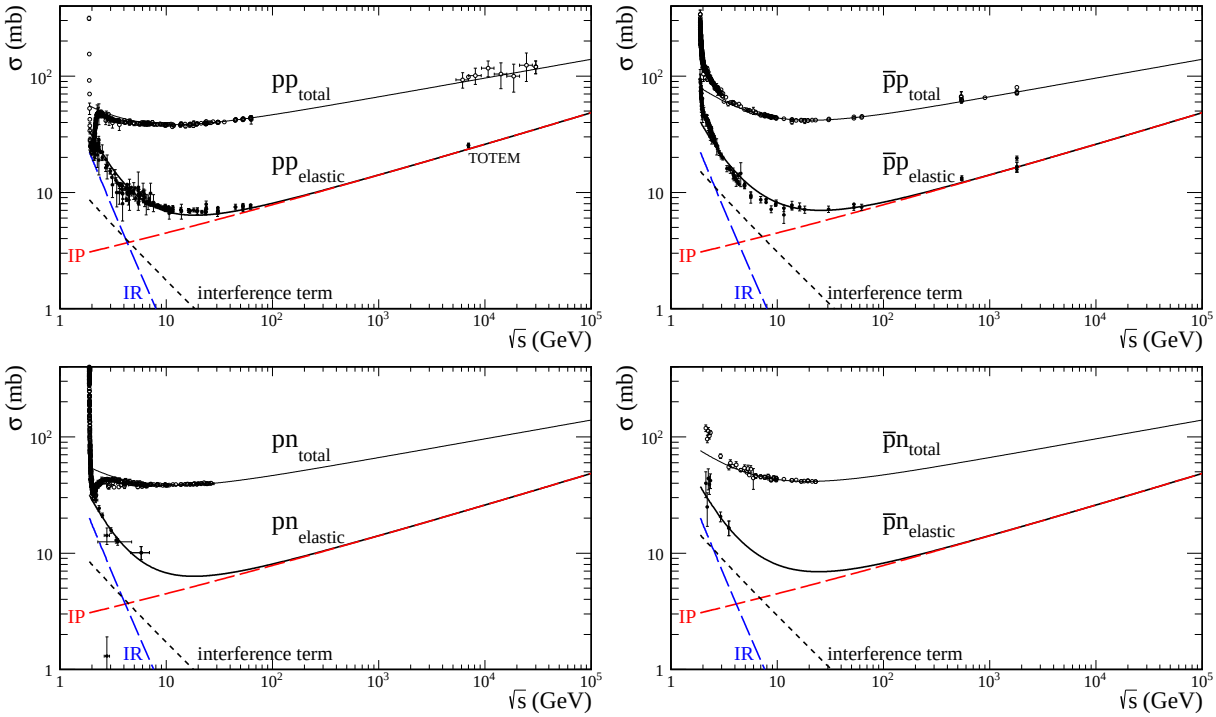

Figure 2.6: Integrated cross section for the NN total and elastic scattering. The lines are explained in the main text and in Fig. 2.2. The experimental data are taken from PDG [96,124] and from a recent publication by the TOTEM Collaboration [140] at $\sqrt{s} = 7$ TeV which cover the $|t|$ range $0.005 - 0.4$ GeV^2.

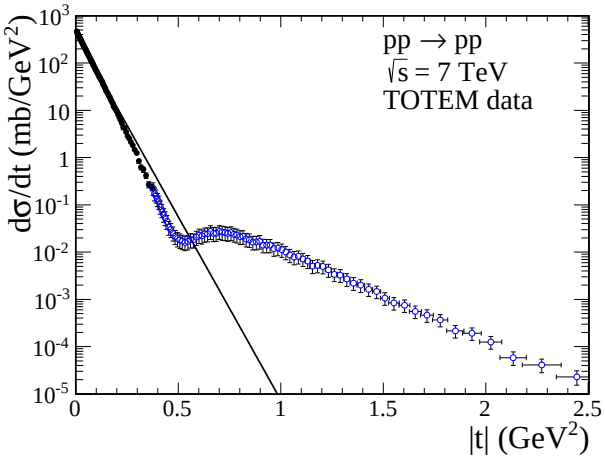

Figure 2.7: Differential distribution for pp elastic scattering at $\sqrt{s} = 7$ TeV. The CERN-LHC-TOTEM experimental data [140], which cover the $|t|$ range $0.005 - 0.4$ GeV^2, were collected using Roman Pot detectors very close to the outgoing beam. The data measurement in the higher $|t|$ range are taken from [142].

2.3 Central diffractive mechanism

We shall study exclusive central meson pair production in proton-proton (proton-antiproton) collisions:

$$p(p_a, \lambda_a)p(p_b, \lambda_b) \to p(p_1, \lambda_1) + M(p_3)\bar{M}(p_4) + p(p_2, \lambda_2)\,. \tag{2.22}$$

Here $p_{a,b}$, $p_{1,2}$ and $\lambda_{a,b}$, $\lambda_{1,2}$ denote the four-momenta and helicities of the protons, respectively, and central system $M(p_3)\bar{M}(p_4)$ denotes a meson pair ($\pi^+\pi^-$ or K^+K^-) with corresponding four-momenta p_3 and p_4.

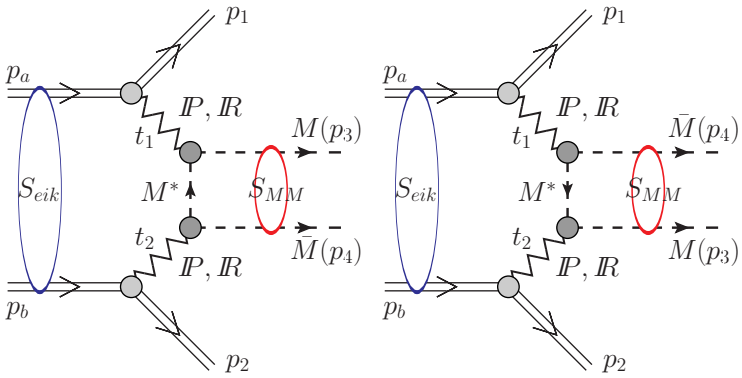

Figure 2.8: A sketch of the central double diffractive mechanism of exclusive production of meson pairs including the Regge exchanges ($I\!P$, $I\!R$) and an intermediate (off-shell) meson exchange (M^*). The absorptive corrections due to proton-proton interactions and meson-meson rescattering (indicated by the blobs) are very relevant at high energies.

The dominant mechanism of the exclusive production of pion/kaon meson pair at high energies is sketched in Fig. 2.8. This mechanism is relatively simple compared to that of the $pp \to nn\pi^+\pi^+$ reaction [4], see Fig. 4.43 in Section 4.7. In calculations of the amplitude related to the central diffractive mechanism (2.22) for the $pp \to pp\pi^+\pi^-$ reaction we follow the general rules of Pumplin and Henyey [122] (for early rough estimates see also Refs. [126, 143] and references therein). This mechanism can be used to calculate an expected non-resonant background and can be modelled using a "non-perturbative" framework, mediated by pomeron-pomeron fusion with an intermediate off-shell meson (M^*) exchange.

The Born amplitude for the $pp \to pp\pi^+\pi^-$ reaction can be written as

$$|\mathcal{M}^{Born}|^2 = |\mathcal{M}_{I=0}|^2 + |\mathcal{M}_{I=1}|^2 + |\mathcal{M}_{I=2}|^2 , \tag{2.23}$$

where I denotes the isospin of the $\pi^+\pi^-$ system. The isospin amplitudes can be decomposed to the Regge ingredients as

$$\mathcal{M}_{I=0} = \mathcal{M}^{I\!P I\!P} + \mathcal{M}^{I\!P f_{2I\!R}} + \mathcal{M}^{f_{2I\!R} I\!P} + \mathcal{M}^{f_{2I\!R} f_{2I\!R}} + \langle 1,0;1,0 \,|\, 0,0\rangle \, \mathcal{M}^{\rho_{I\!R}\rho_{I\!R}} , \tag{2.24}$$

$$\mathcal{M}_{I=1} = \mathcal{M}^{I\!P \rho_{I\!R}} + \mathcal{M}^{\rho_{I\!R} I\!P} + \mathcal{M}^{f_{2I\!R}\rho_{I\!R}} + \mathcal{M}^{\rho_{I\!R} f_{2I\!R}} , \tag{2.25}$$

$$\mathcal{M}_{I=2} = \langle 1,0;1,0 \,|\, 2,0\rangle \, \mathcal{M}^{\rho_{I\!R}\rho_{I\!R}} , \tag{2.26}$$

where the Clebsch-Gordan coefficients $\langle j_1, m_1; j_2, m_2 \,|\, j, m\rangle$ are

$$\langle 1,0;1,0 \,|\, 0,0\rangle = \sqrt{2/3} \quad \text{and} \quad \langle 1,0;1,0 \,|\, 2,0\rangle = -\sqrt{1/3} .$$

Not only leading double pomeron exchanges contribute, but also the subleading f_{2R} and ρ_R reggeon exchanges. For the pomeron-pomeron fusion we have C-parity $C = +1$ and $I = 0$.

In order to deeper insight we calculate the percentage shared by the isospin contributions (2.24), (2.25), and (2.26) to the total cross section in the $pp \to pp\pi^+\pi^-$ reaction. At low energy $\sqrt{s} = 5.5$ GeV (PANDA), where the dominance of the reggeon exchanges is justified, we get [5] $\sigma_{I=0} : \sigma_{I=1} : \sigma_{I=2}$ = 97.339% : 2.258% : 0.003% of total cross section. At higher energies $\sqrt{s} = 18.9$ GeV (COMPASS) ($\sigma_{tot} = 66.2$ μb) and $\sqrt{s} = 62$ GeV (ISR) ($\sigma_{tot} = 115.1$ μb) the contributions of isospin $I = 1$ and $I = 2$ amplitudes are even smaller: 98.941% : 1.058% : 0.001% and 99.907% : 0.093% : $<$ 0.001%, respectively. This can be summarized:

$$|\mathcal{M}_{I=0}|^2 \gg |\mathcal{M}_{I=1}|^2 \gg |\mathcal{M}_{I=2}|^2 . \tag{2.27}$$

[5] In this calculations we used exponential type of off-shell pion form factor discussed below (2.29) and $\Lambda_{off,E} = 1$ GeV. In order to exclude resonance regions we used (2.20) with the parameters $W_0 = 2$ GeV and $a_0 = 0.2$ GeV. We obtained the total cross section $\sigma_{tot} = 0.6$ μb at $\sqrt{s} = 5.5$ GeV.

Table 2.2: A percentage share of cross sections for different combinations of Regge exchanges in diagrams in Fig. 2.8.

$\sqrt{s}$	$I\!P I\!P$	$I\!P f_{2R}$ ($f_{2R} I\!P$)	$f_{2R} f_{2R}$
5.5 GeV	3.2	7.6	16.8
18.9 GeV	9.8	8.8	6.5
62 GeV	21.3	9.4	1.6

In similar way, in Table 2.2 we present a percentage shared by cross sections for the individual Regge exchanges in the $\mathcal{M}_{I=0}$ amplitude (2.24). The $\rho_R \rho_R$ component is negligible (see the strength parameters Table 2.1) and was omitted in further analysis. One can observe that at lower energies the subleading f_{2R} exchanges constitutes a large contribution to the total cross section and must be included in addition to the pomeron exchanges. Furthermore, there is a large interference effect between components in the amplitude of about 55-60%. (respect to the total cross section in full phase space). As we shall see in the results section imposing limitations on meson rapidity $|y_M| < 1$ and go to higher energies reduces the role of subleading f_{2R} exchanges, however, due to their non-negligible interference effects with the leading $I\!P I\!P$ term we keep them in our calculations.

Thus, the Born amplitude with the intermediate meson M^* exchange follows

$$\begin{aligned} \mathcal{M}^{Born} &= M_{13}(s_{13}, t_1) F_{M^*}(\hat{t}) \frac{1}{\hat{t} - m^2_{M^*}} F_{M^*}(\hat{t}) M_{24}(s_{24}, t_2) \\ &\quad + M_{14}(s_{14}, t_1) F_{M^*}(\hat{u}) \frac{1}{\hat{u} - m^2_{M^*}} F_{M^*}(\hat{u}) M_{23}(s_{23}, t_2) \,, \end{aligned} \tag{2.28}$$

where the $M_{ik}(s_{ik}, t_i)$ elastic amplitudes denotes "interaction" between forward proton ($i = 1$) or backward proton ($i = 2$) and one of the two mesons ($k = 3$ for M or $k = 4$ for $\bar{M}$). $s_{ik} = W^2_{ik}$, where W_{ik} is the center-of-mass energy in the (ik) subsystems. The energy dependence of the subsystem amplitudes M_{ik} is parametrised in terms of the pomeron and the f_{2R} reggeon exchanges, as explained in Section 2.2. We found the corresponding strength parameters from fitting total meson-nucleon cross sections as a function of the center-of-mass energy [113] to the world experimental data [96, 124], see Table 2.1). In order to exclude resonance regions the M_{ik} terms are "corrected" by a purely phenomenological smooth cut-off correction factors (2.20). At high subsystem energies $W_{ik} > 20$ GeV only the pomeron exchange survive.

The extra form factors, $F(\hat{t}/\hat{u})$, "correct" for the off-shellness of the intermediate mesons in the middle of the diagrams, see Fig. 2.8. In the following for brevity we shall use notation $\hat{t}/\hat{u}$ which means off-shell $\hat{t}$ or $\hat{u}$-channel meson exchange. Because the form of the form factor is unknown, in particular at higher values of $|\hat{t}/\hat{u}|$ (see the $< |\hat{t}| > (M_{M\bar{M}}$ distributions in Fig. 2.9), they are treat as a phenomenological input in our model and are parametrised as

$$F_{M^*}(\hat{t}/\hat{u}) = \exp\left(\frac{\hat{t}/\hat{u} - m^2_{M^*}}{\Lambda^2_{off,E}}\right) , \tag{2.29}$$

$$F_{M^*}(\hat{t}/\hat{u}) = \frac{\Lambda^2_{off,M} - m^2_{M^*}}{\Lambda^2_{off,M} - \hat{t}/\hat{u}} , \tag{2.30}$$

$$F_{M^*}(\hat{t}/\hat{u}) = \exp\left(-\sqrt{-(\hat{t}/\hat{u} - m^2_{M^*})}/\Lambda_{off}\right) . \tag{2.31}$$

All form factors are normalized to unity on the meson-mass-shell, i.e. if the squared four-momentum transfer is equal to $m^2_{M^*}$. In general, the parameter Λ_{off} is not known precisely but, in principle, could be fitted to the normalized experimental data. From our general experience in hadronic physics we expect $\Lambda_{off} \sim 1$ GeV. How to extract the off-shell parameters will be discussed in Section 2.6.

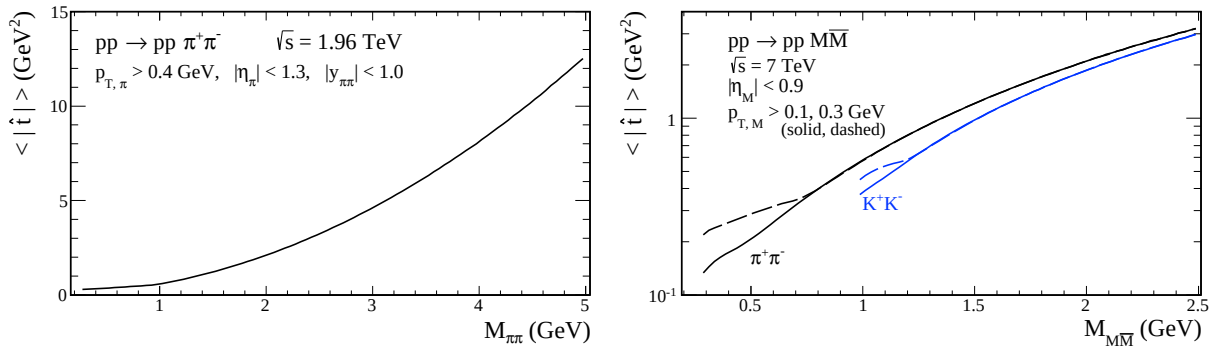

Figure 2.9: Mean value of $|\hat{t}|$ as a function of two-meson invariant mass for the $pp \to pp\pi^+\pi^-$ (black lines) and the $pp \to ppK^+K^-$ (blue lines) reactions at $\sqrt{s} = 1.96$ GeV (left panel) and 7 TeV (right panel). These calculations were done with the usual (mesonic) propagator and with the cut-off parameter $\Lambda_{off,E} = 1$ GeV.

2.3.1 Reggeization of the exchanged meson

The intermediate pion/kaon exchange as a meson exchange is a correct description at rather low energies. At higher energies we may have to account for the fact that the exchanged object in $\hat{t}/\hat{u}$-channel is not a simple meson but can correspond to a whole family of exchanges, that is, the pion/kaon reggeization is required. We have written $\hat{s}, \hat{t}, \hat{u}$ to stress that these are quantities for a subprocess rather than for a full reaction. In order to preserve meson physics at low pion-pion energies ($\hat{s} < 1$ GeV) and get the Regge form of the amplitude at higher energies $\hat{s}$ we propose to use a generalized propagator

$$\frac{1}{\hat{t}/\hat{u} - m^2_{M^*}} \to \beta_M(\hat{s}) \frac{1}{\hat{t}/\hat{u} - m^2_{M^*}} + \beta_R(\hat{s}) \mathcal{P}^{M^*}(\hat{t}/\hat{u}, \hat{s}) \,, \tag{2.32}$$

where we have introduced the pion/kaon Regge propagator (see [144, 145]) with the Euler's gamma function $\mathcal{P}^{M^*} = \mathcal{P}^K = \mathcal{P}^\pi$

$$\mathcal{P}^{M^*}(\hat{t}/\hat{u}, \hat{s}) = \frac{\pi \alpha'_{M^*}}{2\Gamma(\alpha_{M^*}(\hat{t}/\hat{u}) + 1)} \frac{1 + \exp(-i\pi\alpha_{M^*}(\hat{t}/\hat{u})}{\sin \pi\alpha_{M^*}(\hat{t}/\hat{u})} \left(\frac{\hat{s}}{\hat{s}_0}\right)^{\alpha_{M^*}(\hat{t}/\hat{u})} \,, \tag{2.33}$$

gives a suppression for large values of $\hat{t}/\hat{u}$. [6] The scale parameter $\hat{s}_0$ is taken as 1 GeV^2 and $\alpha_{M^*}(\hat{t}/\hat{u}) = \alpha'_{M^*}(\hat{t}/\hat{u} - m^2_{M^*})$ is the Regge trajectory to which the exchanged meson belongs with the slope parameter $\alpha'_{M^*} = \alpha'_\pi = \alpha'_K = 0.7$ GeV^{-2}. We have introduced also extra phenomenological functions $\beta_M(\hat{s})$ and $\beta_R(\hat{s})$ which role is to interpolate between the meson and Regge exchange. We parametrise them as

$$\beta_M(\hat{s}) = \exp\left(-(\hat{s} - 4m^2_{M^*})/\Lambda^2_{int}\right) \,, \quad \beta_R(\hat{s}) \;=\; 1 - \beta_M(\hat{s}) \,, \tag{2.35}$$

where the parameter Λ_{int} can be fitted to experimental data.

2.3.2 Proton-proton rescattering

In a more microscopic approach one has to include the absorption effects due to proton-proton interaction and the meson-meson final state interaction (FSI) (see 2.7.2) marked in Fig. 2.8

[6] For simplicity, we may replace the meson propagator by form:

$$\frac{1}{\hat{t}/\hat{u} - m^2_{M^*}} \to \frac{1}{\hat{t}/\hat{u} - m^2_{M^*}} \left(\frac{\hat{s}}{\hat{s}_0}\right)^{\alpha_{M^*}(\hat{t}/\hat{u})} \,. \tag{2.34}$$

Sometimes in the literature a different form for the $\hat{t}/\hat{u}$-dependence of the reggeized meson exchange is used, see for example Eq. (8) of [146].

by the blobs. The first type of the interaction was studied e.g. for three-body reactions [147]. For the four-body reaction discussed here a similar effect is expected, i.e. large energy-dependent damping of the cross section which is often embodied in the soft gap survival probability.

The absorptive corrections due to pp-interactions to the bare amplitude (Eq. (2.28)) can be written as:

$$\mathcal{M}^{pp-rescatt.}_{pp\to ppM\bar{M}} = i\int \frac{d^2\boldsymbol{k}_\perp}{2(2\pi)^2}\frac{A_{pp}(s,k_\perp^2)}{s}\mathcal{M}^{Born}_{pp\to ppM\bar{M}}(\boldsymbol{p}^*_{a\perp}-\boldsymbol{p}_{1\perp},\boldsymbol{p}^*_{b\perp}-\boldsymbol{p}_{2\perp})\,, \tag{2.36}$$

where $p_a^* = p_a - k_\perp$, $p_b^* = p_b + k_\perp$ and $k_\perp$ is the transverse momentum exchanged in the blob. $A_{pp}(s,k_\perp^2)$ is an elastic proton-proton amplitude for the appropriate energy (2.9). Again the Donnachie-Landshoff parametrisation [113] of the total pp or $p\bar{p}$ cross sections can be used to calculate the rescattering amplitude.

The amplitude for the exclusive process $pp \to ppM\bar{M}$ (with the four-momenta $p_a + p_b \to p_1 + p_2 + p_3 + p_4$) which includes the proton-proton interactions can be written as

$$\begin{aligned}\mathcal{M}_{pp\to ppM\bar{M}}(s,y_3,y_4,\boldsymbol{p}_{1\perp},\boldsymbol{p}_{2\perp},\boldsymbol{p}_{m\perp}) &= \mathcal{M}^{Born}_{pp\to ppM\bar{M}}(s,y_3,y_4,\boldsymbol{p}_{1\perp},\boldsymbol{p}_{2\perp},\boldsymbol{p}_{m\perp}) \\ &\quad +\mathcal{M}^{pp-rescatt.}_{pp\to ppM\bar{M}}(s,y_3,y_4,\boldsymbol{p}_{1\perp},\boldsymbol{p}_{2\perp},\boldsymbol{p}_{m\perp})\,,\end{aligned} \tag{2.37}$$

where the auxiliary quantity $\boldsymbol{p}_{m\perp} = \boldsymbol{p}_{3\perp} - \boldsymbol{p}_{4\perp}$.

The $2 \to 4$ amplitude described above (2.37) is used to calculate the corresponding cross section including limitations of the four-body phase-space. The details how to conveniently reduce the number of kinematical integration variables are discussed in Appendix A.

2.4 Other diffractive processes

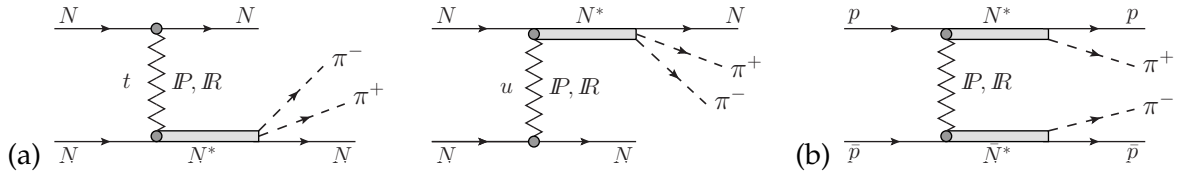

Figure 2.10: Resonance contributions leading to the $pp \to pp\pi^+\pi^-$ channel through diffractive single resonance excitation (DSRE) (panels (a)) and leading to the $p\bar{p} \to p\bar{p}\pi^+\pi^-$ channel through diffractive double resonance excitation (DDRE) (panel (b)).

Up to now we have discussed only central diffractive (CD) contribution to the $pp \to pp\pi^+\pi^-$ reaction. In general, there are also contributions with diffractive single or double proton/antiproton excitations followed by the nucleon resonance decays shown in Fig. 2.10. At high energy the first mechanism (panel (a)) contribute both to the $pp \to pp\pi^+\pi^-$ and $p\bar{p} \to p\bar{p}\pi^+\pi^-$ reaction while the second mechanism (panel (b)) only to the $p\bar{p} \to p\bar{p}\pi^+\pi^-$ reaction. In single and double diffractive dissociation, one or both of the protons get diffractively excited, and the proton remnants are very much forward focussed. The charge exchange reactions in proton-proton collisions (e.g. $pp \to \Delta^0 + \Delta^{++} \to p\pi^- + p\pi^+$ with dominating the pion-trajectory exchange at low energies and the ρ-trajectory exchange at high energies) were recently examined in Ref. [148]. The charge exchange reactions can, however, also be initiated by the exchange of a photon.

In general, there are also contributions with other diffractive processes leading to K^+K^- production shown in Fig.2.11 The exclusive $pp \to ppK^+K^-$ reaction was studied only at low energies [149, 150], where the dominant mechanisms are exclusive $a_0(980)$ and $f_0(980)$ production [149] or excitation of nucleon and Λ resonances [150].

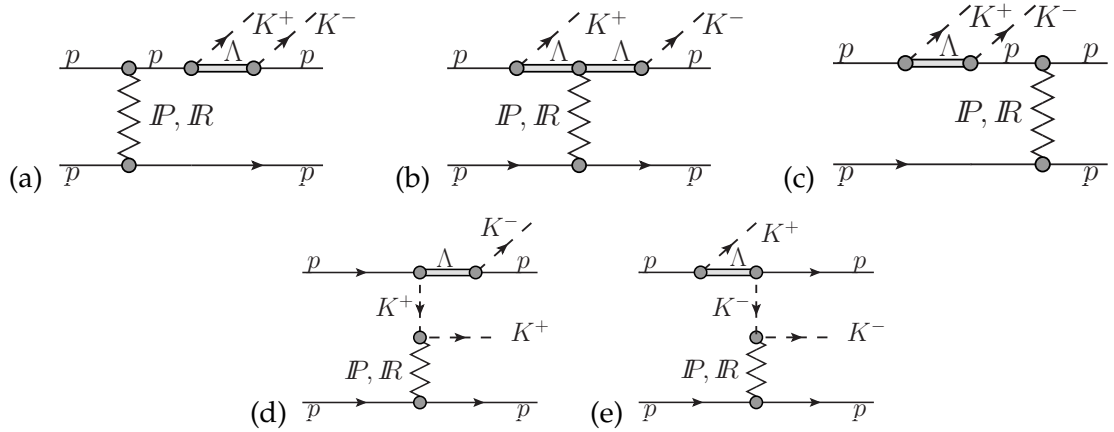

Figure 2.11: Other diffractive contributions leading to the $pp \to ppK^+K^-$ channel.

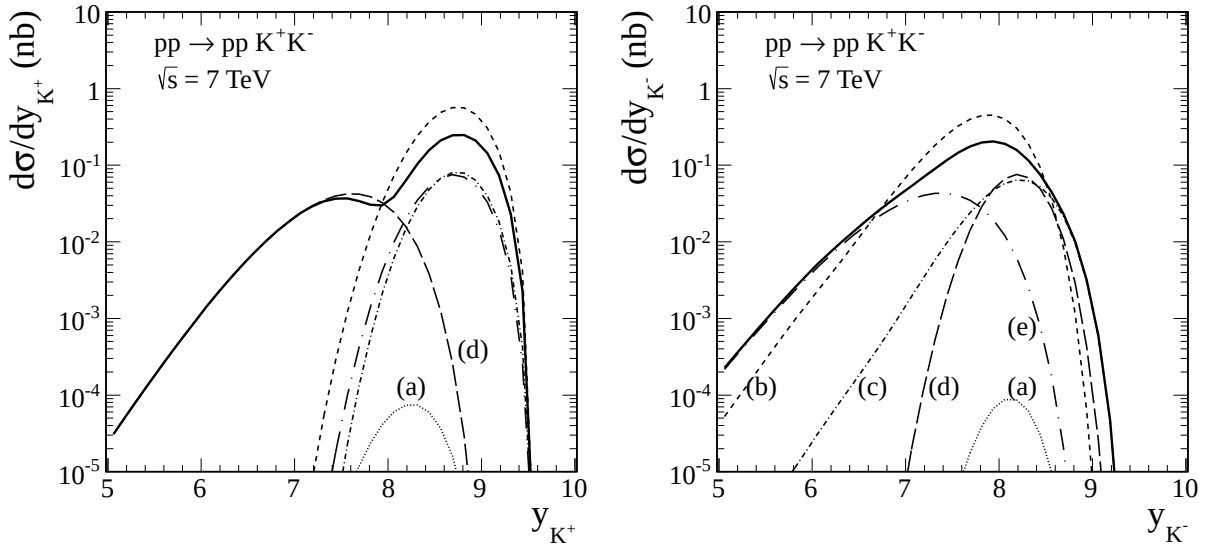

Figure 2.12: Differential cross sections $d\sigma/dy_{K^+}$ (left panel) and $d\sigma/dy_{K^-}$ (right panel) for the $pp \to ppK^+K^-$ reaction at $\sqrt{s} = 7$ TeV. The solid line represents the coherent sum of all amplitudes. The dotted, dashed, dash-dotted, long-dashed, long-dash-dotted lines correspond to contributions from diagrams (a) - (e) in Fig.2.11. The reggeization of particle exchange was included here.

It is straightforward to evaluate the new diffractive contributions of diagrams (a) - (e).

The Born amplitudes are given below:

$$\begin{aligned}
\mathcal{M}^{(a)}_{\lambda_a\lambda_b\to\lambda_1\lambda_2K^+K^-} &= \bar{u}(p_1,\lambda_1)i\gamma_5 S_\Lambda(p^2_{1fl})i\gamma_5 S_p(p^2_{1fp})u(p_a,\lambda_a)\, g^2_{\Lambda KN}\, F^2_p(p^2_{1fp})\, F^2_\Lambda(p^2_{1fl}) \\
&\quad \times is C^{NN}_{\mathbb{P}} \left(\frac{s}{s_0}\right)^{\alpha_{\mathbb{P}}(t_2)-1} \exp\left(\frac{B^{NN}_{\mathbb{P}} t_2}{2}\right) \delta_{\lambda_2\lambda_b}, \qquad (2.38) \\
\mathcal{M}^{(b)}_{\lambda_a\lambda_b\to\lambda_1\lambda_2K^+K^-} &= \bar{u}(p_1,\lambda_1)i\gamma_5 S_\Lambda(p^2_{1fl})S_\Lambda(p^2_{1il})i\gamma_5 u(p_a,\lambda_a)\, g^2_{\Lambda KN}\, F^2_\Lambda(p^2_{1il})\, F^2_\Lambda(p^2_{1fl}) \\
&\quad \times is_{124} C^{\Lambda N}_{\mathbb{P}} \left(\frac{s_{124}}{s_0}\right)^{\alpha_{\mathbb{P}}(t_2)-1} \exp\left(\frac{B^{\Lambda N}_{\mathbb{P}} t_2}{2}\right) \delta_{\lambda_2\lambda_b} \\
&\quad \times \left(s_{134}/s^{pKK}_{th}\right)^{\alpha_\Lambda(p^2_{1il})-1/2}, \qquad (2.39) \\
\mathcal{M}^{(c)}_{\lambda_a\lambda_b\to\lambda_1\lambda_2K^+K^-} &= \bar{u}(p_1,\lambda_1) S_p(p^2_{1ip})i\gamma_5 S_\Lambda(p^2_{1il})i\gamma_5 u(p_a,\lambda_a)\, g^2_{\Lambda KN}\, F^2_\Lambda(p^2_{1il})\, F^2_p(p^2_{1il}) \\
&\quad \times is_{12} C^{NN}_{\mathbb{P}} \left(\frac{s_{12}}{s_0}\right)^{\alpha_{\mathbb{P}}(t_2)-1} \exp\left(\frac{B^{NN}_{\mathbb{P}} t_2}{2}\right) \delta_{\lambda_2\lambda_b} \\
&\quad \times \left(s_{14}/s^{pK}_{th}\right)^{\alpha_N(p^2_{1ip})-1/2} \left(s_{34}/s^{KK}_{th}\right)^{\alpha_\Lambda(p^2_{1il})-1/2}, \qquad (2.40) \\
\mathcal{M}^{(d)}_{\lambda_a\lambda_b\to\lambda_1\lambda_2K^+K^-} &= \bar{u}(p_1,\lambda_1)i\gamma_5 S_\Lambda(p^2_{1fl})i\gamma_5 u(p_a,\lambda_a)\, S_K(p^2_{1fk})\, g^2_{\Lambda KN}\, F^2_\Lambda(p^2_{1fl})\, F^2_K(p^2_{1fk}) \\
&\quad \times is_{23} C^{KN}_{\mathbb{P}} \left(\frac{s_{23}}{s_0}\right)^{\alpha_{\mathbb{P}}(t_2)-1} \exp\left(\frac{B^{KN}_{\mathbb{P}} t_2}{2}\right) \delta_{\lambda_2\lambda_b} \\
&\quad \times \left(s_{134}/s^{pKK}_{th}\right)^{\alpha_K(p^2_{1fk})-1}, \qquad (2.41) \\
\mathcal{M}^{(e)}_{\lambda_a\lambda_b\to\lambda_1\lambda_2K^+K^-} &= \bar{u}(p_1,\lambda_1)i\gamma_5 S_\Lambda(p^2_{1il})i\gamma_5 u(p_a,\lambda_a)\, S_K(p^2_{1ik})\, g^2_{\Lambda KN}\, F^2_\Lambda(p^2_{1il})\, F^2_K(p^2_{1ik}) \\
&\quad \times is_{24} C^{KN}_{\mathbb{P}} \left(\frac{s_{24}}{s_0}\right)^{\alpha_{\mathbb{P}}(t_2)-1} \exp\left(\frac{B^{KN}_{\mathbb{P}} t_2}{2}\right) \delta_{\lambda_2\lambda_b} \\
&\quad \times \left(s_{14}/s^{pK}_{th}\right)^{\alpha_K(p^2_{1ik})-1} \left(s_{13}/s^{pK}_{th}\right)^{\alpha_\Lambda(p^2_{1il})-1/2}, \qquad (2.42)
\end{aligned}$$

where $s_0 = 1$ GeV^2 and $s^{pK}_{th} = (m_N + m_K)^2$, $s^{pKK}_{th} = (m_N + 2m_K)^2$. In the above equations $u(p_i,\lambda_i)$, $\bar{u}(p_f,\lambda_f) = u^\dagger(p_f,\lambda_f)\gamma^0$ are the Dirac spinors (normalized as $\bar{u}(p)u(p) = 2m_N$) of the initial and outgoing protons with the four-momenta p and the helicities λ. Here $s_{ij} = (p_i + p_j)^2$, $s_{ijk} = (p_i + p_j + p_k)^2$ are squared invariant masses of the (i,j) and (i,j,k) systems. The four-momenta squared of the virtual particles are: $p^2_{1il,2il} = (p_{a,b} - p_3)^2$, $p^2_{1fl,2fl} = (p_{1,2} + p_4)^2 = s_{14,24}$, $p^2_{1ik,2ik} = (p_{1il,2il} - p_{1,2})^2$, $p^2_{1fk,2fk} = (p_{a,b} - p_{1il,2il})^2$, $p^2_{1ip,2ip} = (p_{1il,2il} - p_4)^2$, $p^2_{1fp,2fp} = (p_{1fl,2fl} + p_3)^2 = s_{134,234}$. While the four-momenta squared of transferred kaons and protons are < 0, it is not the case for transferred Λ's, where $p^2_{1il,2il} < m^2_\Lambda$. The propagators for the intermediate particles are respectively

$$S_K(k^2) = \frac{i}{k^2 - m^2_K}, \quad S_p(k^2) = \frac{i(k_\nu\gamma^\nu + m_N)}{k^2 - m^2_N}, \quad S_\Lambda(k^2) = \frac{i(k_\nu\gamma^\nu + m_\Lambda)}{k^2 - m^2_\Lambda}. \qquad (2.43)$$

The form factors, $F_i(k^2)$, correct for the off-shellness of the virtual particles and are parametrised as

$$F_i(k^2) = \exp\left(\frac{-|k^2 - m^2_i|}{\Lambda^2_{off}}\right), \qquad (2.44)$$

where the parameter $\Lambda_{off} = 1$ GeV is taken in practical calculations. In our calculation the ΛKN coupling constant is taken as $g^2_{\Lambda KN} = 14$ [151].

The Regge parameters in diagram (b) in Fig.2.11 (see Eq.(2.39)) are not known precisely and are assumed to be $C^{\Lambda N}_{\mathbb{P}} \approx C^{NN}_{\mathbb{P}}$ (see Table 2.1) and $B^{\Lambda N}_{\mathbb{P}} \approx B^{NN}_{\mathbb{P}} = 9$ GeV^{-2}. To reproduce the

high-energy Regge dependence the amplitudes given in Eqs (2.39 - 2.42) are corrected, e.g. the amplitude of (2.41) is multiplied by a factor $(s_{134}/s_{th}^{pKK})^{\alpha_K(p_{1fk}^2)-1}$. The parameters of the Regge trajectories used in the calculation are given as $\alpha_K(k^2) = 0.7(k^2 - m_K^2)$, $\alpha_p(k^2) = -0.3 + 0.9k^2$, $\alpha_\Lambda(k^2) = -0.6 + 0.9k^2$ for the kaon, proton and Λ exchanges, respectively.

In Fig.2.12 we present rapidity distribution of K^+ (left panel) and rapidity distribution of K^- (right panel) including only diagrams shown in Fig.2.11. The contribution for individual diagrams (a) - (e) are also shown. In the discussed here new mechanism not only protons but also kaons are produced dominantly in very forward or very backward directions. The two kaons have, however, similar rapidities which means that there is no gap between kaons. This means that both kaons are preferentially produced very forward or very backward forming a large size gap between kaons and one of the protons (backward or forward, respectively). Please note a very limited range of rapidities shown in the figure. The reggeization leads to an extra damping of the cross section. The cross section is much smaller than that for the DPE mechanism discussed above. It is particularly interesting that the distributions for K^+ and K^- have slightly different shape.

2.5 Review of new experimental results

The recent experiments at COMPASS, RHIC, Tevatron, and LHC are expected to provide new opportunities for studying the central exclusive production of mesons at high energies in the exclusive processes $pp \to pM\bar{M}p$ and $p\bar{p} \to pM\bar{M}\bar{p}$ (Tevatron). Here we present the preliminary measurements of the invariant mass spectra of two charged pions only. Much more new data sets will soon be available.

The physics motivation is understanding of the scalar meson spectrum and perturbative and non-perturbative aspects of meson production. One of the goals of these experiments is to study the existence and signatures of exotic mesons and glueball (i.e. objects composed entirely of valence gluons) candidates at central rapidities, in continuation of the efforts that were made in the past [115]. Since pomerons are considered to have no valence quark contribution, pomeron-pomeron fusion was proposed to be well suited for the production of glueballs.

This process can be realised in a fixed-target experiment by the scattering of a proton beam on a proton target $p_{beam}p_{target} \to p_{fast}\pi^+\pi^- p_{slow}$, where a system of $\pi^+\pi^-$ particles is produced centrally. In Fig. 2.13 we show the $\pi^+\pi^-$ invariant mass distribution measured at the fixed-target experiments at CERN Omega spectrometer [152] and by the COMPASS Collaboration at CERN SPS [153–155]. In the COMPASS experiment in order to separate the $\pi^+\pi^-$ system from the fast proton, a cut on the invariant mass combinations $M_{p\pi} > 1.5$ GeV was introduced and after this kinematic cuts the centrally $\pi\pi$ system lies in the region $|x_F| \leqslant 0.25$. At all three different centre-of-mass energies the $\rho(770)$, the $f_2(1270)$ and the sharp drop due to the $f_0(980)$, can be observed. Above the $\pi\pi$ threshold, there is a maximum corresponding probably to the σ (or $f_0(500)$) resonance, then close to 1 GeV a characteristic dip due to the $f_0(980)$ meson and the enhancement at $1.2 - 1.4$ GeV related to the tensor $f_2(1270)$ meson and other scalar mesons present in the $\pi\pi$ channel. The relative yield of $\rho(770)$ signal decreased rapidly with increasing $\sqrt{s}$ up to the ISR energies where the ρ signal almost vanishes [156]. On the other hand the enhancement at low masses as well as $f_0(980)$ remain particularly unchanged.

It is worth mentioning that in the previous experiments at $\sqrt{s} = 23.8$ GeV [152] (WA76 Collaboration) and $\sqrt{s} = 29.1$ GeV [90] (WA102 Collaboration) a study of the centrally produced $\pi^+\pi^-$ and K^+K^- channels in pp collisions has been performed. The suppression of ρ and $f_2(1270)$ signals in the low t region ($t < 0.3$ GeV^2) has been observed at $\sqrt{s} = 12.7, 23.8$ GeV, see Fig. 29 in Ref. [152]. In the latter paper a study of resonance production rate as a function of the difference in the transverse momentum vectors (dP_T) between the particles exchanged from vertices has been performed. An analysis of the dP_T dependence of the four-momentum transfer behaviour shows that the $\rho^0(770)$, $\phi(1020)$, $f_2(1270)$ and $f_2'(1525)$ mesons are suppressed at small dP_T in contrast to the scalar $f_0(980)$, $f_0(1500)$ and $f_0(1710)$ mesons. Different distributions

are observed in the azimuthal angle (defined as the angle between the $p_\perp$ vectors of the two outgoing protons) for the different resonances [90]. For more information about some differential distributions from previously carried out experiments we refer to Section 3.2.

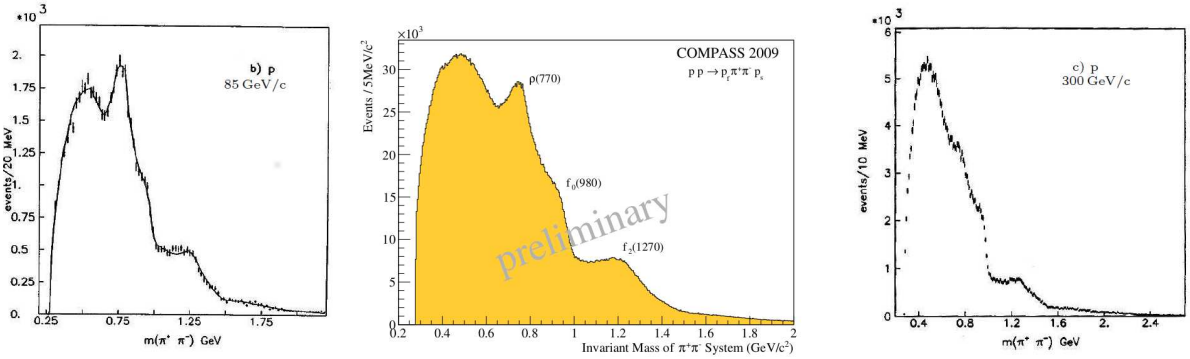

Figure 2.13: Invariant mass spectrum of $\pi^+\pi^-$ system measured with the COMPASS [154, 155] (central panel) and the Omega [152] (left and right panel) at three proton beam energies $P_{lab} = 85, 190, 300$ GeV correspond to the centre-of-mass energies $\sqrt{s} = 12.7, 18.9, 23.8$ GeV, respectively.

In Fig. 2.14 the preliminary spectrum of the invariant mass of $\pi^+\pi^-$ pairs produced in central exclusive process (2.22) is presented. The exclusive measurement was obtained with the STAR detector at RHIC at $\sqrt{s} = 200$ GeV with forward protons tagged using Roman Pots (at very small four-momentum transfer squared range $0.003\ \text{GeV}^2 < -t_1, -t_2 < 0.035\ \text{GeV}^2$) and using two opposite charge tracks reconstructed in the STAR Time Projection Chamber (TPC) [157] (for the centrally produced mesons $|\eta_M| < 1$ and with transverse momentum $p_{\perp,M} > 0.15$ GeV). The spectrum is not corrected for acceptance, but preliminary acceptance study indicates that corrections will not change shape of the spectrum significantly [158]. This spectrum is dominated by the low invariant mass pairs and it shows the same characteristic features to the one published by the AFS Collaboration at ISR [156]. There is very small like-sign (non-exclusive) background, which gives a measure of exclusivity of the process. Preparation for analogous measurement at $\sqrt{s} = 500$ GeV and higher four-momentum transfers ($0.1\ \text{GeV}^2 < -t_1, -t_2 < 1.5\ \text{GeV}^2$) is in progress.

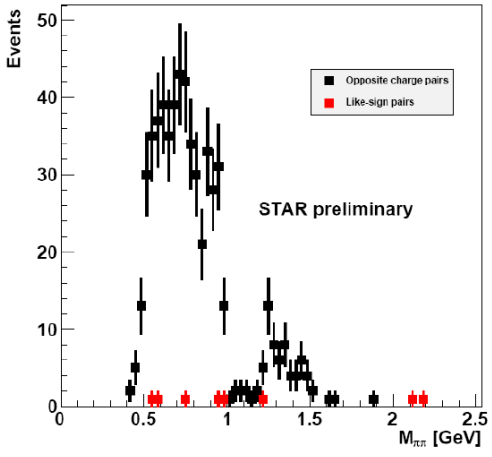

Figure 2.14: Invariant mass distribution of $\pi^+\pi^-$ pairs produced in central exclusive process $pp \to p\pi^+\pi^-p$ at $\sqrt{s} = 200$ GeV measured by the STAR detector, at very small four-momentum transfer squared $-t$ range $0.003\ \text{GeV}^2 < -t_1, -t_2 < 0.035\ \text{GeV}^2$, $|\eta_M| < 1$ and with transverse momentum $p_{\perp,M} > 0.15$ GeV [158]. The spectrum is not corrected for acceptance.

Fig. 2.15 shows the low mass region on a linear scale, and at both energies $\sqrt{s} = 0.9, 1.96$ TeV. The $f_0(980)$ signal is seen, and a dominant enhancement in the region of $f_2(1270)$ resonance (also dominant in $\gamma\gamma \to \pi^+\pi^-$). A possible shoulder on the high mass side ($f_0(1370)$)

is followed by a distinct change of slope at 1500 MeV, which was also seen at lower energies [156]. While the cross section shapes are similar at the two energies, they differ in detail as seen in the ratio plot. In Refs. [159–161] the authors observe that the ratio is lower in the region of the $f_2(1270)$ than it is below 1 GeV, expected to be dominated by S-wave. They also find that the mean $p_{\perp,\pi\pi}$ has a minimum in the $f_2(1270)$ region, and rises abruptly at 1.5 GeV. There is more rapidity available for proton dissociation at 1.96 TeV [161], the beam rapidities being 6.87 and 7.64 while the detector extends to $\eta = 5.9$ in both cases.

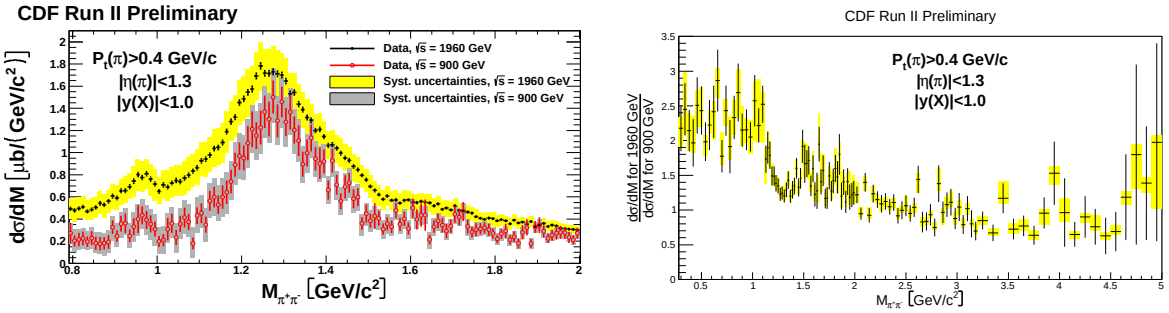

Figure 2.15: Invariant mass distribution of two particles, assumed to be $\pi^+\pi^-$ produced in proton-antiproton collisions at $\sqrt{s} = 0.9, 1.96$ TeV (the red and black data points, respectively) measured by the CDF detector at the Fermilab Tevatron [161]. The $\pi^+\pi^-$-pair was required to have $|y_{\pi\pi}| < 1$, $|\eta_M| < 1.3$, $p_{\perp,M} > 0.4$ GeV, and there are no other particles detected in $|\eta| < 5.9$. The distribution shown [161] is corrected for acceptance. The right panel shows ratio of cross sections $d\sigma/dM_{\pi\pi}$ at $\sqrt{s} = 1.96$ GeV and 0.9 TeV as a function of mass. In both cases rapidity gaps extend to $\eta = 5.9$, and p-dissociation is included.

In Fig. 2.16 we show the invariant mass of two-pions measured by the ALICE Collaboration at the LHC at CERN which analysed meson production in double gap events in minimum-bias proton-proton collisions at $\sqrt{s} = 7$ TeV [162] in the pseudorapidity range $|\eta_M| < 0.9$ and with transverse momenta $p_{\perp,M} \geqslant 0.3$ GeV. The information from the V0, T0, FMD, SPD and TPC detectors define the gaps spanning the range $-3.7 < \eta_M < -0.9$ and $0.9 < \eta_M < 5.1$, see [162]. Events with and without detector signals in these two ranges are defined to be no-gap and double gap events, respectively. A double rapidity gap can be induced by a combination of the pomeron, reggeon and photon exchanges. Also in this experiment the like-sign pairs are estimated to be very small (less than 5%, see Fig. 3 in [162]). In the double gap distribution the $\rho(770)$ ($J^{PC} = 1^{--}$) state is strongly suppressed while other resonant-like structure $f_0(980)$ (0^{++}) and $f_2(1270)$ (2^{++}) states can be seen.

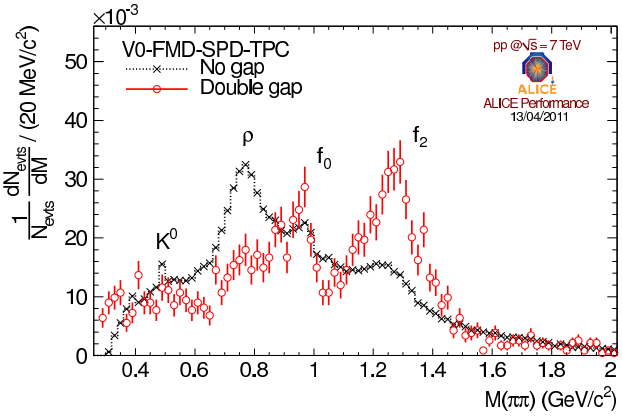

Figure 2.16: Invariant mass distributions of pion pair produced in proton-proton collisions at $\sqrt{s} = 7$ TeV measured by the ALICE detector for double and for no-gap events (left panel) and distribution of like and unlike sign pion pairs (right panel) in the pseudorapidity range $|\eta_M| < 0.9$ and with transverse momenta $p_{\perp,M} \geqslant 0.3$ GeV [162]. The distribution shown is not corrected for acceptance.

2.6 Model results

2.6.1 Comparison with low energy data

Let us start our predictions with integrated cross section, before we go to differential distributions. In Fig.2.17 we present the total cross section for the $pp \to pp\pi^+\pi^-$ reaction, i.e. the cross section integrated over full phase space, as a function of the center-of-mass energy. We show the experimental cross sections for the $pp \to pp\pi^+\pi^-$ reaction (the filled black circles) and for the $p\bar{p} \to p\bar{p}\pi^+\pi^-$ reaction (the filled blue triangles) which are more than 1 mb for ($2.5 < \sqrt{s} < 10$) GeV. This is a significant contribution to the total nucleon-nucleon cross section. For references of experimental data see [3]. Our results depend on the value of the nonperturbative, a priori unknown, parameter of the form factor responsible for off-shell effects of exchanged mesons. The low-$M_{\pi\pi}$ ($M_{\pi\pi} < 1.45$ GeV) and high-$M_{\pi\pi}$ (the Regge formalism) rescattering contributions discussed in Sections 1.1 and 1.6, respectively, are found to be negligible compared with the experimental data. Clearly for low energies ($\sqrt{s} < 20$ GeV) neither exclusive double diffraction nor the pion-pion rescattering constitute the dominant mechanism, see Section 2.4. Here the production of single and double nucleon resonance states is the dominant mechanism; e.g. the single Roper resonance excitation and its decay, see Section 1.1. In central diffraction, a hadronic system is formed by the fusion of two pomerons/reggeons. We show theoretical predictions of central diffractive contribution including the absorptive corrections due to pp-rescattering and for different model parameters. The cross section for the central diffractive contribution slowly grows with energy. The search for double pomeron exchange (DPE) mechanism contribution leads to an upper limits of $\simeq 20$ μb (for $M_{\pi\pi} \leqslant 0.7$ GeV) [163], (49 ± 5.5) μb [164], (30 ± 11) μb [165] and (44 ± 15) μb [166]. The experimental value of the cross section taken from [165] was obtained for $M_{p\pi} > 2$ GeV and no limitation on $M_{\pi\pi}$; reduces however to 9 μb for $M_{\pi\pi} \leqslant 0.6$ GeV [165]. We should remember, however, that the DPE cross section is quite sensitive to kinematical cuts which are used to define DPE candidate events.

Fig. 2.18 shows the theoretical uncertainties for the central diffractive contributions at midrapidity of both pions $y_\pi < 1$. We show the theoretical uncertainties due to different values of the cut-off parameter in form factor (2.29). The coherent sum of all Regge exchanges is shown by the black lines while the $I\!P I\!P$ exchange contribution alone by the blue lines. As we will discuss below, there is a large interference between Regge exchanges in the amplitude. The bare cross section rises with c.m.s. energy while the absorption corrections lower the rise; from a factor ~ 2 at $\sqrt{s} = 20$ GeV to a factor ~ 5 at $\sqrt{s} = 14$ TeV In general, the higher energy the higher absorption effects. We predict that the integrated cross section of meson pair production will decrease gently with c.m.s. energy.

In Fig.2.19 we compare our results with the experimental data [164, 167–174]. The experimental cuts on the rapidity of both pions ($y_\pi > 1.0$ see the left panel, $y_\pi > 1.5$ see the right panel) and $x_{F,p} \geqslant 0.9$ of both protons (A.16) are included in the calculations. As explained in the figure caption, we use different values of the off-shell meson form-factor parameter. In the calculations the absorption effects due to pp-rescattering have been included. Furthermore, we see that requiring $x_{F,p} > 0.9$ on both protons is especially important at lower energies $\sqrt{s} < 60$ GeV. The large discrepancy between experimental cross sections [172] (in the left panel the full triangle versus other experimental points) is the result of fitting the slope in t-distribution, i.e. their large error is due to the uncertainty in the extrapolation to low $|t| \approx 0$.

In Fig. 2.20 we show the two-meson invariant mass distribution at the center-of-mass energy of the CERN ISR $\sqrt{s} = 62$ GeV and with the experimental cuts on the rapidity of both mesons $|y_M| \leqslant 1.5$ and on the longitudinal momentum fractions $|x_{F,p}| > 0.9$ of both outgoing protons. We compare our results with the two-pion/kaon invariant mass spectrum from [174] (see Ref. [173] for early studies) [7]. The experimental data show some peaks above the non-

[7] The mass spectrum of the exclusive K^+K^- system at the CERN ISR is shown e.g. in Ref. [156] at $\sqrt{s} = 63$ GeV and in Ref. [173] at $\sqrt{s} = 62$ GeV.

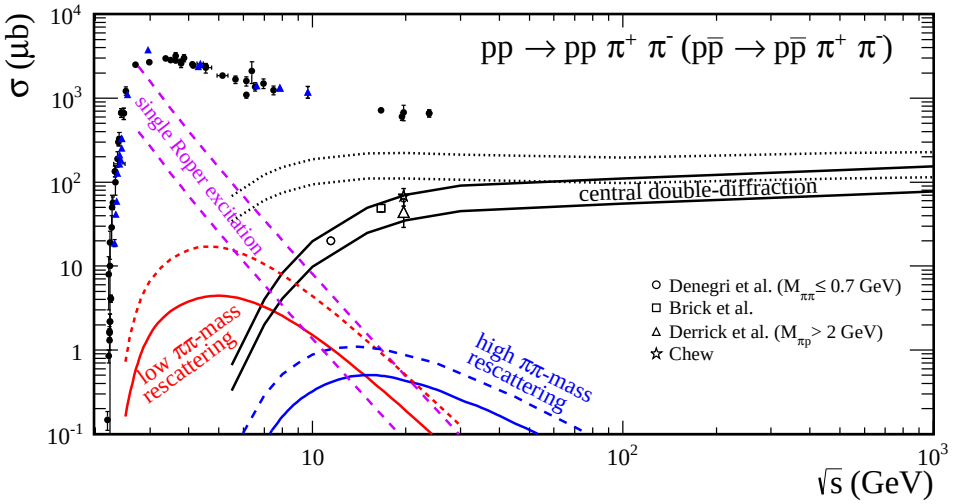

Figure 2.17: The total cross section (integrated over full phase space) for the $pp \to pp\pi^+\pi^-$ reaction as a function of the center-of-mass energy. We compare the pion-pion rescattering and the central diffractive contributions as well as the single Roper resonance excitation contribution with the experimental data. The theoretical uncertainties for these contributions are shown. The open symbols represent DPE contribution from Refs. [163–166] and filled symbols show the cross sections for the $pp \to pp\pi^+\pi^-$ reaction (black circles) and the $p\bar{p} \to p\bar{p}\pi^+\pi^-$ reaction (blue triangles); for references of experimental data see [3]. Details about the low $\pi\pi$-mass rescattering and the single Roper resonance excitation contributions can be found in Fig. 1.6 of Section 1.1. The high $\pi\pi$-mass rescattering contribution was obtained with the exponential type of πNN form factor for $\Lambda^2_{off,E} = 0.5\,\text{GeV}^2$ (the lower line) and $\Lambda^2_{off,E} = 1\,\text{GeV}^2$ (the upper line) and $B^{\pi\pi}_{\rho_{\mathbb{R}}} = 4\,\text{GeV}^{-2}$, see Section 1.6. In calculating the central diffractive contribution we take into account the absorption corrections. We exclude resonance regions multiplying the πN subsystem amplitudes (in Eq. (2.28)) by a purely phenomenological smooth cut-off correction factor (2.20) with parameters $W_0 = 1.5$ GeV, $a_0 = 0.2$ GeV and $W_0 = 2$ GeV, $a_0 = 0.2$ GeV, see the dotted and solid lines, respectively. We show results for $\Lambda^2_{off,E} = 1\,\text{GeV}^2$ (the lower lines) and $\Lambda^2_{off,E} = 1.6\,\text{GeV}^2$ (the upper lines).

resonant background which correspond to the $\pi^+\pi^-/K^+K^-$ resonances (σ, $f_2(1270)/f_2'(1525)$, $f_0(1500)$, etc.) which are not included explicitly in the calculations. These resonant states interfere with the continuum contribution; the production of lower mass resonances was recently examined in Ref. [13], see also Chapter 3. In the bottom panels we show the coherent sum of all (the upper line) as well as an individual Regge contributions (similarly as in Fig. 1.34 in Section 1.6). Absorption effects due to pp-interaction have been included in this calculation. The results depend on the value of the nonperturbative, a priori unknown parameter of the form factor (2.29) responsible for off-shell meson effects. Our model with the $\Lambda_{off,E}$ parameter fitted to the data provides an educated extrapolation to the unmeasured region $M_{M\bar{M}} \gtrsim 2$ GeV. We show results with the cut-off parameters $\Lambda^2_{off,E} = 1, 1.6, 2\,\text{GeV}^2$ as represented by the solid lines from bottom to top, respectively.

2.6.2 Predictions for high energy experiments

The distribution in the (y_3, y_4) space is particularly interesting. In Fig.2.21 we show distributions for the exclusive central diffractive and the pion-pion rescattering contributions for three c.m. energies $\sqrt{s} = 0.5, 1.96$ and 7 TeV. The shape of the distributions strongly depends on the collision energy. In the first case the pions are emitted preferentially in the same hemispheres, i.e. $y_3, y_4 > 0$ or $y_3, y_4 < 0$. One can see a shape of the ridge form elongated along the line $y_3 = y_4$. The minimum of the cross section on the top of the ridge occurs when $y_3 = y_4 = 0$ and two maxima close to the phase space ends. The minimum occurs in the part of the phase space where the pomeron-pomeron contribution dominates, i.e. when both W_{ik} are comparable and large. The maxima are related to the dominance of the pomeron-reggeon and reggeon-pomeron mechanisms, i.e. where one of W_{ik} is small and the second one is large. The

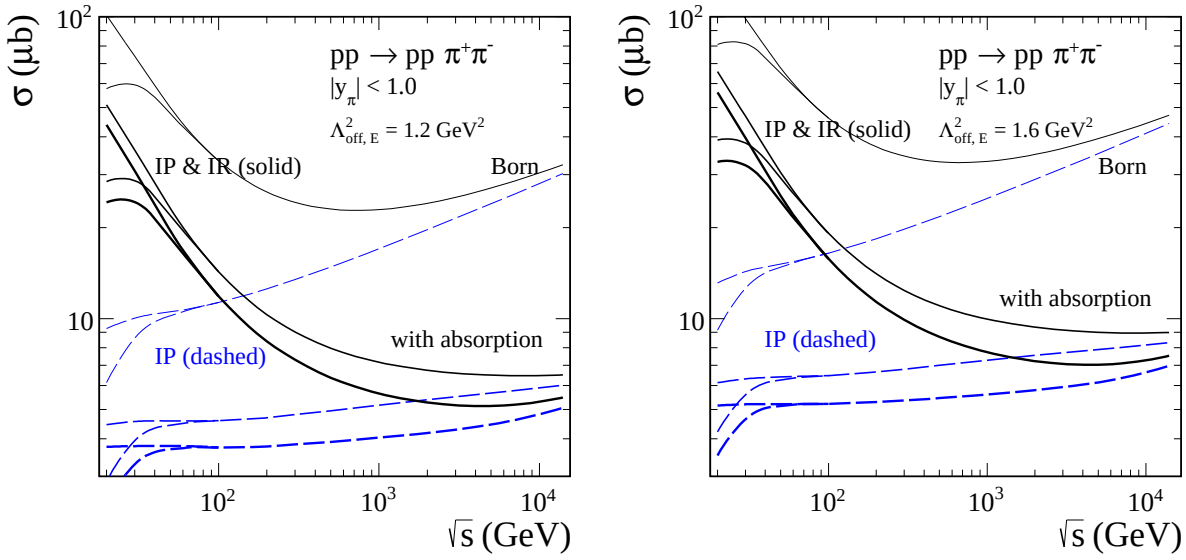

Figure 2.18: The integrated cross section at midrapidity of both pions $y_\pi < 1.0$ for the $pp \to pp\pi^+\pi^-$ reaction as a function of the center-of-mass energy. We present the central diffractive contribution with different components in the amplitude. The coherent sum of $\mathbb{P}\mathbb{P}$, $\mathbb{R}\mathbb{P}$, $\mathbb{P}\mathbb{R}$ and $\mathbb{R}\mathbb{R}$ exchanges is shown by the black solid lines. The contribution of $\mathbb{P}\mathbb{P}$ exchange alone is presented by the blue dashed lines. Results correspond to different values of the cut-off parameter in form factor (2.29): $\Lambda^2_{off,E} = 1.2$ GeV^2 (left panel) and $\Lambda^2_{off,E} = 1.6$ GeV^2 (right panel). At energies $\sqrt{s} < 60$ GeV the top and bottom lines correspond to calculations with $W_0 = 1.5$ GeV and 2 GeV (2.20), respectively. The role of absorption effects is also shown. The thick lower line is calculated by enhancing the absorptive amplitude (2.36) by a factor $c_{abs} = 1.2$.

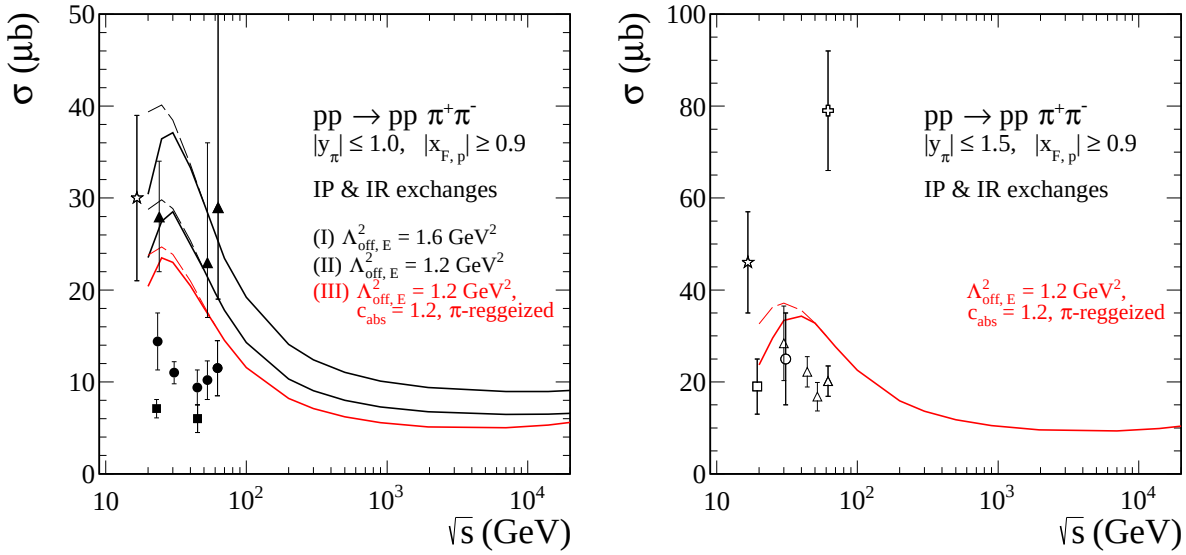

Figure 2.19: Cross section for the $pp \to pp\pi^+\pi^-$ reaction integrated over phase space with cuts relevant for a given experiment [164, 167–174]. The theoretical results are corrected by extrapolations to low energies by formula (2.20) with $W_0 = 2$ GeV and $a_0 = 0.2$ GeV and include the absorption effects. The experimental value from [168] (marked as open circle in the right panel) was obtained for the forward rapidity gaps $\Delta y = |y_p - y_\pi| > 2$. We show results for different values of the parameter $\Lambda^2_{off,E} = 1.2$ GeV^2 (the lower lines), $\Lambda^2_{off,E} = 1.6$ GeV^2 (the upper lines). For comparison, the dashed lines at low energies show the results without cut on $x_{F,p}$.

reggeon-reggeon contribution is completely negligible which is due to the fact that both W_{ik} cannot be small simultaneously. In the second case, for the pion-pion rescattering mechanism, the

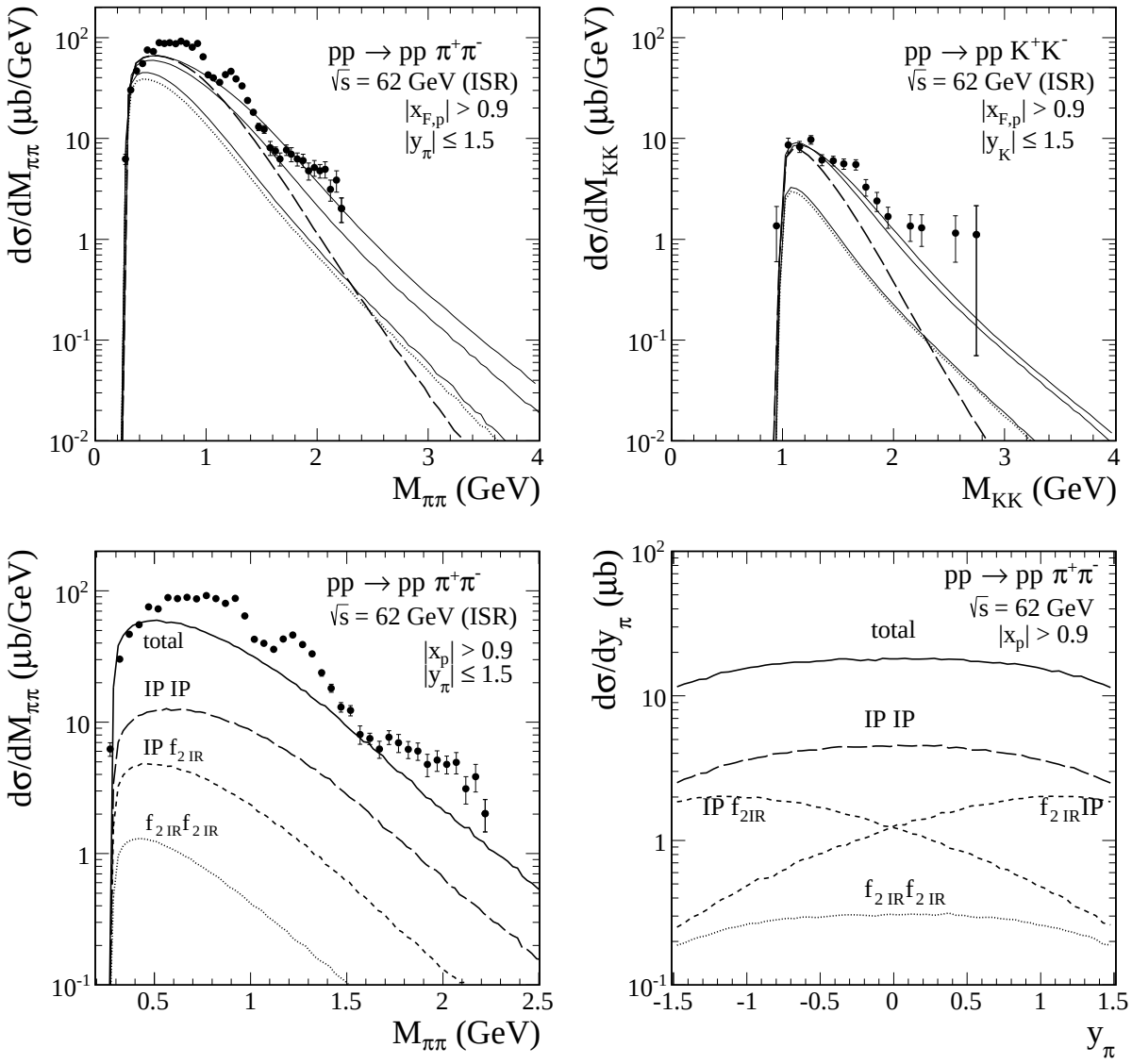

Figure 2.20: In the top panels we show the differential cross section $d\sigma/dM_{M\bar{M}}$ for the $pp \to pp\pi^+\pi^-$ reaction (left panel) and the $pp \to ppK^+K^-$ reaction (right panel) at $\sqrt{s} = 62$ GeV with experimental cuts relevant for the CERN ISR experimental data from [173, 174]. The proton-proton rescattering effects has been included in the calculations. In the top panels we show results for different values of the cut-off parameter $\Lambda^2_{off,E} = 1, 1.6, 2$ GeV^2 correspond to the solid lines from bottom to top, respectively. We include also the smooth cut-off formula (2.20) ($W_0 = 2$ GeV and $a_0 = 0.2$ GeV). The dotted line is calculated for $\Lambda_{off,E} = 1$ GeV and the absorptive amplitude (2.36) is multiplied somewhat arbitrarily by an extra factor $c_{abs} = 1.2$. The long-dashed line represent result obtained for $\Lambda^2_{off} = 2$ GeV^2 with the generalized off-shell meson propagator (2.32), where $\Lambda_{int} = 2$ GeV. In the bottom panels we show the individual Regge exchange contributions to the cross section and their coherent sum (total, the solid line) as a function of the two-pion invariant mass (left panel) and the pion rapidity (right panel) calculated for the usual (mesonic) pion propagator and $\Lambda^2_{off,E} = 1.6$ GeV^2. The double-pomeron exchanges ($I\!P I\!P$) are plotted by the long-dashed line, the pomeron-f_2 reggeon ($I\!P f_{2R}$) and the f_2 reggeon-pomeron ($f_{2R} I\!P$) exchanges by the short-dashed line, and the double-reggeon exchanges ($f_{2R} f_{2R}$) by the dotted line.

cross section drops quickly with $\sqrt{s}$. The rescattered pions are emitted preferentially in different hemispheres, i.e. (π^+ at positive y_3 and π^- at negative y_4) or (π^+ at negative y_3 and π^- at positive y_4). While at low energies (PANDA) both contributions overlap, see Fig. 1.34, at high energies (RHIC, Tevatron, LHC) they are well separated, i.e. can, at least in principle, be measured.

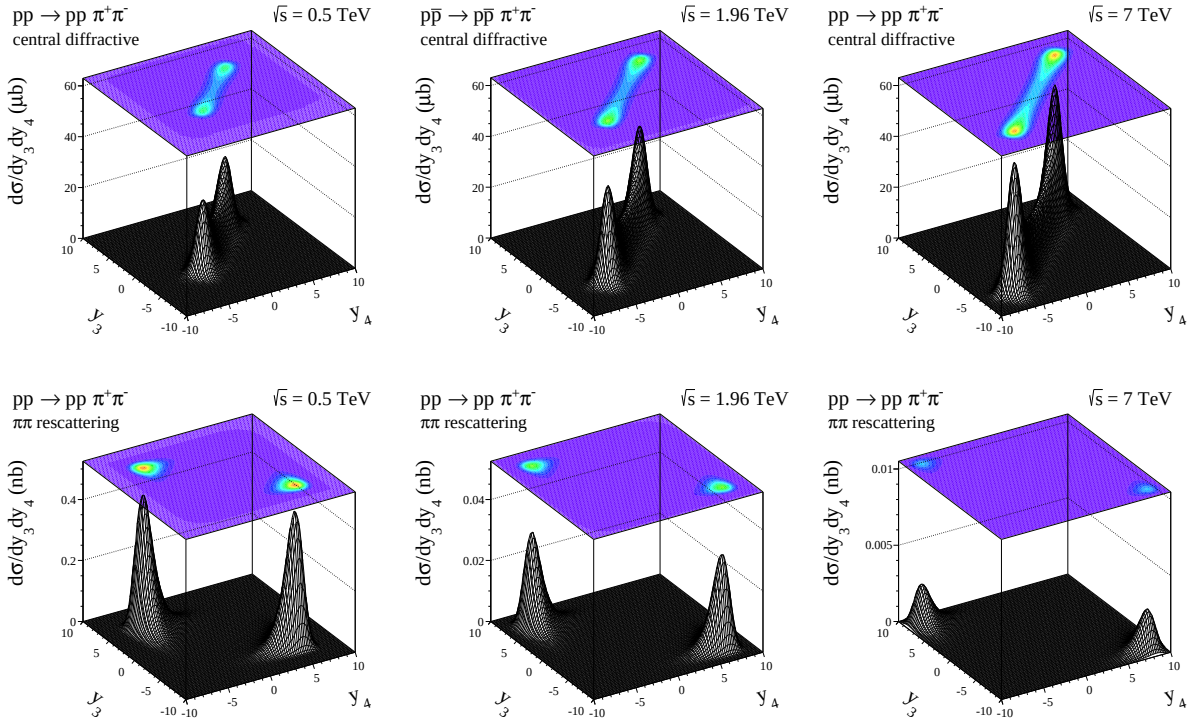

Figure 2.21: Differential cross section in (y_3, y_4) space for the central diffractive (top panels) and the pion-pion rescattering (bottom panels) contributions for different incident energies $\sqrt{s} = 0.5, 1.96, 7$ TeV. In this calculation for the central diffractive contribution we used the cut-off parameter $\Lambda^2_{off,E} = 2$ GeV^2, while for the pion-pion rescattering contribution $\Lambda = \Lambda_{off,M} = 1$ GeV and $B^{\pi\pi}_{\rho_{\mathbb{R}}} = 6$ GeV^{-2}.

In Fig.2.22 we show distributions in the (Z_1, Z_2) space for both contributions. The $Z_{1,2}$ variables used to define the exclusive double-pomeron exchange (DPE) region (see e.g. [164,166]) are given as

$$Z_1 = \ln(s/s_{134}), \quad Z_2 = \ln(s/s_{234}), \tag{2.45}$$

where s is the square of the total center-of-mass energy, $s_{ijk} = M^2_{ijk}$ is the invariant mass squared of the $p\pi\pi$ system, and $M^2_{ijk}/s \simeq 1 - |x_{F,i}|$ for nucleon i.

The 'camel-like' shape of the meson rapidity distribution requires a separate discussion. In our calculation we include both pomeron and reggeon exchanges. In Fig.2.23 (top panels) we show the cross section in pion rapidity at the RHIC, Tevatron and LHC energies for all ingredients included (total, thick solid line) and when only some Regge exchanges are included. The $\mathbb{P}\mathbb{P}$ cross section peaks at midrapidities of pions, while $\mathbb{P}f_{2\mathbb{R}}$ and $f_{2\mathbb{R}}\mathbb{P}$ at backward and forward pion rapidities, respectively. At higher energies each of the "isolated" cross section peaks in different region of pion rapidities. When interfering the Regge components in the amplitude produce significant enhancements of the cross section at forward/backward rapidities. It would be desirable to identify the 'camel-like' structure experimentally. At even more forward/backward rapidities one may expect single-diffraction contributions (e.g. diffractive production of nucleon resonances and their decays) not included in the present analysis. In the bottom panels we show the two-pion invariant-mass distribution. We recall that at the lowest energy the pion-pion rescattering and the central diffractive components strongly overlap. While the central diffractive component dominates at low two-pion invariant masses, the pion-pion rescattering component dominates only at very large invariant masses ($M_{\pi\pi} \gtrsim 20$ GeV at $\sqrt{s} = 0.2$ GeV, see Fig. 12 in [3]). At the Tevatron and LHC energies the central diffractive component dominates over the pion-pion rescattering in the whole range of $M_{\pi\pi}$.

In Fig. 2.24 we show differential distributions in pion rapidity for the $pp \to pp\pi^+\pi^-$

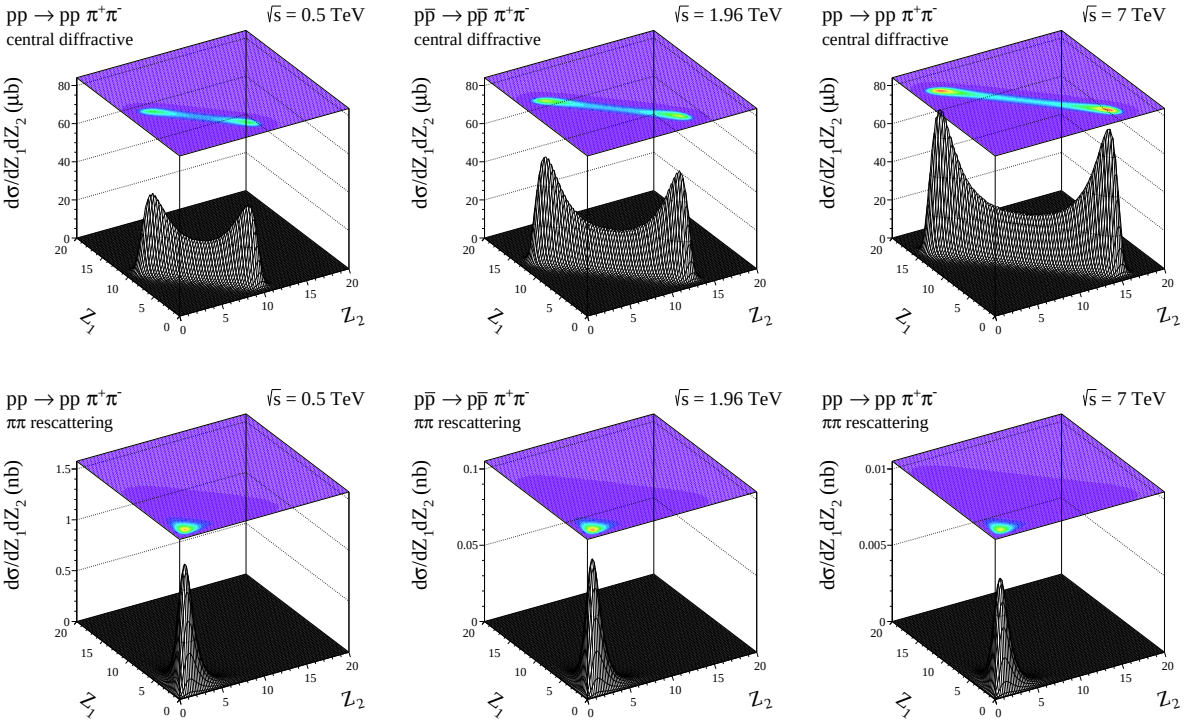

Figure 2.22: Differential cross section in (Z_1, Z_2) space for the central diffractive (top panels) and the pion-pion rescattering (bottom panels) contributions for different incident energies $\sqrt{s} = 0.5, 1.96, 7$ TeV. In this calculation for the central diffractive contribution we used the cut-off parameter $\Lambda^2_{off,E} = 2$ GeV^2, while for the pion-pion rescattering contribution $\Lambda = \Lambda_{off,M} = 1$ GeV and $B^{\pi\pi}_{\rho_{\mathbb{R}}} = 6$ GeV^{-2}.

reaction at $\sqrt{s} = 0.5, 1.96, 14$ TeV without (upper lines) and with (bottom lines) absorption effects. The integrated cross section slowly rises with incident energy. The reader is asked to notice that the energy dependence of the cross section at $y_\pi \approx 0$ is reversed by the absorption effects which are stronger at higher energies.

RHIC

We present predictions of two-meson pair production in the $pp \to ppM\bar{M}$ reaction for the RHIC experiment with the corresponding cuts. We shall show how the absorptive effects due to pp-interaction and the uncertainties of the off-shell meson form factor parameters affect our final results.

In Fig. 2.25 (top panels) we show the $t = t_1 = t_2$ distribution for the $pp \to pp\pi^+\pi^-$

Table 2.3: The integrated cross sections in μb for the exclusive $\pi^+\pi^-$ production at RHIC energies. The corresponding cuts in the calculations were imposed: $p_{\perp,\pi} > 0.15$ GeV, $|\eta_\pi| < 1$ on both pions, and 0.003 GeV$^2 < -t_1, -t_2 < 0.035$ GeV^2 at $\sqrt{s} = 200$ GeV or 0.1 GeV$^2 < -t_1, -t_2 < 1.5$ GeV^2 at 500 GeV. The different values of the off-shell-pion form-factor parameters (2.29) have been used: $\Lambda^2_{off,E} = 1.0$ GeV^2 and 1.6 GeV^2 (for the second case result in the parentheses).

Model	200 GeV	500 GeV
Born, cuts on $p_{\perp,\pi}, \eta_\pi$	14.85	13.16
with pp-rescattering, cuts on $p_{\perp,\pi}, \eta_\pi$	5.78	4.52
Born, cuts on $p_{\perp,\pi}, \eta_\pi$ and t	0.79 (1.53)	2.29 (4.60)
with pp-rescattering, cuts on $p_{\perp,\pi}, \eta_\pi$ and t	0.37 (0.69)	0.77 (1.41)

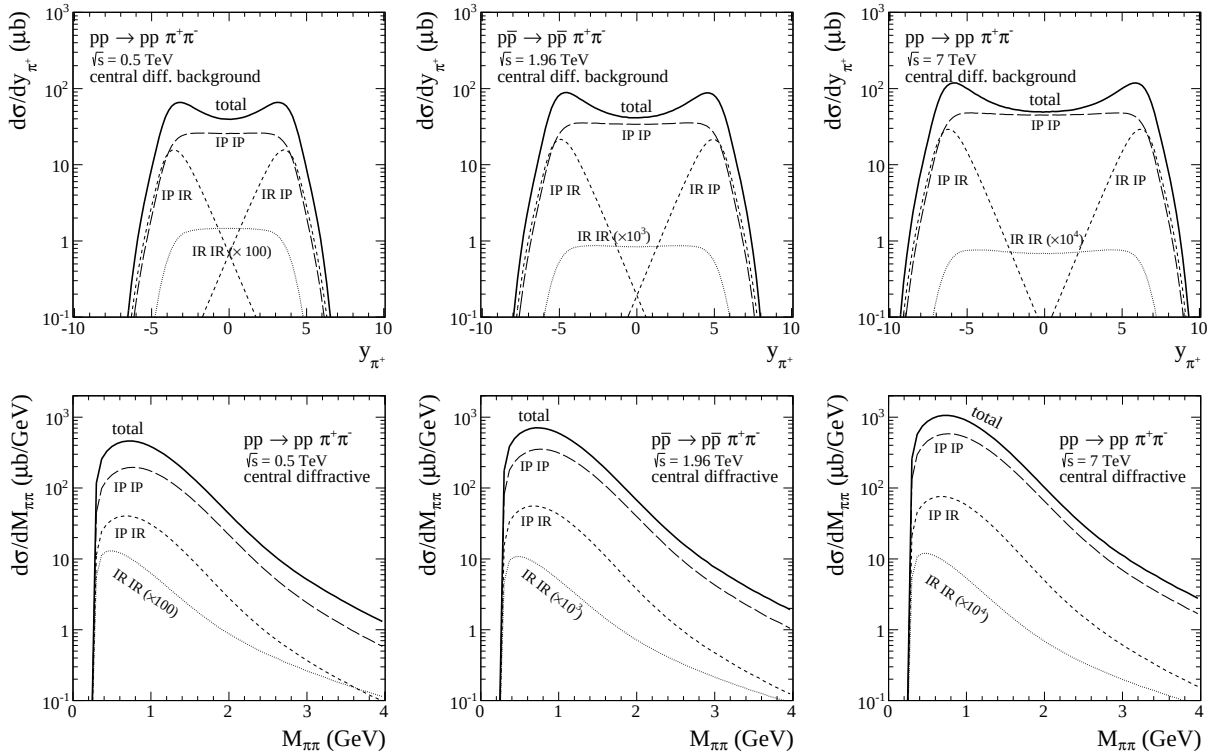

Figure 2.23: The distributions in pion rapidity (top panels) and in the two-pion invariant mass (bottom panels) for different center-of-mass energies. The different lines correspond to the situation when all (total, the solid line) and only some components in the amplitude are included. The usual (mesonic) propagator of the off-shell pion and the exponential form of form factors (2.29) with the cut-off parameter $\Lambda^2_{off,E} = 2$ GeV^2 have been used. Here the absorption effects were not included. The double-pomeron exchange ($I\!P I\!P$) is plotted by the long-dashed line, the pomeron-f_2 reggeon ($I\!P f_{2R}$) and the f_2 reggeon-pomeron ($f_{2R} I\!P$) exchanges by the short-dashed line, and the double-f_2 reggeon exchange ($f_{2R} f_{2R}$) by the dotted line.

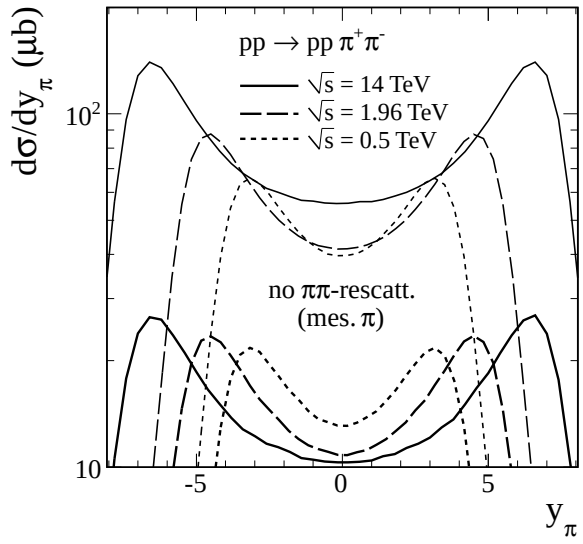

Figure 2.24: Differential cross section $d\sigma/dy_\pi$ for the $pp \to pp\pi^+\pi^-$ reaction at $\sqrt{s} = 0.5, 1.96, 14$ TeV with $\Lambda^2_{off,E} = 2$ GeV^2. The results without (upper lines) and with (bottom lines) absorption effects due to pp-interaction are shown. The $\pi\pi$-rescattering effects was not included in the calculations.

reaction at two c.m. energies $\sqrt{s} = 0.2, 0.5$ TeV with the corresponding cuts on both pions $p_{\perp,\pi} > 0.15$ GeV and $|\eta_\pi| < 1$. The results without and with the absorptive corrections due to pp-interaction are shown. We can see from Table 2.3 that the predicted cross section at $\sqrt{s} = 200$ GeV is larger than at $\sqrt{s} = 500$ GeV even without the absorption effects. This fact highlights a huge role of interference effects in the amplitude due to presence of subleading f_{2R} exchange. In the calculations we use a typical "soft" exponential form of the off-shell-meson form factor (2.29) for two cut-off parameters $\Lambda^2_{off,E} = 1.0, 1.6$ GeV^2 corresponding to the dotted and dashed lines, respectively. In bottom panels we present distributions in proton transverse momentum $p_{\perp,p}$ with the same cuts on both pions (the upper lines) and with the additional cut on t (the lower lines): 0.003 GeV^2 $< -t_1, -t_2 <$ 0.035 GeV^2 at $\sqrt{s} = 200$ GeV or 0.1 GeV^2 $< -t_1, -t_2 <$ 1.5 GeV^2 at 500 GeV.

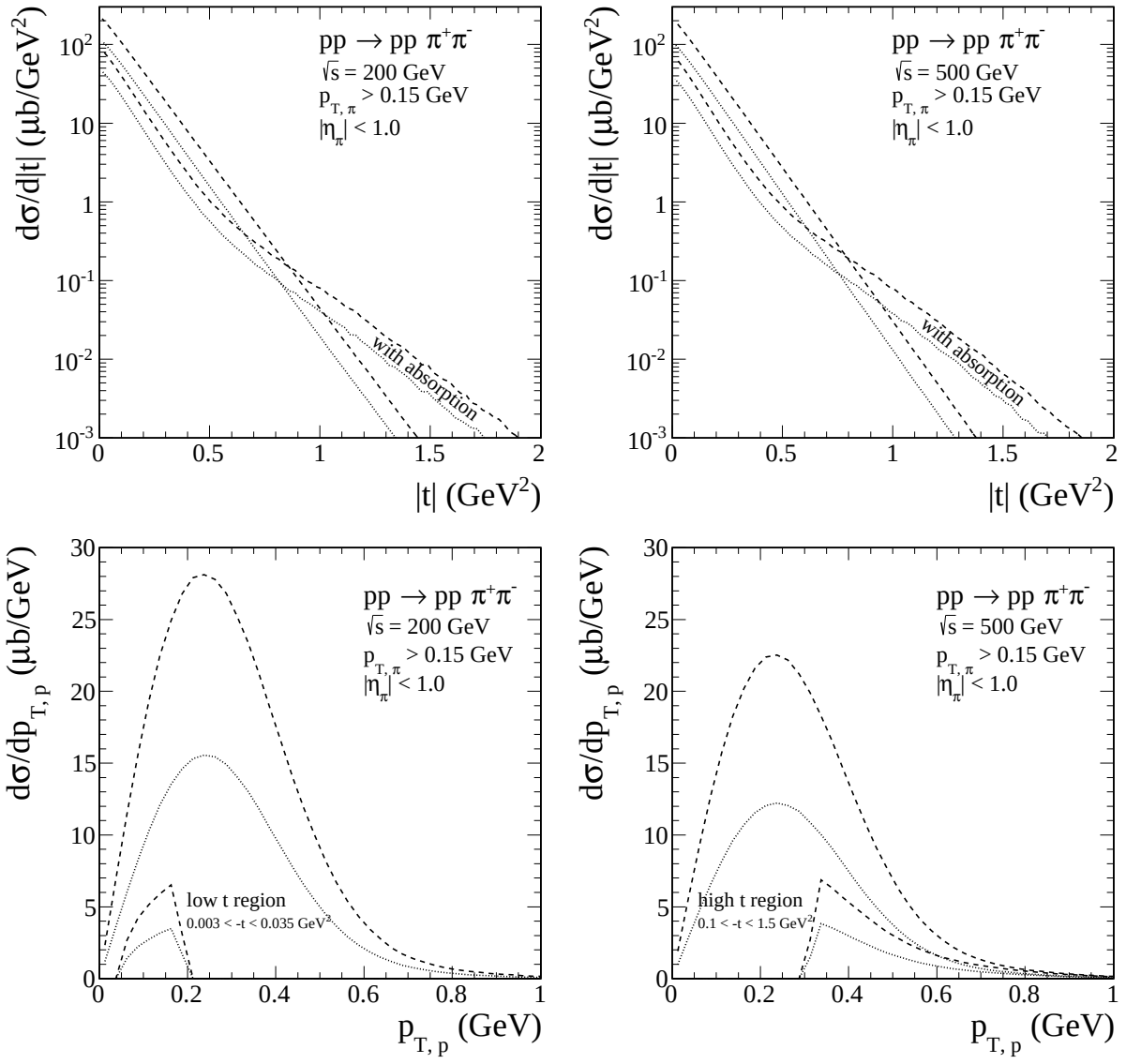

Figure 2.25: Differential cross sections $d\sigma/dt$ (top panels) and $d\sigma/dp_{\perp,p}$ (bottom panels) at the RHIC c.m. energies $\sqrt{s} = 200$ GeV (left panels) and 500 GeV (right panels) with the cuts on both pions $p_{\perp,\pi} > 0.15$ GeV and $|\eta_\pi| < 1$. In bottom panels we show the distributions in proton transverse momentum without and with extra limitation on the momentum transfer squared: 0.003 GeV^2 $< -t_1, -t_2 <$ 0.035 GeV^2 at $\sqrt{s} = 200$ GeV and 0.1 GeV^2 $< -t_1, -t_2 <$ 1.5 GeV^2 at 500 GeV. Absorption effects due to the pp-interaction have been included in this calculation. The dotted and dashed lines correspond to $\Lambda^2_{off,E} = 1.0, 1.6$ GeV^2, respectively.

In Fig. 2.26 we show the $M_{\pi\pi}$ two-pion invariant mass distribution and in the $p_{\perp,\pi}$ pion transverse momentum distribution as well as the $p_{\perp,\pi\pi}$ distribution; $p_{\perp,34} = |\vec{p}_{3\perp} + \vec{p}_{4\perp}| = \sqrt{(p_{3x} + p_{4x})^2 + (p_{3y} + p_{4y})^2}$. Results for $\sqrt{s} = 0.2, 0.5$ TeV (the red lines) and 0.5 TeV (the black lines) with cuts on both pions $p_{\perp,\pi} > 0.15$ GeV and $|\eta_\pi| < 1$ are shown. The absorption effects included in these calculations reduce the Born cross section by about a factor 3.

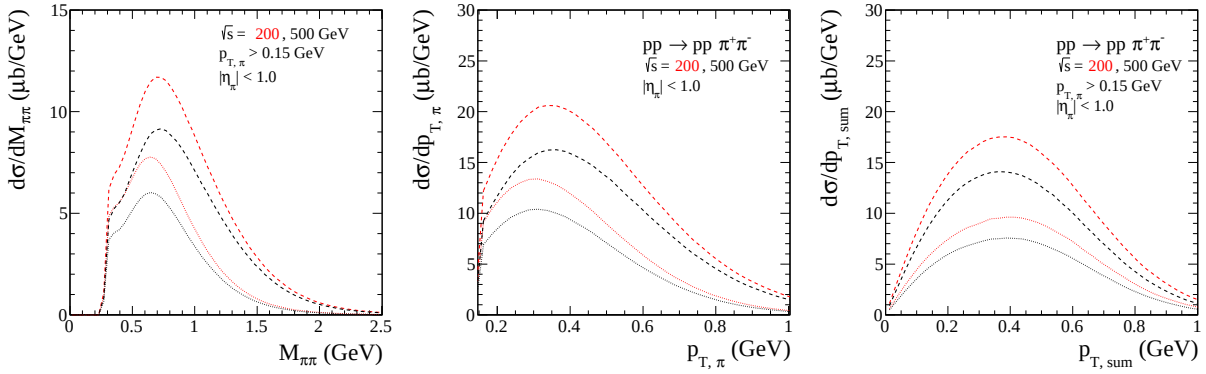

Figure 2.26: Differential cross sections $d\sigma/dM_{\pi\pi}$ (left panel), $d\sigma/dp_{\perp,\pi}$ (center panel), and $d\sigma/dp_{\perp,\pi\pi}$ (right panel) at the RHIC energies $\sqrt{s} = 0.2$ TeV (the red lines) and 0.5 TeV (the black lines) with the cuts on both pions $p_{\perp,\pi} > 0.15$ GeV and $|\eta_\pi| < 1$. The dotted and dashed lines correspond to $\Lambda^2_{off,E} = 1.0, 1.6$ GeV^2, respectively. The absorption effects due to pp-interaction have been included.

In Fig. 2.27 (left panel) we show two-pion invariant mass distribution at $\sqrt{s} = 0.2, 0.5$ TeV with the corresponding cuts, see the red and black lines, respectively. In the next two panels we show results both for the pions (the black lines) and for the kaons (the blue lines) at $\sqrt{s} = 0.2$ TeV (left panel) and 0.5 TeV (right panel) in different t ranges.

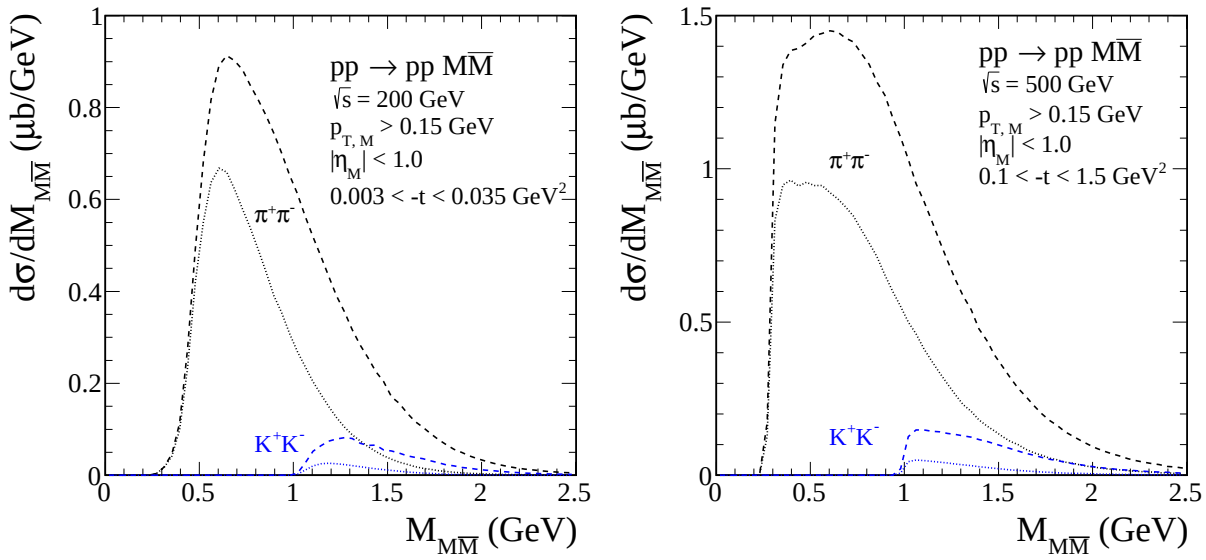

Figure 2.27: Two-pion (the black lines) and two-kaon (the blue lines) invariant mass distributions at $\sqrt{s} = 0.2$ TeV (left panel) and 0.5 TeV (right panel) with the cuts on both mesons $p_{\perp,M} > 0.15$ GeV and $|\eta_M| < 1$ with the corresponding limitation on both t. Absorption effects due to the pp-interaction have been included. Here $\Lambda^2_{off,E} = 1.0, 1.6$ GeV^2 correspond to the dotted and dashed lines, respectively.

In Fig. 2.28 we show the $p_{\perp,M}$ (top panels) and the $p_{\perp,M\bar{M}}$ (bottom panels) distributions for the $pp \to pp\pi^+\pi^-$ reaction (the black lines) and the $pp \to ppK^+K^-$ reaction (the blue lines).

In Fig. 2.29 we present the cross sections in the two-dimensional space: $(p_{\perp,\pi}, M_{\pi\pi})$ (top panels) and $(p_{\perp,\pi\pi}, M_{\pi\pi})$ (bottom panels) for two considered c.m. energies and relevant t

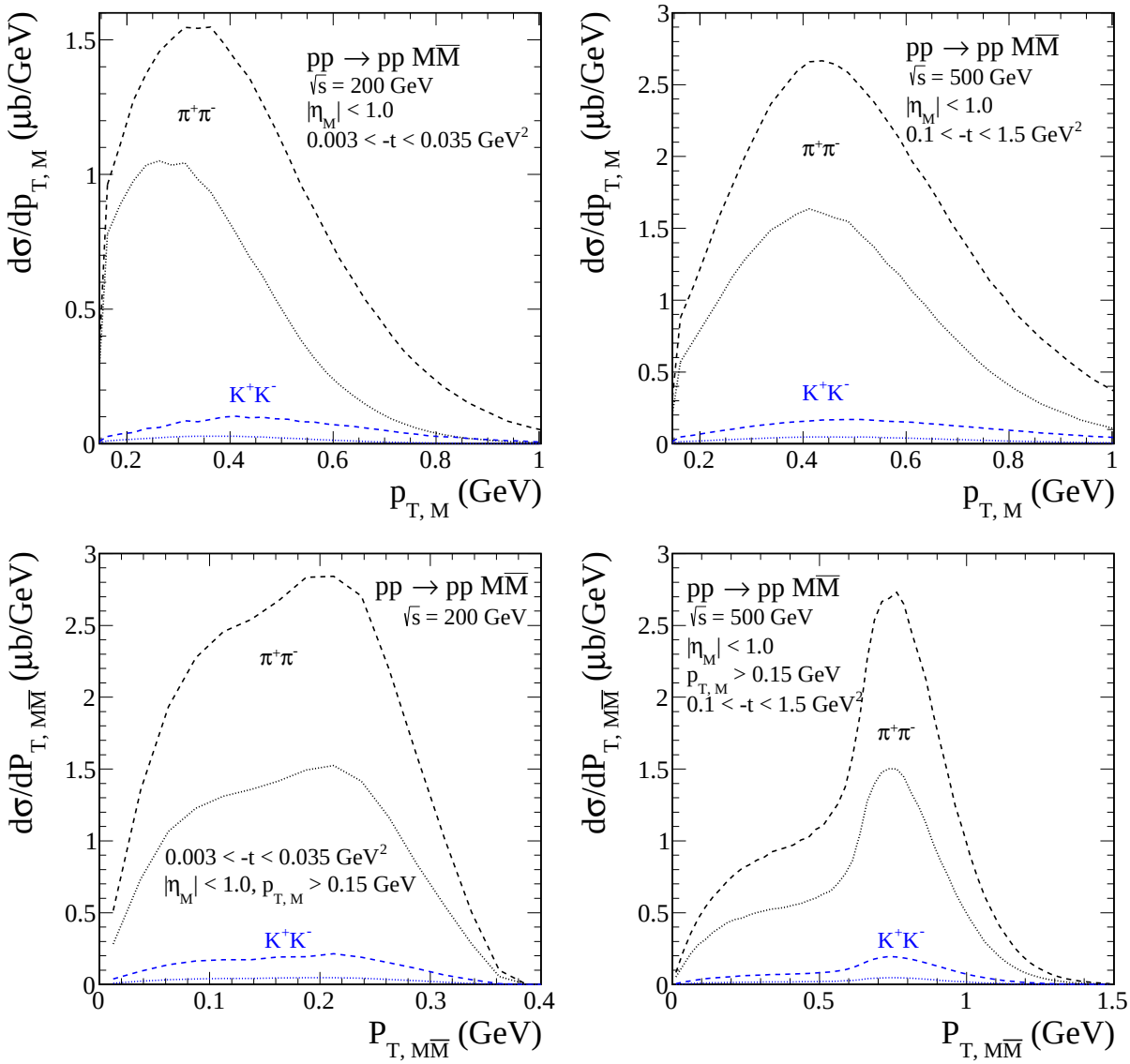

Figure 2.28: Differential cross sections $d\sigma/dp_{\perp,M}$ (top panels) and $d\sigma/dp_{\perp,sum}$ (bottom panels) at $\sqrt{s} =$ 0.2 TeV (left panel) and 0.5 TeV (right panel) We show the distributions without and with limitation on both t. Here $\Lambda^2_{off,E} = 1.0, 1.6$ GeV^2 correspond to the dotted and dashed lines, respectively. Absorption effects due to the pp-interaction have been included in this calculation.

ranges.

Finally, we consider what additional information can be provided by measuring the momenta of the outgoing intact protons. In particular, a measurement of the distribution in the relative azimuthal angle between the $p_\perp$ vectors of the outgoing protons (Fig. 2.30 (top panels)) can provide a fully differential test of the soft survival factors. The ϕ_{pp} distribution is sensitive, in general, to both the structure of the production subprocess and spin/parity of the centrally produced state, as well as absorption effects due to the pp-interaction. For comparison, the bottom panels present the $\phi_{\pi\pi}$ distributions. We can see how these angular distributions depend on cuts in t imposed on phase space. In Fig. 2.31 we show the cross sections in the two-dimensional space $(p_{\perp,p}, \phi_{pp})$ at $\sqrt{s} = 200$ GeV without (left panel) and with the absorption effects due to the pp-interaction (right panel). We can observe a very distinct dip structure with the ϕ_{pp} distribution reaching a minimum at a certain value of ϕ_{pp}. This is a consequence of the destructive interference between the bare and screened amplitudes in Eq. (2.37).

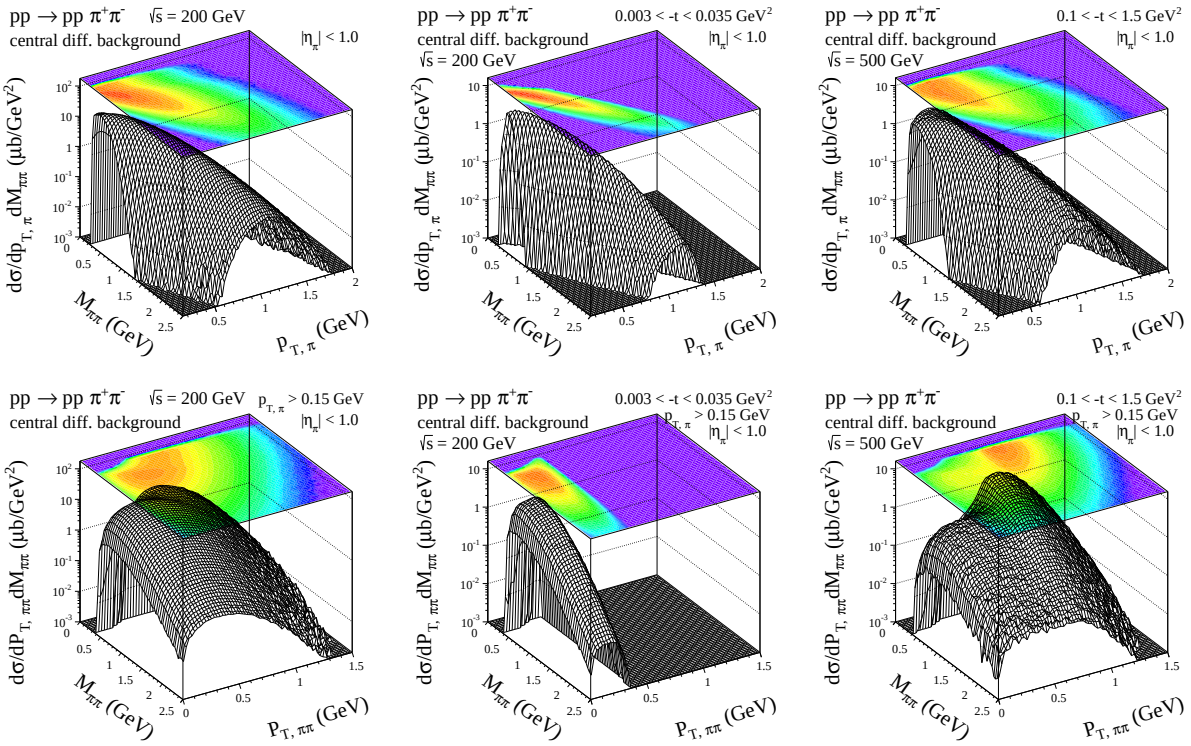

Figure 2.29: Differential cross section in two-dimensional space for different variables for the two-pion central diffractive contribution at $\sqrt{s} = 200, 500$ GeV. In this calculation the cut-off parameter $\Lambda^2_{off,E} = 1.6\,\mathrm{GeV}^2$ and the absorption effects due to the pp-interaction have been included.

Tevatron

In the few plots presented below we discuss the different aspects of our non-resonant central diffractive model of production of meson pair in the $p\bar{p} \to p\bar{p}M\bar{M}$ reaction at the Tevatron c.m. energy $\sqrt{s} = 1.96$ TeV and with the corresponding cuts on both mesons: $p_{\perp,M} > 0.4$ GeV, $|\eta_M| < 1.3$, and $|y_{M\bar{M}}| < 1$, where $y_{M\bar{M}}$ is the rapidity of central $M\bar{M}$ system expressed by formula

$$y_{34} = \frac{1}{2} \ln \left(\frac{(p_{30} + p_{40}) + (p_{3z} + p_{4z})}{(p_{30} + p_{40}) - (p_{3z} + p_{4z})} \right) , \tag{2.46}$$

with the four-momenta p_3 (π^+ or K^+ meson) and p_4 (π^- or K^- meson).

We shall show how the uncertainties due to the off-shell form factor type affect our final results. In the calculations we include the enhanced absorptive effects due to the $p\bar{p}$-interaction, i.e. the absorptive amplitude is multiplied somewhat arbitrarily by a factor $c_{abs} = 1.2$. We should also consider the possibility of additional meson-meson rescattering, that is, due to final-state interactions. However, following [146, 175], it may be necessary to introduce an additional factor corresponding to the small Poisson probability of not to emit other secondary particles in the $I\!P I\!P \to M\bar{M}$ subprocess. We refer the reader to [146, 175] for a more detailed discussion of this issue. This suppression factor may be described as the reggeization of the meson M^* exchange, see (2.34). More precisely, we expect no additional suppression in the lower mass resonance region $M_{M\bar{M}} = \sqrt{\hat{s}} < m_R$, while in the region $M_{M\bar{M}} = \sqrt{\hat{s}} \geqslant m_R$ we take the form: $\exp(-c \ln(\hat{s}/\hat{s}_0))$ with $\hat{s}_0 = m_R^2$, where $m_R = m_{f_2(1270)}$ for the case of $M\bar{M} = \pi^+\pi^-$ production and $m_{f_2'(1525)}$ for the case of K^+K^- production. In both cases the parameter c defines the strength of this additional 'Poisson suppression', and can, in principle, be extracted from data [161, 176]. In the present calculations we take $c = 0.5$.

In Fig. 2.32 we show the invariant mass distributions of pion pair (left panel) and the kaon pair (right panel) produced in the $p\bar{p} \to p\bar{p}M\bar{M}$ reaction at $\sqrt{s} = 1.96$ TeV (top panels) and

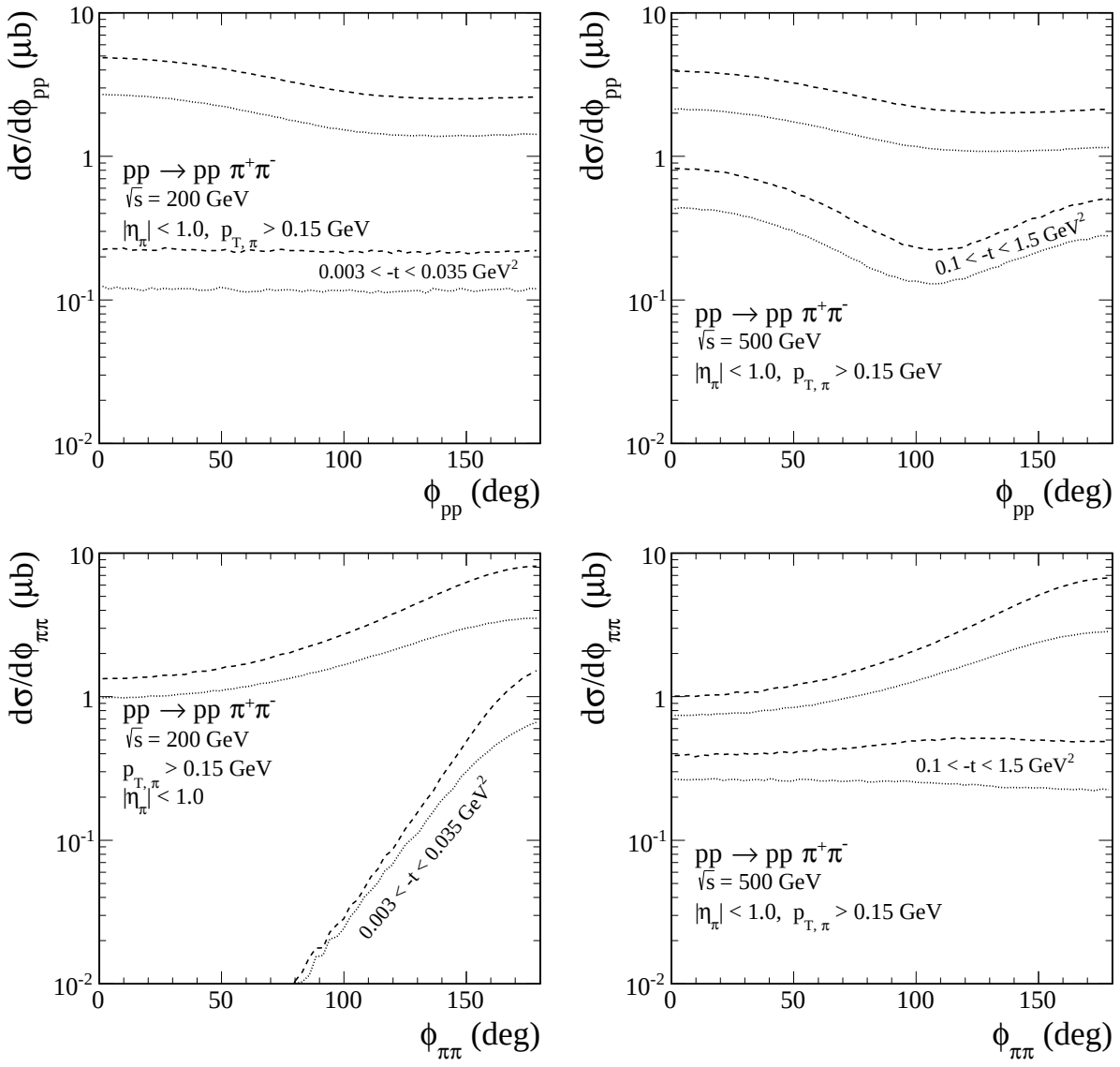

Figure 2.30: Differential cross sections $d\sigma/d\phi_{pp}$ and $d\sigma/d\phi_{\pi\pi}$ at the RHIC energies. Here $\Lambda^2_{off,E} = 1.0, 1.6$ GeV^2 correspond to the dotted and dashed lines, respectively. Absorption effects due to the pp-interaction have been included in this calculation.

in the $pp \to ppM\bar{M}$ reaction at $\sqrt{s} = 62$ GeV (bottom panels). One can observe that our predictions are sensitive to the form of the off-shell meson form factor (2.29) - (2.31) given in Section 2.3 with the cut-off parameters $\Lambda^2_{off,E} = 1.0$ GeV^2 (1), $\Lambda^2_{off,M} = 0.7$ GeV^2 (2), and $\Lambda_{off} = 1.2$ GeV (3), respectively. The choice of form factor leads to dramatically different behaviour at higher $\hat{t}/\hat{u}$ (Fig. 2.9), beyond the region probed by the ISR data, that is, in the region $M_{M\bar{M}} < 1.5$ GeV. Since in the calculations we use the 'Poisson suppression' formula with a factor $c = 0.5$, which operates at higher $M_{M\bar{M}}$ and in effective way describes the additional particle contributions in the $M\bar{M}$ subproces, we do not include any meson reggeization. We note that preliminary measurements of two-pion invariant mass distribution by the CDF Collaboration have been presented in [161] (see also [176]). In Table 2.4 we collected some values of the integrated cross sections at $\sqrt{s} = 1.96$ TeV for exclusive $\pi^+\pi^-$ production with and without the 'Poisson suppression' formula. We can see that the M_{KK} distribution is below the $M_{\pi\pi}$ distribution with the same choice of model parameters, with the exception of form-factor type (2.31) where it should be taken other parametrisation. At invariant mass larger than 2 GeV the KK contribution constitutes about 40% of the $\pi\pi$ contribution.

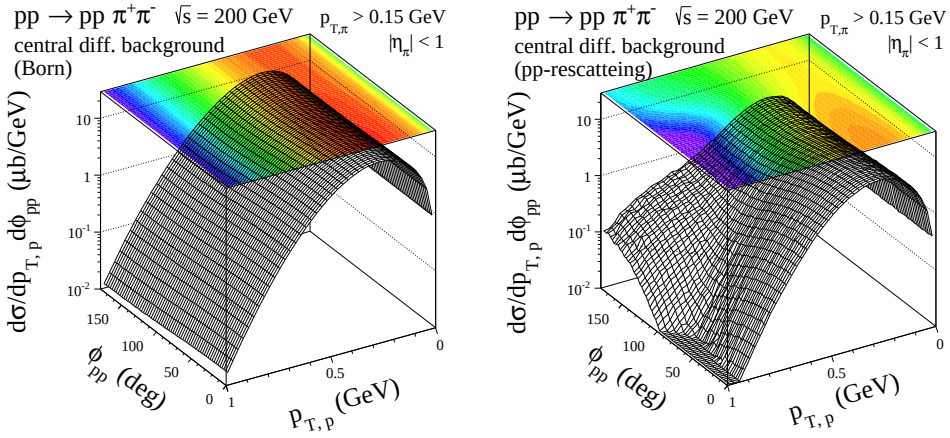

Figure 2.31: Differential cross section in two-dimensional $(p_{\perp,p}, \phi_{pp})$ space for the two-pion central diffractive contribution at $\sqrt{s} = 200$ GeV without (left panel) and with the absorption effects due to the pp-interaction (right panel). In this calculation the cut-off parameter $\Lambda^2_{off,E} = 1.0\,\mathrm{GeV}^2$ has been used.

Table 2.4: The integrated cross sections in μb for exclusive $\pi^+\pi^-$ production at $\sqrt{s} = 1.96$ TeV with cuts for the CDF experiment [161]: $p_{\perp,\pi} > 0.4$ GeV and $|\eta_\pi| < 1.3$ of both pions, and the rapidity of $\pi^+\pi^-$ system $|y_{\pi\pi}| < 1$. The three choices of the pion off-shell form-factors have been used: (1) (2.29) for $\Lambda_{off,E} = 1.0$ GeV , (2) (2.30) for $\Lambda^2_{off,M} = 0.7$ GeV^2, and (3) (2.31) for $\Lambda_{off} = 1.2$ GeV. We show results with the additional Poisson suppression for a factor $c = 0.5$ and without this effect (in the parentheses).

Model / form-factor type	(1) (2.29)	(2) (2.30)	(3) (2.31)
Born	4.82 (5.44)	5.41 (6.88)	5.99 (8.49)
with pp-rescattering ($c_{abs} = 1.2$)	0.92 (1.04)	0.97 (1.21)	1.04 (1.44)

Another observable which can be very sensitive to the choice of meson off-shell form factor is the meson transverse momentum distribution. In Fig. 2.33 we show the $p_{\perp,\pi}$, $p_{\perp,\pi\pi}$, η_π, and the angular distribution of the π^+ meson $\cos\theta^{r.f.}_{\pi^+}$, where $cos\theta^{r.f.}_{\pi^+}$ is the angle of the π^+ meson with respect to the beam axis, in the $\pi^+\pi^-$ rest frame, see Eq. (A.39) of Appendix A.

In Fig. 2.34 we show the $\cos\theta^{r.f.}_{\pi^+}$ distribution for two ranges of two-pion invariant mass: $2m_\pi < M_{\pi\pi} < 1\,\mathrm{GeV}$ (left panel) and $1\,\mathrm{GeV} < M_{\pi\pi} < 1.5\,\mathrm{GeV}$ (right panel) without and with all kinematical cuts included as well as with individual cut on $p_{\perp,\pi}$, $|\eta_\pi|$, or $|y_{\pi\pi}|$, see the upper and lower solid lines, respectively. The influence of individual cuts to the angular distribution is also shown. We can see that these cuts strongly modify the shape of the angular distribution.

In Fig. 2.36 we present cross section in the two-dimensional spaces $(p_{\perp,\pi\pi}, M_{\pi\pi})$, $(p_{\perp,\pi}, M_{\pi\pi})$, and $(cos\theta^{r.f.}_{\pi^+}, M_{\pi\pi})$ for Tevatron cuts on some kinematical variables. One can observe that different parametrisations of pion off-shell form factor (2.29) - (2.31) give different characteristic of distributions, in particularly, at higher $M_{\pi\pi}$.

In Fig. 2.37 (top panels) we show the dependence of $< p_{\perp,\pi} >$ and $< p_{\perp,\pi\pi} >$ as a function of two-pion invariant mass. It has been already shown that the cuts $p_{\perp,\pi} > 0.4$ GeV on both pions strongly distort the region of low $M_{\pi\pi} < 1$ GeV. Since the distributions have a rapid change of the slope below $M_{\pi\pi} > 1$ GeV and increase slowly at higher masses.

A few of distributions in $p_{\perp,\pi}$, $p_{\perp,\pi\pi}$, $cos\theta^{r.f.}_{\pi}$, and η_π for some $M_{\pi\pi}$ mass ranges at $\sqrt{s} =$ 1.96 TeV are shown in Figs. 2.38, 2.39, 2.40, and 2.41, respectively. The π^+ meson distributions are equivalent to the π^- meson distributions.

In Figs. 2.42, 2.43, and 2.44 we present results of $< P_{L_{even}}(\cos\theta^{r.f.}_{\pi^+}) > (M_{\pi\pi})$. Note that

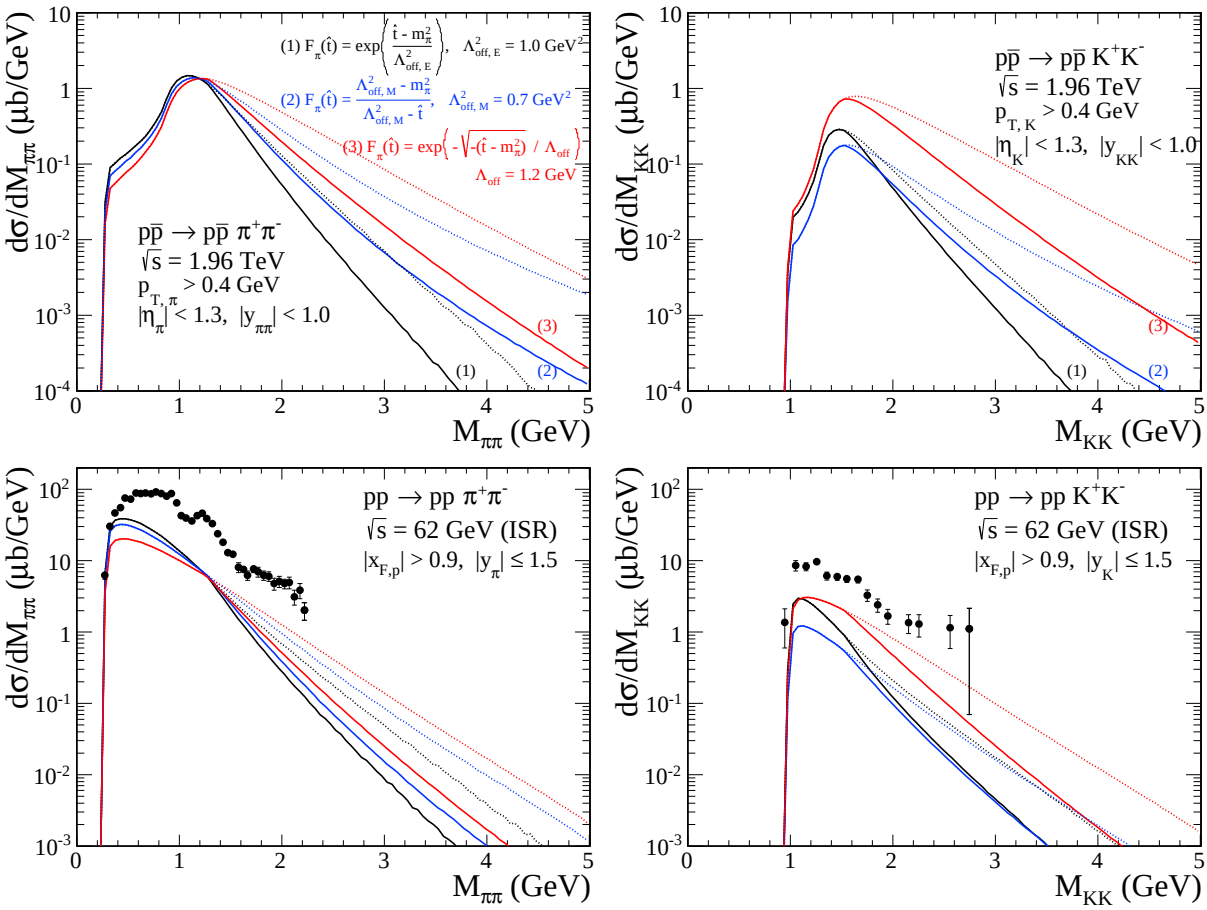

Figure 2.32: Two-pion (left panel) and two-kaon (right panel) invariant mass distributions at $\sqrt{s} = 1.96$ TeV (top panels) and at $\sqrt{s} = 62$ GeV (bottom panels). We show results for three different forms of off-shell meson form factor given in Section 2.3 with the cut-off parameters $\Lambda^2_{off,E} = 1.0$ GeV^2 (1), $\Lambda^2_{off,M} = 0.7$ GeV^2 (2), and $\Lambda_{off} = 1.2$ GeV (3) given by the black, blue and red lines, respectively. We present results without the Poisson suppression (the upper dotted lines) and with the Poisson suppression (the lower solid lines), where we take a factor $c = 0.5$. In the calculations we do not include any meson reggeization. The enhanced absorptive effects due to the $p\bar{p}$-interaction were included, i.e. the absorptive amplitude was multiplied somewhat arbitrarily by a factor $c_{abs} = 1.2$.

the predicted angular distributions are even in $\cos\theta^{r.f.}$ and so the odd L contributions vanish, i.e. $< P_{L_{odd}}(\cos\theta^{r.f.}_{\pi^+}) > (M_{\pi\pi}) = 0$. One can observe that the contribution of $L = 4$ is small at lower energy when cuts are neglected and significant already at $M_{\pi\pi} \approx 1$ GeV when cuts are applied, This suggests that kinematical cuts may distort the partial wave content. This makes conclusions more difficult. The average contributions can be calculated as

$$< P_L(\cos\theta^{r.f.}) > (M_{\pi\pi}) = \frac{\int d\mathcal{PS}\ P_L(\cos\theta^{r.f.})\ d\sigma/d\mathcal{PS}(M_{\pi\pi})}{\int d\mathcal{PS}\ d\sigma/d\mathcal{PS}(M_{\pi\pi})}\,, \tag{2.47}$$

where the integral is done over phase space. These contributions satisfy the relation:

$$< P_L(\cos\theta^{r.f.}_{\pi^+}) > (M_{\pi\pi}) = (-1)^L < P_L(\cos\theta^{r.f.}_{\pi^-}) > (M_{\pi\pi})\,. \tag{2.48}$$

We can see in Fig. 2.43 that cut on $\cos\theta^{r.f.}$ strongly modify the region of $M_{\pi\pi} < 1$ GeV, see also Fig. 2.36 (bottom panels). The difference between the form factors (2.29) - (2.31) is huge at higher invariant masses and thus such observables may prove very useful in distinguishing between these choices. We found that these distributions are largely unaffected by the absorption effects. We note that preliminary measurements of these distributions by the CDF Collaboration

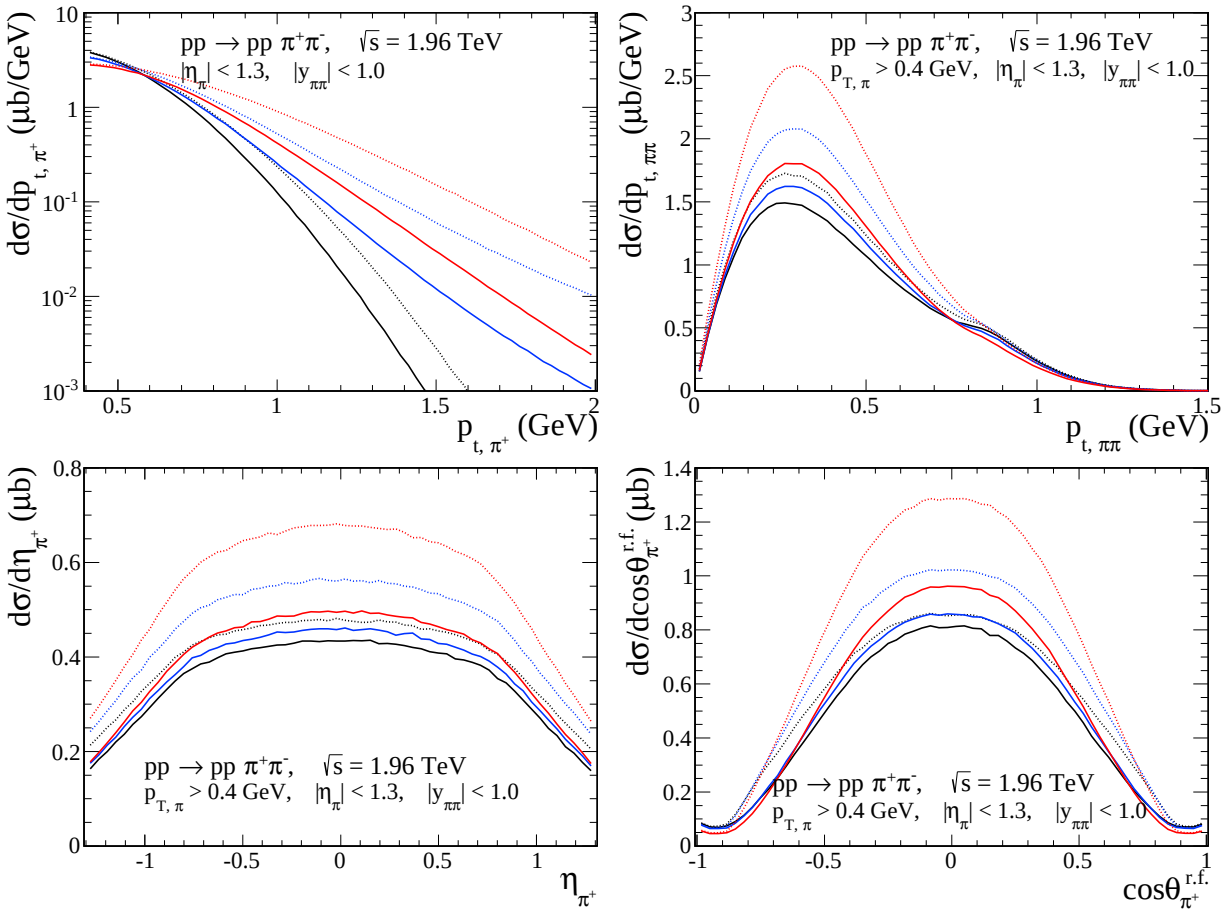

Figure 2.33: Differential cross sections at $\sqrt{s} = 1.96$ TeV. We show results for three different forms of off-shell meson form factor given in Section 2.3 with the cut-off parameters $\Lambda^2_{off,E} = 1.0$ GeV^2, $\Lambda^2_{off,M} = 0.7$ GeV^2, and $\Lambda_{off} = 1.2$ GeV correspond to black, blue and red lines, respectively. The other details are the same as in Fig. 2.32.

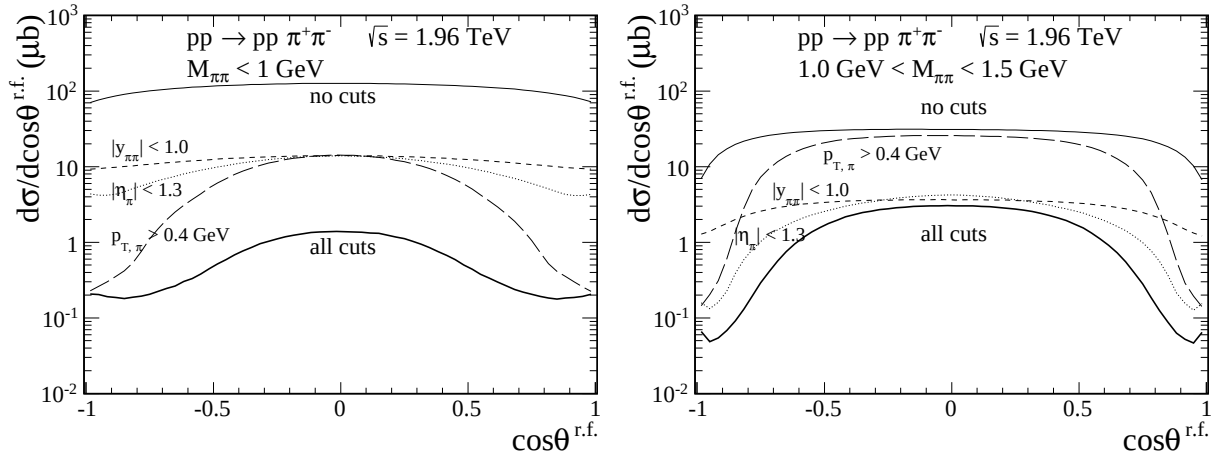

Figure 2.34: The $\cos\theta^{r.f.}_{\pi^+}$ distribution for two ranges of two-pion invariant mass: $2m_\pi < M_{\pi\pi} < 1$ GeV (left panel) and 1 GeV $< M_{\pi\pi} <$ 1.5 GeV (right panel), without (the upper thin solid line) and with all kinematical cuts imposed (the lower thick solid line). The long-dashed, the dotted, and the short-dashed lines correspond to the contributions with cut on $p_{\perp,\pi} > 0.4$ GeV of both pions, $|\eta_\pi| < 1.3$ of both pions, and the rapidity of the $\pi^+\pi^-$ system $|y_{\pi\pi}| < 1$, respectively.

have been presented in [161] (see also [176]) and are in good agreement at higher $M_{\pi\pi}$ with our predictions, but with exception of typical exponential form (2.29).

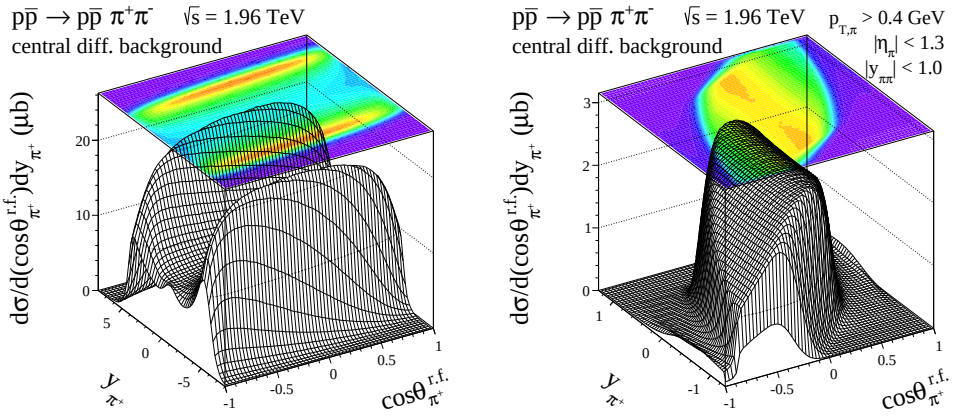

Figure 2.35: Differential cross section in two-dimensional $(y_{\pi^+}, \cos\theta^{r.f.}_{\pi^+})$ space for the central diffractive contribution at $\sqrt{s} = 1.96$ TeV in the full phase space (left panel) and with the additional cuts imposed (right panel). In this calculation the exponential type of the off-shell form factor has been used with the cut-off parameter $\Lambda_{off,E} = 1$ GeV and no absorption effects due to the $p\bar{p}$-interaction.

The angular distribution $z = \cos\theta^{r.f.}_{\pi^+}$ in the recoil $\pi\pi$ center of mass system with z-axis parallel to the proton direction can be expanded in terms of Legendre palynomials as:

$$\frac{d\sigma}{dz} = \sum_L a_L P_L(z)\,. \tag{2.49}$$

The expansion coefficients can be calculated as:

$$a_L = \int_{-1}^{1} dz\; P_L(z)\frac{d\sigma}{dz}(z)\,. \tag{2.50}$$

It is useful to define:

$$\tilde{a}_L = \frac{\int_{-1}^{1} dz\; P_L(z)\frac{d\sigma}{dz}(z)}{\int_{-1}^{1} dz\; \frac{d\sigma}{dz}}\,. \tag{2.51}$$

They have a simple interpretation of relative contribution of different partial waves with respect to that of $L = 0$. This can be generalized to include interesting dependence on two-pion invariant mass as follows:

$$\tilde{a}_L(M_{\pi\pi}) = \frac{\int_{-1}^{1} dz\; P_L(z)\frac{d\sigma}{dzdM_{\pi\pi}}(z)}{\int_{-1}^{1} dz\; \frac{d\sigma}{dzdM_{\pi\pi}}}\,. \tag{2.52}$$

The normalized expansion coefficients can be calculated from the final $d\sigma/dz$ or $d\sigma/(dzdM_{\pi\pi})$ distributions obtained by binning in the four-body integration. This method seems equivalent to the previous calculations of $< P_L >$.

LHC

Now we present results for production of two-meson pairs in the $pp \to ppM\bar{M}$ reaction and with the corresponding cuts for the ALICE experiment at the LHC ($\sqrt{s} = 7$ TeV): $p_{\perp,M} > 0.1$ GeV or 0.3 GeV and $|\eta_M| < 0.9$ on both mesons. We present results for the $pp \to pp\pi^+\pi^-$ (black lines) and the $pp \to ppK^+K^-$ (blue lines) reactions at $\sqrt{s} = 7$ TeV.

In our model we include the pomeron and secondary reggeon exchange contributions. It was mention that the type of off-shell meson form factor strongly modify the higher values of $M_{M\bar{M}}$. Here we consider the exponential type of form factor (2.29) with the cut-off parameter $\Lambda^2_{off,E} = 1.2$ GeV^2 (left panels). In the right panels we show calculations with two choice of

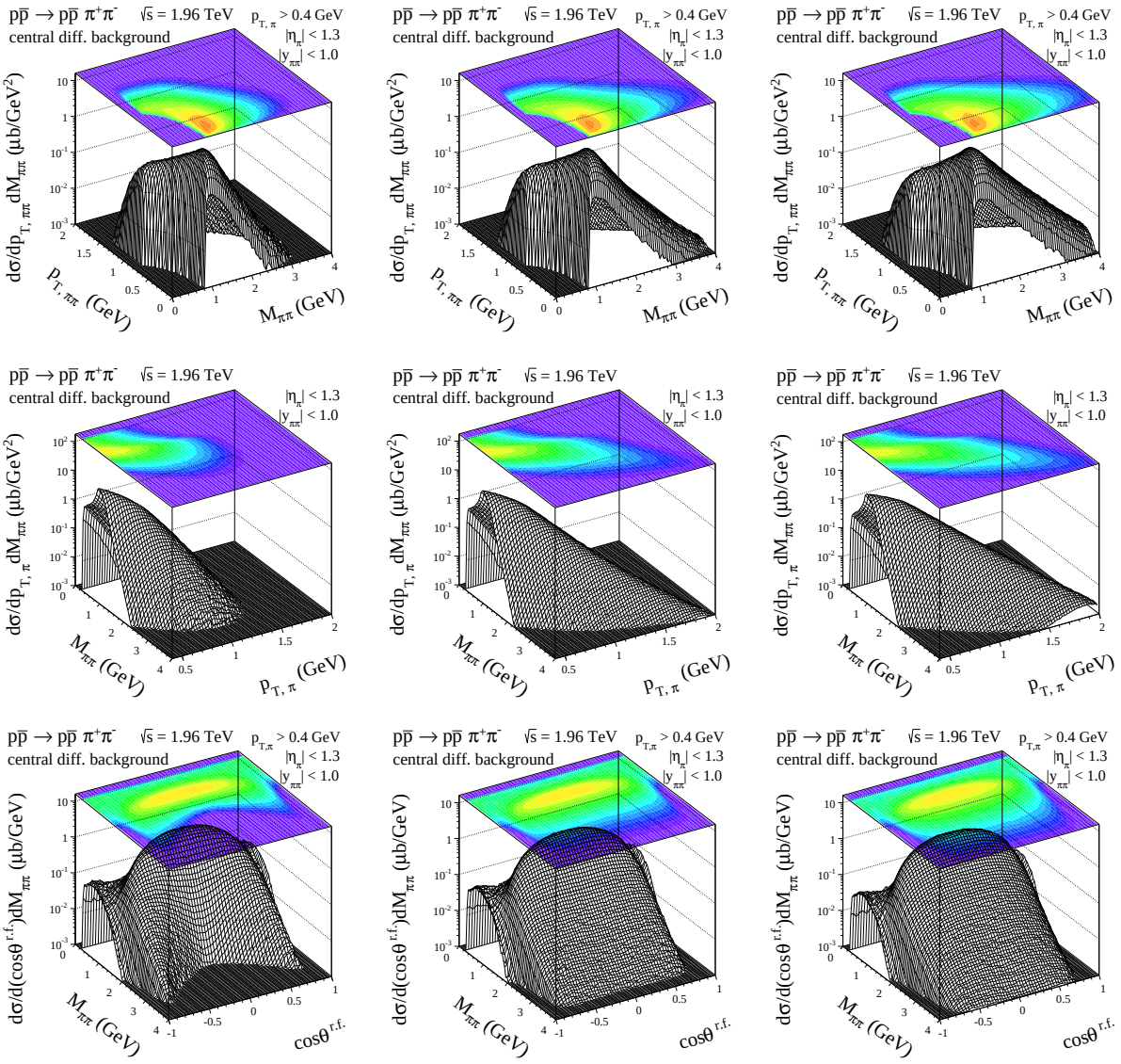

Figure 2.36: Differential cross section for the central diffractive contribution in two-dimensional spaces $(p_{\perp,\pi\pi}, M_{\pi\pi})$, $(p_{\perp,\pi}, M_{\pi\pi})$, and $(cos\theta^{r.f.}_{\pi^+}, M_{\pi\pi})$ at $\sqrt{s} = 1.96$ TeV and for cuts on some kinematical variables. The three columns present results with different forms of off-shell meson form factor given in Section 2.3 with the cut-off parameters $\Lambda^2_{off,E} = 1.0$ GeV^2, $\Lambda^2_{off,M} = 0.7$ GeV^2, and $\Lambda_{off} = 1.2$ GeV, respectively. The absorption effects due to the $p\bar{p}$-interaction enhanced by a factor $c_{abs} = 1.2$ have been included in the calculations. Results were calculated with the Poisson suppression ($c = 0.5$) and the standard pion propagator.

$\Lambda^2_{off,E} = 1.2, 1.6$ GeV^2 correspond to the solid and the dotted line, respectively. We show how the uncertainties of the form factor parameters affect our final results. The short-dashed lines correspond to the results without the absorptive corrections. In the calculations we include the soft absorptive effects due to the pp-interaction. The thick solid lines correspond to the results with the absorptive corrections (for comparison, see the long-dashed lines which show the result when the absorptive amplitude is multiplied by an extra factor $c_{abs} = 1.2$).

It was mention in the section above that at large masses $M_{M\bar{M}}$ the possibility to produce additional particles in the pomeron/reggeon fusion subprocess is rather high. Here we do not include this effect and the calculations were done only with the usual (mesonic) propagator, that is, do not include any meson reggeization. However, as we can see in Fig. 2.20 (top panels), the off-shell meson reggeization formula (2.33) suppresses the cross section, for example, at larger values of two-meson invariant masses or equivalently at larger values of meson transverse

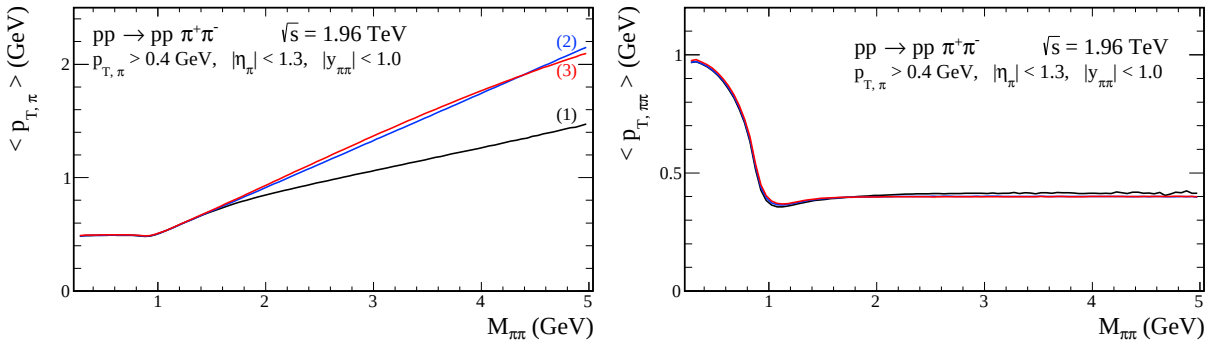

Figure 2.37: Mean value of $p_{\perp,\pi}$ and $p_{\perp,\pi\pi}$ as a function of two-pion invariant mass. We show results for three different forms of pion off-shell form factor given in Section 2.3 with the cut-off parameters $\Lambda^2_{off,E} = 1.0$ GeV^2 (1), $\Lambda^2_{off,M} = 0.7$ GeV^2 (2), and $\Lambda_{off} = 1.2$ GeV (3) given by the black, blue and red lines, respectively. Results were calculated with the Poisson suppression ($c = 0.5$) and the standard pion propagator.

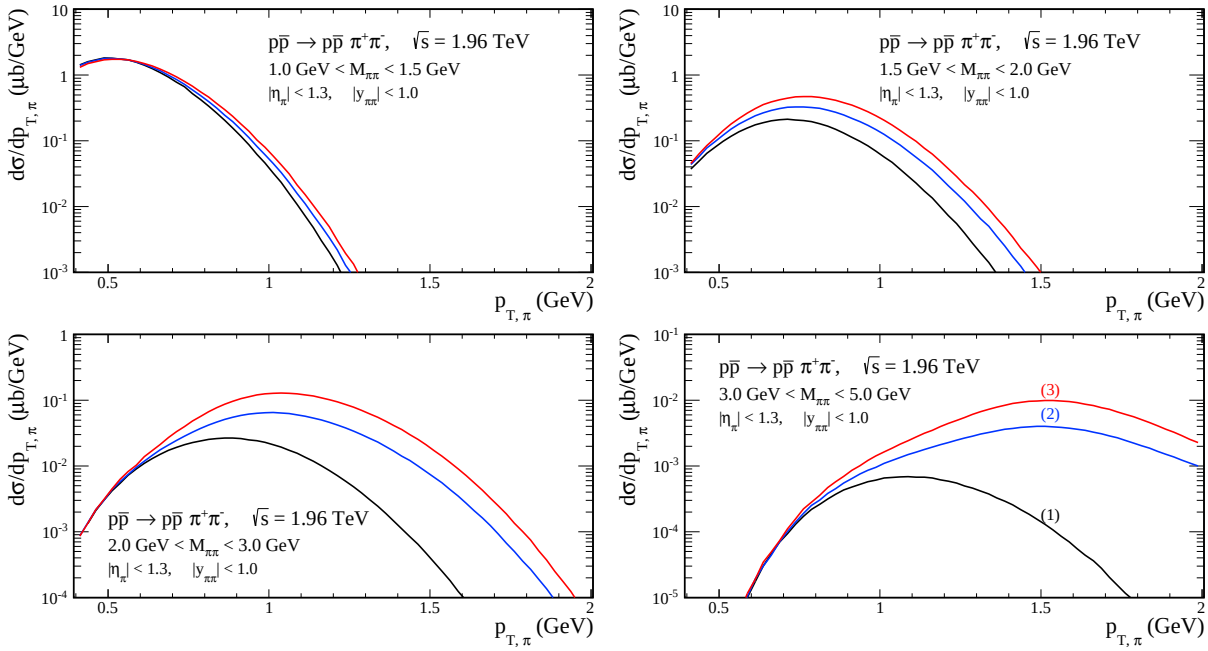

Figure 2.38: The $p_{\perp,\pi}$ distribution for a few $M_{\pi\pi}$ windows for the $p\bar{p} \to p\bar{p}\pi^+\pi^-$ reaction at $\sqrt{s} = 1.96$ TeV using the three choices of pion off-shell form factor given in Section 2.3. Results were calculated with the Poisson suppression ($c = 0.5$) and the standard pion propagator. Absorption effects due to the $p\bar{p}$-interaction enhanced by a factor $c_{abs} = 1.2$ have been included in this calculation.

momenta.

In Fig. 2.45 we present the meson transverse momenta distribution (top panels), the invariant mass distribution (centre panels), and the $p_{\perp,\pi\pi}$ distribution (bottom panels) both for the pions and kaons (the black and blue lines, respectively). The dashed lines correspond to the Born calculations and the solid and long-dashed lines to calculations with the absorption effects due to the pp-rescattering. The long-dashed lines show the result obtained by multiplying the absorption amplitude by a factor $c_{abs} = 1.2$. In Fig. 2.46 we present the differential cross section in two-dimensional spaces $(p_{\perp,\pi}, M_{\pi\pi})$ and $(p_{\perp,\pi\pi}, M_{\pi\pi})$, the top and bottom panels, respectively. The dependence of $< p_{\perp,M} >$ and $< p_{\perp,M\bar{M}} >$ as a function of two-meson invariant mass is presented in Fig. 2.47. It is worth recalling that the absorption effects change the shape of $p_{\perp,p}$ and t distributions, see Fig. 2.49, and strongly modify the distribution in relative azimuthal angle between the outgoing protons ϕ_{pp}, see Fig. 2.50. The $\phi_{M\bar{M}}$ distribution peaks in the back-to-back

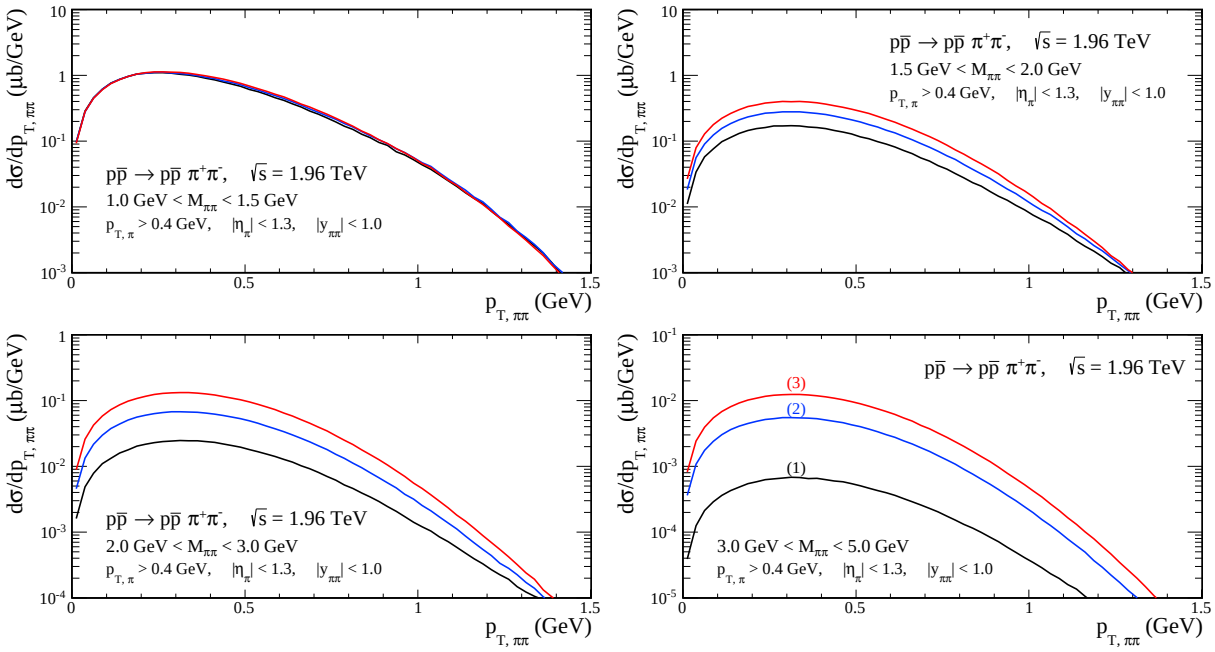

Figure 2.39: The $p_{\perp,\pi\pi}$ distribution for a few $M_{\pi\pi}$ windows for the $p\bar{p} \to p\bar{p}\pi^+\pi^-$ reaction at $\sqrt{s} = 1.96$ TeV. Here $\Lambda^2_{off,E} = 1.0$ GeV^2, $\Lambda^2_{off,M} = 0.7$ GeV^2, and $\Lambda_{off} = 1.2$ GeV correspond to the black, blue, and red lines, respectively. Results were calculated with the Poisson suppression ($c = 0.5$) and the standard pion propagator. Absorption effects due to the $p\bar{p}$-interaction enhanced by a factor $c_{abs} = 1.2$ have been included in this calculation.

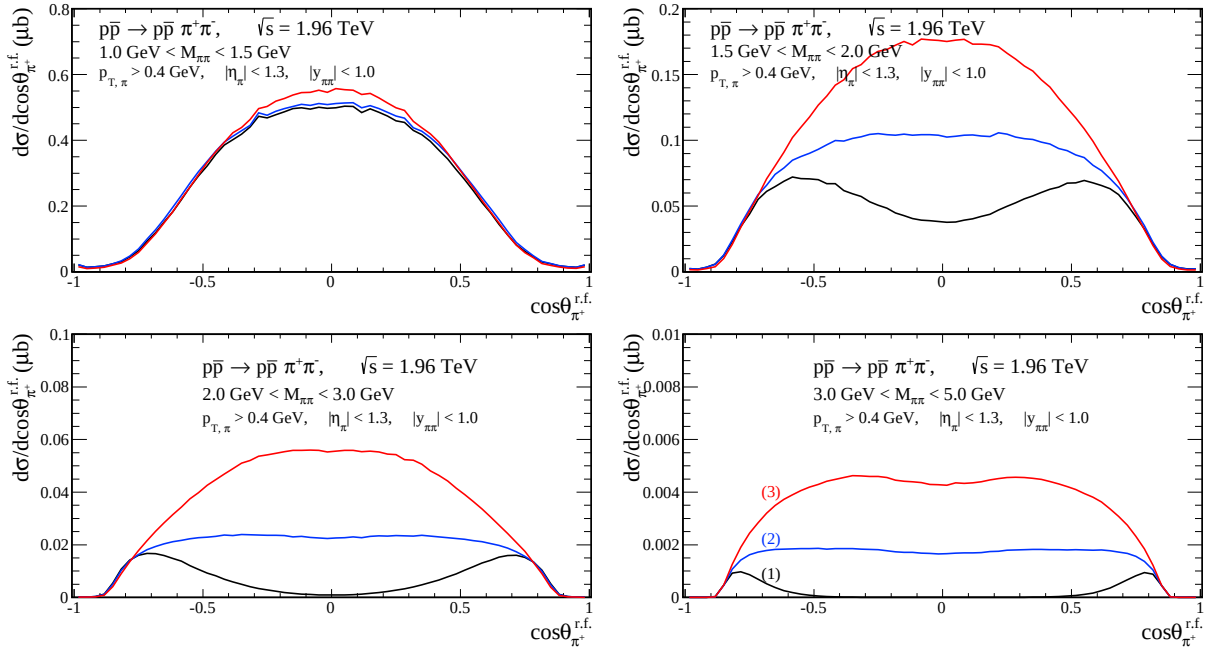

Figure 2.40: The $cos\theta^{r.f.}_{\pi^+}$ distribution for a few $M_{\pi\pi}$ windows for the $p\bar{p} \to p\bar{p}\pi^+\pi^-$ reaction at $\sqrt{s} = 1.96$ TeV using the three choices of pion off-shell form factor given in Section 2.3. Results were calculated with the Poisson suppression ($c = 0.5$) and the standard pion propagator. Absorption effects due to the $p\bar{p}$-interaction enhanced by a factor $c_{abs} = 1.2$ have been included in this calculation.

configuration $\phi_{M\bar{M}} = \pi$.

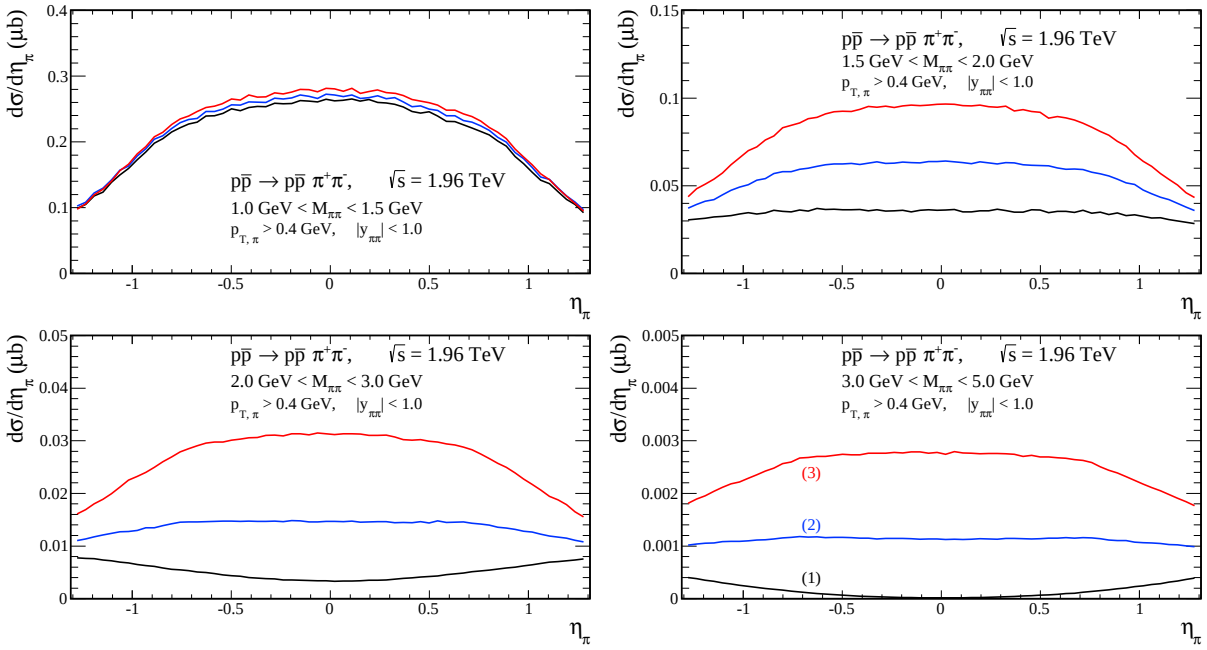

Figure 2.41: The η_π distribution for a few $M_{\pi\pi}$ windows for the $p\bar{p} \to p\bar{p}\pi^+\pi^-$ reaction at $\sqrt{s} = 1.96$ TeV using the three choices of pion off-shell form factor given in Section 2.3. Results were calculated with the Poisson suppression ($c = 0.5$) and the standard pion propagator. Absorption effects due to the $p\bar{p}$-interaction enhanced by a factor $c_{abs} = 1.2$ have been included in this calculation.

Table 2.5: The integrated cross sections in μb for exclusive $\pi^+\pi^-$ production at $\sqrt{s} = 7$ TeV with the corresponding cuts on both mesons in the calculations. Different values of the off-shell-pion form-factor parameters (2.29) have been used: $\Lambda^2_{off,E} = 1.2$ GeV^2, 1.6 GeV^2 (result in the parentheses). In the case of calculation with pp-rescattering first values (blue) correspond to the results when the absorptive amplitude was multiplied by an extra factor $c_{abs} = 1.2$.

Model	$\pi^+\pi^-$	K^+K^-
Born, cuts on $p_{\perp,M} > 0.1$ GeV and $\lvert\eta_M\rvert < 0.9$	19.70 (29.55)	1.16 (2.74)
Born, cuts on $p_{\perp,M} > 0.3$ GeV and $\lvert\eta_M\rvert < 0.9$	10.76 (18.36)	0.77 (2.01)
with pp-rescattering, $p_{\perp,M} > 0.1$ GeV and $\lvert\eta_M\rvert < 0.9$	3.44 (4.86) - 4.32 (6.18)	0.18 (0.42) - 0.24 (0.54)
with pp-rescattering, $p_{\perp,M} > 0.3$ GeV and $\lvert\eta_M\rvert < 0.9$	1.67 (2.74) - 2.14 (3.53)	0.12 (0.30) - 0.15 (0.38)

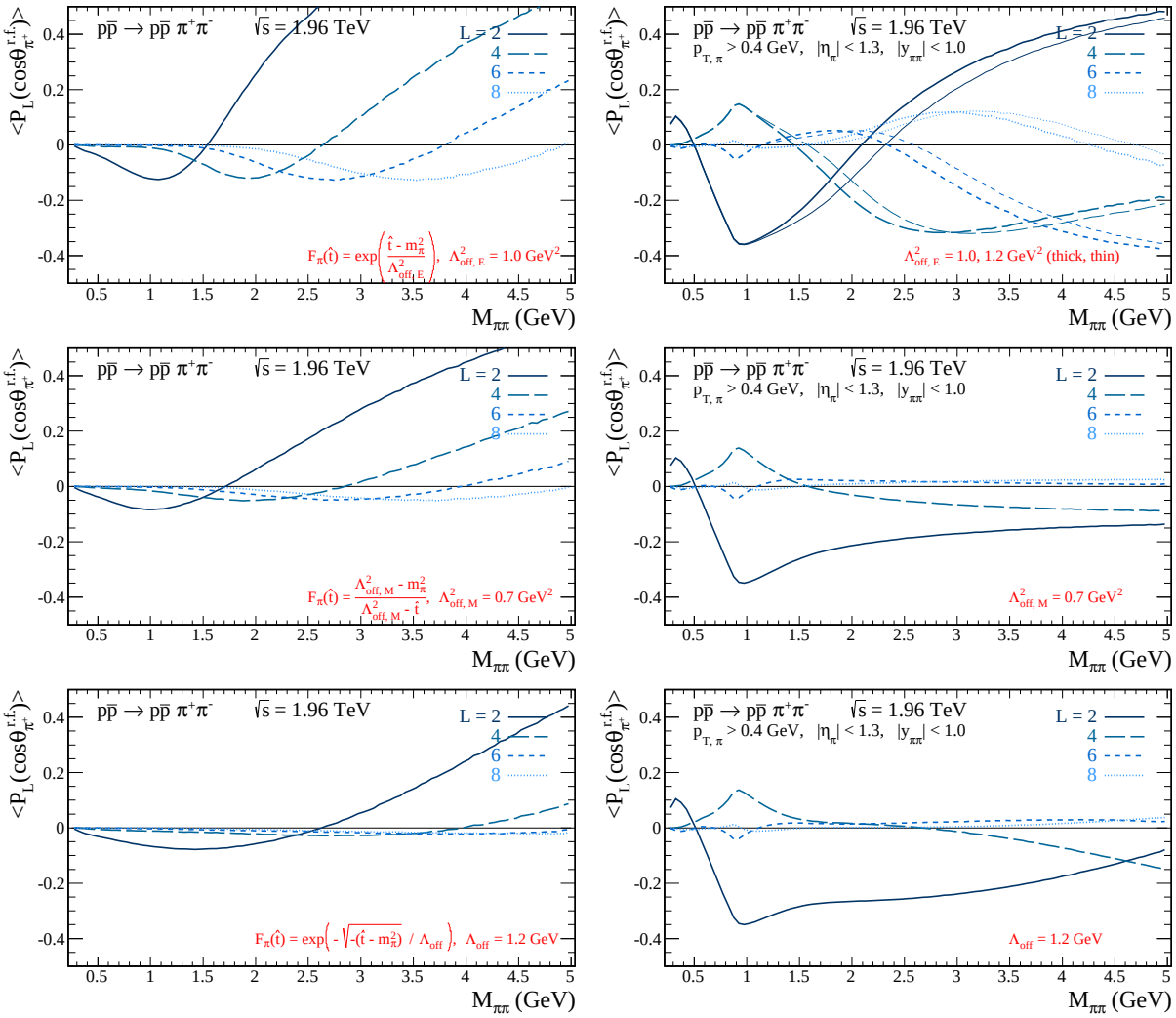

Figure 2.42: Mean value of the first even Legendre polynomials $P_L(\cos\theta^{r.f.}_{\pi^+})$ as a function of two-pion invariant mass without (left panels) and with the additional cuts (right panels) $p_{\perp,\pi} > 0.4$ GeV, $|\eta_\pi| < 1.3$, and $|y_{\pi\pi}| < 1.0$ imposed, as in [161, 176]. The results correspond to three types of off-shell pion form factors (2.29) - (2.31), given in Section 2.3, with the cut-off parameters $\Lambda^2_{off,E} = 1.0$ GeV^2 (the thick lines), $\Lambda^2_{off,E} = 1.2$ GeV^2 (the thin lines), $\Lambda^2_{off,M} = 0.7$ GeV^2, and $\Lambda_{off} = 1.2$ GeV.

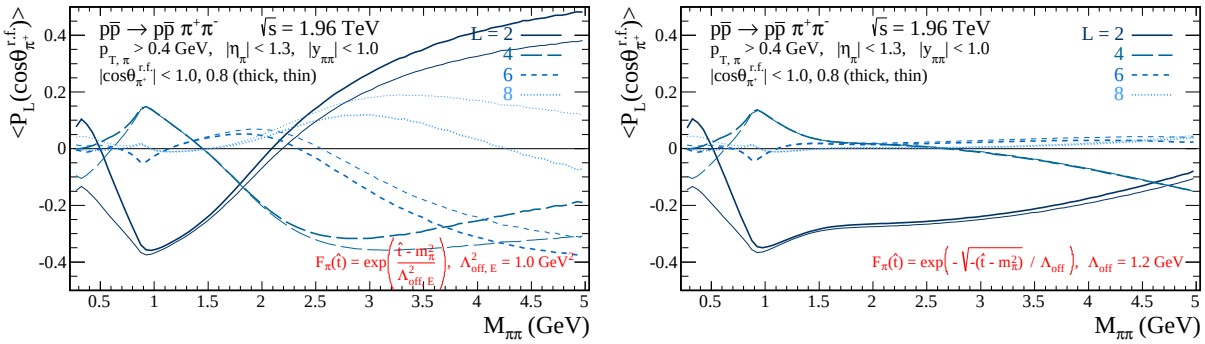

Figure 2.43: The same as Fig. 2.42 (right panel), but for the additional cut on $|\cos\theta^{r.f.}_{\pi^+}| < 0.8$ (the thin lines). Here, we present results for two type of off-shell meson form factors (2.29) and (2.31).

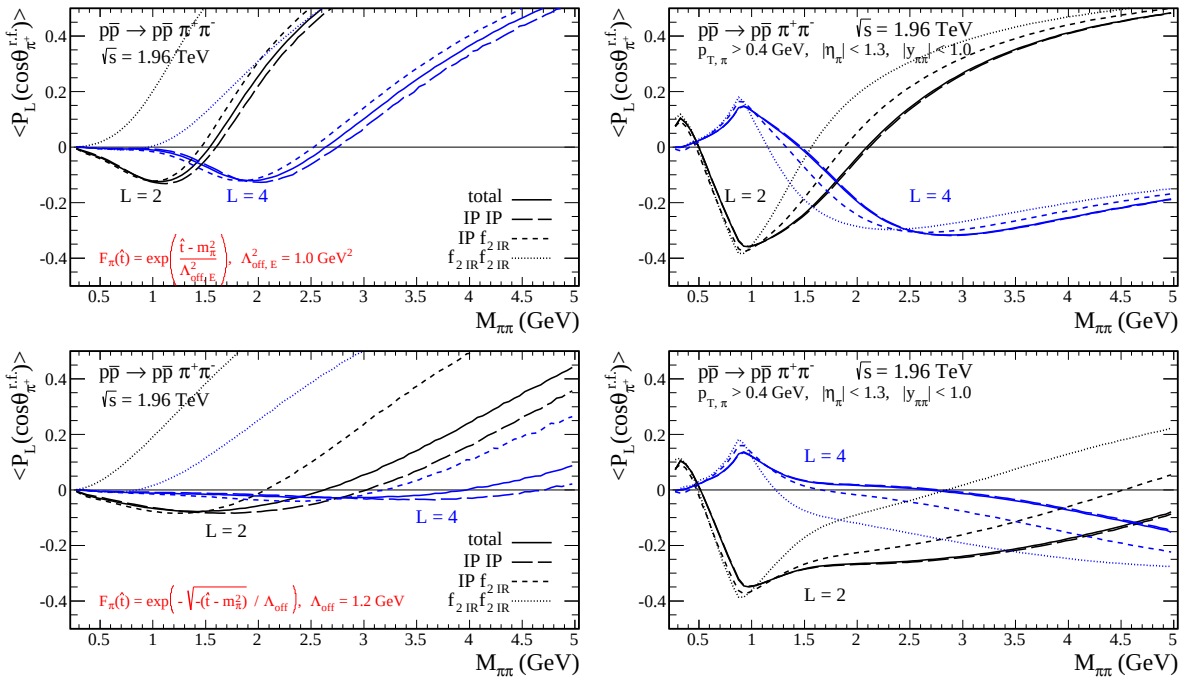

Figure 2.44: Mean values of the Legendre polynomials $P_{L=2,4}(\cos\theta^{r.f.}_{\pi^+})$ as a function of two-pion mass in the full phase space (left panels) and with the additional cuts (right panels). The $L = 2$ contributions correspond to the black lines, while the $L = 4$ contributions correspond to the blue lines. Here, we present results for two type of off-shell meson form factors given by Eq. (2.29) (top panels), and Eq. (2.31) (bottom panels). The solid line represents the coherent sum of all the Regge exchanges included in the amplitude, while the long-dashed line when the double-pomeron exchanges only, the dashed line correspond to the pomeron-reggeon exchanges, and the dotted line to the double-reggeon exchanges. We note that preliminary measurements of these distributions by the CDF Collaboration have been presented in [161] (see also [176]).

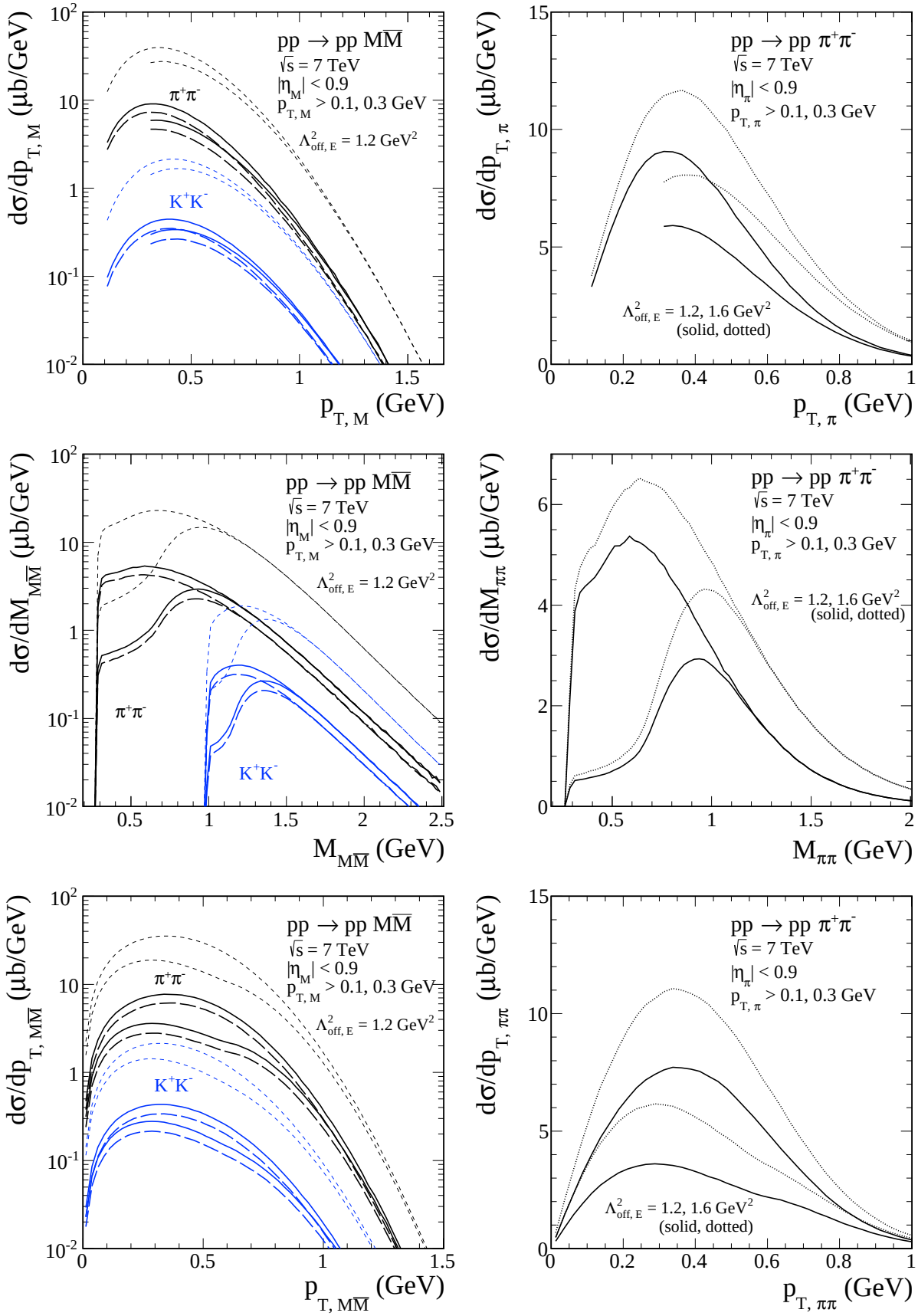

Figure 2.45: Differential cross sections $d\sigma/dp_{\perp,M}$ (top panels), $d\sigma/dM_{M\bar{M}}$ (centre panels), and $d\sigma/dp_{\perp,\pi\pi}$ (bottom panels) at $\sqrt{s} = 7$ TeV. Results without (the dashed lines) and with (the solid and long-dashed lines) absorption effects due to the pp-interaction are shown. The long-dashed lines show the result obtained by multiplying the absorption amplitude by a factor $c_{abs} = 1.2$. The black lines correspond to the pions and the blue lines to the kaons. These calculations were done with the usual (mesonic) propagator and with the cut-off parameter $\Lambda^2_{off,E} = 1.2, 1.6\,\mathrm{GeV}^2$in the off-shell meson form factor (2.29).

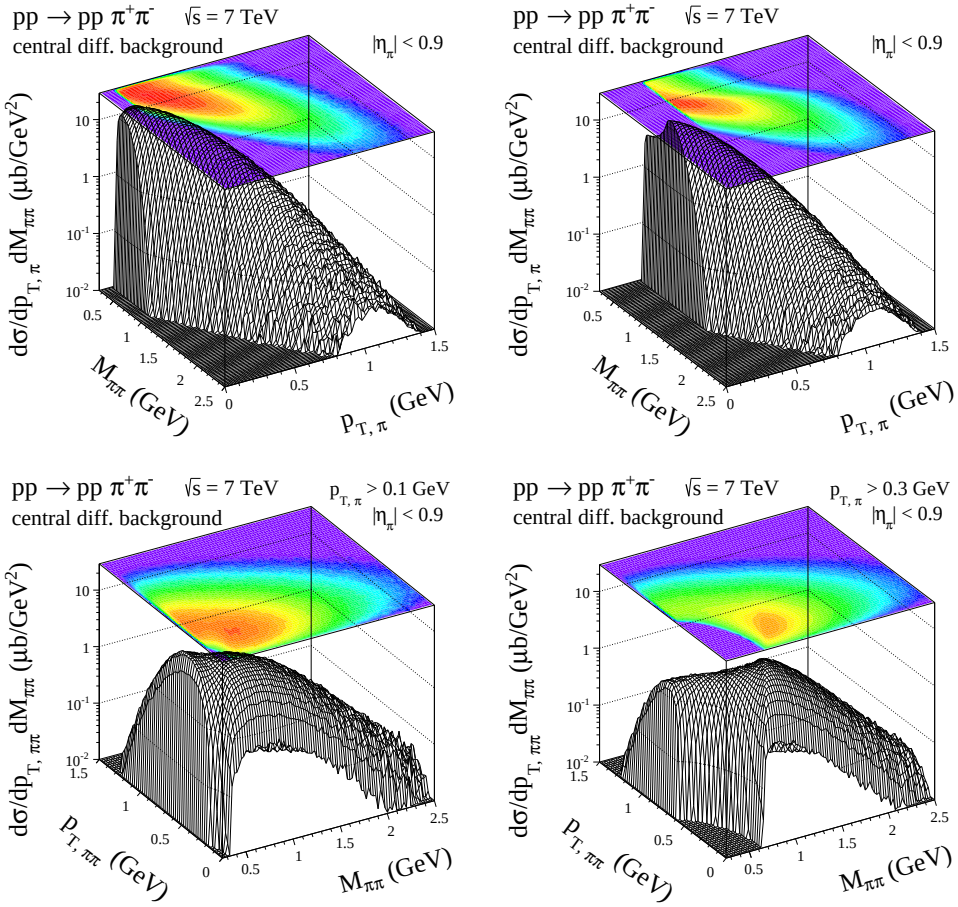

Figure 2.46: Distribution in $(p_{\perp,\pi}, M_{\pi\pi})$ space (top panels) and in $(p_{\perp,\pi\pi}, M_{\pi\pi})$ space (bottom panels). In these calculation cuts on both meson pseudorpidities $|\eta_M| < 0.9$ and transverse momenta $p_{\perp,M} > 0.1$ GeV (left panel) or 0.3 GeV (right panel) have been included. In this calculation the cut-off parameter $\Lambda^2_{off,E} = 1.2$ GeV^2 and the absorption effects due to the $p\bar{p}$-interaction have been included.

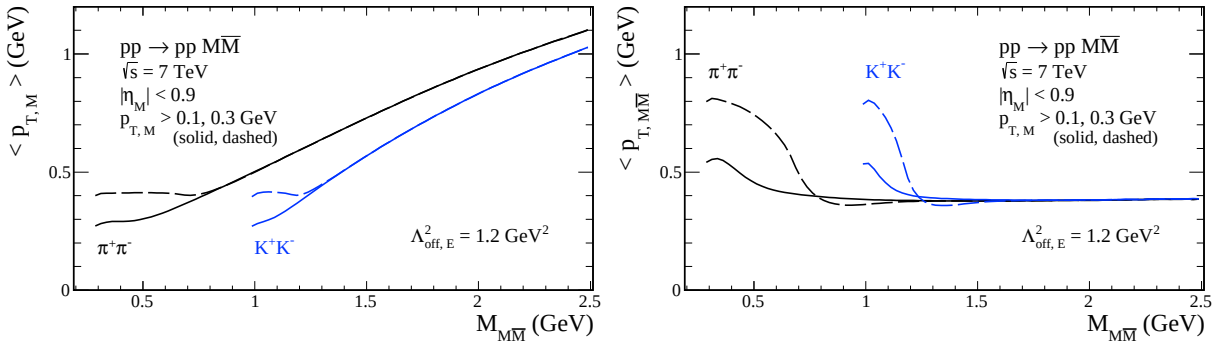

Figure 2.47: Mean value of the $p_{\perp,M}$ (left panel) and $p_{\perp,M\bar{M}}$ (right panel) as a function of two-meson invariant mass. The black lines correspond to the pions and the blue lines to the kaons. In these calculation cuts on both meson pseudorpidities $|\eta_M| < 0.9$ and transverse momenta $p_{\perp,M} > 0.1$ GeV (the solid lines) or 0.3 GeV (the dashed lines) were imposed. The usual (mesonic) propagator and the cut-off parameter $\Lambda^2_{off,E} = 1.2$ GeV^2 have been used.

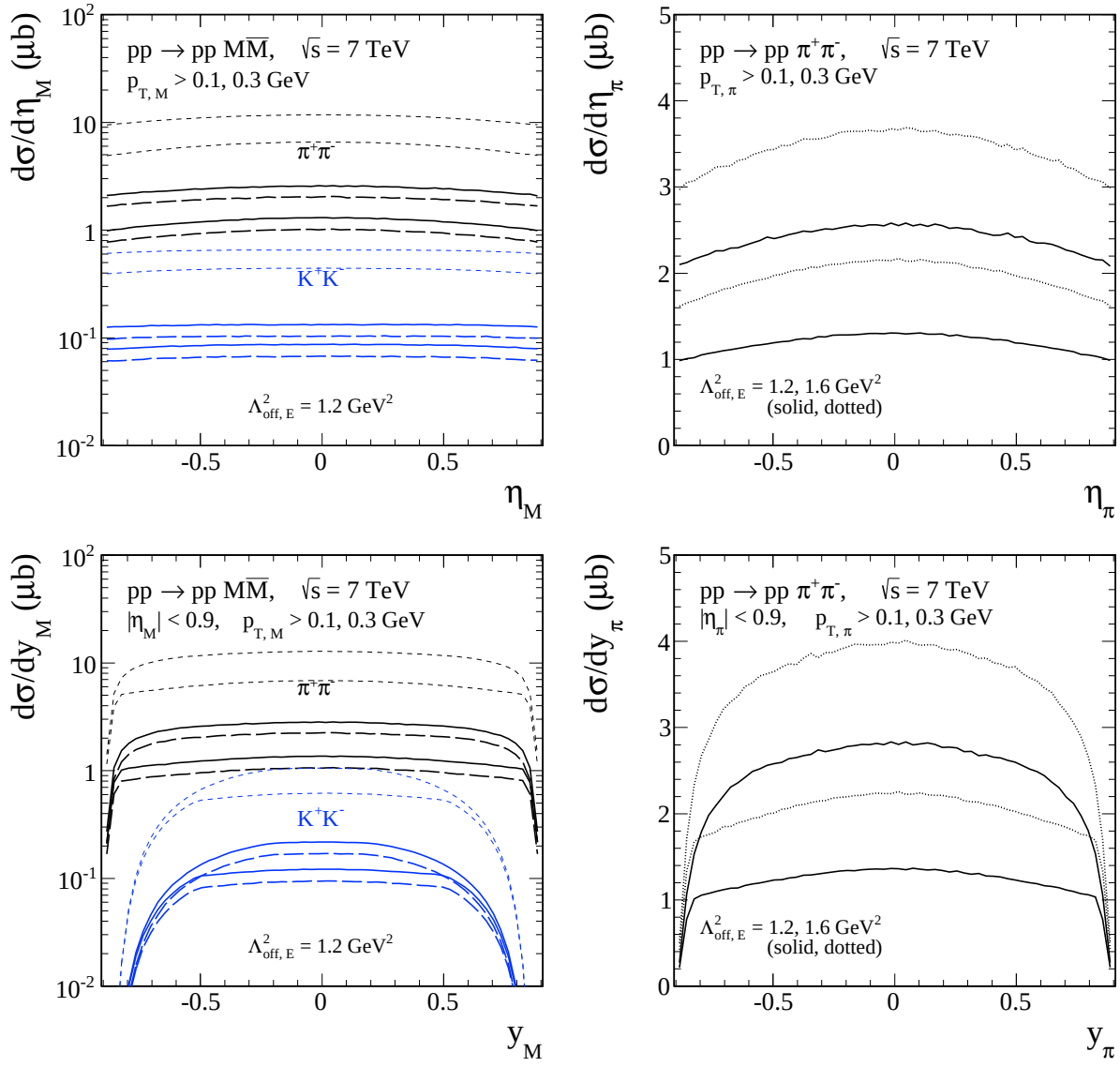

Figure 2.48: Differential cross sections $d\sigma/d\eta_M$ (top panels) and $d\sigma/dy_M$ (bottom panels) at $\sqrt{s} = 7$ TeV, without (the dashed lines) and with (the solid and long-dashed lines) the absorption effects due to the pp-interaction. The long-dashed lines show the result obtained by multiplying the absorption amplitude by a factor $c_{abs} = 1.2$. The black lines correspond to the pions and the blue lines to the kaons. These calculations were done with the usual (mesonic) propagator and with the cut-off parameter $\Lambda^2_{off,E} = 1.2, 1.6\,\mathrm{GeV}^2$.

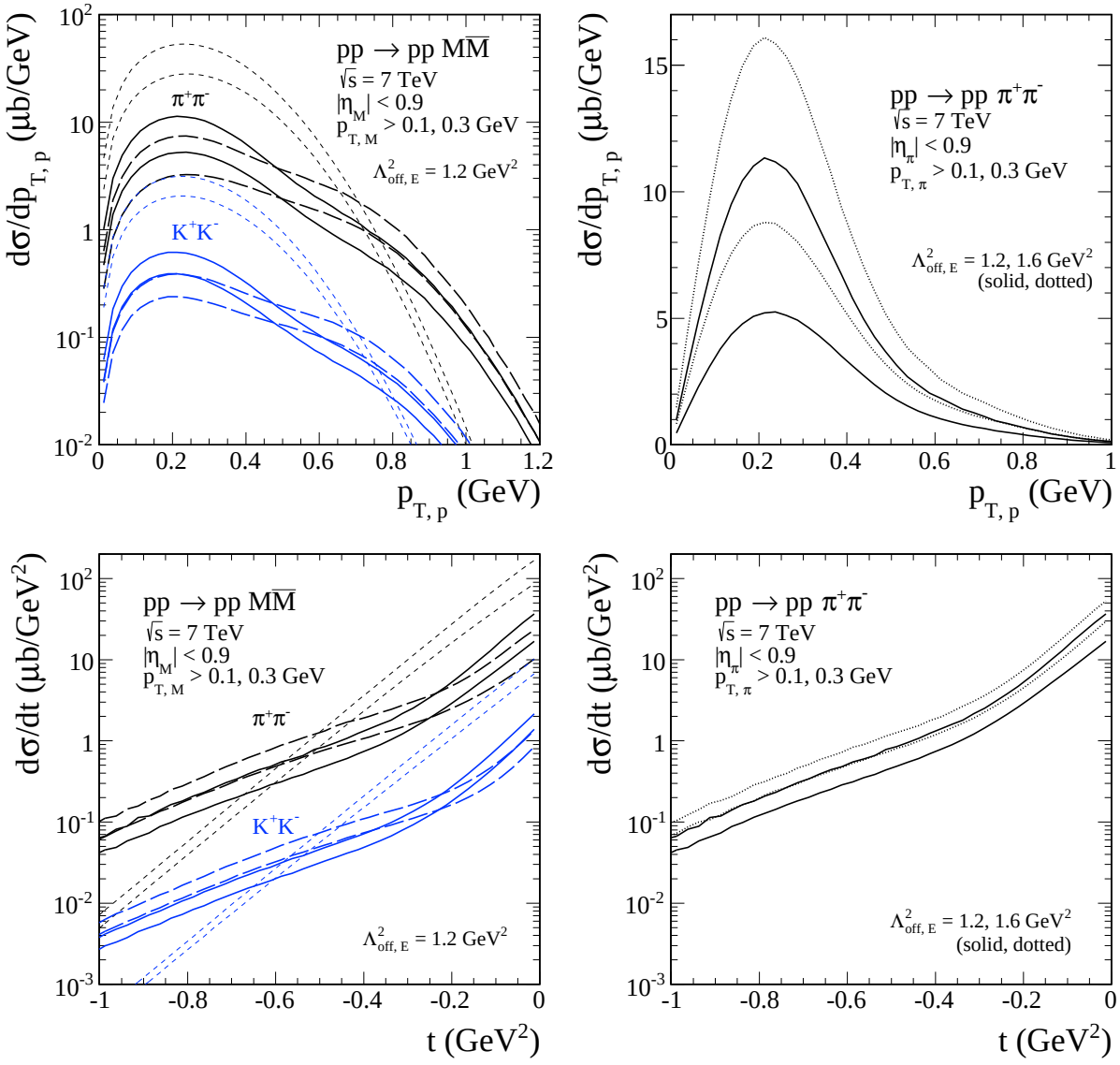

Figure 2.49: Differential cross sections $d\sigma/dp_{\perp,p}$ (top panels) and $d\sigma/dt$ (bottom panels) at $\sqrt{s} = 7$ TeV, without (the dashed lines) and with (the solid and long-dashed lines) the absorption effects due to the pp-interaction. The long-dashed lines show the result obtained by multiplying the absorption amplitude by a factor $c_{abs} = 1.2$. The black lines correspond to the pions and the blue lines to the kaons. These calculations were done with the usual (mesonic) propagator and with the cut-off parameter $\Lambda^2_{off,E} = 1.2, 1.6$ GeV^2.

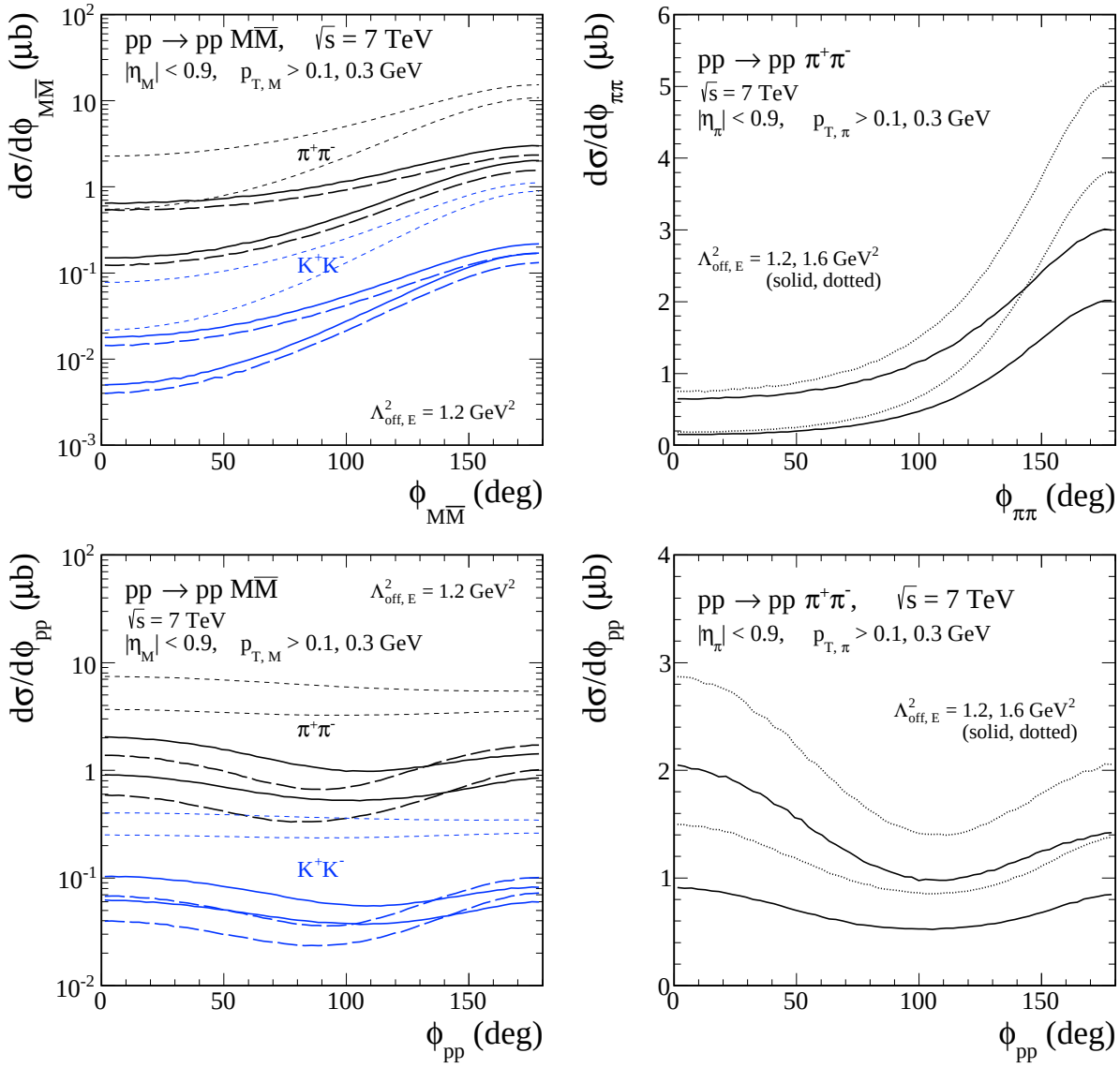

Figure 2.50: Differential cross sections $d\sigma/d\phi_{M\bar{M}}$ (top panels) and $d\sigma/d\phi_{pp}$ (bottom panels) at $\sqrt{s}$ = 7 TeV, without (the dashed lines) and with (the solid and long-dashed lines) the absorption effects due to the pp-interaction. The long-dashed lines show the result obtained by multiplying the absorption amplitude by a factor $c_{abs} = 1.2$. The black lines correspond to the pions and the blue lines to the kaons. These calculations were done with the usual (mesonic) propagator and with the cut-off parameter $\Lambda^2_{off,E} = 1.2, 1.6\,\mathrm{GeV}^2$.

2.7 Measurement of χ_{c0} meson via $\chi_{c0} \to \pi^+\pi^-$ and K^+K^- decays

The mechanism of exclusive production of mesons at high energies became recently a very active field of research (see e.g. Ref. [128] and references therein). Central exclusive production processes represent a very promising and novel way to study QCD in hadron-hadron collisions. Recently, there is a growing interest in understanding exclusive three-body reactions $pp \to ppR$ at high energies, where the meson (resonance) R is produced in the central rapidity region. The four-body $pp \to ppM\bar{M}$ reactions constitute an irreducible background to the exclusive χ_{c0} meson production in a relevant channel. The two-pion background to exclusive production of $f_0(1500)$ meson was already discussed in Ref. [1]. The recent works concentrated on the production of χ_c mesons (see e.g. Refs. [104, 106, 177–179] and references therein) where the QCD mechanism is similar to the exclusive production of the Higgs boson.

The CDF Collaboration has measured the cross section for exclusive production of χ_c mesons in proton-antiproton collisions at the Tevatron [180], by selecting events with large rapidity gaps separating the centrally produced state from the dissociation products of the incoming protons. In this experiment χ_c mesons are identified via decay to the $J/\psi + \gamma$ with $J/\psi \to \mu^+\mu^-$ channel. The cross section $d\sigma/dy|_{y=0} = 76 \pm 10$ (stat) ± 10 (syst) nb, assuming all the events were $\chi_{c0}(3415)$, has been measured [180]. At the Tevatron the experimental invariant mass resolution was not sufficient to distinguish between scalar, axial and tensor χ_c. While the branching fractions to this channel for axial and tensor mesons are large [96] ($\mathcal{B} = (34.4 \pm 1.5)\%$ and $\mathcal{B} = (19.5 \pm 0.8)\%$, respectively) the branching fraction for the scalar meson is very small $\mathcal{B} = (1.16 \pm 0.08)\%$ [96]. On the other hand, theoretical calculations [177] have shown that the cross section for exclusive χ_{c0} production obtained within the k_t-factorization is much bigger than that for χ_{c1} and χ_{c2}. As a consequence, all χ_c mesons give similar contributions to the $J/\psi + \gamma$ decay channel. Clearly, the measurement via decay to the $J/\psi + \gamma$ channel at Tevatron cannot provide precise cross section for different species of χ_c.

Could other decay channels be used? The scalar χ_{c0} meson decays into several two-body channels (e.g. $\pi\pi$, K^+K^-, $p\bar{p}$) or four-body hadronic modes (e.g. $\pi^+\pi^-\pi^+\pi^-$, $\pi^+\pi^-K^+K^-$). The branching ratios are shown in Table 2.6. The observation of χ_{c0} production via two-body decay channels is of special interest for studying the dynamics of heavy quarkonia. The measurement of exclusive production of χ_{c0} meson in proton-(anti)proton collisions via $\chi_{c0} \to \pi^+\pi^-, K^+K^-$ decays has been already discussed in Refs. [6, 8, 18]. The advantage of this channel is that the $\pi^+\pi^-$ continuum has been studied recently [3] and is relatively well known. In addition the axial χ_{c1} does not decay to the $\pi\pi$ channel and the branching ratio for the χ_{c2} decay into two pions is smaller. A much smaller cross section for χ_{c2} production as obtained from theoretical calculation than that for χ_{c0} means that only χ_{c0} will contribute to the signal.

Table 2.6: Branching fractions for the χ_{cJ} two- and four-body hadronic decays, taken from Ref. [96].

Channel	$\mathcal{B}(\chi_{c0})$	$\mathcal{B}(\chi_{c1})$	$\mathcal{B}(\chi_{c2})$
$\pi^+\pi^-$	$(0.56 \pm 0.03) \times 10^{-2}$	–	$(0.16 \pm 0.01) \times 10^{-2}$
K^+K^-	$(0.610 \pm 0.035) \times 10^{-2}$	–	$(0.109 \pm 0.008) \times 10^{-2}$
$p\bar{p}$	$(2.28 \pm 0.13) \times 10^{-4}$	$(0.73 \pm 0.04) \times 10^{-4}$	$(0.72 \pm 0.04) \times 10^{-4}$
$\pi^+\pi^-\pi^+\pi^-$	$(2.27 \pm 0.19) \times 10^{-2}$	$(0.76 \pm 0.26) \times 10^{-2}$	$(1.11 \pm 0.11) \times 10^{-2}$
$\pi^+\pi^-K^+K^-$	$(1.80 \pm 0.15) \times 10^{-2}$	$(0.45 \pm 0.10) \times 10^{-2}$	$(0.92 \pm 0.11) \times 10^{-2}$

We wish to calculate differential distributions for the exclusive production χ_{c0} meson with the UGDFs taken from the literature relevant for small gluon virtualities (transverse momenta). This process is especially important because the χ_{c0} has the same quantum numbers as the Higgs boson (apart from its strong interactions) and is produced the same way but with a c-loop replacing the t-loop, so it is a good test of the theoretical calculations. We shall use matrix element for the off-shell gluons as obtained in Ref. [104]. The expected non-resonant

background can be modeled using a "non-perturbative" framework, mediated by the pomeron-pomeron fusion with an intermediate off-shell pion/reggeon exchanged between the final-state particle pairs. Thus, we consider $pp(\bar{p}) \to pp(\bar{p})\pi^+\pi^-$ reaction as a genuine four-body process with exact kinematics which can be easily used when kinematical cuts are improved.

Exclusive charmonium decays have been a subject of interest at the e^+e^- colliders as they are an excellent laboratory for studying quark-gluon dynamics at relatively low energies. Thus, a measurement of many exclusive hadronic χ_c decays as possible is very valuable. Although these χ_c states are not directly produced in e^+e^- collisions, they are copiously produced in the radiative decays $\psi(2S) \to \gamma\chi_c$, each of which has a branching ratio of around 9% [96]. The CLEO Collaboration has studied exclusive $\chi_{c(0,1,2)}$ decays into four-hadron final states involving two charged and two neutral mesons [181]: $\pi^+\pi^-\pi^0\pi^0$, $K^+K^-\pi^0\pi^0$, $p\bar{p}\pi^0\pi^0$, $K^+K^-\eta\pi^0$ and $K^\pm\pi^\mp K^0\pi^0$. The BESIII Collaboration has studied two-body $\chi_{c(0,2)}$ decays into $\pi^0\pi^0$ and $\eta\eta$ [182] [8] and four-body $\chi_{c(0,1,2)}$ decays into $\pi^0\pi^0\pi^0\pi^0$ [183] final states, where χ_{cJ} signals appear in radiative photon energy spectrum. Recently the BESIII Collaboration performed a measurement of the hadronic decays of the three χ_{cJ} states to $p\bar{p}K^+K^-$ ($\bar{p}K^+\Lambda(1520)$, $\Lambda(1520)\bar{\Lambda}(1520)$ and $\phi p\bar{p}$) [184]. In the proton-(anti)proton collisions the continuum backgrounds are expected to be larger than in the e^+e^- collisions.

2.7.1 Diffractive QCD amplitude for exclusive χ_{c0} production

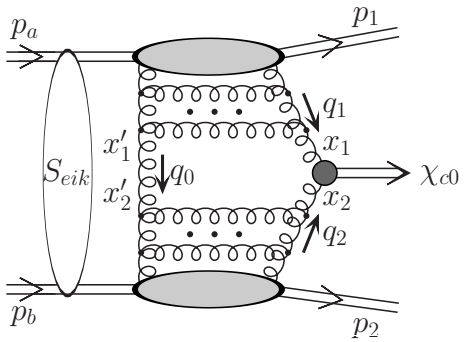

Figure 2.51: The QCD mechanism of exclusive diffractive production of χ_{c0} meson including the absorptive correction.

The QCD mechanism for the diffractive production of heavy central system has been proposed by Khoze, Martin and Ryskin (KMR) and developed in collaboration with Kaidalov and Stirling for Higgs production (see e.g. Refs. [99–103]). In the framework of this approach the amplitude of the exclusive $pp \to pp\chi_{c0}$ process is described by the diagram shown in Fig. 2.51, where the hard subprocess $g^*g^* \to \chi_{c0}$ is initiated by the fusion of two off-shell gluons and the soft part is represented in terms of the off-diagonal unintegrated gluon distributions (UGDFs). The formalism used to calculate the exclusive χ_{c0} meson production is explained in detail elsewhere [104] and so we will only review relevant aspects here.

The amplitude for the exclusive χ_{c0} meson production can be written as

$$\begin{aligned}\mathcal{M}_{pp\to pp\chi_c}(s,y,-\boldsymbol{p}_{1\perp},-\boldsymbol{p}_{2\perp}) &= \mathcal{M}^{Born}_{pp\to pp\chi_c}(s,y,-\boldsymbol{p}_{1\perp},-\boldsymbol{p}_{2\perp}) \\ &\quad +\mathcal{M}^{rescatt.}_{pp\to pp\chi_c}(s,y,-\boldsymbol{p}_{1\perp},-\boldsymbol{p}_{2\perp})\,. \end{aligned} \tag{2.53}$$

[8] The χ_{c1} decay into these final states are not considered as they are forbidden by the spin-parity conservation.

We can write the Born amplitude [104] as

$$\mathcal{M}^{Born}_{pp\to pp\chi_c}(s,y,-\boldsymbol{p}_{1\perp},-\boldsymbol{p}_{2\perp}) = \\ \frac{s}{2}\pi^2\frac{1}{2}\frac{1}{N_c^2-1}\mathrm{Im}\int d^2q_{0\perp}V(\boldsymbol{q}_{1\perp},\boldsymbol{q}_{2\perp})\frac{f^{off}_{g,1}(x_1,x',q^2_{0\perp},q^2_{1\perp},t_1)f^{off}_{g,2}(x_2,x',q^2_{0\perp},q^2_{2\perp},t_2)}{q^2_{0\perp}\,q^2_{1\perp}\,q^2_{2\perp}}\,, \quad (2.54)$$

where the objects $f^{off}_{g,1/g,2}$ are skewed (or off-diagonal) unintegrated gluon distributions of both nucleons. $t_{1,2}$ are the momentum transfers along each nucleon line, $q_{1\perp}$, $q_{2\perp}$, $q_{0\perp}$, $x_{1,2}$, $x'_1 \sim x'_2 \ll x_{1,2}$ are the transverse momenta and the longitudinal momentum fractions for active and screening gluons, respectively. UGDFs are nondiagonal both in the x and q_t^2 space. The usual off-diagonal gluon distributions are nondiagonal only in x. In the limit $x_{1,2} \to x'_{1,2}$, $q^2_{0\perp} \to q^2_{1/2\perp}$ and $t_{1,2} \to 0$ they become the usual UGDFs.

The vertex factor $V(\boldsymbol{q}_{1\perp},\boldsymbol{q}_{2\perp})$ describes the coupling of two virtual gluons to χ_{c0} meson is obtained in heavy quark approximation (including virtualities of active gluons) and can be written as

$$V(\boldsymbol{q}_{1\perp},\boldsymbol{q}_{2\perp}) = K_{NLO}\frac{8ig_s^2}{M}\frac{\mathcal{R}'(0)}{\sqrt{\pi M N_c}}\frac{3M^2\boldsymbol{q}_{1\perp}\boldsymbol{q}_{2\perp} - 2\boldsymbol{q}^2_{1\perp}\boldsymbol{q}^2_{2\perp} - (\boldsymbol{q}_{1\perp}\boldsymbol{q}_{2\perp})(\boldsymbol{q}^2_{1\perp}+\boldsymbol{q}^2_{2\perp})}{(M^2+\boldsymbol{q}^2_{1\perp}+\boldsymbol{q}^2_{2\perp})^2}\,, \quad (2.55)$$

where M is the χ_{c0} mass, $g_s^2 = 4\pi\alpha_s(M^2)$ and the strong coupling constant is calculated in the leading order and extended to the nonperturbative region according to Shirkov-Solovtsov analytical model [112]. The value of the P-wave radial wave function at the origin is taken to be [185] $\mathcal{R}'_{\chi_{cJ}}(0) = \sqrt{0.075}$ GeV$^{5/2}$ and the radiative corrections factor in the vertex K_{NLO} is known [186–188], $K_{NLO} \simeq 1.68$.

The rescattering correction shown in Fig. 2.51 by the extra blob can be written in the form

$$\mathcal{M}^{rescatt.}_{pp\to pp\chi_c}(s,y,-\boldsymbol{p}_{1\perp},-\boldsymbol{p}_{2\perp}) = \int\frac{d^2\boldsymbol{k}_\perp}{2(2\pi)^2}\frac{A_{pp}(s,k^2_\perp)}{s}\mathcal{M}^{Born}_{pp\to pp\chi_c}(s,y,\boldsymbol{k}_{1\perp},\boldsymbol{k}_{2\perp})\,, \quad (2.56)$$

where $\boldsymbol{k}_{1\perp} = -\boldsymbol{p}_{1\perp} - \boldsymbol{k}_\perp$ and $\boldsymbol{k}_{2\perp} = -\boldsymbol{p}_{2\perp} - \boldsymbol{k}_\perp$ with momentum transfer $\boldsymbol{k}_\perp$. The amplitude for elastic proton-proton scattering at an appropriate energy is parametrised as (2.9)

$$A_{pp}(s,k^2_\perp) = A_0(s)\,\exp(-Bk^2_\perp/2) \quad (2.57)$$

with the leading pomeron exchange and the effective slope (2.21) adjusted to the elastic NN scattering data. From the optical theorem we have $\mathrm{Im}A_0(s,t=0) = s\sigma_{tot}(s)$ (the real part is small in the high energy limit).

The KMR UGDFs, unintegrated over $q_\perp$, are calculated from the conventional (integrated) distributions $g(x,q^2_\perp)$ and the so-called Sudakov form factor $\sqrt{T_g(q^2_\perp,\mu^2)}$ as follows:

$$f^{KMR}_g(x,x',Q^2_\perp,\mu^2;t) = R_g\frac{\partial}{\partial\ln q^2_\perp}\left[xg(x,q^2_\perp)\sqrt{T_g(q^2_\perp,\mu^2)}\right]_{q^2_\perp=Q^2_\perp}F(t)\,. \quad (2.58)$$

The Sudakov factor suppresses real emissions from the active gluon during the evolution, so that the rapidity gaps survive up to the hard scale μ. The factor R_g approximately accounts for the single $\ln Q^2_\perp$ skewed effect [189]. In the calculations presented here we take $R_g = 1.3$, and the value of the hard scale is $\mu^2 = M^2$. The choice of the scale is somewhat arbitrary, and consequences of this choice were discussed in Ref. [104].

In Ref. [190] a procedure was presented which allows to calculate the generalized (or skewed) parton distributions of the proton, $\overline{H}(x,\xi;q^2_\perp,\mu^2)$, unintegrated over the partonic transverse momenta, from the conventional parton distributions, $q(x,\mu^2)$ and $g(x,\mu^2)$, for small values of the skewedness parameter $\xi^2 \ll 1$ and any x. The momentum fractions carried by the

emitted and absorbed partons are defined as $x_{1,2} = x \pm \frac{1}{2}\xi$ with support $-1 \leq x \leq 1$. The result is a simple approximate phenomenological form for the distribution:

$$\overline{H}_g\left(\frac{\xi}{2}, \xi; q_\perp^2, \mu^2\right) = \sqrt{T_g(q_\perp^2, \mu^2)}\left[R_g \frac{\partial x g(x, q_\perp^2)}{\partial \ln q_\perp^2} + x g(x, q_\perp^2) \frac{N_c \alpha_s}{2\pi}\left(\ln \frac{\mu + \frac{1}{2}q_\perp}{q_\perp} + 1.2\frac{\mu^2}{\mu^2 + q_\perp^2}\right) + 5\,\frac{\alpha_s}{2\pi}\left(x u_{\rm val}(x, q_\perp^2) + x d_{\rm val}(x, q_\perp^2)\right)\right]_{x=\xi}. \quad (2.59)$$

In evaluating f_g's we have used the GRV NLO [108] and GJR NLO [191, 192] collinear gluon distributions, which allow to use rather low values of gluon transverse momenta $Q_\perp^2 = q_{0\perp}^2,\ q_{1\perp}^2,\ q_{2\perp}^2 \geq 0.5$ GeV^2. The collinear distributions such as CTEQ and MRST are defined for higher factorization scales ($Q_\perp^2 > 1$ GeV^2), and therefore are less useful in the applications discussed here.

The t-dependence of the unintegrated gluon distribution f_g's is not well known and is isolated in the effective form factors of the QCD pomeron-proton vertex, which are parametrised in the forward scattering limit in the exponential form as $F(t) = \exp(b\,t/2)$ with the t-slope parameter $b = 4$ GeV^{-2}. Then the integral in Eq. (2.56) can be evaluated as [193]

$$\mathcal{M}^{rescatt.}_{pp\to pp\chi_c}(s, y, -\boldsymbol{p}_{1\perp}, -\boldsymbol{p}_{2\perp}) = \frac{iA_0}{4\pi s(B + 2b)} \exp\left(\frac{b^2|\boldsymbol{p}_{1\perp} - \boldsymbol{p}_{2\perp}|^2}{2(B + 2b)}\right) \times \mathcal{M}^{Born}_{pp\to pp\chi_c}(s, y, -\boldsymbol{p}_{1\perp}, -\boldsymbol{p}_{2\perp}). \quad (2.60)$$

In practical integrations of the exclusive χ_{c0} meson cross section we choose the transverse momenta of outgoing nucleons $(p_{1\perp}, p_{2\perp})$, the meson rapidity (y) and the relative azimuthal angle between outgoing nucleons (ϕ_{12}).

In Fig. 2.52 we show distributions of the central exclusive χ_{c0} production cross section at $\sqrt{s} = 14$ TeV without (dashed line) and with (solid line) absorptive corrections. These calculations were done with GJR NLO [191, 192] collinear gluon distribution, to generate the KMR UGDFs (see Eq. (2.58)), which allows to use low values of the gluon transverse momenta $Q_\perp^2 \geq Q_{cut}^2 = 0.5$ GeV^2. The bigger the value of the cut-off parameter, the smaller the cross section (see Ref. [104]). In the calculations we take the value of the hard scale to be $\mu^2 = M^2$. The bigger μ^2, the smaller the cross section [104]. The absorption effects lead to a damping of the cross section. In most distributions the shape is almost unchanged. Exception is the distribution in proton transverse momentum where the absorption effects lead to a damping of the cross section at small proton $p_\perp$ and an enhancement of the cross section at large proton $p_\perp$. In relative azimuthal angle distribution we observe a minimum at $\phi_{12} \sim \pi/2$. Transverse momentum distribution of χ_{c0} shows a small minimum at $p_\perp \sim 2.5$ GeV. The main reason of its appearance is the functional dependence of matrix elements on its arguments [104].

In Fig. 2.53 we compare distributions of the central exclusive χ_{c0} production cross section at $\sqrt{s} = 14$ TeV calculated for two collinear gluon distributions: GRV94 NLO (upper lines) and GJR08 NLO (bottom lines). We show results here only for distributions with absorptive corrections calculated with the KMR off-diagonal UGDFs given by Eq. (2.58) (solid lines) and with off-diagonal UGDFs given in the phenomenological form given by Eq. (2.59). The peaks at large rapidities appear only when we use formula (2.58). In this region one of off-diagonal UGDFs changes a sign. This shows limitations in applying formula (2.58).

2.7.2 Background mechanism with $M\bar{M}$ rescattering

The full amplitude for the four-body process (2.22) is a sum of the Born and rescattering amplitudes

$$\mathcal{M}^{full}_{pp\to ppM\bar{M}} = \mathcal{M}^{Born} + \mathcal{M}^{pp-rescattering} + \mathcal{M}^{M\bar{M}-rescattering}. \quad (2.61)$$

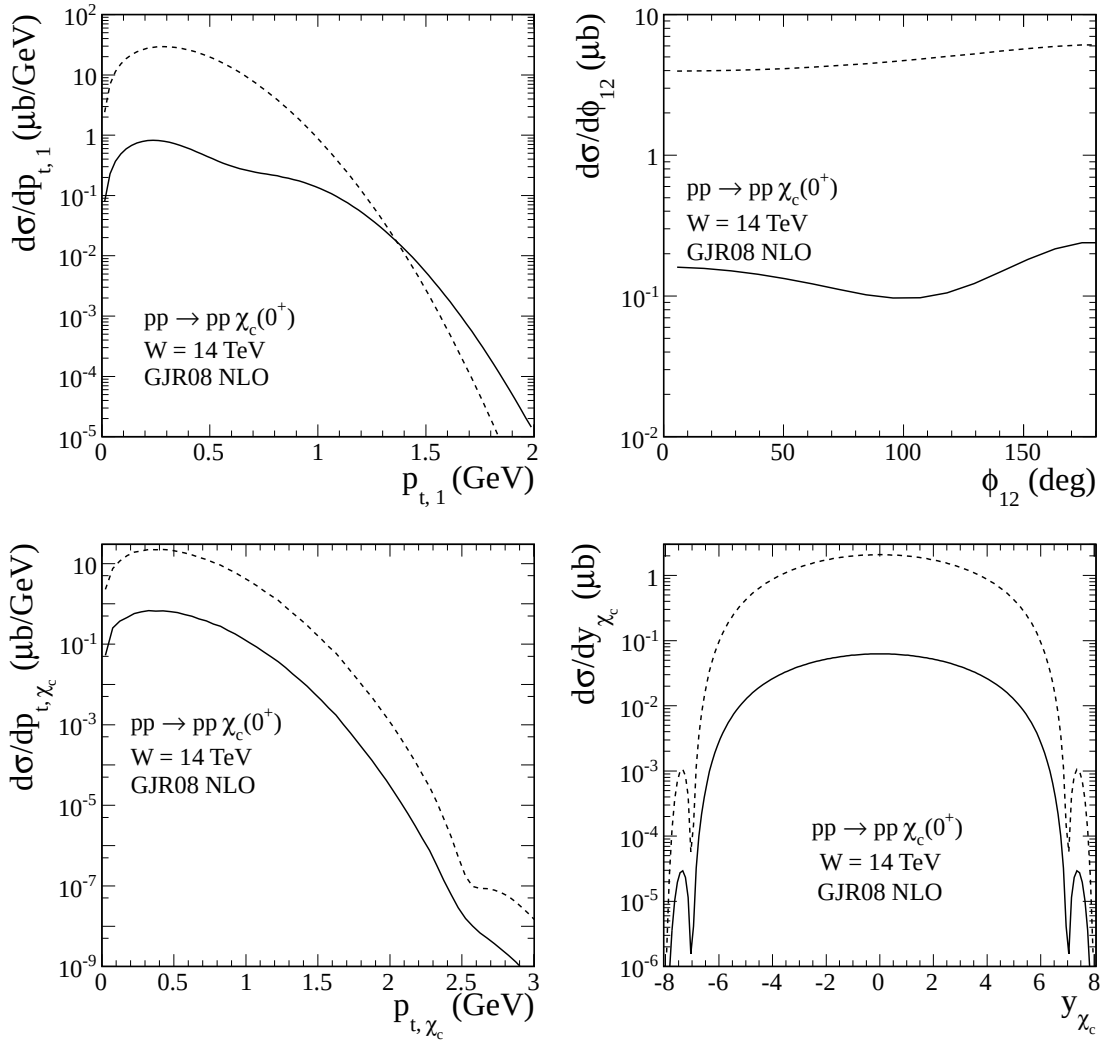

Figure 2.52: Differential cross sections for the $pp \to pp\chi_{c0}$ reaction at $\sqrt{s} = 14$ TeV without (dashed line) and with (solid line) the absorption effects taken into account. These calculations were done with the GJR08 NLO [191, 192] distribution to generate UGDFs.

The formulae presented so far (see Section 2.3) does not include the $M\bar{M}$ rescattering. Inclusion of $M\bar{M}$ rescattering at low energies is rather difficult and is often done with the help of the Lippmann-Schwinger formalism.

When going from the Born approximation to the higher-order diagrams with the pion-pion FSI the following replacement is formally required:

$$\frac{F^A_{off}(k)F^B_{off}(k)}{k^2-m_\pi^2} \to \int \frac{d^4k}{(2\pi)^4}\frac{1}{k^2-m_\pi^2}\frac{F^A_{off}(k,k_3)}{k_3^2-m_\pi^2}\frac{F^B_{off}(k,k_4)}{k_4^2-m_\pi^2}\sum_{ij}\mathcal{M}^{off-shell}_{\pi_i\pi_j\to\pi^\pm\pi^\mp}(k_3k_4 \to p_3p_4)\,, \quad (2.62)$$

where the sum runs over different isospin combinations of pions. In general the integral above is complicated (singularities, unknown elements), the vertex form factors (A and B) with two pions being off-mass-shell are not well known, and even the off-shell matrix element is not fully under control. Usually a serious simplifications are done to make the calculation useful on a practical level. Limiting to the S-wave ($L = 0$) one can correct the Born amplitude by a phenomenological function which causes an enhancement close to the two-pion threshold and damping at $M_{\pi\pi} \sim 0.8$ GeV. Dealing with higher partial waves is more complicated, see e.g. [41]. At even larger $M_{\pi\pi}$ the interaction becomes absorptive and was not much studied. Some work can be found in Ref. [111]. Clearly much more theoretical afford is required. In the present approach we are interested rather at somewhat larger pion-pion energies close to the χ_{c0} mass.

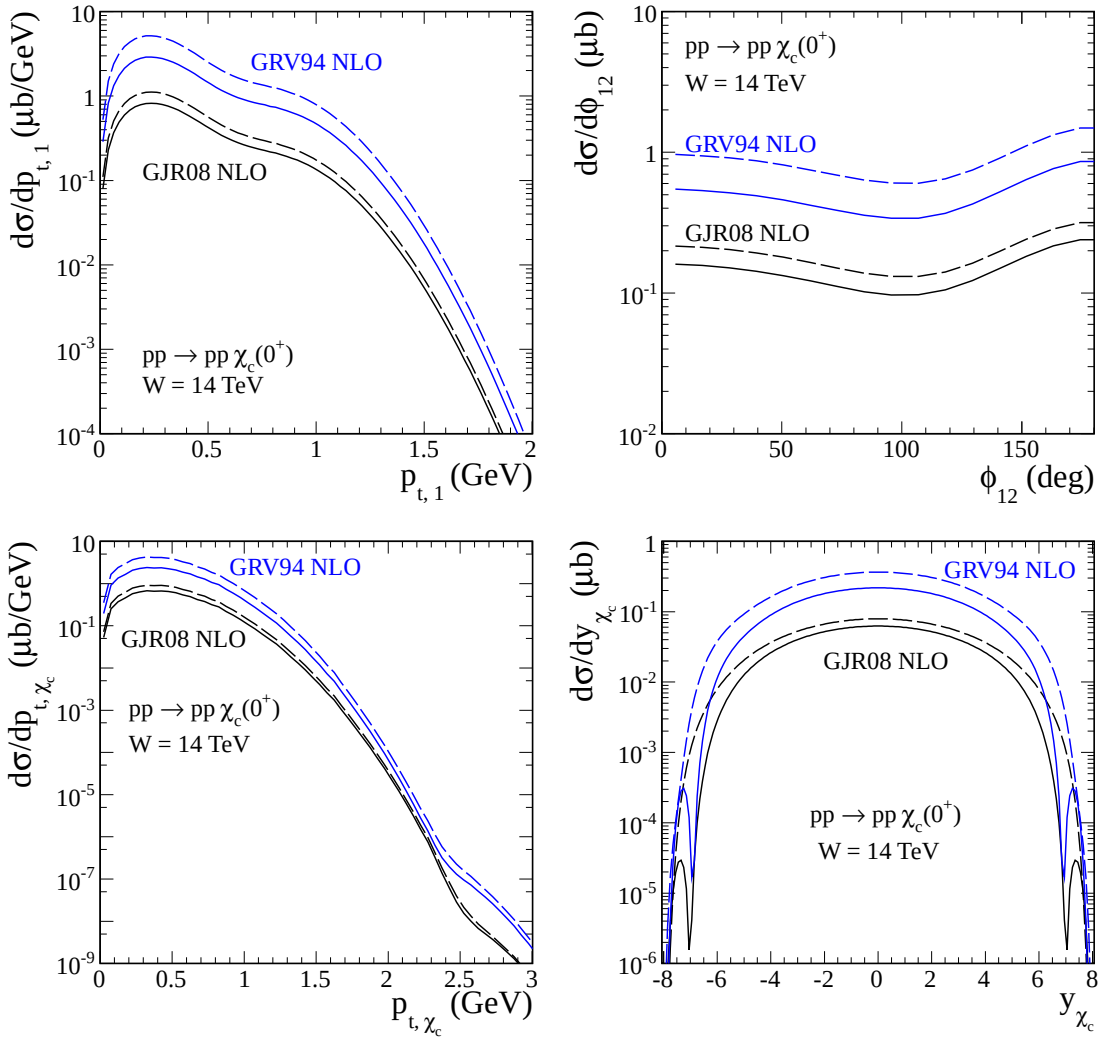

Figure 2.53: Differential cross sections for the $pp \to pp\chi_{c0}$ reaction at $\sqrt{s} = 14$ TeV with the absorption effects taken into account. The results with the KMR off-diagonal UGDFs given by Eq. (2.58) (solid lines) and with off-diagonal UGDFs given by Eq. (2.59) (dashed lines) are shown. These calculations were done for GRV94NLO GDFs (upper lines) and GJR08NLO GDFs (bottom lines).

The pion-pion rescattering contribution leads to a redistribution of the strength but seems to modify the pion-pion integrated cross section very little [122]. The effect of pion-pion FSI must be, however, included if the spectrum of invariant mass is studied. At high invariant masses one may expect also a strong damping due to absorption in the pion-pion subsystem. Only low-invariant-mass spectra were studied in the past experiments [156]. The experiments at the LHC could study the potential damping of large-mass dipion production and therefore could shed more light on the not fully understood problem of absorption effects in a few-body hadronic systems.

The pion-pion interaction at high energies was studied e.g. in Refs. [111, 194]. In full analogy to those works at the higher energies one can include the pion-pion rescattering for our four-body reaction by replacing the normal (or reggeized) pion propagators (including vertex form factors) as:

$$\begin{aligned} \frac{F_\pi^2(\hat{t})}{\hat{t} - m_\pi^2} &\to \frac{i}{16\pi^2 \hat{s}} \int d^2\kappa \frac{F_\pi^2(\hat{t}_1)}{\hat{t}_1 - m_\pi^2} \mathcal{M}_{\pi^+\pi^- \to \pi^+\pi^-}(\hat{t}_2)\,, \\ \frac{F_\pi^2(\hat{u})}{\hat{u} - m_\pi^2} &\to \frac{i}{16\pi^2 \hat{s}} \int d^2\kappa \frac{F_\pi^2(\hat{u}_1)}{\hat{u}_1 - m_\pi^2} \mathcal{M}_{\pi^+\pi^- \to \pi^+\pi^-}(\hat{u}_2) \end{aligned} \tag{2.63}$$

for t and u diagrams, respectively. The integration is over momentum in the loop (see [194]). Above we have written $\hat{s}, \hat{t}, \hat{u}$ to stress that these are quantities for a subprocess rather than for a full reaction. The quantities $\hat{t}_1$, $\hat{t}_2$, $\hat{u}_1$ and $\hat{u}_2$ are four-momenta squared of the exchanged objects in the first and the second step of the rescattering process. Other details are explained in [111]. The corresponding pion-pion rescattering amplitude is to be added to the amplitudes given by Eq. (2.37).

The Regge parametrisation of the $\pi^+\pi^- \to \pi^+\pi^-$ scattering amplitude from Ref. [111] includes both the pomeron as well as the f_2 and ρ reggeon exchanges very important at the energies considered here. The low pion-pion subenergies ($W_{\pi\pi} < 2$ GeV) require a special care of resonant scattering, coupled channel effects, which goes beyond the scope of the present work. The Regge-type interaction applies at higher energies. At low energies the Regge type of interactions is not realistic and should be switched off. To achieve this requirement we can multiply the Regge amplitude by an extra (in principle unknown) threshold factor $S_{thr}(\hat{s})$. In the present approach we take it in a simple purely phenomenological form:

$$S_{thr}(\hat{s}) = \begin{cases} 0, & \hat{s} \leqslant \hat{s}_{thr}, \\ 1 - \exp(-(\hat{s} - \hat{s}_{thr})/\Delta\hat{s}), & \hat{s} > \hat{s}_{thr} \end{cases} \tag{2.64}$$

with $\Delta\hat{s}$ being the only free parameter and $\Delta\hat{s} = 9$ GeV^2 value is taken. As s_{thr} we take $(2m_K)^2$. Below this value physics is certainly different and a resonant $\pi\pi$-rescattering known as σ-meson and a $\pi\pi - KK$ coupled-channel approach are necessary. We leave this low-energy part, not important for the χ_{c0} background, for an independent analysis. So-modified Regge amplitude will be used then to included extra pion-pion interactions in Eq. (2.63).

The $KK \to KK$ subprocess amplitude for t and u diagrams in Fig. 2.8 is written in the high-energy approximation

$$\begin{aligned} \frac{F_K^2(\hat{t})}{\hat{t} - m_K^2} &\to \frac{i}{16\pi^2\hat{s}} \int d^2\kappa \frac{F_K^2(\hat{t}_1)}{\hat{t}_1 - m_K^2} M_{K^+K^- \to K^+K^-}(\hat{s}, \hat{t}_2)\,, \\ \frac{F_K^2(\hat{u})}{\hat{u} - m_K^2} &\to \frac{i}{16\pi^2\hat{s}} \int d^2\kappa \frac{F_K^2(\hat{u}_1)}{\hat{u}_1 - m_K^2} M_{K^-K^+ \to K^-K^+}(\hat{s}, \hat{u}_2)\,. \end{aligned} \tag{2.65}$$

The elastic amplitudes in the $KK \to KK$ subprocesses are written as

$$M_{KK\to KK}(\hat{s}, \hat{t}_2/\hat{u}_2) = \beta'_M(\hat{s}) A^{V-exch.}_{KK\to KK}(\hat{t}_2/\hat{u}_2) + \beta'_R(\hat{s}) A^{Regge}_{KK\to KK}(\hat{s}, \hat{t}_2/\hat{u}_2)\,, \tag{2.66}$$

for the vector meson ($V = \rho, \omega, \phi$) exchanges and $\beta'_M(\hat{s}) = \exp(-(\hat{s} - 4m_K^2)/\Delta\hat{s})$, $\beta'_R(\hat{s}) = 1 - \beta'_M(\hat{s})$, $\Delta\hat{s} = 9$ GeV^2.

The Regge-type interaction which includes the pomeron and reggeon (f_2, a_2, ρ and ω) exchanges applies at higher s_{34} energies:

$$\begin{aligned} A^{Regge}_{K^+K^-\to K^+K^-}(\hat{s}, \hat{t}_2) &= \eta_i\, \hat{s}\, C_i^{KK} \left(\frac{\hat{s}}{\hat{s}_0}\right)^{\alpha_i(\hat{t}_2)-1} \exp\left(\frac{B_i^{KK}}{2}\hat{t}_2\right), \\ A^{Regge}_{K^-K^+\to K^-K^+}(\hat{s}, \hat{u}_2) &= \eta_i\, \hat{s}\, C_i^{KK} \left(\frac{\hat{s}}{\hat{s}_0}\right)^{\alpha_i(\hat{u}_2)-1} \exp\left(\frac{B_i^{KK}}{2}\hat{u}_2\right), \end{aligned} \tag{2.67}$$

where the scale parameter $\hat{s}_0 = 1$ GeV^2 and the C_i^{KK} coupling constants can be evaluated assuming Regge factorisation (1.68) and are listed in Table 2.1.

At low s_{34} energies the Regge type of interactions is not realistic and rather $V = \rho, \omega, \phi$ meson exchanges must be taken into account:

$$\begin{aligned} A^{V-exch.}_{K^+K^-\to K^+K^-}(\hat{t}_2) &= g_{KKV} F_{KKV}(\hat{t}_2) \frac{(p_3^{*\mu} + p_3^\mu) P_{\mu\nu} (p_4^{*\nu} + p_4^\nu)}{\hat{t}_2 - m_V^2 + i m_V \Gamma_V} g_{KKV} F_{KKV}(\hat{t}_2)\,, \\ A^{V-exch.}_{K^-K^+\to K^-K^+}(\hat{u}_2) &= g_{KKV} F_{KKV}(\hat{u}_2) \frac{(p_3^{*\mu} + p_4^\mu) P_{\mu\nu} (p_4^{*\nu} + p_3^\nu)}{\hat{u}_2 - m_V^2 + i m_V \Gamma_V} g_{KKV} F_{KKV}(\hat{u}_2)\,, \end{aligned} \tag{2.68}$$

where $P_{\mu\nu}(k) = -g_{\mu\nu} + k_\mu k_\nu / m_V^2$ and the KKV coupling constants g_{KKV} are given from SU(3) symmetry relations $2\,g_{KK\omega} = \sqrt{2}\,g_{KK\phi} = 2\,g_{KK\rho} = g_{\rho\pi\pi} = 6.04$ [195], where the value of $g_{\rho\pi\pi}$ is determined by the decay width of the ρ meson.

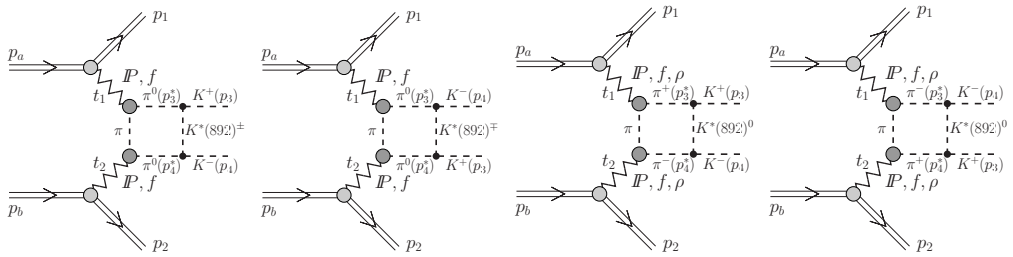

Figure 2.54: The central diffractive mechanism of exclusive production of K^+K^- pairs via the $K^*(892)$ meson exchanges.

Again the $\pi\pi \to KK$ subprocess amplitude is written in the high-energy approximation as

$$\begin{aligned}
\frac{F_\pi^2(\hat{t})}{\hat{t} - m_\pi^2} &\to \frac{i}{16\pi^2 \hat{s}} \int d^2\kappa \frac{F_\pi^2(\hat{t}_1)}{\hat{t}_1 - m_\pi^2} M^{K^*-exch.}_{\pi\pi\to K^+K^-}(\hat{t}_2)\,, \\
\frac{F_\pi^2(\hat{u})}{\hat{u} - m_\pi^2} &\to \frac{i}{16\pi^2 \hat{s}} \int d^2\kappa \frac{F_\pi^2(\hat{u}_1)}{\hat{u}_1 - m_\pi^2} M^{K^*-exch.}_{\pi\pi\to K^-K^+}(\hat{u}_2)\,,
\end{aligned} \tag{2.69}$$

with

$$\begin{aligned}
M^{K^*-exch.}_{\pi\pi\to K^+K^-}(\hat{t}_2) &= g_{\pi KK^*} F_{\pi KK^*}(\hat{t}_2) \frac{(p_3^{*\mu} + p_3^\mu) P_{\mu\nu} (p_4^{*\nu} + p_4^\nu)}{\hat{t}_2 - m_{K^*}^2 + i m_{K^*}\Gamma_{K^*}} g_{\pi KK^*} F_{\pi KK^*}(\hat{t}_2)\,, \\
M^{K^*-exch.}_{\pi\pi\to K^-K^+}(\hat{u}_2) &= g_{\pi KK^*} F_{\pi KK^*}(\hat{u}_2) \frac{(p_3^{*\mu} + p_4^\mu) P_{\mu\nu} (p_4^{*\nu} + p_3^\nu)}{\hat{u}_2 - m_{K^*}^2 + i m_{K^*}\Gamma_{K^*}} g_{\pi KK^*} F_{\pi KK^*}(\hat{u}_2)\,,
\end{aligned} \tag{2.70}$$

where now $P_{\mu\nu}(k) = -g_{\mu\nu} + k_\mu k_\nu / m_{K^*}^2$ and we take $g_{\pi KK^*} = -\frac{1}{2}\, g_{\rho\pi\pi}$ [195].

The quantities $F(k^2)$ in Eqs. (2.68 and 2.70) describe couplings of extended ω and K^* mesons, respectively, and are parametrised in the exponential form:

$$F(k^2) = \exp\left(\frac{B_V}{4}(k^2 - m_V^2)\right)\,. \tag{2.71}$$

Consistent with the definition of the coupling constant the form factors are normalized to unity when ω or K^* meson is on-mass-shell. We take $B_V = 4$ GeV^{-2}.

The amplitudes given by formula (2.70) are corrected by the factors $(\hat{s}/\hat{s}_0)^{\alpha_{K^*}(k^2)-1}$ to reproduce the high-energy Regge dependence. We take K^* meson trajectory as $\alpha_{K^*}(k^2) = 0.25 + \alpha'_{K^*}\, k^2$, with $\alpha'_{K^*} = 0.83$ GeV^{-2} [144, 145].

To demonstrate the role of the KK-rescattering corrections below we present various differential distributions without (the upper lines) and with (the two bottom lines) absorption effects. In Fig. 2.55 we show the distributions of kaon rapidity y_K for the $pp \to ppK^+K^-$ reaction at $\sqrt{s} = 0.5, 1.96, 7$ TeV. In our calculation we include both pomeron and reggeon exchanges which produce the 'camel-like' shape of the distributions. The reader is asked to notice, by comparison of the doted lines with the long-dashed lines, that the energy dependence of the cross section at $y_K \approx 0$ is reversed by the absorption effects which are stronger at higher energies. The integrated cross section slowly rises with incident energy.

In Fig. 2.56 we show differential distributions for the $pp \to ppK^+K^-$ reaction at $\sqrt{s} =$ 7 TeV without (dotted line) and with (solid line) the absorptive corrections. In most distributions the shape is almost unchanged. The only exception is the distribution in proton transverse momentum where we predict a damping of the cross section at small proton $p_\perp$ and an enhancement of the cross section at large proton $p_\perp$. This effect is caused by multiple proton scattering

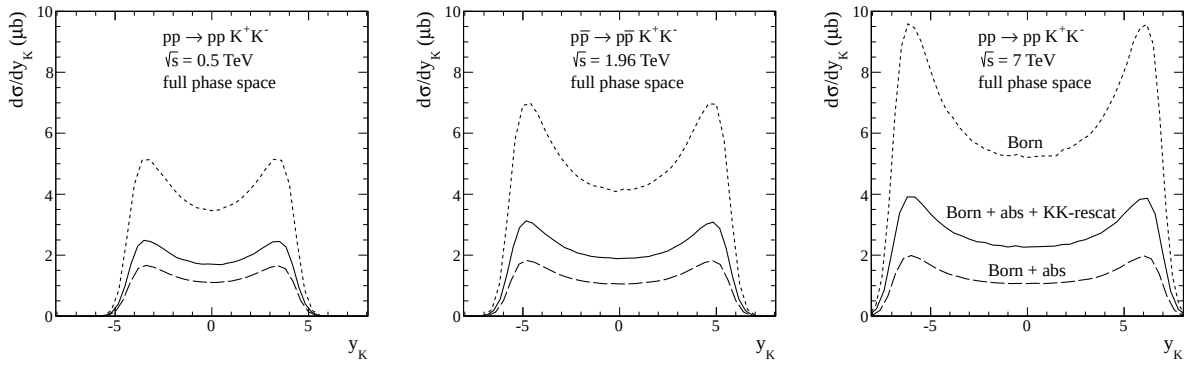

Figure 2.55: Differential cross section $d\sigma/dy_K$ for the $pp \to ppK^+K^-$ reaction at $\sqrt{s} = 0.5, 1.96, 7$ TeV. The results without (upper dotted lines) and with (bottom lines) absorption effects due to pp-interaction (the long-dashed lines) and KK-rescattering (the solid lines) are shown. These calculations were done with the cut-off parameter $\Lambda^2_{off,E} = 2$ GeV^2 and $\Lambda_{int} = 2$ GeV.

(double-scattering in our model). Such an effect is well known e.g. in elastic proton-proton scattering where multiple scattering leads to the appearance of dips and maxima of the t-dependence of the cross section observed in experimental distributions. In the literature for simplicity often three- or four-body cross sections are multiplied by an average gap survival factor which leads to a uniform damping of the cross section. This is not sufficient approximation for some observables as discussed here.

2.7.3 Results

In the present analysis we are interested mostly what happens above $M_{\pi\pi} > 2.5$ GeV, i.e. above the resonance region where there are no yet experimental data points. In Fig. 2.57 (left panel) we compare results without (solid line) and with (dashed lines) the $\pi\pi$-rescattering effect. The calculation without $\pi\pi$-rescattering roughly describe the background below a pronounced $f_2(1270)$ resonance. As seen from the figure the $\pi\pi$-rescattering leads to an extra modification of the shape. While the rescattering with mesonic propagator fails to describe the data the calculation with reggeized pion describes the dipion invariant mass distribution above $M_{\pi\pi} = 2$ GeV with sufficient, for the present purpose, precision. As a consequence of the interference of bare and rescattering amplitudes an extra dip under the $f_2(1270)$ resonance (not included here explicitly) and a shoulder at $M_{\pi\pi} \sim 2$ GeV, which could be wrongly interpreted as resonance(s) appear. Above $M_{\pi\pi} > 2.5$ GeV our predictions does not depend on the "manipulations" done at the KK threshold. At the χ_{c0} mass the $\pi\pi$-rescattering leads therefore to an enhancement compared to the calculation without $\pi\pi$-rescattering. In the right panel we can see that at the χ_{c0} mass the KK-rescattering leads also to an enhancement of the cross section compared to the calculation without KK-rescattering. The contribution from the central diffractive mechanism of exclusive production of K^+K^- pairs via the $K^*(892)$ meson exchanges is small.

Now we wish to compare differential distributions of pions from the χ_{c0} decay with those for the continuum pions. The amplitude for exclusive central diffractive χ_{c0} meson production was calculated within the k_t-factorization approach including virtualities of active gluons [104] and the corresponding cross section is calculated with the help of unintegrated gluon distribution functions (UGDFs) known from the literature. We apply the following simple procedure. In the first step we calculate the two-dimensional distribution $d\sigma(y, p_\perp)/dydp_\perp$, where y and $p_\perp$ is the rapidity and transverse momentum of χ_{c0} meson, respectively. The decay of $\chi_{c0} \to \pi^+\pi^-$ is included then in a simple Monte Carlo program assuming isotropic decay of the scalar χ_{c0} meson in its rest frame. The kinematical variables of pions are transformed to the overall center-of-mass frame where extra cuts are imposed, see Eq. (A.41) of Appendix A. Including the simple cuts allows us to construct several differential distributions in different kinematical

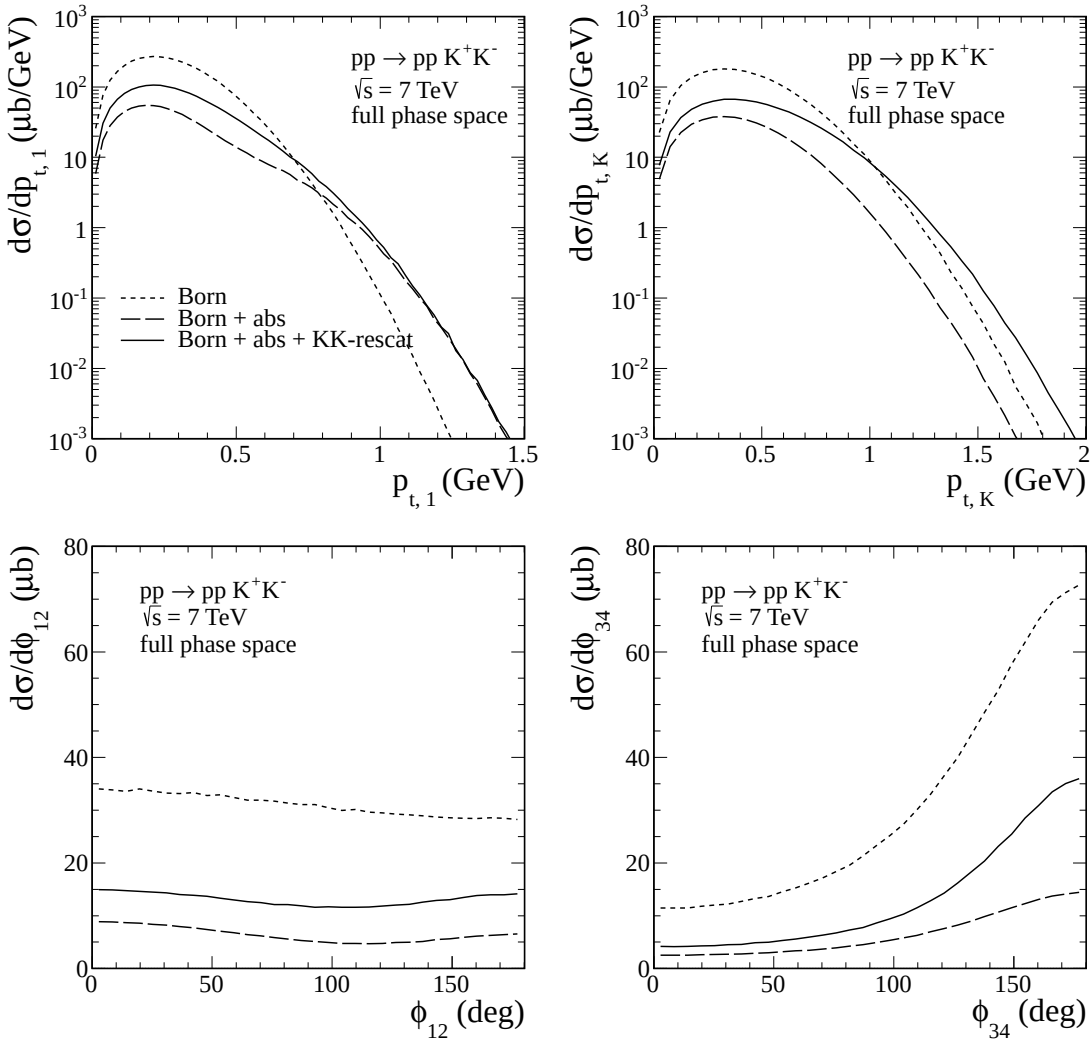

Figure 2.56: Differential cross sections for the $pp \to ppK^+K^-$ reaction at $\sqrt{s} = 7$ TeV without (the upper dotted lines) and with (bottom lines) absorption effects due to pp-interaction (the long-dashed lines) and KK-rescattering (the solid lines). These calculations were done with the cut-off parameter $\Lambda^2_{off} = 2$ GeV^2 and $\Lambda_{int} = 2$ GeV.

variables. In Fig. 2.58 we show distributions in the pion transverse momenta. The pions from the decay are placed at slightly larger transverse momenta. This can be therefore used to get rid of the bulk of the continuum by imposing an extra cut on the pion transverse momenta.

In Fig. 2.59 we show two-pion invariant mass distribution for the central diffractive $\pi\pi$ continuum and the contribution from the decay of the χ_{c0} meson (see the peak at $M_{\pi\pi} \simeq 3.4$ GeV). In these figures the resonant χ_{c0} distribution was parametrised in the Breit-Wigner form:

$$\frac{d\sigma}{dM_{\pi\pi}} = \mathcal{B}(\chi_{c0} \to \pi^+\pi^-)\, \sigma_{pp\to pp\chi_{c0}}\, 2M_{\pi\pi}\, \frac{1}{\pi} \frac{M_{\pi\pi}\Gamma}{(M^2_{\pi\pi} - M^2)^2 + (M_{\pi\pi}\Gamma)^2}\,, \tag{2.72}$$

with parameters according to particle data book [96]. In the calculation of the χ_{c0} distribution we have used GRV94 NLO and GJR08 NLO collinear gluon distributions. The cross sections for the χ_{c0} production and for the background include absorption effects. While upper row shows the cross section integrated over the full phase space at different energies, the lower row shows results including the relevant pion pseudorapidities restrictions $-1 < \eta_{\pi^+}, \eta_{\pi^-} < 1$ (RHIC and Tevatron) and $-2.5 < \eta_{\pi^+}, \eta_{\pi^-} < 2.5$ (LHC).

The question now is whether the situation can be improved by imposing extra cuts. In Fig. 2.60 we show results with additional cuts on both pion transverse momenta $p_{\perp\pi} > 1.5$ GeV.

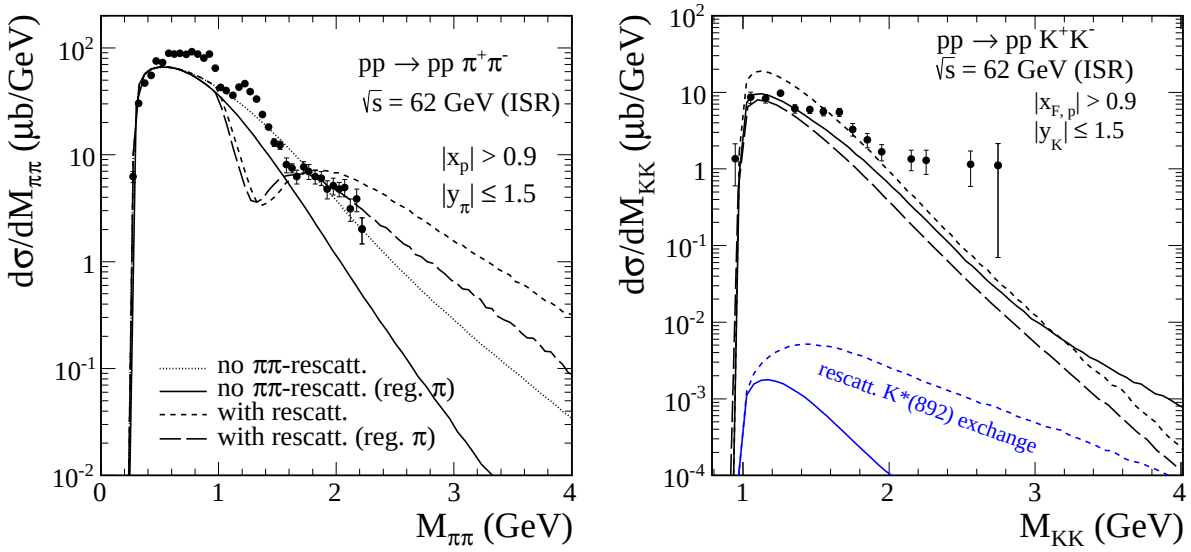

Figure 2.57: Differential cross section $d\sigma/dM_{M\bar{M}}$ for the $pp \to pp\pi^+\pi^-$ (left panel) and the $pp \to ppK^+K^-$ (right panel) reactions at $\sqrt{s} = 62$ GeV with experimental cuts relevant for the CERN ISR experimental data from [174] and [173], respectively. In the calculations we use the cut-off parameter $\Lambda^2_{off,E} = 2$ GeV^2. In the left panel we compare results obtained for the central diffractive mechanism without (the dotted and solid lines) and with (the dashed lines) the $\pi\pi$-rescattering effect, and for usual (mesonic) propagator (the dotted and short-dashed lines) and generalized propagator (the solid and long-dashed lines) given by Eq. (2.32) for $\Lambda_{int} = 2$ GeV. Here the pp-rescattering was included in the calculations. In the right panel we compare results without (the short-dashed line) and with (the solid line) the pp- and KK-rescattering effects. The upper short-dashed line correspond to calculation without these both corrections. The blue short-dashed and solid lines represent central diffractive mechanism via the $K^*(892)$ meson exchange shown in Fig. 2.54 without and with reggeization, respectively.

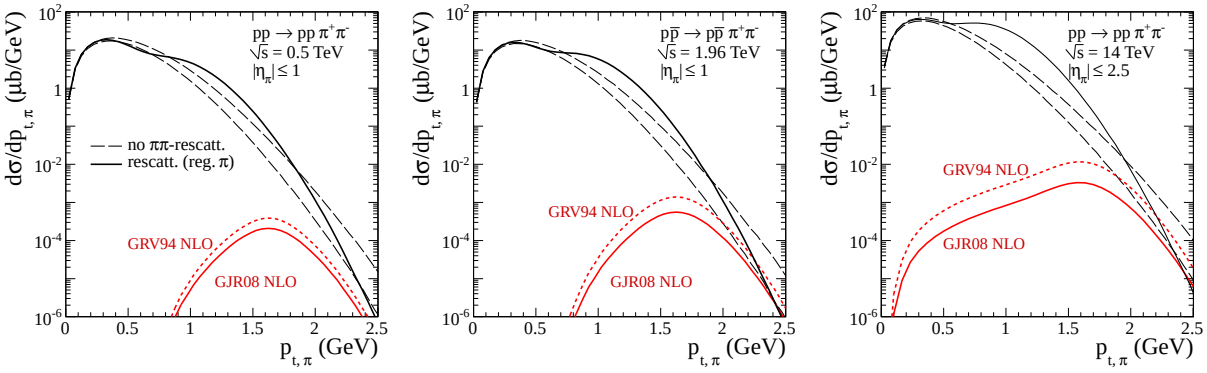

Figure 2.58: Differential cross section $d\sigma/dp_{\perp\pi}$ at $\sqrt{s} = 0.5, 1.96, 14$ TeV with cuts on the pion pseudorapidities. The diffractive background was calculated for the meson propagators and with the cut-off parameters $\Lambda^2_{off} = 1.6, 2$ GeV^2 (lower and upper dashed lines, respectively) and for the generalized pion propagators and the $\pi\pi$-rescattering (solid line). Results for the pions from the decay of the χ_{c0} meson including the $\pi^+\pi^-$ branching ratio, for the GRV94 NLO (upper lines) and GJR08 NLO (bottom lines) gluon distribution used to generate UGDFs, are shown. The proton-proton absorption effects have been included in the calculations.

Now the signal-to-background ratio is somewhat improved especially at the Tevatron and LHC energies. Shown are only purely theoretical predictions. In reality the situation is, however, somewhat worse as both protons and, in particular, pion pairs are measured with a certain precision which leads to an extra smearing in $M_{\pi\pi}$. While the smearing is negligible for the back-

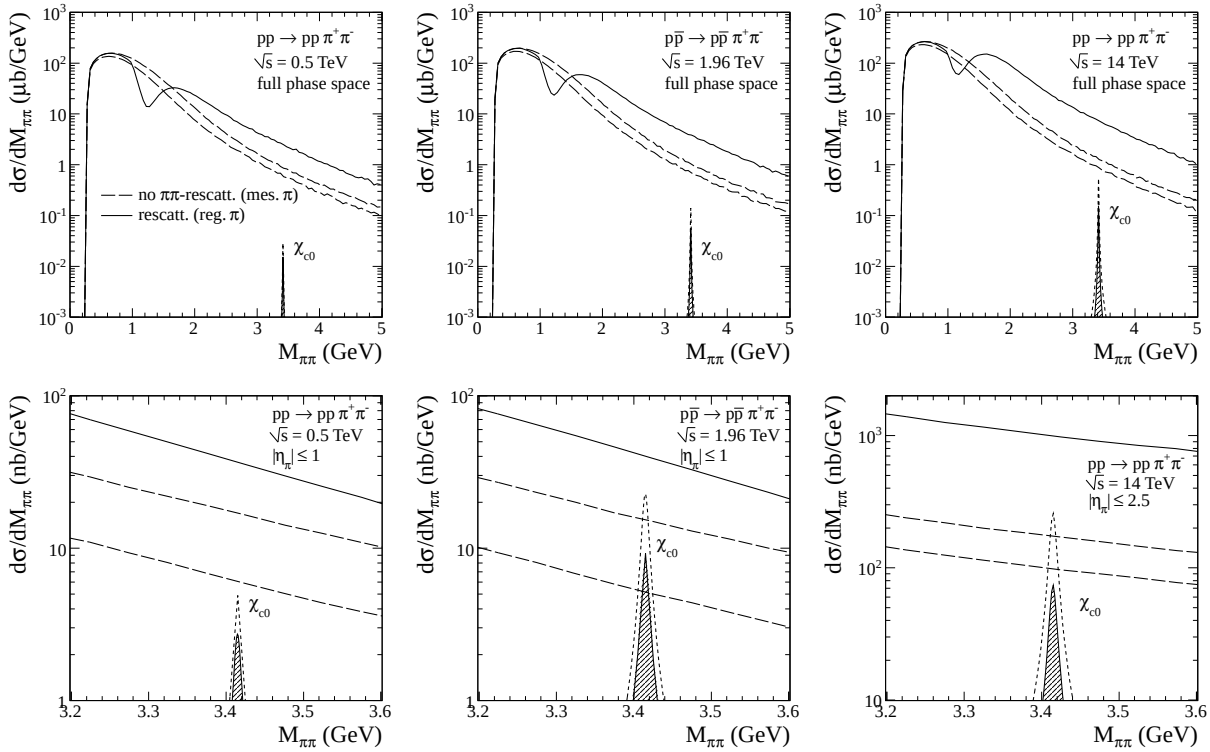

Figure 2.59: The $\pi^+\pi^-$ invariant mass distribution at $\sqrt{s} = 0.5, 1.96, 14$ TeV integrated over the full phase space (upper row) and with the detector limitations in pion pseudorapidities (lower row). The dashed lines represent the $\pi\pi$ continuum with the meson propagators and with the cut-off parameters $\Lambda^2_{off} = 1.6, 2\,\mathrm{GeV}^2$ (lower and upper dashed lines, respectively) and the solid lines are for the generalized pion propagators and for the $\pi\pi$-rescattering. The χ_{c0} contribution is calculated with GRV94 NLO (dotted lines) and GJR08 NLO (filled areas) collinear gluon distributions. The absorption effects for the χ_{c0} meson and for the background have been included in the calculations.

ground, it leads to a modification of the Breit-Wigner peak for the χ_{c0} meson [9]. The results with more modern GJR GDF are smaller by about a factor of 2-3 than those for somewhat older GRV GDF.

The main experimental task is to measure the distributions in the χ_{c0} rapidity and transverse momentum. Can one recover such distributions based on the measured ones in spite of the severe cuts on pion kinematical variables? In Fig. 2.61 we show the two-dimensional ratio of the cross sections for the χ_{c0} meson in its rapidity and transverse momentum:

$$\mathrm{Ratio}(y, p_\perp) = \frac{d\sigma^{pp\to pp\chi_{c0}(\to\pi^+\pi^-)}_{\text{with cuts}}/dydp_\perp}{d\sigma^{pp\to pp\chi_{c0}}/dydp_\perp}\,. \tag{2.73}$$

The numerator includes limitations on η_π and $p_{\perp,\pi}$. These distributions provide a fairly precise evaluation of the expected acceptances when experimental cuts are imposed. The experimental data could be corrected by our two-dimensional acceptance function to recover the distributions of interest.

Now we wish to compare differential distributions of kaon from the χ_{c0} decay with those for the continuum kaons at different energies. In Fig. 2.62 we show two-kaon invariant mass distribution for the central diffractive KK continuum and the contribution from the decay of the χ_{c0} meson and the contribution from the decay of the ϕ meson. The cross section for exclusive production of the ϕ meson has been calculated within a pQCD k_t-factorization approach in

[9] An additional experimental resolution not included here can be taken into account by an extra convolution of the Breit-Wigner shape with an additional Gaussian function.

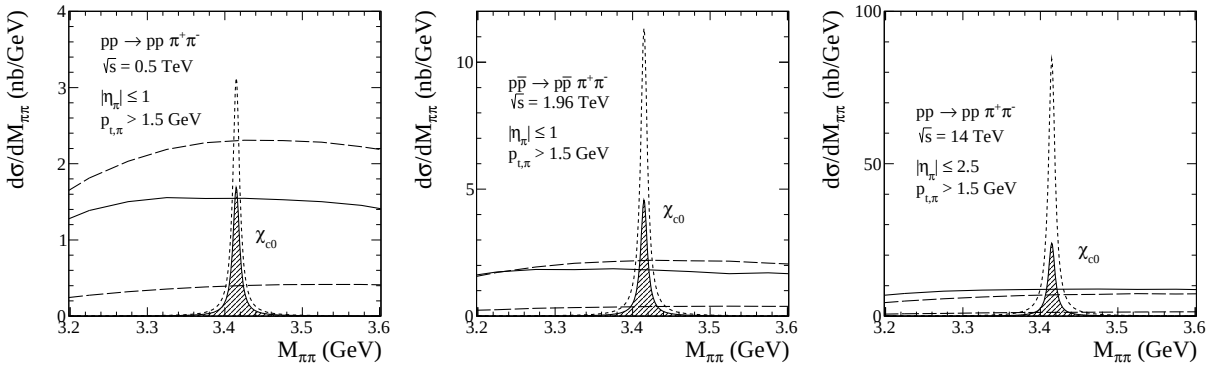

Figure 2.60: The $\pi^+\pi^-$ invariant mass distribution at $\sqrt{s} = 0.5, 1.96, 14$ TeV with the relevant restrictions in the pion pseudorapidities and pion transverse momenta. The dashed lines present the $\pi\pi$ continuum with the meson propagators and with the cut-off parameters $\Lambda^2_{off} = 1.6, 2$ GeV^2 (lower and upper dashed lines, respectively) and for the generalized pion propagators and the $\pi\pi$-rescattering. In calculating the χ_{c0} contribution we use GRV94 NLO (dotted lines) and GJR08 NLO (filled areas) collinear gluon distributions. The absorption effects for the χ_{c0} meson and for the background have been included in the calculations. Clear χ_{c0} signal with relatively small background for the Tevatron and LHC energies can be observed when imposing the extra cuts on $p_{\perp\pi}$.

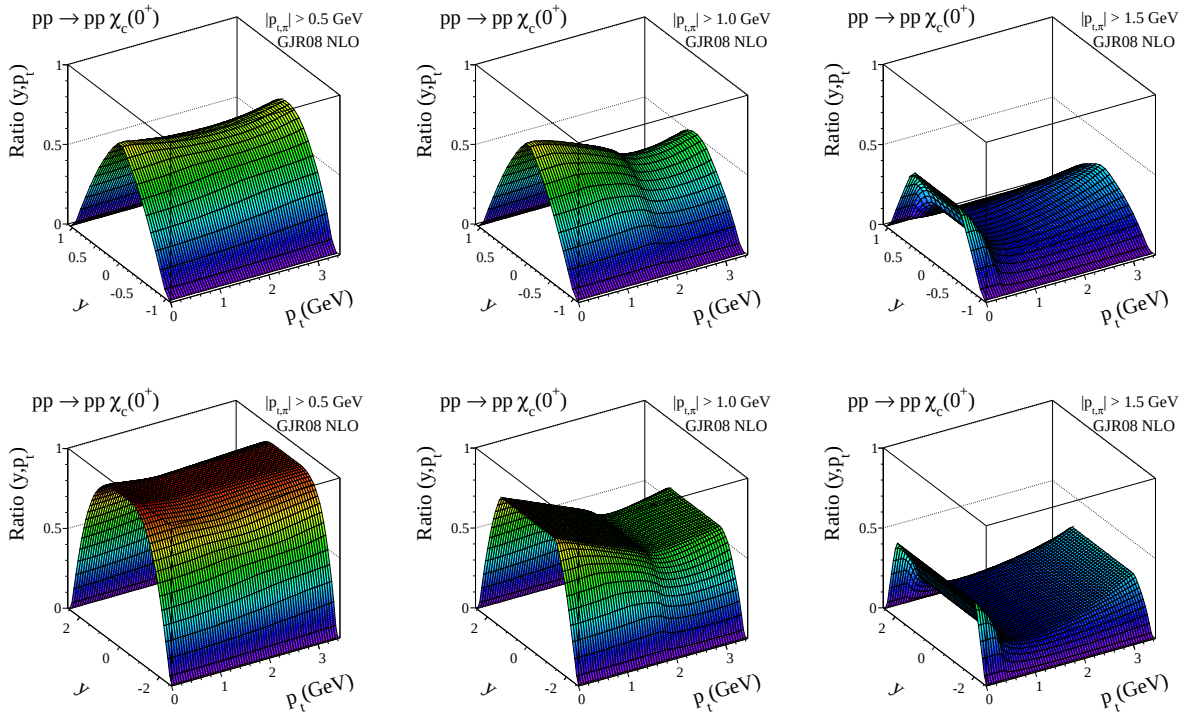

Figure 2.61: Ratio of the two-dimensional cross sections for the χ_{c0} meson in its rapidity and transverse momentum (in $(y, p_\perp)$ space) for the $pp \to pp\chi_{c0}$ reaction with the relevant limitations on the pion pseudorapidities and a few lower cuts on the pion transverse momenta $p_{\perp\pi}$. These calculations were done with GJR08 NLO [191, 192] GDFs. The upper row is for the STAR detector ($|\eta_\pi| < 1$) and the lower row for the ATLAS or CMS detectors ($|\eta_\pi| < 2.5$).

Ref. [196]. In these figures the resonant $\mathcal{R} = \phi, \chi_{c0}$ distributions was parametrised in the Breit-Wigner form; similarly as for $\pi^+\pi^-$ decay (2.72). The cross sections for the ϕ and χ_{c0} production and for the background include absorption effects. One can be observed a clear χ_{c0} signal with relatively small background for the detector limitations in kaon pseudorapidities. In Fig. 2.63 we show distributions in the kaon transverse momenta. An extra cut on the kaon transverse mo-

menta can significantly improve the signal-to-background ratio. It is not the case for the kaons from the ϕ decay which are placed at lower $p_{\perp,K}$.

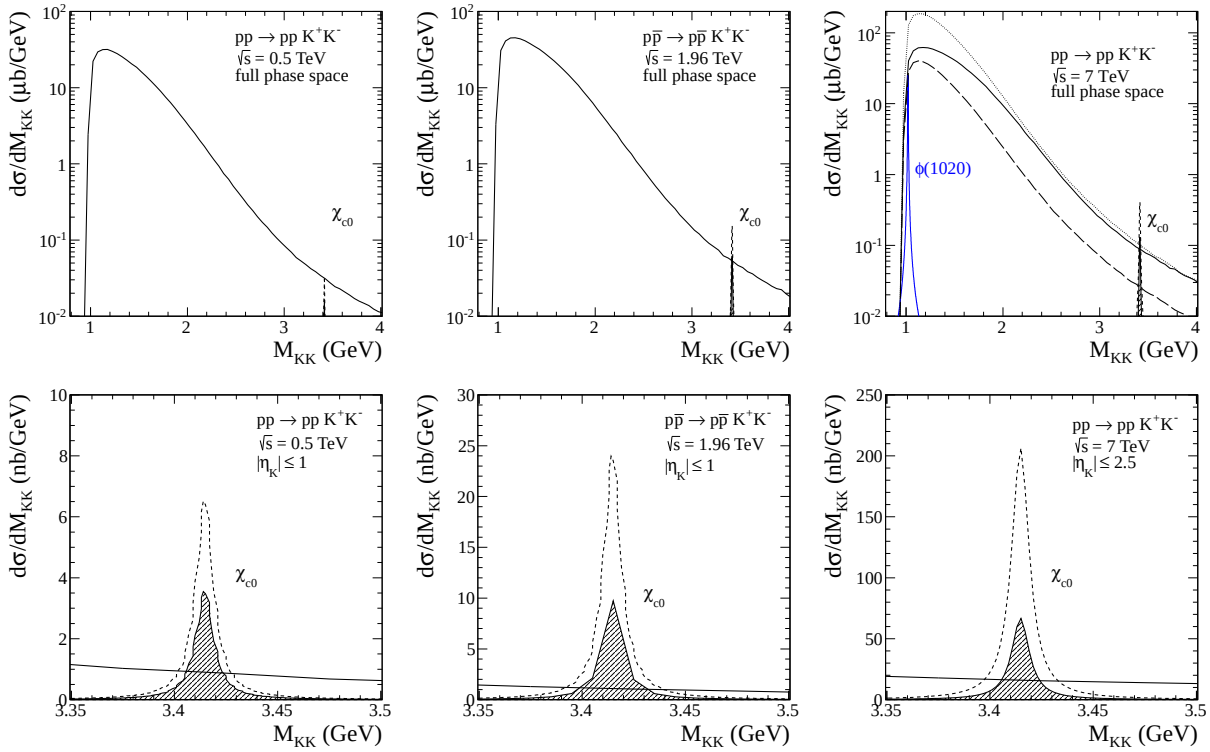

Figure 2.62: The K^+K^- invariant mass distribution at $\sqrt{s} = 0.5, 1.96$ and 7 TeV. While the upper row shows the cross section integrated over the full phase space, the lower row shows results including the relevant kaon pseudorapidity restrictions $-1 < \eta_{K^+}, \eta_{K^-} < 1$ (RHIC and Tevatron) and $-2.5 < \eta_{K^+}, \eta_{K^-} < 2.5$ (LHC). The solid lines present the KK continuum with the cut-off parameter $\Lambda^2_{off,E} = 2$ GeV^2. The χ_{c0} contribution is calculated with the GRV94 NLO (dotted lines) and GJR08 NLO (filled areas) collinear gluon distributions. The cross section for the ϕ meson contribution at $\sqrt{s} = 7$ TeV is calculated as in Ref. [196]. The absorption effects have been included in the calculations.

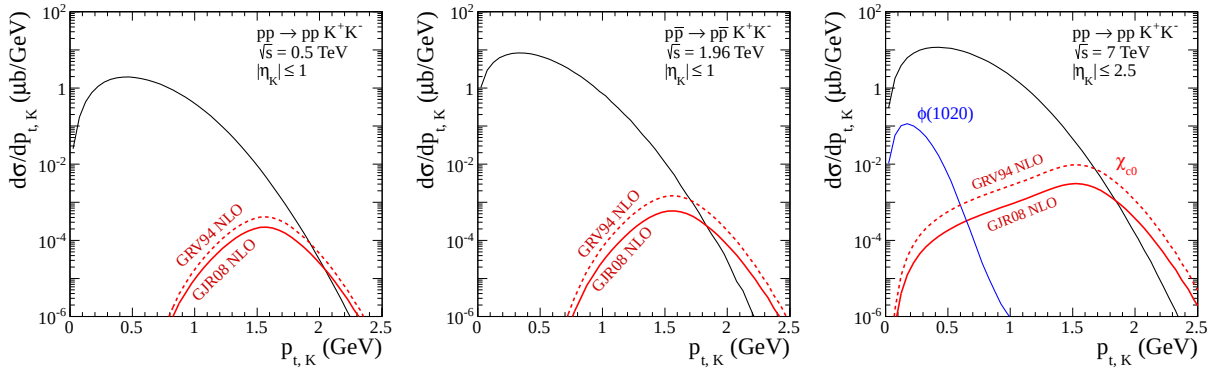

Figure 2.63: Differential cross section $d\sigma/dp_{\perp,K}$ at $\sqrt{s} = 0.5, 1.96, 7$ TeV with cuts on the kaon pseudorapidities. The diffractive background was calculated with the cut-off parameter $\Lambda^2_{off} = 2$ GeV^2. Results for the kaons from the decay of the χ_{c0} meson including the K^+K^- branching ratio, for the GRV94 NLO (upper lines) and GJR08 NLO (bottom lines) GDFs, are shown. In the right panel ϕ meson contribution is shown in addition. The absorption effects have been included in the calculations.

Finally, in Table 2.7 we have collected numerical values of the integrated cross sections (see $\sigma_{pp\to pp\chi_{c0}}$ in Eq. (2.72)) for exclusive χ_{c0} meson production for some selected GDFs at different energies. The new $\pi^+\pi^-$ and K^+K^- data obtained in CDF at the Tevatron in the central

region and presented in [161] can provide an upper limit on χ_{c0} cross sections of $d\sigma/dy|_{y=0}$ = 21.4 ± 4.2 (syst.) nb and 18.9 ± 3.8 (syst.) nb, respectively. The data presented there do not show a significant $\chi_{c0}(3415)$ signal.

Table 2.7: Integrated cross sections in nb (with absorption corrections included) for exclusive χ_{c0} production at different energies with GRV94 NLO [108] and GJR08 NLO [191, 192] collinear gluon distributions. In these calculations we have taken into account the relevant limitations in the pion/kaon pseudorapidities $|\eta_{\pi/K}| < 1$ at RHIC and Tevatron, $|\eta_{\pi/K}| < 2.5$ at LHC and lower cut on both pion/kaon transverse momenta $p_{\perp,\pi/K} > 1.5$ GeV.

$\sqrt{s}$	full phase space		with cuts on $\eta_{\pi/K}$		with cuts on $\eta_{\pi/K}$ and $p_{\perp,\pi/K}$	
(TeV)	GRV	GJR	GRV	GJR	GRV	GJR
0.5	82.9	44.0	17.3/17.9	9.4/9.7	5.7/9.1	3.1/4.9
1.96	406.3	165.1	63.7/65.7	25.9/26.7	20.7/32.8	8.3/13.2
7	1076.7	347.7	540.0/548.6	176.3/177.1	60.4/114.5	20.7/36.6
14	1566.3	449.2	735.0/744.7	210.9/213.7	152.1/244.2	43.1/69.4

2.8 Measurement of $\pi^+\pi^-$ pairs at the LHC with Forward Proton Tagging

The dominant mechanism of the exclusive production of the $\pi^+\pi^-$ pairs at high energies is sketched in Fig. 2.8. The formalism used in calculations is explained in detail in Section 2.3, see also [3, 6, 8]. In this calculation the absorption effects due to proton-proton interaction only has been included. The cross section is obtained by integration over the four-body phase space, which was reduced to 8 dimensions and performed numerically. A weighted Monte Carlo generator based on this model has been developed and was used in the following analysis, see [7] for more details.

2.8.1 Exclusive measurement

The final state of the $pp \to pp\pi^+\pi^-$ consists of four charged particles – two protons and two pions. At the LHC the pions are produced in the rapidity range $|y_\pi| < 10$, whereas the protons are scattered at very small angles (of the order of microradians) into the accelerator beam pipe. Therefore, to perform a fully exclusive measurement, there is a need of two different types of detectors (see Fig. 2.64): a central detector (for pion detection) and very forward detectors (for proton tagging). The analysis presented here assumes ATLAS as the central detector and ALFA as the proton tagging detectors, see [7].

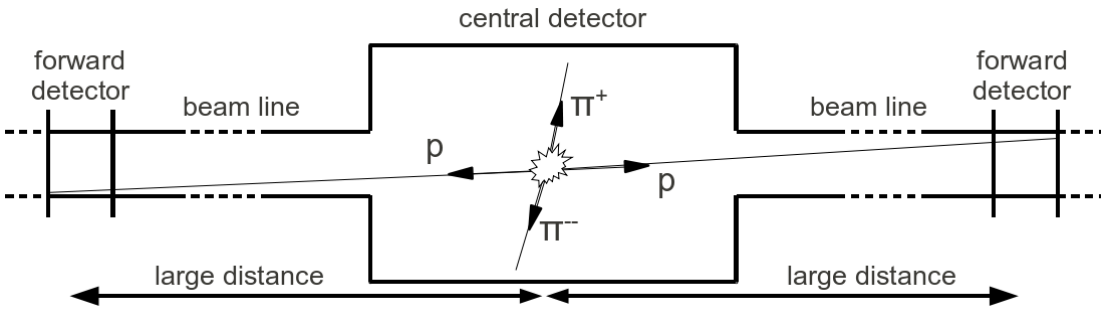

Figure 2.64: A scheme of the measurement concept – pions are registered in the central detectors, whereas protons in the very forward detectors.

The ATLAS detector [197] is located at the LHC Interaction Point 1 (IP1). It has been designed as a general purpose detector with a large acceptance in pseudorapidity, full azimuthal angle coverage, good charged particle momentum resolution and a good electromagnetic calorimetry completed by full-coverage hadronic calorimetry. The ATLAS tracking detector provides measurement of charged particles momenta in the $|\eta_\pi| < 2.5$ region and the calorimeter covers $|\eta_\pi| < 4.9$.

The ALFA (Absolute Luminosity For ATLAS) detectors [198] are designed for proton-proton elastic scattering measurement in the Coulomb-nuclear amplitude interference region. These detectors are placed about 240 m from the IP1, symmetrically on both sides, inside roman pots. These are special devices that allow to place detectors inside the beam pipe and to control the distance between their edge and the proton beam. This is of primordial importance for the detectors safety, since the proton beam can cause serious radiation damage. Measurement of protons scattered at very small angles (like in the elastic scattering) requires a special tune of the LHC accelerator with very small angular dispersion at the IP. This is granted by a high value of the betatron function (β^*). Due to limited radiation hardness, the ALFA detector will be used only during dedicated runs.

It is worth mentioning that at the LHC, apart from ALFA, there are also similar stations of the TOTEM [199] experiment placed around the CMS central detector. Although, the present study was carried out for ALFA and ATLAS, similar results can be expected for TOTEM and CMS. In addition, two other proton tagging detectors are presently at the planning stage – AFP (ATLAS Forward Proton) for ATLAS and HPS (High Precision Spectrometer) for CMS. Their purpose is to tag forward protons during high luminosity LHC runs and to look at high-$p_\perp$ signals. The acceptance of these detectors will be completely different than the one of ALFA and TOTEM. Actually, the AFP and HPS detectors will be able to detect protons which lost some part of their initial energy [200] and will not register protons originating from elastic scattering. Since for the $pp \to p\pi^+\pi^-p$ process the energy loss of the protons is rather small, only the tails of this signal could be seen in AFP or HPS. Taking into account the fact that these detectors will work during normal LHC runs, when there will be many independent interactions in one bunch crossing, it is clear that exclusive pion pair production can be measured only with help of ALFA or TOTEM.

A crucial element of the $pp \to p\pi^+\pi^-p$ measurement is the tagging of the forward protons with the ALFA detectors. Thus, a very important ingredient of this analysis is a proper simulation of the proton transport from the Interaction Point to the ALFA stations through the LHC magnetic lattice. One needs to remember that the ALFA detectors are designed only for the special LHC runs so a corresponding description of the LHC magnets has to be used in the simulation. In this analysis the $\sqrt{s} = 7$ TeV and $\beta^* = 90$ m LHC optics was taken.

2.8.2 Results

The cross section for exclusive $\pi^+\pi^-$ production at $\sqrt{s} = 7$ TeV is 234 μb [7]. The requirement that both protons are tagged in the ALFA stations causes that not all events can be fully registered. This is due to limited acceptance of the detectors. In fact, the visible cross section depends on the distance between the ALFA detector edge and the beam centre (it will be changed during runs, accordingly to beam conditions). This dependence is presented in Fig. 2.65 (left panel). For the rest of the present analysis a distance of 4 mm is assumed, which corresponds to 75 μb of cross section visible in the ALFA detectors. Fig. 2.65 (right panel) presents the distribution of forward proton transverse momentum before and after requesting that protons are tagged in ALFA.

Pions produced in the discussed process will be measured in the central detector. The pion pseudorapidity distribution is presented in Fig. 2.66 (left panel), whereas the right panel of Fig. 2.66 shows a correlation between pseudorapidities of both pions. The model used for the simulation predicts a strong correlation between the pseudorapidities of π^+ and π^-, which is

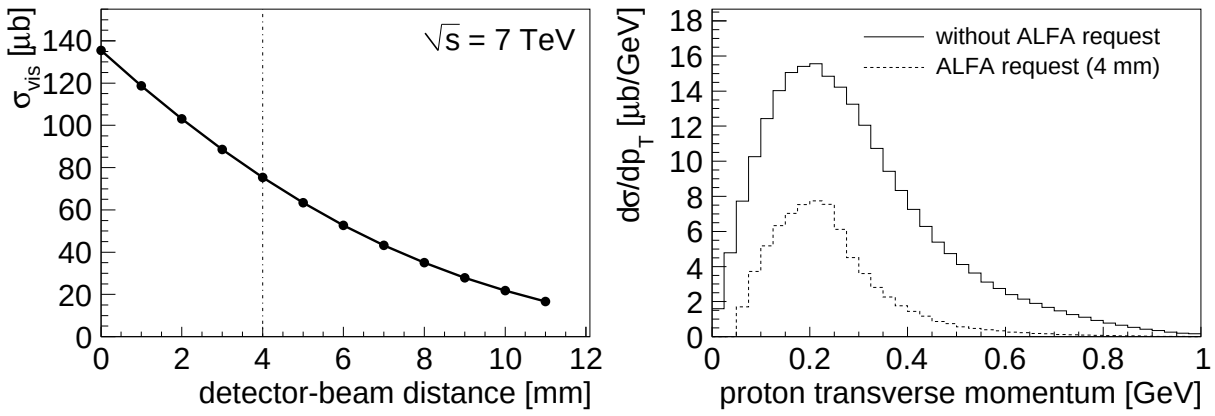

Figure 2.65: Left panel shows the cross section for $pp \to p\pi^+\pi^- p$ with both protons tagged by the ALFA detectors as a function of the distance between the detectors edge and the beam centre (assumed to be identical in all ALFA stations). Right panel shows the proton transverse momentum distribution; the dotted line marks the distribution for the events with both protons tagged by ALFA detectors positioned at 4 mm.

not expected for pions originating from $pp \to p\pi^+\pi^0\pi^- p$ or $pp \to p\pi^+\pi^-\pi^+\pi^- p$ processes[10]. Although the majority of the events contains pions with η_π too large to be detected in ATLAS, the remaining cross section is still large enough to make the measurement possible.

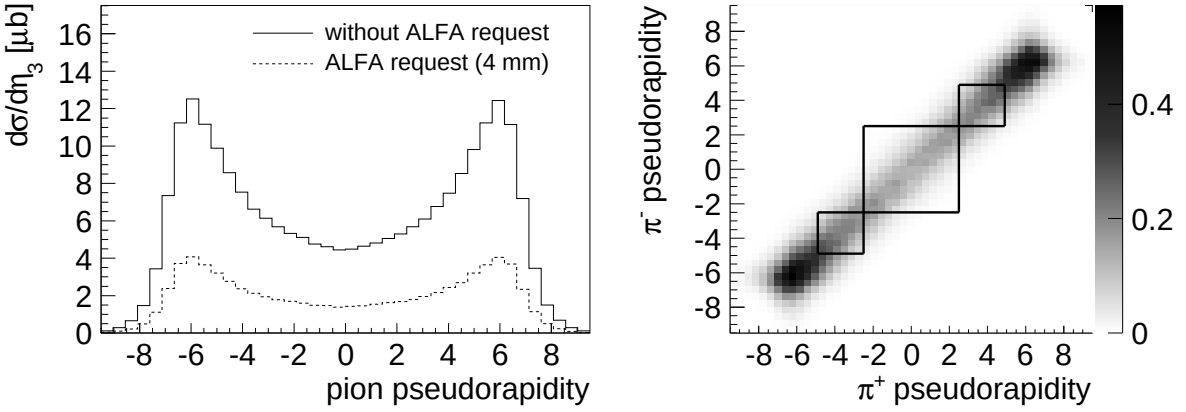

Figure 2.66: Left panel shows the total cross section as a function of pion pseudorapidity. Right panel shows the correlation between the pion pseudorapidies. The black frames represent regions of tracker ($|\eta_\pi| < 2.5$) and forward calorimeters ($|\eta_\pi| < 4.9$).

The pions can be detected in the ATLAS tracking detector ($|\eta_\pi| < 2.5$) or in the ATLAS calorimetry system ($|\eta_\pi| < 4.9$). From the experimental point of view these are two different measurements, as the tracker enables the particle momentum and charge determination, whereas the calorimeter is sensitive only to the particle energy. One should note that the preferable measurement is the one with the tracker, as it provides very high precision and allows to efficiently discriminate against the like-charge background pairs. Since the correlation between the pseudorapidities of both pions is very large, the following analysis is performed independently for the tracking detector ($|\eta_\pi| < 2.5$) and the forward calorimetry ($2.5 < |\eta_\pi| < 4.9$).

The two adequate distributions: pion transverse momentum in the central region ($|\eta_\pi| < 2.5$) and pion energy in the forward region ($2.5 < |\eta_\pi| < 4.9$) are presented in Fig. 2.67 (left panel) and Fig. 2.68 (left panel). Requirement of both protons being tagged in the ALFA detectors in-

[10]Such reactions are a natural background, when only two pions are inside the detector acceptance. This contribution can be estimated experimentally by studying the three and four pion final states.

fluences the shapes of the distributions only very little, but it reduces both by a factor close to three.

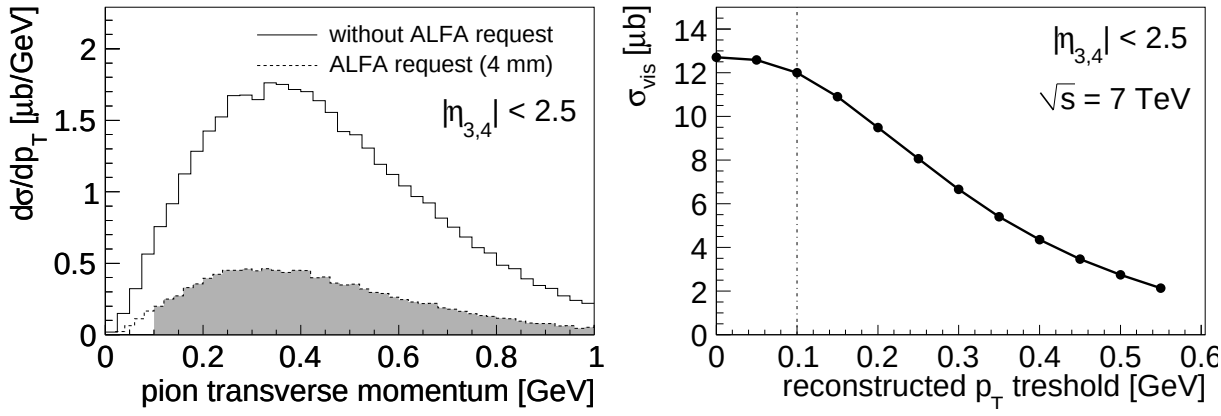

Figure 2.67: Left panel shows the pion transverse momentum distribution in the tracking detector. Right panel shows the cross section for $|\eta_\pi| < 2.5$ as a function of $p_{\perp,\pi}$ threshold. The grey area and the dash-dotted line marks the lower boundary of the region accessible by the main ATLAS detector.

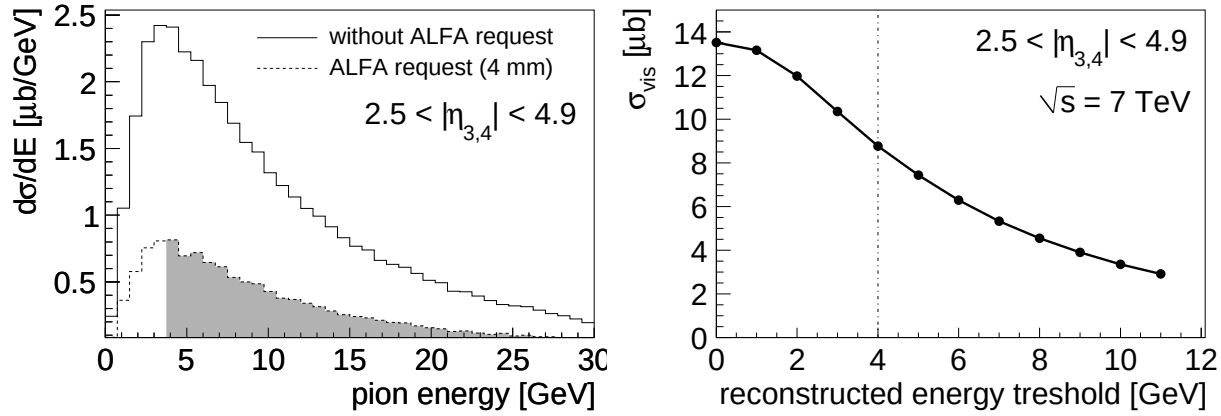

Figure 2.68: Left panel shows the pion energy distribution in the calorimeter. Right panel shows the cross section for $4.9 < |\eta_\pi| < 2.5$ as a function of energy threshold. The grey area and the dash-dotted line marks the lower boundary of the region accessible by the main ATLAS detector.

Obviously, the number of events that can be observed depends on the minimal pion transverse momentum and minimal pion energy that are experimentally accessible. Fig. 2.67 (right panel) and Fig. 2.68 (right panel) show the visible cross section as a function of reconstruction thresholds for measurements in the tracker and the calorimeter. Clearly, the cross section falls very steeply with increasing thresholds values. The vertical dash-dotted lines show the thresholds that should be possible to obtain: measurements of $p_{\perp,\pi} = 0.1$ GeV were performed for ATLAS minimum bias analysis [201] and particles with energy $E_\pi > 4$ GeV were shown to be well above the noise [202]. It should be mentioned that in the minimum bias analysis the efficiency for such low-$p_{\perp,\pi}$ tracks was quite small (about 10%). However, in that analysis, the reconstruction algorithms had to simultaneously deal with many particle tracks. For very clean events that are considered in this work (only two tracks) it should be possible to adjust the reconstruction to obtain a much better efficiency.

An interesting study that can be made when data are collected is the measurement of the $\pi^+\pi^-$ invariant mass distribution. Fig. 2.69 presents the theoretical predictions and a possible measurement with 100 μb^{-1} integrated luminosity (30 hours of data acquisition time assuming the luminosity value of 10^{27} $cm^{-2}s^{-1}$) for pions detected in the ATLAS tracker (systematic uncer-

tainty of such a measurement is not considered, only the statistical errors are presented). If the collected statistics is high enough, it should be possible to see resonances, especially the $f_2(1270)$ meson, on top of the presented distribution.

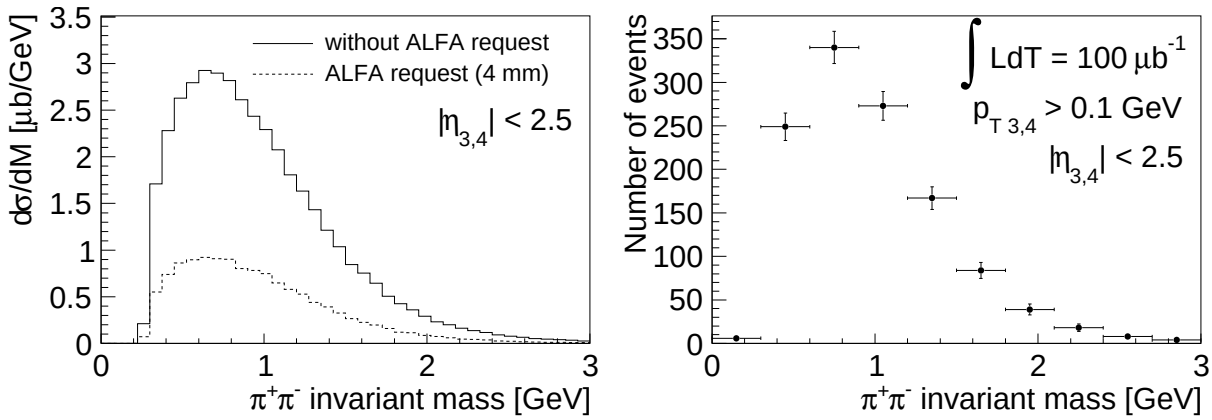

Figure 2.69: Left panel shows the distribution of $\pi^+\pi^-$ invariant mass reconstructed in the tracking detector. Right panel shows a possible measurement of the $\pi^+\pi^-$ invariant mass distribution for 100 μb^{-1} integrated luminosity (only the statistical errors are plotted).

2.9 Conclusions

We have calculated several differential observables for the exclusive $pp \to ppM\bar{M}$ and $p\bar{p} \to p\bar{p}M\bar{M}$ reactions, where in the $M\bar{M}$ central system we have charged pion or kaon pairs. Both central diffractive and pion-pion rescattering processes were considered. In the first case, the full amplitude was calculated in a simple model with parameters adjusted to the low energy data, i.e. the energy dependence of the amplitudes of MN subsystems was parametrised in the Regge form which describes total and elastic cross section for MN scattering. This parametrisation includes both leading pomeron trajectory as well as subleading reggeon exchanges. Even at relatively high energies the inclusion of reggeon exchanges is crucial as amplitudes with different combination of exchanges interfere or/and MN subsystem energies can be relatively small $W_{\pi N} < 10$ GeV. The latter happens when $y_{\pi^+}, y_{\pi^-} \gg 0$ or $y_{\pi^+}, y_{\pi^-} \ll 0$. In this region of the phase space one can expect a competition of single diffractive mechanism. In the present analysis we have excluded baryon resonance contributions. Further work is required to estimate contribution of such a processes.

We have predicted large cross sections of the order of 100 μb for RHIC, Tevatron and LHC which allows to hope that presented by us distributions will be measured. At high energies we find a preference for the same hemisphere (same-sign rapidity) emission of π^+ and π^-. At ISR energies the same size emission is about 50% while at LHC energies the same hemisphere emission constitutes about 90% of all cases. The integrated cross section of the central diffractive component grows slowly with incident energy if absorption effects are ignored. The absorption effects may even reverse the trend. The energy dependence of the "diffractive" central production of two-pions is quite different than the one for elastic scattering, single- or double-diffraction. This is due to the specificity of the reaction, where rather the subsystem energies dictate the energy dependence of the process.

In the second case the pion-pion amplitude was parametrised using a recent phase shift analysis at the low pion-pion energies and a Regge form of the continuum obtained by assumption of Regge factorization. The factorization assumption is made to estimate the process contribution. The two contributions occupy slightly different parts of the phase space, have different energy dependence and in principle can be resolved experimentally. The interference of amplitudes of the both processes is almost negligible.

The general situation at high energies is sketched in Fig.2.70. The central diffractive (CD) contribution lays along the diagonal $y_3 = y_4$ and the classical double pomeron exchange (DPE) is placed in the center $y_3 \approx y_4$. While the diffractive single resonance excitation (DSRE) contribution (the Roper resonance excitation is a good example) from diagrams in Fig. 2.11 is predicted at $y_3, y_4 \sim y_{beam}$ or $y_3, y_4 \sim y_{target}$, i.e. situated at the end points of the CD contribution, the diffractive double resonance excitation (DDRE) contribution is predicted at ($y_3 \sim y_{beam}$ and $y_4 \sim y_{target}$) or ($y_3 \sim y_{target}$ and $y_4 \sim y_{beam}$), i.e. well separated from the central diffractive contribution. The seperation in the (y_3, y_4) space can be used to seperate the two contributions experimentally. We have calculated also contributions of several diagrams where kaons are emitted from the proton lines (Fig. 2.11). These mechanisms contribute at forward and backward regions but the corresponding cross section is rather small at the LHC and also do not disturb the observation of the central diffractive component.

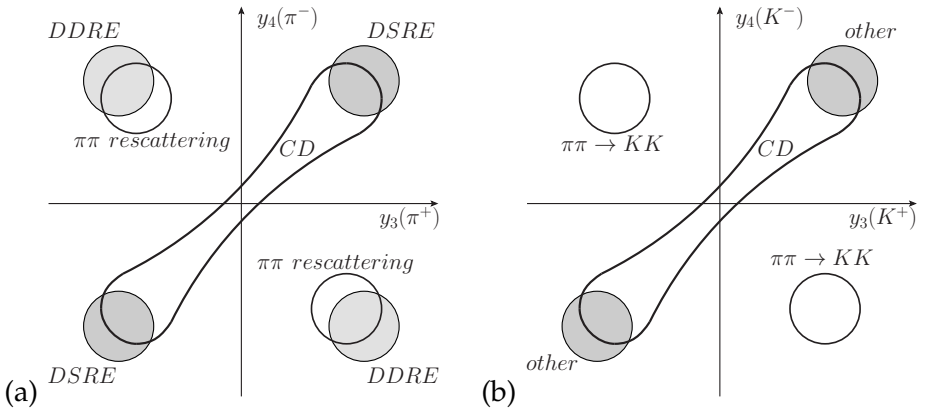

Figure 2.70: A schematic localization of different mechanisms at high energies leading to the $\pi^+\pi^-$ production (panel (a)) and the K^+K^- production (panel (b)).

We have analysed a possibility to measure the exclusive production of χ_{c0} meson in the proton-(anti)proton collisions at the LHC, Tevatron and RHIC via $\chi_{c0} \to \pi^+\pi^-$ and K^+K^- decay channels. It was realized recently that at the Tevatron the measurement of exclusive production of χ_c via decay in the $J/\psi + \gamma$ channel cannot give production cross sections for different species of χ_c. In this decay channel the contributions of χ_c mesons with different spins are similar and experimental resolution is not sufficient to distinguish them. However, at the LHC situation should be better. Since the cross section for exclusive χ_{c0} production in the $\pi\pi$ or KK channel is much larger than that for χ_{c1} and χ_{c2} these two-meson channels should provide an useful information about the χ_{c0} exclusive production. We have performed detailed studies of several differential distributions and demonstrated how to impose extra cuts in order to improve the signal-to-background ratio. We have shown that relevant measurements at Tevatron and LHC are possible. At RHIC the signal-to-background ratio is much worse but measurements should be possible as well. Imposing cuts distorts the original distributions for χ_{c0} in rapidity and transverse momentum. We have demonstrated how to recover the original distributions and presented the correction functions for some typical experimental situations.

Finally, a possibility of measuring the central diffractive process at the LHC was investigated for the ATLAS central detector and the ALFA very forward detectors. We recall that tagged protons, can act as a very sensitive test of the models of soft diffraction (absorption effects). There are three main experimental parameters that limit the visible cross section: the distance between the ALFA detector edge and the proton beam centre, a minimal $p_{\perp,\pi}$ that can be measured in the tracking detector (for pions produced in $|\eta_\pi| < 2.5$) and minimal energy that can be measured in the calorimeter (for $2.5 < |\eta_\pi| < 4.9$ range). For the values of these parameters set to 4 mm, 0.1 GeV and 4 GeV, respectively, the visible cross section is 21 μb. For 100 μb^{-1} of integrated luminosity that can be collected during the ALFA runs this gives over 2000 events within the detector acceptance.

Chapter 3

Central Exclusive Diffractive Production of Scalar and Pseudoscalar Mesons

Double pomeron exchange mechanism is known to be responsible also for high-energy central production of mesons with $I^G = 0^+$. While it is clear that the effective pomeron must be a colour singlet, the spin structure of the pomeron and its coupling to hadrons is, however, not finally established. It is commonly assumed that the pomeron has effectively a vectorial nature; see for instance [93–95, 114, 131] for the history and many references. This model of the pomeron is being questioned in [13, 203]. Here we wish to concentrate on central exclusive meson production in the nonperturbative region using the notion of effective pomeron. In general, such an object may have a nontrivial spin structure. In the present analysis we explore the hypothesis of "tensorial pomeron" in the central meson production. The theoretical arguments for considering an effective tensorial ansatz for the nonperturbative pomeron are discussed in detail in [13]. Hadronic correlation observables could be particularly sensitive to the spin aspects of the pomeron.

Indeed, tests for the helicity structure of the pomeron have been devised in [204] for diffractive contributions to electron-proton scattering, that is, for virtual-photon–proton reactions. For central meson production in proton-proton collisions such tests were discussed in [93–95] and in the following we shall compare our results with those of Ref. [93–95] whenever suitable.

There are some attempts to obtain the pomeron-pomeron-meson vertex in special models of the pomeron. In [93–95] results were obtained from the assumption that the pomeron acts as a $J^{PC} = 1^{++}$ conserved and non-conserved current. The general structure of helicity amplitudes of the simple Regge behaviour was also considered in Ref. [102, 205]. On the other hand, the detailed structure of the amplitudes depends on dynamics and cannot be predicted from the general principles of Regge theory. The mechanism for central production of scalar glueball based on the "instanton" structure of QCD vacuum was considered in [206–209].

Recent activity in the field concentrated rather on perturbative aspects of the pomeron. For instance, the production of heavy objects (χ_c mesons [6, 210], Higgs bosons [211], dijets [211], W^+W^- pairs [11], etc.) has been considered in the language of unintegrated gluon distributions. Exclusive $\pi^+\pi^-$ [3, 6, 175, 179] and K^+K^- [8] pairs production mediated by pomeron-pomeron fusion has been a subject of both theoretical and experimental studies. Particularly interesting is the transition between the nonperturbative (small meson transverse momenta) and perturbative (large meson transverse momenta) regimes.

In this Chapter we shall consider some examples of central meson production and compare results of our calculations for the "tensorial pomeron" with those for the "vectorial pomeron" as well as with experimental data whenever possible. The aim of the present study is to explore the potential of exclusive processes in order to better pin down the nature of the pomeron exchange. Therefore, we shall limit ourselves to Born level calculations leaving other, more complicated, effects for further studies. Nevertheless, we hope that our studies will be

useful for planned or just being carried out experiments [1]. In Section 3.1 we discuss the formalism. We present amplitudes for the exclusive production of scalar and pseudoscalar mesons and we also briefly report some experimental activity in this field. In Section 3.3 we compare results of our calculations with existing data, mostly those from the WA102 experiment [90, 91, 115, 212–214]. In Appendices B and C we discuss properties and useful relations for the tensorial and vectorial pomeron, respectively. In Appendices A and D we have collected some useful formulae concerning details of the calculations.

3.1 Formalism - Tensorial versus Vectorial Pomeron

3.1.1 Basic elements

We shall study exclusive central meson production in proton-proton collisions at high energies

$$p(p_a, \lambda_a) + p(p_b, \lambda_b) \to p(p_1, \lambda_1) + M(k) + p(p_2, \lambda_2)\,. \tag{3.1}$$

Here $p_{a,b}$, $p_{1,2}$ and $\lambda_{a,b}$, $\lambda_{1,2}$ denote, respectively, the four-momenta and helicities of the protons and $M(k)$ denotes a meson with $I^G = 0^+$ and four-momentum k. Our kinematic variables are defined as follows

$$\begin{aligned} &q_1 = p_a - p_1, \quad q_2 = p_b - p_2, \quad k = q_1 + q_2, \\ &s = (p_a + p_b)^2 = (p_1 + p_2 + k)^2, \quad s_{13} = (p_1 + k)^2, \quad s_{23} = (p_2 + k)^2, \\ &t_1 = q_1^2, \quad t_2 = q_2^2, \quad m_M^2 = k^2\,. \end{aligned} \tag{3.2}$$

For the totally antisymmetric symbol $\varepsilon_{\mu\nu\rho\sigma}$ we use the convention $\varepsilon_{0123} = 1$. Further kinematic relations, in particular those valid in the high-energy small-angle limit, are discussed in Appendix A.1.

At high c.m. energies $\sqrt{s}$ the dominant contribution to (3.1) comes from pomeron-pomeron ($\mathbb{P}\mathbb{P}$) fusion; see Fig.3.1. Non-leading terms arise from reggeon-pomeron ($\mathbb{R}\mathbb{P}$) and reggeon-reggeon ($\mathbb{R}\mathbb{R}$) exchanges. We shall be mainly interested in the $\mathbb{P}\mathbb{P}$-fusion giving the

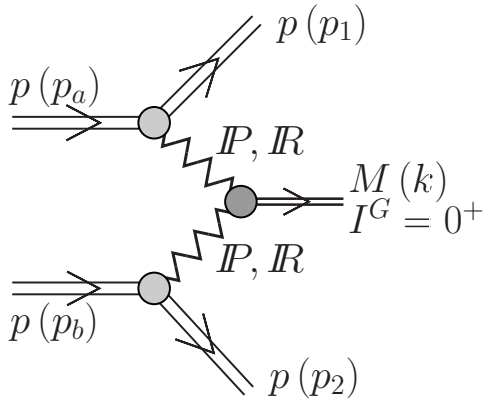

Figure 3.1: The exchange mechanisms for central exclusive meson production in proton-proton collisions.

meson M. It is clear from Fig.3.1 that in order to calculate this contribution we must know the $\mathbb{P}pp$ vertex, the effective $\mathbb{P}$ propagator and the $\mathbb{P}\mathbb{P}M$ vertex. This propagator and these vertices will now be discussed, both, for the tensorial and vectorial ansatz for the pomeron $\mathbb{P}$.

[1] Predictions for experiments at RHIC, Tevatron, and LHC are rather straightforward and will be presented elsewhere.

3.1.2 Scalar and pseudoscalar meson production

In this section we study central production of scalar and pseudoscalar mesons, that is, the reaction (3.1) with $J^{PC} = 0^{++}$ and 0^{-+} mesons M. We shall consider pomeron-pomeron fusion, see Fig.3.1, for both, the tensorial- and the vectorial-pomeron approaches. In Table B.2 of Appendix B we list mesons M in which we are interested. There we also give the values of the lowest orbital angular momentum l and of the corresponding total spin S which can lead to the production of M in the fictitious fusion of two tensorial and vectorial "pomeron particles". The lower the values of l is, the lower is the angular momentum barrier in the reaction.

We discuss first the tensor-pomeron case. For scalar mesons, $J^{PC} = 0^{++}$, the effective Lagrangians and the vertices for $\mathbb{P}\mathbb{P} \to M$ are discussed in Appendix B. For the tensorial pomeron the vertex corresponding to the lowest values of (l, S), that is $(l, S) = (0, 0)$ plus $(2, 2)$, is given in (B.20). For pseudoscalar mesons, $J^{PC} = 0^{-+}$, the tensorial pomeron-pomeron-meson $(\mathbb{P}\mathbb{P}\tilde{M})$ coupling corresponding to $(l, S) = (1, 1)$, see Table B.1 of Appendix B, has the form

$$\mathcal{L}'_{\mathbb{P}\mathbb{P}\tilde{M}}(x) = -\frac{2}{M_0}\, g'_{\mathbb{P}\mathbb{P}\tilde{M}}\, \left[\partial_\rho \mathbb{P}_{\mu\nu}(x)\right]\, \left[\partial_\sigma \mathbb{P}_{\kappa\lambda}(x)\right]\, g^{\mu\kappa}\, \varepsilon^{\nu\lambda\rho\sigma}\, \tilde{\chi}(x)\,. \tag{3.3}$$

Here $\tilde{\chi}(x)$ and $\mathbb{P}_{\mu\nu}(x)$ are the pseudoscalar meson and effective tensor-pomeron field operators, respectively; $M_0 \equiv 1$ GeV, and $g'_{\mathbb{P}\mathbb{P}\tilde{M}}$ is a dimensionless coupling constant. The $\mathbb{P}\mathbb{P}\tilde{M}$ vertex

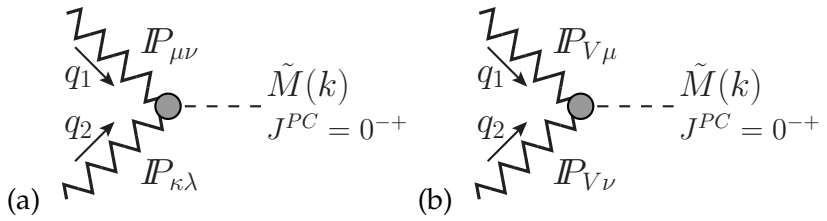

Figure 3.2: A sketch of the pomeron-pomeron-pseudoscalar meson vertex for the tensorial (a) and vectorial (b) pomeron fusion.

corresponding to $(l, S) = (1, 1)$ obtained from (3.3), see Fig.3.2 (a), including a form factor, reads as follows:

$$\begin{aligned} i\Gamma'^{(\mathbb{P}\mathbb{P}\to\tilde{M})}_{\mu\nu,\kappa\lambda}(q_1, q_2) &= i\,\frac{g'_{\mathbb{P}\mathbb{P}\tilde{M}}}{2M_0}\, \left(g_{\mu\kappa}\varepsilon_{\nu\lambda\rho\sigma} + g_{\nu\kappa}\varepsilon_{\mu\lambda\rho\sigma} + g_{\mu\lambda}\varepsilon_{\nu\kappa\rho\sigma} + g_{\nu\lambda}\varepsilon_{\mu\kappa\rho\sigma}\right)(q_1 - q_2)^\rho k^\sigma \\ &\quad \times F_{\mathbb{P}\mathbb{P}\tilde{M}}(q_1^2, q_2^2)\,, \end{aligned} \tag{3.4}$$

where the meson four-momentum $k = q_1 + q_2$. Another form for the $\mathbb{P}\mathbb{P}\tilde{M}$ coupling corresponding to $(l, S) = (3, 3)$ is

$$\begin{aligned} \mathcal{L}''_{\mathbb{P}\mathbb{P}\tilde{M}}(x) &= -\frac{g''_{\mathbb{P}\mathbb{P}\tilde{M}}}{M_0^3}\, \varepsilon^{\mu_1\mu_2\nu_1\nu_2}\, (\partial_{\mu_1}\tilde{\chi}(x)) \\ &\quad \times \left[\left(\partial_{\mu_3}\mathbb{P}_{\mu_4\nu_1}(x) - \partial_{\mu_4}\mathbb{P}_{\mu_3\nu_1}(x)\right)\, \overset{\leftrightarrow}{\partial}_{\mu_2}\, \left(\partial^{\mu_3}\mathbb{P}^{\mu_4}_{\nu_2}(x) - \partial^{\mu_4}\mathbb{P}^{\mu_3}_{\nu_2}(x)\right)\right], \end{aligned} \tag{3.5}$$

where the asymmetric derivative has the form $\overset{\leftrightarrow}{\partial}_\mu = \overset{\rightarrow}{\partial}_\mu - \overset{\leftarrow}{\partial}_\mu$. From (3.5) we get the vertex, including a form factor, as follows

$$\begin{aligned} i\Gamma''^{(\mathbb{P}\mathbb{P}\to\tilde{M})}_{\mu\nu,\kappa\lambda}(q_1, q_2) &= i\,\frac{g''_{\mathbb{P}\mathbb{P}\tilde{M}}}{M_0^3}\, \{\varepsilon_{\nu\lambda\rho\sigma}\left[q_{1\kappa}q_{2\mu} - (q_1q_2)g_{\mu\kappa}\right] + \varepsilon_{\mu\lambda\rho\sigma}\left[q_{1\kappa}q_{2\nu} - (q_1q_2)g_{\nu\kappa}\right] \\ &\quad + \varepsilon_{\nu\kappa\rho\sigma}\left[q_{1\lambda}q_{2\mu} - (q_1q_2)g_{\mu\lambda}\right] + \varepsilon_{\mu\kappa\rho\sigma}\left[q_{1\lambda}q_{2\nu} - (q_1q_2)g_{\nu\lambda}\right]\}(q_1 - q_2)^\rho k^\sigma \\ &\quad \times F_{\mathbb{P}\mathbb{P}\tilde{M}}(q_1^2, q_2^2) \end{aligned} \tag{3.6}$$

with $g''_{\boldsymbol{PP}\tilde{M}}$ a dimensionless coupling constant. As complete vertex we take the sum of (3.4) and (3.6)

$$i\Gamma^{(\boldsymbol{PP}\to\tilde{M})}_{\mu\nu,\kappa\lambda}(q_1,q_2) = i\Gamma'^{(\boldsymbol{PP}\to\tilde{M})}_{\mu\nu,\kappa\lambda}(q_1,q_2) + i\Gamma''^{(\boldsymbol{PP}\to\tilde{M})}_{\mu\nu,\kappa\lambda}(q_1,q_2)\,. \tag{3.7}$$

It can be checked that this vertex satisfies the identities

$$\begin{aligned}
&\Gamma^{(\boldsymbol{PP}\to\tilde{M})}_{\mu\nu,\kappa\lambda}(q_1,q_2) = \Gamma^{(\boldsymbol{PP}\to\tilde{M})}_{\kappa\lambda,\mu\nu}(q_2,q_1)\,,\\
&g^{\mu\nu}\Gamma^{(\boldsymbol{PP}\to\tilde{M})}_{\mu\nu,\kappa\lambda}(q_1,q_2) = 0\,, \quad g^{\kappa\lambda}\Gamma^{(\boldsymbol{PP}\to\tilde{M})}_{\mu\nu,\kappa\lambda}(q_1,q_2) = 0\,.
\end{aligned} \tag{3.8}$$

Now we can write down the $\mathbb{P}\boldsymbol{P}\boldsymbol{P}$-fusion contributions to the Born amplitudes for the scalar and pseudoscalar meson exclusive production. We find for a 0^{++} meson M

$$\begin{aligned}
&\langle p(p_1,\lambda_1), p(p_2,\lambda_2), M(k) \,|\, \mathcal{T} \,|\, p(p_a,\lambda_a), p(p_b,\lambda_b)\rangle \;|_{\boldsymbol{PP}} \equiv\\
&\mathcal{M}^{2\to3}_{\lambda_a\lambda_b\to\lambda_1\lambda_2 M}\;|_{\boldsymbol{PP}} = (-i)\bar{u}(p_1,\lambda_1) i\Gamma^{(\boldsymbol{P}pp)}_{\mu_1\nu_1}(p_1,p_a) u(p_a,\lambda_a)\\
&\qquad\qquad \times i\Delta^{(\boldsymbol{P})\,\mu_1\nu_1,\kappa_1\lambda_1}(s_{13},t_1)\;\; i\Gamma^{(\boldsymbol{PP}\to M)}_{\kappa_1\lambda_1,\kappa_2\lambda_2}(q_1,q_2)\;\; i\Delta^{(\boldsymbol{P})\,\kappa_2\lambda_2,\mu_2\nu_2}(s_{23},t_2)\\
&\qquad\qquad \times \bar{u}(p_2,\lambda_2) i\Gamma^{(\boldsymbol{P}pp)}_{\mu_2\nu_2}(p_2,p_b) u(p_b,\lambda_b)\,.
\end{aligned} \tag{3.9}$$

Here $\Delta^{(\boldsymbol{P})}$ and $\Gamma^{(\boldsymbol{P}pp)}$ denote the effective propagator and proton vertex function, respectively, for the tensorial pomeron. For the explicit expressions, see Appendix B, (B.1) to (B.4) and for the $\mathbb{P}\boldsymbol{P}\boldsymbol{P}M$ vertex (B.20). For a pseudoscalar meson $\tilde{M}$ the amplitude is similar with $\Gamma^{(\boldsymbol{PP}\to M)}_{\kappa_1\lambda_1,\kappa_2\lambda_2}$ replaced by $\Gamma^{(\boldsymbol{PP}\to\tilde{M})}_{\kappa_1\lambda_1,\kappa_2\lambda_2}$ in (3.9).

Explicitly we obtain from (3.9), using the expressions from Appendix B, the amplitude for exclusive production of a scalar meson M as

$$\begin{aligned}
&\mathcal{M}^{2\to3}_{\lambda_a\lambda_b\to\lambda_1\lambda_2 M}\;|_{\boldsymbol{PP}} = -\,(3\beta_{\boldsymbol{P}NN})^2\; F_1(t_1)\, F_1(t_2)\, F_{\boldsymbol{PP}M}(t_1,t_2)\\
&\times\bar{u}(p_1,\lambda_1)\gamma^{\mu_1}(p_1+p_a)^{\nu_1} u(p_a,\lambda_a)\;\frac{1}{2s_{13}}\left(-is_{13}\alpha'_{\boldsymbol{P}}\right)^{\alpha_{\mathbb{P}}(t_1)-1}\\
&\times\;\Big[g'_{\boldsymbol{PP}M} M_0\Big(g_{\mu_1\mu_2}g_{\nu_1\nu_2} + g_{\mu_1\nu_2}g_{\nu_1\mu_2} - \frac{1}{2}g_{\mu_1\nu_1}g_{\mu_2\nu_2}\Big) + \frac{g''_{\boldsymbol{PP}M}}{2M_0}\\
&\times\Big(q_{1\mu_2}q_{2\mu_1}g_{\nu_1\nu_2} + q_{1\mu_2}q_{2\nu_1}g_{\mu_1\nu_2} + q_{1\nu_2}q_{2\mu_1}g_{\nu_1\mu_2} + q_{1\nu_2}q_{2\nu_1}g_{\mu_1\mu_2} - 2(q_1q_2)(g_{\mu_1\mu_2}g_{\nu_1\nu_2} + g_{\nu_1\mu_2}g_{\mu_1\nu_2})\Big)\Big]\\
&\times\frac{1}{2s_{23}}\left(-is_{23}\alpha'_{\boldsymbol{P}}\right)^{\alpha_{\mathbb{P}}(t_2)-1}\;\bar{u}(p_2,\lambda_2)\gamma^{\mu_2}(p_2+p_b)^{\nu_2} u(p_b,\lambda_b)\,.
\end{aligned} \tag{3.10}$$

The coupling constants $\beta_{\boldsymbol{P}NN}$, $g'_{\boldsymbol{PP}M}$, and $g''_{\boldsymbol{PP}M}$ are defined in (B.1), (B.16), and (B.18), and the form factors F_1 and $F_{\boldsymbol{PP}M}$ in (B.2) and (B.21), respectively. Similarly, we obtain the amplitude for production of a pseudoscalar meson $\tilde{M}$ as

$$\begin{aligned}
&\mathcal{M}^{2\to3}_{\lambda_a\lambda_b\to\lambda_1\lambda_2\tilde{M}}\;|_{\boldsymbol{PP}} = -(3\beta_{\boldsymbol{P}NN})^2\, F_1(t_1)\, F_1(t_2)\, F_{\boldsymbol{PP}\tilde{M}}(t_1,t_2)\\
&\times\bar{u}(p_1,\lambda_1)\gamma^{\mu_1}(p_1+p_a)^{\nu_1} u(p_a,\lambda_a)\;\frac{1}{2s_{13}}\left(-is_{13}\alpha'_{\boldsymbol{P}}\right)^{\alpha_{\mathbb{P}}(t_1)-1}\\
&\times\;\Big[\Big(\frac{g_{\boldsymbol{PP}\tilde{M}}}{2M_0} - \frac{g''_{\boldsymbol{PP}\tilde{M}}}{M_0^3}(q_1q_2)\Big)\Big(g_{\mu_1\mu_2}\varepsilon_{\nu_1\nu_2\rho\sigma} + g_{\nu_1\mu_2}\varepsilon_{\mu_1\nu_2\rho\sigma} + g_{\mu_1\nu_2}\varepsilon_{\nu_1\mu_2\rho\sigma} + g_{\nu_1\nu_2}\varepsilon_{\mu_1\mu_2\rho\sigma}\Big)\\
&+\frac{g''_{\boldsymbol{PP}\tilde{M}}}{M_0^3}\Big(\varepsilon_{\nu_1\nu_2\rho\sigma}q_{1\mu_2}q_{2\mu_1} + \varepsilon_{\mu_1\nu_2\rho\sigma}q_{1\mu_2}q_{2\nu_1} + \varepsilon_{\nu_1\mu_2\rho\sigma}q_{1\nu_2}q_{2\mu_1} + \varepsilon_{\mu_1\mu_2\rho\sigma}q_{1\nu_2}q_{2\nu_1}\Big)\Big](q_1-q_2)^\rho k^\sigma\\
&\times\frac{1}{2s_{23}}\left(-is_{23}\alpha'_{\boldsymbol{P}}\right)^{\alpha_{\mathbb{P}}(t_2)-1}\;\bar{u}(p_2,\lambda_2)\gamma^{\mu_2}(p_2+p_b)^{\nu_2} u(p_b,\lambda_b)\,;
\end{aligned} \tag{3.11}$$

see (3.4), (3.6), (B.1), (B.2), and (B.21).

The same steps can now be repeated in the model of the vector pomeron. The Born amplitude for the production of a 0^{++} meson M via $I\!P_V I\!P_V$-fusion can be written as

$$\begin{aligned}\mathcal{M}^{2\to3}_{\lambda_a\lambda_b\to\lambda_1\lambda_2 M}\,|_{I\!P_V I\!P_V} &= (-i)\bar{u}(p_1,\lambda_1) i\Gamma^{(I\!P_V pp)}_{\mu_1}(p_1,p_a) u(p_a,\lambda_a) \\ &\times i\Delta^{(I\!P_V)\,\mu_1\nu_1}(s_{13},t_1)\;\; i\Gamma^{(I\!P_V I\!P_V\to M)}_{\nu_1\nu_2}(q_1,q_2)\;\; i\Delta^{(I\!P_V)\,\nu_2\mu_2}(s_{23},t_2) \\ &\times \bar{u}(p_2,\lambda_2) i\Gamma^{(I\!P_V pp)}_{\mu_2}(p_2,p_b) u(p_b,\lambda_b)\,. \end{aligned} \tag{3.12}$$

The effective Lagrangian and the vertices for $I\!P_V I\!P_V \to M$ are discussed in Appendix C; see (C.1), (C.2), and (C.9). Explicitly we obtain

$$\begin{aligned}\mathcal{M}^{2\to3}_{\lambda_a\lambda_b\to\lambda_1\lambda_2 M}\,|_{I\!P_V I\!P_V} &= -(3\beta_{I\!PNN})^2\, F_1(t_1)\, F_1(t_2)\, F_{I\!P I\!P M}(t_1,t_2) \\ &\times \bar{u}(p_1,\lambda_1)\gamma^{\mu_1} u(p_a,\lambda_a)\, g_{\mu_1\nu_1}\, \left(-is_{13}\alpha'_{I\!P}\right)^{\alpha_{I\!P}(t_1)-1} \\ &\times \Big[\frac{2}{M_0}\, g'_{I\!P_V I\!P_V M}\, g^{\nu_1\nu_2} + \frac{2}{M_0^3}\, g''_{I\!P_V I\!P_V M}\left(q_2^{\nu_1} q_1^{\nu_2} - (q_1q_2) g^{\nu_1\nu_2}\right)\Big] \\ &\times g_{\nu_2\mu_2}\, \left(-is_{23}\alpha'_{I\!P}\right)^{\alpha_{I\!P}(t_2)-1}\, \bar{u}(p_2,\lambda_2)\gamma^{\mu_2} u(p_b,\lambda_b)\,. \end{aligned} \tag{3.13}$$

Now we turn to the production of a pseudoscalar meson $\tilde{M}$ via $I\!P_V I\!P_V$-fusion. The first step is to construct an effective coupling Lagrangian $I\!P_V I\!P_V \tilde{M}$. Traditionally this is done in analogy to the $\gamma\gamma\pi^0$ coupling which is given by the Adler-Bell-Jackiw anomaly (for a review see chapter 22 of [215]). In this way we get

$$\mathcal{L}'_{I\!P_V I\!P_V \tilde{M}}(x) = \frac{g'_{I\!P_V I\!P_V \tilde{M}}}{16 M_0}\, \left[\partial_\mu I\!P_{V\nu}(x) - \partial_\nu I\!P_{V\mu}(x)\right]\, \left[\partial_\rho I\!P_{V\sigma}(x) - \partial_\sigma I\!P_{V\rho}(x)\right]\, \varepsilon^{\mu\nu\rho\sigma}\, \tilde{\chi}(x) \tag{3.14}$$

with $g'_{I\!P_V I\!P_V \tilde{M}}$ a dimensionless coupling constant.

The corresponding vertex, including a form factor, reads as follows (see Fig.3.2 (b)):

$$i\Gamma'^{(I\!P_V I\!P_V\to\tilde{M})}_{\mu\nu}(q_1,q_2) = i\,\frac{g'_{I\!P_V I\!P_V \tilde{M}}}{2M_0}\, \varepsilon_{\mu\nu\rho\sigma} q_1^\rho q_2^\sigma\, F_{I\!P I\!P \tilde{M}}(q_1^2,q_2^2)\,. \tag{3.15}$$

It is easy to see that in the fictitious reaction (C.4) the coupling (3.14), (3.15) gives $(l,S)=(1,1)$. Note that in our framework we have for $I\!P_T I\!P_T$-fusion two values, $(l,S)=(1,1)$ and $(3,3)$, which can lead to a pseudoscalar meson; see Table B.1 in Appendix B. Correspondingly, we have two independent couplings, (3.3) and (3.5). For $I\!P_V I\!P_V$-fusion, on the other hand, we find from Table C.1 in Appendix C that only $(l,S)=(1,1)$ can lead to a pseudoscalar meson, thus, only the coupling (3.14) is possible there. This clear difference between the $I\!P_T$ and $I\!P_V$ ansätze can be exploited for experimentally distinguishing the two cases.

The amplitude for the production of a $J^{PC}=0^{-+}$ meson $\tilde{M}$ via $I\!P_V I\!P_V$-fusion can now be written down as in (3.12) with the $I\!P_V I\!P_V \tilde{M}$ vertex from (3.15). Explicitly this gives

$$\begin{aligned}\mathcal{M}^{2\to3}_{\lambda_a\lambda_b\to\lambda_1\lambda_2\tilde{M}}\,|_{I\!P_V I\!P_V} = \quad & -(3\beta_{I\!PNN})^2\, F_1(t_1)\, F_1(t_2)\, F_{I\!P I\!P\tilde{M}}(t_1,t_2)\, \frac{g'_{I\!P_V I\!P_V \tilde{M}}}{2M_0^3} \\ &\times \bar{u}(p_1,\lambda_1)\gamma^{\mu_1} u(p_a,\lambda_a)\, g_{\mu_1\nu_1}\, \left(-is_{13}\alpha'_{I\!P}\right)^{\alpha_{I\!P}(t_1)-1} \\ &\times \epsilon^{\nu_1\nu_2\rho\sigma}\, q_{1\rho} q_{2\sigma} \\ &\times g_{\nu_2\mu_2}\, \left(-is_{23}\alpha'_{I\!P}\right)^{\alpha_{I\!P}(t_2)-1}\, \bar{u}(p_2,\lambda_2)\gamma^{\mu_2} u(p_b,\lambda_b)\,. \end{aligned} \tag{3.16}$$

In [216] also (vector pomeron)-(vector pomeron) fusion was considered as the dominant mechanism of the η'-meson production. In order to estimate this contribution, the Donnachie-Landshoff energy dependence of the pomeron exchange [113] was used.

We shall now consider the high-energy small-angle limit, see Appendix A.1, for both the tensorial and vectorial pomeron fusion reactions giving the mesons M and $\tilde{M}$. With (A.9) to (A.21) we get from (3.10) and (3.11) for the tensorial pomeron

$$\begin{aligned}
\mathcal{M}^{2\to3}_{\lambda_a\lambda_b\to\lambda_1\lambda_2 M}\,|_{\boldsymbol{PP}} \;&\cong\; -2s\,(3\beta_{\boldsymbol{P}NN})^2\,F_1(t_1)\,F_1(t_2)\,F_{\boldsymbol{PP}M}(t_1,t_2)\\
&\quad\times\frac{M_0}{m_M^2}\Big(g'_{\boldsymbol{PP}M}+g''_{\boldsymbol{PP}M}\,\frac{1}{M_0^2}\,\vec{p}_{1\perp}\cdot\vec{p}_{2\perp}\Big)\\
&\quad\times\left(-is_{13}\alpha'_{\boldsymbol{P}}\right)^{\alpha_{\boldsymbol{P}}(t_1)-1}\;\left(-is_{23}\alpha'_{\boldsymbol{P}}\right)^{\alpha_{\boldsymbol{P}}(t_2)-1}\\
&\quad\times\delta_{\lambda_1\lambda_a}\delta_{\lambda_2\lambda_b}\,, \qquad (3.17)\\
\mathcal{M}^{2\to3}_{\lambda_a\lambda_b\to\lambda_1\lambda_2\tilde{M}}\,|_{\boldsymbol{PP}} \;&\cong\; -(3\beta_{\boldsymbol{P}NN})^2\,F_1(t_1)\,F_1(t_2)\,F_{\boldsymbol{PP}\tilde{M}}(t_1,t_2)\\
&\quad\times\frac{1}{m_{\tilde{M}}^2}\Big[\frac{g'_{\boldsymbol{PP}\tilde{M}}}{M_0}+\frac{g''_{\boldsymbol{PP}\tilde{M}}}{sM_0^3}\Big((q_1,p_2+p_b)(q_2,p_1+p_a)-(q_1,q_2)(p_1+p_a,p_2+p_b)\Big)\Big]\\
&\quad\times\varepsilon_{\mu\nu\rho\sigma}(p_1+p_a)^\mu(p_2+p_b)^\nu(q_1-q_2)^\rho k^\sigma\\
&\quad\times\left(-is_{13}\alpha'_{\boldsymbol{P}}\right)^{\alpha_{\boldsymbol{P}}(t_1)-1}\;\left(-is_{23}\alpha'_{\boldsymbol{P}}\right)^{\alpha_{\boldsymbol{P}}(t_2)-1}\\
&\quad\times\delta_{\lambda_1\lambda_a}\delta_{\lambda_2\lambda_b}\\
&\cong\; -4s\,(3\beta_{\boldsymbol{P}NN})^2\,F_1(t_1)\,F_1(t_2)\,F_{\boldsymbol{PP}\tilde{M}}(t_1,t_2)\\
&\quad\times\frac{1}{m_{\tilde{M}}^2M_0}|\vec{p}_{1\perp}||\vec{p}_{2\perp}|\sin\phi_{pp}\Big(g'_{\boldsymbol{PP}\tilde{M}}+g''_{\boldsymbol{PP}\tilde{M}}\,\frac{2}{M_0^2}|\vec{p}_{1\perp}||\vec{p}_{2\perp}|\cos\phi_{pp}\Big)\\
&\quad\times\left(-is_{13}\alpha'_{\boldsymbol{P}}\right)^{\alpha_{\boldsymbol{P}}(t_1)-1}\;\left(-is_{23}\alpha'_{\boldsymbol{P}}\right)^{\alpha_{\boldsymbol{P}}(t_2)-1}\\
&\quad\times\delta_{\lambda_1\lambda_a}\delta_{\lambda_2\lambda_b}\,. \qquad (3.18)
\end{aligned}$$

For the vectorial pomeron we get in this limit from (3.13) and (3.16) the expressions (3.17) and (3.18), respectively, but with the replacements:

$$g'_{\boldsymbol{PP}M}\to\frac{2m_M^2}{M_0^2}\,g'_{\boldsymbol{P}_V\boldsymbol{P}_VM}\,,\quad g''_{\boldsymbol{PP}M}\to\frac{2m_M^2}{M_0^2}\,g''_{\boldsymbol{P}_V\boldsymbol{P}_VM}\,, \qquad (3.19)$$

$$g'_{\boldsymbol{PP}\tilde{M}}\to\frac{m_{\tilde{M}}^2}{4M_0^2}\,g'_{\boldsymbol{P}_V\boldsymbol{P}_V\tilde{M}}\,,\quad g''_{\boldsymbol{PP}\tilde{M}}\to 0\,. \qquad (3.20)$$

We see that for the vectorial pomeron the term $\propto\cos\phi_{pp}\sin\phi_{pp}$ in (3.18) is absent.

Going now from high to intermediate collision energies we must expect besides pomeron-pomeron fusion also reggeon-pomeron (pomeron-reggeon) and reggeon-reggeon fusion to become important; see Fig.3.1. The relevant scales for these non-leading terms should be given by the subenergies squared s_{13} and s_{23} in (3.2). We have to consider for the first non-leading contributions those from the Regge trajectories with intercept $\alpha_{\boldsymbol{R}}(0)\approx 0.5$, that is, the f_2, a_2, ω and ρ trajectories which we shall denote by $f_{2\boldsymbol{R}}$, $a_{2\boldsymbol{R}}$, $\omega_{\boldsymbol{R}}$ and $\rho_{\boldsymbol{R}}$, respectively. In [13, 203] effective propagators for these reggeons and reggeon-proton-proton vertices are given. The $C=+1$ reggeons $f_{2\boldsymbol{R}}$ and $a_{2\boldsymbol{R}}$ are treated as effective tensor exchanges, the $C=-1$ reggeons $\omega_{\boldsymbol{R}}$ and $\rho_{\boldsymbol{R}}$ as effective vector exchanges.

To give an example we discuss the contribution of $\omega_{\boldsymbol{R}}\omega_{\boldsymbol{R}}$-fusion to the production of a pseudoscalar meson $\tilde{M}$; see Fig.3.1 with $\boldsymbol{R}=\omega_{\boldsymbol{R}}$ and $M\to\tilde{M}$. The effective $\omega_{\boldsymbol{R}}$ propagator and the $\omega_{\boldsymbol{R}}pp$ vertex are given in [13, 203] as follows:

- $\omega_{\boldsymbol{R}}$ propagator

$$i\Delta^{(\omega_{\boldsymbol{R}})}_{\mu\nu}(s,t)=i\,g_{\mu\nu}\,\frac{1}{M_-^2}\,\left(-is\alpha'_{\boldsymbol{R}}\right)^{\alpha_{\boldsymbol{R}}(t)-1} \qquad (3.21)$$

  with the parameters of the Regge trajectory (2.12), see [114]. In this calculations we use $\alpha'_{\boldsymbol{R}}=0.9\,\mathrm{GeV}^{-2}$ and the mass scale $M_-=1.41$ GeV.

- $\omega_{I\!R} pp$ vertex

$$i\Gamma_{\mu}^{(\omega_{I\!R} pp)}(p',p) = -i\, g_{\omega_{I\!R} pp}\, F_1\big((p'-p)^2\big)\, \gamma_\mu\,, \tag{3.22}$$

where $g_{\omega_{I\!R} pp} = 8.65$.

For the $\omega_{I\!R}\omega_{I\!R}\tilde{M}$ vertex we shall make an ansatz in complete analogy to (3.14), (3.15) for the vectorial pomeron. We get then

$$i\Gamma_{\mu\nu}^{(\omega_{I\!R}\omega_{I\!R}\to\tilde{M})}(q_1,q_2) = i\,\frac{g_{\omega_{I\!R}\omega_{I\!R}\tilde{M}}}{2M_0}\,\varepsilon_{\mu\nu\rho\sigma} q_1^\rho q_2^\sigma\, F_{\omega_{I\!R}\omega_{I\!R}\tilde{M}}(q_1^2,q_2^2)\,, \tag{3.23}$$

where $g_{\omega_{I\!R}\omega_{I\!R}\tilde{M}}$ is a dimensionless coupling constant.

Using (3.21) to (3.23) the Born amplitude for the $\omega_{I\!R}\omega_{I\!R}$-fusion giving a pseudoscalar meson $\tilde{M}$ can be parametrised as

$$\begin{aligned}
\mathcal{M}^{2\to3}_{\lambda_a\lambda_b\to\lambda_1\lambda_2\tilde{M}}\,|_{\omega_{I\!R}\omega_{I\!R}} = \quad & (g_{\omega_{I\!R} pp})^2\, F_1(t_1)\, F_1(t_2)\, F_{\omega_{I\!R}\omega_{I\!R}\tilde{M}}(t_1,t_2)\,\frac{g_{\omega_{I\!R}\omega_{I\!R}\tilde{M}}}{2M_0} \\
& \times \bar{u}(p_1,\lambda_1)\gamma^{\mu_1}u(p_a,\lambda_a) \\
& \times g_{\mu_1\nu_1}\,(M_-)^{-2}\,\left(-is_{13}\alpha'_{I\!R}\right)^{\alpha_{I\!R}(t_1)-1} \\
& \times \epsilon^{\nu_1\nu_2\rho\sigma}\, q_{1\rho} q_{2\sigma} \\
& \times g_{\nu_2\mu_2}\,(M_-)^{-2}\,\left(-is_{23}\alpha'_{I\!R}\right)^{\alpha_{I\!R}(t_2)-1} \\
& \times \bar{u}(p_2,\lambda_2)\gamma^{\mu_2}u(p_b,\lambda_b)\,.
\end{aligned} \tag{3.24}$$

At even lower energies, for s_{13} and s_{23} near the threshold value $s_{thr} = (m_p + m_{\tilde{M}})^2$, respectively $s_{thr} = (m_p + m_M)^2$ for a 0^{++} meson M, the exchange of reggeons in Fig.3.1 should be replaced by particle exchanges. As an example we give the amplitudes for η and η' production at low energies $\sqrt{s_{13}}$ and $\sqrt{s_{23}}$. It is known from the low energy phenomenology that both $\rho\rho$ and $\omega\omega$ mesons couple to η and η' mesons. The $\omega\omega\tilde{M}$ vertex required for constructing the meson-exchange current is derived from the Lagrangian densities [2]

$$\mathcal{L}_{\omega\omega\tilde{M}}(x) = \frac{g_{\omega\omega\tilde{M}}}{2m_\omega}\,\left[\partial_\mu\omega_\nu(x)\right]\left[\partial_\rho\omega_\sigma(x)\right]\,\varepsilon^{\mu\nu\rho\sigma}\,\tilde{\chi}(x) \tag{3.25}$$

and reads

$$i\Gamma_{\mu\nu}^{(\omega\omega\to\tilde{M})}(q_1,q_2) = i\,\frac{g_{\omega\omega\tilde{M}}}{m_\omega}\,\varepsilon_{\mu\nu\rho\sigma} q_1^\rho q_2^\sigma\, F_{\omega\omega\tilde{M}}(q_1^2,q_2^2)\,. \tag{3.26}$$

The Born amplitude for the $\omega\omega$-fusion giving $\tilde{M} = \eta'$ or η can be written as

$$\begin{aligned}
\mathcal{M}^{2\to3}_{\lambda_a\lambda_b\to\lambda_1\lambda_2\tilde{M}}\,|_{\omega\omega} = \quad & (g_{\omega pp})^2\, F_\omega(t_1)\, F_\omega(t_2)\, F_{\omega\omega\tilde{M}}(t_1,t_2)\,\frac{g_{\omega\omega\tilde{M}}}{m_\omega} \\
& \times \bar{u}(p_1,\lambda_1)\gamma^{\mu_1}u(p_a,\lambda_a) \\
& \times \frac{-g_{\mu_1\nu_1} + q_{1\mu_1}q_{1\nu_1}/m_\omega^2}{t_1 - m_\omega^2}\,\epsilon^{\nu_1\nu_2\rho\sigma}\, q_{1\rho} q_{2\sigma}\,\frac{-g_{\nu_2\mu_2} + q_{2\nu_2}q_{2\mu_2}/m_\omega^2}{t_2 - m_\omega^2} \\
& \times \bar{u}(p_2,\lambda_2)\gamma^{\mu_2}u(p_b,\lambda_b)\,.
\end{aligned} \tag{3.27}$$

The coupling constants $g_{\omega\omega\eta'} = 4.9$ [217,219], $g_{\omega\omega\eta} = 4.84$ [218,220] are known from low energy phenomenology. In the present calculations we take the ωpp coupling constant $g_{\omega pp} = 10$. Here we use form factors $F_{\omega\omega\tilde{M}}(t_1,t_2) = F_\omega(t_1)\,F_\omega(t_2)$ for both exponential (B.25) or monopole (B.24) approaches. At larger subsystem energies squared, $s_{13}, s_{23} \gg s_{thr}$, one should use reggeons

[2] The Lagrangian (3.25) is as given in (2.11) of [217] and (A.11b) of [218] taking into account that we use the opposite sign convention for $\varepsilon_{\mu\nu\rho\sigma}$; see after (3.2).

rather than mesons. The "reggeization" of the amplitude given in Eq. (3.27) is included here only approximately by a factor assuring asymptotically correct high energy dependence

$$\mathcal{F} = \left(\frac{s_{13}}{s_{thr}}\right)^{\frac{2}{\pi}\arctan[(s_{13}-s_{thr})/\Lambda^2_{thr}](\alpha_{I\!R}(t_1)-1)} \left(\frac{s_{23}}{s_{thr}}\right)^{\frac{2}{\pi}\arctan[(s_{23}-s_{thr})/\Lambda^2_{thr}](\alpha_{I\!R}(t_2)-1)}, \tag{3.28}$$

where $\Lambda_{thr} = 1$ GeV and $\alpha_{I\!R}(0) = 0.5$ and $\alpha'_{I\!R} = 0.9$ GeV^{-2}.

3.2 Existing experimental data

A big step in the investigation of central meson production process (3.1) was taken by the WA91 and WA102 Collaborations, which reported remarkable kinematical dependences and different effects; see Ref. [90, 91, 115, 212–214, 221]. The WA102 experiment at CERN was the first to discover a strong dependence of the cross section on the azimuthal angle between the momenta transferred to the two protons, a feature that was not expected from standard pomeron phenomenology. This result inspired some phenomenological works [93–95] pointing to a possible analogy between the pomeron and vector particles as had been suggested in [113, 222–228] (see also chapter 3.7 of [114]).

Close and his collaborators have even proposed to use transverse momentum correlations of outgoing protons as a tool to discriminate different intrinsic structures of the centrally produced object ("glueball filter"); see [92–95]. In particular, the production of scalar mesons such as $f_0(980)$, $f_0(1500)$, $f_0(1710)$ was found to be considerably enhanced at small $dP_\perp$, while the production of pseudoscalars such as η, η' at large $dP_\perp$; see Fig.3 of [115]. Here $dP_\perp = |d\vec{P}_\perp|$ with $d\vec{P}_\perp$ the difference of the transverse momenta of the two outgoing protons in (3.1); see (A.5). In Ref. [90, 115] a study was performed of resonance production rates as a function of $dP_\perp$. It was observed that all the undisputed $q\bar{q}$ states (i.e. η, η', $f_1(1285)$ etc.) are suppressed as $dP_\perp \to 0$, whereas the glueball candidates, e.g. $f_0(1500)$, $f_2(1950)$ are prominent. It is also interesting that the $f_1(1420)$ state disappears at small $dP_\perp$ relative to large $dP_\perp$. As can be seen from [115] the $\rho^0(770)$, $f_2(1270)$, and $f_2'(1525)$ mesons are produced preferentially at large $dP_\perp$ and their cross sections peak at $\phi_{pp} = \pi$, i.e. the outgoing protons are on opposite sides of the beam. [3] In contrast, for the 'enigmatic' $f_0(980)$, $f_0(1500)$ and $f_0(1710)$ states the cross sections peak at $\phi_{pp} = 0$. So far, no dynamical explanation of this empirical observation has been suggested, so the challenge for theory is to understand the dynamics behind this "glueball filter".

In Ref. [152] the study of the $|t| = |t_1 + t_2|$ dependence of the resonances observed in the $\pi^+\pi^-$ and K^+K^- mass spectra at $\sqrt{s} = 23.8$ GeV was considered. It has been observed that $\rho(770)$, $\phi(1020)$, $f_2(1270)$ and $f_2'(1525)$ resonances are produced more at the high-$|t|$ region ($|t| > 0.3$ GeV^2) and at low $|t|$ their signals are suppressed. The suppression of the ρ and $f_2(1270)$ signals in the low-$|t|$ region is also present at $\sqrt{s} = 12.7$ GeV for the $\pi^+p \to \pi^+(\pi^+\pi^-)p$ reaction; see [152]. In addition, the $dP_\perp$, ϕ_{pp} and $|t|$ distributions observed in the analysis of the $\pi^+\pi^-$ final state for the $f_0(1370)$ and $f_0(1500)$ mesons are similar to what was found in the $\pi^+\pi^-\pi^+\pi^-$ channel [91].

The ratios of the experimental cross sections for the different mesons at $\sqrt{s} = 29.1$ GeV and 12.7 GeV has also been determined, see Table 3.1. Moreover, the WA76 Collaboration reported that the ratio of the $\rho^0(770)$ cross section at 23.8 GeV and 12.7 GeV is 0.44 ± 0.07; cf. [115].

[3] Here ϕ_{pp} is the azimuthal angle between the momentum vectors of the outgoing protons; see (A.4).

Table 3.1: Experimental results for the ratios of the cross sections for the different mesons at $\sqrt{s} = 29.1$ GeV and 12.7 GeV.

	η'	$\rho(770)$	$f_0(980)$	$f_0(1500)$	$f_2(1270)$
$\frac{\sigma(\sqrt{s}=29.1\,GeV)}{\sigma(\sqrt{s}=12.7\,GeV)}$	0.72 ± 0.16 [214]	0.36 ± 0.05 [90]	1.28 ± 0.21 [90]	1.07 ± 0.14 [90]	0.98 ± 0.13 [90]

Since the $I = 1$ states cannot be produced by pomeron-pomeron fusion, the ρ meson signal decreases at high energy. However, large enhancement of the ρ signal at $\sqrt{s} = 29.1$ GeV and strong correlation between the directions of the outgoing protons have been observed [212, 221]. Similarly, in the case of the ω meson production, where some 'non-central' mechanisms are possible [5], the cross section is more than twice larger than for the $f_0(1500)$ meson, the lightest scalar glueball candidate [1, 115].

We turn now to our present calculations of cross sections and distributions for the central production reaction (3.1) with scalar and pseudoscalar mesons.

3.3 Model results

Now we wish to compare results of our calculations with existing experimental data. Theoretical predictions for production of various J^{PC} mesonic states for RHIC, Tevatron and LHC, with parameters fixed from the fit to the WA102 experimental data, can then be easily done.

3.3.1 Scalar meson production

We start with discussing the WA102 data at $\sqrt{s} = 29.1$ GeV where total cross sections are given in Table 1 of Ref. [115]. We show these cross sections for the mesons of interest to us in Table 3.2. We assume that here the energy is high enough that we can consider only pomeron-pomeron-meson ($\mathbb{P}\mathbb{P}M$) fusion. We have then determined the corresponding $\mathbb{P}\mathbb{P}M$ coupling constants by approximately fitting the results of our calculations to the total cross sections given in Table 3.2 and the shapes of experimental differential distributions (specific details will be given when discussing differential distributions below). The results depend also on the pomeron-pomeron-meson form factors (B.21), as discussed in Appendix B, which are not well known, in particular for larger values of t. In Table 3.3 we show our results for these $\mathbb{P}\mathbb{P}M$ coupling constants for the tensorial and vectorial pomeron ansätze. The figures in bold face represent our "best" fit. We show the resulting total cross sections, from the coupling $g'_{\mathbb{P}\mathbb{P}M}$ alone, from $g''_{\mathbb{P}\mathbb{P}M}$ alone, and from the total which includes, of course, the interference term between the two components. The column "no cuts, total" has to be compared to the experimental results shown in Table 3.2. For the cross section with the cuts in $|t_1 t_2|$ only normalised differential distributions are available; see below. Thus, our results for the corresponding cross sections are predictions to be checked in future experiments.

In Fig.3.3 we present our result for the integrated cross sections of the exclusive $f_0(980)$ (left panel) and $f_0(1500)$ (right panel) scalar meson production as a function of centre-of-mass energy $\sqrt{s}$. For this calculation we have taken into account pion-pion fusion and pomeron-pomeron fusion; see Fig.3.1. The $\pi\pi$-fusion mechanism has been discussed in Section 1.4.1 and in Ref. [1]. We see that at low energy the $\pi\pi$-fusion contribution dominates, i.e. grows quickly from the threshold, has a maximum at $\sqrt{s} \approx 5 - 7$ GeV and then slowly drops with increasing energy. This contribution was calculated with monopole vertex form factor (B.24) with parameters $\Lambda_{\pi NN} = 0.8$ GeV, $\Lambda_{\pi\pi M} = 1$ GeV (the lower line) and $\Lambda_{\pi NN} = 1.2$ GeV, $\Lambda_{\pi\pi M} = 1$ GeV (the upper line). In this calculation the coupling constants were calculated from the corresponding partial decay width (1.28) ($g_{f_0(1500)\pi\pi} = 1.4$ GeV and $g_{f_0(980)\pi\pi} = 1.55$ GeV). The difference between the lower and upper curves represents the uncertainties on the pion-pion component. At intermediate energies other exchange processes such as the pomeron-$f_{2\mathbb{R}}$, $f_{2\mathbb{R}}$-pomeron and $f_{2\mathbb{R}}$-$f_{2\mathbb{R}}$ exchanges are possible. For the $f_{2\mathbb{R}}pp$ vertex and the $f_{2\mathbb{R}}$ exchange effective propagator we shall make an ansatz in complete analogy to (B.1) and (B.3) for the tensorial pomeron, respectively, with the coupling constant $g_{f_{2\mathbb{R}}pp} = 11.04$ and the trajectory as (2.12); see [13, 203]. The $f_{2\mathbb{R}}f_{2\mathbb{R}}f_0(980)$ and $f_{2\mathbb{R}}\mathbb{P}_T f_0(980)$ vertices should have the general structure of the $\mathbb{P}_T\mathbb{P}_T f_0(980)$ vertex (B.20), but, of course, with different and independent coupling constants. In panel (c) we show results with $\mathbb{P}_T\mathbb{P}_T$ (black solid line (1)) and $f_{2\mathbb{R}}f_{2\mathbb{R}}$ (violet solid line (3)) exchanges, obtained

Table 3.2: Experimental results for total cross sections of various mesons in pp collisions at $\sqrt{s} =$ 29.1 GeV; from Table 1 of Ref. [115].

	η	η'	$f_0(980)$	$f_0(1370)$	$f_0(1500)$	$f_0(1710)$	$f_0(2000)$
$\sigma(\mu\text{b})$	3.86 ± 0.37	1.72 ± 0.18	5.71 ± 0.45	1.75 ± 0.58	2.91 ± 0.30	0.25 ± 0.07	3.14 ± 0.48

Table 3.3: The values of the pomeron-pomeron-meson coupling constants of the two models of the pomeron exchanges are approximately fitted to reproduce the experimental total cross sections from Table 3.2 and shapes of differential distributions of the WA102 data as discussed below. The resulting cross sections (in μb) for scalar meson central production at $\sqrt{s} = 29.1$ GeV without cuts and with cuts in $|t_1 t_2|$ are also shown. The figures in bold face represent our "best fit" values for the $I\!P I\!P M$ coupling constants.

Vertex	$g'_{I\!P I\!P M}$ $(0,0)$ term	$g''_{I\!P I\!P M}$ $(2,2)$ term	σ (μb) at $\sqrt{s} = 29.1$ GeV								
			no cuts			$\lvert t_1 t_2\rvert \leqslant 0.01$ GeV^4			$\lvert t_1 t_2\rvert \geqslant 0.08$ GeV^4		
			$(0,0)$	$(2,2)$	total	$(0,0)$	$(2,2)$	total	$(0,0)$	$(2,2)$	total
$I\!P_T I\!P_T f_0(980)$	**0.788**	**4**	5.73	1.16	5.71	3.56	0.12	3.51	0.21	0.41	0.3
	0.75	**5.5**	5.19	2.19	5.83	3.22	0.23	3.23	0.19	0.77	0.55
$I\!P_V I\!P_V f_0(980)$	**0.27**	**0.8**	5.37	0.48	5.72	2.85	0.04	2.87	0.34	0.2	0.49
	0.26	1.1	4.98	0.9	5.71	2.64	0.07	2.69	0.31	0.38	0.63
	0.24	**1.5**	4.24	1.67	5.7	2.25	0.12	2.36	0.27	0.71	0.9
	0.2	2	2.94	2.97	5.69	1.56	0.22	1.76	0.19	1.27	1.36
$I\!P_T I\!P_T f_0(1500)$	**1.22**	**6**	2.69	0.53	2.9	1.55	0.05	1.56	0.12	0.19	0.21
	1	**10**	1.81	1.47	2.83	1.04	0.14	1.13	0.08	0.53	0.47
$I\!P_V I\!P_V f_0(1500)$	**0.208**	**0.725**	2.64	0.32	2.9	1.37	0.02	1.39	0.17	0.13	0.28
	0.185	1.22	2.08	0.89	2.91	1.09	0.06	1.14	0.13	0.38	0.48
	0.164	**1.5**	1.64	1.35	2.91	0.85	0.1	0.94	0.1	0.57	0.64
$I\!P_T I\!P_T f_0(1370)$	**0.81**	–	1.75	–	–	1.02	–	–	0.07	–	–
$I\!P_V I\!P_V f_0(1370)$	**0.165**	–	1.75	–	–	0.91	–	–	0.11	–	–

for the coupling constants $(g'_{I\!P I\!P M}, g''_{I\!P I\!P M}) = (0.788, 4)$ and $(g'_{f_{2R} f_{2R} M}, g''_{f_{2R} f_{2R} M}) = (9.5, 80)$, respectively. We see that fixing the $I\!P_T$ or f_{2R} contributions to the point at $\sqrt{s} = 29.1$ GeV the $I\!P_T$ curve is below, the f_{2R} curve above the experimental point at $\sqrt{s} = 12.7$ GeV. Clearly, we have to include all $I\!P_T$ and f_{2R} exchanges. The corresponding curve (2) reproduces the experiment. The individual contributions are also shown in Fig.3.3(c), corresponding to $(g'_{I\!P I\!P M}, g''_{I\!P I\!P M}) = (0.47, 2.4)$, $(g'_{I\!P f_{2R} M}, g''_{I\!P f_{2R} M}) = (g'_{f_{2R} I\!P M}, g''_{f_{2R} I\!P M}) = (0.63, 3.2)$, $(g'_{f_{2R} f_{2R} M}, g''_{f_{2R} f_{2R} M}) = (0.79, 3.9)$. In panel (d) we show results at larger c.m. energies $\sqrt{s}$ for two parameter sets of the $I\!P_T I\!P_T f_0(1500)$ coupling constants $(g'_{I\!P I\!P M}, g''_{I\!P I\!P M}) = (1.22, 6)$ (the black solid line) and $(g'_{I\!P I\!P M}, g''_{I\!P I\!P M}) = (1, 10)$ (the blue solid line). The resulting cross sections with cuts in rapidity of $f_0(1500)$ meson are also shown.

In Fig.3.4 we show the distribution in azimuthal angle ϕ_{pp} between outgoing protons for central exclusive $f_0(1370)$ meson production by the fusion of two tensor (solid line) or two vector (long-dashed line) pomerons at $\sqrt{s} = 29.1$ GeV. The results of the two models of pomeron exchanges are compared with the WA102 data. The tensorial pomeron with the $(l, S) = (0, 0)$ coupling alone already describes the azimuthal angular correlation for $f_0(1370)$ meson reasonable well. The vectorial pomeron with the $(l, S) = (0, 0)$ term alone is disfavoured here. The preference of the $f_0(1370)$ for the $\phi_{pp} \approx \pi$ domain in contrast to the enigmatic $f_0(980)$ and $f_0(1500)$ scalars has been observed by the WA102 Collaboration [90].

The distributions in azimuthal angle ϕ_{pp} between the outgoing protons for the central exclusive production of the$f_0(980)$ and $f_0(1500)$ mesons at $\sqrt{s} = 29.1$ GeV are shown in Fig.3.5 and 3.6, respectively. We compare results obtained by the fusion of two pomerons (the tensor pomeron exchanges are shown in panels (a) - (c) and the vector pomeron exchanges are shown in panels (d) - (f)) with the data measured by the WA102 Collaboration in [90] (the black filled points) and [214] (the blue circle points). In the left panels we show the ϕ_{pp} distribution without experimental cuts, the middle panels show the ϕ_{pp} distribution for $|t_1 t_2| \leqslant 0.01$ GeV^4 and the right panels show the corresponding distribution for $|t_1 t_2| \geqslant 0.08$ GeV^4. Note that in [90]

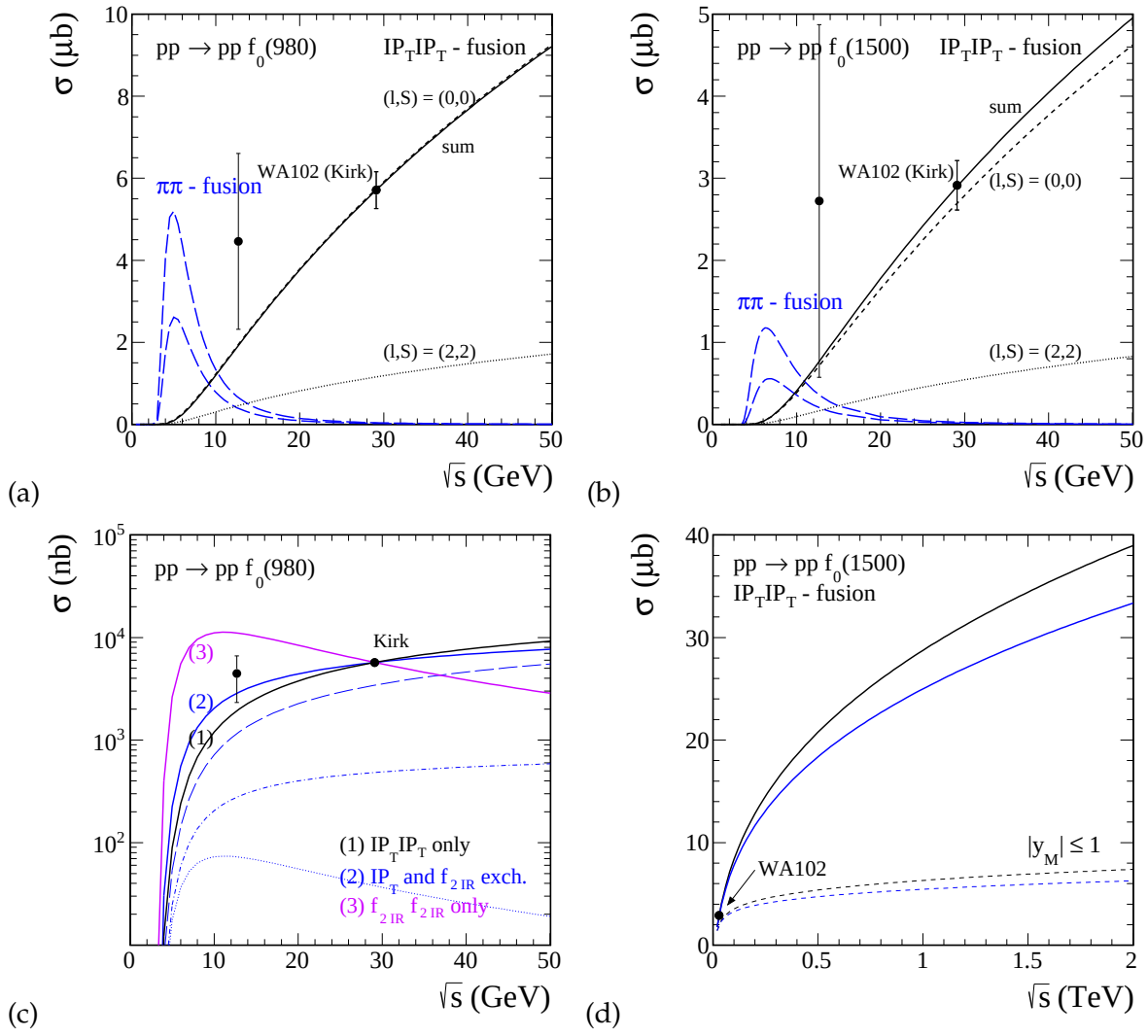

Figure 3.3: The integrated cross section as a function of the proton-proton center-of-mass energy for the $pp \to ppf_0(980)$ (panel (a)) and $pp \to ppf_0(1500)$ (panel (b)) reactions. We show data points obtained by the WA102 experiment [90, 115]. The two long-dashed lines peaked at $\sqrt{s} \approx 5-7$ GeV correspond to pion-pion fusion contribution. The pomeron-pomeron fusion dominates at higher energies. In panels (a) and (b) we show the individual contributions to the cross section with $(l,S) = (0,0)$ (short-dashed line) and $(l,S) = (2,2)$ (dotted line). In panels (a) and (b) we show results when only the $I\!P_T I\!P_T$-fusion is included. In panel (c) the black solid line (1) represents the $I\!P_T I\!P_T$-fusion, the blue solid line (2) correspond to the results with tensor pomeron and f_{2R} exchanges (the long-dashed, dash-dotted and dotted lines represent the $I\!P_T I\!P_T$, $I\!P_T f_{2R}$ and $f_{2R} f_{2R}$ contributions, respectively). The violet solid line (3) represents the $f_{2R} f_{2R}$-fusion alone normalized to the total cross section from [115] as given in our Table 3.2. Panel (d) shows the $I\!P_T I\!P_T$ contributions obtained for two parameter sets of (l,S) components (see Table 3.3 and 3.6) normalized to the data point at $\sqrt{s} = 29.1$ GeV.

and [214] only normalised distributions are given. We have multiplied these distributions with the value of the total cross sections from Table 3.2 for panels (a) and (d). For panels (b), (c), (e), and (f) we have multiplied the normalised data distributions given in [214] with the cross sections obtained from our calculations in the tensorial and vectorial pomeron models, respectively; see Table 3.3. These normalisation factors are different for the $I\!P_T$ and $I\!P_V$ cases. Therefore, also the data shown in panels (b) and (e), as well as in (c) and (f), are different. Also note that the difference in the data from [90] and [214] shown in panels (a) and (d) has an experimental origin. Correspondingly, in the panels (a) the black filled and the blue circle experimental points are described by the tensorial pomeron exchanges for different values of (l,S). For the $f_0(980)$ (Fig.3.5(a)) we obtain $(g'_{PPM}, g''_{PPM}) = (0.788, 4)$ (the black solid line) and $(g'_{PPM}, g''_{PPM}) = (0.75, 5.5)$ (the blue

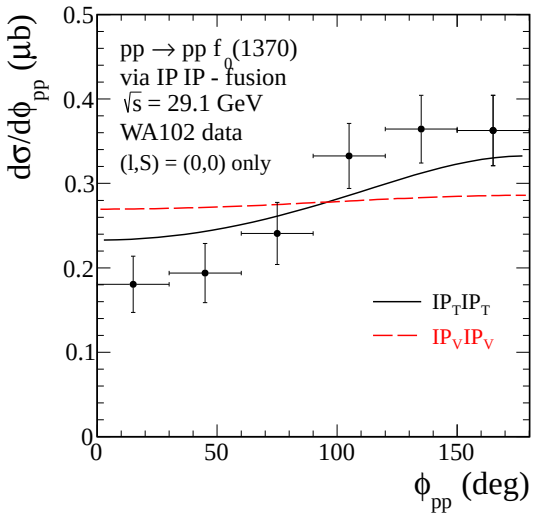

Figure 3.4: The distribution in azimuthal angle between the outgoing protons for central exclusive $f_0(1370)$ meson production by a fusion of two tensor (solid line) and vector (long-dashed line) pomerons at $\sqrt{s} = 29.1$ GeV. The WA102 experimental data points from [90] have been normalized to the total cross section from [115] as given in our Table 3.2. The corresponding $\mathbb{P}\mathbb{P}M$ coupling constants are given in Table 3.3.

solid line), respectively. The values of the couplings for $f_0(1500)$ production shown in Fig.3.6(a) are $(g'_{\mathbb{P}\mathbb{P}M}, g''_{\mathbb{P}\mathbb{P}M}) = (1.22, 6)$ (the black solid line) and $(g'_{\mathbb{P}\mathbb{P}M}, g''_{\mathbb{P}\mathbb{P}M}) = (1, 10)$ (the blue solid line), respectively. From our results we conclude that both (l, S) contributions are necessary if the distributions in azimuthal angle are to be described accurately. The $(l, S) = (2, 2)$ contribution increases the cross section at large ϕ_{pp} while decreasing it for small ϕ_{pp}. The panels (d) - (f) show the results obtained for two vector pomerons coupling to the mesons. The curves represent contributions from different (l, S) couplings collected in Table 3.3. In the panel (d) of Fig.3.5 ($f_0(980)$ production) the black long-dashed line corresponds to $(g'_{\mathbb{P}\mathbb{P}M}, g''_{\mathbb{P}\mathbb{P}M}) = (0.27, 0.8)$ and the blue long-dashed line to $(g'_{\mathbb{P}\mathbb{P}M}, g''_{\mathbb{P}\mathbb{P}M}) = (0.24, 1.5)$. For $f_0(1500)$ production shown in panel (d) of Fig.3.6 the black long-dashed line corresponds to $(g'_{\mathbb{P}\mathbb{P}M}, g''_{\mathbb{P}\mathbb{P}M}) = (0.208, 0.725)$, the blue long-dashed line to $(g'_{\mathbb{P}\mathbb{P}M}, g''_{\mathbb{P}\mathbb{P}M}) = (0.164, 1.5)$. With these values we are able to describe well the black filled and blue circle experimental points, respectively. For panels (e) and (f) we have multiplied the normalised data from [214] with the cross sections obtained from our calculations. In panels (g) - (i) the results obtained with the two models of pomeron are compared. From Fig.3.5 and 3.6 we conclude that, especially for $|t_1 t_2| \geqslant 0.08$ GeV^4, the tensorial pomeron ansatz is in better (qualitative) agreement with the data than the vectorial ansatz. But let us recall that for panels (b), (c), (e), and (f) the normalisation is taken from the models themselves for lack of experimental information.

At present we have calculated only so-called bare amplitudes which are subjected to absorption corrections. The absorption effects lead usually to a weak energy dependent damping of the cross sections. At the energy of the WA102 experiment ($\sqrt{s} = 29.1$ GeV) the damping factor is expected to be at most of the order of 2 and should increase with rising collision energy. The absorption effects both in initial and final states have been considered in Ref. [205]. It was stressed in Ref. [205] that at the WA102 energies absorptive effects are not so significant and the azimuthal angle dependence looks like the "bare" one.

In Fig.3.7 we show the distributions in transferred four-momentum squared t between the initial and final protons at $\sqrt{s} = 29.1$ GeV for $f_0(980)$, $f_0(1370)$, and $f_0(1500)$ mesons. While for $f_0(1370)$ the $(l, S) = (0, 0)$ coupling is sufficient (see discussion of azimuthal correlations in Fig.3.4) for $f_0(980)$ and $f_0(1500)$ both the $(0, 0)$ and $(2, 2)$ couplings are included. A different structure of the central vertex for vector and tensor leads to a difference in t distribution; see panels (a) - (c). The difference seems, however, too small to be verified experimentally. In addition,

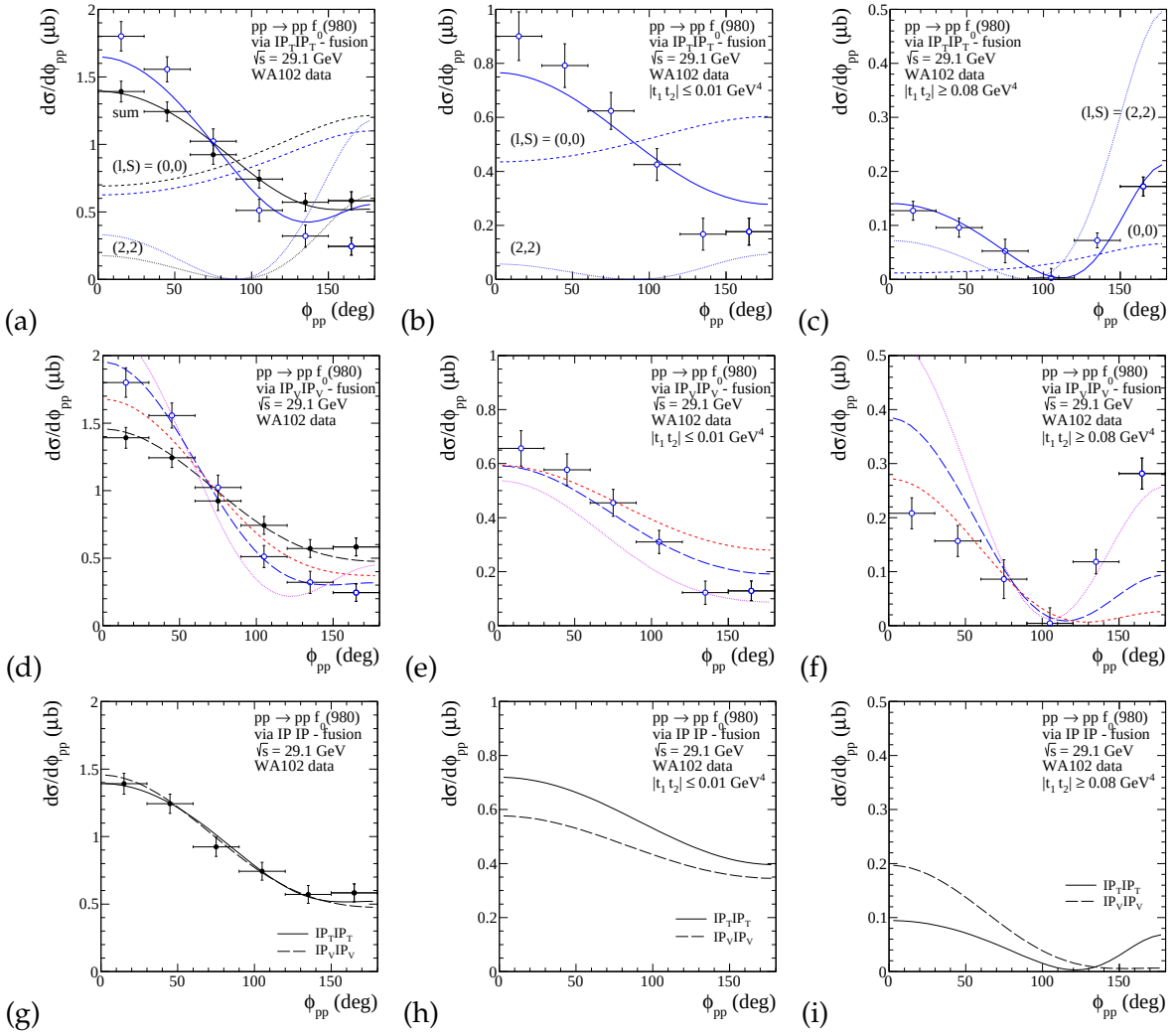

Figure 3.5: The distribution in azimuthal angle between outgoing protons for the central exclusive $f_0(980)$ meson production by the fusion of both tensor (panels (a) - (c)) and both vector (panels (d) - (f)) pomerons at $\sqrt{s} = 29.1$ GeV. Results in the left panels and the WA102 data points from [90] (black filled points) and from [214] (blue open points) have been normalized to the value of the total cross section given in Table 3.2, obtained from Ref. [115]. The ϕ_{pp} distributions have also been analysed in two intervals of $|t_1 t_2|$ and compared with experimental data. These data are obtained from [214] with the normalisation calculated in the tensorial and vectorial pomeron models themselves. We show in panels (a) - (c) the results in the tensorial pomeron model. For tensorial pomeron the individual contributions to the cross sections with $(l, S) = (0, 0)$ (short-dashed line) and $(l, S) = (2, 2)$ (dotted line) are also shown. Panels (d) - (f) show the results obtained for the vectorial pomeron model. In panels (g) - (i) the results obtained in the two models of pomeron are compared.

in panels (a) - (c) we compare distributions obtained for two types of pomeron-pomeron-meson form factors of the exponential form (B.23) and the monopole form (B.21). The calculations with the exponential form factor (B.23) and for the cut-off parameter $\Lambda_E^2 = 0.6$ GeV^2 give a sizeable decrease of the cross sections at large $|t|$. In panel (d) we show contributions for two tensor pomerons (the line (1)) and f_{2R} reggeons (the line (3)) exchanges alone, since the contribution with tensorial pomeron and f_{2R} reggeon is included as well (the line (2)). We conclude that the $f_{2R} f_{2R}$ component alone does not describe the WA102 data. In panels (e) and (f) we show a decomposition of the t-distribution into $(0, 0)$ and $(2, 2)$ components for the tensor pomeron exchanges. At $t = 0$ the $(2, 2)$ component vanishes, in contrast to the $(0, 0)$ component. Therefore, the latter dominates at small $|t|$. As previously, we show lines for the two parameter sets obtained from the fits to the two different experimental azimuthal angular correlations (see panels (a) in Fig.3.5 and 3.6).

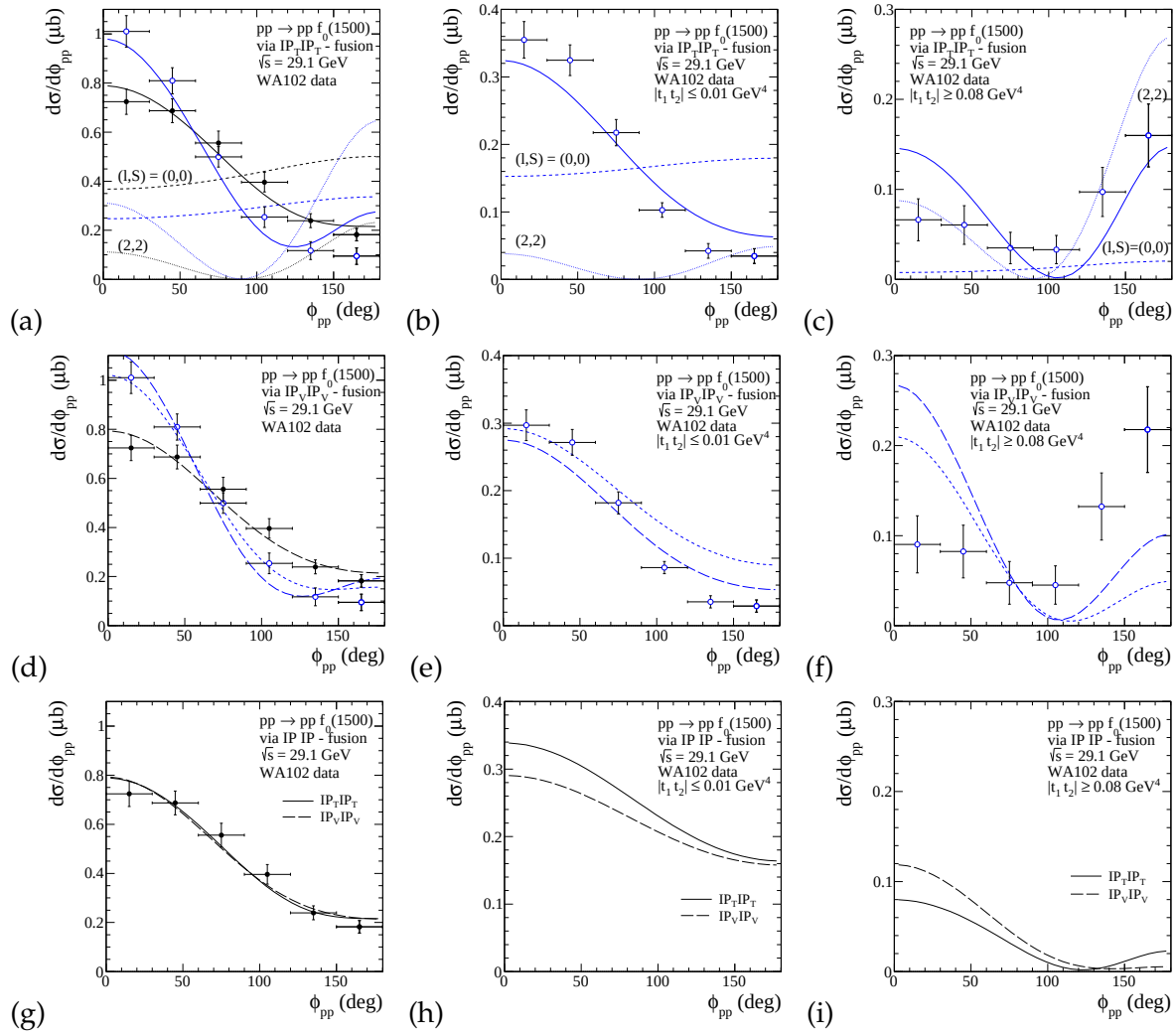

Figure 3.6: Same as Fig.3.5, but for the central exclusive $f_0(1500)$ meson production.

In Fig.3.8 we present different differential observables (in proton and meson transverse momenta as well as in the so-called "glueball filter variable" $dP_\perp$) at $\sqrt{s} = 29.1$ GeV for the central exclusive production of three different scalar mesons, $f_0(980)$ (left panel), $f_0(1500)$ (middle panel) and $f_0(1370)$ (right panel). As explained in the figure caption we show results for both tensor (solid line) and vector (long-dashed line) pomerons as well as the individual spin (l, S) contributions for tensor pomeron only. The coherent sum of the $(0, 0)$ and $(2, 2)$ components is shifted to smaller $dP_\perp$ with respect to the $(0, 0)$ component alone. This seems to be qualitatively consistent with the WA102 Collaboration result presented in Table 2 of Ref. [115]. Further studies how different scalar mesons are produced as a function of $dP_\perp$ will be presented in the next section; see discussion of Fig.3.18. For meson transverse momentum one can see a shift in the opposite direction.

In Fig.3.9 we show distributions in transverse momenta of protons, mesons and in the $dP_\perp$ for the $f_0(980)$ meson production. The three tensorial scenarios of meson production, as in Fig.3.7 (b), are presented. One conclusion is that the $f_{2R}f_{2R}$ contribution, indicated in the figure as curve (3), does not give the expected $dP_\perp$ distribution as in Table 2 of Ref. [115].

In Fig.3.10 we show distributions in rapidity of $f_0(980)$ and $f_0(1500)$ mesons and the corresponding distributions in pseudorapidity η_M at $\sqrt{s} = 29.1$ GeV. In these observables both (l, S) components and their coherent sum have similar shape. The minimum in the pseudorapidity distributions can be understood as a kinematic effect; see Appendix A.1. In addition, for the $f_0(980)$ meson production we have included the tensorial f_{2R} contributions; see the central pan-

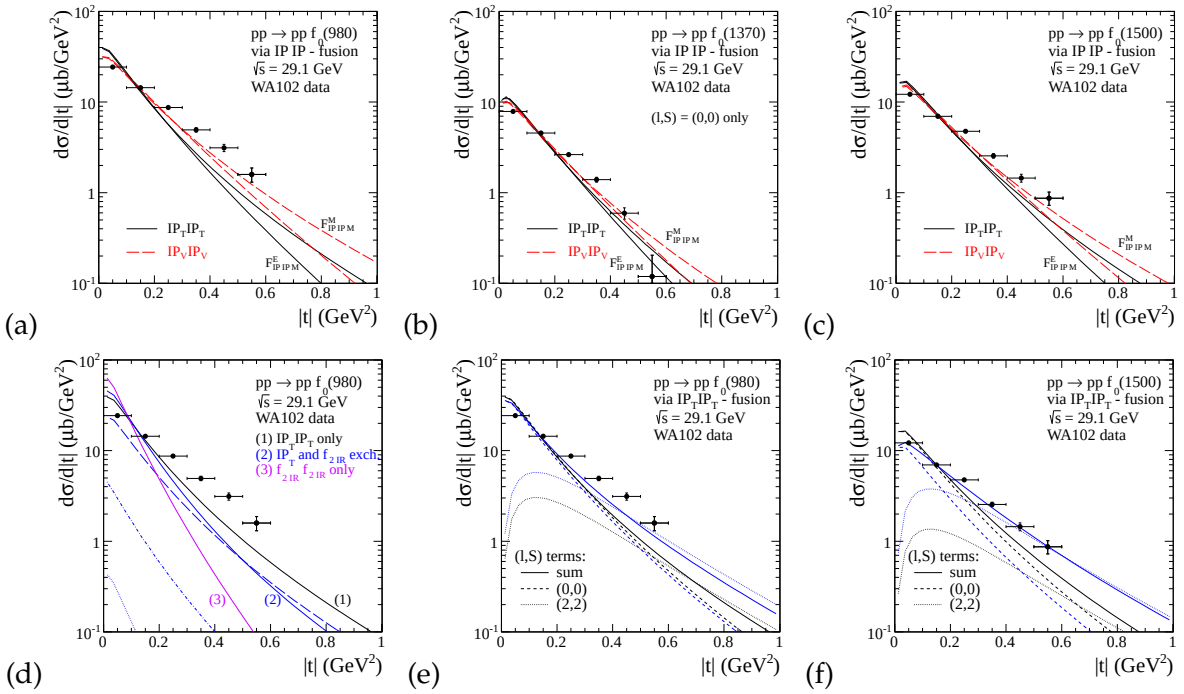

Figure 3.7: The t distributions for $f_0(980)$ (panels (a), (d) and (e)), $f_0(1370)$ (panel (b)), and $f_0(1500)$ (panels (c) and (f)) meson production at $\sqrt{s} = 29.1$ GeV. The WA102 experimental data points from [90] have been normalized to the value of the total cross sections given in Table 3.2 as obtained from [115]. In panels (a) - (c) the results for the fusion of two tensor (solid line) and two vector (long-dashed line) pomerons are shown. The lower lines correspond to calculations with the exponential form factor (B.23) and for the cut-off parameter $\Lambda_E^2 = 0.6$ GeV^2, the upper lines to calculations with the monopole form factor (B.21) for $\Lambda_0^2 = 0.5$ GeV^2. In panel (d) the black solid line (1) corresponds to the $I\!P_T I\!P_T$-fusion only, the blue solid line (2) corresponds to the tensor pomeron and f_{2R} exchanges (the long-dashed, dash-dotted and dotted lines present the $I\!P_T I\!P_T$, $I\!P_T f_{2R}$ ($f_{2R} I\!P_T$) and $f_{2R} f_{2R}$ contributions, respectively), and the violet solid line (3) presents the $f_{2R} f_{2R}$-fusion alone normalized to the integrated cross section from [115]. In panels (e) and (f) we show the individual spin contributions to the cross sections with $(l, S) = (0, 0)$ (short-dashed line) and $(l, S) = (2, 2)$ (dotted line) as well as lines for the two sets of couplings fixed previously by comparison with the experimental azimuthal angular correlations (see panels (a) in Fig.3.5 and 3.6).

els. The $I\!P_T I\!P_T$ and the $f_{2R} f_{2R}$ exchanges contribute at midrapidity of the meson, while the $I\!P_T f_{2R}$ and $f_{2R} I\!P_T$ exchanges at backward and forward meson rapidity, respectively. The interference of these components in the amplitude produces an enhancement of the cross section at large meson (pseudo)rapidity.

In Fig.3.11 we show the distribution in Feynman-x_F for the central exclusive $f_0(980)$ meson (the only available experimentally) production at $\sqrt{s} = 29.1$ GeV. The good agreement of the $I\!P_T I\!P_T$-fusion result (see the solid line in the left panel) with the WA102 data suggests that for the tensor pomeron model the pomeron-reggeon and reggeon-reggeon contributions are small.

Up to now we have observed some differences of the results for $(l, S) = (0, 0)$ and $(2, 2)$ couplings. The differences can be made better visible in two-dimensional distributions. In Fig.3.12 we show, as an example, two-dimensional distributions in $(dP_\perp, \phi_{pp})$. We show results for the fusion of two tensor (left panels) and two vector (right panels) pomerons. In panels (a) and (b) we show the results for both (l, S) components added coherently. In panels (c, d) and (e, f) we show the individual components for $(l, S) = (0, 0)$ and $(2, 2)$, respectively. The distributions for both cases are very different. By comparing panels (a) and (b) to panels (c, e) and (d, f), respectively, we see that the interference effects are rather large.

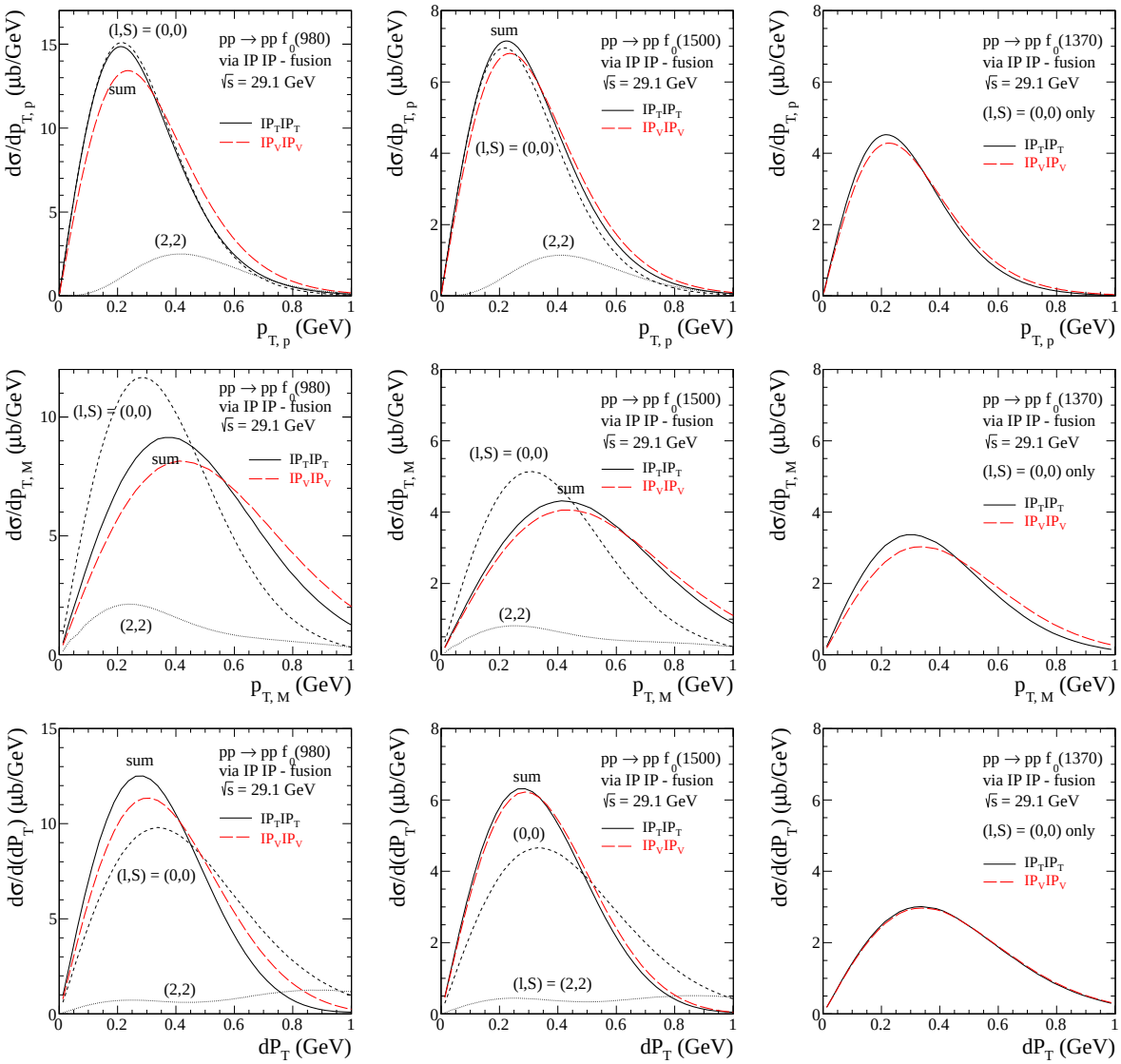

Figure 3.8: The different differential observables for the central exclusive production of $f_0(980)$ (left panel), $f_0(1500)$ (central panel) and $f_0(1370)$ (right panel) mesons by the fusion of two tensor (solid line) and two vector (long-dashed line) pomerons at $\sqrt{s} = 29.1$ GeV. The results have been normalized to the value of the total cross sections given in Table 3.2. For the tensorial pomeron case we show the individual spin contributions to the cross sections with $(l, S) = (0, 0)$ (short-dashed line) and $(l, S) = (2, 2)$ (dotted line).

3.3.2 Pseudoscalar meson production

We turn now to the presentation of our results for pseudoscalar mesons. It is known that the η and η' mesons, the isoscalar members of the nonet of the lightest pseudoscalar mesons, play an important role in the understanding of various aspects of nonperturbative effects of QCD; see for instance [230]. The η'-meson being dominantly $(\alpha\,|s\bar{s}\rangle + \beta\,|gg\rangle)$ state, with presence of a sizeable gluonic component [231], is particularly interesting for our study as here the pomeron-pomeron fusion should be the dominant mechanism in central production. For central production of the η meson the situation may be more complicated and requires consideration of additional f_{2R} reggeon exchanges [216, 232]. In contrast to η' production, no good fit with (tensorial or vectorial) pomeron-pomeron component only is possible for the η meson production. Therefore we have decided to include in addition $f_{2R}\mathbb{P}$, $\mathbb{P}f_{2R}$ and $f_{2R}f_{2R}$ contributions

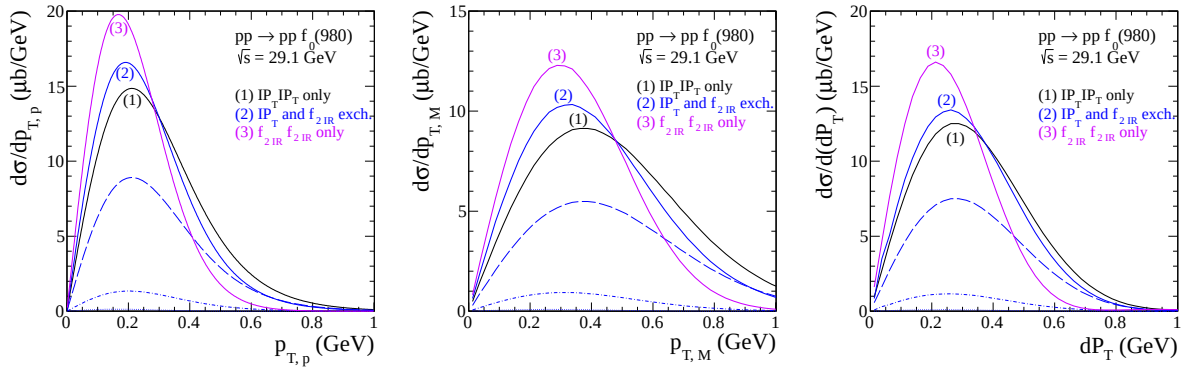

Figure 3.9: Different differential observables for the central exclusive production of $f_0(980)$ meson at $\sqrt{s} = 29.1$ GeV. The results have been normalized to the value of the total cross section given in Table 3.2. The black solid line (1) corresponds to the $I\!P_T I\!P_T$-fusion, the blue solid line (2) to the results with tensor pomeron and f_{2R} exchanges (the long-dashed, dash-dotted and dotted lines present the $I\!P_T I\!P_T$, $I\!P_T f_{2R}$, and $f_{2R} f_{2R}$ contributions, respectively), and the violet solid line (3) presents the $f_{2R} f_{2R}$-fusion alone normalized to the integrated cross section from [115].

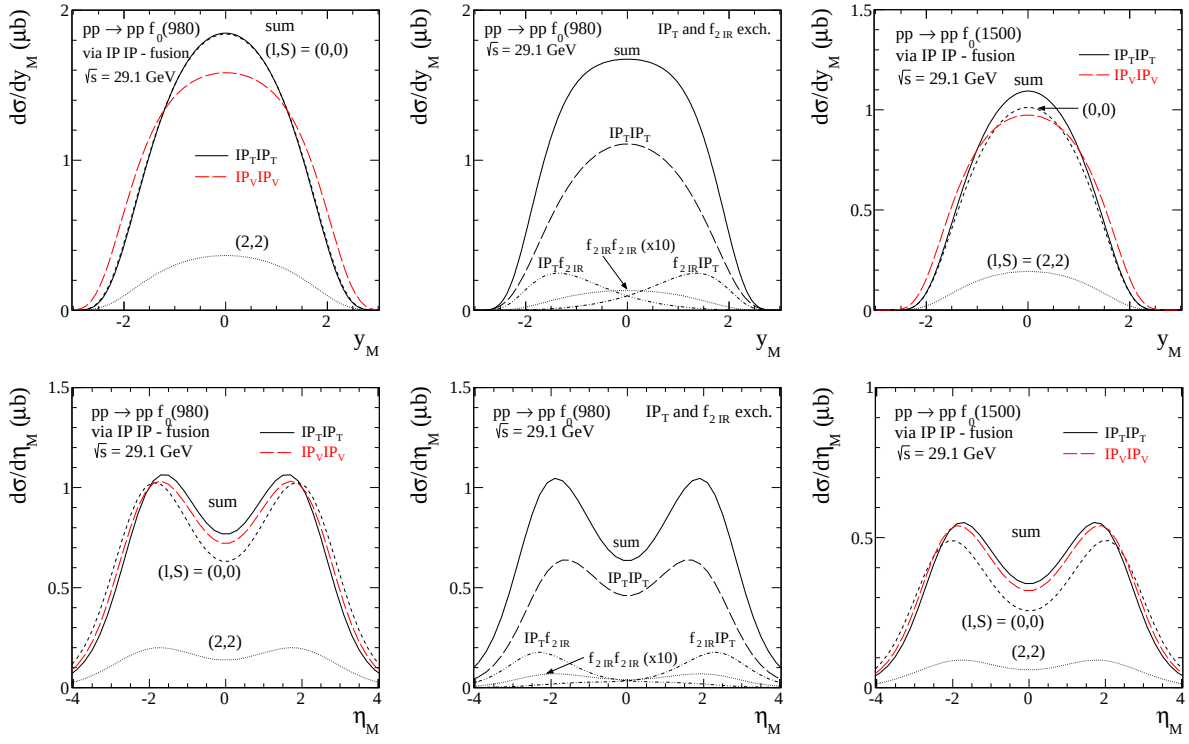

Figure 3.10: Rapidity and pseudorapidity distributions of $f_0(980)$ and $f_0(1500)$ produced by the fusion of two tensor (solid line) and two vector (long-dashed line) pomerons at $\sqrt{s} = 29.1$ GeV. The results have been normalized to the value of the total cross sections given in Table 3.2. For tensorial pomeron the individual contributions of $(l, S) = (0, 0)$ (short-dashed line), $(l, S) = (2, 2)$ (dotted line), and their coherent sum (solid line) are shown. In the center panels we show the results for the $f_0(980)$ meson production included the tensorial f_{2R} contributions.

into our analysis. [4] The corresponding coupling constants were roughly fitted to existing experimental differential distributions (some specific details will be given when discussing differential distributions); see Table 3.4. We recall from the discussion in Section 3.1.2 that for the tensorial

[4] In addition some other 'non-central' mechanisms are possible [5, 9, 10]. One of them is diffractive excitation of $N(1535)$ $J^P = 1/2^-$ which decays into the $p + \eta$ channel with branching fraction of about 50 % [96]. The issue of diffractive excitation of nucleon resonances is so far not well understood and requires further studies.

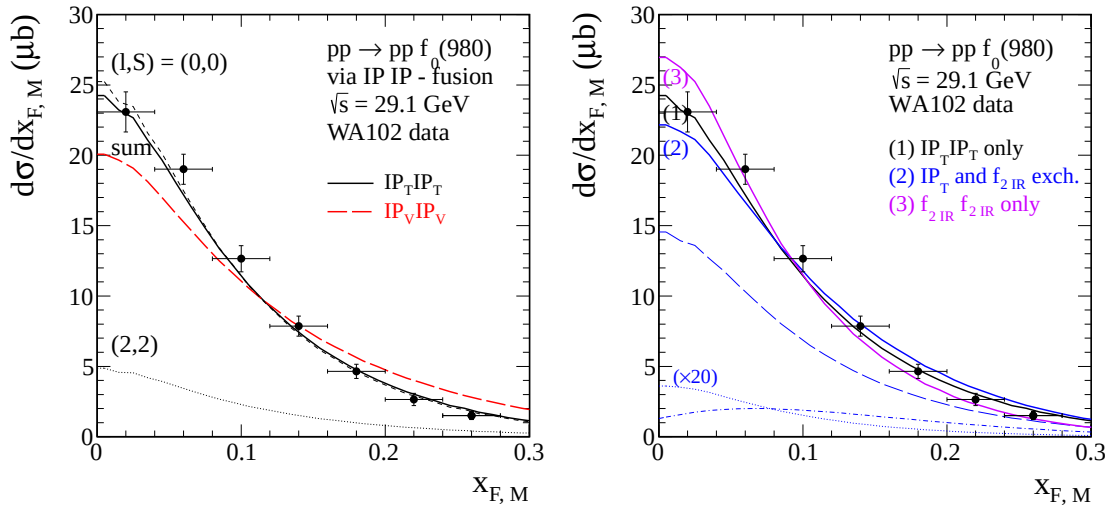

Figure 3.11: The $x_{F,M}$ distribution for the central exclusive $f_0(980)$ meson production at $\sqrt{s} = 29.1$ GeV. The WA102 experimental data points from [229] have been normalized to the values of the total cross section given in Table 3.2. In the left panel we show the results obtained by the fusion of two tensor pomerons. In addition, the individual $(l, S) = (0, 0)$ and $(2, 2)$ contributions denoted by the short-dashed and dotted lines, respectively, are presented. In the right panel the black solid line (1) corresponds to the $I\!P_T I\!P_T$-fusion, the blue solid line (2) to the results with tensor pomeron and f_{2R} exchanges (the long-dashed, dash-dotted and dotted lines represent the $I\!P_T I\!P_T$, $I\!P_T f_{2R}$ and $f_{2R} f_{2R}$ (enlarged by a factor 20) contributions, respectively), and the violet solid line (3) represents the $f_{2R} f_{2R}$-fusion contribution alone normalized to the value of the total cross section given in Table 3.2.

Table 3.4: The values of the pomeron-pomeron-meson $\tilde{M}$ coupling constants of the two models of the pomeron exchanges which are approximately fitted to reproduce the correct normalization, see Table 3.2, and shapes of differential distributions of the WA102 experiment. In addition, the cross sections (in μb) for the individual (l, S) contributions at $\sqrt{s} = 29.1$ GeV are shown.

Meson $\tilde{M}$	Exchanges	$g'_{I\!P I\!P \tilde{M}}$ $(1,1)$ term	$g''_{I\!P I\!P \tilde{M}}$ $(3,3)$ term	σ (μb) at $\sqrt{s} = 29.1$ GeV		
				$(1,1)$	$(3,3)$	total
η	$I\!P_T I\!P_T$, $I\!P_T f_{2R}$, $f_{2R} I\!P_T$, $f_{2R} f_{2R}$	0.8, 2.45, 2.45, 2	1.4, 4.29, 4.29, 3.5	5.05	0.85	3.85
	$I\!P_T I\!P_T$	2	2.25	4.83	0.55	3.85
	$I\!P_V I\!P_V$	8.47	-	3.86	–	–
η'	$I\!P_T I\!P_T$	2.61	1.5	1.86	0.05	1.71
	$I\!P_V I\!P_V$	6.08	-	1.72	–	–

pomeron two $I\!P I\!P \tilde{M}$ couplings, $(l, S) = (1, 1)$ and $(3, 3)$, are possible. For the vectorial pomeron we have only $(l, S) = (1, 1)$. As will be discussed below in addition to pomeron-pomeron fusion the inclusion of secondary reggeons is required for a simultaneous description of $d\sigma/d\phi_{pp}$, $d\sigma/dt$ and $d\sigma/dx_F$ experimental data for the η production.

In Fig.3.13 we present energy dependences of the cross sections for η (panels (a) and (c)) and η' (panels (b) and (d)) meson production. It was argued in Ref. [232] that f_{2R}-pomeron and pomeron-f_{2R} exchanges could be important for both η and η' central production. For comparison, we show the results where f_{2R} exchanges are included for η production. We observe a large interference of different components in the amplitude (the long-dashed line denotes the pomeron-pomeron component, the dash-dotted line – f_{2R}-pomeron (or pomeron-f_{2R}) component, and the dotted line – $f_{2R} f_{2R}$ component). In the diffractive mechanism we use vertex form factor given by Eqs. (B.21) and (B.22). Our results have been normalized to the experimental total cross sections given in Table 3.2 and take into account (see the dash-dotted line in panels (a) and (b)) the limited Feynman-x_F domain $0 \leqslant x_{F,M} \leqslant 0.1$ for the corresponding data points; see [213]. Moreover, at lower energies we can expect large contributions from $\omega\omega$ exchanges due to the large coupling of the ω meson to the nucleon. The dashed bottom and

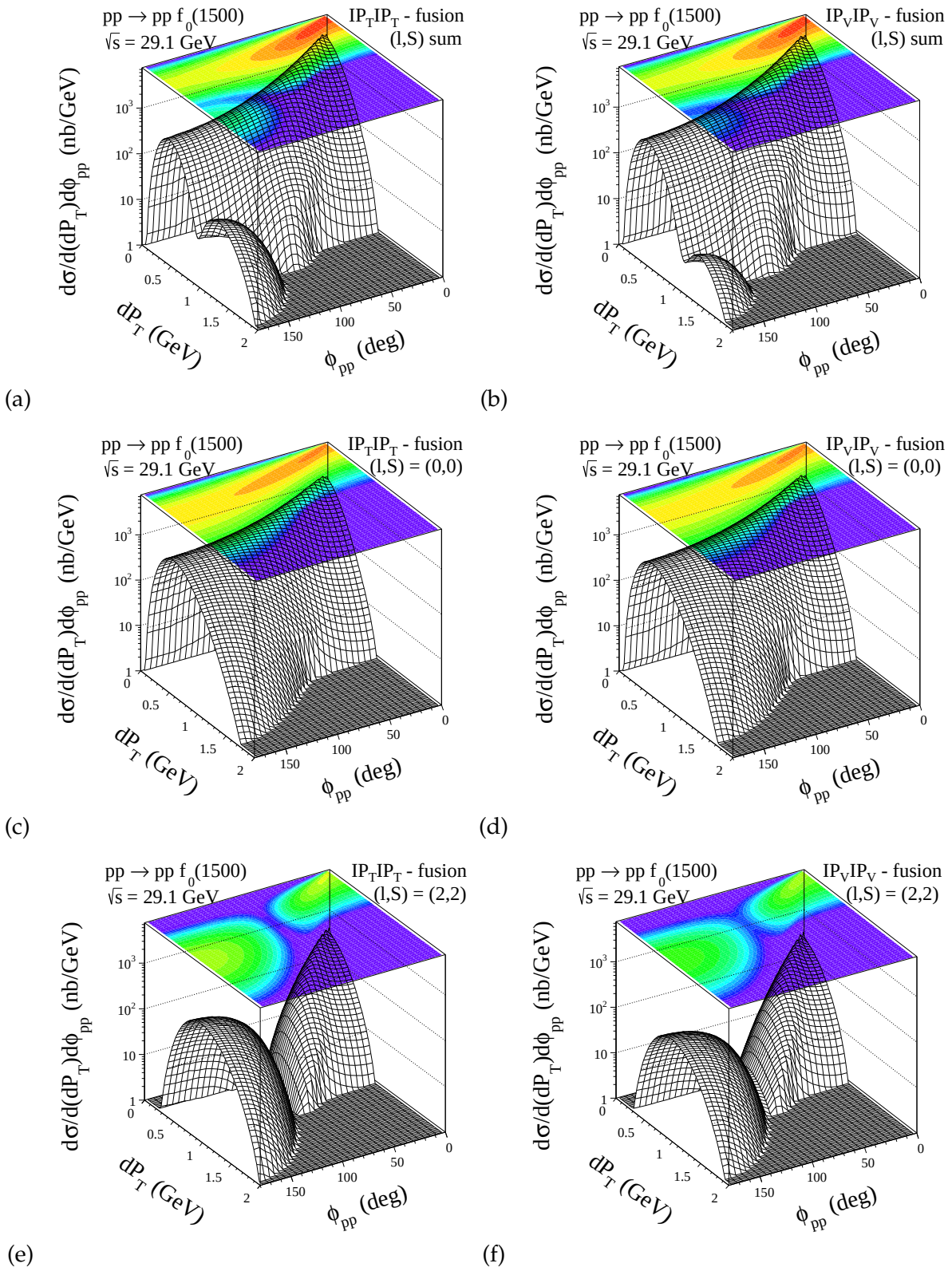

Figure 3.12: Distributions in $(dP_\perp, \phi_{pp})$ for the central exclusive $f_0(1500)$ meson production via the tensorial (left panels) and vectorial (right panels) pomeron exchanges at $\sqrt{s} = 29.1$ GeV. The individual contributions of $(l, S) = (0, 0)$ (panels (c) and (d)) and $(l, S) = (2, 2)$ (panels (e) and (f)) are shown separately.

upper lines at low energies represent the $\omega\omega$-contribution calculated with the monopole (B.24) and exponential (B.25) form factors, respectively. In the case of meson exchanges we use values of the cut-off parameters $\Lambda_E = \Lambda_M = 1.4$ GeV. We have taken rather maximal Λ_E and Λ_M

in order to obtain an upper limit for this contribution. As explained in Section 3.1.2 at higher subsystem squared energies s_{13} and s_{23} the meson exchanges are corrected to obtain the high energy behaviour appropriate for reggeon exchange, cf. Eq. (3.28). In both panels (a) and (b) in Fig. 3.13 the dotted line represents the $\omega_{I\!R}\omega_{I\!R}$-contribution calculated with coupling constant $g_{\omega_{I\!R}\omega_{I\!R}\tilde{M}} = 60$. Due to charge-conjugation invariance the η and η' cannot be produced by ω-pomeron exchange and isospin conservation forbids ρ-pomeron exchange. In the region of small momentum transfer squared the contribution from other processes such as photon-(vector meson) and photon-photon fusion is possible [233], but the cross section is expected to be several orders of magnitude smaller [105, 234] than for the double pomeron processes [5].

In Fig.3.14 we show the cross section as a function of the azimuthal angle ϕ_{pp} between the transverse momentum vectors of the two outgoing protons; see (A.4). The vertex form factor (B.21) was used in calculations. For tensor pomeron the strengths of the $(l, S) = (1, 1)$ and $(3, 3)$ were adjusted to roughly reproduce the azimuthal angle distribution. The contribution of the $(1, 1)$ component alone is not able to describe the azimuthal angular dependence (see panel (b)). For both models the theoretical distributions are somewhat skewed with respect to a simple $\sin^2(\phi_{pp})$ dependence as obtained e.g. from vector-vector-pseudoscalar coupling alone without phase space effects. The small deviation in this case is due to phase space angular dependence. The matrix element squared itself is proportional to $\sin^2(\phi_{pp})$. For comparison, the dash-dotted line in the panel (c) corresponds to $\gamma\gamma$-fusion for the η' production calculated as in [105].

In Fig.3.15 we present distribution in $|t_1|$ and $|t_2|$, which are, of course identical. Therefore we label them by $|t|$. As can be seen from panels (a) and (c) the results for the tensorial exchanges give a better description of t distribution than the vector pomeron exchanges. The t-dependence of η and η' production is very sensitive to the form factor $F_{I\!P I\!P M}(t_1, t_2)$, cf. (B.21), in the pomeron-pomeron-meson vertex.

In Fig.3.16 we present the $d\sigma/dx_F$ distribution. We see that η (panels (a) and (b)) and η' (panels (c) and (d)) meson distributions are peaked at $x_{F,M} \approx 0$, which is consistent with the dominance of the pomeron-pomeron exchange. In the calculations we use the pomeron-pomeron-meson couplings collected in Table 3.4. For the description of the η production in the case of the tensorial pomeron the $f_{2I\!R}$ exchanges in the amplitude were included. In panel (a) the solid line corresponds to the model with tensorial pomeron plus $f_{2I\!R}$ exchanges and the long-dashed line to the model with vectorial pomeron. The enhancement of the η distribution at larger values of $x_{F,M}$ can be explained by significant $f_{2I\!R}$-pomeron and pomeron-$f_{2I\!R}$ exchanges. As can be seen from panel (a) these contributions have maxima at $x_{F,M} \neq 0$. The corresponding couplings constants were fixed to differential distributions of the WA102 Collaboration [213]. In panel (b) we show for the tensorial pomeron the individual contributions to the cross section with $(l, S) = (1, 1)$ (the short-dashed line), $(l, S) = (3, 3)$ (the dotted line), and their coherent sum (the solid line). In panel (c) we show the Feynman-x_F distribution of the η' meson and the theoretical curves for $I\!P_T I\!P_T$ and $I\!P_V I\!P_V$ fusion, respectively. The diffractively scattered outgoing protons are placed at $x_F \approx \pm 1$; see panel (d).

In Fig.3.17 we present distributions in meson transverse momentum $p_{\perp,M}$ and proton transverse momentum $p_{\perp,p}$. As already explained above for η meson production we include in addition tensorial reggeon exchanges. Their individual contributions are shown in the left panels. In addition, we show the individual spin contributions to the cross section with $(l, S) = (1, 1)$ (short-dashed line) and $(l, S) = (3, 3)$ (dotted line). The coherent sum of $(1, 1)$ and $(3, 3)$ tensorial components is shifted with respect to the $(1, 1)$ vectorial component alone.

In Fig.3.18 we present the "glueball variable" $dP_\perp$ distribution. Theoretical predictions of $dP_\perp$ seem to be qualitatively consistent with the WA102 data presented in Table 2 of Ref. [115]. We show results for the mesons of interest to us in Table 3.5. In addition, in Fig.3.18(d), the ratio of production at small $dP_\perp$ to large $dP_\perp$ has been compared with the experimental results taken

[5] In Ref. [209] the authors considered glueballs and η' production in semiclassical theory based on interrupted tunneling (instantons) or QCD sphaleron production and predicted cross section (with the cut $0 \leqslant x_{F,M} \leqslant 0.1$) $\sigma(\eta') \approx 255$ nb in comparison to the 588 ± 63 nb observed empirically [213].

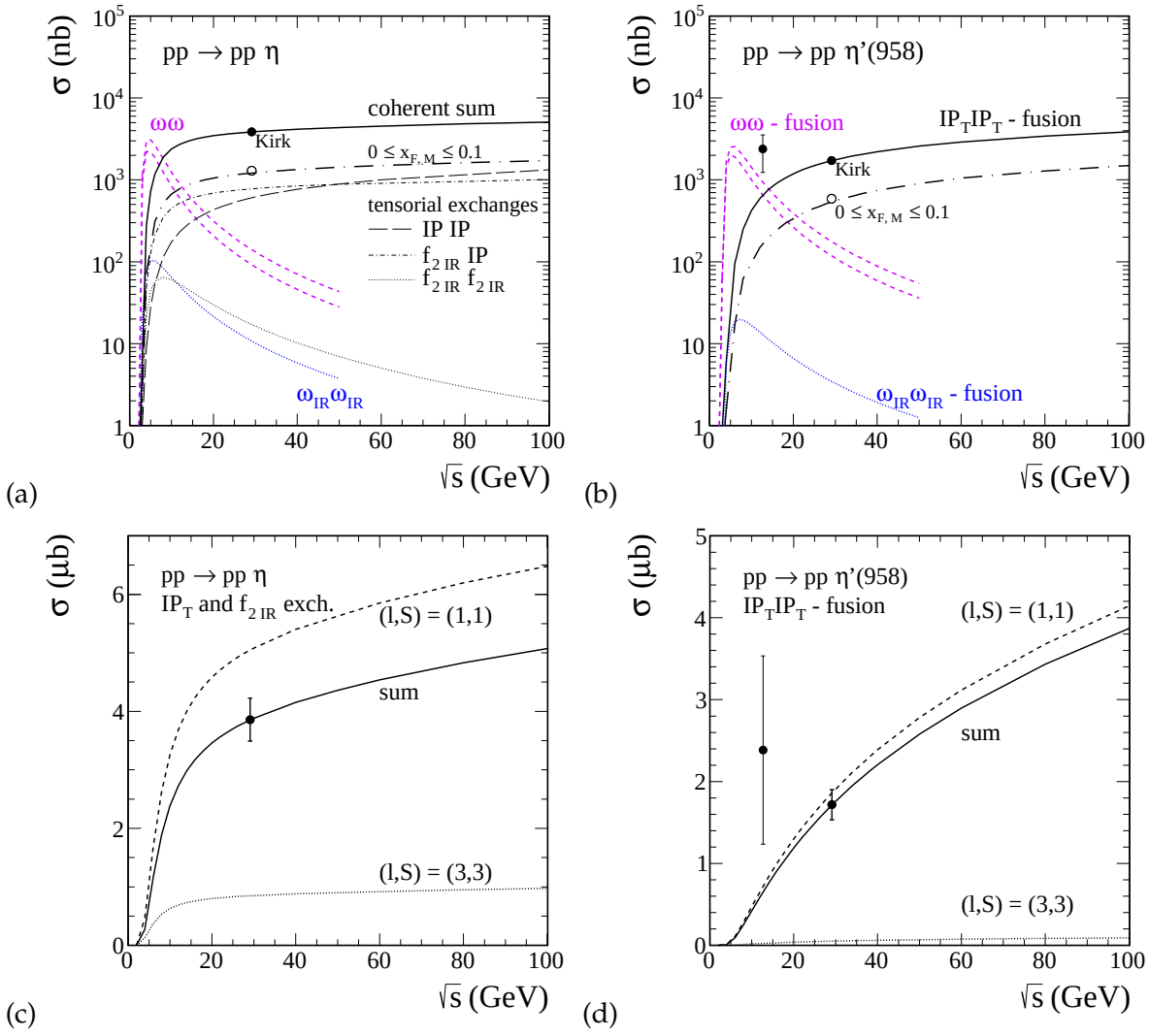

Figure 3.13: Cross section for the $pp \to pp\eta$ (panel a) and $pp \to pp\eta'(958)$ (panel b) reaction as a function of proton-proton center-of-mass energy $\sqrt{s}$. The experimental data are from the WA102 experiment at $\sqrt{s} = 29.1$ GeV; see Table 3.2 obtained from [115], and for the Feynman-x_F interval $0 \leqslant x_{F,M} \leqslant 0.1$ [213]. There is also a data point at $\sqrt{s} = 12.7$ GeV obtained from Table 3.1. The $\omega\omega$-fusion contribution is important only at lower energies while tensorial pomeron fusion contribution dominates at higher energies. In the diffractive mechanism we use vertex form factor (B.21) and the value of coupling constants collected in Table 3.4. For the η meson production the tensorial contributions of $I\!P I\!P$, $f_{2R} I\!P$ ($I\!P f_{2R}$) and $f_{2R} f_{2R}$ exchanges were included. Their coherent sum is shown by the solid line. For the η' meson production the solid line represents the cross section obtained via tensor pomeron exchanges only. For comparison, in the panels (c) and (d), we show the individual contributions to the cross section with $(l, S) = (1, 1)$ (short-dashed line) and $(l, S) = (3, 3)$ (dotted line).

from [115]; see also [90]. It can be observed that scalar mesons which could have a large 'gluonic component' have a large value for this ratio. The fact that $f_0(1370)$ and $f_0(1500)$ have different ϕ_{pp} and $dP_\perp$ dependences confirms that these are not simply J dependent phenomena. This is also true for the $J = 2$ states, where the $f_2(1950)$ has a different ϕ_{pp} dependence compared to the $f_2(1270)$ and $f_2'(1525)$ states; see Fig.5 of [115]. The $dP_\perp$ and ϕ_{pp} effects are in our present work understood as being due to the fact that in general more than one coupling structure, $I\!P I\!P M$ respectively $I\!P I\!P \tilde{M}$, is possible. It remains a challenge for theory to predict these coupling structure from calculations in the framework of QCD.

In Fig.3.19 we show two-dimensional distributions in $(dP_\perp, \phi_{pp})$ for the η (left panels) and $\eta'(958)$ (right panels) meson production in the fusion of two tensor pomerons. In panels (a) and (b) we show the result for (l, S) components added coherently. In panels (c) - (d) and

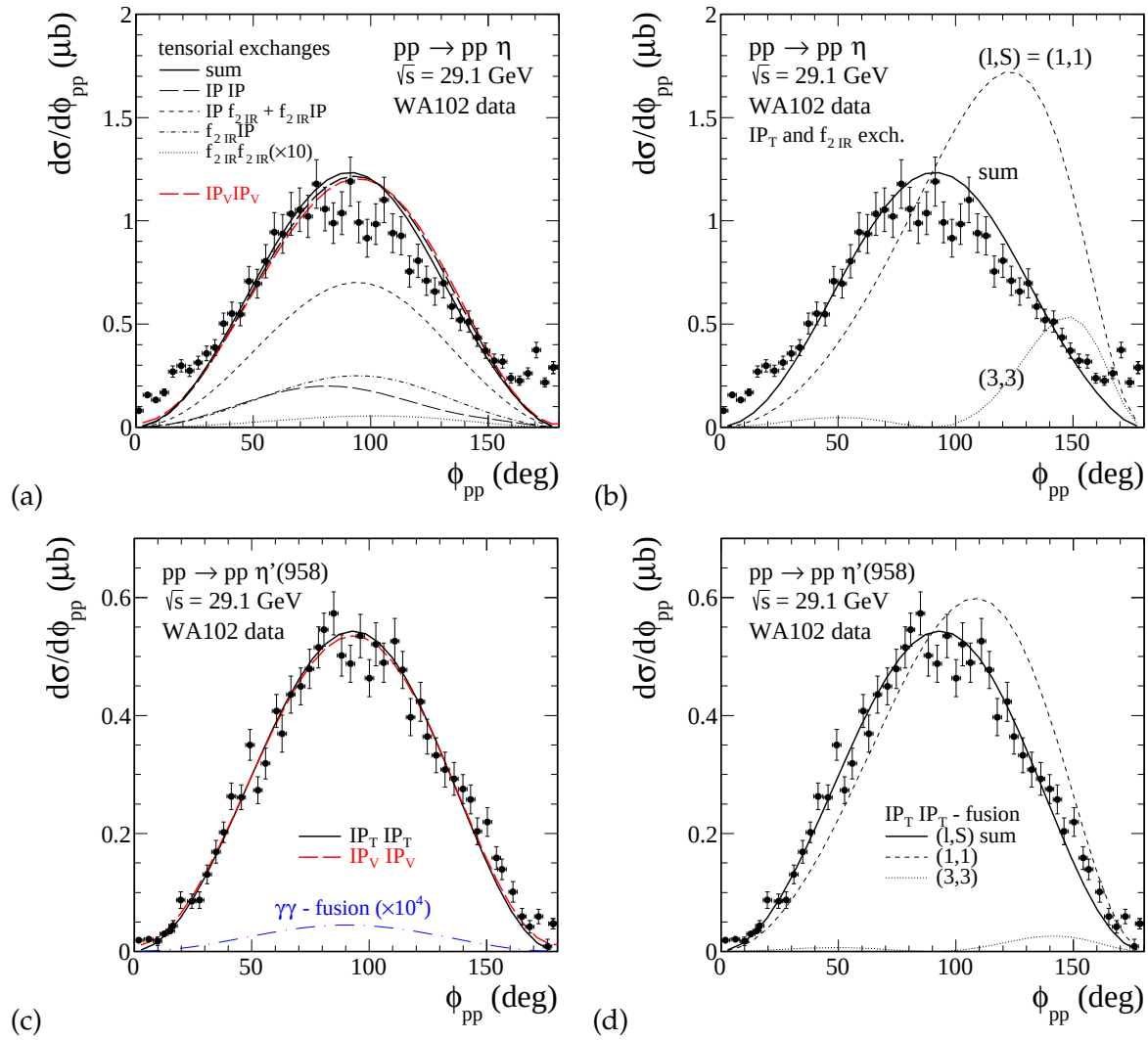

Figure 3.14: Differential cross section $d\sigma/d\phi_{pp}$ for the $pp \to pp\eta$ and $pp \to pp\eta'(958)$ reactions at $\sqrt{s} = 29.1$ GeV. The WA102 experimental data from [213] have been normalized to the values of the total cross sections given in Table 3.2. Panel (a) shows the results for η production. The solid line is the result for the tensorial pomeron including two (l,S) couplings as well as $f_{2R}\mathbb{P}$, $\mathbb{P}f_{2R}$, and $f_{2R}f_{2R}$ exchanges. The red long-dashed line corresponds to vector pomeron exchange only and $(l,S) = (1,1)$ coupling. In panel (b) the two (l,S) contributions from the tensorial pomeron exchanges and their total are shown. In panel (c) we show the results for η' production for the case of tensor and vector pomeron exchanges as well as the $\gamma\gamma$-fusion enlarged by a factor 10^4. Panel (d) shows the results for $\mathbb{P}_T\mathbb{P}_T$-fusion.

(e) - (f) we show the individual spin components for $(l,S) = (1,1)$ and $(3,3)$, respectively. By comparing panels (a) - (f) we infer that the interference effects are rather large.

For completeness, differential distributions in the η or η' rapidity and pseudorapidity are shown in Fig. 3.20. As explained in the figure caption we show results for both tensor (solid line) and vector (long-dashed line) pomerons as well as the individual spin (l,S) contributions for tensorial case. For η production the f_{2R} exchanges in the amplitude were included in addition which modify the y_M and η_M distributions. The dip in the η_M distribution for $|\eta_M| \to 0$ is a kinematic effect; see Appendix A.1.

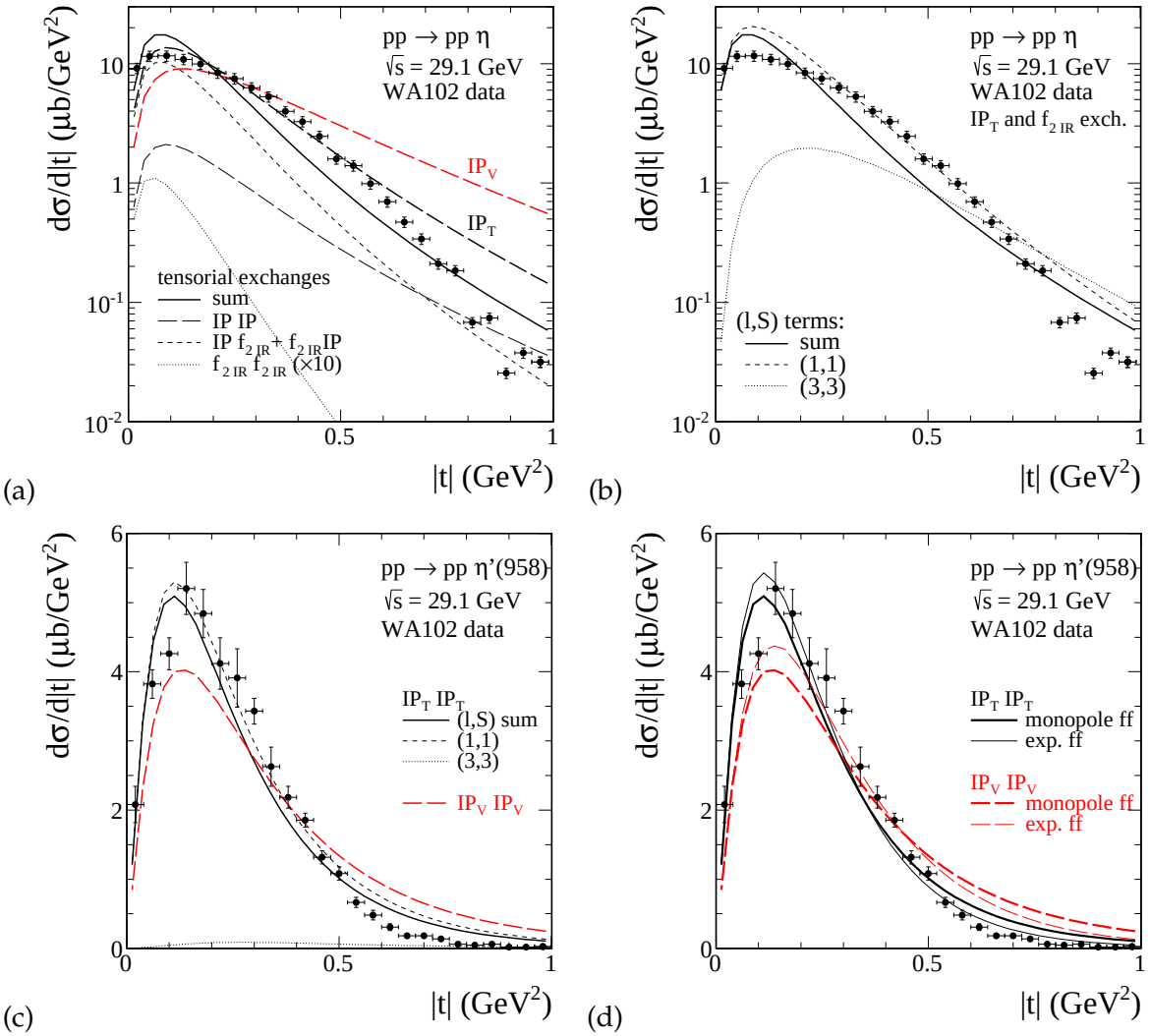

Figure 3.15: Differential cross section $d\sigma/d|t|$ for the $pp \to pp\eta$ (panels (a) and (b)) and $pp \to pp\eta'$ (panels (c) and (d)) reactions at $\sqrt{s} = 29.1$ GeV. The WA102 experimental distributions from [213] have been normalized to the values of the total cross sections given in Table 3.2. The solid line corresponds to the model with tensorial pomeron while the dashed line to the model with vectorial pomeron. For η production the f_{2R} exchanges were included in addition. In the present calculations we use vertex form factor given by Eqs. (B.21) and (B.22). For comparison, in panel (d), we also show the results for exponential form factor (B.23) and for $\Lambda_E^2 = 0.7$ GeV^2.

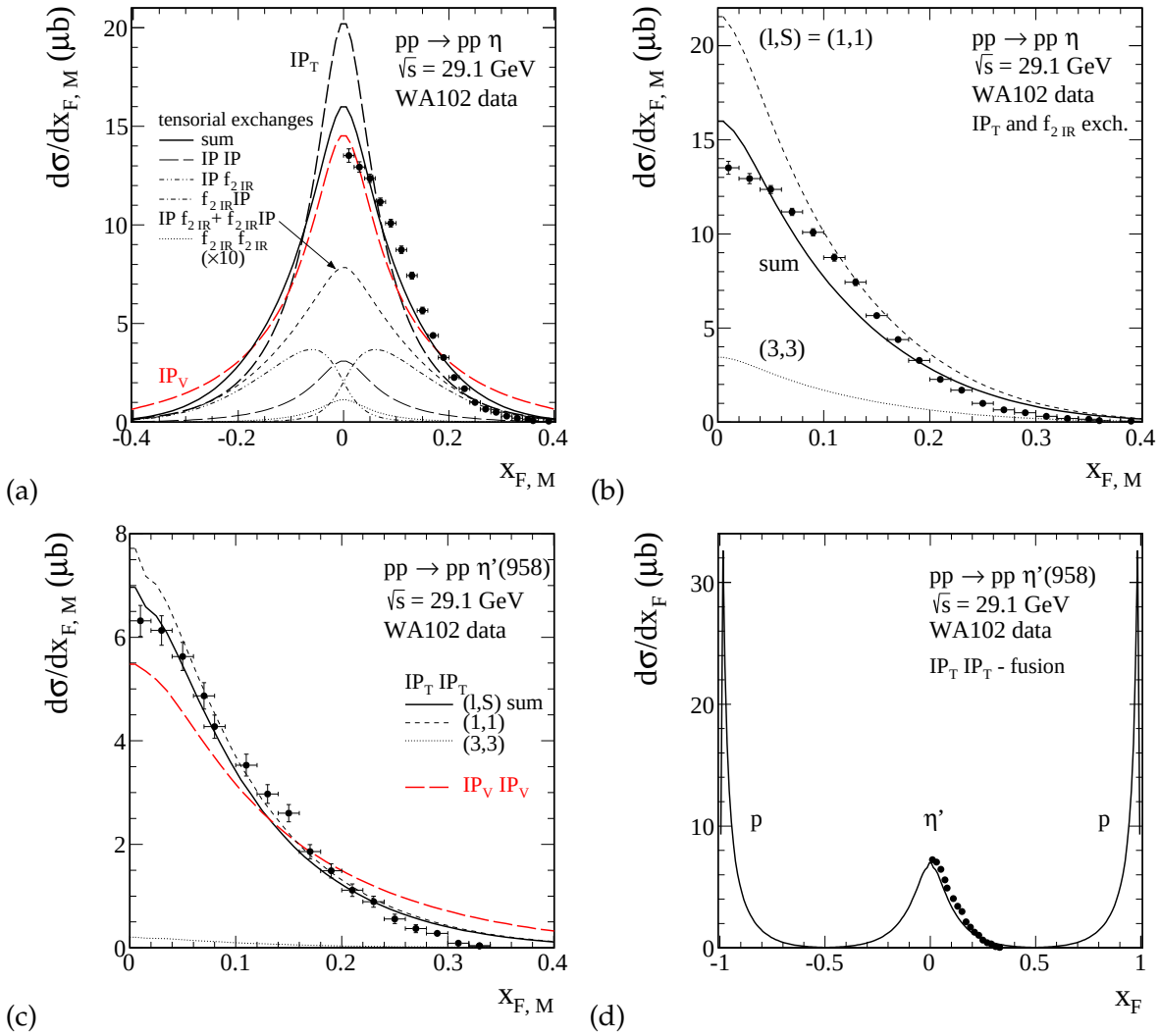

Figure 3.16: Differential cross section $d\sigma/dx_{F,M}$ for the $pp \to pp\eta$ (panels (a) and (b)) and $pp \to pp\eta'$ (panels (c) and (d)) reactions at $\sqrt{s} = 29.1$ GeV. The WA102 experimental data [213] are shown for comparison and have been normalized to the values of the total cross sections given in Table 3.2. In the present calculations we use vertex form factor (B.21) and two model of pomeron exchanges. In panel (a) the results for the tensorial pomeron and f_{2R} exchanges are shown; the pomeron-pomeron component peaks at $x_{F,M} = 0$ (the long-dashed line), the pomeron-f_{2R} (f_{2R}-pomeron) peaks at backward (forward) $x_{F,M}$, respectively, and the coherent sum of pomeron-f_{2R} and f_{2R}-pomeron component effectively dominates in the central region of $x_{F,M}$ (the short-dashed line). In panels (b) and (c) we show the individual contributions to the cross section with $(l,S) = (1,1)$ (the short-dashed line), $(3,3)$ (the dotted line), and their coherent sum (the solid line). The long-dashed line in panel (c) corresponds to the model with vectorial pomeron. In panel (d) the x_F distributions for η' (at $x_F = 0$) and for the protons (at $x_F \to \pm 1$) are shown for the $I\!P_T I\!P_T$ fusion.

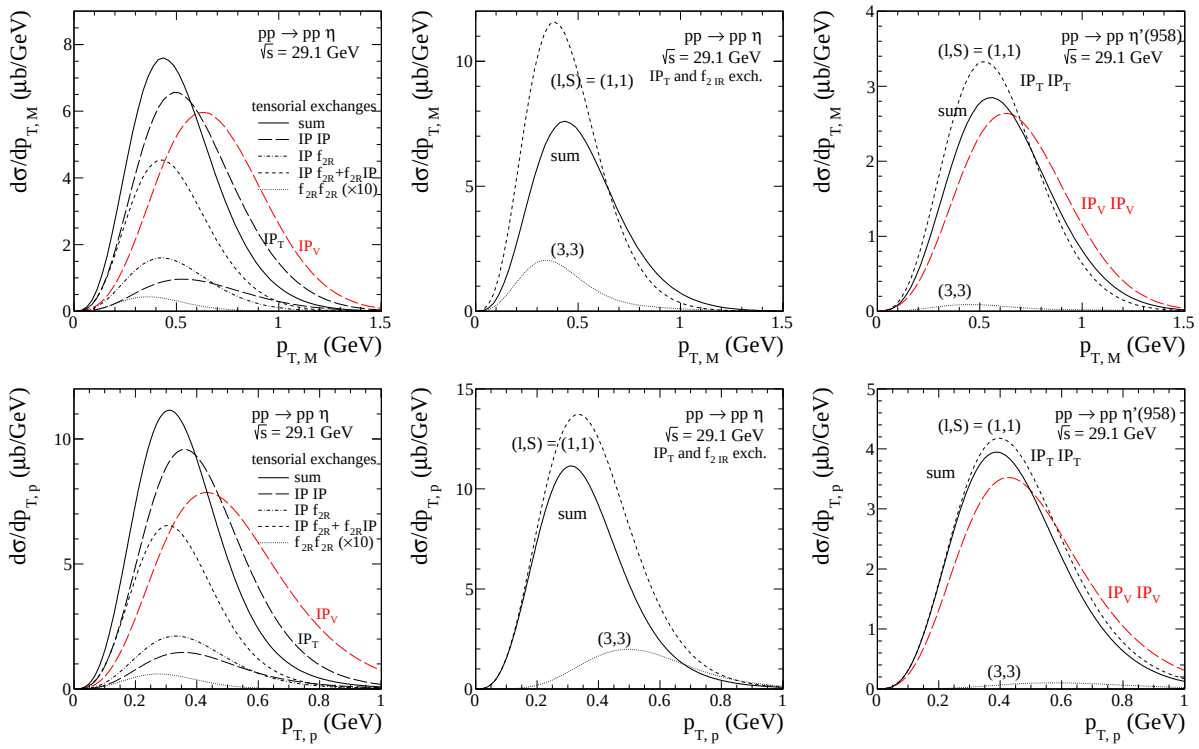

Figure 3.17: Differential cross sections $d\sigma/dp_{\perp,M}$ and $d\sigma/dp_{\perp,p}$ (the forward proton p_1) for the central exclusive η and η' meson production at $\sqrt{s} = 29.1$ GeV. The solid line corresponds to the model with tensorial pomeron while the dashed line to the model with vectorial pomeron. For η production the f_{2R} exchanges in the amplitude were included in addition as discussed in the text. We show for the tensorial case also the individual contributions to the cross section with $(l,S) = (1,1)$ (short-dashed line) and $(l,S) = (3,3)$ (dotted line).

Table 3.5: Results of meson production as a function of $dP_\perp$ expressed as a percentage of its total contribution at the WA102 collision energy $\sqrt{s} = 29.1$ GeV. The numbers in parentheses are obtained for second parameter set of (l,S) components, see Table 3.3, to describe the blue circle points in Fig.3.5 and 3.6. In addition, the ratios of $\frac{d\sigma/d(dP_\perp \leqslant 0.2\text{ GeV})}{d\sigma/d(dP_\perp \geqslant 0.5\text{ GeV})}$ are given. The experimental numbers are from Table 2 of Ref. [115].

Meson	Exchanges	$dP_\perp \leqslant 0.2$ GeV	$0.2 \leqslant dP_\perp \leqslant 0.5$ GeV	$dP_\perp \geqslant 0.5$ GeV	Ratio
η	$I\!P_T$ and f_{2R}	3.0	46.8	50.1	0.06
	$I\!P_T I\!P_T$	1.8	33.4	64.8	0.03
	$I\!P_V I\!P_V$	1.1	21.0	77.8	0.01
	exp.	6 ± 2	34 ± 2	60 ± 3	0.10 ± 0.03
η'	$I\!P_T I\!P_T$	1.4	28.3	70.4	0.02
	$I\!P_V I\!P_V$	1.2	22.1	76.7	0.02
	exp.	3 ± 2	32 ± 2	64 ± 3	0.05 ± 0.03
$f_0(980)$	$I\!P_T$ and f_{2R}	25.3	59.2	15.2	1.67
	$I\!P_T I\!P_T$	22.7 (23.9)	57.9 (57.0)	19.3 (19.1)	1.18 (1.25)
	$I\!P_V I\!P_V$	19.3 (21.6)	54.9 (56.4)	25.9 (21.9)	0.74 (0.99)
	exp.	23 ± 2	51 ± 2	26 ± 3	0.88 ± 0.12
$f_0(1370)$	$I\!P_T I\!P_T$	15.5	49.0	35.5	0.44
	$I\!P_V I\!P_V$	15.2	48.5	36.3	0.42
	exp.	18 ± 4	32 ± 2	50 ± 3	0.36 ± 0.08
$f_0(1500)$	$I\!P_T I\!P_T$	22.5 (23.7)	57.8 (54.3)	19.7 (22.0)	1.15 (1.07)
	$I\!P_V I\!P_V$	20.4 (22.4)	56.0 (54.9)	23.6 (22.7)	0.86 (0.99)
	exp.	24 ± 2	54 ± 3	22 ± 4	1.05 ± 0.18

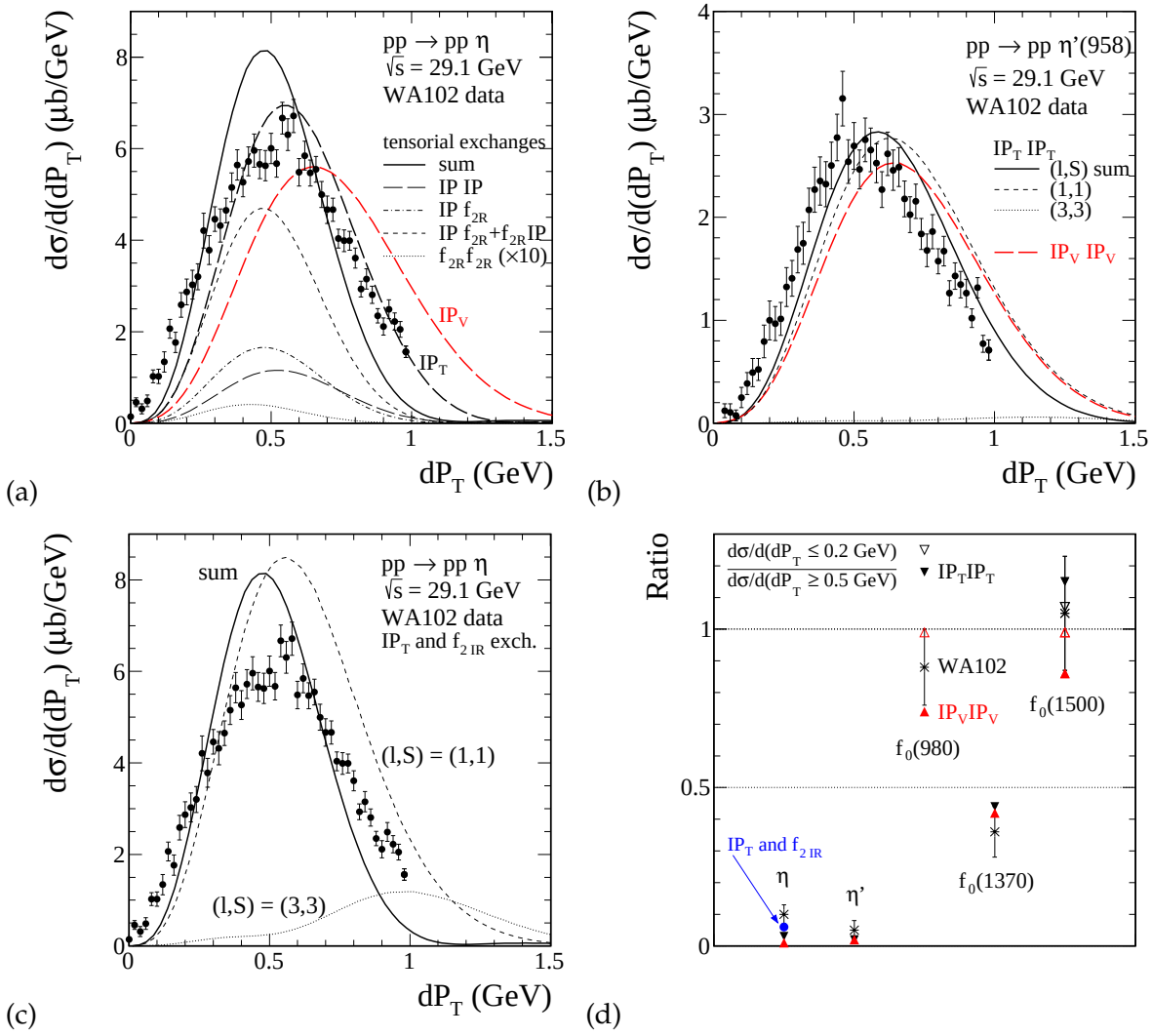

Figure 3.18: Differential cross section $d\sigma/d(dP_\perp)$ for the central exclusive η (panels (a) and (c)) and η' (panel (b)) mesons production at $\sqrt{s} = 29.1$ GeV. The WA102 experimental distributions from [213] have been normalized to the values of the total cross sections from Table 3.2. Results for the tensorial and vectorial pomeron models are presented. For η production the f_{2R} exchanges in the amplitude were included in addition. The (l, S) contributions to the differential cross sections are also shown. Panel (d) shows the ratio of production at small $dP_\perp$ to large $dP_\perp$ for each pseudoscalar and scalar meson discussed here and collected in Table 3.5. Experimental results for the ratio are taken from Table 2 of Ref. [115]. For the $f_0(980)$ and $f_0(1500)$ meson production we show results obtained for the two sets of (l, S) contributions fitted to the experimental azimuthal angular correlations data shown in Fig.3.5 and 3.6. For the $f_0(980)$ and $f_0(1500)$ the filled points correspond to $(g'_{P_TP_TM}, g''_{P_TP_TM}) = (0.788, 4)$ and $(1.22, 6)$, the open points to $(g'_{P_TP_TM}, g''_{P_TP_TM}) = (0.75, 5.5)$ and $(1, 10)$, respectively, see Table 3.3.

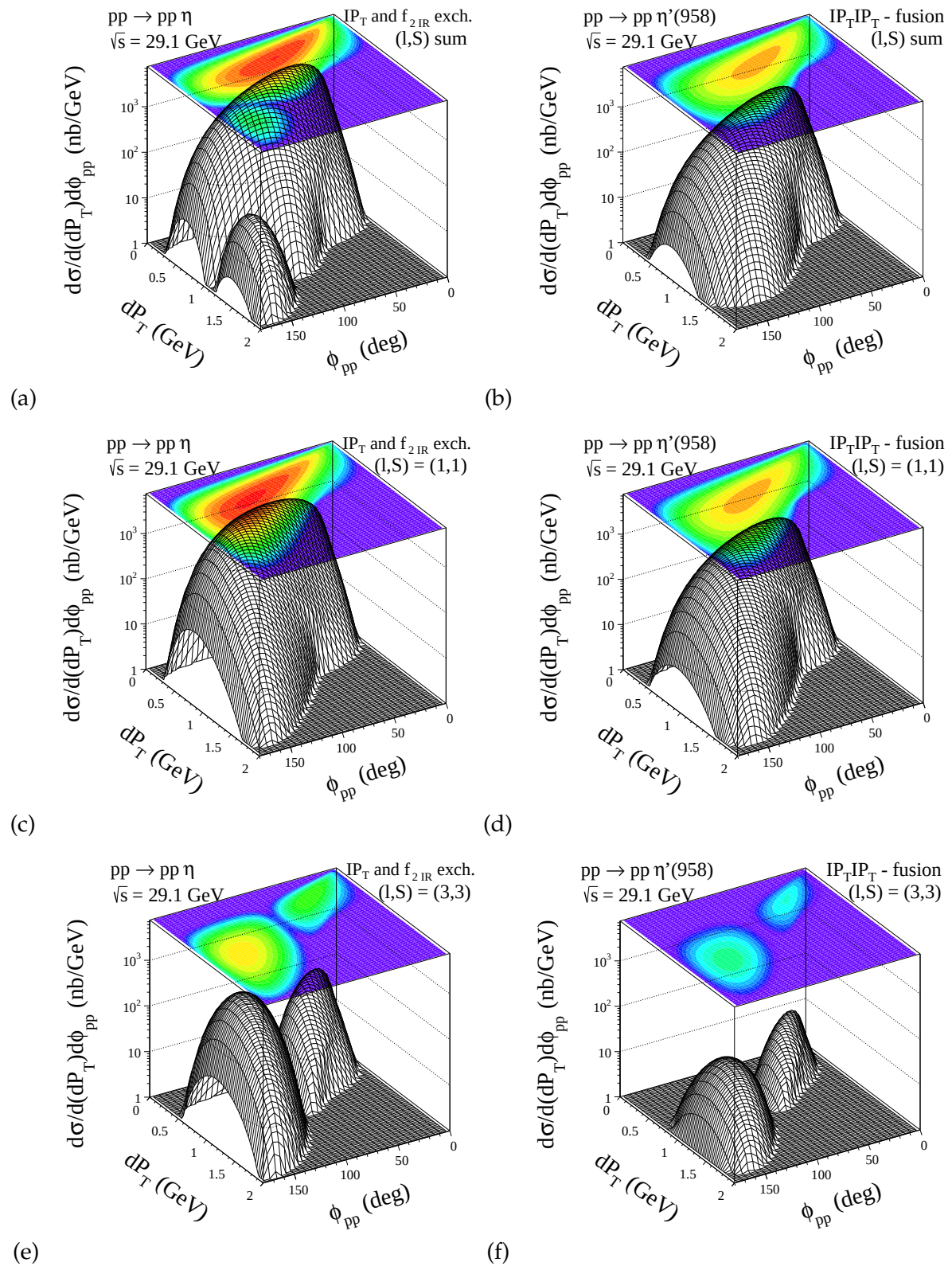

Figure 3.19: Distributions in $(dP_\perp, \phi_{pp})$ for the η (left panels) and $\eta'(958)$ (right panels) meson production at $\sqrt{s} = 29.1$ GeV, Results for η meson correspond to the model with the tensor pomeron and f_2-reggeon exchanges while η' meson production to the model with tensorial pomeron only. The individual contributions of $(l, S) = (1, 1)$ (panels (c) and (d)) and $(l, S) = (3, 3)$ (panels (e) and (f)) are shown separately.

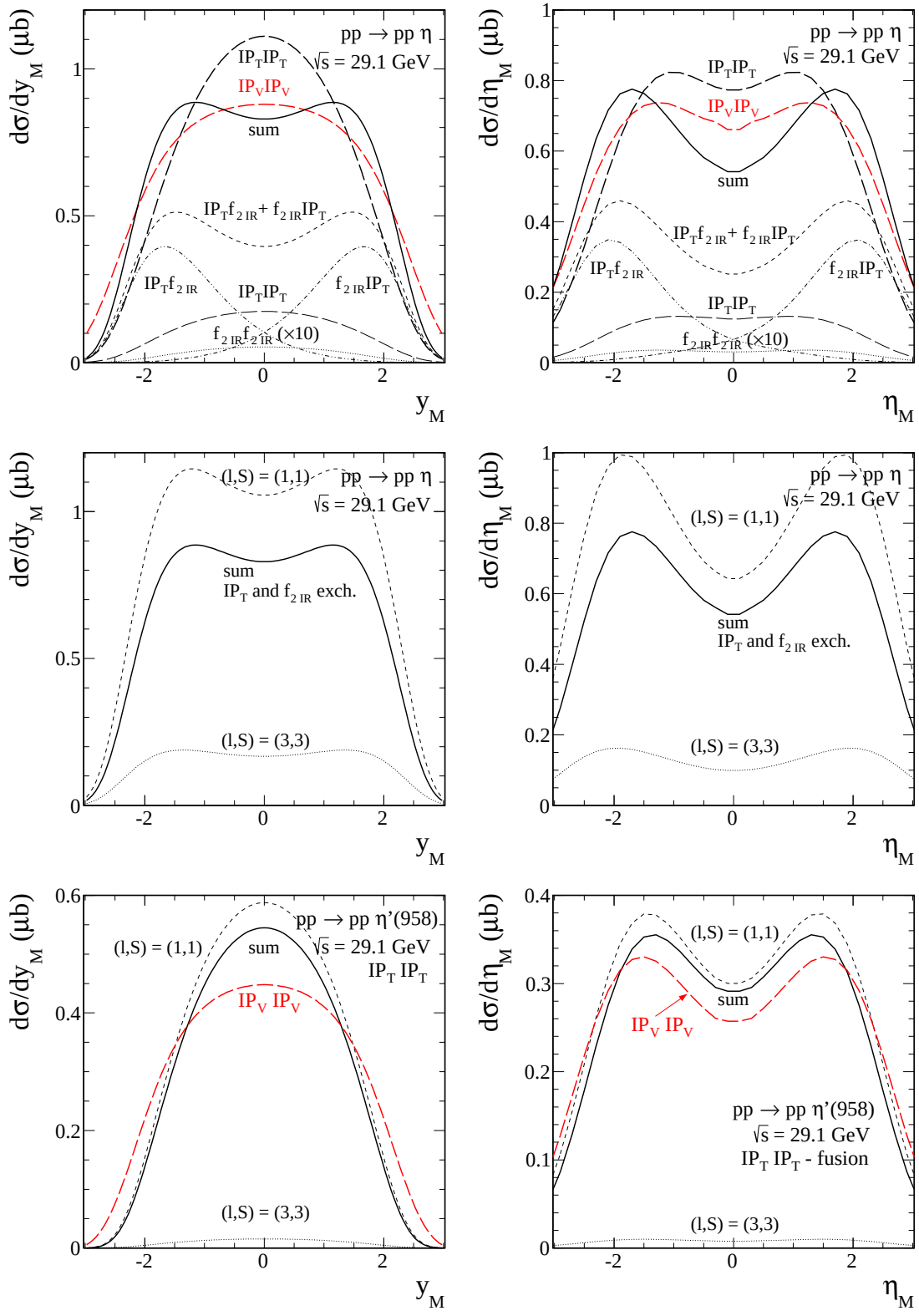

Figure 3.20: Differential cross section $d\sigma/dy_M$ and $d\sigma/d\eta_M$ for the η and η' production at $\sqrt{s} = 29.1$ GeV. The solid line corresponds to the model with tensorial pomeron while the long-dashed line to the model with vectorial pomeron. The different lines correspond to the situation when all or only some components of the pomeron and f_{2R} exchanges in the amplitude are included (the pomeron-pomeron component dominates at midrapidities of η and the pomeron-reggeon (reggeon-pomeron) peaks at backward (forward) rapidities of η, respectively).

3.4 Conclusions

We have analysed proton-proton collisions with the exclusive central production of scalar and pseudoscalar mesons. We have presented the predictions of two different models of the soft pomeron. The first one is the commonly used model with vectorial pomeron which is, however, difficult to be supported from a theoretical point of view. The second one is a recently proposed model of tensorial pomeron, which, in our opinion, has better theoretical foundations. We have presented formulae for corresponding pomeron-pomeron-meson vertices and amplitudes for the $pp \to pMp$ reaction. In general, different couplings with different orbital angular momentum and spin of two "pomeron particles" are possible. In most cases one has to add coherently amplitudes for two couplings. The corresponding coupling constants are not known and have been fitted to existing experimental data.

We have performed calculations of several differential distributions. We wish to emphasize that the tensorial pomeron can, at least, equally well describe experimental data on the exclusive meson production discussed here as the less theoretically justified vectorial pomeron frequently used in the literature. This has been illustrated for the production of several scalar and pseudoscalar mesons. The existing low-energy experimental data do not allow to clearly distinguish between the two models as the presence of subleading reggeon exchanges is at low energies very probable for many reactions. This seems to be the case for the η meson production. In these cases we have included in our analysis also exchanges of subleading trajectories which improve the agreement with experimental data. Production of η' meson seems to be less affected by contributions from subleading exchanges.

For the resonances decaying e.g. into the $\pi\pi$ channel an interference of the resonance signals with the two-pion continuum has to be included in addition. This requires a consistent model of the resonances and the non-resonant background. It would clearly be interesting to extend the studies of central meson production in diffractive processes to higher energies, where the dominance of the pomeron exchange can be better justified. Furthermore, absorption effects are frequently taken into account by simply multiplying cross sections with a gap survival factor. But absorption effects may also change the shapes of t_1/t_2, ϕ_{pp}, etc. distributions. The deviation from "bare" distributions probably is more significant at high energies where the absorptive corrections should be more important.

To summarise: our study of scalar and pseudoscalar meson production certainly shows the potential of these reactions for testing the nature of the soft pomeron. Pseudoscalar meson production could be of particular interest in this respect since there the distribution in the azimuthal angle ϕ_{pp} between the two outgoing protons may contain, for the tensorial pomeron, a term which is not possible for the vectorial pomeron; see the discussion after (3.15) and after (3.20) in Section 3.1.2. Clearly, our study can be extended to the central exclusive production of other mesons like the $f_2(1270)$ meson. Our main aim in these studies was to provide detailed models for central meson production, for both the tensorial and the vectorial pomeron ansatz, where all measurable distributions of the particles in the final state can be calculated. The models contain only a few free coupling parameters to be determined by experiment. The hope is, of course, that future experiments will be able to select soft pomeron model. In any case, our models should provide good "targets" for experimentalists to shoot at. Supposing that only one model survives the experimental tests we have then the theoretical challenge of deriving the corresponding $\mathbb{P}\mathbb{P}M$ coupling constants from QCD.

Future experimental data on exclusive meson production at high energies should thus provide good information on the spin structure of the pomeron and on its couplings to the nucleon and the mesons. On the other hand, the low energy data could help in understanding the role of subleading trajectories. Several experimental groups, e.g. COMPASS [153–155], STAR [158], CDF [159–161] (see for more information [176]), ALICE [162], ATLAS [7] have potential to make very significant contributions to this program aimed at understanding the spin structure of the soft pomeron.

Chapter 4

Exclusive Diffractive Bremsstrahlung at High Energies

It was realized over the last decade that the measurement of forward particles can be an interesting and useful supplement to the multipurpose LHC detectors for central particles detection (ATLAS/CMS) and for proton tagging (ALFA/TOTEM) [199, 235]. Here we consider processes

$$h_1(p_a)h_2(p_b) \to h_1(p_1)h_2(p_2) + X(p_3)\,, \tag{4.1}$$

where X represents a very forward system in the final state (e.g. π^0, ω, γ, n) which could be measured with the help of Zero Degree Calorimeters (ZDCs). The ZDCs are installed at about 140 meters on each side of the interaction region. They will measure the spectra of very forward photons, neutrons and π^0 mesons radiated off the initial and final state protons in the pseudorapidity region $|\eta| > 8.5$ at CMS [236], $|\eta| > 8.3$ at ATLAS [237], and $|\eta| > 6$ at RHIC [238]. The main effort concentrated on the design and construction of forward proton detectors [239]. Furthermore, the proposed Forward Shower Counters, to detect and trigger on rapidity gaps in diffractive events, would improve the measurements at the LHC significantly [240]. In addition to a measurement of the elastic pp cross section the bremsstrahlung photons could allow for the evaluation of the total pp cross section, luminosity and relative alignment of the ZDCs and of the Roman Pot detectors.

4.1 Exclusive π^0 meson production

The exclusive process $pp \to pp\pi^0$ was measured in detail only near to the pion threshold at the IUCF (Bloomington) [241, 242], CELSIUS (Uppsala) [243–245] and the COSY (Jülich) [246]. The total cross section for single pion production grows from threshold to about 10 μb at the c.m. energy $\sqrt{s} \approx 3$ GeV. Although only a few partial waves are involved close to threshold, the theoretical description is not easy (see e.g. [247–249] and references therein). For a summary of close-to-threshold meson production experiments in hadronic interactions see [250].

What happens when the energy increases? In the range of center-of-mass energies $\sqrt{s} = 3 - 10$ GeV the nucleon resonances can be excited via meson exchange processes. Evidence of proton excitation can be observed in the $p\pi^0$ mass spectrum (Δ^+ or N^{*+}). A nice summary of the intermediate energy data for $pp \to pp\pi^0$ can be found in Ref. [251]. In this region of energy the corresponding cross section systematically decreases which is consistent with the meson exchange picture. When energy increases further the role of many of the nucleon resonances diminishes and the mechanism becomes simpler.

In Refs [115, 213] a study of pseudoscalar mesons produced centrally by the CERN-WA102 Collaboration at $\sqrt{s} = 29.1$ GeV was performed. The results show that the η and η' mesons appear to have a similar production mechanism which considerably differs from that for

the π^0 production [213]. To our knowledge this was never explained theoretically. The WA102 Collaboration concentrated on very central production of mesons and therefore measured protons with large Feynman x_F (A.16). This condition eliminates contribution of the diffractive mechanisms discussed here. Reactions of this type $pp \to pMp$ are expected to be mediated by double exchange processes, with a mixture of pomeron-pomeron, reggeon-pomeron, and reggeon-reggeon exchanges. For instance, the η and η' mesons are produced dominantly by double pomeron exchange (see [13] and references therein). For the central exclusive π^0 production at intermediate energies the ρ-ω exchange may be the dominant mechanism. The ρ-a_2 exchange could be another potential candidate. The validity of these exchanges could be verified experimentally by the COMPASS Collaboration (see [153]).

In this Section we wish to concentrate on the production of single neutral pions in the $pp \to pp\pi^0$ reaction at large energies (RHIC, LHC). We hope that this process could be measured, at least in some corners of the phase space, at the LHC. We shall refer also to $pp \to p(n\pi^+)$ and $np \to (p\pi^-)p$ reactions measured at lower energies at Intersecting Storage Rings (ISR) and Fermilab in the 1970's [252–257] (for a nice review we refer to [126]). The mechanism of these reactions is closely related to the $pp \to pp\pi^0$ reaction discussed here and will be therefore a good reference point for our calculation. As discussed in the past, the dominant hadronic bremsstrahlung-type mechanism is the Drell-Hiida-Deck (DHD) mechanism for diffractive production of πN final states in NN collisions [258, 259]; for a review, see e.g. [125, 126].

The π^0's can be also produced by $\gamma\gamma$, $\gamma\omega$ and $\omega\gamma$ exchanges, but not by $\gamma I\!P$-fusion since the π^0 meson has positive C-parity. Unlike pomeron which corresponds to the vacuum quantum numbers and so to the positive charge conjugation the odderon ($\mathcal{O}$), the hypothetical counterpart of the pomeron ($I\!P$), is characterised by odd charge parity $C = 1$ (and $I = 0$), i.e. it carries the same quantum numbers as the ω Regge pole. Therefore, the $\gamma\mathcal{O}$ and $\mathcal{O}\gamma$ exchanges are also possible, however, the soft odderon couples very weakly to the nucleon. In Refs. [234, 260] the authors discussed some results of exclusive pseudoscalar meson production in high energy ep scattering. It was shown in [260, 261] (see also [262]) that odderon exchange leads to a much larger inelastic than elastic π^0 production cross section. As shown in Ref. [260], the photon exchange is larger than the odderon exchange only at very small transverse momenta of π^0. Here we shall consider the odderon contribution in proton-proton collisions using a simple phenomenological approach for the odderon exchange. We shall discuss how it can be separated from the contribution of photon-photon fusion.

4.1.1 π^0-bremsstrahlung mechanisms

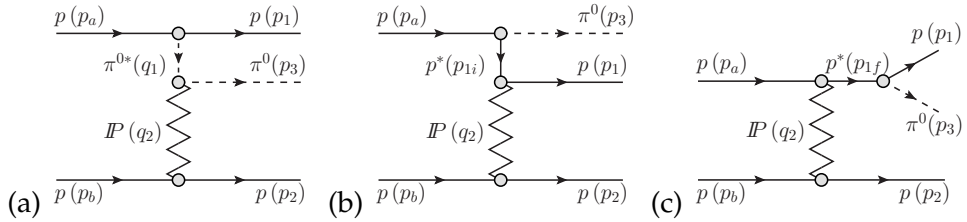

Figure 4.1: Diagrams of the π^0-bremsstrahlung amplitudes driven by the pomeron exchange in proton-proton collisions: (a) pion exchange, (b) proton exchange, and (c) direct production. The direct-channel p^* in (c) is an off-shell proton, not a proton resonance. Some kinematical variables are shown in addition.

The exclusive π^0 meson production mechanism is similar to exclusive production of the ω meson [5] and γ [10]. The diffractive π^0-bremsstrahlung mechanisms are driven by the pomeron/reggeon ($I\!P/I\!R$) exchanges as depicted in Fig.4.1. At high c.m. energies $\sqrt{s}$ the dominant contribution comes from the pomeron exchange. There are two processes when the π^0 meson emitted by one of the protons interacts with the second proton (diffractive π^0 rescatter-

ing), [1] as depicted in Fig.4.1(a), and four processes in which protons interact and the π^0 emission may occur, see Figs.4.1(b) and 4.1(c). In general, the amplitudes of these processes may interfere but in practise the interference is negligible as the two processes are well separated in rapidity as will be discussed in Section 4.2. The Born amplitudes for these processes, see Fig.4.1, can be written as

$$\begin{aligned}
\mathcal{M}^{(\pi-\text{exchange})}_{\lambda_a\lambda_b\to\lambda_1\lambda_2\pi^0} &= \bar{u}(p_1,\lambda_1) i\gamma_5 u(p_a,\lambda_a)\, S_\pi(t_1,s_{13})\, g_{\pi NN}\, F_{\pi^* NN}(t_1) F_{I\!P\pi^*\pi}(t_1) \\
&\quad \times A^{\pi N}_{I\!P}(s_{23},t_2)\,/(2s_{23})(q_1+p_3)_\mu\, \bar{u}(p_2,\lambda_2)\gamma^\mu u(p_b,\lambda_b)\,, \qquad (4.2)\\
\mathcal{M}^{(p-\text{exchange})}_{\lambda_a\lambda_b\to\lambda_1\lambda_2\pi^0} &= g_{\pi NN}\, \bar{u}(p_1,\lambda_1)\gamma^\mu S_N(p^2_{1i}) i\gamma_5 u(p_a,\lambda_a)\, F_{\pi NN^*}(p^2_{1i})\, F_{I\!PN^*N}(p^2_{1i}) \\
&\quad \times A^{NN}_{I\!P}(s_{12},t_2)\,/(2s_{12})\, \bar{u}(p_2,\lambda_2)\gamma_\mu u(p_b,\lambda_b)\,, \qquad (4.3)\\
\mathcal{M}^{(\text{direct production})}_{\lambda_a\lambda_b\to\lambda_1\lambda_2\pi^0} &= g_{\pi NN}\, \bar{u}(p_1,\lambda_1) i\gamma_5 S_N(p^2_{1f})\gamma^\mu u(p_a,\lambda_a)\, F_{\pi N^* N}(p^2_{1f})\, F_{I\!PNN^*}(p^2_{1f}) \\
&\quad \times A^{NN}_{I\!P}(s,t_2)\,/(2s)\, \bar{u}(p_2,\lambda_2)\gamma_\mu u(p_b,\lambda_b)\,, \qquad (4.4)
\end{aligned}$$

where $u(p,\lambda)$, $\bar{u}(p',\lambda') = u^+(p',\lambda')\gamma^0$ are the Dirac spinors of the incident and outgoing protons with the four-momentum p and the helicities λ; normalized as $\bar{u}(p')u(p) = 2m_p$. The factors $1/(2s_{ij})$ or $1/(2s)$ appear here as a consequence of using spinors. The four-momenta squared of intermediate particles are defined in Fig.4.1 and $p^2_{1i,2i} = (p_{a,b} - p_3)^2$, $p^2_{1f,2f} = (p_{1,2} + p_3)^2$, $q^2_{1,2} = (p_{a,b} - p_{1,2})^2$, the four-momentum transfers along the pomeron line $t_{1,2} = q^2_{1,2}$ and $s_{ij} = (p_i + p_j)^2$ are squared invariant masses of the (i,j) system. In the present study we use a generalized pion propagator $S_\pi(t_i, s_{ik})$ (see 2.32) at an appropriate $p\pi$ subsystem energy and t. Here we use the parameter $\Lambda_{int} \cong 1$ GeV. The propagator of the off-shell proton is

$$S_N(p^2) = \frac{i(\not{p} + m_p)}{p^2 - m_p^2}\,, \qquad (4.5)$$

where $\not{p} = p_\mu\gamma^\mu$.

The energy dependence of the ab elastic scattering amplitude $A^{qb}_{I\!P}(s,t)$ was parametrised in the Regge-like form, see Eq. (2.9). If the energy in the πp or the pp system is small, then the secondary exchanges (trajectories) are also important, e.g. we have in Eq. (4.2) $A^{\pi^0 p} = A_{I\!P} + A_{f_2}$. The strength parameters C_i, the values of signature factors η_i, and the (linear) Regge trajectories $\alpha_i(t)$ ((2.11), (2.12), and Fig. 2.1) are taken from the Donnachie-Landshoff analysis [113] of the total NN and πp cross sections, see Table 2.1. The running slope for elastic ab scattering can be written as (2.10), where $B^{NN}_{I\!P} = 9\,\text{GeV}^{-2}$, $B^{\pi N}_{I\!P} = 5.5\,\text{GeV}^{-2}$ and $B^{NN}_{I\!R} = 6\,\text{GeV}^{-2}$, $B^{\pi N}_{I\!R} = 4\,\text{GeV}^{-2}$ for pomeron and reggeon exchanges, respectively.

Usually a high-energy approximate formula is used in the literature in calculating differential cross sections. We use a precise calculation of the phase space (see e.g., [1]). This is important if one wants to go to lower energies and/or to large rapidities. As will be discussed in the next section, for this particular reaction the cross section has maximum just at large rapidities, where the often used formula is too approximate. In the high-energy limit we can obtain

$$(q_1 + p_3)_\mu\, \bar{u}(p_2,\lambda_2)\gamma^\mu u(p_b,\lambda_b) \cong (q_1 + p_3)_\mu\, (p_2 + p_b)^\mu \delta_{\lambda_2\lambda_b} \cong 2s_{23}\, \delta_{\lambda_2\lambda_b}\,. \qquad (4.6)$$

In the bremsstrahlung processes discussed here the intermediate nucleons are off-mass shell. In the above equations (4.3) and (4.4) the off-shell effects related to the non-point-like protons in the intermediate state are included by the following form factors:

$$F(p^2) = \frac{\Lambda_N^4}{(p^2 - m_p^2)^2 + \Lambda_N^4}\,. \qquad (4.7)$$

[1] Discussed here diffractive mechanisms of exclusive π^0 production are similar to the diffractive mechanism of $pp \to pp\omega$ [5] and $pp \to pp\gamma$ [10] processes.

Such a form was used e.g. in Ref. [263] for ω photoproduction. In general, the cutoff parameters in the form factors are not known but could be fitted in the future to the (normalized) experimental data. From our general experience in hadronic physics we expect $\Lambda_N \sim 1$ GeV. We shall discuss how the uncertainties of the form factors influence our final results.

The pion-nucleon coupling constant $g_{\pi NN}$ is relatively well known [45, 97]. In our calculations we take $g^2_{\pi NN}/4\pi = 13.5$. $F_{\pi^* NN}(t)$ is a vertex form factor due to the extended nature of particles involved. Unfortunately, the off-shell form factor is not well known as it is due to nonperturbative effects related to the internal structure of the respective objects. This discussion of form factors applies also to other $I\!P\pi^*\pi$ vertices in (4.2). We parametrise these form factors in the simple exponential form,

$$F_{\pi^* NN}(t) = F_{I\!P\pi^*\pi}(t) = \exp\left(\frac{t - m_\pi^2}{\Lambda_\pi^2}\right), \tag{4.8}$$

which is conventionally normalized to unity on the pion-mass shell and $\Lambda_\pi = 1$ GeV is a reasonable choice.

We improve the parametrisation of p-exchange amplitude (4.3) to reproduce the high-energy Regge dependence by the factor $(s_{13}/s_{thr})^{\alpha_N(p_{1i}^2)-\frac{1}{2}}$ or by the factor $(s_{23}/s_{thr})^{\alpha_N(p_{2i}^2)-\frac{1}{2}}$, where the threshold factor $s_{thr} = (m_p + m_{\pi^0})^2$ and the nucleon trajectory is $\alpha_N(p^2_{1i,2i}) = -0.3 + \alpha'_N\, p^2_{1i,2i}$ with $\alpha'_N = 0.9\ \mathrm{GeV}^{-2}$, see Fig. 2.1(b).

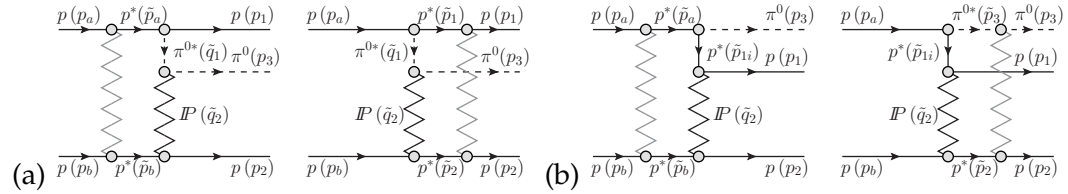

Figure 4.2: Typical absorptive correction diagrams to: (a) pion exchange and (b) proton exchange. The stars attached to protons and π^0 meson denote the fact that they are off-mass shell.

Let us estimate absorptive corrections $\delta\mathcal{M}$ shown in Fig.4.2. Diagrams which involve the elastic scattering of the incident protons are termed "initial-state" absorption. From physical reasons discussed in [126, 264] the diagrams, when the transition of excited proton $p^* \to p\pi^0$ occurs inside, do not contribute significantly at high energies. Diagrams with the "final-state" absorption corrections provide the dominant absorptive effect [264]. In the eikonal approximation which takes into account contribution of elastic rescatterings the absorbed amplitudes can be expressed as

$$\mathcal{M}_{\rm abs}(-\boldsymbol{p}_{1\perp}, -\boldsymbol{p}_{2\perp}) = \mathcal{M}(-\boldsymbol{p}_{1\perp}, -\boldsymbol{p}_{2\perp}) - \delta\mathcal{M}(-\boldsymbol{p}_{1\perp}, -\boldsymbol{p}_{2\perp}), \tag{4.9}$$

where $\delta\mathcal{M}$ for the diagrams with "initial-state" absorption is the sum of convolution integral

$$\begin{aligned}
&\delta\mathcal{M}^{\text{initial state abs}}_{\lambda_a\lambda_b\to\lambda_1\lambda_2\pi^0}(-\boldsymbol{p}_{1\perp}, -\boldsymbol{p}_{2\perp}) = \frac{i}{8\pi^2 s}\int d^2k_\perp\, A^{NN}_{\lambda_a\lambda_b\to\lambda'_a\lambda'_b}(s, \boldsymbol{k}_\perp) \\
&\times\left[\mathcal{M}^{(\pi-\text{exchange})}_{\lambda'_a\lambda'_b\to\lambda_1\lambda_2\pi^0}(-\tilde{\boldsymbol{p}}_{1\perp}, -\tilde{\boldsymbol{p}}_{2\perp}) + \mathcal{M}^{(p-\text{exchange})}_{\lambda'_a\lambda'_b\to\lambda_1\lambda_2\pi^0}(-\tilde{\boldsymbol{p}}_{1\perp}, -\tilde{\boldsymbol{p}}_{2\perp})\right]
\end{aligned} \tag{4.10}$$

and in the case of diagrams with "final-state" absorption we have

$$\begin{aligned}
&\delta\mathcal{M}^{\text{final state abs}}_{\lambda_a\lambda_b\to\lambda_1\lambda_2\pi^0}(-\boldsymbol{p}_{1\perp}, -\boldsymbol{p}_{2\perp}) = \\
&\frac{i}{8\pi^2}\int d^2k_\perp \frac{1}{s_{12}}\mathcal{M}^{(\pi-\text{exchange})}_{\lambda_a\lambda_b\to\lambda'_1\lambda'_2\pi^0}(-\tilde{\boldsymbol{p}}_{1\perp}, -\tilde{\boldsymbol{p}}_{2\perp})\, A^{NN}_{\lambda'_1\lambda'_2\to\lambda_1\lambda_2}(s_{12}, \boldsymbol{k}_\perp) \\
&+\frac{i}{8\pi^2}\int d^2k_\perp \frac{1}{s_{23}}\mathcal{M}^{(p-\text{exchange})}_{\lambda_a\lambda_b\to\lambda_1\lambda'_2\pi^0}(-\tilde{\boldsymbol{p}}_{1\perp}, -\tilde{\boldsymbol{p}}_{2\perp})\, A^{\pi N}_{\lambda'_2\to\lambda_2}(s_{23}, \boldsymbol{k}_\perp),
\end{aligned} \tag{4.11}$$

where the two-dimensional transverse vectors $-\tilde{\boldsymbol{p}}_{1\perp} = -\boldsymbol{p}_{1\perp} + \boldsymbol{k}_\perp$ and $-\tilde{\boldsymbol{p}}_{2\perp} = -\boldsymbol{p}_{2\perp} - \boldsymbol{k}_\perp$ are the transverse components of the momenta of final state protons and $\boldsymbol{k}_\perp$ is the momentum transfer. $A^{el}(s, \boldsymbol{k}_\perp)$ is an elastic scattering amplitude given by Eq.(2.9) at an appropriate energy and for the momentum transfer $\boldsymbol{k}_\perp$. Since in our calculations we include effective pomeron and reggeon exchanges, i.e. pomerons and reggeons describing approximately nucleon-nucleon or pion-nucleon elastic scattering, no explicit absorption corrections have to be included in addition.

Experience from hadronic phenomenology (for several analyses of two-body reactions see [265]) suggest that the purely elastic rescattering taken into account by Eq. (4.9) are insufficient, and inelastic intermediate states (screening corrections) lead to an enhancement of absorptive corrections. This is sometimes included in a phenomenological way by a factor λ_{sc} ($\lambda_{sc} > 1$). Taking into account absorption corrections, the DHD mechanism was shown to give a reasonable explanation for the main properties of the low-mass diffractive dissociation [266]. The effect of the absorption in diffractive dissociation is also discussed in [267].

4.1.2 $\gamma\gamma$ and $\gamma\omega$ exchanges

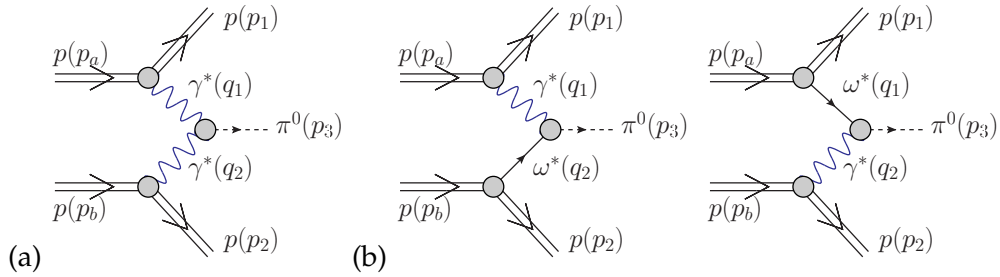

Figure 4.3: A sketch of the photon-photon (a) and photon-omega meson (b) exchanges leading to production of π^0 meson in proton-proton collisions.

In the following we wish to investigate competitive mechanisms to the diffractive mechanisms discussed in the previous subsection. The new mechanisms, never discussed so far in the literature, are shown schematically in Fig.4.3. In the most general case the corresponding Born amplitudes read

$$\begin{aligned}
\mathcal{M}^{\gamma\gamma-\text{exchange}}_{\lambda_a\lambda_b\to\lambda_1\lambda_2\pi^0} &= e\,\bar{u}(p_1,\lambda_1)\gamma^\mu u(p_a,\lambda_a)\,F_1(t_1) \\
&\times\frac{g_{\mu\mu'}}{t_1}\,(-i)\,e^2\,\epsilon^{\mu'\nu'\rho\sigma}\,q_{1,\rho}q_{2,\sigma}\,F_{\gamma^*\gamma^*\to\pi^0}(t_1,t_2)\,\frac{g_{\nu\nu'}}{t_2} \\
&\times e\,\bar{u}(p_2,\lambda_2)\gamma^\nu u(p_b,\lambda_b)\,F_1(t_2)\,, \qquad (4.12)\\
\mathcal{M}^{\gamma\omega-\text{exchange}}_{\lambda_a\lambda_b\to\lambda_1\lambda_2\pi^0} &= e\,\bar{u}(p_1,\lambda_1)\gamma^\mu u(p_a,\lambda_a)\,F_1(t_1) \\
&\times\frac{g_{\mu\mu'}}{t_1}\,(-i)\,g_{\gamma\omega\pi^0}\,\epsilon^{\mu'\nu'\rho\sigma}\,q_{1,\rho}q_{2,\sigma}\,F_{\gamma^*\omega^*\to\pi^0}(t_1,t_2)\,\frac{-g_{\nu\nu'}+\frac{q_\nu q_{\nu'}}{m_\omega^2}}{t_2-m_\omega^2} \\
&\times g_{\omega NN}\,\bar{u}(p_2,\lambda_2)\gamma^\nu u(p_b,\lambda_b)\,F_{\omega NN}(t_2)\,\mathcal{F}(s_{23},t_2)\,, \qquad (4.13)\\
\mathcal{M}^{\omega\gamma-\text{exchange}}_{\lambda_a\lambda_b\to\lambda_1\lambda_2\pi^0} &= g_{\omega NN}\,\bar{u}(p_1,\lambda_1)\gamma^\mu u(p_a,\lambda_a)\,F_{\omega NN}(t_1)\,\mathcal{F}(s_{13},t_1) \\
&\times\frac{-g_{\mu\mu'}+\frac{q_\mu q_{\mu'}}{m_\omega^2}}{t_1-m_\omega^2}\,(-i)\,g_{\gamma\omega\pi^0}\,\epsilon^{\mu'\nu'\rho\sigma}\,q_{1,\rho}q_{2,\sigma}\,F_{\gamma^*\omega^*\to\pi^0}(t_2,t_1)\,\frac{g_{\nu\nu'}}{t_2} \\
&\times e\,\bar{u}(p_2,\lambda_2)\gamma^\nu u(p_b,\lambda_b)\,F_1(t_2)\,. \qquad (4.14)
\end{aligned}$$

At larger subsystem energies, $s_{ij} \gg s_{thr}$, one should rather use reggeons than mesons. The "reggeization" is included here only approximately by a factors $\mathcal{F}(s_{ik}, t_i)$ (1.66) assuring asymptotically correct high energy dependence and $\Lambda_{thr} \simeq 1$ GeV.

The $\gamma^* NN$ vertices are parametrised by the proton's Dirac electromagnetic form factor (B.2). The central vertices involve off-shell particles. The t dependences of $F_{\gamma^*\gamma^*\to\pi^0}(t_1,t_2)$ electromagnetic off-shell form factor are the least known ingredients in formula (4.12). It is known experimentally only for one virtual photon $\gamma\gamma^* \to \pi^0$ (see [268]). In the present calculation we use a vector meson dominance model inspired parametrisation of the $\gamma^*\gamma^* \to \pi^0$ transition form factor,

$$F_{\gamma^*\gamma^*\to\pi^0}(t_1,t_2) = \frac{F_{\gamma^*\gamma^*\pi^0}(0,0)}{(1-t_1/m_\rho^2)(1-t_2/m_\rho^2)}\,, \tag{4.15}$$

where m_ρ is the ρ meson mass. The form factor is normalized to $F_{\gamma^*\gamma^*\pi^0}(0,0) = \frac{N_c}{12\pi^2 f_\pi}$, where $N_c = 3$ is the number of quark colors and $f_\pi = 93$ MeV is the pion decay constant.

The coupling of the omega meson to the nucleon is described by the coupling constant $g^2_{\omega NN}/4\pi = 10$ and the corresponding form factor is taken in the exponential form:

$$F_{\omega NN}(t) = \exp\left(\frac{t-m_\omega^2}{\Lambda^2_{\omega NN}}\right)\,, \tag{4.16}$$

where $\Lambda_{\omega NN} = 1$ GeV. The $g_{\omega\pi^0\gamma} \simeq 0.7$ GeV^{-1} constant was obtained from the omega partial decay width as discussed in Ref. [5]. The $\gamma\omega$ and $\omega\gamma$ form factors are taken in the following factorized form:

$$F_{\gamma^*\omega^*\to\pi^0}(t_1,t_2) \;=\; \frac{m_\rho^2}{m_\rho^2-t_1}\exp\left(\frac{t_2-m_\omega^2}{\Lambda^2_{\omega\pi\gamma}}\right)\,. \tag{4.17}$$

The factor describing the virtual photon coupling is taken as in the vector dominance model. In practical calculations we take $\Lambda_{\omega\pi\gamma} = 0.8$ GeV [5] as found from the fit to the $\gamma p \to \omega p$ experimental data.

In the high energy limit we can write a relatively simple formula of two-photon fusion amplitude squared and averaged over initial and summed over final spin polarizations (see [105]):

$$\overline{|\mathcal{M}^{\gamma\gamma-\text{exchange}}_{pp\to pp\pi^0}|^2} \cong 4s^2e^8\frac{F_1^2(t_1)}{t_1^2}\frac{F_1^2(t_2)}{t_2^2}|F_{\gamma^*\gamma^*\to\pi^0}(t_1,t_2)|^2\,|\mathbf{q}_{1\perp}|^2|\mathbf{q}_{2\perp}|^2\sin^2(\phi_{12})\,, \tag{4.18}$$

where $\phi_{12} = \phi_1 - \phi_2$ is the azimuthal angle between the two outgoing protons.

The amplitude for processes shown in Fig.4.3 are calculated numerically for each point in the phase space. In calculating cross section we perform integration in $\log_{10}(p_{1\perp})$ and $\log_{10}(p_{2\perp})$ instead in $p_{1\perp}$ and $p_{2\perp}$, which is useful numerically because of photon propagators.

4.1.3 $\gamma\mathcal{O}$ and $\mathcal{O}\gamma$ exchanges

As will be shown in Section 4.2, at the π^0 midrapidity only the $\gamma\gamma \to \pi^0$, out of the mechanisms considered so far, contributes, i.e. the corresponding cross section is rather small. This gives a chance to search for $\gamma\mathcal{O}$ and $\mathcal{O}\gamma$ exchange processes shown in Fig.4.4. We should keep in mind that the odderon couples to quarks rather more weakly than does the pomeron. The $\gamma p \to \pi^0 p$ reaction was proposed some time ago as a good candidate for identifying the odderon exchange, the $C = -1$ partner of the pomeron [260, 269]. They have predicted cross section of about 341 nb at the HERA energy. However, the search performed at HERA [270] was negative and found only an upper limit for this process $\sigma_{\gamma p\to\pi^0 p} < 49$ nb. Ewerz and Nachtmann [271] found an explanation of this discrepancy within a nonperturbative approach using approximate chiral symmetry and partially conserved axial vector current (PCAC). They have found that the amplitude for diffractive neutral pion production is proportional to m_π^2 and vanishes in the chiral limit ($m_\pi \to 0$). They have estimated that the cross section is probably damped by a factor of

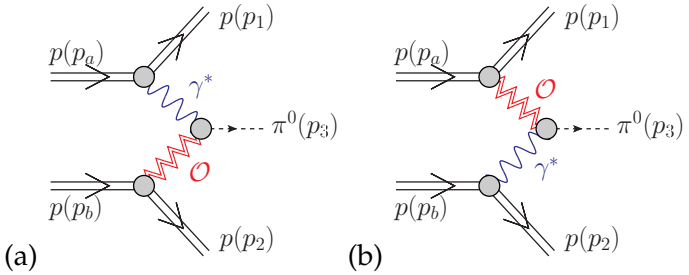

Figure 4.4: Diagrams with the photon-odderon (a) and odderon-photon (b) exchanges in the $pp \to pp\pi^0$ reaction.

50 (see [272]) compared to the early estimate in [260]. The exclusive production of neutral pions at midrapidity can be used to search for odderon exchange as well as to test the predictions of Ref. [271].

The cross section for photon-odderon and odderon-photon exchanges can be estimated in the Equivalent Photon Approximation (EPA). In this approach the distribution of the neutral pions can be written as

$$\begin{aligned}\frac{d\sigma}{dy dp_\perp^2} &= z_1 f(z_1) \frac{d\sigma_{\gamma p\to\pi^0 p}}{dt_2}\left(s_{23}, t_2 \approx -p_\perp^2\right) \\ &+ z_2 f(z_2) \frac{d\sigma_{\gamma p\to\pi^0 p}}{dt_1}\left(s_{13}, t_1 \approx -p_\perp^2\right) ,\end{aligned} \tag{4.19}$$

where $f(z)$ is an elastic photon flux in the proton; an explicit formula can be found e.g. in [273]. In the formula above, $z_{1/2} = \frac{m_\perp}{\sqrt{s}} \exp(\pm y)$ with $m_\perp = \sqrt{m_\pi^2 + p_\perp^2}$.

The differential cross section $\gamma p \to \pi^0 p$ is parametrised as

$$\frac{d\sigma_{\gamma p\to\pi^0 p}}{dt} = -B^2\, t\, \exp(Bt)\, \sigma_{\gamma p\to\pi^0 p} \tag{4.20}$$

and vanishes at $t = 0$ which is due to helicity flip in the $\gamma \to \pi^0$ transition. The slope parameter can be expected to be typically as for other soft processes $B \sim 4 - 8$ GeV^{-2}. At the LHC and at midrapidities typical energies in the photon-proton subsystems are similar as at the HERA. In the following we shall consider two scenarios: HERA upper limit ($\sigma_{\gamma p\to\pi^0 p} = 49$ nb) and Ewerz-Nachtmann estimate ($\sigma_{\gamma p\to\pi^0 p} = 6$ nb).

4.2 Results

Now we present results of our calculations of cross sections and distributions of the exclusive π^0 meson production in proton-proton collisions. The rapidity distributions of π^0 are shown in Fig.4.5 at center-of-mass energies $\sqrt{s} = 45$ GeV (ISR), 500 GeV (RHIC), and 14 TeV (LHC). We present results for the π^0-bremsstrahlung mechanism driven by the pomeron (the black solid lines) or driven by the photon exchange (the green solid lines) as well as photon-photon fusion (the blue dotted lines) and photon-omega (omega-photon) exchange processes (the violet dashed lines) not discussed so far in the literature. The higher the energy, the two π^0-bremsstrahlung contributions become better separated. At the LHC energy and in the rapidity region $-2 < y_{\pi^0} < 2$ the two-photon fusion mechanism dominates over the diffractive π^0-bremsstrahlung mechanism. The cross section for the π^0-bremsstrahlung contribution at the LHC energy and at midrapidity is much smaller than e.g. for the production of heavy quarkonia: J/ψ [147], Υ [274] or χ_{c0} [6, 104]. Clearly an experimental measurement there would be a challenge. The $\gamma\omega$ or $\omega\gamma$ exchanges have been found to be significant only in backward or forward rapidities, respectively, and are small at midrapidities due to ω-reggeization.

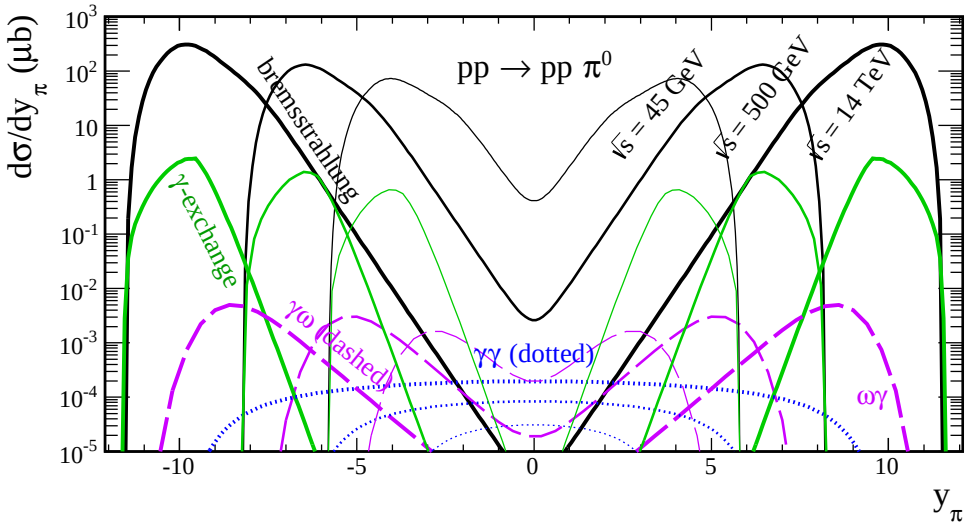

Figure 4.5: The distribution of π^0 in rapidity at $\sqrt{s} = 45$ GeV (ISR), 500 GeV (RHIC), and 14 TeV (LHC). The π^0-bremsstrahlung contribution via the pomeron and photon exchanges (the black and green solid lines, respectively) and the $\omega\gamma$ ($\gamma\omega$) exchanges (the violet dashed lines) peak at forward (backward) region of y_{π^0}, respectively. The $\gamma\gamma$ fusion (the blue dotted lines) peaks at midrapidity region. In this calculation we have used $\Lambda_N = \Lambda_\pi = 1$ GeV of the hadronic form factors. No absorption effects are included here.

Let us look now how absorption effects discussed in the theory section (see Fig.4.2) can modify the results obtained with the "bare" amplitudes (see Fig.4.1). In Fig.4.6 we present, in addition, individual contributions for the π^0-bremsstrahlung mechanism. We observe a large cancellation between the two terms in the amplitude (between the initial (p-exchange) and final state radiation (direct production)). Because of destructive interference of "bare" and absorptive correction amplitudes, the resulting cross section is by a factor 2 to 3 smaller than that for the "bare" amplitude. The difference between the solid ($\Lambda_N = \Lambda_\pi = 1$ GeV) and dashed ($\Lambda_N = 0.6$ GeV and $\Lambda_\pi = 1$ GeV) curves represents the uncertainties of the form factor parameters.

In Fig.4.7 we show corresponding distribution in π^0 meson pseudorapidity. At large y_{π^0} another mechanism may come into the game – diffractive excitation of nucleon resonances. The resonances may occur when the energy in the πN subsystem $W_{\pi N} \in \mathcal{R}$, where $\mathcal{R}$ is the nucleon resonance domain. In Fig.4.8 we present the average value of subsystem energies $\langle W_{13} \rangle$ and $\langle W_{23} \rangle$ as a function of y_{π^0} at $\sqrt{s} = 0.5, 14$ TeV. If $\langle W_{13} \rangle (y_{\pi^0}) \in \mathcal{R}$ or $\langle W_{23} \rangle (y_{\pi^0}) \in \mathcal{R}$ then an extra strength due to resonance excitation may occur. Only some baryon resonances can be excited diffractively [2]. At the LHC they can occur for $8 < |y_{\pi^0}| < 11$ and at the RHIC for $4.5 < |y_{\pi^0}| < 7.5$. One way to introduce resonances in the DHD model is to include them as intermediate states in the direct production term in Eq.(4.4) (see also Fig.4.1(c)). The reader can find some theoretical attempts in Ref. [275].

In Fig.4.9 we show corresponding distribution in proton pseudorapidity again without (upper lines) and with (lower lines) absorption effects and for two sets of Λ_π and Λ_N parameters. At the LHC protons could be measured by the ALFA (ATLAS) or TOTEM (CMS) detectors.

The effect of absorption on transverse momentum spectra of protons and neutral pions is more complicated. In Fig.4.10 we show distribution in transverse momentum of outgoing protons. Absorption causes a transverse momentum dependent damping of the cross section at small $p_{\perp,p}$ and an enhancement at large $p_{\perp,p}$ (compare upper and lower solid line).

In Fig.4.11 we show distribution in transverse momentum of π^0 meson. As in the previous figure we show results without and with absorption effects. The distributions are peaked

[2] As it was described by the Gribov-Morrison rule for the production of a resonance by pomeron exchange (see e.g. Section 3.9 in [114]): $P_{out} = (-1)^{\Delta J} P_{in}$, where ΔJ is the change in spin between the incident particle and the outgoing resonance, P_{in} is the parity of the incident particle and P_{out} the parity of the outgoing resonance.

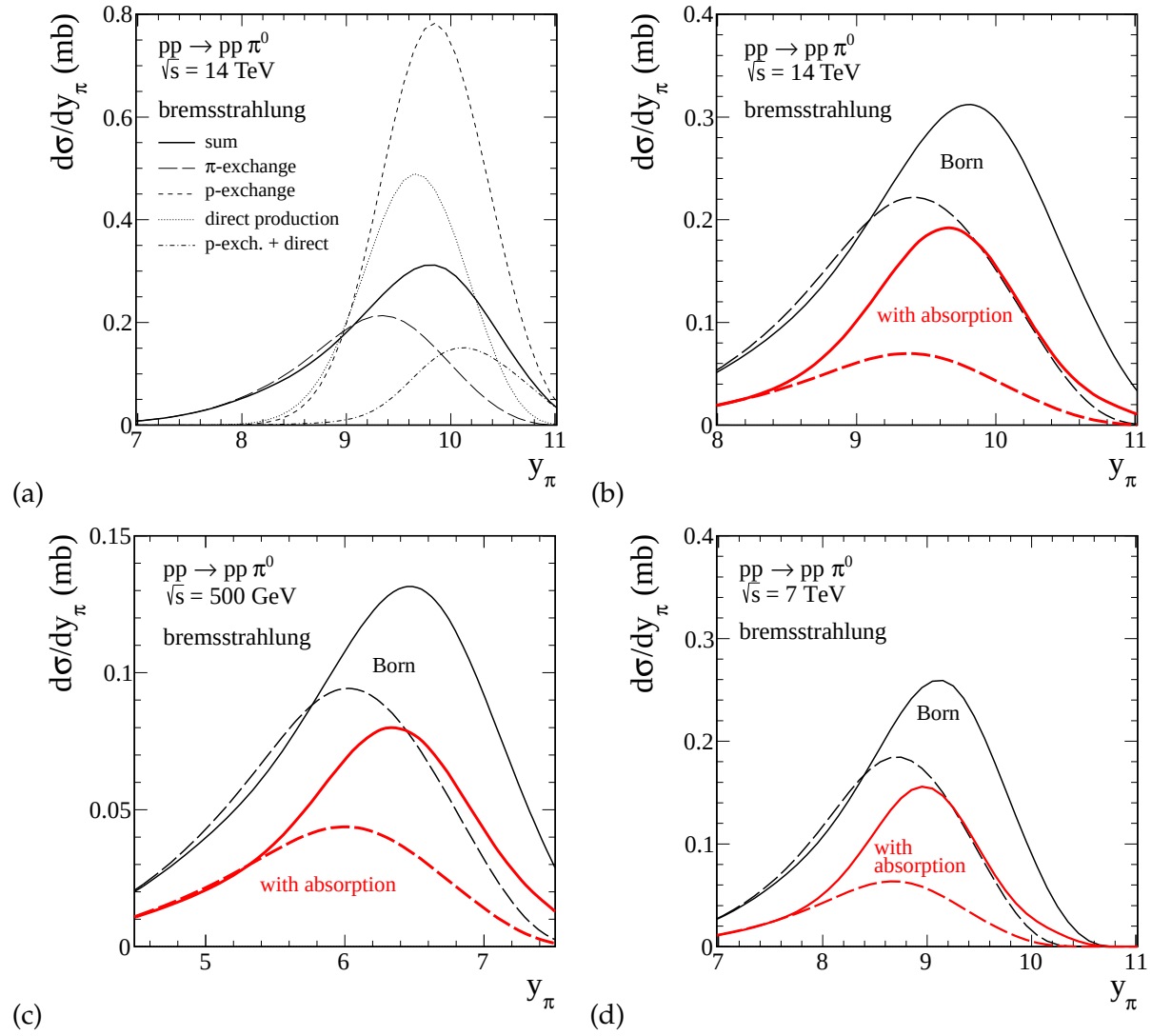

Figure 4.6: The distribution of π^0 in rapidity for $\sqrt{s} = 0.5, 7, 14$ TeV. In panel (a) we show individual contributions to the Born cross section. A large cancellation between the initial (p-exchange) and final state radiation (direct production) can be observed. In panels (b)-(d) the upper solid line corresponds to calculations without absorption effects, the lower solid line with absorption effects. The solid lines are for $\Lambda_N = \Lambda_\pi = 1$ GeV while the dashed lines are for $\Lambda_N = 0.6$ GeV and $\Lambda_\pi = 1$ GeV.

at $p_{\perp,\pi} \sim 0.2$ GeV.

In Fig.4.12 we show distribution in the square of four-momentum transfer between initial and final protons. In panels (a) and (b) we show separate contributions of different exchange terms. As in the previous figure we show results without and with absorption effects. One can observe much large tails of distributions in t_1 than in t_2 ($y_{\pi^0} > 0$ was assumed).

In Fig.4.13 we show distribution in two-dimensional space (t_1, t_2) for the π^0-bremsstrahlung contribution at $\sqrt{s} = 14$ TeV (top panels) and $\sqrt{s} = 500$ GeV (bottom panels) without (left panel) and with (right panel) absorption effects. The distributions in t_1 or t_2 are different because we have limited to the case of $y_{\pi^0} > 0$ only. The distributions discussed here could in principle be obtained with the TOTEM detector at CMS to supplement the ZDC detector for the measurement of neutral pions. Similar analysis could be done by the ALFA detector for proton tagging at ATLAS.

The pion energy spectrum for $y_{\pi^0} > 0$ drops relatively slowly with pion energy which is shown in Fig.4.14. We show results without and with absorption effects.

In Fig.4.15 we compare distribution in invariant mass of the forward produced $p\pi^0$

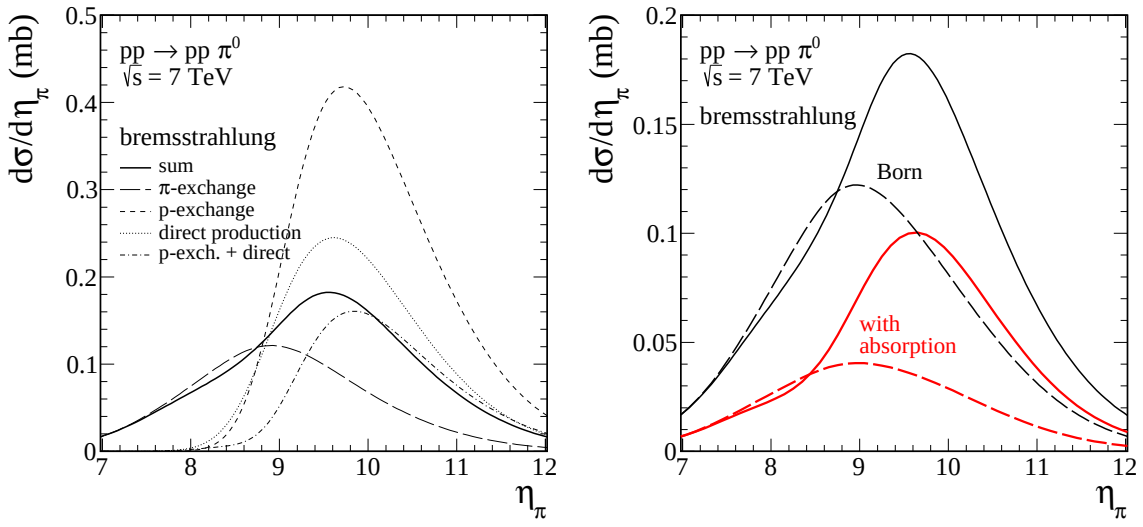

Figure 4.7: The distribution of π^0 meson in pseudorapidity for $\sqrt{s} = 7$ TeV. In the left panel we show individual contributions to the Born cross section. In the right panel the results without (upper lines) and with (lower lines) absorption effects and for two sets of Λ_π and Λ_N parameters are presented. The solid lines are for $\Lambda_N = \Lambda_\pi = 1$ GeV while the dashed lines are for $\Lambda_N = 0.6$ GeV and $\Lambda_\pi = 1$ GeV.

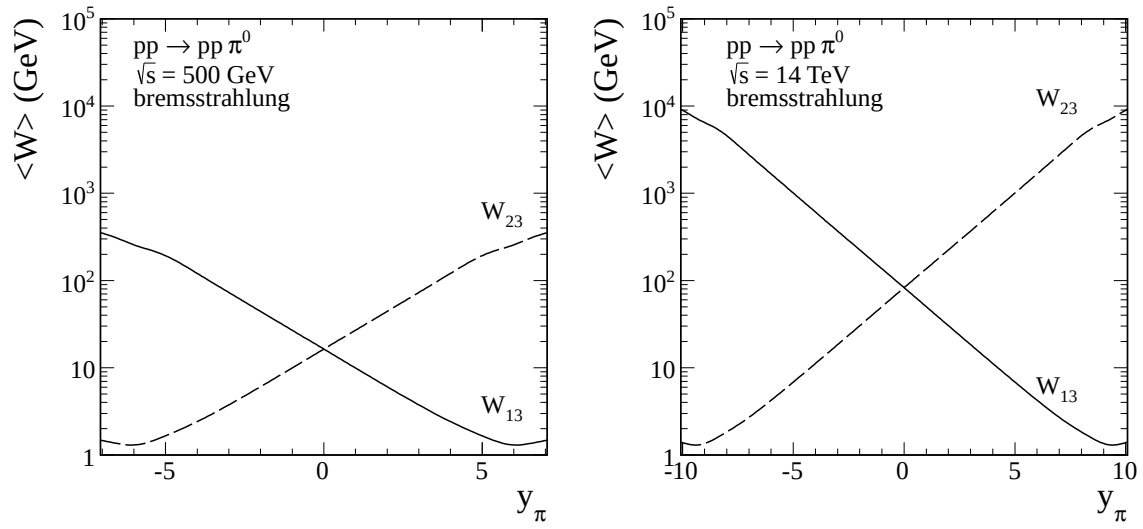

Figure 4.8: The average value of subsystem energies $\langle W_{13}\rangle\,(y_{\pi^0})$ (solid line) and $\langle W_{23}\rangle\,(y_{\pi^0})$ (dashed line) at $\sqrt{s} = 0.5, 14$ TeV. Here $\Lambda_N = \Lambda_\pi = 1$ GeV.

system for the π^0-bremsstrahlung contribution and $y_{\pi^0} > 0$. The discussed here $pp \to pp\pi^0$ process gives a sizable contribution to the low mass $(M_X > m_p + m_{\pi^0})$ single diffractive cross section.

In Fig.4.16 we show correlation function in azimuthal angle between outgoing protons. As can be seen in panel (d) the π^0-bremsstrahlung contribution is peaked at back-to-back configuration ($\phi_{12} = \pi$). For comparison, the contribution for $\gamma\gamma$- and $\gamma\omega$-fusions are peaked at $\phi_{12} = \pi/2$ and are much smaller. We observe a strong cancellation between the initial and the final state radiation. There is (see panels (a)-(c)) a sizeable difference in shape between the result obtained with the "bare" amplitude and the result with inclusion of absorption effects. We doubt if such a correlation can be measured at the LHC in the future.

In Fig.4.17 we show distribution in two-dimensional space (t_2, M_{13}). One can observe different behavior of slope in four-momentum transfer squared t_2 for different masses of the $p\pi^0$ system. A similar effect was observed for $pp \to p(n\pi^+)$ [253] and $np \to (p\pi^-)p$ [256, 257] reac-

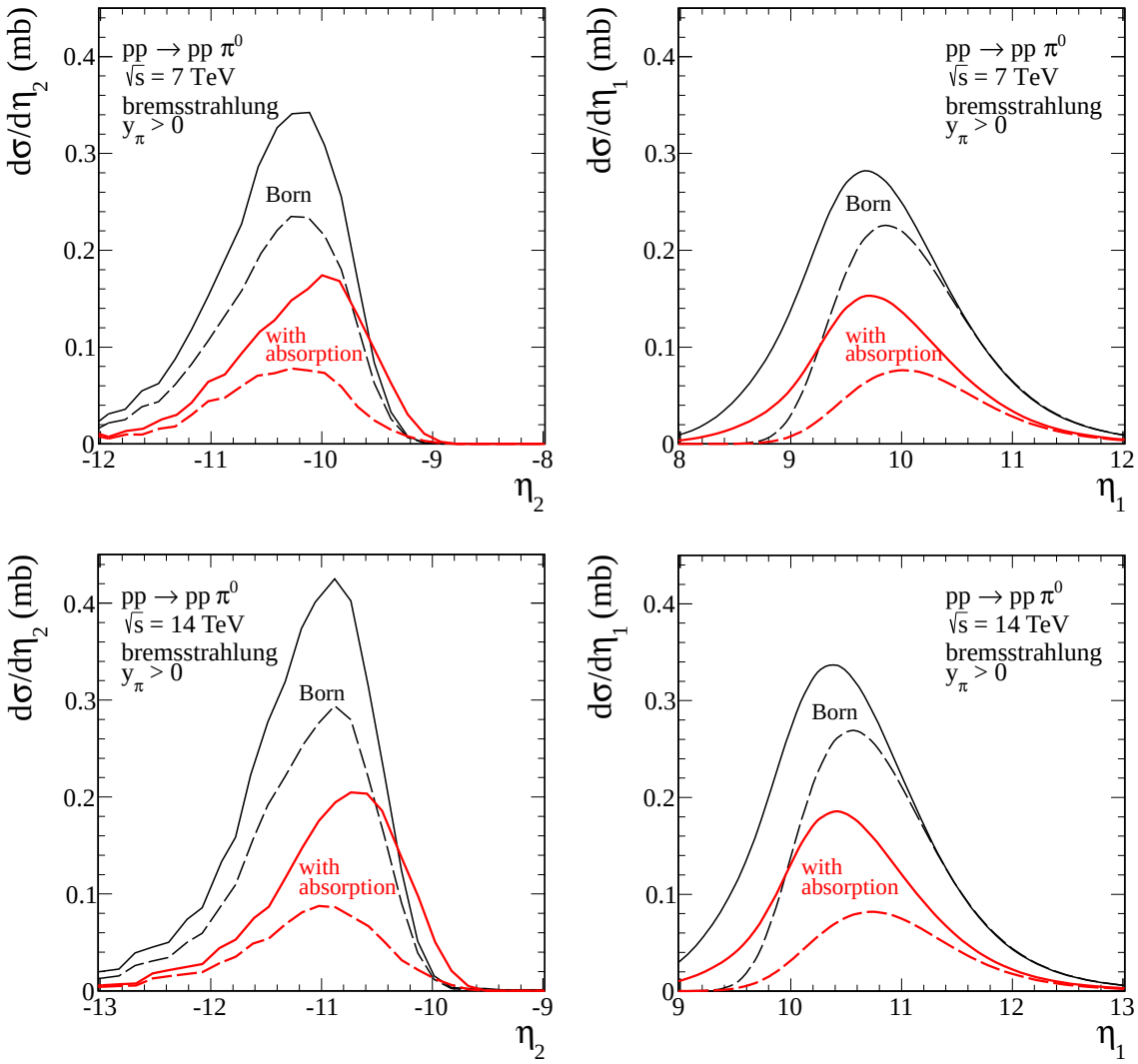

Figure 4.9: The distribution in pseudorapidity of protons in the backward (left panel) and forward (right panel) hemisphere at $\sqrt{s} = 7$ and 14 TeV and for $y_{\pi^0} > 0$. Here $\Lambda_N = \Lambda_\pi = 1$ GeV (solid line) or $\Lambda_N = 0.6$ GeV and $\Lambda_\pi = 1$ GeV (dashed line).

tions at much lower energies. As can be seen in Figs.4.12 and 4.15 the large contribution comes from the π-exchange diagram and the baryon-exchange terms are suppressed due to amplitude cancellations. The differential cross section peaks for invariant masses close to threshold and disappears rapidly with increasing invariant mass, giving an approximately exponential behavior for large masses. The absorptive effects could be partially responsible for the irregular structure in two-dimensional space (t_2, M_{13}) at small $|t_2|$ and $M_{13} \sim 1.3$ GeV.

In Fig.4.18 we show corresponding two-dimensional (M_{13}, y_{π^0}) distributions. We can see characteristic features of distribution at large $p_1\pi$ subsystem energy $M_{p_1\pi} \approx 3.5$ GeV. It is due to presence of different components (amplitudes), that is, the pion exchange mechanism contributes at $y_\pi \approx 6$ while the proton exchange mechanism at $y_\pi \approx 11$, see also Figs. 4.6(a) and 4.15(d). There is a window for another mechanisms such as the diffractive excitation of nucleon resonances; see Fig. 4.8 (right panel).

In Table 4.1 we have collected numerical values of the integrated cross section $\sigma^{DHD}_{pp\to pp\pi^0}$ taking into account only the forward region ($y_{\pi^0} > 0$). Our results depend on the Λ parameters of the hadronic form factors. The cross section obtained from ISR experiments (see e.g., Ref. [253]) are roughly reproduced.

For completeness, in Fig.4.19 (left panel) we compare the photon-odderon and odderon-

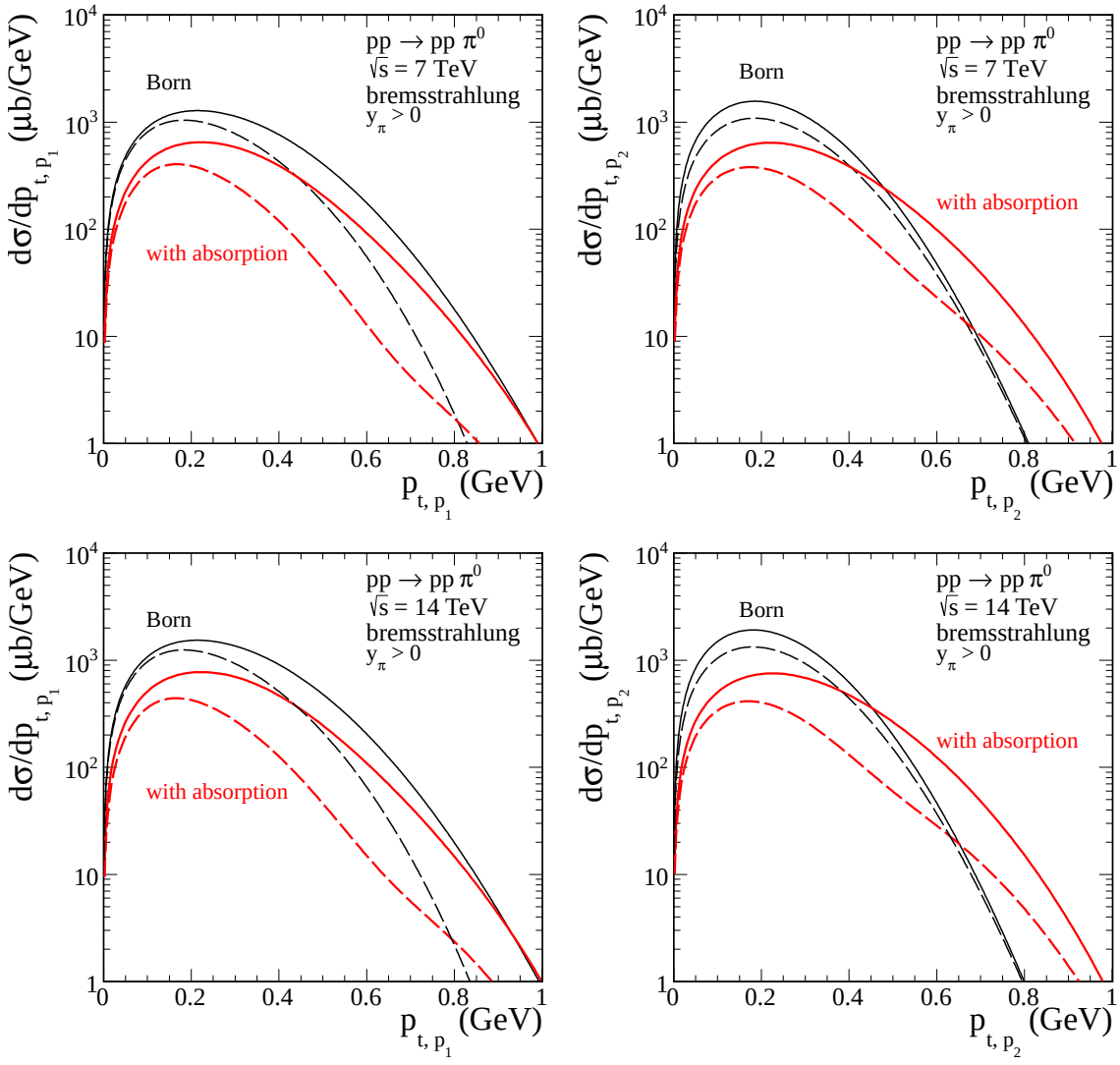

Figure 4.10: The distribution of outgoing protons in transverse momentum for $\sqrt{s} = 7, 14$ TeV and for $y_{\pi^0} > 0$. As in the previous figure we show results without and with absorption effects. Here $\Lambda_N = \Lambda_\pi = 1$ GeV (solid line) or $\Lambda_N = 0.6$ GeV and $\Lambda_\pi = 1$ GeV (dashed line).

photon contributions with the $\gamma\gamma$ contribution. We show results for $B = 6$ GeV^{-2} and two different estimates of the $\gamma p \to \pi^0 p$ cross section (energy independent) as specified in the figure caption. The total cross section for the odderon contributions, corresponding to the HERA upper limit, is less than 20 nb in the rapidity region $|y_{\pi^0}| < 2.5$. The corresponding cross section is more than an order of magnitude larger than the photon-photon contribution. In the right panel we make similar comparison of the two contributions for transverse momentum distribution of neutral pions and in the region $|y_{\pi^0}| < 2.5$. We show the photon-odderon contribution for different values of slope parameters B in Eq. (4.20). The curve corresponding to the HERA upper limit is considerably larger than the photon-photon contribution starting from $p_{\perp,\pi^0} > 0.2$ GeV. Even with the Ewerz and Nachtmann limit, one can observe deviations from the $\gamma\gamma$ curve at transverse momenta $p_{\perp,\pi^0} > 0.3$ GeV. The cut on meson $p_{\perp,\pi^0}$ should enhance relative odderon contribution. In principle, the ALICE collaboration could try to measure the transverse momentum distribution of exclusively produced neutral pions.

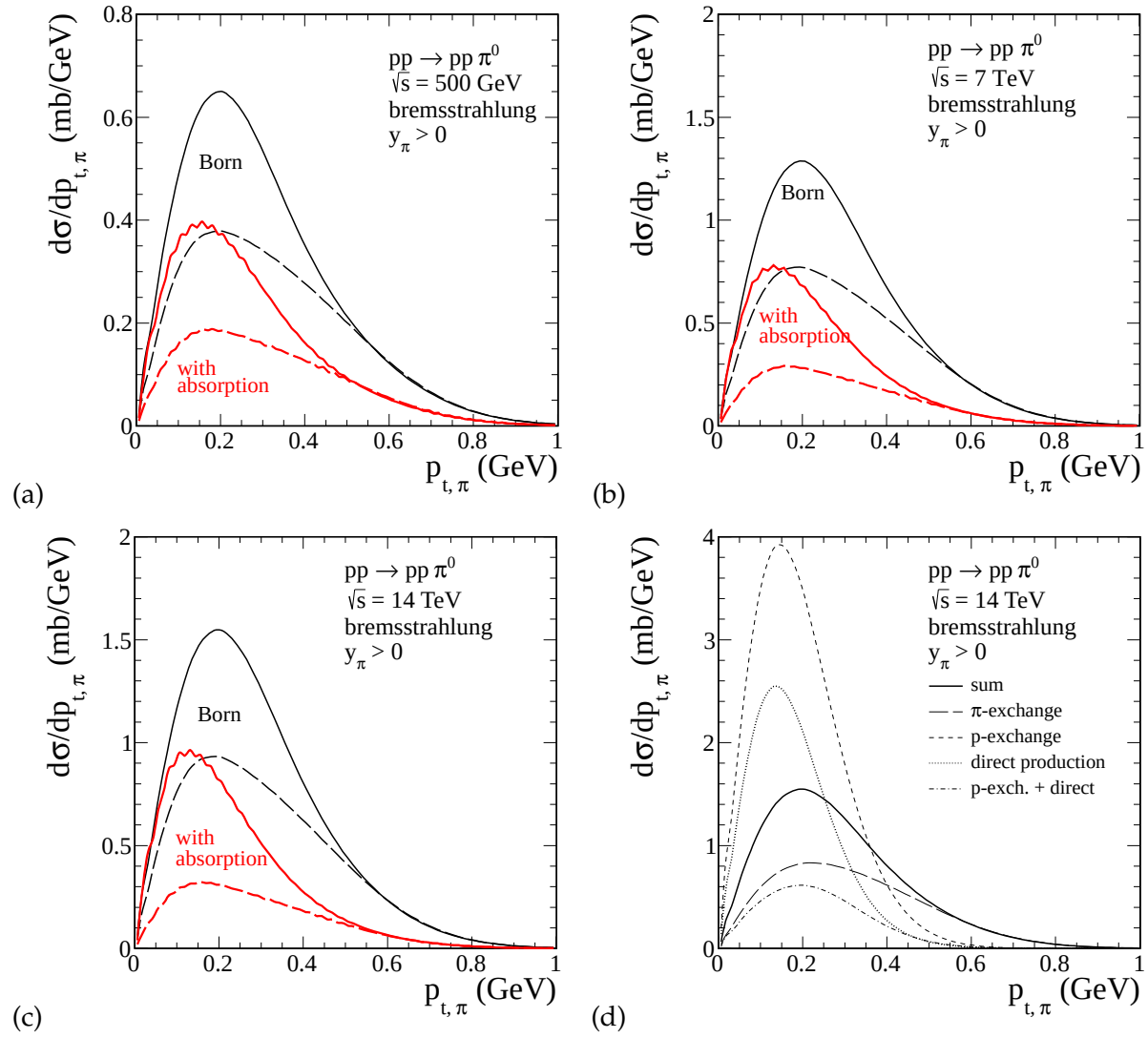

Figure 4.11: The distribution of π^0 mesons in transverse momentum for $\sqrt{s} = 0.5, 7, 14$ TeV and for $y_{\pi^0} > 0$. In panels (a)-(c), as in the previous figures, we show theoretical uncertainties (in e.g. form factors). Here $\Lambda_N = \Lambda_\pi = 1$ GeV (solid line) or $\Lambda_N = 0.6$ GeV and $\Lambda_\pi = 1$ GeV (dashed line). In panel (d) we show individual contributions to the Born cross section.

4.2.1 A comment on single diffractive cross section at low proton excitations

The measurement of inelastic proton-proton cross section is one of the standard and obligatory measurements at each collision energy. At the LHC single diffraction (SD) and double diffraction (DD) processes constitute a large contribution to the inelastic cross section (about a half). Unfortunately it is very difficult to truly measure the cross section for the low mass excitation at the LHC and often educated extrapolations are required. Usually $1/M^2$ triple-Regge fit is used for this purpose. Do we have expertise on the very low mass excitations? This issue was critically discussed recently [275]. The authors presented predictions of a dual-Regge model with a nonlinear proton Regge trajectory [276] with parameters fitted to the single diffractive cross section measured at low energies (for a review of the low energy SD data see e.g. [126,277]). In their fit the low mass excitation is dominated by the excitation of the proton resonances $N^*(1440)$ with $J^P = \frac{1}{2}^+$ and $N^*(1680)$ with $J^P = \frac{5}{2}^+$. While the presence of the latter is rather natural – it is a member of the same Regge trajectory as proton, see Fig. 2.1(b) – the huge contribution of the Roper resonance is not so clear to us. The low-energy experimental SD data [277] show up a huge peak at the nominal position of the Roper resonance. This is the region where the absorbed Drell-Hiida-Deck mechanism (the nonresonant background model) predicts an en-

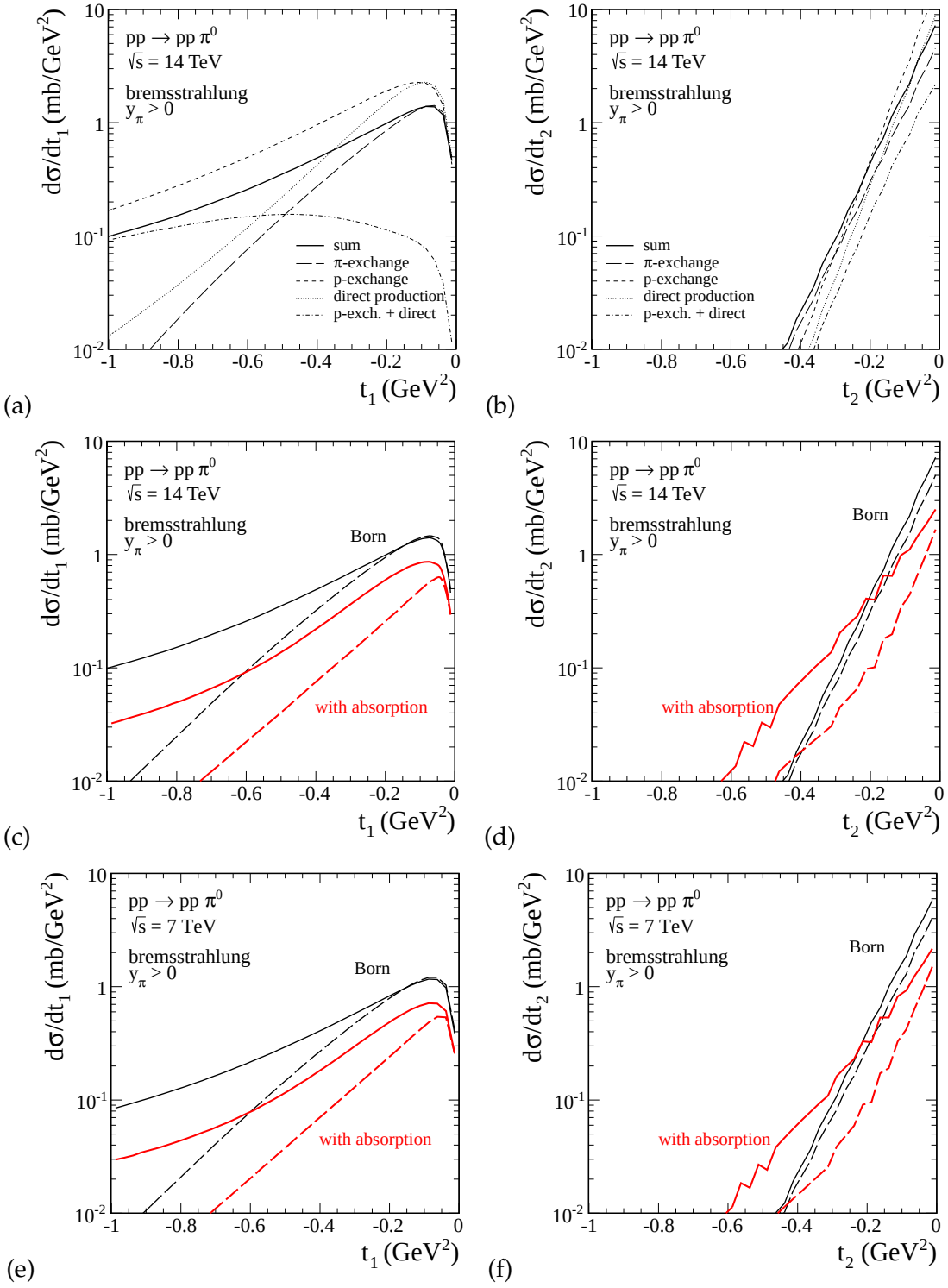

Figure 4.12: Distribution in the four-momentum transfer squared between initial and final protons at $\sqrt{s} = 7, 14$ TeV and for $y_{\pi^0} > 0$. In panels (a) and (b) we show individual contributions to the Born cross section. The theoretical uncertainties are shown in panels (c)-(f). Here $\Lambda_N = \Lambda_\pi = 1$ GeV (solid line) or $\Lambda_N = 0.6$ GeV and $\Lambda_\pi = 1$ GeV (dashed line).

hancement (see Fig.4.15). The arguments against large Roper contribution in single diffraction at high energies were exposed in Ref. [278]. We wish to emphasize that the DHD contribution was not included in the analysis of the SD mass spectrum in [275] where only a purely mathematical fit was used. The fitted background seems to have quite different properties than the discussed here DHD mechanism with absorption (different both in M_X and in t). In our opinion

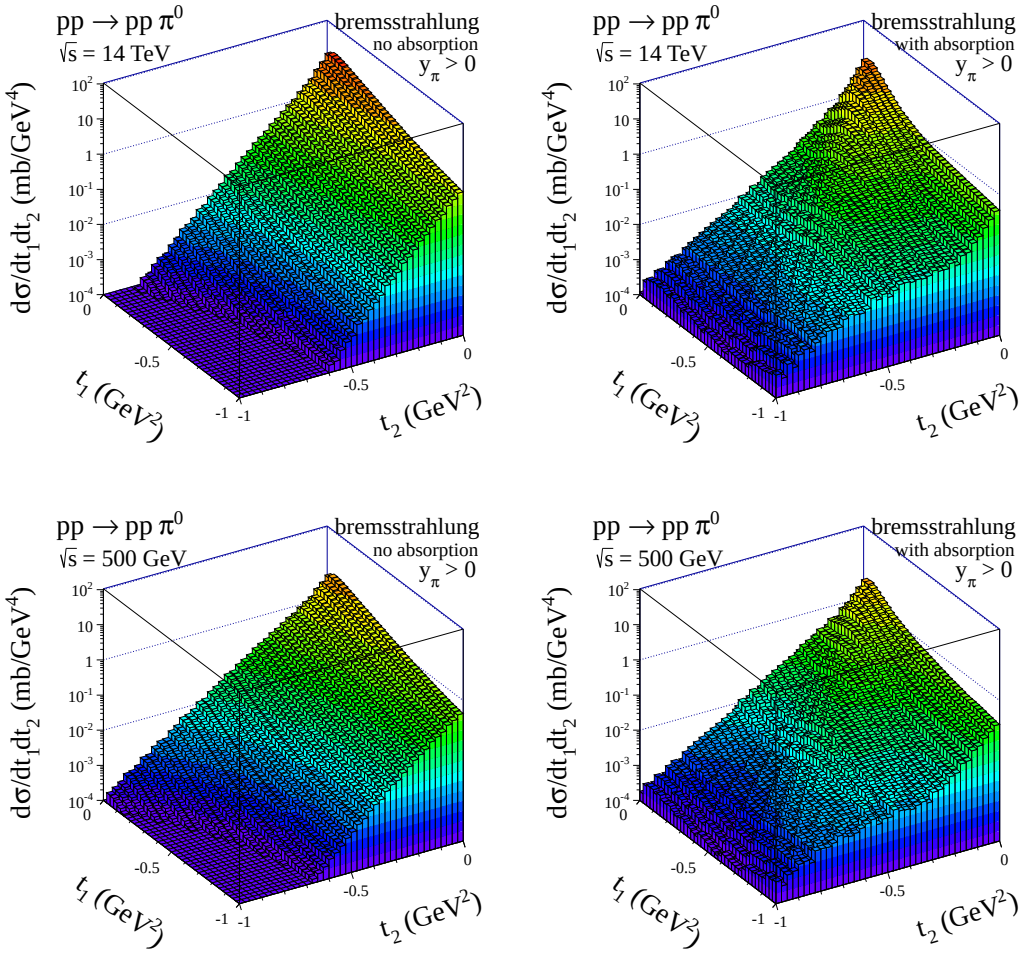

Figure 4.13: Distribution in (t_1, t_2) for the π^0-bremsstrahlung contribution at $\sqrt{s} = 14$ TeV (top panels) and $\sqrt{s} = 500$ GeV (bottom panels) and for $y_{\pi^0} > 0$ without (left panels) and with (right panels) absorption effects. Here $\Lambda_N = \Lambda_\pi = 1$ GeV.

inclusion of a realistic absorbed DHD contribution could dramatically change, or even eliminate, the contribution of the Roper resonance. This issue requires further studies.

The resonances contributing to the SD cross section discussed in [275] naturally contribute also to the $pp \to pp\pi^0$ channel and the corresponding cross section is

$$\sigma^{N^*}_{pp\to pp\pi^0} = \sigma^{N^*}_{SD} \times BR(N^* \to N\pi) \times \frac{1}{3}\,. \tag{4.21}$$

The last factor comes from the fact that the considered diffractively excited baryon resonances have isospin $I = \frac{1}{2}$. The branching fractions $BR(N^* \to N\pi)$ have been measured [96] and are about 65% for both discussed states. The same situation occurs in the $pp \to p(n\pi^+)$ and $np \to (p\pi^-)p$ reactions (a factor 2 larger cross section), where no clear signal of the Roper $N^*(1440)$ resonance was identified (see e.g., [253–255]) while the $N^*(1680)$ resonance was observed [3]. The situation should be better clarified in the future. The discussed there resonances were not included in our analysis but could be included in principle.

Our DHD mechanism contributes to the single diffraction cross section as

$$\sigma^{DHD}_{SD} = 3\,\sigma^{DHD}_{pp\to pp\pi^0}\,. \tag{4.22}$$

[3] In Ref. [253] results on diffractive dissociation of protons into $(n\pi^+)$ in pp collisions at the CERN ISR $\sqrt{s} = 45$ GeV energy were shown and the cross sections $\sigma_{pp\to p(n\pi^+)} = (400 \pm 110)\ \mu$b, $\sigma_{pp\to pN^*(1680)} = (170 \pm 60)\ \mu$b was reported.

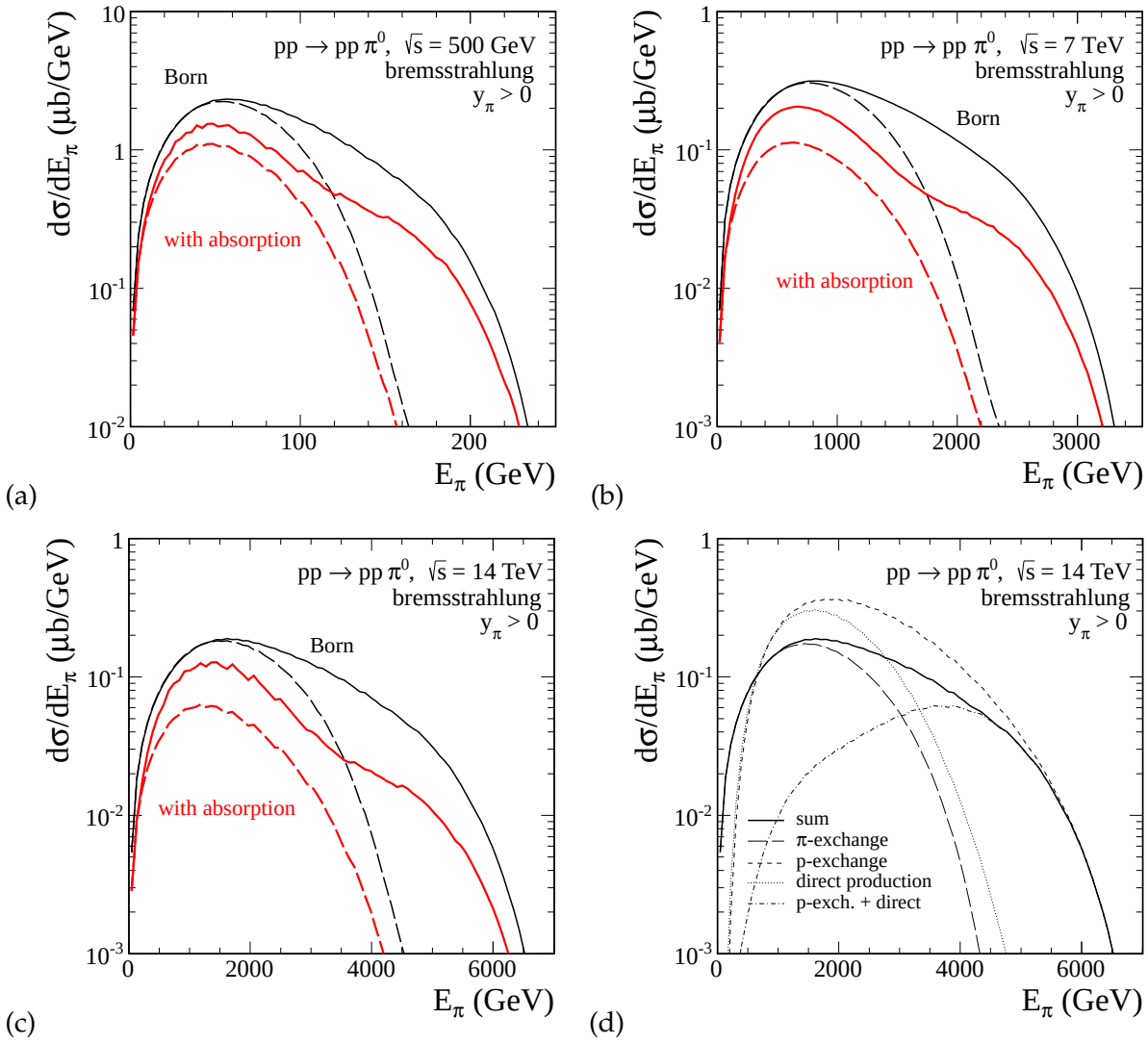

Figure 4.14: Energy spectrum of pions at $\sqrt{s} = 0.5, 7$ and 14 TeV and for $y_{\pi^0} > 0$. Theoretical uncertainties are shown in panels (a)-(c). Here $\Lambda_N = \Lambda_\pi = 1$ GeV (solid lines) or $\Lambda_N = 0.6$ GeV and $\Lambda_\pi = 1$ GeV (dashed lines). In panel (d) we show individual contributions to the Born cross section.

The factor 3 comes from the isospin symmetry of the $NN\pi$ coupling constant. Taking our numbers from Table 4.1 we predict certainly not a negligible contribution to the total inelastic cross section at high energies (for both-side SD the $\sigma^{DHD}_{pp\to pp\pi^0}$ should be multiplied by a factor 2). To our knowledge the DHD contribution is not included in the existing Monte Carlo codes simulating high-energy diffractive processes.

In Fig. 4.20 we present inclusive transverse momentum spectra of the neutral pions. For an example, the experimental spectra in the forward rapidity ranges were measured by the Large Hadron Collider forward (LHCf) experiment at $\sqrt{s} = 7$ TeV [279]. The π^0s are identified by their decay into two photons. The inclusive cross section of π^0 production is given by the expression

$$\frac{1}{\sigma_{inel}} E\frac{d^3\sigma}{dp^3} = \frac{1}{\sigma_{inel}} \frac{d^3\sigma}{d\phi dy\, p_\perp dp_\perp} \Rightarrow \frac{1}{\sigma_{inel}} \frac{d^2\sigma}{\pi dy d(p_\perp^2)} \Rightarrow \frac{1}{\sigma_{inel}} \frac{d\sigma}{2\pi\, p_\perp dp_\perp} \frac{1}{\Delta y}, \tag{4.23}$$

where the inelastic cross section $\sigma_{inel} = 73.6$ mb was assumed for proton-proton collisions at $\sqrt{s} = 7$ TeV [280]. The second form of Eq. (4.23) is obtained using the identity $dy/dp_z = 1/E$, and the third form represents average over ϕ.

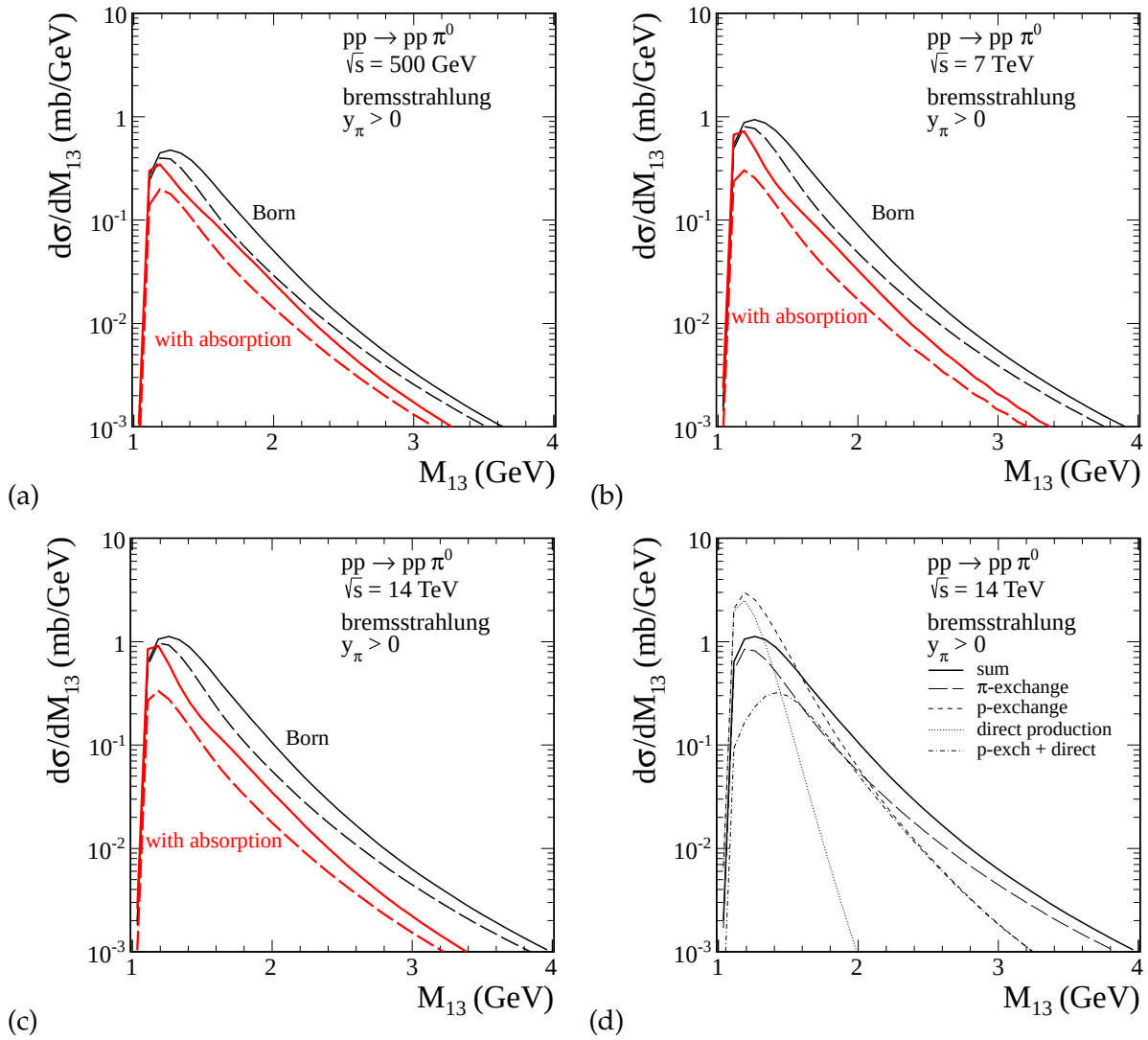

Figure 4.15: Distribution in proton-pion invariant mass M_{13} at $\sqrt{s} = 0.5, 7, 14$ TeV and for $y_{\pi^0} > 0$. Theoretical uncertainties are presented in panels (a) - (c). Here $\Lambda_N = \Lambda_\pi = 1$ GeV (solid line) or $\Lambda_N = 0.6$ GeV and $\Lambda_\pi = 1$ GeV (dashed line). In panel (d) we show individual contributions to the Born cross section.

Table 4.1: The integrated value of cross sections in μb for the $pp \to pp\pi^0$ reaction at $\sqrt{s} = 45$ GeV (ISR), 500 GeV (RHIC), 7 and 14 TeV (LHC). Here $y_{\pi^0} > 0$ is taken into account only. The lower limit corresponds to the result when $\Lambda_N = 0.6$ GeV and $\Lambda_\pi = 1$ GeV and the upper limit when $\Lambda_N = \Lambda_\pi = 1$ GeV.

Model	$\sqrt{s} = 45$ GeV	$\sqrt{s} = 500$ GeV	$\sqrt{s} = 7$ TeV	$\sqrt{s} = 14$ TeV
No absorption	$103 - 146$	$177 - 251$	$337 - 481$	$402 - 575$
Absorption in initial state	$46 - 76$	$62 - 125$	$85 - 273$	$94 - 357$
Absorption in final state	$60 - 91$	$84 - 139$	$118 - 244$	$128 - 290$

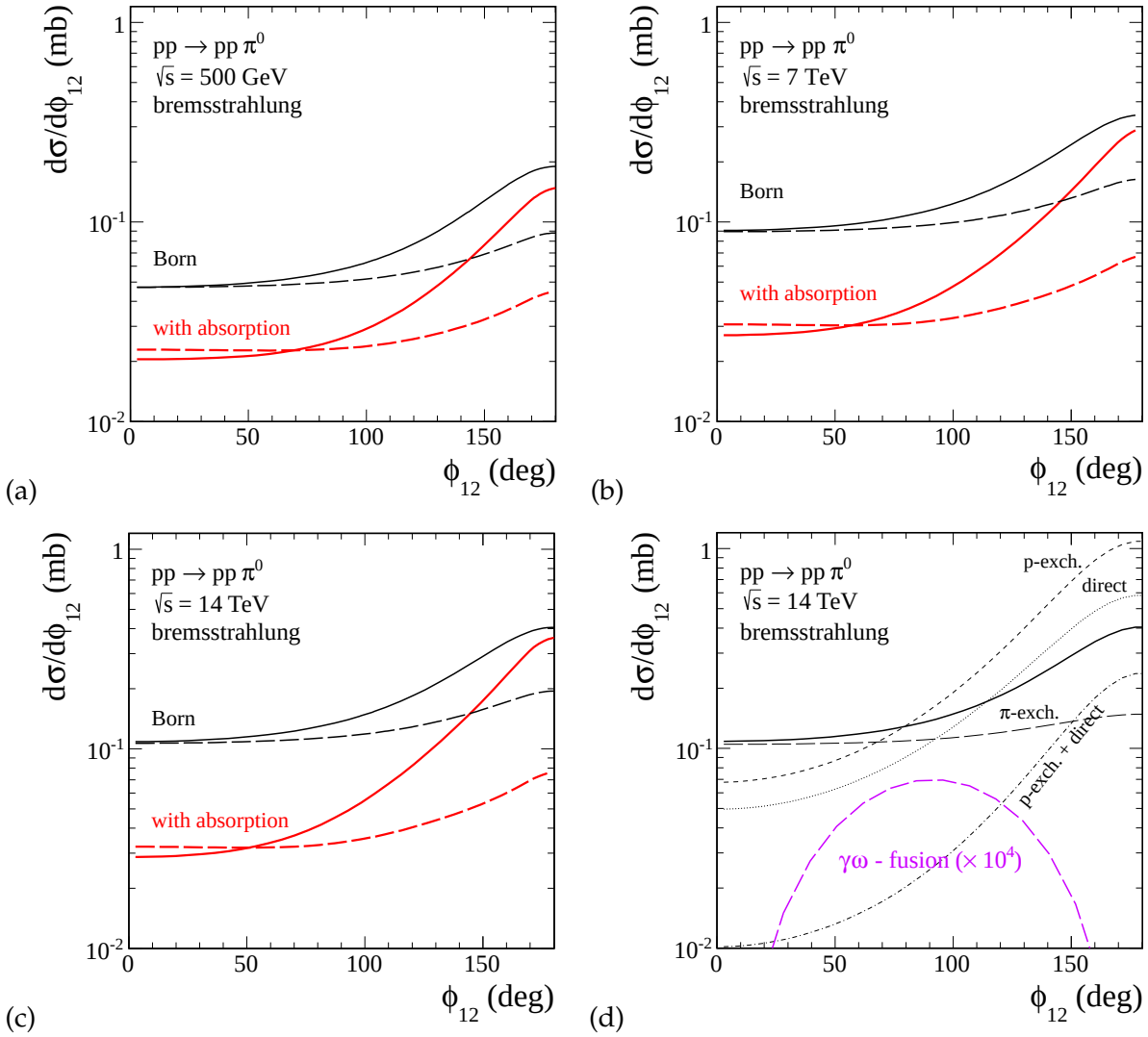

Figure 4.16: The distribution in azimuthal angle between outgoing protons for $\sqrt{s} = 0.5, 7$, and 14 TeV are presented in panels (a), (b), and (c), respectively, without (black lines) and with (red lines) absorption effects. Here $\Lambda_N = \Lambda_\pi = 1$ GeV (solid lines) or $\Lambda_N = 0.6$ GeV and $\Lambda_\pi = 1$ GeV (dashed lines). The difference between the results with various of Λ parameters of form factors illustrates theoretical uncertainties. In panel (d) we show individual bremsstrahlung contributions to the Born cross section and also the $\gamma\omega$-fusion contribution enlarged by a factor 10^4 (violet dashed line).

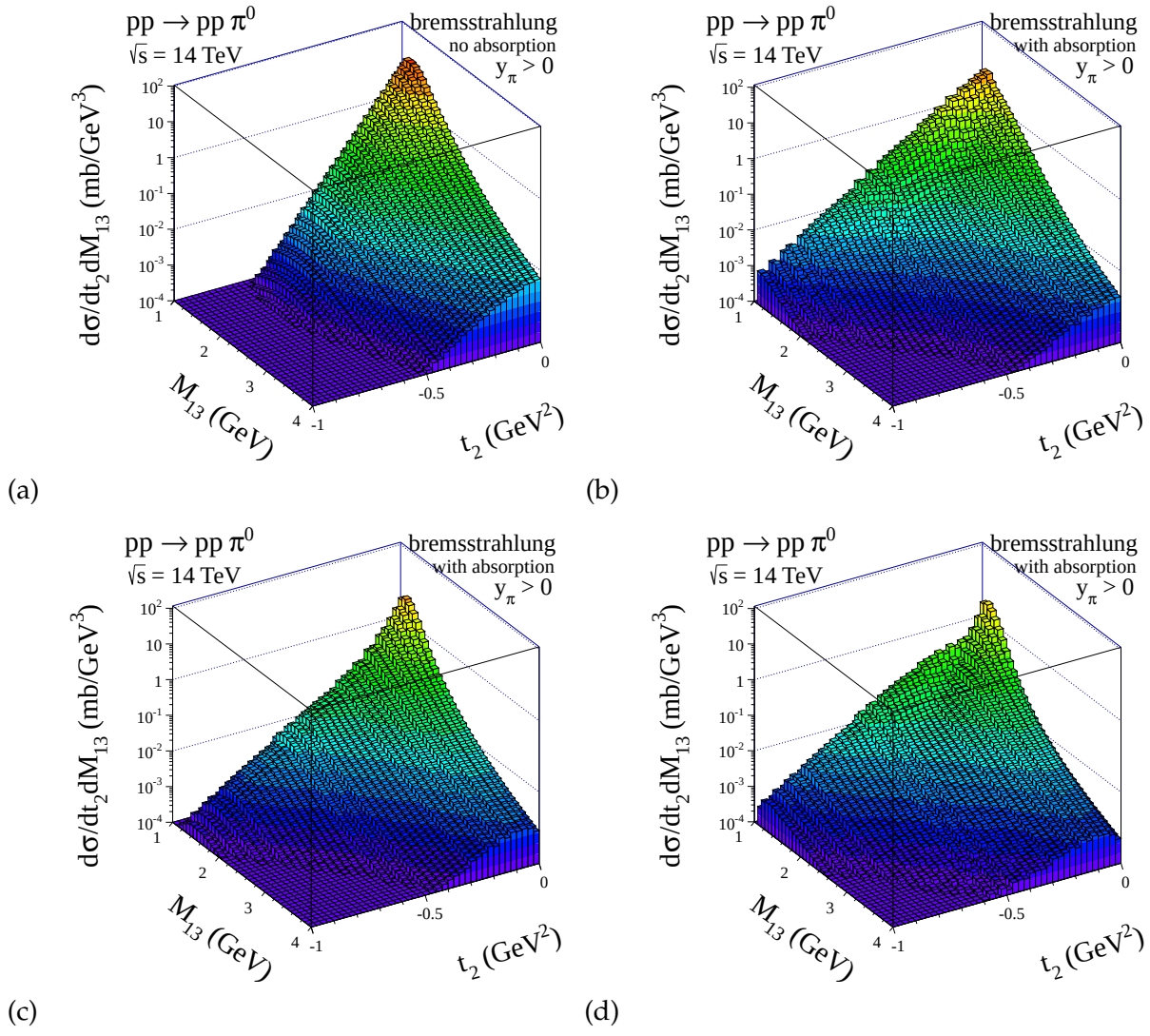

Figure 4.17: Distribution in (t_2, M_{13}) for the π^0-bremsstrahlung contribution at $\sqrt{s} = 14$ TeV and for $y_{\pi^0} > 0$ without [panel (a)] and with absorption effects in the final state only [panels (b) and (c)] and absorption effects in the initial state only [panel (d)]. Here $\Lambda_N = \Lambda_\pi = 1$ GeV [panels (a) and (b)] and $\Lambda_N = 0.6$ GeV, $\Lambda_\pi = 1$ GeV [panels (c) and (d)].

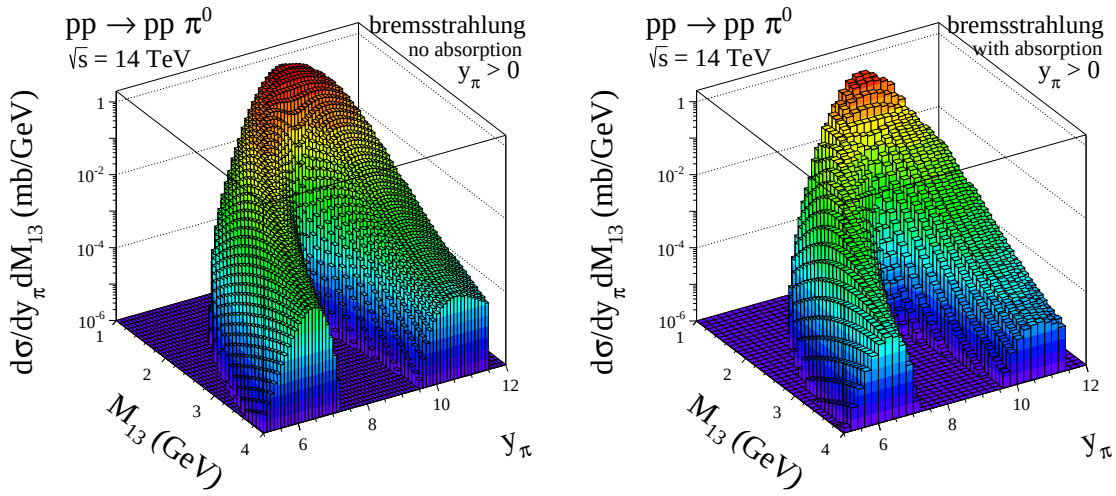

Figure 4.18: Distribution in (M_{13}, y_{π^0}) at $\sqrt{s} = 14$ TeV and $y_{\pi^0} > 0$ for the π^0-bremsstrahlung contribution without (left panel) and with (right panel) absorption effects. Here $\Lambda_N = \Lambda_\pi = 1$ GeV.

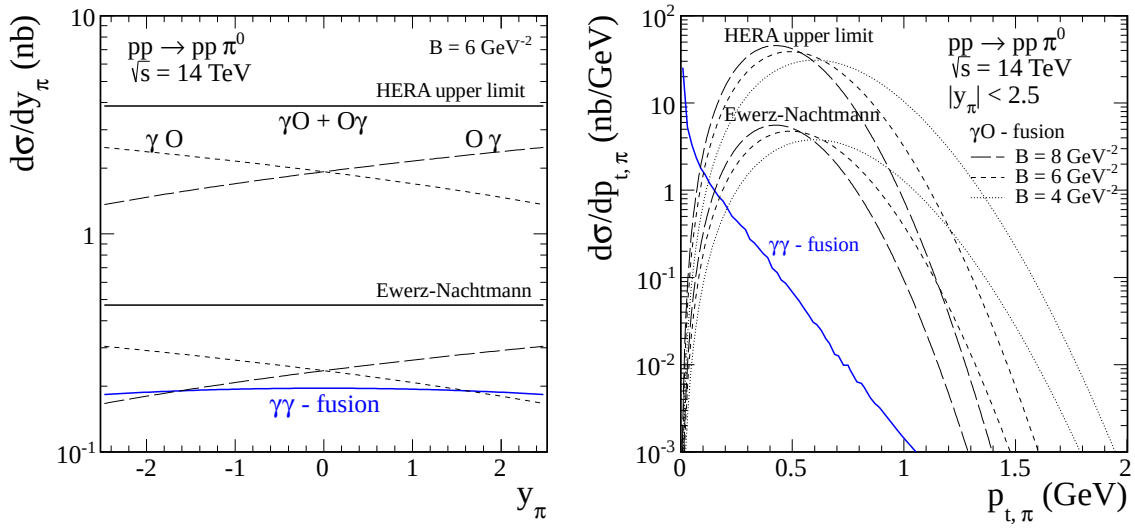

Figure 4.19: Rapidity distribution of neutral pions (left panel) produced in $\gamma\mathcal{O}$-fusion and $\mathcal{O}\gamma$-fusion (black upper solid lines) compared to the $\gamma\gamma$ contribution (blue lowest solid line) for $\sqrt{s} = 14$ TeV. Individual contributions of photon-odderon (short dashed line) and odderon-photon (long dashed line) are shown separately. We show predictions for the HERA upper limit ($\sigma_{\gamma p \to \pi^0 p} = 49$ nb) and for the Ewerz-Nachtmann estimate ($\sigma_{\gamma p \to \pi^0 p} = 6$ nb). In the right panel we make similar comparison of contributions of the two mechanisms for transverse momentum distribution of π^0's in the rapidity region $-2.5 < y_{\pi^0} < 2.5$. For the odderon contributions we have used different values of slope parameters $B = 4, 6, 8\,\mathrm{GeV}^{-2}$.

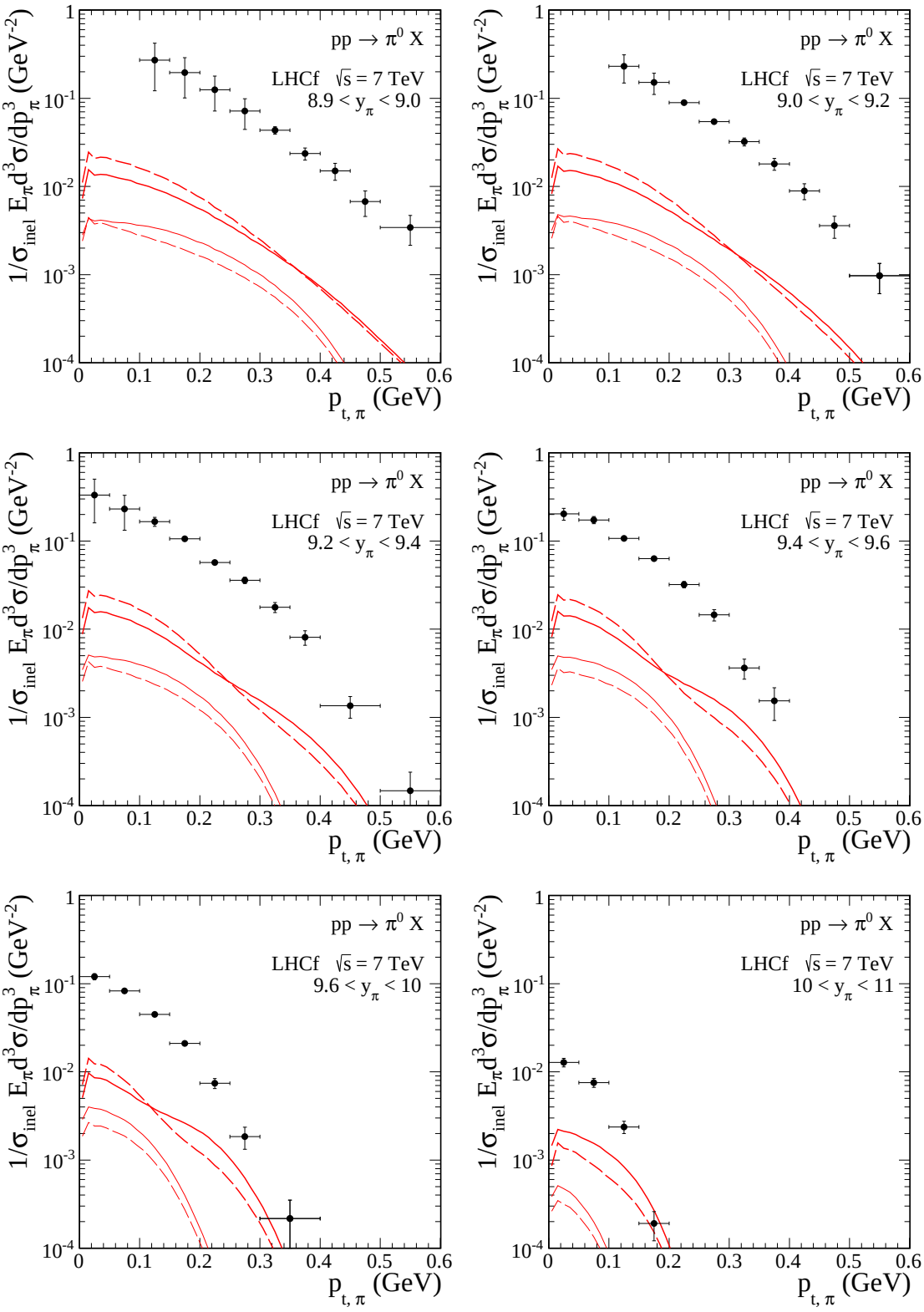

Figure 4.20: The inclusive neutral pion transverse momentum spectra in different ranges of π^0 rapidity at $\sqrt{s} = 7$ TeV. Experimental results from LHCf experiment [279] are compared with our theoretical predictions of two absorbed DHD model calculations. The solid lines correspond to calculations for the "final-state" absorption corrections and the dashed lines for the "initial-state" absorption corrections. In order to estimate theoretical uncertainties of our contributions two sets of cut-off parameters $\Lambda_N = \Lambda_\pi = 1$ GeV (the upper lines) and $\Lambda_N = 0.6$ GeV, $\Lambda_\pi = 1$ GeV (the lower lines) was used.

4.3 Exclusive ω meson production

The (virtual) photoproduction of vector mesons in $\gamma^* p$ collisions is also vivid and active field of research. Here the main interest was related to the wealth of experimental data obtained by the H1 and ZEUS Collaborations at the HERA collider. For a review of the experimental and theoretical status until 2006, see [281]. The subject continues to be actively researched also in recent years. The focus being e.g. on saturation phenomena in the small-x gluon distribution [282], on models based on the general principles of Regge theory [283], as well as on investigations of systematic treatment of higher twist contributions in the high Q^2 limit [284].

The exclusive photoproduction of vector mesons can also be studied in hadron-hadron collisions [285]. Here the dominant mechanism is photon-pomeron (pomeron-photon) fusion which for heavy vector quarkonia (J/Ψ, Υ) probes the proton's gluon density at small x (see e.g. [147, 274, 286]). Recently also the quasi-diffractive large-t, the large rapidity gap, the photoproduction of vector mesons in hadronic collisions has attracted some interest, see e.g. [287, 288], the latter calculation using a theoretical framework developed in [289, 290]. These works have in common that they involve a hard scale of some sort, either the large mass of a heavy quark, or a large momentum transfer.

The soft mechanism of exclusive light vector meson production in proton-proton collisions at high energies was almost not studied in the literature; the exception is the ϕ meson [196] and the ω meson [5]. Here we will show that exclusive production of ω mesons in proton-proton collisions is very different than similar processes for ϕ [196], J/Ψ [147] or Υ [274]. The $pp \to pp\omega$ process was studied before only close to its production threshold. Various theoretical models (see Refs. [291–296]) were developed to describe the lower-energy data [297] (for more references, see [5]). Here the dominant mechanisms are meson exchange processes as well as the ω-meson bremsstrahlung driven by meson exchanges. How the situation changes at high-energy is very interesting. While at low energy the meson exchanges (π, ρ, ω, σ) are the driving t-channel exchanges, for the ω-bremsstrahlung at high energy their role is taken over by the pomeron exchange. The latter will be treated here purely phenomenologically. A similar hadronic bremsstrahlung-type mechanism is the Deck-mechanism for diffractive production of πN final states in pp collisions [258, 259], for a review, see e.g. [125].

We intend to make predictions for being in operation colliders RHIC, Tevatron and LHC. The hadronic bremsstrahlung mechanisms are expected to be enhanced for exclusive production of ω meson compared to other vector mesons as the $g_{\omega NN}$ coupling constant is known to be large from low-energy phenomenology [46, 296, 298]. We will also show how important are the photoproduction mechanisms discussed in Refs. [147, 196, 274] in the context of exclusive heavy vector quarkonium production. At this point it is interesting to remember, that the exclusive production of vector mesons at high energies has been proposed as a promising channel for a discovery/study of the odderon [299, 300]. This fact is simply related to the odd C-parity of the vector meson. It now turns out, that for the exclusive J/Ψ and Υ mesons production, the main competitor to the odderon-pomeron fusion mechanism exchange is the photoproduction mechanism. Moreover, in Ref. [301] the authors noted that the measurement of the η_c ($c\bar{c}$ bound state) photo- or electroproduction is a useful tool for probing the QCD odderon and is similar to the measurement of the J/Ψ photo- or electroproduction which probes the BFKL pomeron implied by QCD [4].

In this regard it is important to stress, that the unique hadronic bremsstrahlung mechanism active in the exclusive ω-production precludes an interpretation of a possible excess over

[4]The magnitude of the η_c photoproduction cross section was estimated to be equal about $11 - 45$ pb [301]. The photoproduction cross section is also characterized by the relatively weak t dependence at large t, where the diagrams with the gluons coupling to three different quarks in a proton dominate. The t-dependence of the differential cross section was also discussed in Ref. [301]. It should be noted that the two gluon exchange mechanism of diffractive J/Ψ production generates strong suppression of the differential cross-section in the large-t region due to the nucleon form-factor effects. This fact can be useful in experimental separation of the η_c mesons produced through the odderon exchange from those which are the decay products of the diffractively produced J/Ψ mesons.

photoproduction in terms of an odderon. Indeed, as will be shown below, the strong coupling of the ω to protons entails a surprisingly large cross section for central ω production at high energies. This is despite the fact that formally the t-channel exchange of ω's is decreasing with the size of the rapidity gap in comparison to the odderon.

In this context we mention, that it has also been proposed to search for the odderon in the photoproduction of C-even pion pairs. Their interference with the pomeron-produced C-odd pions will lead to characteristic angular asymmetries [302, 303] (for the case of large photon virtualities, see [304]). While in principle photoproduction of continuum pion pairs is just as well possible as the production of vector meson resonances studied here, the relevant asymmetries will be heavily diluted by the C-even pion pairs produced from the pomeron-pomeron fusion.

4.3.1 Photoproduction mechanism for $\gamma p \to \omega p$

Pomeron exchange

Let us concentrate on the $\gamma p \to \omega p$ reaction which is a building block for the $pp \to pp\omega$ reaction. Photoproduction of the vector meson in photon-proton collisions is very interesting from both experimental and theoretical side. The corresponding cross sections have been measured by the ZEUS Collaboration at HERA at virtuality of photon $Q^2 \simeq 0$ GeV^2 for ω photoproduction [305] and at large values Q^2 for ω electroproduction $ep \to ep\omega$ [306]. The amplitude for

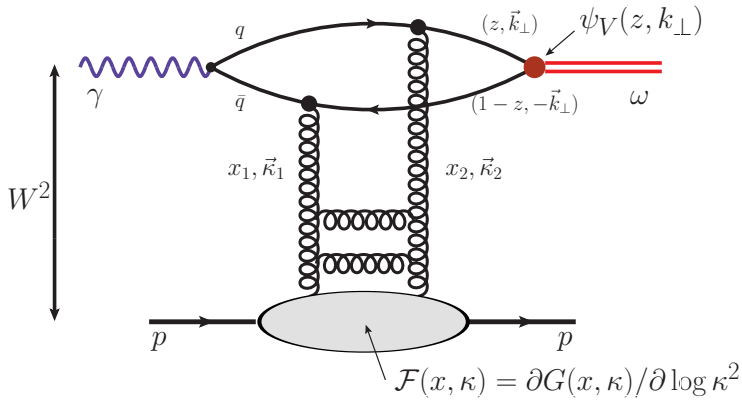

Figure 4.21: A sketch of the amplitude for exclusive photoproduction $\gamma p \to \omega p$ process. Some kinematical variables are shown in addition.

this reaction is shown schematically in Fig.4.21. The pomeron exchange is modelled by a pQCD gluon ladder. The details how to calculate the amplitude are explained in Refs. [274, 281]. The following representation for the imaginary part of the amplitude for the transverse polarization for forward photoproduction $\gamma p \to \omega p$ process is used:

$$\mathrm{Im}\mathcal{M}(W, \Delta^2 = 0, Q^2 = 0) = W^2 \frac{c_V \sqrt{4\pi\alpha_{em}}}{4\pi^2} \int dz d^2\boldsymbol{k}\, d^2\boldsymbol{\kappa} \psi_V(z, \boldsymbol{k}^2) \mathcal{F}(x_{eff}, \boldsymbol{\kappa}^2) I(z, \boldsymbol{k}, \boldsymbol{\kappa}), \tag{4.24}$$

where the precise form of the function $I(z, \boldsymbol{k}, \boldsymbol{\kappa})$ derives from the quark loop in Fig.4.21 and can be found in [281]. Here $\mathcal{F}(x_{eff}, \boldsymbol{\kappa}^2)$ is an unintegrated gluon distribution, taken from [307], which following [281] is evaluated at $x_{eff} = c_{skewed}(m_\omega^2/W^2)$, $c_{skewed} = 0.41$. Notice that this particular unintegrated glue incorporates also the region of soft gluon transverse momenta $\boldsymbol{\kappa}$, where it can be viewed as a model of the soft pomeron in terms of nonperturbative gluons. The process at hand is sensitive to this domain of soft momenta. The charge-isospin factor c_V is $c_\omega = 1/\sqrt{2}(e_u + e_d) = 1/(3\sqrt{2})$.

The full amplitude for the $\gamma p \to \omega p$ process at finite momentum transfer is given as

$$\mathcal{M}(W, \Delta^2, Q^2 = 0) = (i + \tilde{\rho})\, \mathrm{Im}\mathcal{M}(W, \Delta^2 = 0, Q^2 = 0)\, \exp\left(\frac{-B(W)\Delta^2}{2}\right), \tag{4.25}$$

where $\tilde{\rho}$ is a ratio of real to imaginary part of the amplitude and $B(W)$ is the slope parameter dependent on the photon-proton center-of-mass energy and is parametrised as $B(W) = B_0 + 2\alpha'_{eff} \ln(W^2/W_0^2)$ with: $W_0 = 95$ GeV, $B_0 = 11$ GeV^{-2}, $\alpha'_{eff} = 0.25$ GeV^{-2} [308].

Our amplitude is normalized to the total cross section:

$$\sigma(\gamma p \to \omega p) = \frac{1+\tilde{\rho}^2}{16\pi B(W)} \left| \mathrm{Im} \frac{\mathcal{M}(W, \Delta^2 = 0, Q^2 = 0)}{W^2} \right|^2 . \tag{4.26}$$

The radial light-cone wave function of the vector meson can be regarded as a function of three-momentum $\boldsymbol{p} = (\vec{p}, p_z)$, where $\vec{p} = \vec{k}$, $p_z = (2z-1)M/2$ then

$$\psi_V(z, \vec{k}^2) \to \psi_V(p^2), \ \frac{dz d^2\vec{k}}{z(1-z)} \to \frac{4d^3\boldsymbol{p}}{M}, \ p^2 = \frac{M^2 - 4m_q^2}{4} . \tag{4.27}$$

Following [281], in our calculation we use a Gaussian wave function, representing a standard harmonic-oscillator type quark model, which turned out to be superior over a Coulomb wave function (which has a power-law tail in momentum space) for J/Ψ, Υ and ϕ mesons exclusive photoproduction [147, 196, 274]

$$\psi_V(p^2) = N \exp\left(-\frac{p^2 a_1^2}{2} \right) . \tag{4.28}$$

The parameter a_1 is obtained by fitting to the electronic decay width

$$\Gamma(V \to e^+e^-) = \frac{4\pi\alpha_{em}^2 c_V^2}{3m_\omega^3} \cdot g_V^2 , \tag{4.29}$$

where $\Gamma(\omega \to e^+e^-) = 0.6$ keV [96] and imposing the normalization condition

$$1 = \frac{N_c 4\pi}{(2\pi)^3} \int_0^\infty p^2 dp \, 4M \psi_V^2(p^2) . \tag{4.30}$$

In our calculation we use leading-order approximation, i.e. we neglect a possible NLO K-factor. The parameter g_V can be expressed in terms of the ω-meson wave function as [281]

$$g_V = \frac{8N_c}{3} \int \frac{d^3\vec{p}}{(2\pi)^3} (M + m_q) \, \psi_V(p^2) . \tag{4.31}$$

Having in view theoretical uncertainties in defining light quark mass it is treated here as a model parameter. In Fig.4.22 we show the total cross section for the exclusive $\gamma p \to \rho^0 p$ (left panel) and $\gamma p \to \omega p$ (right panel) processes as a function of the γp center-of-mass energy $W_{\gamma p}$ for the photon virtuality $Q^2 = 0$ GeV^2. Our results for exclusive ρ^0 and ω mesons production are compared with the corresponding experimental data. For the ρ^0 meson we present results for three different values of the u and d quark masses assumed here to be identical. The dashed line (bottom) is for $m_q = 0.33$ GeV, the dotted line (top) for $m_q = 0.22$ GeV and the thick solid line (fitted to experimental data) for $m_q = 0.3$ GeV. Because the results for $m_q = 0.3$ GeV give the best description of experimental data, this mass will be used in further calculations. In our calculation the Gaussian wave function is used. We see that it gives quite good description of the high-energy ω-meson data. At low energies the pion exchange mechanism dominates [263, 313].

Pion exchange

The amplitude for the π-exchange shown in Fig.4.23 can be written as:

$$\begin{aligned} \mathcal{M}^{\pi^0-exch.}_{\lambda_\gamma, \lambda_N \to \lambda_\omega, \lambda_{N'}} &= g_{\omega\pi^0\gamma} \, F_{\omega\pi\gamma}(t) \, \varepsilon^{\beta\mu\nu\lambda} \, k_\mu \, k'_\nu \, \varepsilon_\beta(k, \lambda_\gamma) \, \varepsilon^*_\lambda(k', \lambda_\omega) \\ &\times g_{\pi^0 NN} \, F_{\pi NN}(t) \, \frac{1}{t - m_\pi^2} \, \bar{u}(p_{N'}, \lambda_{N'}) \mathrm{i}\gamma_5 u(p_N, \lambda_N) . \end{aligned} \tag{4.32}$$

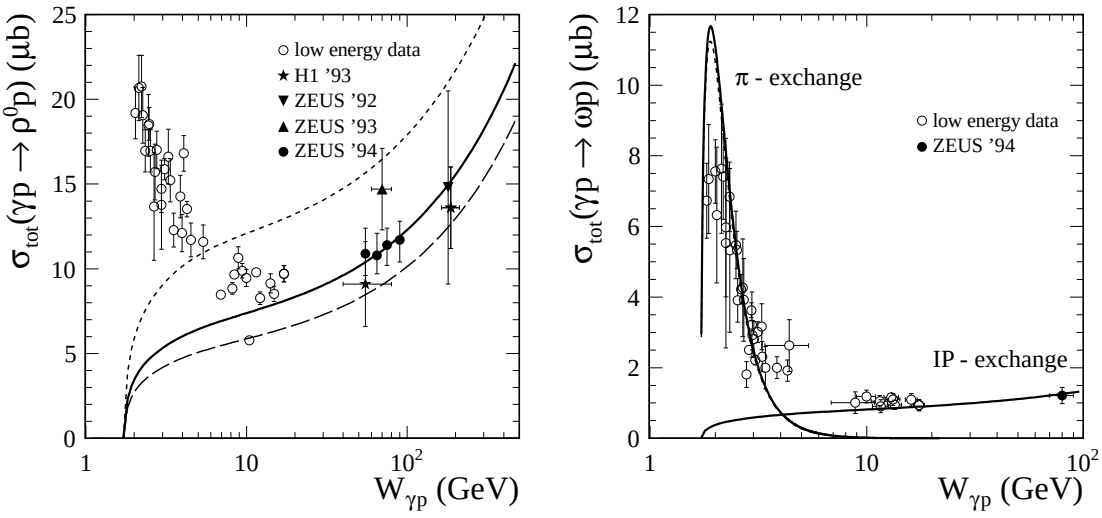

Figure 4.22: Total cross section for the photoproduction $\gamma p \to \rho^0 p$ (left panel) and $\gamma p \to \omega p$ (right panel) processes as a function of the photon-proton center-of-mass energy. In the calculation of the $I\!P$-exchange mechanism the Gaussian wave function of the ρ^0 and ω mesons is used. At low energies π-exchange is the dominant mechanism. The curves are described in the text. Our results are compared with the HERA data [305,309–312] (solid marks) and with a compilation of low energy data (open circles); see Ref. [5] for more references.

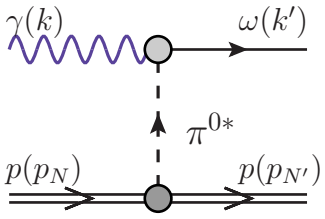

Figure 4.23: Diagram with the π-exchange for exclusive photoproduction $\gamma p \to \omega p$.

The $g_{\omega\pi^0\gamma}$ coupling constant in the formula above is obtained from the ω partial decay width through the relation:

$$\Gamma(\omega \to \pi^0\gamma) = \mathcal{BR}(\omega \to \pi^0\gamma) \cdot \Gamma_{tot} = \frac{g^2_{\omega\pi^0\gamma}}{96\pi} \cdot m^3_\omega \left(1 - \frac{m^2_\pi}{m^2_\omega}\right)^3 . \tag{4.33}$$

Taking experimental partial decay width $\Gamma(\omega \to \pi^0\gamma)$ from [96] we get $g_{\omega\pi^0\gamma} \approx 0.7$ GeV^{-1} which is consistent with the values used in Refs. [263,314] [5]. The pion-nucleon coupling constant $g_{\pi NN}$ is relatively well known [45]. In our calculations the coupling constant $g^2_{\pi NN}/4\pi = 13.5$. $\varepsilon_\beta(k,\lambda_\gamma)$ and $\varepsilon^*_\lambda(k',\lambda_\omega)$ are the polarization vectors of the photon and ω meson, respectively.

We describe the low energy data shown in Fig.4.22 (right panel) with $\Lambda_{mon} \approx 0.7$ GeV for the monopole form factors by the dashed line

$$F(t) = \frac{\Lambda^2_{mon} - m^2_\pi}{\Lambda^2_{mon} - t} \tag{4.34}$$

[5] Please note different normalization convention of the coupling constant in all the references.

or with $\Lambda_{exp} \approx 0.8$ GeV for the exponential form factors by the solid line

$$F(t) = \exp\left(\frac{t - m_\pi^2}{\Lambda_{exp}^2}\right) . \tag{4.35}$$

The cut-off parameters obtained from the fit are significantly smaller than e.g. those used in the Bonn model [46, 298]. Such soft form factors may be due to active coupling with the πN and ρN channels not included explicitly both here nor in the literature. The pion exchange describes only angular distributions at forward angles. At larger angles there are other mechanisms as nucleon exchanges or s-channel nucleon resonances [263, 315]. A more refined analysis in the peak region would require description of new very precise CLAS Collaboration data [316] for full range of angular distributions. Such an analysis would need to include also channel couplings discussed above.

The form factors found here will be used when discussing $\gamma\pi^0$ and $\pi^0\gamma$ exchanges in the $pp \to pp\omega$ reaction.

4.3.2 $\gamma I\!P$ and $I\!P\gamma$ exchanges

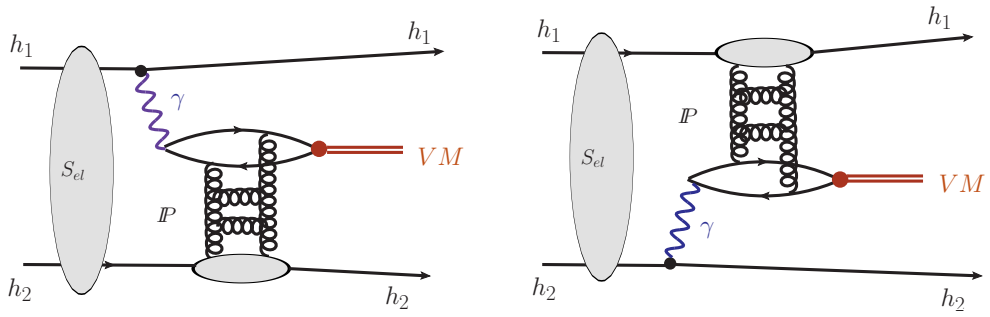

Figure 4.24: A sketch of the exclusive photoproduction $pp \to pp\omega$ amplitudes with absorptive corrections.

The diagrams for the pp and $p\bar{p}$ collisions in Fig.4.24 show schematically the amplitudes for photon-pomeron (pomeron-photon) exchanges with absorptive correction, including elastic rescattering. The full amplitude (with absorptive correction) for the $pp \to pp\omega$ or $p\bar{p} \to p\bar{p}\omega$ reactions can be written as

$$\begin{aligned} \boldsymbol{M}(\vec{p}_1, \vec{p}_2) &= \int \frac{d^2\vec{k}}{(2\pi)^2} S_{el}(\vec{k})\, \boldsymbol{M}^{(0)}(\vec{p}_1 - \vec{k}, \vec{p}_2 + \vec{k}) \\ &= \boldsymbol{M}^{(0)}(\vec{p}_1, \vec{p}_2) - \delta\boldsymbol{M}(\vec{p}_1, \vec{p}_2) , \end{aligned} \tag{4.36}$$

where

$$S_{el}(\vec{k}) = (2\pi)^2\delta^{(2)}(\vec{k}) - \frac{1}{2}T(\vec{k}) , \;\; T(\vec{k}) = \sigma_{tot}^{pp}(s)\, \exp\Big(-\frac{1}{2}B_{el}\vec{k}^2\Big) . \tag{4.37}$$

Here $\vec{p}_1$ and $\vec{p}_2$ are the transverse momenta of outgoing protons (RHIC, LHC) or proton and antiproton (Tevatron). In practical evaluations we take $B_{el} = 14$ GeV^{-2}, $\sigma_{tot}^{pp} = 52$ mb for the RHIC energy $W = 200$ GeV, $B_{el} = 17$ GeV^{-2}, $\sigma_{tot}^{p\bar{p}} = 76$ mb [317] for the Tevatron energy $W = 1.96$ TeV and $B_{el} = 21$ GeV^{-2}, $\sigma_{tot}^{pp} = 100$ mb for the LHC energy $W = 14$ TeV.

The Born-amplitude (without absorptive correction) can be written in the form of a two-dimensional vector (corresponding to the two transverse (linear) polarizations of the final state vector meson) [147] as

$$\begin{aligned} \boldsymbol{M}^{(0)}(\vec{p}_1, \vec{p}_2) &= e_1\frac{2}{z_1}\frac{\vec{p}_1}{t_1}\mathcal{F}_{\lambda_1'\lambda_1}(\vec{p}_1, t_1)\mathcal{M}_{\gamma^* h_2 \to V h_2}(s_2, t_2, Q_1^2) \\ &+ e_2\frac{2}{z_2}\frac{\vec{p}_2}{t_2}\mathcal{F}_{\lambda_2'\lambda_2}(\vec{p}_2, t_2)\mathcal{M}_{\gamma^* h_1 \to V h_1}(s_1, t_1, Q_2^2) , \end{aligned} \tag{4.38}$$

where $\mathcal{M}_{\gamma^* h_2 \to V h_2}(s_2, t_2, Q_1^2)$ and $\mathcal{M}_{\gamma^* h_1 \to V h_1}(s_1, t_1, Q_2^2)$ are the amplitudes for photoproduction discussed above (see (4.25)). Because of the presence of the Dirac electromagnetic form factor of the proton/antiproton only small Q_1^2 and Q_2^2 enter the amplitude for the hadronic process. This means that in practice one can put $Q_1^2 = Q_2^2 = 0$ GeV^2 for the $\gamma^* p \to V p$ amplitudes. We have used the assumption of s-channel helicity conservation in the $\gamma \to \omega$ transition, $\lambda_\gamma = \lambda_V$.

The absorptive correction for the amplitude have the form:

$$\delta \boldsymbol{M}(\vec{p}_1, \vec{p}_2) = \int \frac{d^2\vec{k}}{2(2\pi)^2}\, T(\vec{k})\, \boldsymbol{M}^{(0)}(\vec{p}_1 - \vec{k}, \vec{p}_2 + \vec{k})\,. \tag{4.39}$$

The differential cross section is expressed in terms of the full amplitude $\boldsymbol{M}$ as

$$d\sigma = \frac{1}{512\pi^4 s^2} |\boldsymbol{M}|^2\, dy_\omega dt_1 dt_2\,, d\phi\,. \tag{4.40}$$

where y_ω is rapidity of the ω meson, $t_{1,2} \simeq -\vec{p}_{1,2}^{\,2}$ and ϕ is the azimuthal angle between transverse momenta $\vec{p}_1$ and $\vec{p}_2$. [6]

4.3.3 $\gamma\pi^0$ and $\pi^0\gamma$ exchanges

As shown in Fig.4.22 the QCD mechanism does not describe the huge close-to-threshold enhancement of the cross section. This indicates a presence of another mechanisms of omega photoproduction. Neutral pion exchange is the best candidate which describes the low energy data as discussed in 4.3.1 (Pion exchange). Therefore for the $pp \to pp\omega$ reaction we should include also photon-pion and pion-photon exchanges. The underlying mechanisms are shown in Fig. 4.25.

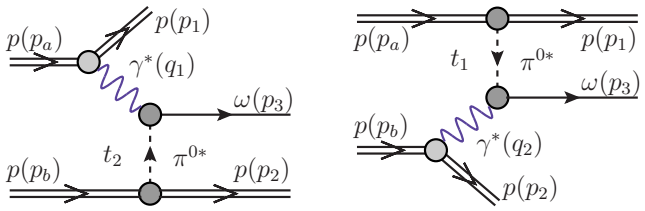

Figure 4.25: Diagrams with the $\gamma\pi^0$ and $\pi^0\gamma$ exchange amplitudes in the $pp \to pp\omega$ reaction.

The amplitudes for the two new processes can be written easily as:

$$\begin{aligned}
\mathcal{M}^{\gamma\pi^0-exchange}_{\lambda_a\lambda_b\to\lambda_1\lambda_2\lambda_3} &= e\, F_1(t_1)\, \bar{u}(p_1,\lambda_1)\gamma^\alpha u(p_a,\lambda_a) \\
&\times \frac{-g_{\alpha\beta}}{t_1}\, g_{\omega\pi^0\gamma} F_{\gamma\pi\to\omega}(t_1,t_2)\, \varepsilon^{\beta\mu\nu\lambda}\, q_{1\mu}\, p_{3\nu} \varepsilon^*_\lambda(p_3,\lambda_3) \\
&\times g_{\pi^0 NN} F_{\pi NN}(t_2)\, \frac{1}{t_2 - m_\pi^2}\, \bar{u}(p_2,\lambda_2) \mathrm{i}\gamma_5 u(p_b,\lambda_b)\,, \qquad (4.41) \\
\mathcal{M}^{\pi^0\gamma-exchange}_{\lambda_a\lambda_b\to\lambda_1\lambda_2\lambda_3} &= g_{\pi^0 NN} F_{\pi NN}(t_1)\, \frac{1}{t_1 - m_\pi^2}\, \bar{u}(p_1,\lambda_1) \mathrm{i}\gamma_5 u(p_a,\lambda_a) \\
&\times \frac{-g_{\alpha\beta}}{t_2}\, g_{\omega\pi^0\gamma} F_{\gamma\pi\to\omega}(t_2,t_1)\, \varepsilon^{\beta\mu\nu\lambda}\, q_{2\mu}\, p_{3\nu} \varepsilon^*_\lambda(p_3,\lambda_3) \\
&\times e\, F_1(t_2)\, \bar{u}(p_2,\lambda_2)\gamma^\alpha u(p_b,\lambda_b)\,, \qquad (4.42)
\end{aligned}$$

where $F_1(t_{1,2})$ are the Dirac electromagnetic form factors of participating protons. The $g_{\omega\pi^0\gamma}$ constant was obtained from the omega partial decay width as discussed in 4.3.1 (Pion exchange).

[6] In the following for brevity we shall use notation $t_{1,2}$ which means t_1 or t_2.

The coupling of the pion to the nucleon $g^2_{\pi NN}/4\pi = 13.5$ is relatively well known (see e.g. [45]) and the corresponding form factor is taken in the exponential form:

$$F_{\pi NN}(t_{1,2}) = \exp\left(\frac{t_{1,2} - m_\pi^2}{\Lambda^2_{\pi NN}}\right). \tag{4.43}$$

The central vertices involve off-shell particles. Here the $\gamma\pi^0$ and $\pi^0\gamma$ form factors $F_{\gamma\pi\to\omega}(t_1, t_2)$ are taken in the factorized form given by Eq. (4.17). In practical calculations we take: $\Lambda_{\pi NN}$ = 0.8 GeV and $\Lambda_{\omega\pi\gamma}$ = 0.8 GeV as found from the fit to the $\gamma p \to \omega p$ experimental data.

At high-energies often light-cone form factors are used instead of the t_1 or t_2 dependent ones discussed above (see Eq.(4.43)). In such an approach the pion is rather a constituent of the initial proton. Then the form factors are parametrised in terms of the squared invariant masses of the πN system:

$$\begin{aligned} M^2_{2,\pi N}(z_2, p^2_{2t}) &= \frac{m_N^2 + p^2_{2t}}{z_2} + \frac{m_\pi^2 + p^2_{2t}}{1 - z_2}, \\ M^2_{1,\pi N}(z_1, p^2_{1t}) &= \frac{m_N^2 + p^2_{1t}}{z_1} + \frac{m_\pi^2 + p^2_{1t}}{1 - z_1}, \end{aligned} \tag{4.44}$$

where the longitudinal momentum fractions of outgoing protons with respect to the initial protons can be calculated from energies and z-components of momenta of participating protons

$$\begin{aligned} z_2 &= (p_{20} - p_{2z})/(p_{b0} - p_{bz}), \\ z_1 &= (p_{10} + p_{1z})/(p_{a0} + p_{az}). \end{aligned} \tag{4.45}$$

The light-cone form factors are parametrised then as

$$\begin{aligned} F_{\pi NN}(M^2_{2,\pi N}) &= \exp\left(-\frac{M^2_{2,\pi N}(z_2, p^2_{2t}) - m_N^2}{2\Lambda^2_{LC}}\right), \\ F_{\pi NN}(M^2_{1,\pi N}) &= \exp\left(-\frac{M^2_{1,\pi N}(z_1, p^2_{1t}) - m_N^2}{2\Lambda^2_{LC}}\right). \end{aligned} \tag{4.46}$$

The parameter Λ_{LC} in the light-cone parametrisation was fitted in Ref. [318] to the data on forward nucleon production and the value $\Lambda_{LC} = 1.1$ GeV was found.

The amplitude for processes shown in Fig.4.25 is calculated numerically for each point in the phase space. In calculating cross section we perform integration in $\log_{10}(p_{1\perp})$ (for $\gamma\pi$-exchange) and $\log_{10}(p_{2\perp})$ (for $\pi\gamma$-exchange) instead in $p_{1\perp}$ and $p_{2\perp}$.

4.3.4 ω-bremsstrahlung mechanisms

The strong coupling of the ω meson to the nucleon causes that the hadronic bremsstrahlung mechanisms become important. The bremsstrahlung mechanisms for exclusive production of ω discussed here are shown schematically in Fig.4.26. In the case of ω production the diagrams with intermediate nucleon resonances are negligible (see [96]). Because at high energy the pomeron is the driving mechanism of bremsstrahlung it is logical to call the mechanisms diffractive bremsstrahlung to distinguish from the low-energy bremsstrahlung driven by meson exchanges.

It is straightforward to evaluate the contribution of diagrams shown in Fig.4.26. The

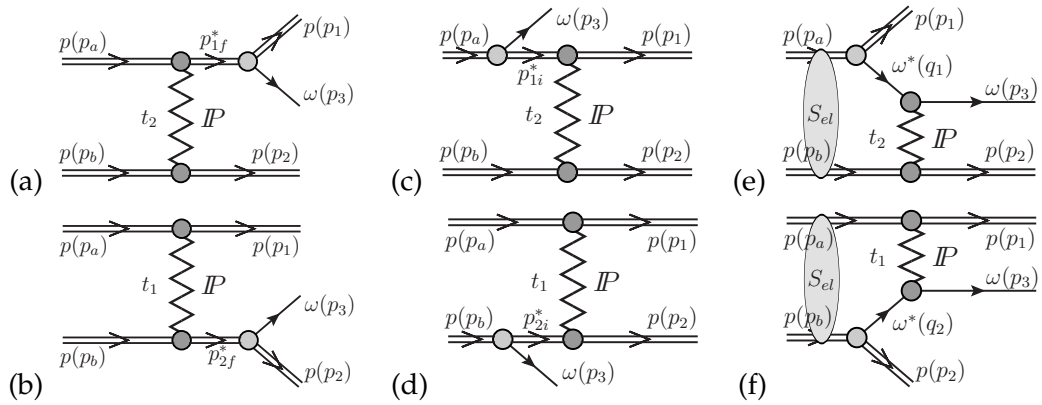

Figure 4.26: Diagrams of the ω bremsstrahlung amplitudes. The absorption effects due to proton-proton interaction are included.

Born amplitudes read:

$$\mathcal{M}^{(a)}_{\lambda_a\lambda_b\to\lambda_1\lambda_2\lambda_3} = \bar{u}(p_1,\lambda_1)\varepsilon^*_\mu(p_3,\lambda_3)\gamma^\mu S_N(p^*_{1f})u(p_a,\lambda_a)\; g_{\omega NN}\; F_{\omega N^*N}(p^{*2}_{1f})\; F_{I\!PNN^*}(p^{*2}_{1f})$$
$$\times \mathrm{i}s_{ab}C^{NN}_{I\!P}\left(\frac{s_{ab}}{s_0}\right)^{\alpha_{I\!P}(t_2)-1}\exp\left(\frac{B^{NN}_{I\!P}t_2}{2}\right)\;\delta_{\lambda_2\lambda_b}, \tag{4.47}$$

$$\mathcal{M}^{(b)}_{\lambda_a\lambda_b\to\lambda_1\lambda_2\lambda_3} = \bar{u}(p_2,\lambda_2)\varepsilon^*_\mu(p_3,\lambda_3)\gamma^\mu S_N(p^{*2}_{2f})u(p_b,\lambda_b)\; g_{\omega NN}\; F_{\omega N^*N}(p^{*2}_{2f})\; F_{I\!PNN^*}(p^{*2}_{2f})$$
$$\times \mathrm{i}s_{ab}C^{NN}_{I\!P}\left(\frac{s_{ab}}{s_0}\right)^{\alpha_{I\!P}(t_1)-1}\exp\left(\frac{B^{NN}_{I\!P}t_1}{2}\right)\;\delta_{\lambda_1\lambda_a}, \tag{4.48}$$

$$\mathcal{M}^{(c)}_{\lambda_a\lambda_b\to\lambda_1\lambda_2\lambda_3} = \bar{u}(p_1,\lambda_1)S_N(p^{*2}_{1i})\varepsilon^*_\mu(p_3,\lambda_3)\gamma^\mu u(p_a,\lambda_a)\; g_{\omega NN}\; F_{\omega NN^*}(p^{*2}_{1i})\; F_{I\!PN^*N}(p^{*2}_{1i})$$
$$\times \mathrm{i}s_{12}C^{NN}_{I\!P}\left(\frac{s_{12}}{s_0}\right)^{\alpha_{I\!P}(t_2)-1}\left(\frac{s_{13}}{s_{thr}}\right)^{\alpha_N(p^{*2}_{1i})-1}\exp\left(\frac{B^{NN}_{I\!P}t_2}{2}\right)\;\delta_{\lambda_2\lambda_b}, \tag{4.49}$$

$$\mathcal{M}^{(d)}_{\lambda_a\lambda_b\to\lambda_1\lambda_2\lambda_3} = \bar{u}(p_2,\lambda_2)S_N(p^{*2}_{2i})\varepsilon^*_\mu(p_3,\lambda_3)\gamma^\mu u(p_b,\lambda_b)\; g_{\omega NN}\; F_{\omega NN^*}(p^{*2}_{2i})\; F_{I\!PN^*N}(p^{*2}_{2i})$$
$$\times \mathrm{i}s_{12}C^{NN}_{I\!P}\left(\frac{s_{12}}{s_0}\right)^{\alpha_{I\!P}(t_1)-1}\left(\frac{s_{23}}{s_{thr}}\right)^{\alpha_N(p^{*2}_{2i})-1}\exp\left(\frac{B^{NN}_{I\!P}t_1}{2}\right)\;\delta_{\lambda_1\lambda_a}. \tag{4.50}$$

The amplitudes for the interaction with emitted ω meson:

$$\mathcal{M}^{(e)}_{\lambda_a\lambda_b\to\lambda_1\lambda_2\lambda_3} = \bar{u}(p_1,\lambda_1)\gamma^\mu u(p_a,\lambda_a)S_{\mu\nu}(t_1)\varepsilon^{\nu*}(p_3,\lambda_3)\; g_{\omega NN}\; F_{\omega^*NN}(t_1)F_{I\!P\omega^*\omega}(t_1)$$
$$\times \mathrm{i}s_{23}C^{\omega N}_{I\!P}\left(\frac{s_{23}}{s_0}\right)^{\alpha_{I\!P}(t_2)-1}\left(\frac{s_{13}}{s_{thr}}\right)^{\alpha_\omega(t_1)-1}\exp\left(\frac{B^{\omega N}_{I\!P}t_2}{2}\right)\;\delta_{\lambda_2\lambda_b}, \tag{4.51}$$

$$\mathcal{M}^{(f)}_{\lambda_a\lambda_b\to\lambda_1\lambda_2\lambda_3} = \bar{u}(p_2,\lambda_2)\gamma^\mu u(p_b,\lambda_b)S_{\mu\nu}(t_2)\varepsilon^{\nu*}(p_3,\lambda_3)\; g_{\omega NN}\; F_{\omega^*NN}(t_2)F_{I\!P\omega^*\omega}(t_2)$$
$$\times \mathrm{i}s_{13}C^{\omega N}_{I\!P}\left(\frac{s_{13}}{s_0}\right)^{\alpha_{I\!P}(t_1)-1}\left(\frac{s_{23}}{s_{thr}}\right)^{\alpha_\omega(t_2)-1}\exp\left(\frac{B^{\omega N}_{I\!P}t_1}{2}\right)\;\delta_{\lambda_1\lambda_a}, \tag{4.52}$$

where $s_0 = 1\,\mathrm{GeV}^2$ and $s_{thr} = (m_N + m_\omega)^2$. The absorption effect for the hadronic bremsstrahlung contributions requires a short comment. Since in practice for the pomeron exchanges in diagrams (a) - (d) we use phenomenological interactions which effectively describe the total and elastic data an additional use of absorption would be a double counting. This is not the case for diagrams (e) and (f) where the interaction is between ω-meson and proton. Consequently in the latter case we include absorption effects in full analogy to that described in section about photoproduction. The factor $g_{\omega NN}$ is the omega nucleon coupling constant. Different values have been used in the literature [46, 298]. In our calculation we assume coupling constant $g^2_{\omega NN}/4\pi = 10$. Similar value was used in Refs. [294, 296].

In the above equations $u(p_i,\lambda_i)$, $\bar{u}(p_f,\lambda_f) = u^\dagger(p_f,\lambda_f)\gamma^0$ are the Dirac spinors (normalized as $\bar{u}(p)u(p) = 2m_N$) of the initial and outgoing protons with the four-momentum p and the helicities λ. The propagators of nucleons and ω meson can be written as

$$S_N(p^{*2}_{1f,2f}) = \frac{\mathrm{i}(p^*_{1f,2f_\nu}\gamma^\nu + m_N)}{p^{*2}_{1f,2f} - m_N^2}\,, \tag{4.53}$$

$$S_N(p^{*2}_{1i,2i}) = \frac{\mathrm{i}(p^*_{1i,2i_\nu}\gamma^\nu + m_N)}{p^{*2}_{1i,2i} - m_N^2}\,, \tag{4.54}$$

$$S_{\mu\nu}(t) = \frac{-g_{\mu\nu} + \frac{q_\mu q_\nu}{m_\omega^2}}{t - m_\omega^2}\,, \tag{4.55}$$

where $t_{1,2} = (p_{a,b} - p_{1,2})^2 = q^2_{1,2}$, $p^{*2}_{1i,2i} = (p_{a,b} - p_3)^2$, $p^{*2}_{1f,2f} = (p_{1,2} + p_3)^2$ are the four-momenta squared of objects in the middle of diagrams and $s_{ij} = (p_i + p_j)^2$ are squared invariant masses of the (i,j) system.

Using the known strength parameters for the NN and πN scattering fitted to the corresponding total cross sections (the Donnachie-Landshoff model [113]) we obtain $C_{I\!P}^{NN} = 21.7$ mb and $C_{I\!P}^{\omega N} = C_{I\!P}^{\pi N} = 13.63$ mb, see Table 2.1. The pomeron trajectory determined from elastic and total cross sections is taken in the linear approximation in t, see Eq. (2.11) and Fig. 2.1(a). We take the slope parameters: $B_{I\!P}^{\omega N} = B_{I\!P}^{\pi N} = 5.5\ \mathrm{GeV}^{-2}$ and $B_{I\!P}^{NN} = 9\ \mathrm{GeV}^{-2}$ (2.10).

The extra factors $F_{\omega NN}$ and $F_{I\!PNN}$ (or $F_{I\!P\omega\omega}$) allow for modification when one of the nucleons or the ω-meson is off its mass shell. We parametrise all the form factors in the following exponential form:

$$\begin{aligned}
&F_{\omega NN}(p^{*2}_{1f,2f}) = \exp\left(\frac{-(p^{*2}_{1f,2f} - m_N^2)}{\Lambda^2}\right), F_{I\!PNN}(p^{*2}_{1f,2f}) = \exp\left(\frac{-(p^{*2}_{1f,2f} - m_N^2)}{\Lambda^2_{I\!PNN}}\right),\\
&F_{\omega NN}(p^{*2}_{1i,2i}) = \exp\left(\frac{p^{*2}_{1i,2i} - m_N^2}{\Lambda^2}\right), F_{I\!PNN}(p^{*2}_{1i,2i}) = \exp\left(\frac{p^{*2}_{1i,2i} - m_N^2}{\Lambda^2_{I\!PNN}}\right),\\
&F_{\omega NN}(t_{1,2}) = \exp\left(\frac{t_{1,2} - m_\omega^2}{\Lambda^2}\right), F_{I\!P\omega\omega}(t_{1,2}) = \exp\left(\frac{t_{1,2} - m_\omega^2}{\Lambda^2_{I\!P\omega\omega}}\right).
\end{aligned} \tag{4.56}$$

In general, the cut-off parameters are not known but could be fitted to the (normalized) experimental data. From our general experience in hadronic physics we expect $\Lambda \approx \Lambda_{I\!PNN} \approx \Lambda_{I\!P\omega\omega} = 1$ GeV. We shall discuss how the uncertainties of the form factors influence our final results.

The amplitudes above, (4.51 and 4.52), are corrected by the Regge-like factors to reproduce the high-energy Regge dependence: $(s_{13}/s_{thr})^{\alpha_\omega(t_1)-1}$ and $(s_{23}/s_{thr})^{\alpha_\omega(t_2)-1}$, where $s_{thr} = (m_p + m_\omega)^2$, respectively. We improve also the parametrisation of the amplitudes (4.49, 4.50) by the factors $\left(\frac{s_{i3}}{s_{thr}}\right)^{\alpha_N(p^{*2}_{1i,2i})-1}$, where we assume the nucleon trajectory $\alpha_N(p^{*2}_{1i,2i}) = -0.3 + \alpha'_N\, p^{*2}_{1i,2i}$, with $\alpha'_N = 0.9\ \mathrm{GeV}^{-2}$.

We have chosen a representation for the polarization vectors of the ω-meson in the helicity states $\lambda_3 = 0, \pm 1$. The polarization vectors are defined in the proton-proton center-of-mass frame, where $p = (E_3, p_3\cos\phi\sin\theta, p_3\sin\phi\sin\theta, p_3\cos\theta)$, as

$$\begin{aligned}
\varepsilon(p_3,0) &= \frac{E_3}{m_\omega}\left(\frac{p_3}{E_3}, \cos\phi\sin\theta, \sin\phi\sin\theta, \cos\theta\right),\\
\varepsilon(p_3,\pm 1) &= \frac{1}{\sqrt{2}}(0, i\sin\phi \mp \cos\theta\cos\phi, -i\cos\phi \mp \cos\theta\sin\phi, \pm\sin\theta)\,.
\end{aligned} \tag{4.57}$$

It is easy to check that they fulfill the relation $\varepsilon^\nu(p,\lambda)\varepsilon^*_\nu(p,\lambda) = -1$ and $p^\nu\varepsilon_\nu(p,\lambda) = 0$.

The exclusive production of ω-mesons in the fragmentation region of either proton can also be understood as a diffractive excitation of a two-body ωp-Fock state of the physical proton.

This is best formalized by a Fock state decomposition of the protons light-cone wave function in terms of meson-baryon Fock states. A comprehensive treatment of meson-cloud effects with applications to deep-inelastic scattering and baryon form factors within this framework has been developed in [318, 319], for a review and references see [50]. For the problem at hand, we can write schematically

$$|p\rangle_{phys} = \sqrt{Z}\Big(|p\rangle_{bare} + \int dz d^2\vec{k}_\perp \, \Psi_{\omega p}(z,\vec{k}_\perp) \, |p(1-z,-\vec{k_\perp}); \omega(z,\vec{k_\perp})\rangle + \dots \Big) \,. \tag{4.58}$$

Here, the "bare" proton state represents, for example, a three-quark core of the physical proton, $\Psi_{\omega p}$ is the light-cone wave function of the ωp-Fock state. The ω-meson in the two-body Fock state carries a fraction z of light-cone plus-momentum of the physical proton and transverse momentum $\vec{k}_\perp$; for simplicity helicity labels are suppressed. The invariant mass of the virtual ωp system is then given as

$$M^2_{\omega p} = \frac{\vec{k}^2_\perp + m^2_\omega}{z} + \frac{\vec{k}^2_\perp + m^2_N}{(1-z)} \,, \tag{4.59}$$

and enters the radial part of the wave function in terms of the ωNN-form factor

$$F_{\omega NN}(M^2_{\omega p}) = \exp\Big(- \frac{M^2_{\omega p} - m^2_N}{2\Lambda^2_{LC}} \Big) \,. \tag{4.60}$$

The parameter Λ_{LC} which controls the momentum distribution of ω-mesons in the Fock state is taken as $\Lambda_{LC} = 1.1$ GeV [318].

In accordance with the classic Good-Walker formalism [127], diffractive excitation of the ωp-state now occurs because interactions of the "bare" proton and the two-body ωN-state differ. We can write the ωp scattering state as:

$$|\omega p\rangle_{scatt} = \Big(\hat{S}_{\omega p} - \hat{S}_p \Big) \, |\omega p\rangle \,, \tag{4.61}$$

where $\hat{S}_{\omega p}$ and $\hat{S}_p$ are the elastic scattering matrices for the ωp and p interactions with the target. Assuming, that the S-matrix of the two-body state factorizes, $\hat{S}_{\omega p} = \hat{S}_\omega \, \hat{S}_p$, one can show that Eq.(4.61) generates precisely the diagrams (a), (c), and (e) of Fig.4.26. Diagrams (b), (d), and (f) can be obtained by an obvious symmetrization. In practical evaluation, these diagrams will give similar expressions in momentum space as the ones obtained in the reggeized field theory model (the "standard approach" discussed above), modulo the absence of Regge-factors and the careful replacement of all ωNN-form factors by their light-cone counterparts given in Eq.(4.60).

Notice that this description of diffractive dissociation, which treats the ω-meson as a nonperturbative parton of the proton has a good physical motivation only in the fragmentation region of the proton(s). When the ω-meson is produced in the central rapidity domain, the reggeization of the crossed channel exchanges must be taken into account. For Reggeon exchanges however the light-cone wave function formalism described above is ill defined [320]. Therefore, for a description of midrapidity ω production, one would have to add the reggeized ω exchange. We do not do this here, as the final result would not differ much from the reggeized field theory diagrams (the "standard approach"). At rapidities close to the proton fragmentation region the difference between the "standard approach" and the light-cone wave function treatment can serve as an indicator for the model dependence of our predictions for this particular soft process. Finally let us note, that at the high energies of interest the deviation from factorization

$$\delta\hat{S} = \hat{S}_{\omega p} - \hat{S}_\omega \, \hat{S}_p \,, \tag{4.62}$$

is quantified by the shadowing or absorption correction.

4.4 Results

First of all, we will discuss the role of the ωNN form factors and the ω meson reggeization effect [321] for several differential distributions. In Fig.4.27 we present differential cross sections $d\sigma/dW_{13}$, $d\sigma/dy_\omega$, and $d\sigma/dp_{\perp,\omega}$ for the $pp \to pp\omega$ reaction at $\sqrt{s} = 14$ TeV. We show results with Mandelstam variable dependent form factors (top panels), which we will call standard in the following, and with light-cone form factors (bottom panels). The long dashed, dashed and dotted lines correspond to contributions from diagrams (a), (c) and (e), respectively. In the top panel we show results for the standard spin-1/2 propagators in diagrams (a) and (c) as well as with meson reggeization, see the black and blue lines, respectively. The thick solid line presents the coherent sum of all amplitudes. The light-cone form factors lead to much steeper dependence of the cross section on W_{13} (W_{23}) than the standard form factors. The reggeization leads to an extra damping of the large W_{13} (W_{23}) cross section. The distribution in y_ω is closely related to that for W_{13} (W_{23}). As seen the reggeization makes the $p_{\perp,\omega}$ distribution steeper.

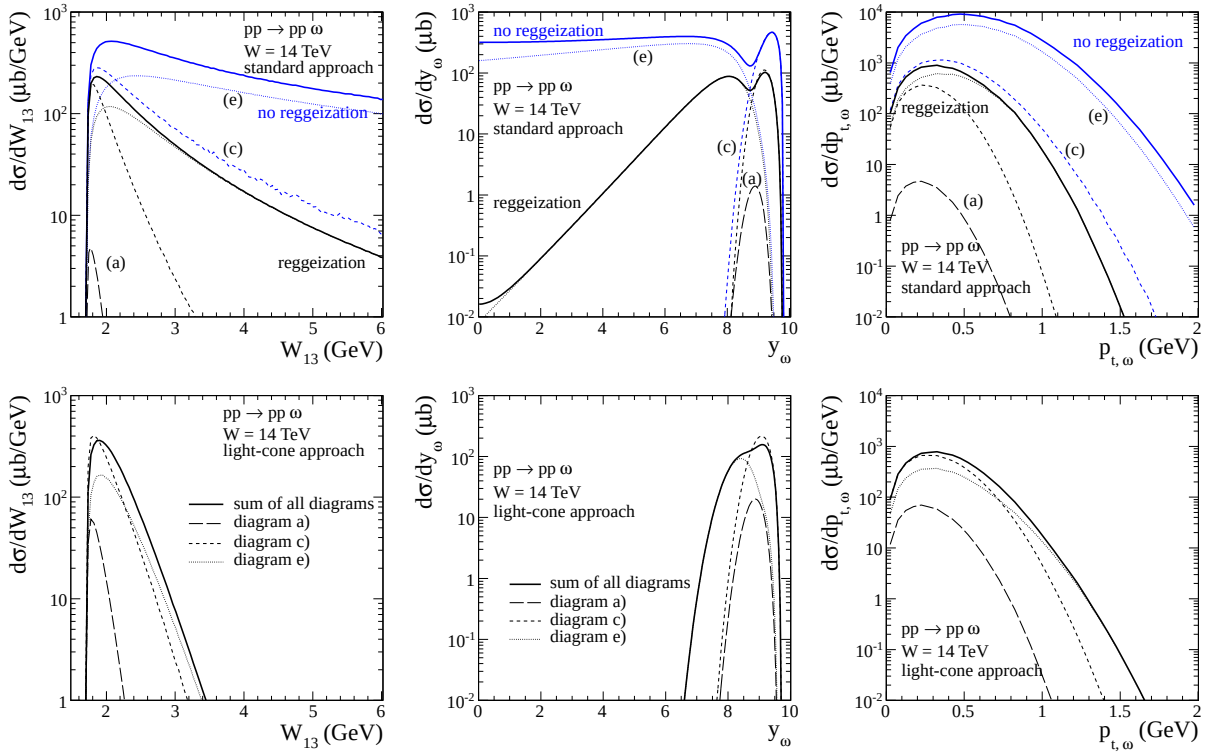

Figure 4.27: Differential cross sections $d\sigma/dW_{13}$, $d\sigma/dy_\omega$, and $d\sigma/dp_{\perp,\omega}$ for the $pp \to pp\omega$ reaction at $\sqrt{s} = 14$ TeV for the hadronic bremsstrahlung mechanisms. The top panels are for results with Mandelstam variable dependent ωNN form factors and with reggeization included while the light-cone approach results are shown in the bottom panels. The thick solid line represents the result for the coherent sum of all amplitudes shown in Fig.4.26.

Now, we present differential distributions for three different c.m. energies: $\sqrt{s} = 200$ GeV (RHIC), $\sqrt{s} = 1960$ GeV (Tevatron) and $\sqrt{s} = 14$ TeV (LHC). This includes rapidity and transverse momentum of ω meson distributions as well as azimuthal correlations between outgoing protons. In Fig.4.28 we present rapidity distribution of the ω meson for the two considered approaches. In the first approach we use the standard ωNN form factors (upper panels) and in the second approach we use the light-cone form factors (bottom panels) for the omega-nucleon-nucleon coupling. The distributions for the standard form factors extend more towards midrapidities. We show the $\gamma I\!P$ ($I\!P\gamma$), $\gamma\pi^0$ ($\pi^0\gamma$) as well as diffractive bremsstrahlung mechanisms. At "low" energy (RHIC) the discussed hadronic bremsstrahlung mechanisms dominate over the $\gamma I\!P$ and $I\!P\gamma$ ones. The cross section for the hadronic bremsstrahlung contribution is two-orders of magnitude bigger than that for the ($\gamma I\!P$, $I\!P\gamma$) contribution. The latter mechanism

is known to be the dominant one for J/Ψ and Υ mesons production [147, 274]. A recent analysis at the Tevatron seems to confirm this claim [180]. Increasing the center-of-mass energy the hadronic bremsstrahlung components move to large rapidities. The $\gamma\pi^0$ (left peak) and the $\pi^0\gamma$ (right peak) components are separated. The separation in rapidity means also lack of interference effects which is very different compared to the $\gamma I\!P$ ($I\!P\gamma$) mechanism [7]. At the LHC energy at midrapidities the photoproduction mechanisms with $I\!P$-exchange dominate over the hadronic bremsstrahlung ones. We predict a narrow plateau around $y_\omega \approx 0$ and a significant increase when going to large $|y_\omega|$. Experimental observation of the increase would confirm the bremsstrahlung mechanisms discussed here. Only at the highest LHC energy the region of very small rapidities is free of the hadronic bremsstrahlung contributions.

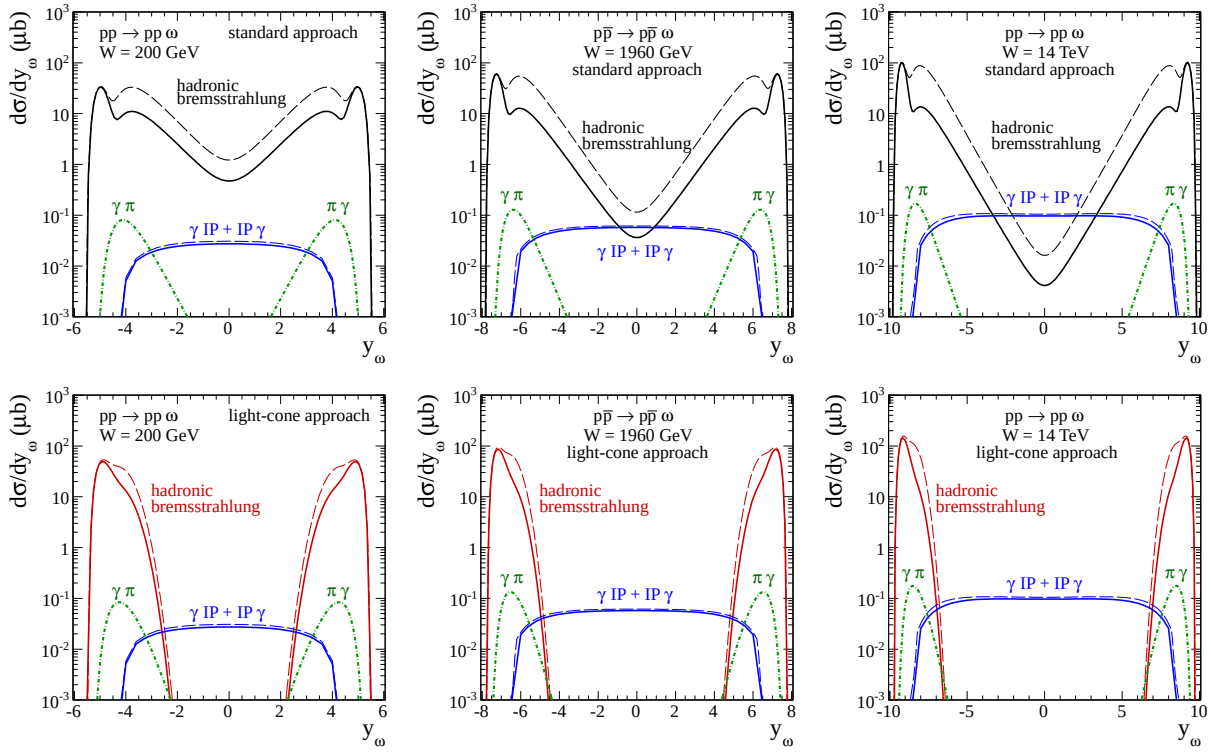

Figure 4.28: Differential cross sections $d\sigma/dy_\omega$ for the $pp(\bar{p}) \to pp(\bar{p})\omega$ reaction at $\sqrt{s}$ = 0.2, 1.96, 14 TeV in the full rapidity range. The upper panels are for results with Mandelstam variable dependent ωNN form factors and with reggeization included while the light-cone form factors correspond to the bottom panels. In the latter case the Regge exchanges are evidently not included. The difference between the results with standard and light-cone form factors illustrates theoretical uncertainties. The blue lines correspond to the QCD $\gamma I\!P$ and $I\!P\gamma$ mechanism. The green dash-dotted lines represent the contribution of diagrams for the $\gamma\pi^0$ (left peak) and $\pi^0\gamma$ (right peak) exchanges. The dashed lines in the figures represent the contributions without absorption, while the thick solid lines include the absorption.

How precise are our estimations of the bremsstrahlung contribution? In Fig.4.29 we show the uncertainty band related to the choice of the form factor parameter. Similar uncertainty band can be expected due to the choice of the proton-proton-omega coupling constant. Our previous conservative estimation was rather a lower limit. While the hadronic bremsstrahlung contributions are subjected to rather large theoretical uncertainties. The $\gamma I\!P$ ($I\!P\gamma$) contributions are fairly precisely estimated. Deviations from the pQCD contribution at midrapidities may be caused by either the difficult to predict hadronic bremsstrahlung contributions or by the very interesting pomeron-odderon contributions. The rise of the cross section with increasing $|y_\omega|$ would be a clear signal of the hadronic bremsstrahlung contributions, while a sizeable deviation

[7] The interference beetwen the two mechanisms $\gamma I\!P$ and $I\!P\gamma$ is proportional to $e_1 e_2(\vec{p}_1 \cdot \vec{p}_2)$ and introduces a charge asymmetry as well as an angular correlations between the outgoing protons.

of the cross section normalization a potential signal of the odderon exchange.

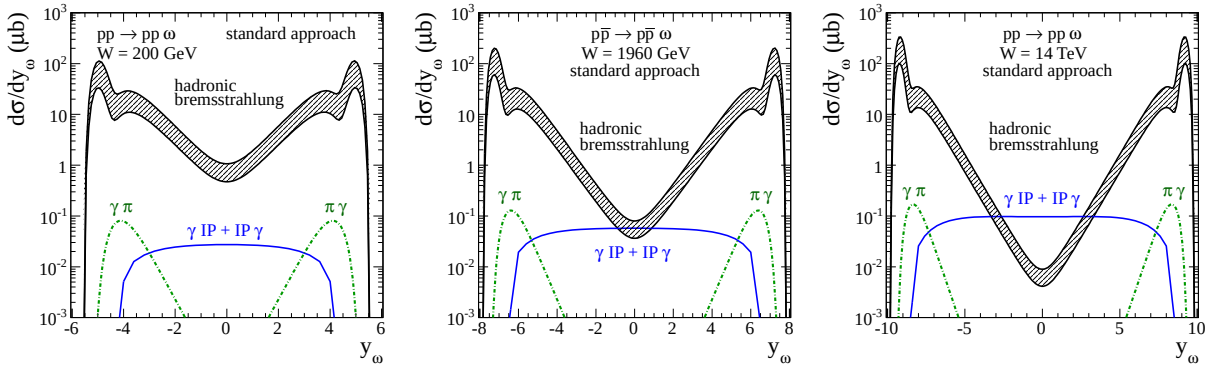

Figure 4.29: Differential cross sections $d\sigma/dy_\omega$ for the $pp(\bar{p}) \to pp(\bar{p})\omega$ reaction at $\sqrt{s}$ = 0.2, 1.96, 14 TeV in the full rapidity range. The uncertainty band for the hadronic bremsstrahlung contributions related to the choice of the form factor parameter for $\Lambda = 1$ GeV (lower limit) and $\Lambda = 1.2$ GeV (upper limit).

In Fig.4.30 (top panels) we show the distribution in the ω meson transverse momentum. In this case the integration is done over full range of meson rapidities. The dashed lines are for the Born level calculations while the thick lines include effect of absorption. The hadronic bremsstrahlung contributions calculated in the light-cone approach are similar to those in the standard approach. The distribution of the photon-pomeron contribution for the $p\bar{p}$ scattering is somewhat different than that for the pp scattering. This is caused by different signs of the interference terms (different combination of electric charges). The distribution of the $\gamma\pi^0$ ($\pi^0\gamma$) contribution (green dash-dotted line) is very similar to that of the $\gamma I\!P$ ($I\!P\gamma$) contribution (blue lines).

In Fig.4.30 (bottom panels) we show distribution in relative azimuthal angle between outgoing protons. For the $\gamma\pi^0$ mechanism the maximum occurs at $\phi_{12} \approx \pi/2$ which is dictated by a specific tensorial coupling $\gamma\pi^0 \to \omega$. The azimuthal distribution for the $\gamma\pi^0$ mechanism is very different than for the hadronic bremsstrahlung contributions which peak at $\phi_{12} = \pi$, especially for the light-cone form factors. In principle, the azimuthal angle correlations could be used therefore to separate the different mechanisms. One can clearly see that the absorption effects (dashed lines) lead to extra decorrelation in azimuth compared to the Born-level results (thick solid lines). In general the azimuthal angle correlations are rapidity dependent. Quite different distributions for the $\gamma I\!P$ ($I\!P\gamma$) contribution have been predicted for the Tevatron and RHIC or LHC. The correlation function for this mechanism is caused totally be the interference of the $\gamma I\!P$ and $I\!P\gamma$ contributions (see [147]). This interference is different for pp- and $p\bar{p}$-collisions because proton and antiproton have opposite charges.

The distributions in the full (pseudo)rapidity range are rather theoretical and may be difficult to measure. One may expect that in practice only limited range of ω meson (pseudo)rapidity around $y_\omega = 0$ will be available experimentally. Therefore, as an example, we have made an extra calculation for a limited rapidity range. In Fig.4.31 (top panels) we show the ω meson transverse momentum distributions for $|y_\omega| < 1$. Here, as can be seen from Fig.4.28, it is enough to include only the hadronic bremsstrahlung diagrams (e) and (f). In this case standard form factors are used only. Please note (see Fig.4.28) that in the case of light-cone form factors the hadronic bremsstrahlung mechanism does not contribute to the restricted rapidity region. For comparison we show the contributions of photoproduction mechanisms which are calculated fairly precisely as discussed before. This is very useful in the context of the searches for odderon. In the bottom panels we show angular correlations between outgoing protons for $|y_\omega| < 1$. In the case of light-cone form factors only the photoproduction mechanism contributes. Testing such distributions together with rapidity distributions could provide therefore new information on the mysterious odderon exchange.

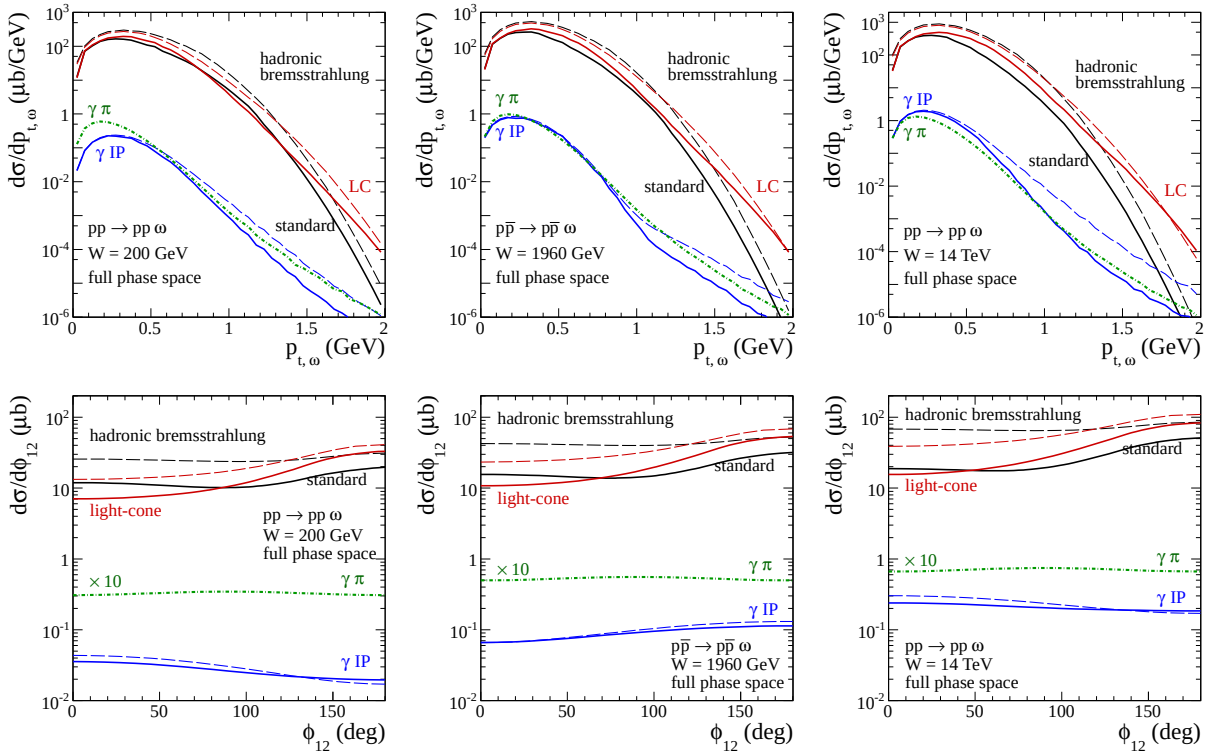

Figure 4.30: Differential cross sections $d\sigma/dp_t$ (top panels) and $d\sigma/d\phi_{12}$ (bottom panels) for the $pp(\bar{p}) \to pp(\bar{p})\omega$ reaction at $\sqrt{s}$ = 0.2, 1.96, 14 TeV in the full rapidity range. Here the reggeized propagators of omega and nucleons are used. The dashed lines represent the contribution without absorption, while the thick solid lines include the absorption.

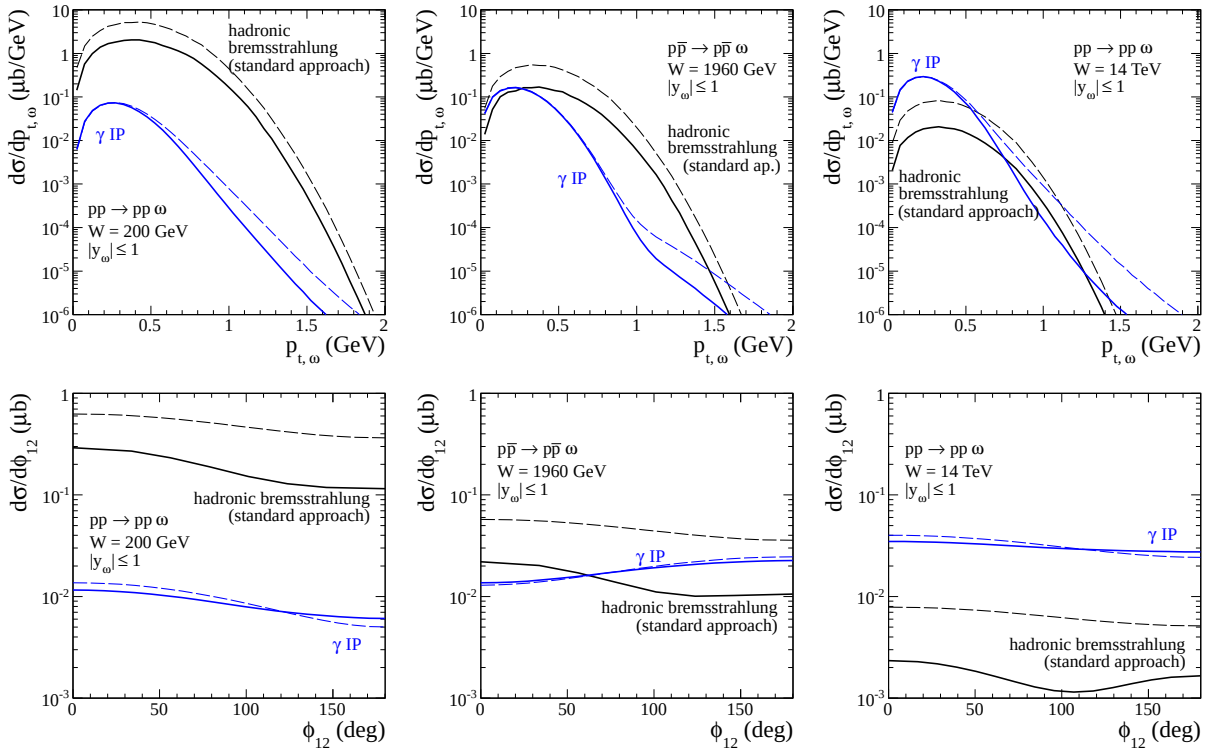

Figure 4.31: Differential cross sections $d\sigma/dp_t$ (top panels) and $d\sigma/d\phi_{12}$ (bottom panels) for the $pp(\bar{p}) \to pp(\bar{p})\omega$ reaction at $\sqrt{s}$ = 0.2, 1.96, 14 TeV for the limited rapidity range $|y_\omega| < 1$. Here the reggeized propagators of omega and standard ωNN form factors are used. The dashed lines represent the contribution without absorption, while the thick solid lines include the absorption.

4.5 Exclusive photon production

We wish to present a first detailed studies of single photon bremsstrahlung in the exclusive process $pp \to pp\gamma$ at the LHC energy $\sqrt{s} = 14$ TeV. We shall include γ-bremsstrahlung diagrams as well as some new diagrams characteristic exclusively for proton-proton scattering, not present e.g. in e^+e^- scattering. We take into account diagrams which arise in the vector-dominance model as well as photon-pion (pion-photon) and photon-pomeron (pomeron-photon) exchange processes. We shall try to identify the region of the phase space where one can expect a dominance of one of the processes through detailed studies of several differential distributions.

4.5.1 γ-bremsstrahlung mechanisms

The photon bremsstrahlung was intensively studied in nucleon-nucleon collisions at low energies (see e.g. [322–328] and references therein). There the dominant mechanisms are nucleon current (off-shell nucleon) and/or mesonic current (photon emitted from the middle of exchanged mesons) contributions driven by meson exchanges. At high energies the exclusive diffractive γ-bremsstrahlung mechanism was almost not studied in the literature [8]. The exclusive production mechanism is similar to $pp \to pp\omega$ [5] and $pp \to pp\pi^0$ [9] processes, where the dominant hadronic bremsstrahlung-type mechanism is the Drell-Hiida-Deck (DHD) mechanism [258, 259] for diffractive production of πN final states (for a nice review we refer to [126] and references therein).

In the presented approach we consider a so-called vector model of the pomeron, called sometimes Donnachie-Landshoff model. This model is known to have some deficiencies. For example, in Ref. [331] it was shown that this model when applied to quark-antiquark production in deep-inelastic scattering violates gauge invariance. The main problems there are for virtual photons and for the coupling of the pomeron to quark and antiquark. Here we consider real photons and coupling to protons. Coupling of anything to extended, off-shell objects, like nucleons, requires a special care. This is especially true when electromagnetic interaction comes into game (see e.g. [323]). The introduction of form factors for extended objects is one of potential sources of gauge invariance violation, which can be easily checked for an academic case when the effective pomeron exchange is replaced by the t-channel photon exchange. There are no general and systematic methods how to treat this problem. In general, in effective theories contact terms appear. The simple pomeron model considered here is certainly not the final word in the field. Furthermore there are good arguments that tensor pomeron could be an alternative [13, 203]. Further studies are necessary to find optimal model for the effective pomeron exchange and how the form factors for off-shell non-point-like particles should be constructed to preserve gauge invariance.

The bremsstrahlung mechanisms for exclusive production of photons discussed here are shown schematically in Fig.4.32. In the case of γ production the diagrams with intermediate nucleon resonances (see [96]) should be negligible. The pronounced at low energy proton to Δ isobar transitions are suppressed in high energy regime.

[8] The $pp \to pp\gamma$ process at high energies was discussed also in Ref. [329, 330] and it was proposed to use the exclusive photon bremsstrahlung to measure or estimate elastic proton-proton cross section at the LHC. Only approximate formulas for the diffractive bremsstrahlung were given there. The participating particles were treated there as point-like particles. No differential distributions for the exclusive bremsstrahlung have been discussed.

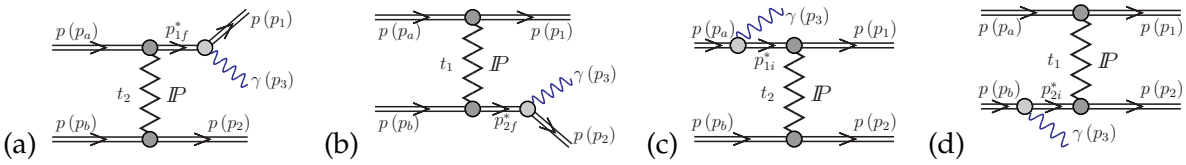

Figure 4.32: Diagrams of the γ-bremsstrahlung amplitudes driven by the pomeron exchange.

The Born amplitudes of diagrams shown in Fig. 4.32 can be written as

$$\mathcal{M}^{(a)\ \boldsymbol{P}-exch.}_{\lambda_a\lambda_b\to\lambda_1\lambda_2\lambda_3} = e\,\bar{u}(p_1,\lambda_1)\not{\epsilon}^*(p_3,\lambda_3)S_N(p_{1f}^2)\gamma^\mu u(p_a,\lambda_a)\,F_{\gamma N^*N}(p_{1f}^2)\,F_{\boldsymbol{P}NN^*}(p_{1f}^2)$$
$$\times is\,C^{NN}_{\boldsymbol{P}}\left(\frac{s}{s_0}\right)^{\alpha_{I\!P}(t_2)-1}\exp\left(\frac{B^{NN}_{\boldsymbol{P}}t_2}{2}\right)\frac{1}{2s}\,\bar{u}(p_2,\lambda_2)\gamma_\mu u(p_b,\lambda_b)\,, \quad (4.63)$$

$$\mathcal{M}^{(b)\ \boldsymbol{P}-exch.}_{\lambda_a\lambda_b\to\lambda_1\lambda_2\lambda_3} = e\,\bar{u}(p_2,\lambda_2)\not{\epsilon}^*(p_3,\lambda_3)S_N(p_{2f}^2)\gamma^\mu u(p_b,\lambda_b)\,F_{\gamma N^*N}(p_{2f}^2)\,F_{\boldsymbol{P}NN^*}(p_{2f}^2)$$
$$\times is\,C^{NN}_{\boldsymbol{P}}\left(\frac{s}{s_0}\right)^{\alpha_{I\!P}(t_1)-1}\exp\left(\frac{B^{NN}_{\boldsymbol{P}}t_1}{2}\right)\frac{1}{2s}\,\bar{u}(p_1,\lambda_1)\gamma_\mu u(p_a,\lambda_a)\,, \quad (4.64)$$

$$\mathcal{M}^{(c)\ \boldsymbol{P}-exch.}_{\lambda_a\lambda_b\to\lambda_1\lambda_2\lambda_3} = e\,\bar{u}(p_1,\lambda_1)\gamma^\mu S_N(p_{1i}^2)\not{\epsilon}^*(p_3,\lambda_3)u(p_a,\lambda_a)\,F_{\gamma NN^*}(p_{1i}^2)\,F_{\boldsymbol{P}N^*N}(p_{1i}^2)$$
$$\times is_{12}\,C^{NN}_{\boldsymbol{P}}\left(\frac{s_{12}}{s_0}\right)^{\alpha_{I\!P}(t_2)-1}\exp\left(\frac{B^{NN}_{\boldsymbol{P}}t_2}{2}\right)\frac{1}{2s_{12}}\,\bar{u}(p_2,\lambda_2)\gamma_\mu u(p_b,\lambda_b)\,, \quad (4.65)$$

$$\mathcal{M}^{(d)\ \boldsymbol{P}-exch.}_{\lambda_a\lambda_b\to\lambda_1\lambda_2\lambda_3} = e\,\bar{u}(p_2,\lambda_2)\gamma^\mu S_N(p_{2i}^2)\not{\epsilon}^*(p_3,\lambda_3)u(p_b,\lambda_b)\,F_{\gamma NN^*}(p_{2i}^2)\,F_{\boldsymbol{P}N^*N}(p_{2i}^2)$$
$$\times is_{12}\,C^{NN}_{\boldsymbol{P}}\left(\frac{s_{12}}{s_0}\right)^{\alpha_{I\!P}(t_1)-1}\exp\left(\frac{B^{NN}_{\boldsymbol{P}}t_1}{2}\right)\frac{1}{2s_{12}}\,\bar{u}(p_1,\lambda_1)\gamma_\mu u(p_a,\lambda_a)\,, \quad (4.66)$$

where $u(p,\lambda)$, $\bar{u}(p',\lambda') = u^\dagger(p',\lambda')\gamma^0$ are the Dirac spinors (normalized as $\bar{u}(p')u(p) = 2m_p$) of the initial and outgoing protons with the four-momentum p and helicities λ. The four-momenta squared of virtual nucleons in the middle of diagrams are defined as $t_{1,2} = q^2_{1,2} = (p_{a,b} - p_{1,2})^2$, $p^2_{1i,2i} = (p_{a,b} - p_3)^2$, $p^2_{1f,2f} = (p_{1,2} + p_3)^2$ and $s_{ij} = W^2_{ij} = (p_i + p_j)^2$ are squared invariant masses of the (i,j) system. The propagators of the intermediate nucleons can be written as (4.5). The polarization vectors of real photon ($\not{\epsilon}^*(p_3,\pm1) = \gamma^\nu\epsilon^*_\nu(p_3,\pm1)$) are defined as (4.57), where θ is the polar angle and ϕ is the azimuthal angle of an emitted photon.

We use interaction parameters of Donnachie-Landshoff [113] with $C^{NN}_{\boldsymbol{P}} = 21.7$ mb and the linear pomeron trajectory (2.11). We take the pomeron slope parameter $B^{NN}_{\boldsymbol{P}} = 9$ GeV^{-2} which approximately describes a running slope (2.10) for proton-proton elastic scattering. Since in our calculations we include the pomeron exchange describing approximately the nucleon-nucleon elastic scattering no explicit absorption corrections have to be included in addition. In our approach the off-shell effects related to the non-point-like protons in the intermediate state are included by the form factors (4.7).

We could "improve" the parametrisation of the amplitudes (4.65) and (4.66) to reproduce the high-energy Regge dependence by the factors $\left(s_{13}/m_p^2\right)^{\alpha_N(p^2_{1i})-\frac{1}{2}}$ and $\left(s_{23}/m_p^2\right)^{\alpha_N(p^2_{2i})-\frac{1}{2}}$, respectively, where the nucleon trajectory is $\alpha_N(p^2_{1i,2i}) = -0.3 + \alpha'_N\,p^2_{1i,2i}$, with $\alpha'_N = 0.9$ GeV^{-2}, see Fig. 2.1(b). We leave the problem of consistent nucleon reggeization in the context of high-energy photon bremsstrahlung for future studies.

The amplitudes of bremsstrahlung driven by the t-channel photon exchange can be

written as

$$\begin{aligned}
\mathcal{M}^{(a)\,\gamma-exch.}_{\lambda_a\lambda_b\to\lambda_1\lambda_2\lambda_3} &= e^3\,\bar{u}(p_1,\lambda_1)\not{\varepsilon}^*(p_3,\lambda_3)S_N(p_{1f}^2)\gamma^\mu u(p_a,\lambda_a)\;F_1(t_2)^2\;\bar{u}(p_2,\lambda_2)\gamma_\mu u(p_b,\lambda_b)\,,\\
\mathcal{M}^{(b)\,\gamma-exch.}_{\lambda_a\lambda_b\to\lambda_1\lambda_2\lambda_3} &= e^3\,\bar{u}(p_2,\lambda_2)\not{\varepsilon}^*(p_3,\lambda_3)S_N(p_{2f}^2)\gamma^\mu u(p_b,\lambda_b)\;F_1(t_1)^2\;\bar{u}(p_1,\lambda_1)\gamma_\mu u(p_a,\lambda_a)\,,\\
\mathcal{M}^{(c)\,\gamma-exch.}_{\lambda_a\lambda_b\to\lambda_1\lambda_2\lambda_3} &= e^3\,\bar{u}(p_1,\lambda_1)\gamma^\mu S_N(p_{1i}^2)\not{\varepsilon}^*(p_3,\lambda_3)u(p_a,\lambda_a)\;F_1(t_2)^2\;\bar{u}(p_2,\lambda_2)\gamma_\mu u(p_b,\lambda_b)\,,\\
\mathcal{M}^{(d)\,\gamma-exch.}_{\lambda_a\lambda_b\to\lambda_1\lambda_2\lambda_3} &= e^3\,\bar{u}(p_2,\lambda_2)\gamma^\mu S_N(p_{2i}^2)\not{\varepsilon}^*(p_3,\lambda_3)u(p_b,\lambda_b)\;F_1(t_1)^2\;\bar{u}(p_1,\lambda_1)\gamma_\mu u(p_a,\lambda_a)\,,
\end{aligned} \tag{4.67}$$

where the $\gamma^* NN$-vertices are parametrised by the proton Dirac electromagnetic form factors (B.2) only, that is, without including the proton off-shell form factors (4.7). We checked that the amplitudes (4.67) are gauge invariant, i.e. replacing photon polarization vector by its momentum vector produces a vanishing result.

4.5.2 Bremsstrahlung of ω mesons; $\omega I\!P$ and $I\!P\omega$ exchanges

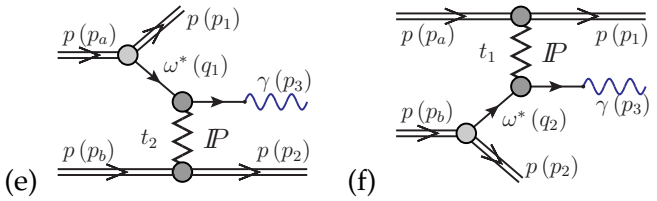

Figure 4.33: Diagrams of the bremsstrahlung amplitudes with virtual-ω meson (reggeon) and its transformation to final state photon.

In Section 4.3 we have discussed bremsstrahlung of ω mesons, see also Ref. [5]. There one includes processes when ω meson emitted by an (anti)proton interacts with the second (anti)proton. The Born amplitudes for the interaction with emitted virtual-ω meson and its subsequent transformation to a photon, shown in Fig.4.33, are obtained by multiplied the amplitudes (4.51) and (4.52) by a transition factor $C_{\omega\to\gamma}$. The transformation of ω meson to photon is obtained within the vector dominance model [332] and $C_{\omega\to\gamma} = \sqrt{\alpha_{em}/20.5} \simeq 0.02$, $\alpha_{em} = e^2/(4\pi)$. For completeness of this analysis we should include also amplitudes for the interaction with emitted (virtual) ρ meson. Because of isospin, there is no mixing between the intermediate ω and ρ mesons. The transition of ρ meson to photon is more probable $C_{\rho\to\gamma} = \sqrt{\alpha_{em}/2.54} \simeq 0.05$ whereas the coupling constant $g_{\rho NN}$ is small compared with $g_{\omega NN}$ – in consequence the $\rho I\!P$ contribution is comparable to the $\omega I\!P$ contribution.

4.5.3 Pion cloud; $\gamma\pi^0$ and $\pi^0\gamma$ exchanges

In our present analysis we include also $\gamma\pi^0$ and $\pi^0\gamma$ exchanges. The underlying mechanisms are shown in Fig.4.34. Such diagrams are dictated by the presence of pion cloud in the nucleon (see e.g. [318]).

The amplitudes for the two new processes can be written as (4.41) and (4.42), but with the replacements $g_{\omega\pi^0\gamma}F_{\gamma\pi\to\omega}(t_1,t_2)$ by $F_{\gamma\pi\to\gamma}(t_1,t_2)$. For the central vertices involving off-shell particles the $\gamma\pi^0$ form factors are taken in the factorized form

$$F_{\gamma\pi\to\gamma}(t_1,t_2) = \frac{N_c}{12\pi^2 f_\pi}\frac{m_\rho^2}{m_\rho^2 - t_1}\exp\left(\frac{t_2 - m_\pi^2}{\Lambda^2_{\gamma\pi\to\gamma}}\right) \tag{4.68}$$

with the pion decay constant $f_\pi = 93$ MeV and $N_c = 3$. The factor describing the virtual photon coupling is taken as in the vector dominance model. In practical calculations we take $\Lambda_{\gamma\pi\to\gamma} = 1$ GeV. In the calculations the corresponding hadronic form factor is taken in the exponential form (4.43), where we used $\Lambda_{\pi NN} = 1$ GeV.

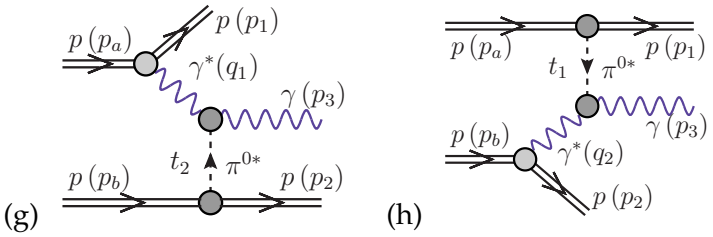

Figure 4.34: Diagrams with the $\gamma\pi^0$ and $\pi^0\gamma$ exchanges in the $pp \to pp\gamma$ reaction.

4.5.4 Photon rescattering; $\gamma I\!P$ and $I\!P\gamma$ exchanges

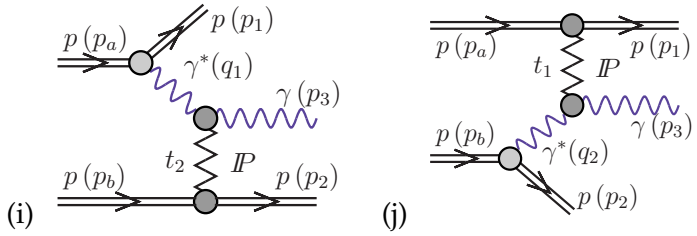

Figure 4.35: Diagrams with the $\gamma I\!P$ and $I\!P\gamma$ exchanges for the $pp \to pp\gamma$ reaction.

At high energy there is still another type of diagrams (mechanisms) shown in Fig.4.35. We shall call them in the following diagrams (i) and (j) for simplicity. Here the intermediate photon couples to one of the protons through electromagnetic form factors and interacts (at high energies) with the second proton exchanging pomeron (phenomenology) or gluonic ladder in the QCD language (see e.g. [147]). This is a counterpart of the diagrams (g) and (h) (see Fig.4.34) relevant at lower γp subenergies.

The amplitude of the three-body process can be written in terms of the amplitude for elastic γp scattering. For not too large t the $\gamma p \to \gamma p$ amplitude can be simply parametrised as

$$\mathcal{M}_{\gamma p\to\gamma p}(s,t) \cong is\sigma_{tot}^{\gamma p}(s)\exp\left(\frac{B_{\gamma p}}{2}t\right) . \tag{4.69}$$

Such an amplitude gives, however, correct total cross section by construction. In the calculations presented in the Result section we shall use the simple Donnachie-Landshoff fit to the world data on photon-proton total cross section [113] in which the pomeron and subleading reggeon exchanges have been included [9]

$$\begin{aligned}&\sigma_{tot}^{\gamma p}(s) = C_{I\!P}^{\gamma p}s^{\alpha_{I\!P}(0)-1} + C_{I\!R}^{\gamma p}s^{\alpha_{I\!R}(0)-1},\\ &C_{I\!P}^{\gamma p} = 0.0677\text{ mb}, \quad C_{I\!R}^{\gamma p} = 0.129\text{ mb}, \quad \alpha_{I\!P}(0) = 1.0808, \quad \alpha_{I\!R}(0) = 0.5475\,.\end{aligned} \tag{4.70}$$

In general, the slope parameter could be found by fitting to elastic γp scattering data which are, however, unknown and very difficult to measure. Since the incoming photon must first fluctuate to the $q\bar{q}$ state which interacts by the pomeron exchange with a proton before forming the outgoing vector meson, it seems reasonable to use a hadronic slope for a first estimation. In practical calculations we shall use $B_{\gamma p}(s) = B_{\pi p}(s)$ with its energy dependence, see Eq.(2.10).

Having fixed the elementary $\gamma p \to \gamma p$ amplitude we can proceed to our three-body photon rescattering amplitude. Limiting to large energies and small transverse momenta t_1 and

[9] In the reggeon contribution the f_2 exchange dominates over the a_2 exchange similarly as in the hadronic reactions, see e.g. [114].

t_2, helicity conserving processes, the matrix element can be written as

$$\begin{aligned}\mathcal{M}_{\lambda_a\lambda_b\to\lambda_1\lambda_2\lambda_3} &\cong \delta_{\lambda_2\lambda_b}\mathcal{M}_{\gamma p\to\gamma p}(s_{23},t_2)\frac{eF_1(t_1)}{t_1}(p_a+p_1)^\mu\varepsilon^*_\mu(p_3,\lambda_3)\delta_{\lambda_1\lambda_a} \\ &+ \delta_{\lambda_1\lambda_a}\mathcal{M}_{\gamma p\to\gamma p}(s_{13},t_1)\frac{eF_1(t_2)}{t_2}(p_b+p_2)^\mu\varepsilon^*_\mu(p_3,\lambda_3)\delta_{\lambda_2\lambda_b}\,. \end{aligned} \tag{4.71}$$

Using $\vec{q}_{1,2\perp} = -\vec{p}_{1,2\perp}$ we have then

$$\begin{aligned}\mathcal{M}_{\lambda_a\lambda_b\to\lambda_1\lambda_2\lambda_3} &\cong \delta_{\lambda_2\lambda_b}\mathcal{M}_{\gamma p\to\gamma p}(s_{23},t_2)\frac{eF_1(t_1)}{t_1}\frac{2}{z_1}\frac{V^*(q_{1\perp},\lambda_3)}{\sqrt{1-z_1}}\delta_{\lambda_1\lambda_a} \\ &+ \delta_{\lambda_1\lambda_a}\mathcal{M}_{\gamma p\to\gamma p}(s_{13},t_1)\frac{eF_1(t_2)}{t_2}\frac{2}{z_2}\frac{V^*(q_{2\perp},\lambda_3)}{\sqrt{1-z_2}}\delta_{\lambda_2\lambda_b}\,, \end{aligned} \tag{4.72}$$

where the longitudinal momentum fractions of outgoing protons $z_{1,2}$ are

$$z_1 \cong \frac{s_{23}}{s}, \quad z_2 \cong \frac{s_{13}}{s}, \quad z_1, z_2 < 1 \tag{4.73}$$

and $V(q_\perp,\lambda_3)$ can be calculated from x,y-components of momenta of participating protons (see [147])

$$V(q_\perp,\lambda_3=\pm1) = \mathbf{e}^{(\lambda_3)}_\mu q^\mu_\perp = -\frac{1}{\sqrt{2}}\left(\lambda_3\, q_x + i q_y\right)\,. \tag{4.74}$$

The cross section for $\gamma\pi^0$ exchange and $\gamma I\!P$ exchange mechanisms can be also calculated in the Equivalent Photon Approximation (EPA) (see Eq. 4.19). The differential distribution of elastic scattering at high energies can be calculated in the standard way

$$\frac{d\sigma_{\gamma p\to\gamma p}}{dt}(s,t) = \frac{|\mathcal{M}_{\gamma p\to\gamma p}(s,t)|^2}{16\pi s^2}\,. \tag{4.75}$$

First energy and the longitudinal momentum of photon is calculated as a function of photon rapidity and transverse momentum $p_\perp = \sqrt{p_x^2+p_y^2}$

$$E_\gamma = p_\perp\cosh y, \quad p_z = p_\perp\sinh y\,. \tag{4.76}$$

We get

$$p_z = \sqrt{E_\gamma^2 - p_\perp^2} \;\text{ for } y>0, \;\text{ and }\; p_z = -\sqrt{E_\gamma^2-p_\perp^2} \;\text{ for } y<0\,. \tag{4.77}$$

Then energies in the photon-proton subsystems can be calculated approximately as

$$\begin{aligned} s_{13} &\approx (p_{a0}+E_\gamma)^2 - (p_{az}+p_z)^2\,, \\ s_{23} &\approx (p_{b0}+E_\gamma)^2 - (p_{bz}+p_z)^2\,. \end{aligned} \tag{4.78}$$

The fractional energy losses, z_1 and z_2, of the protons with four-momenta p_a and p_b, respectively, can be obtained from Eq.(4.73).

4.6 Results

We shall show results of the differential distributions for the exclusive γ-bremsstrahlung mechanisms. The amplitudes for processes discussed in the section above are calculated numerically for each point in the phase space. In calculating cross section of the three-body process we perform integrations in $\xi_1 = \log_{10}(p_{1\perp}/1\,\text{GeV})$ and $\xi_2 = \log_{10}(p_{2\perp}/1\,\text{GeV})$ instead in $p_{1\perp}$ and $p_{2\perp}$, in the photon (pseudo)rapidity η_γ and the relative azimuthal angle between the outgoing protons $\phi_{12} = \phi_1 - \phi_2$.

The photon energy spectrum drops relatively slowly with photon energy as is shown in Fig.4.36 (left panel). The ZDC detectors (at ATLAS or CMS) can measure only photons above some energy threshold (e.g. $E_\gamma > 50$ GeV). In the calculation of γ-bremsstrahlung presented here we assume $E_\gamma > 100$ GeV as an example. Corresponding distributions in the photon transverse momentum are shown in Fig.4.36 (right panel). The contribution of γ-bremsstrahlung is concentrated at very small transverse momenta which is consistent with very small photon emission angle (large pseudorapidity). The other distributions have rather similar shape and vanish at $p_{\perp,\gamma} = 0$ GeV. The exact shape may depend somewhat on the functional form and values of cut-off parameters of off-shell form factors taking into account the non-point-like nature of the vertices involved. Here we have fixed the values of the corresponding form factors at typical hadronic scales.

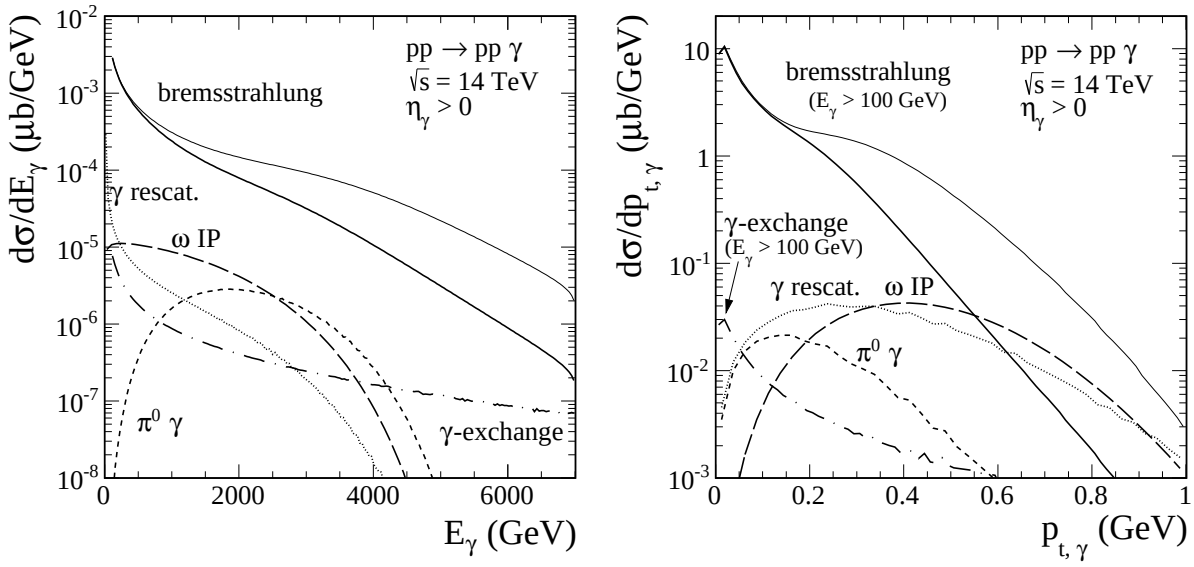

Figure 4.36: Energy spectrum of photons (left panel) and distribution in transverse momentum of photons (right panel) for all processes considered here at $\sqrt{s} = 14$ TeV and for $\eta_\gamma > 0$. For the diffractive γ-bremsstrahlung we have imposed $E_\gamma > 100$ GeV and used two values of $\Lambda_N = 0.8, 1$ GeV (the lower and upper solid line, respectively) in the proton off-shell form factors (4.7).

In Fig.4.37 we show auxiliary distribution in $\xi_1 = \log_{10}(p_{1\perp}/1\,\mathrm{GeV})$ (left panel) and $\xi_2 = \log_{10}(p_{2\perp}/1\,\mathrm{GeV})$ (right panel), where $p_{1\perp}$ and $p_{2\perp}$ are outgoing proton transverse momenta. For example $\xi = -1$ means proton transverse momenta 0.1 GeV. The biggest contribution for the diffractive γ-bremsstrahlung comes from the region $\xi_i \approx -0.5$ (i.e, $p_{i\perp} \approx 0.3$ GeV). The distributions in ξ_1 or ξ_2 are different because we have limited to the case of $\eta_\gamma > 0$ only.

In Fig.4.38 we show corresponding two-dimensional distributions in (ξ_1, ξ_2) in the full range of photon (pseudo)rapidity. Quite different pattern can be seen for different mechanisms. For the γ-bremsstrahlung we observe an enhancement along the diagonal. This enhancement is a reminiscence of the elastic scattering for which $\xi_1 = \xi_2$. The photon rescattering on the pion cloud (panel c) and the photon rescattering with pomeron exchange (panel d) as well as the γ-bremsstrahlung via γ exchange (panel e) contributions are concentrated at quite small ξ_1 or ξ_2.

The photon (pseudo)rapidity distribution is particularly interesting. In Fig.4.39 we show both distribution for photon η_γ (left panel) and corresponding distribution for outgoing protons η_p (right panel) for all considered processes. In this variable both protons and photons are localized in a similar region of pseudorapidities (or equivalently polar angles). The diffractive γ-bremsstrahlung clearly gives the largest contribution. It is also concentrated at very large η_γ i.e. in the region where ZDC detectors can be used. We observe a large cancellation between the corresponding terms in the amplitude (4.63) and (4.65) (see left panel) or (4.64) and (4.66).

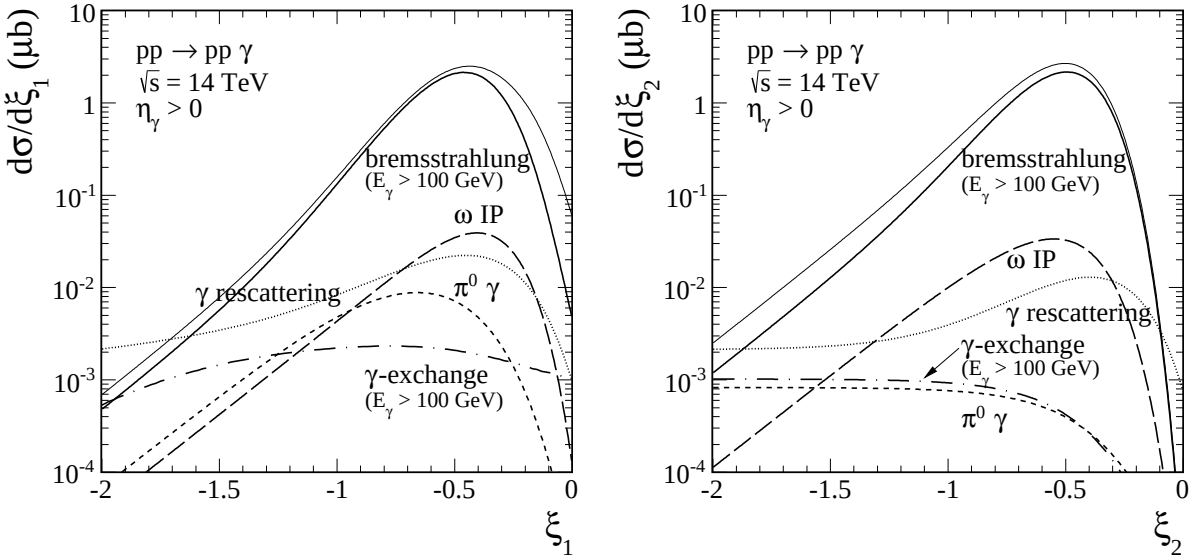

Figure 4.37: Distribution in $\xi_1 = \log_{10}(p_{1\perp}/1\,\mathrm{GeV})$ (left panel) and $\xi_2 = \log_{10}(p_{2\perp}/1\,\mathrm{GeV})$ (right panel) at $\sqrt{s} = 14$ TeV and for $\eta_\gamma > 0$. For the diffractive γ-bremsstrahlung $E_\gamma > 100$ GeV and we have used two values of $\Lambda_N = 0.8, 1$ GeV (see the lower and upper solid line, respectively).

The γ-rescattering process with pomeron exchange clearly dominates in the region of $\eta_\gamma < 6$. The cross section for this process is rather small. Clearly an experimental measurement there would be a challenge.

In a first experimental trial one could measure only photons and perform a check for rapidity gap in the midrapidity region. If protons are measured in addition, one could analyze also some new observables related to protons. In Fig.4.40 we show distribution in the four-momentum transfer squared between initial and final protons. One can observe a change of slope of the t distribution which is caused by the bremsstrahlung of photons. In our simplified model we have assumed a constant (in t_1 and t_2) energy-dependent slope.

In Fig.4.41 we show distribution in two-dimensional space (t_1, t_2). For the γ-bremsstrahlung (left panel) one can observe a ridge when $t_1 \simeq t_2$ which is reminiscence of elastic scattering. The distributions discussed here could, in principle, be obtained with the TOTEM detector at CMS main detector to supplement the ZDC detector for the measurement of photons.

In Fig.4.42 we compare distribution in photon-(forward proton) subsystem energy for all considered processes (left panel). The discussed here $pp \to pp\gamma$ process gives a sizeable contribution to the low mass $(M_X > m_p)$ single diffractive cross section. If both protons are measured one could also study correlations in the relative azimuthal angle between outgoing protons (right panel). One can observe a large enhancement at back-to-back configurations for the γ-bremsstrahlung which reminds the elastic scattering case ($\phi_{12} = \pi$). The contributions for other mechanisms are significantly smaller and weakly depend on ϕ_{12}.

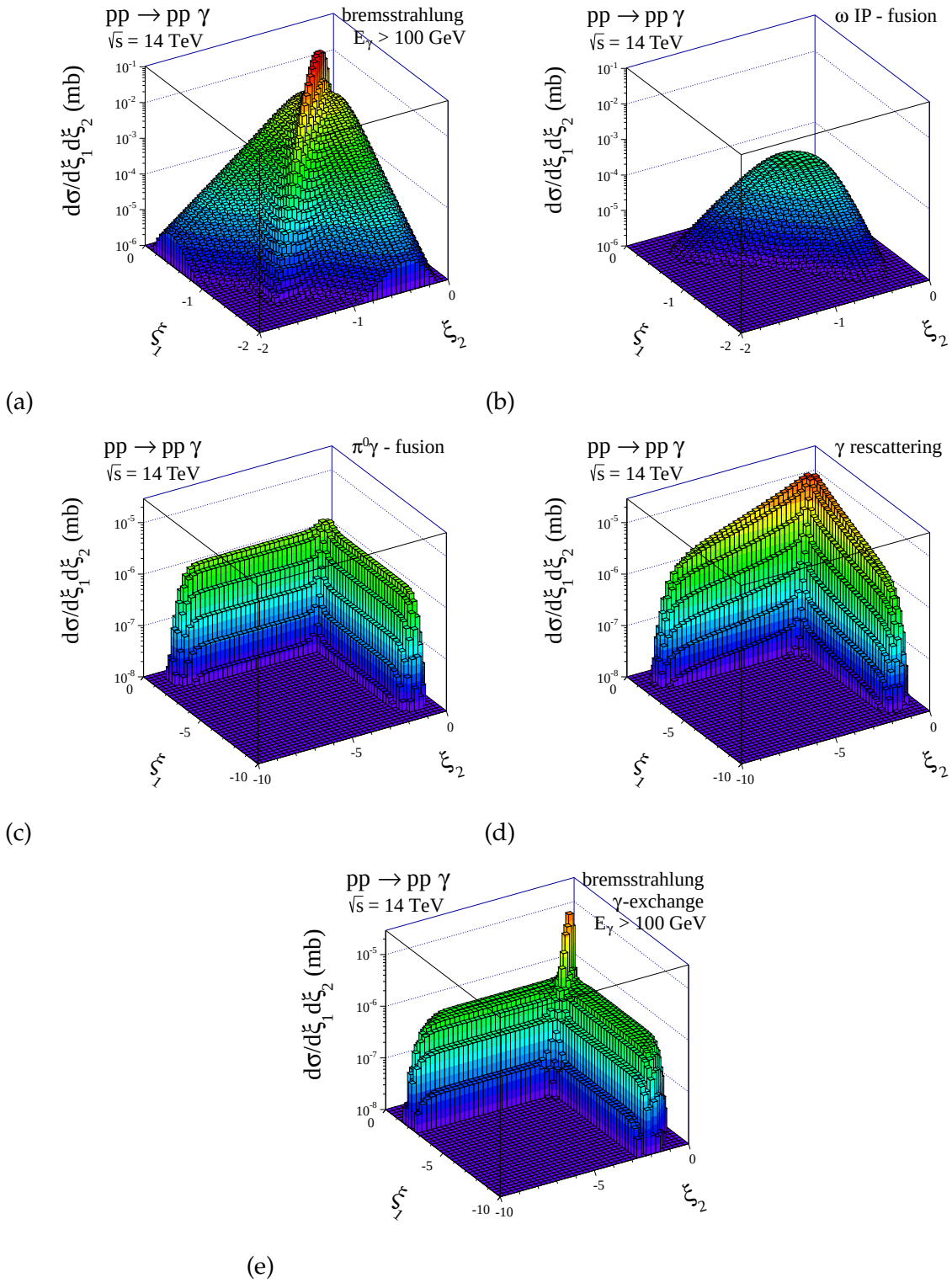

Figure 4.38: Distribution in $(\xi_1, \xi_2) = (\log_{10}(p_{1\perp}/1\,\text{GeV}), \log_{10}(p_{2\perp}/1\,\text{GeV}))$ for the diffractive γ-bremsstrahlung (a), the ω-rescattering (b), the pion-cloud (c), the γ-rescattering (d), and the bremsstrahlung via γ-exchange (e) mechanisms at $\sqrt{s} = 14$ TeV. For the bremsstrahlung mechanisms we have imposed in addition $E_\gamma > 100$ GeV. In the calculations of the diffractive γ-bremsstrahlung we used $\Lambda_N = 1$ GeV in the proton off-shell form factors.

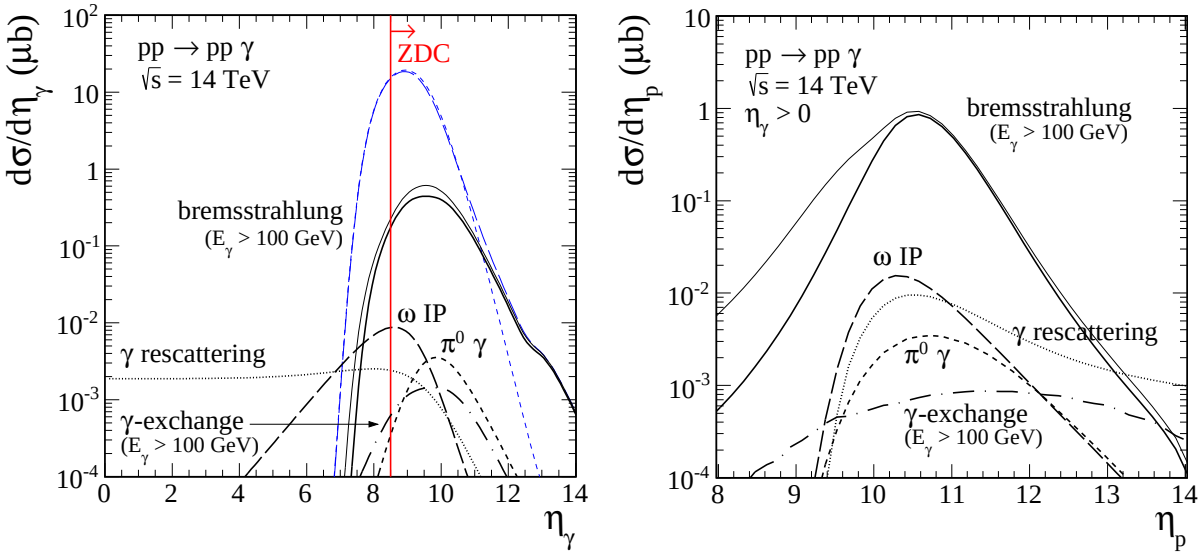

Figure 4.39: Distribution in (pseudo)rapidity of emitted photons (left panel) and in pseudorapidity of outgoing protons (right panel) at $\sqrt{s} = 14$ TeV. For the diffractive γ-bremsstrahlung we have imposed $E_\gamma > 100$ GeV and used two values of $\Lambda_N = 0.8, 1$ GeV (see the lower and upper solid line, respectively). A large cancellation between the initial (4.65) and final state radiation (4.63) is shown (see the blue short-dashed and the blue long-dashed lines, respectively). The lower pseudorapidity limit for the CMS ZDC detector $\eta_\gamma > 8.5$ is shown in addition by the vertical line.

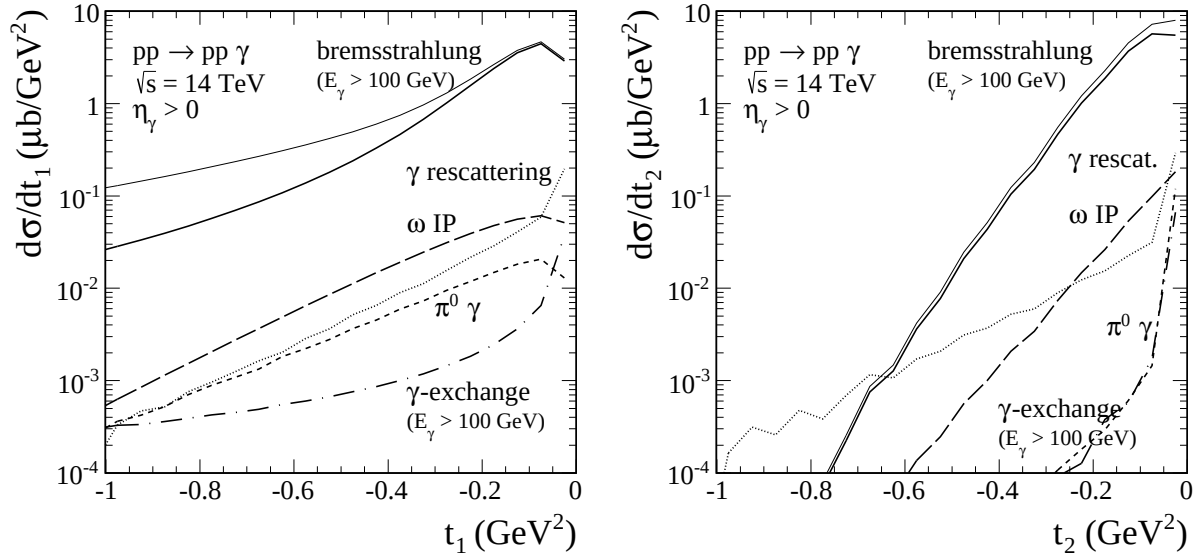

Figure 4.40: Distribution in four-momentum squared t_1 (left panel) and t_2 (right panel) at $\sqrt{s} = 14$ TeV and for $\eta_\gamma > 0$. For the diffractive γ-bremsstrahlung we have imposed $E_\gamma > 100$ GeV and used two values of $\Lambda_N = 0.8, 1$ GeV (see the lower and upper solid line, respectively).

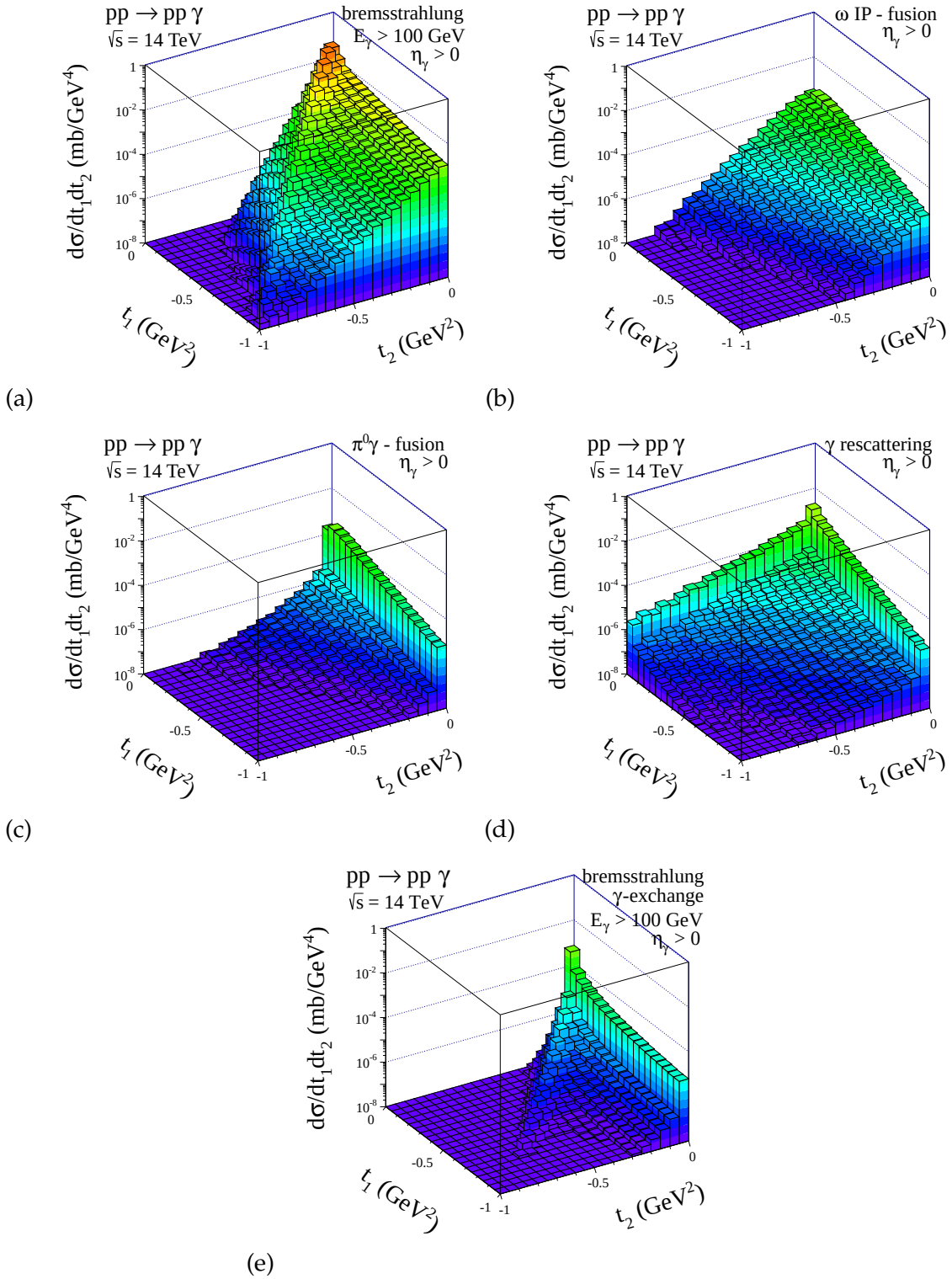

Figure 4.41: Distribution in (t_1, t_2) at $\sqrt{s} = 14$ TeV and $\eta_\gamma > 0$ for the diffractive bremsstrahlung (a) ($E_\gamma > 100$ GeV and $\Lambda_N = 1$ GeV), the ω-rescattering (b), the pion cloud (c), the γ-rescattering (d), and the bremsstrahlung via γ-exchange (e) ($E_\gamma > 100$ GeV) contributions.

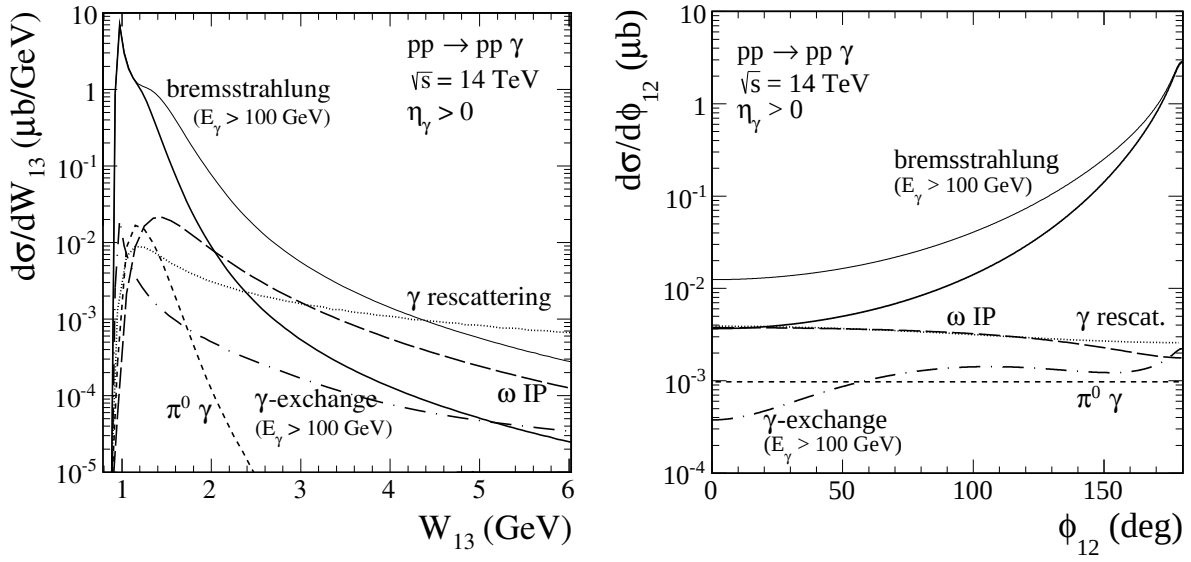

Figure 4.42: Distribution in the γp subsystem energy W_{13} (left panel) and in the relative azimuthal angle between outgoing protons ϕ_{12} for all processes considered here at $\sqrt{s} = 14$ TeV and for $\eta_\gamma > 0$. For the diffractive γ-bremsstrahlung we have imposed $E_\gamma > 100$ GeV and used two values of $\Lambda_N = 0.8, 1$ GeV (see the lower and upper solid line, respectively).

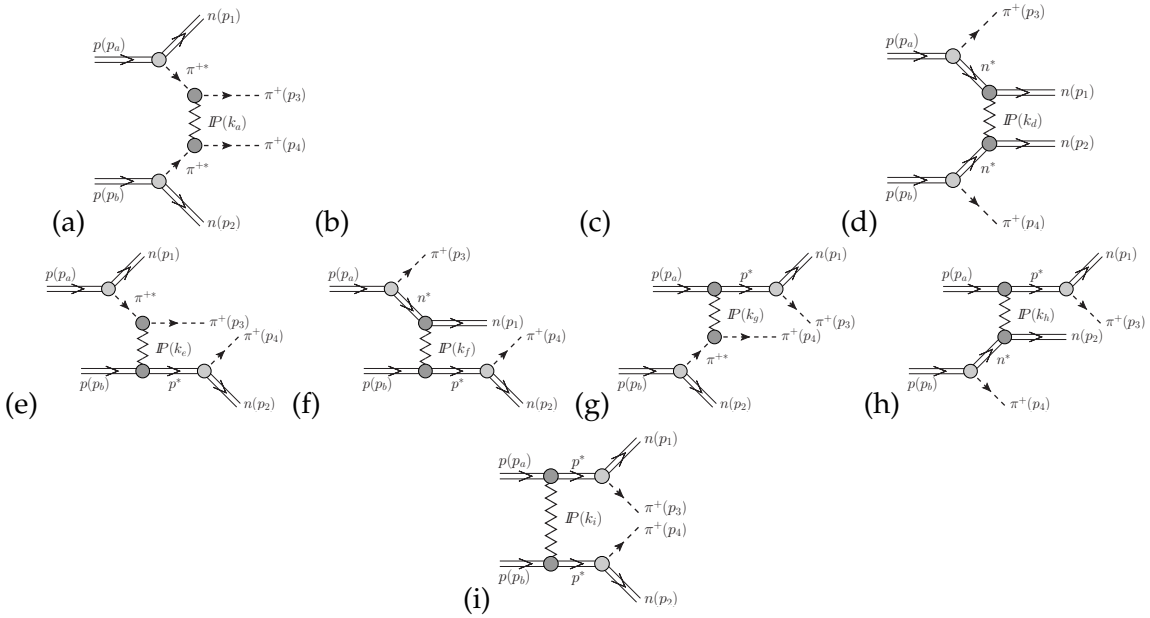

Figure 4.43: Diagrams for the exclusive production of $\pi^+\pi^+$ in pp collisions at high energies. The stars attached to π^+, n and p denote the fact they are off-mass-shell. k_a–k_i are four-vectors of the exchanged pomerons.

4.7 Exclusive $pp \to nn\pi^+\pi^+$ reaction

Here we shall study the $pp \to nn\pi^+\pi^+$ reaction with two forward neutrons in the final state which could be addressed for the ZDCs measurements at high energies (see [4]):

$$p(p_a, \lambda_a)p(p_b, \lambda_b) \to n(p_1, \lambda_1)n(p_2, \lambda_2)\pi^+(p_3)\pi^+(p_4)\,, \tag{4.79}$$

where $p_{a,b}$, $\lambda_{a,b}$ and $p_{1,2}$, $\lambda_{1,2}$ denote the four-momenta and helicities of the ingoing protons and outgoing neutrons, respectively.

The total and elastic cross sections are basic objects of the scattering theory. While the proton-proton, proton-antiproton or pion-proton can be directly measured (see e.g. [96]) the pion-pion scattering is not directly accessible. It was suggested recently [333] how to extract the total $\pi^+\pi^+$ cross section in the high-energy region. Here it was suggested to use scattering of virtual π^+'s which couple to the nucleons with well known coupling constant and are subsequently promoted by the interaction onto their mass shell in the final state. The final pions are then associated with outgoing neutrons. The energy dependence of the total and possibly elastic cross section of pion-pion scattering would be very useful and supplementary information for the groups which model the soft hadron-hadron interactions (see e.g. [334]). It was shown recently that the CMS (Compact Muon Spectrometer) Collaboration ZDC's provide a unique possibility to measure the $\pi^+\pi^+$ total cross section [333]. Can a similar method be used to extract the elastic $\pi^+\pi^+$ scattering by analysis of the $pp \to nn\pi^+\pi^+$ reaction? We wish to address this issue in this Section. [10]

Even at high-energy the major part of the phase space of a few-body reactions is populated in soft processes which cannot be calculated within perturbative QCD. Only limited corner of the phase space, where particles are produced at large transverse momenta, can be addressed in the framework of pQCD. At high energy the Regge approach is the most efficient tool to describe total cross section, elastic scattering as well as different $2 \to 2$ reactions [114, 130]. We shall show how to construct the amplitude for the considered $2 \to 4$ process in terms of several $2 \to 2$ soft amplitudes. In the present analysis we will also include absorption effects as was done recently for three-body processes [147].

4.7.1 Diffractive amplitudes of exclusive $pp \to nn\pi^+\pi^+$ reaction

The diffractive mechanisms involving pomeron and reggeon exchanges are shown in Fig.4.43. In principle, in all diagrams shown the intermediate nucleon can be replaced by nucleon excited states. It is known that diffractive excitation of nucleons to inelastic states is rather large and constitutes about $1/3$ of the elastic scattering. This number is, however, not relevant in our case, as it is to large extend due to the Deck type mechanism [126] which is included explicitly in our calculation. A microscopic calculation must unavoidably include not only the structure of the nucleon but also of the nucleon excited states. The cross section for $pp \to p + N\pi\pi$ of our interest is, however, only a fraction of mb [336]. That the contribution of excited discrete state is small can be also seen in the following way. First of all the diffractive transitions to discrete excited states are known to be much weaker than the elastic one. Secondly the $g_{NN^*\pi}$ coupling constants are much smaller than the $g_{NN\pi}$ coupling constant, see e.g. Refs. [25, 337]. Finally, the exact strength of the diffractive transitions are not known phenomenologically. Therefore in the following we neglect the contributions of diagrams with excited nucleon states.

The amplitude squared, averaged over the initial and summed over the final polarization states, for the $pp \to nn\pi^+\pi^+$ reaction can be written as:

$$\overline{|\mathcal{M}|^2} = \frac{1}{4}\sum_{\lambda_a\lambda_b\lambda_1\lambda_2} |\mathcal{M}^{(a)}_{\lambda_a\lambda_b\to\lambda_1\lambda_2} + ... + \mathcal{M}^{(i)}_{\lambda_a\lambda_b\to\lambda_1\lambda_2}|^2\,. \tag{4.80}$$

[10] After first version of our paper [4] had been completed, a paper [335] has appeared which also discusses the possibility of extraction of elastic $\pi^+\pi^+$ cross section. In our analysis we take into account many more possible mechanisms for the $pp \to nn\pi^+\pi^+$ reaction.

The Born amplitudes in terms of pomeron exchange shown in Fig.4.43 read:

$$
\begin{aligned}
\mathcal{M}^{(a)}_{\lambda_a\lambda_b\to\lambda_1\lambda_2} &= \bar{u}(p_1,\lambda_1)\mathrm{i}\gamma_5 S_\pi(t_1)u(p_a,\lambda_a)\sqrt{2}g_{\pi NN}F_{\pi NN}(t_1)\\
&\times F_\pi^{off}(t_1)\ \mathrm{i}s_{34}C_{\boldsymbol{P}}^{\pi\pi}\left(\frac{s_{34}}{s_0}\right)^{\alpha_{I\!P}(k_a^2)-1}\exp\left(\frac{B_{\boldsymbol{P}}^{\pi\pi}}{2}k_a^2\right)\ F_\pi^{off}(t_2)\\
&\times\bar{u}(p_2,\lambda_2)\mathrm{i}\gamma_5 S_\pi(t_2)u(p_b,\lambda_b)\sqrt{2}g_{\pi NN}F_{\pi NN}(t_2)\ , \qquad (4.81)\\
\mathcal{M}^{(b)}_{\lambda_a\lambda_b\to\lambda_1\lambda_2} &= \bar{u}(p_1,\lambda_1)\mathrm{i}\gamma_5 S_\pi(t_1)u(p_a,\lambda_a)\sqrt{2}g_{\pi NN}F_{\pi NN}(t_1)\\
&\times F_\pi^{off}(t_1)\ \mathrm{i}s_{23}C_{\boldsymbol{P}}^{\pi N}\left(\frac{s_{23}}{s_0}\right)^{\alpha_{I\!P}(k_b^2)-1}\left(\frac{s_{24}}{s_{thr}}\right)^{\alpha_N(u_2)-\frac{1}{2}}\exp\left(\frac{B_{\boldsymbol{P}}^{\pi N}}{2}k_b^2\right)\ F_n^{off}(u_2)\\
&\times\bar{u}(p_2,\lambda_2)\mathrm{i}\gamma_5 S_n(u_2)u(p_b,\lambda_b)\sqrt{2}g_{\pi NN}F_{\pi NN}(u_2)\ , \qquad (4.82)\\
\mathcal{M}^{(c)}_{\lambda_a\lambda_b\to\lambda_1\lambda_2} &= \bar{u}(p_1,\lambda_1)\mathrm{i}\gamma_5 S_n(u_1)u(p_a,\lambda_a)\sqrt{2}g_{\pi NN}F_{\pi NN}(u_1)\\
&\times F_n^{off}(u_1)\ \mathrm{i}s_{14}C_{\boldsymbol{P}}^{\pi N}\left(\frac{s_{14}}{s_0}\right)^{\alpha_{I\!P}(k_c^2)-1}\left(\frac{s_{13}}{s_{thr}}\right)^{\alpha_N(u_1)-\frac{1}{2}}\exp\left(\frac{B_{\boldsymbol{P}}^{\pi N}}{2}k_c^2\right)\ F_\pi^{off}(t_2)\\
&\times\bar{u}(p_2,\lambda_2)\mathrm{i}\gamma_5 S_\pi(t_2)u(p_b,\lambda_b)\sqrt{2}g_{\pi NN}F_{\pi NN}(t_2)\ , \qquad (4.83)\\
\mathcal{M}^{(d)}_{\lambda_a\lambda_b\to\lambda_1\lambda_2} &= \bar{u}(p_1,\lambda_1)\mathrm{i}\gamma_5 S_n(u_1)u(p_a,\lambda_a)\sqrt{2}g_{\pi NN}F_{\pi NN}(u_1)\\
&\times F_n^{off}(u_1)\ \mathrm{i}s_{12}C_{\boldsymbol{P}}^{NN}\left(\frac{s_{12}}{s_0}\right)^{\alpha_{I\!P}(k_d^2)-1}\left(\frac{s_{13}}{s_{thr}}\right)^{\alpha_N(u_1)-\frac{1}{2}}\left(\frac{s_{24}}{s_{thr}}\right)^{\alpha_N(u_2)-\frac{1}{2}}\\
&\times\exp\left(\frac{B_{\boldsymbol{P}}^{NN}}{2}k_d^2\right)\ F_n^{off}(u_2)\\
&\times\bar{u}(p_2,\lambda_2)\mathrm{i}\gamma_5 S_n(u_2)u(p_b,\lambda_b)\sqrt{2}g_{\pi NN}F_{\pi NN}(u_2)\ , \qquad (4.84)\\
\mathcal{M}^{(e)}_{\lambda_a\lambda_b\to\lambda_1\lambda_2} &= \bar{u}(p_1,\lambda_1)\mathrm{i}\gamma_5 S_\pi(t_1)u(p_a,\lambda_a)\sqrt{2}g_{\pi NN}F_{\pi NN}(t_1)\\
&\times F_\pi^{off}(t_1)\ \mathrm{i}s_{234}C_{\boldsymbol{P}}^{\pi N}\left(\frac{s_{234}}{s_0}\right)^{\alpha_{I\!P}(k_e^2)-1}\exp\left(\frac{B_{\boldsymbol{P}}^{\pi N}}{2}k_e^2\right)\ F_p^{off}(s_{24})\\
&\times\bar{u}(p_2,\lambda_2)\mathrm{i}\gamma_5 S_p(s_{24})u(p_b,\lambda_b)\sqrt{2}g_{\pi NN}F_{\pi NN}(s_{24})\ , \qquad (4.85)\\
\mathcal{M}^{(f)}_{\lambda_a\lambda_b\to\lambda_1\lambda_2} &= \bar{u}(p_1,\lambda_1)\mathrm{i}\gamma_5 S_n(u_1)u(p_a,\lambda_a)\sqrt{2}g_{\pi NN}F_{\pi NN}(u_1)\\
&\times F_n^{off}(u_1)\ \mathrm{i}s_{124}C_{\boldsymbol{P}}^{NN}\left(\frac{s_{124}}{s_0}\right)^{\alpha_{I\!P}(k_f^2)-1}\left(\frac{s_{13}}{s_{thr}}\right)^{\alpha_N(u_1)-\frac{1}{2}}\exp\left(\frac{B_{\boldsymbol{P}}^{NN}}{2}k_f^2\right)\ F_p^{off}(s_{24})\\
&\times\bar{u}(p_2,\lambda_2)\mathrm{i}\gamma_5 S_p(s_{24})u(p_b,\lambda_b)\sqrt{2}g_{\pi NN}F_{\pi NN}(s_{24})\ , \qquad (4.86)\\
\mathcal{M}^{(g)}_{\lambda_a\lambda_b\to\lambda_1\lambda_2} &= \bar{u}(p_1,\lambda_1)\mathrm{i}\gamma_5 S_p(s_{13})u(p_a,\lambda_a)\sqrt{2}g_{\pi NN}F_{\pi NN}(s_{13})\\
&\times F_p^{off}(s_{13})\ \mathrm{i}s_{134}C_{\boldsymbol{P}}^{\pi N}\left(\frac{s_{134}}{s_0}\right)^{\alpha_{I\!P}(k_g^2)-1}\exp\left(\frac{B_{\boldsymbol{P}}^{\pi N}}{2}k_g^2\right)\ F_\pi^{off}(t_2)\\
&\times\bar{u}(p_2,\lambda_2)\mathrm{i}\gamma_5 S_\pi(t_2)u(p_b,\lambda_b)\sqrt{2}g_{\pi NN}F_{\pi NN}(t_2)\ , \qquad (4.87)\\
\mathcal{M}^{(h)}_{\lambda_a\lambda_b\to\lambda_1\lambda_2} &= \bar{u}(p_1,\lambda_1)\mathrm{i}\gamma_5 S_p(s_{13})u(p_a,\lambda_a)\sqrt{2}g_{\pi NN}F_{\pi NN}(s_{13})\\
&\times F_p^{off}(s_{13})\ \mathrm{i}s_{123}C_{\boldsymbol{P}}^{NN}\left(\frac{s_{123}}{s_0}\right)^{\alpha_{I\!P}(k_h^2)-1}\left(\frac{s_{24}}{s_{thr}}\right)^{\alpha_N(u_2)-\frac{1}{2}}\exp\left(\frac{B_{\boldsymbol{P}}^{NN}}{2}k_h^2\right)\ F_n^{off}(u_2)\\
&\times\bar{u}(p_2,\lambda_2)\mathrm{i}\gamma_5 S_n(u_2)u(p_b,\lambda_b)\sqrt{2}g_{\pi NN}F_{\pi NN}(u_2)\ , \qquad (4.88)\\
\mathcal{M}^{(i)}_{\lambda_a\lambda_b\to\lambda_1\lambda_2} &= \bar{u}(p_1,\lambda_1)\mathrm{i}\gamma_5 S_p(s_{13})u(p_a,\lambda_a)\sqrt{2}g_{\pi NN}F_{\pi NN}(s_{13})\\
&\times F_p^{off}(s_{13})\ \mathrm{i}s_{ab}C_{\boldsymbol{P}}^{NN}\left(\frac{s_{ab}}{s_0}\right)^{\alpha_{I\!P}(k_i^2)-1}\exp\left(\frac{B_{\boldsymbol{P}}^{NN}}{2}k_i^2\right)\ F_p^{off}(s_{24})\\
&\times\bar{u}(p_2,\lambda_2)\mathrm{i}\gamma_5 S_p(s_{24})u(p_b,\lambda_b)\sqrt{2}g_{\pi NN}F_{\pi NN}(s_{24})\ , \qquad (4.89)
\end{aligned}
$$

where the energy scale s_0 is fixed at $s_0 = 1$ GeV^2 and $s_{thr} = (m_N + m_\pi)^2$. In our calculations we take $g^2_{\pi NN}/4\pi$ = 13.5. The absorptive corrections are calculated as described e.g. in 2.3.2.

In the above equations $u(p_i, \lambda_i)$, $\bar{u}(p_f, \lambda_f) = u^\dagger(p_f, \lambda_f)\gamma^0$ are the Dirac spinors (normalized as $\bar{u}(p)u(p) = 2m_N$) of the initial protons and outgoing neutrons with the four-momentum p and the helicities of the nucleons λ. The propagators of virtual particles can be written as

$$S_\pi(t_{1,2}) = \frac{\mathrm{i}}{t_{1,2} - m_\pi^2}, \tag{4.90}$$

$$S_n(u_{1,2}) = \frac{\mathrm{i}(\tilde{u}_{1,2_\nu}\gamma^\nu + m_n)}{u_{1,2} - m_n^2}, \tag{4.91}$$

$$S_p(s_{ij}) = \frac{\mathrm{i}(\tilde{s}_{ij_\nu}\gamma^\nu + m_p)}{s_{ij} - m_p^2}, \tag{4.92}$$

where $t_{1,2} = (p_{a,b} - p_{1,2})^2$ and $u_{1,2} = (p_{a,b} - p_{3,4})^2 = \tilde{u}^2_{1,2}$ are the four-momenta squared of transferred pions and neutrons, respectively [11]. $s_{ij} = (p_i + p_j)^2 = \tilde{s}^2_{ij}$ are the squared invariant masses of the (i, j) system, m_π and m_n, m_p are the pion and nucleons masses, respectively.

Using the known strength parameters for the NN and πN scattering fitted to the corresponding total cross sections (the Donnachie-Landshoff model [113]) we obtain $C_{I\!P}^{NN}$, $C_{I\!P}^{\pi N}$ and $C_{I\!P}^{\pi\pi}$ assuming Regge factorization (1.68). The Regge trajectories determined from elastic and total cross sections are given in the linear approximation (2.11). Parameters of Regge exchanges used in the present calculations are listed in Table 2.1. In this calculation we use the t-slope parameters (2.10) of the elastic differential cross section as $B_{I\!P}^{\pi N}$ = 6.5 GeV^{-2}, $B_{I\!P}^{NN}$ = 9 GeV^{-2} and $B_{I\!P}^{\pi\pi}$ = 4 GeV^{-2}. The value of $B_{I\!P}^{\pi\pi}$ is not well known, however, the Regge factorization entails $B_{I\!P}^{\pi\pi} \approx 2B_{I\!P}^{\pi N} - B_{I\!P}^{NN}$ [111]. We have parametrised the $k_a^2, ..., k_i^2$ dependences in the exponential form (see formulas (4.81) – (4.89)).

We improve the parametrisation of the amplitudes for neutron exchange (4.82, 4.83, 4.84, 4.86, 4.88) by the factors $\left(\frac{s_{ij}}{s_{thr}}\right)^{\alpha_N(u_{1,2})-\frac{1}{2}}$ to reproduce the high-energy Regge dependence. The nucleon trajectory is $\alpha_N(u_{1,2}) = -0.3 + \alpha'_N\, u_{1,2}$, with $\alpha'_N = 0.9$ GeV^{-2}, see Fig. 2.1(b).

The extra correction factors $F^{off}_{\pi,N}(k^2)$ (where $k^2 = t_{1,2}, u_{1,2}, s_{ij}$) are due to off-shellness of particles. In the case of our 4-body reaction rather large transferred four-momenta squared k^2 are involved and one has to include non-point-like and off-shellness nature of the particles involved in corresponding vertices. This is incorporated via $F_{\pi NN}(k^2)$ vertex form factors. We parametrise these form factors in the following exponential form:

$$F(t_{1,2}) = \exp\left(\frac{t_{1,2} - m_\pi^2}{\Lambda^2}\right), \tag{4.93}$$

$$F(u_{1,2}) = \exp\left(\frac{u_{1,2} - m_n^2}{\Lambda^2}\right), \tag{4.94}$$

$$F(s_{ij}) = \exp\left(\frac{-(s_{ij} - m_p^2)}{\Lambda^2}\right). \tag{4.95}$$

While four-momenta squared of transferred pions $t_{1,2} < 0$, it is not the case for transferred neutrons where $u_{1,2} < m_n^2$. In our calculation, if not otherwise mentioned, we use the cut-off parameters $\Lambda = \Lambda_{off} = 1$ GeV.

4.7.2 Single and double charge exchanges with subleading reggeons

We wish to include also specific processes with isovector reggeon exchanges ρ^+ and a_2^+. We include processes shown in Fig.4.44. These processes involve $\rho^+\rho^+ \to \pi^+\pi^+$ and $a_2^+a_2^+ \to$

[11] In the following for brevity we shall use notation $t_{1,2}$ which means t_1 or t_2.

$\pi^+\pi^+$ subprocesses. Unfortunately these subprocesses (or the reverse ones) could not be studied experimentally.

The relevant coupling constants in diagrams b) and c) are not known and cannot be obtained from first principles and one has to refer to other reactions involving the same coupling constants. Such reactions are e.g. $\pi^\pm p \to a_2^\pm p$ (where both $I\!P \mp \rho^0$ exchanges are possible), $\pi^- p \to a_2^0 n$, $\pi^- p \to \omega^0 n$ (only ρ^+-reggeon exchange come into game), $\pi^\pm p \to \rho^\pm p$ (π^0, ω^0- and a_2^0-reggeon exchanges) and $\pi^- p \to \rho^0 n$ (π^+, a_2^+-reggeon exchanges).

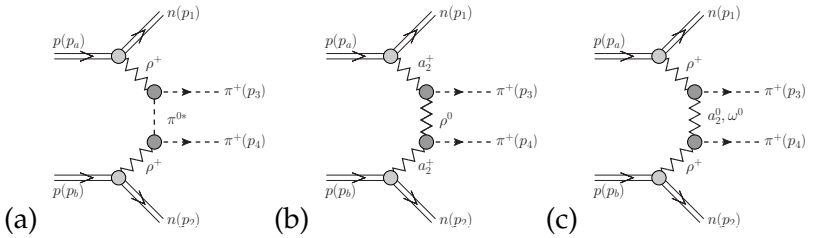

Figure 4.44: Diagrams with subleading charged-reggeon exchanges in the pp collisions at high energies.

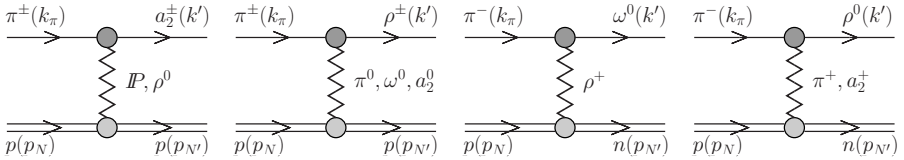

Figure 4.45: Diagrams for various exchanges in πp collisions.

The ρ-meson/reggeon and a_2-meson/reggeon exchanges are known to have not only the nucleon spin-conserving part but also the dominant nucleon spin-flip component while the ω-meson/reggeon exchange to nucleons is mainly spin-conserving. We write the amplitude for the reggeon exchanges (see Fig.4.45) in the following compact phenomenological form: [12]

$$\begin{aligned}\mathcal{M}^{reggeon-exch.}_{\lambda_N\to\lambda_{N'},\lambda_M}(s,t) &= \frac{\sqrt{-(t-t_{min})}}{M_0}\left(\frac{-(t-t_{min})}{4m_N^2}\right)^{|\lambda_{N'}-\lambda_N|/2} r_T^{i\,|\lambda_{N'}-\lambda_N|} \\ &\times \eta_i\; s\; C_i^r \left(\frac{s}{s_0}\right)^{\alpha_i(t)-1} \exp\left(\frac{B_{MN}}{2}(t-t_{min})\right)\; \delta_{|\lambda_M|1}\;, \qquad (4.96)\end{aligned}$$

and the pion exchange amplitude as

$$\begin{aligned}\mathcal{M}^{\pi-exch.}_{\lambda_N\to\lambda_{N'},\lambda_\rho}(s,t) &= g_{\pi NN}\; F_{\pi NN}(t)\; \bar{u}(p_{N'},\lambda_{N'})\mathrm{i}\gamma_5 u(p_N,\lambda_N) \\ &\times (k_\pi^\mu + q^\mu)\epsilon_\mu^*(k',\lambda_\rho)\; \frac{\mathrm{i}}{t-m_\pi^2}\; g_{\rho\pi\pi}\; F_{\rho\pi\pi}(t)\; \left(\frac{s}{s_0}\right)^{\alpha_\pi(t)}\;. \qquad (4.97)\end{aligned}$$

Above the $\sqrt{-(t-t_{min})}/M_0$ factor is due to the meson spin-flip (in the $\pi \to \omega$, $\pi \to \rho$ and $\pi \to a_2$ transitions), M_0 is a reference scale factor taken here M_0 = 1 GeV (which is used here to have the same units for the coupling constants). The double spin-flip components do not interfere with the spin-conserving ones and can be calculated separately. Here we have introduced one more phenomenological (dimensionless) parameter r_T^i which describes coupling for the spin-flip components. It is known to be $r_T^\rho = 7.5$, $r_T^{a_2} \simeq 6.14$, $r_T^\omega \simeq 0.17$ [265] and $r_T^\rho \simeq 8$, $r_T^{a_2} \simeq 4.7$, $r_T^\omega \simeq 0.9$ [338]. In the present calculations we take r_T^ρ = 7.5, $r_T^{a_2}$ = 6 and r_T^ω = 0. The coupling constant $g_{\rho\pi\pi}$ is taken as $g^2_{\rho\pi\pi}/4\pi$ = 2.6. The form factors are parametrised as

[12] For the case of the $\pi^- p \to \omega^0 n$, $\pi^- p \to \rho^0 n$ and $\pi^- p \to a_2^0 n$ reactions the amplitude should be multiplied by $\sqrt{2}$ which is related to isospin Clebsch-Gordan coefficient.

$F(t) = \exp\left((t - m_\pi^2)/\Lambda^2\right)$. We improve the parameterization of the amplitude (4.97) by multiplying by the factor $(s/s_0)^{\alpha_\pi(t)}$, where $\alpha_\pi(t) = \alpha'_\pi(t - m_\pi^2)$ is the pion Regge trajectory with the slope of trajectory $\alpha'_\pi = 1\,\mathrm{GeV}^{-2}$.

We adjust the C_i^r (where $i = I\!P, \rho, \omega, a_2$) coupling constants to the world experimental data often obtained from partial wave analysis in the three-pion system. The effective normalization constants for the auxiliary reactions are related to those in the NN scattering and the $g^i_{\pi\to a_2,\rho,\omega}$ coupling constants we need in our problem as:

$$C_i^r = \sqrt{C_i^{NN}}\, g^i_{\pi\to j}\,. \tag{4.98}$$

Since C_i^{NN} are known from phenomenology (Table 2.1), $g^i_{\pi\to j}$ can be obtained from our fits: $g^{I\!P}_{\pi\to a_2}$ = 1.4 GeV^{-1}, $g^{\rho}_{\pi\to a_2} = g^{a_2}_{\pi\to\rho}$ = 22 GeV^{-1} and $g^{\omega}_{\pi\to\rho} = g^{\rho}_{\pi\to\omega}$ = 4 GeV^{-1}. Having fixed the parameters we can proceed to our four-body $pp \to nn\pi^+\pi^+$ reaction.

In Fig.4.46 we show the total cross section for the $\pi^- p \to a_2^- p$, $\pi^- p \to \omega^0 n$, $\pi^- p \to \rho^0 n$ and $\pi^\pm p \to \rho^\pm p$ reactions as a function of the incident-beam momenta P_{lab}. Our fit is shown by the solid line. In the panel (a) ($\pi^- p \to a_2^- p$ reaction) we show individual contributions of ρ and pomeron exchanges. The pomeron exchange dominates at high energies whereas the ρ exchange at small energies. This separation of mechanisms allows to extract two independent coupling constants. We show also spin-conserving and spin-flip amplitudes separately. In panel (b) we show our fit for the $\pi^- p \to \omega^0 n$. Here only ρ exchange is possible. In panel (c) ($\pi^- p \to \rho^0 n$ reaction) we show contributions for charged pion exchange (parameters fixed from phenomenology) and a_2 exchange (parameters found from the analysis of the $\pi^- p \to a_2^- p$, see panel (a)). Finally in panel d) ($\pi^\pm p \to \rho^\pm p$ reactions) we show contributions for neutral pion exchange, a_2 exchange and ω exchange (relevant coupling constants were found from the analysis of the $\pi^- p \to \omega^0 n$ reaction, see panel (b)).

The diagram (a) in Fig.4.44 is topologically identical to the dominant diagram for the $pp \to pp\pi^+\pi^-$ reaction [3]. There, however, the pomeron-pomeron, pomeron-reggeon and reggeon-pomeron exchanges are the dominant processes. In addition to diagram (a) there is possible also another mechanism with the intermediate pion replaced by a virtual photon. Because it requires two electromagnetic couplings instead of two strong couplings its contribution should be small. Because of the extra photon propagator it could be enhanced when $k_\gamma^2 \to 0$. However then the vertices should tend to zero. Therefore we can safely omit such a diagram.

We write the amplitudes for the diagrams in Fig.4.44 as:

$$\begin{aligned}
\mathcal{M}_{\lambda_a\lambda_b\to\lambda_1\lambda_2} &= \sqrt{2}\left(\frac{-t_1}{4m_N^2}\right)^{|\lambda_1-\lambda_a|/2} r_T^{i\,|\lambda_1-\lambda_a|}\,\eta_{I\!R}\,s_{13}\sqrt{C_{I\!R}^{NN}}\left(\frac{s_{13}}{s_0}\right)^{\alpha_{I\!R}(t_1)-1}\exp\left(\frac{B_{MN}}{2}t_1\right)\\
&\quad\times\mathcal{A}(s_{34},t_a)\\
&\quad\times\sqrt{2}\left(\frac{-t_2}{4m_N^2}\right)^{|\lambda_2-\lambda_b|/2} r_T^{i\,|\lambda_2-\lambda_b|}\,\eta_{I\!R}\,s_{24}\sqrt{C_{I\!R}^{NN}}\left(\frac{s_{24}}{s_0}\right)^{\alpha_{I\!R}(t_2)-1}\exp\left(\frac{B_{MN}}{2}t_2\right)\\
&+ \quad \textit{crossed term}\,,
\end{aligned} \tag{4.99}$$

where $\mathcal{A}(s_{34}, t_a)$ refers to the central part of the diagrams

$$\mathcal{A}^{\pi-exch.}(s_{34},t_a) = F_\pi^{off}(t_a)\sqrt{C_\rho^{\pi\pi}}\,\frac{1}{t_a - m_\pi^2}\sqrt{C_\rho^{\pi\pi}}\,F_\pi^{off}(t_a)\,, \tag{4.100}$$

$$\mathcal{A}^{reggeon-exch.}(s_{34},t_a) = \frac{\sqrt{-t_a}}{M_0}\,\eta_i\,s_{34}\,(g^i_{j\to\pi})^2\left(\frac{s_{34}}{s_0}\right)^{\alpha_i(t_a)-1}\exp\left(\frac{B_{MM}}{2}t_a\right)\frac{\sqrt{-t_a}}{M_0}\,. \tag{4.101}$$

In actual calculations we take $B_{MN} = B_{\pi N}$ and $B_{MM} = B_{\pi\pi}$. Since, in the diagrams in Fig.4.44 and Fig.4.47 we have reggeon exchanges rather than meson exchanges therefore formulas (4.99, 4.101) give rather upper limit for the cross section.

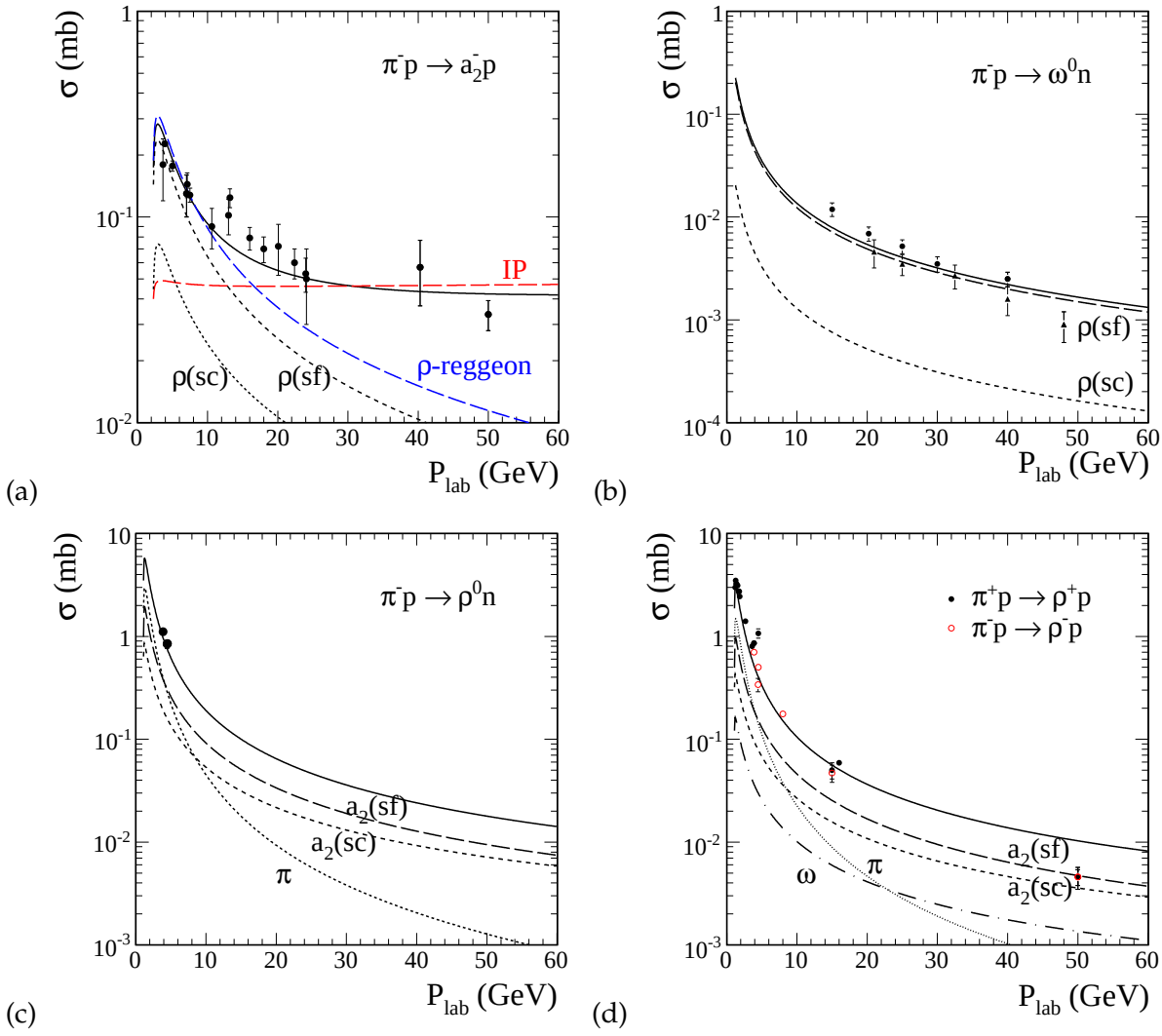

Figure 4.46: The integrated cross section for the $\pi^- p \to a_2^- p$, $\pi^- p \to \omega^0 n$, $\pi^- p \to \rho^0 n$, $\pi^+ p \to \rho^+ p$, and $\pi^- p \to \rho^- p$ reactions as a function of the incident-beam momenta P_{lab}. Corresponding references to experimental data may be found in Ref. [4].

The parameterization of the amplitudes with subleading charged-reggeon exchanges cannot be used in the region of resonances in πN or/and $\pi\pi$ subsystems [3]. Therefore, the amplitude used in the calculations must contain restrictions on the four-body phase space. To exclude the regions of resonances we modify the parameterization of the amplitudes (4.99) by multiplying cross section by a purely phenomenological smooth cut-off correction factor $f_{cont}^{ab}(W_{ab})$ (2.20) for $ab = \pi N$ or $\pi\pi$ system.

There is another class of diagrams shown in Fig.4.47. The diagram (a) represents a generic amplitude with particle sets (A, B, C) collected in Table 4.2. In contrast to the diagrams shown in Fig.4.44, here both pions and subleading reggeons couple to nucleons. We shall not present explicit formulae for the corresponding amplitudes here. We shall show separate contributions of those processes in the Result Section.

In our analysis the $\pi^+ n$ interactions are not taken into account. They would further decrease the cross section. Given other theoretical uncertainties (form factors) it seems not worthy to take over the effort of performing very time-consuming calculations.

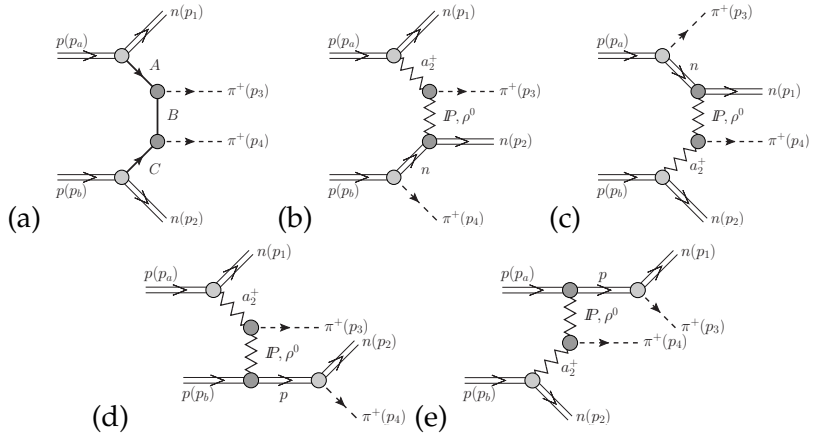

Figure 4.47: Diagrams with subleading reggeon a_2^+ exchange in pp collisions at high energies.

Table 4.2: Different realizations of diagram (a) in Fig.4.47.

A	a_2^+	a_2^+	π^+	a_2^+	π^+
B	$I\!P$	$I\!P$	$I\!P$	ρ^0	ρ^0
C	a_2^+	π^+	a_2^+	π^+	a_2^+

4.8 Results

We shall show our predictions for the $pp \to nn\pi^+\pi^+$ reaction for several differential distributions in different variables at selected center-of-mass energies $\sqrt{s}$ = 500 GeV (RHIC) and $\sqrt{s}$ = 0.9, 2.36 and 7 TeV (LHC). The cross section slowly rises with incident energy. In general, the higher energy the higher absorption effects. The results depend on the value of the nonperturbative, a priori unknown parameter of the form factor responsible for off-shell effects. In Table 4.3 we have collected integrated cross sections for selected energies and different values of the model parameters. We show how the uncertainties of the form factor parameters affect our final results.

In Fig.4.48 we show distributions in pseudorapidity ($\eta = -\ln(\tan\frac{\theta}{2})$, where θ is the angle between the particle momentum and the beam axis) for the $pp \to nn\pi^+\pi^+$ reaction. The discussed reaction is very unique because not only neutrons but also pions are produced dominantly in very forward or very background directions forming a large size gap in pseudorapidity between the produced pions, about 12 units at $\sqrt{s} = 7$ TeV. While neutrons can be measured by the ZDC's the measurement of very forward/backward pions requires further studies. A possible evidence of the reaction discussed here is a signal from both ZDC's and no signal in the central detector.

In Fig.4.49 we present rapidity distributions of pions y_{π^+} and rapidity distributions of neutrons y_n. Please note a very limited range of rapidities shown in the figure. The contributions for individual diagrams (a) – (i) (see Fig.4.43) are also shown. The diagram (d) (from Fig.4.43)

Table 4.3: Full-phase-space integrated cross section (in mb) for exclusive $nn\pi^+\pi^+$ production at selected $\sqrt{s}$ and different values of the form factor parameters. In parentheses we show cross sections including absorption effects.

	$\sqrt{s}$ = 0.5 TeV	$\sqrt{s}$ = 0.9 TeV	$\sqrt{s}$ = 2.36 TeV	$\sqrt{s}$ = 7 TeV
$\Lambda = 0.8$ GeV, $\Lambda_{off} = 1$ GeV	0.34 (0.15)	0.38 (0.16)	0.47 (0.18)	0.59 (0.19)
$\Lambda = \Lambda_{off} = 1$ GeV	0.84 (0.37)	0.95 (0.39)	1.16 (0.42)	1.47 (0.46)
$\Lambda = 1.2$ GeV, $\Lambda_{off} = 1$ GeV	1.45 (0.62)	1.64 (0.66)	2.01 (0.71)	2.55 (0.77)

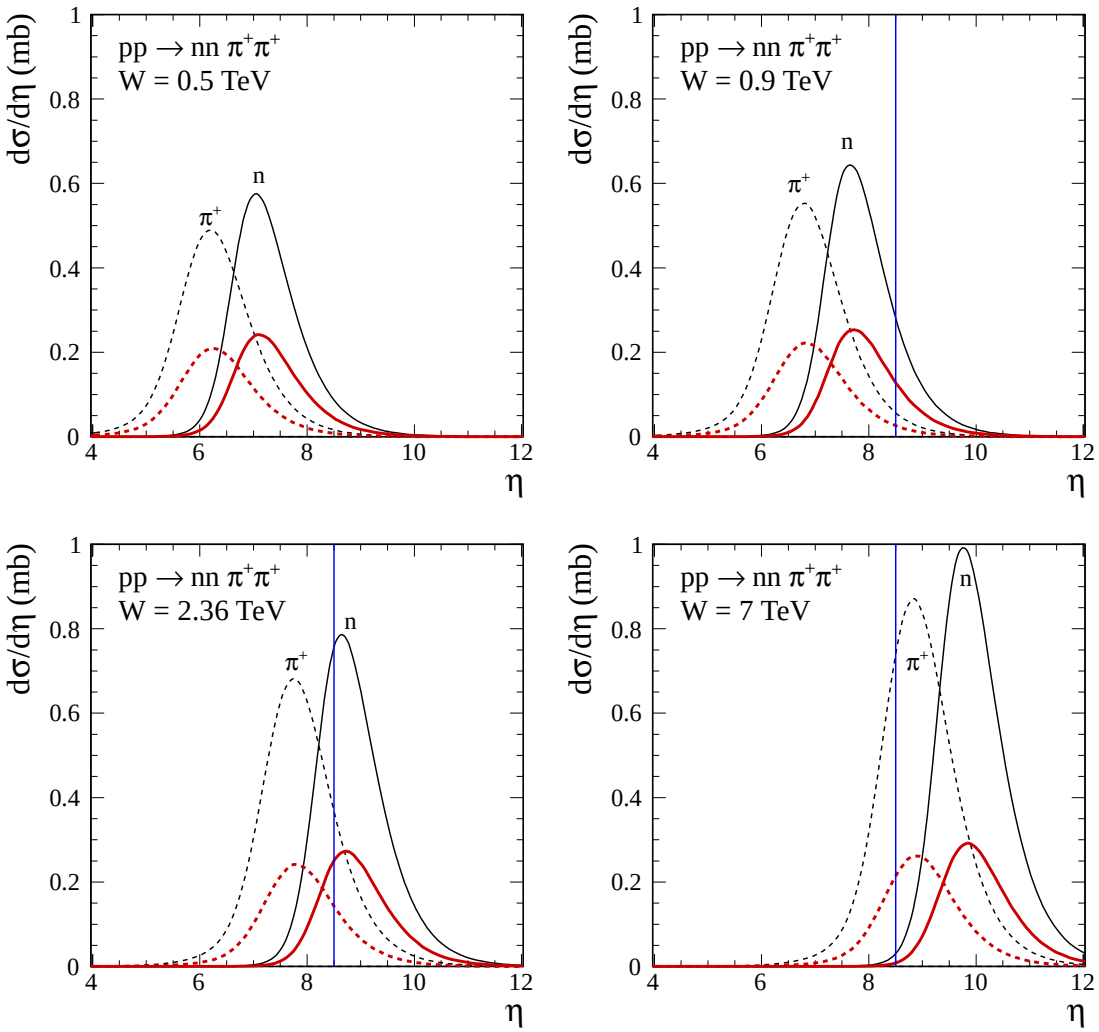

Figure 4.48: Differential cross section $d\sigma/d\eta$ for neutrons (solid lines) and pions (dotted lines) at the center-of-mass energies $\sqrt{s}$ = 0.5, 0.9, 2.36, 7 TeV. The smaller bumps include absorption effects calculated in a way described in 2.3.2. In this calculation we have used $\Lambda = \Lambda_{off}$ = 1 GeV. The vertical lines at $\eta = \pm 8.5$ are the lower limits of the CMS ZDC's. The details related to RHIC ZDC's can be found in Ref. [238, 339].

gives the largest contribution. One can observe specific symmetries between different contributions on the left and right panels. For instance the long-dash-dotted line on the left panel (corresponding to diagram (b)) is symmetric to the dashed line on the right panel (corresponding to diagram (c)). Clearly, a significant interference effect can be seen. There is no region of either pion or neutron rapidity where the diagram (a) dominates. This makes the possibility of extracting of $\pi^+\pi^+$ elastic scattering very difficult.

For completeness, in Fig.4.50 we show the contribution of the diagrams with subleading charged reggeon exchanges (see Fig.4.44) which could not be seen in the previous plot. We show results for the RHIC (left panel) and LHC (right panel) energies. In contrast to the other mechanisms, the corresponding contribution is rather flat over broad range of rapidities. The cross section corresponding to this mechanism is bigger by 2 orders of magnitude for the RHIC energy compared to the LHC energy, but rather small compared to the dominant contributions shown in Fig.4.43. In addition, we show contribution of diagrams of Fig.4.47. They are comparable to those of diagrams shown in Fig.4.44 at midrapidities but much smaller than those from Fig.4.43 at larger rapidities. We show results of diagrams from Fig.4.43 with different values of the form factor parameter $\Lambda = 0.8$ GeV (bottom dashed line) and $\Lambda = 1.2$ GeV (upper dashed

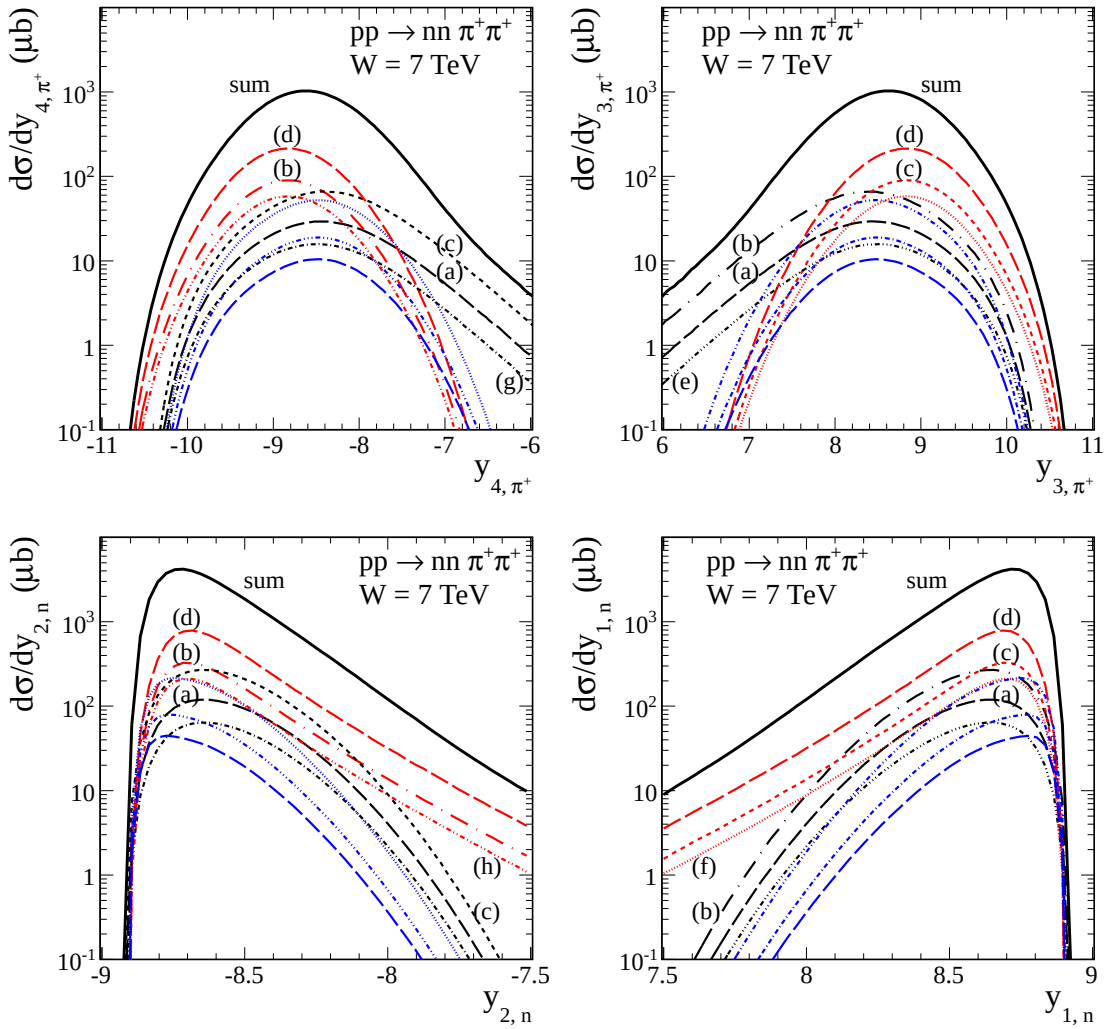

Figure 4.49: Differential cross sections $d\sigma/dy_{\pi^+}$ and $d\sigma/dy_n$ at $\sqrt{s}$ = 7 TeV. The bold solid line represent the coherent sum of all amplitudes. The long-dashed (black), long-dash-dotted, dashed, long-dashed (red online), dash-dot-dot-dotted, dotted, dash-dotted, dash-dot-dotted, long-dashed (blue online) lines correspond to contributions from (a) – (i) diagrams from Fig. 4.43. The red, black and blue lines correspond to diagrams when neutron, pion and proton are off-mass-shell, respectively. No absorption effects were included here.

line) in order to demonstrate the cross section uncertainties.

In Fig.4.51 we present rapidity distributions of pions y_π for double charged reggeon exchanges at $\sqrt{s}$ = 500 GeV (left panel) and $\sqrt{s}$ = 7 TeV (right panel). The bold solid line represent the coherent sum of all amplitudes corresponding to diagrams in Fig.4.44. The contributions for individual diagrams are also shown separately. The diagram (a) in Fig.4.44 gives the largest contribution (long-dashed line). The $a_2^+ - I\!P - a_2^+$ exchange corresponds to the long-dashed-dotted line. One can see that the double reggeon exchange mechanisms shown in Fig.4.44 populate midrapidities of the pions and therefore can be measured either at the RHIC or LHC. In Table 4.4 we have collected cross section for this components. The total contribution is about half of nb at the RHIC (500 GeV) and a few pb at the LHC (7 TeV).

Can the much smaller contribution of diagrams with subleading charged reggeon exchanges be identified experimentally? In Fig.4.52 we show two-dimensional distribution in (y_3, y_4) space. The double-charged reggeon-exchange components from Fig.4.44 are placed along the diagonal $y_3 = y_4$ while the other contributions some distance from the diagonal. Therefore imposing 2-dim cuts in the (y_3, y_4) space one could separate the small double charged

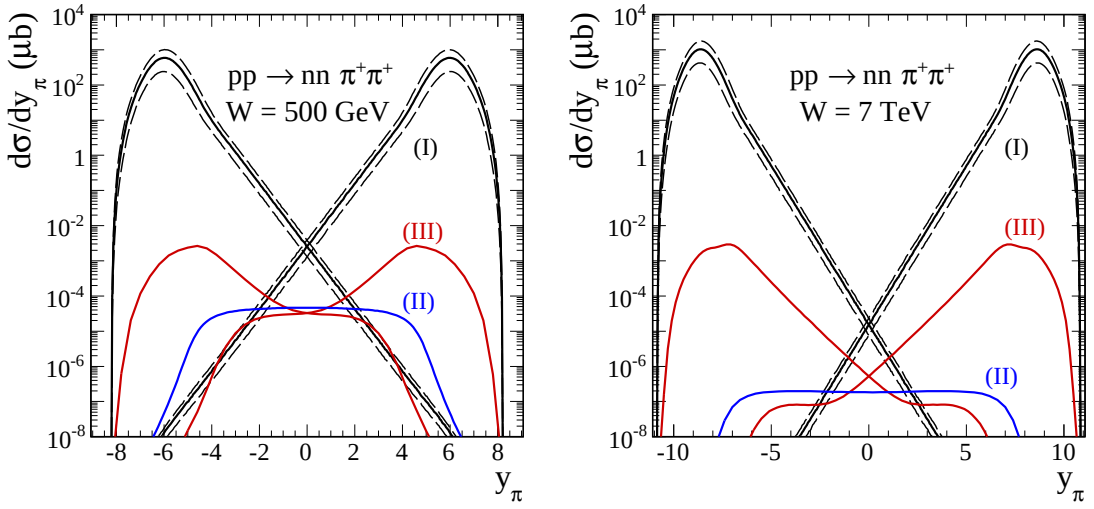

Figure 4.50: Differential cross sections $d\sigma/dy_{\pi^+}$ at $\sqrt{s}$ = 500 GeV (left) and $\sqrt{s}$ = 7 TeV (right). The lines represent the coherent sum of all amplitudes from diagrams in Fig.4.43 (I), Fig.4.47 (III) and the contribution of diagrams in Fig.4.44 (II). No absorption effects were included here.

Table 4.4: Full-phase-space integrated cross section (in nb) for exclusive $\pi^+\pi^+$ production for the amplitude with the double charged reggeon exchanges (diagrams in Fig.4.44) at the center-of-mass energies $\sqrt{s}$ = 0.5, 7 TeV. No absorption effects were included here.

exchange	$\sqrt{s}$ = 0.5 TeV	$\sqrt{s}$ = 7 TeV
$\rho^+ - \pi^0 - \rho^+$	0.43	3.3×10^{-3}
$\rho^+ - a_2^0 - \rho^+$	0.14	1.0×10^{-3}
$a_2^+ - \rho^0 - a_2^+$	0.11	5.4×10^{-4}
$\rho^+ - \omega - \rho^+$	1.5×10^{-4}	1.1×10^{-6}
coherent sum of all amplitudes	0.7	5.1×10^{-3}
$a_2^+ - I\!P - a_2^+$	4.4×10^{-3}	2.5×10^{-3}

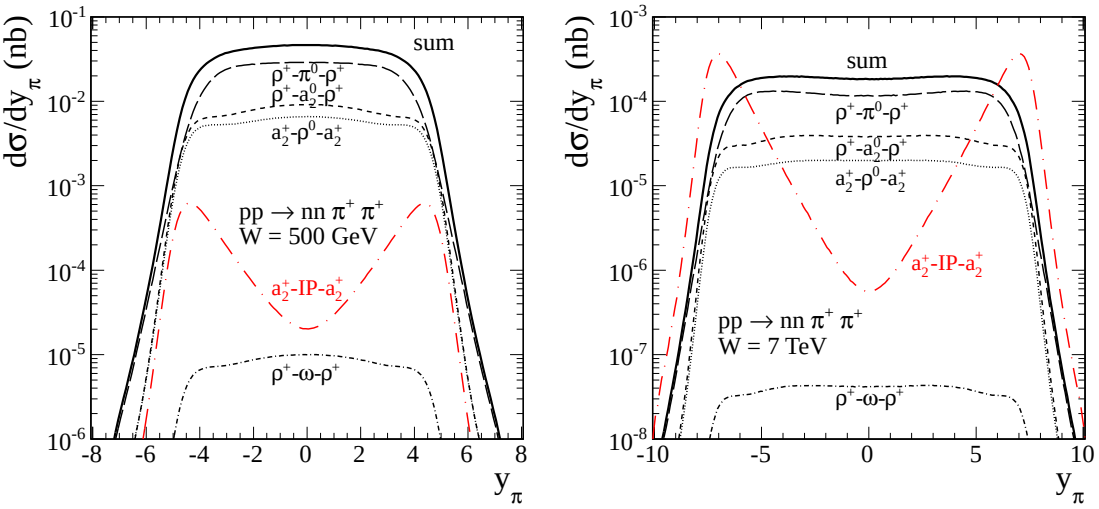

Figure 4.51: Differential cross sections $d\sigma/dy_\pi$ for double charged reggeon exchanges at $\sqrt{s}$ = 500 GeV (left) and $\sqrt{s}$ = 7 TeV (right). The contributions for individual diagrams in Fig.4.44 are shown separately. No absorption effects were included here.

reggeons contribution. A very good one-dimensional observable which can be used for the separation of the processes under discussion could be the differential cross section $d\sigma/dy_{diff}$, where $y_{diff} = y_3 - y_4$ and experimentally charged pions should be taken at random (see Fig.4.53, $y_{\pi,first} = y_3$ or y_4 and $y_{\pi,second} = y_4$ or y_3).

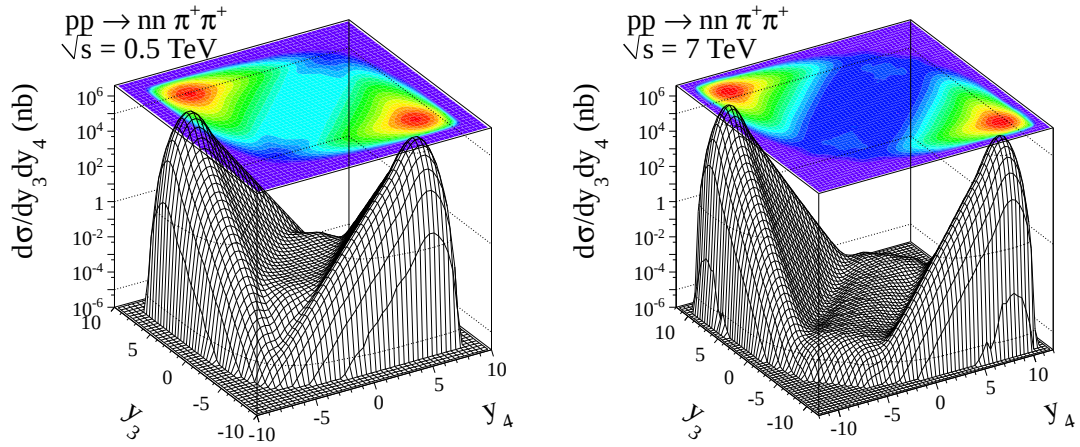

Figure 4.52: Differential cross sections in (y_3, y_4) space at $\sqrt{s}$ = 500 GeV (left) and $\sqrt{s}$ = 7 TeV (right). The coherent sum of all amplitudes from diagrams in Fig.4.43, Fig.4.47, and the contribution placed along the diagonal from diagrams in Fig.4.44 are presented. No absorption effects were included here.

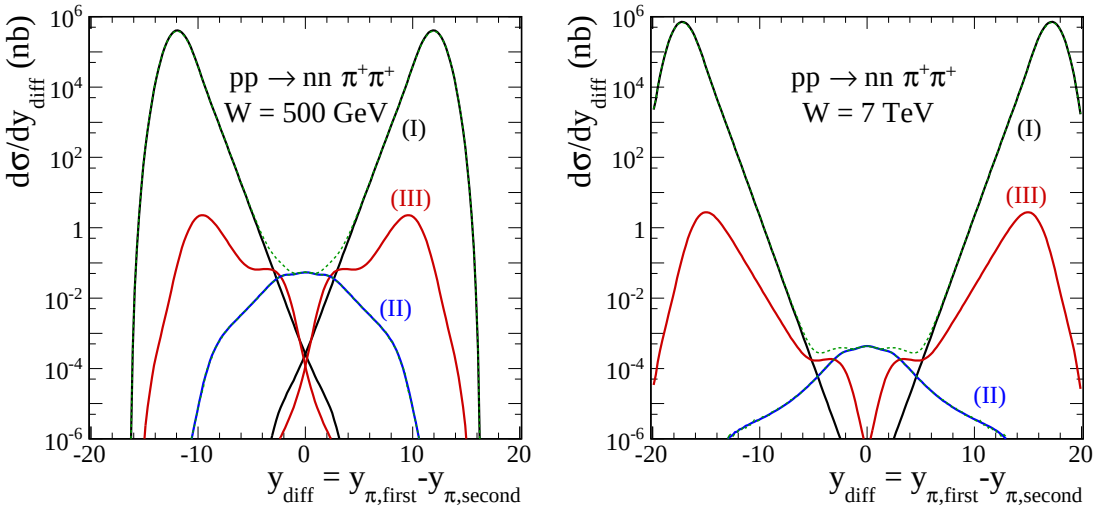

Figure 4.53: Differential cross sections $d\sigma/dy_{diff}$ at $\sqrt{s}$ = 500 GeV (left) and $\sqrt{s}$ = 7 TeV (right). The lines represent the coherent sum of all amplitudes from diagrams in Fig.4.43 (I), Fig.4.47 (III) and the contribution of diagrams in Fig.4.44 (II) placed at $y_{diff} \approx 0$. No absorption effects were included here.

In Fig.4.54 (left panel) we show distribution of neutrons and pions in the Feynman variable x_F (A.16). No absorption effects were included here. In this observable the neutrons and pions are well separated. The position of peaks is almost independent of energy. While pions are produce at relatively small-x_F the neutrons carry large fractions of the parent protons. The situation is qualitatively the same for all energies. The distributions in the transverse momentum of neutrons and pions are shown in Fig.4.54 (right panel). The figure shows that the typical transverse momenta are rather small but large enough to be measured. The distributions for neutrons are rather similar to those for charged pions.

The distribution in pion-pion invariant mass is shown in Fig.4.55. Unique for this reac-

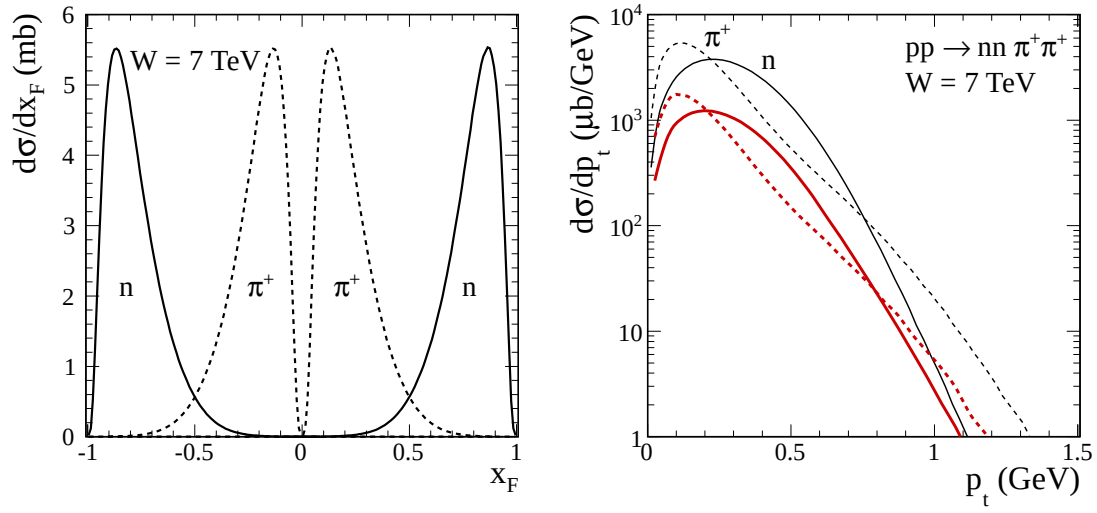

Figure 4.54: Differential cross section $d\sigma/dx_F$ (left panel) and $d\sigma/dp_t$ (right panel) for the $pp \to nn\pi^+\pi^+$ reaction at $\sqrt{s} = 7$ TeV are presented. The solid and dotted lines correspond to the distribution in the transverse momentum of neutrons and pions, respectively. The lower red curves in the right panel correspond to calculations with absorption effects included.

tion, very large two-pion invariant masses are produced (see e.g. Ref. [3]). The larger energy the larger two-pion invariant masses (left panel). The absorption effects almost uniformly reduce the cross section. We show also distributions with different values of the form factor parameter in order to demonstrate the cross section uncertainties (right panel).

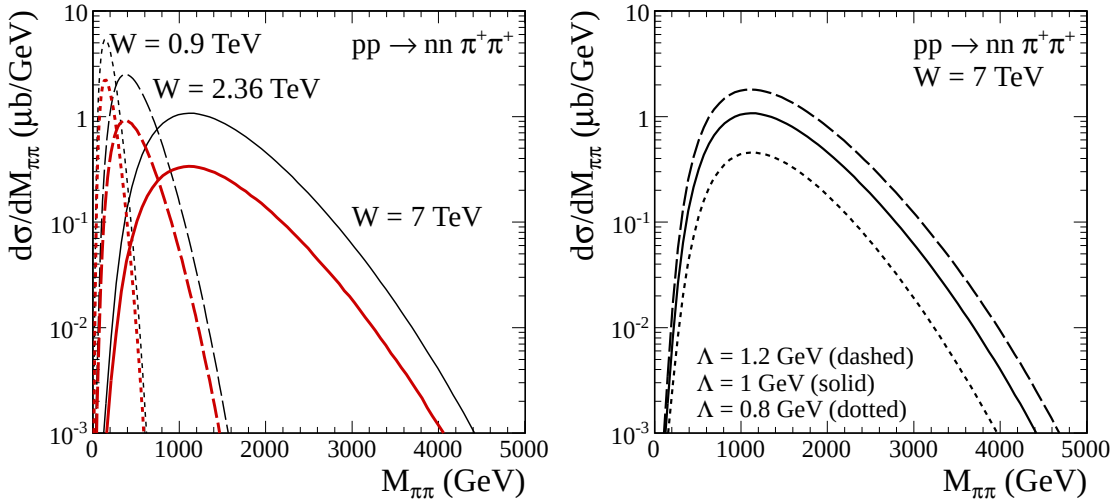

Figure 4.55: Differential cross section $d\sigma/dM_{\pi\pi}$ for the $pp \to nn\pi^+\pi^+$ reaction at $\sqrt{s}$ = 0.9, 2.36, 7 TeV (left panel). The lower curves correspond to calculations with absorption effects. Right panel shows the "bare" cross section obtained with different values of the form factor parameter $\Lambda = 0.8$ GeV (doted line), $\Lambda = 1$ GeV (solid line) and $\Lambda = 1.2$ GeV (dashed line) at $\sqrt{s}$ = 7 TeV..

The energy distributions of neutrons are presented in Fig.4.56. In general, the larger collision energy the larger energy of outgoing neutrons. When combined with the previous plot it becomes clear that the neutrons are produced at very small polar angles (large pseudorapidities) and can be measured by the ZDC's (see also Fig.4.48). There is an attempt to install forward shower counters in the LHC tunnel. Most probably they will not be able to measure energy of the pions but they can signal some activity there. We expect that "some activity" will mean, with a high probability, just one π^+ on one side and the other π^+ on the other side.

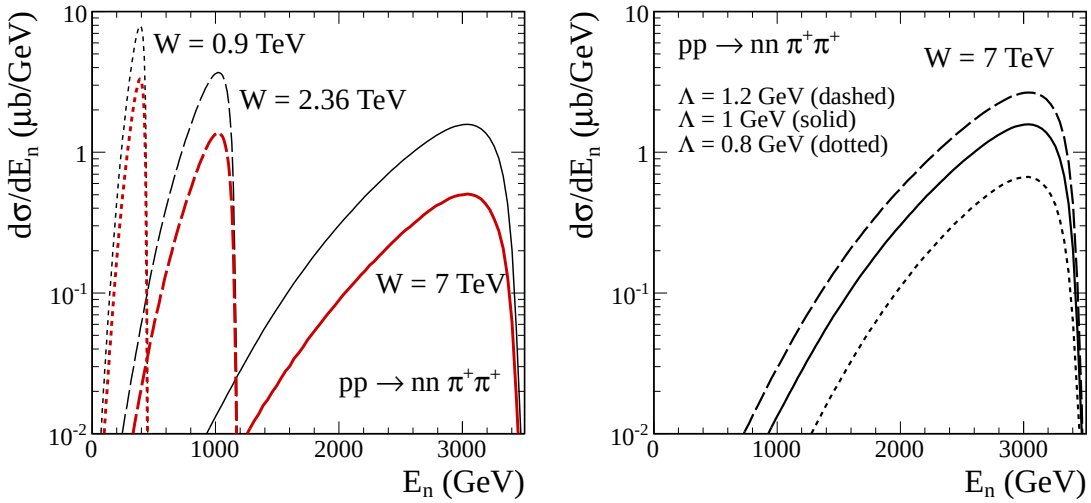

Figure 4.56: Differential cross section $d\sigma/dE_n$ for the $pp \to nn\pi^+\pi^+$ reaction at $\sqrt{s}$ = 0.9, 2.36, 7 TeV (left panel). The lower curves correspond to calculations with absorption effects. Right panel shows the "bare" cross section obtained with different values of the form factor parameter $\Lambda = 0.8$ GeV (dotted line), $\Lambda = 1$ GeV (solid line) and $\Lambda = 1.2$ GeV (dashed line) at $\sqrt{s}$ = 7 TeV.

In Fig.4.57 (left panel) we show two-dimensional correlations between energies of both neutrons measured in both ZDC's. The figure shows that the energies of both neutrons are almost not correlated i.e. the shape (not the normalization) of $d\sigma/dE_{n_1}$ ($d\sigma/dE_{n_2}$) is almost independent of E_{n_2} (E_{n_1}). There should be no problem in measuring energy spectra of neutrons on both sides as well as two-dimensional correlations in (E_{n_1}, E_{n_2}). In Fig.4.57 (right panel) we present the

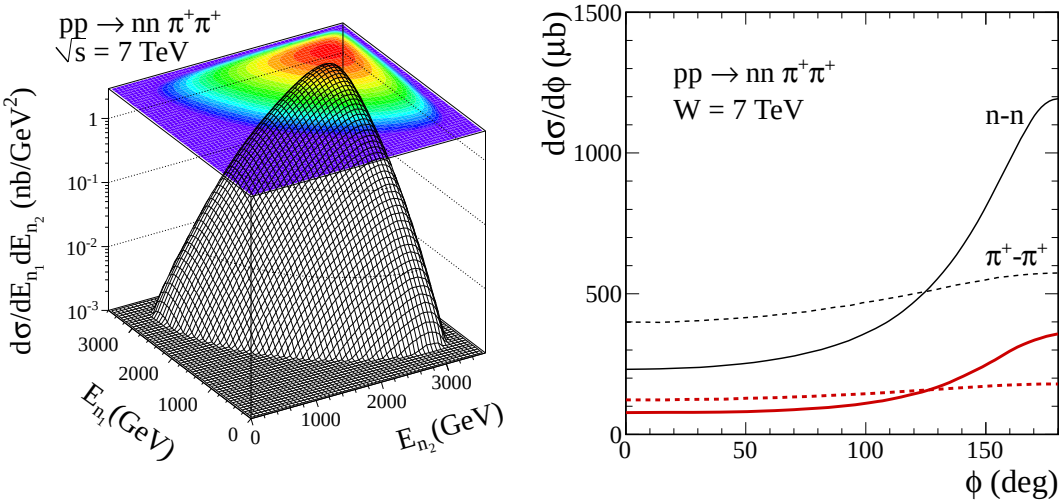

Figure 4.57: Differential cross section $d\sigma/dE_{n_1}dE_{n_2}$ (left panel) for the $pp \to nn\pi^+\pi^+$ reaction at $\sqrt{s}$ = 7 TeV. In the right panel the azimuthal angle correlations between neutrons and beetwen pions are shown. The lower curves correspond to calculations with absorption effects included.

distributions in azimuthal angle ϕ between the transverse momenta of the outgoing neutrons (pions). Clearly a preference of back-to-back emissions can be seen. The measurement of azimuthal correlations of neutrons will be not easy with first version of ZDC's as only horizontal position can be measured. Still correlations of horizontal hit positions on both sides could be interesting. A new correlation observable, taking into account possibilities of the apparatus, should be proposed. In contrast, the two π^+'s are almost not correlated in azimuthal angle. However, such a distribution may be not easy to measure.

Table 4.5: Cross section (no absorption effects) with different experimental cuts on $p_{\perp,\pi}$, η_π and η_n.

	$\sqrt{s}$ (TeV)	$p_{\perp,\pi} >$	$\lvert\eta_\pi\rvert <$	$\lvert\eta_n\rvert_{ZDC} >$	σ (nb)
ALICE	7	0.15	0.9	8.7	6.3×10^{-5}
ALICE	7	0.15	1.2	8.7	1.2×10^{-4}
ATLAS	7	0.5	2.5	8.3	4.9×10^{-4}
CMS	7	0.75	2.4	8.5	4.5×10^{-4}
RHIC	0.5	0.2	1	–	2.0×10^{-2}

We have shown that at present the reaction under consideration can be strictly measured only in a rather limited part of the phase space (midrapidities of pions) where the cross section is rather small and where the charged-reggeon exchanges mechanism dominates. In Table 4.5 we have collected the cross sections in nb for different experiments at the LHC and RHIC. At LHC, where the separation of the double-reggeon exchange mechanism is possible, the cross section is rather small of the order of a fraction of pb. At RHIC the cross section with experimental cuts should be easily measurable as it is of the order of a fraction of nb.

4.9 Conclusions

We have calculated differential cross sections for the exclusive $pp \to pp\pi^0$ reaction at high energies relevant for RHIC and LHC. We have included the π^0-bremsstrahlung from the initial and final state, diffractive π^0-rescattering, photon-photon fusion and photon-omega (omega-photon) fusion processes. The diffractive πN and NN rescattering amplitudes have been related to the total πN and NN cross sections. The Donnachie-Landshoff parametrisation has been used for energy dependence of the latter. Absorptive effects have been included in addition. They lower the cross section by a factor 2 to 3; see Table 4.1.

We have found very large cross sections of the order of mb. The total (integrated over phase space) cross section is almost energy independent. The dominant contributions are placed at large rapidities. The larger c.m. energy, the larger rapidities are populated. On the other hand, the diffractive contribution is absent at midrapidity ($y_{\pi^0} = 0$). The higher the collision energy, the larger the unpopulated region. This opens a window for other mechanisms with much smaller cross section. For example at the LHC the two-photon fusion mechanism "wins" with the diffractive mechanisms at $y_{\pi^0} \approx 0$, where the diffractive contributions are very small. However, the transverse momenta of neutral pions in this region are very small and therefore such pions are very difficult to measure. The $\gamma\omega$ or $\omega\gamma$ exchanges have been found to be significant only in backward or forward rapidities, respectively, and are small at midrapidities due to ω-reggeization. In principle, also a_2-pomeron and pomeron-a_2 exchanges or ρ^0-odderon and odderon-ρ^0 exchanges could play some role but not at midrapidities. In addition, it is rather difficult to make for them realistic predictions. A larger cross section than predicted here at midrapidities would be an interesting surprise.

We have shown several other differential distributions. If one limits to separate regions of $y_{\pi^0} < 0$ or $y_{\pi^0} > 0$ (one-side excitation), then the distributions in proton transverse momenta p_{1t} and p_{2t} are quite different – one reflecting the pion/nucleon exchange and the second reflecting the pomeron exchange. The same is true for the t_1 and t_2 (transferred four-momentum squares) distributions. Analysis of such details would be a useful test of the model. The distribution in the mass of the excited $\pi^0 p$ system peaks at small $M_{\pi p}$ and quickly drops when the mass increases. Such a distribution reminds the spectral shape of the Roper resonance fitted recently to an old single-diffractive data. We have obtained an interesting correlation between the mass of the excited system and the slope of the t distributions well represented in a two-dimensional plot $\frac{d\sigma}{dtdM}(t, M)$. Similar effects were observed in the past for the $pp \to p(n\pi^+)$ and $np \to (p\pi^-)p$

reactions at the CERN ISR and Fermi National Accelerator Laboratory (Fermilab).

At the LHC the π^0 mesons could be measured with the help of Zero Degree Calorimeters. Such measurements are possible only at rather large pseudorapidities $|\eta_{\pi^0}| > 8 - 9$. On the other hand, protons could be measured with the ALFA detector of ATLAS or the TOTEM detector associated with the CMS main detector. Particularly interesting is the distribution in azimuthal angle between outgoing protons, not studied so far, including low-energy $pp \to p(n\pi^+)$ and $np \to (p\pi^-)p$ reactions measured in the 1970's at ISR and Fermilab. The distribution has a maximum at relative angle $\phi_{12} = \pi$. The detailed shape of the distribution is, however, very sensitive to the relative contribution of different ingredients of the model. The sensitive nature of the cancellation between proton-exchange and direct production amplitudes leads to a situation where minor changes in the parametrisations of these amplitudes can have large effects on discussed distributions. Experimental analysis of such a distribution would therefore help in fixing model parameters such as cut-off parameters of hadronic form factors, not known very precisely.

The $pp \to pp\pi^0$ reaction is interesting also in a much broader context. First of all, it may constitute a sizeable fraction of the neutral pion inclusive cross section at very forward/backward (pseudo)rapidities. A comparison with non-diffractive Monte Carlo code would be therefore very valuable. Second, it leads to a production of very energetic photons ($\sim 0.5 - 2$ TeV) from the decay of the forward π^0's. These two issues will be a subject of future investigations. Third, the DHD mechanism contributes sizeable amount to the single diffractive cross section and as a consequence to the total inelastic cross section. This contribution is not included in any of existing Monte Carlo codes. Needless to say, these codes are used when extrapolating the measured high-mass SD cross section down to the πN threshold, which obviously leads to an underestimation of the extracted (measured and extrapolated) cross section for single diffraction and/or inelastic processes. Finally, because the cross section for the discussed reaction is large, detailed studies could help to test model(s) of soft absorption, so important in the context of more fundamental searches such as, e.g., exclusive production of the Higgs boson in diffractive processes.

We have calculated only contributions with intermediate protons in the ground state to the $pp \to pp\pi^0$ reaction. There are also resonance contributions, due to diffractive excitation of some nucleon resonances and their subsequent decays into the $p + \pi^0$ ($\bar{p} + \pi^0$) channels. The dominant contributions are due to N^* resonant states being members of the nucleon trajectory (Fig. 2.1(b)). The $N^*(1680)$ $5/2^+$ state is the best candidate. Although a huge contribution of the Roper resonance $N^*(1440)$ was suggested recently [275], as discussed above, their contribution may be to some extent an artifact of a fit which does not include the non-resonant DHD mechanism, neither in the $pp \to pp\pi^0$ nor in the $pp \to pn\pi^+$ channel. We have considered single exclusive π^0 production. One could think about immediate extension of the present study to double diffractive, double DHD mechanism producing two exclusive π^0's, not considered so far in the literature and not included in any Monte Carlo code. Again we expect a rather large cross section for such an inelastic process.

We have presented first estimates of the photon-odderon and odderon-photon contributions based on the upper limit of the $\gamma p \to \pi^0 p$ cross section obtained at the HERA as well as estimates based on a nonperturbative approach of Ewerz and Nachtmann which makes use of chiral symmetry and PCAC. Based on the HERA upper limit we conclude that the cross section for the contribution to the $pp \to pp\pi^0$ reaction is smaller than 20 nb in the rapidity region $|y_{\pi^0}| < 2.5$. Any deviation from the $\gamma\gamma \to \pi^0$ contribution to transverse momentum distribution of neutral pions at midrapidity would be a potential signal of photon-odderon (odderon-photon) contributions. One can expect potential deviations from the photon-photon contribution at $p_{\perp,\pi^0} \sim 0.5$ GeV. This requires dedicated studies if the considered process could be measured by, e.g., the ALICE Collaboration at the LHC [13]

We have calculated the cross section for $\gamma p \to \omega p$ reaction at high-energy within a

[13]The measurements of the invariant differential cross sections of inclusive π^0 meson production in proton-proton collisions at $\sqrt{s} = 0.9$ TeV and 7 TeV at midrapidity in a wide $p_{\perp,\pi^0}$ range $0.4 - 7$ GeV and $0.3 - 25$ GeV for these two energies, respectively, with the ALICE detector are reported in Ref. [340].

QCD-inspired model. In the presented model the Gaussian wave function was used with parameters adjusted to reproduce the electronic decay width of ω meson. A good description of the HERA experimental data has been achieved, comparable as for the J/Ψ [147] and ϕ [196] mesons. We have predicted the cross sections for the $pp \to pp\omega$ and $p\bar{p} \to p\bar{p}\omega$ reactions at high-energies. In contrast to the exclusive production of J/Ψ and ϕ mesons, in the case of the ω meson different hadronic bremsstrahlung processes are possible due to large nonperturbative coupling of the ω meson to the nucleon.

At low energies the hadronic bremsstrahlung contributions dominate over the photoproduction ones if the standard Mandelstam-dependent form factors are used. With increasing energy the hadronic bremsstrahlung contributions move in rapidity to the fragmentation regions. At high energies the photoproduction mechanisms dominate at midrapidities. We predict a short plateau at midrapidities due to the photoproduction mechanism and a significant increase towards fragmentation regions (large $|y_\omega|$) due to the ω-bremsstrahlung mechanism. The identification of the increase would be a confirmation of the hadronic bremsstrahlung effects discussed here. However, this may be not simple experimentally. The precisely evaluated photoproduction mechanism constitutes a background for the odderon exchange searches.

We have considered also several mechanisms of exclusive single photon production for the $pp \to pp\gamma$ reaction and calculated several differential distributions at high energy. The diffractive γ-bremsstrahlung mechanism turned out to give the biggest cross section concentrated at large photon (pseudo)rapidities. The photons are emitted at only slightly smaller pseudorapidities than the scattered protons. We observe a strong cancellation between the initial and final state radiation. The cross section for the γ-bremsstrahlung is peaked at back-to-back configurations (similar transverse momenta or polar angles of outgoing protons and relative azimuthal angle concentrated close to $\phi_{12} = \pi$). This is a clear reminiscence of elastic scattering. Cut on photon energy ($E_\gamma > 100$ GeV) reduces the region of $\phi_{12} \cong \pi$ significantly and the integrated diffractive bremsstrahlung cross section is only of the order of μb. The cross section for pion-photon or photon-pion exchanges is much smaller. Here both small (photon exchange) and large (pion exchange) four-momentum transfers squared are possible. For this process there is no correlation in azimuthal angle between outgoing protons.

Both the γ-bremsstrahlung and the pion-photon (photon-pion) fusion as well as the virtual-ω–rescattering mechanisms could be studied with the help of Zero Degree Calorimeters (photons) and the ALFA or TOTEM detectors (protons). By imposing several cuts one could select or enhance the contribution of one of the mechanisms. The cross section for pomeron-photon or photon-pomeron exchanges is rather small and concentrated at midrapidities. Furthermore, the transverse momenta of outgoing photons are small and cannot be easily measured with central ATLAS or CMS detectors.

Summarizing, even present LHC equipment allows to study exclusive production of photons. Since this process was never studied at high energies it is worth to make efforts to obtain first experimental cross sections. Since the cross sections are reasonably large one could try to obtain even some differential distributions. This would allow to test our understanding of the diffractive processes and help in pinning down some hadronic and electromagnetic off-shell form factors, difficult to test otherwise.

Finally, we have estimated cross sections and calculated several differential observables for the exclusive $pp \to nn\pi^+\pi^+$ reaction. Because our parameters are extracted from the analysis of known two-body reactions we expect that our predictions of the cross section are fairly precise in spite of the complications of the reaction mechanism. The full amplitude was parametrised in terms of leading pomeron and subleading reggeon exchanges. The first class gives the largest contribution but concentrated at forward or backward pion directions. There are also diagrams with double charged exchanges with subleading reggeons ρ^+ and a_2^+. Although the cross section for these contributions is rather small, it is concentrated at midrapidities of pions where the cross section can be easily measured. The double-exchange reggeons processes can be separated out in the two-dimensional space of rapidities of both pions or in the distribution of the pion rapidity

difference.

Large cross sections have been obtained, even bigger than for the $pp \to pp\pi^+\pi^-$ reaction [3]. Several mechanisms contribute to the cross section, which leads to an enhancement of the cross section due to interference effects. These interference effects cause that the extraction of the elastic $\pi^+\pi^+$ cross section, as proposed recently [335], seems in practice rather impossible. We did not find any corner of the phase space where the relevant diagram dominates. We have included elastic pp-rescattering effects in a way used recently for the three body processes. These effects lead to a substantial damping of the cross section. The bigger energy the larger absorption effect of damping. Other processes (e.g. inelastic intermediate states or final state $\pi^+ n$ interactions) could lead to additional damping. At present there is no full understanding of the absorption effects. We have made predictions for azimuthal angle correlations of outgoing neutrons (back-to-back correlations with a sizeable diffusion). Such distribution should be possible to measure in a future.

The specificity of the reaction is that both neutrons and pions are emitted in very forward/backward directions, producing a huge rapidity gap at midrapidities. While the neutrons could be measured by the ZDC's, the identification of pions may be difficult. We think that the measurement of both neutrons and observation of large rapidity gap is a very good signature of the considered reaction. We expect the cross section for the $nn\pi^+\pi^+\pi^0$, $nn\pi^+\pi^+\pi^0\pi^0$, etc., which could destroy rapidity gaps, to be smaller but a relevant estimates need to be done. In addition, for events with larger number of pions the rapidity gap would be easily destroyed. Therefore the formally kinematically incomplete measurement of two neutrons only could be relatively precise. We have found that the neutrons measured in ZDC's seem to be almost uncorrelated in energies. A future experiment could provide new data to be analysed and could shed new light on absorption effects which are essential for understanding exclusive processes.

Chapter 5

Central Exclusive Diboson Production

We consider the central exclusive production (CEP) of the vector boson pairs in the following processes

$$h_1(p_a) + h_2(p_b) \to h_1(p_1) + V(p_3)V(p_4) + h_2(p_2)\,, \tag{5.1}$$

where VV (e.g. $\gamma\gamma, \gamma Z, ZZ, W^+W^-$) is a diffractive system separated from the two very forward protons (h_1, h_2) by large rapidity gaps. If momenta of the outgoing protons are measured by forward proton detectors placed at 220 m and 420 m from the ATLAS/CMS interaction point [239], the mass of the central system may be reconstructed with very precise resolution [341]. These processes are considered to be very sensitive to New Physics contributions (see Refs. [12, 128] for a review on the topic).

The exclusive reaction $pp \to pHp$ has been intensively studied by the Durham group [99–101, 342, 343] in the last decade. This study was motivated by the clean environment and largely reduced background due to a suppression of $b\bar{b}$ production as a consequence of the spin-parity conservation in the forward limit. In particular, it has been proposed as an alternative way of searching for neutral Higgs bosons and SUSY particles (see Refs. [128, 239]) due to a reduced QCD $b\bar{b}$ background. However, very recent precise calculations of Refs. [211, 344] have shown that the situation with Higgs CEP background in the $b\bar{b}$ channel is more complicated and the signal is to a large extent shadowed by the exclusive non-reducible continuum $b\bar{b}$ production. In addition, reducible backgrounds from a misidentification of gluonic jets as b-quark jets can be very difficult to separate [345]. Since the total cross section for the Higgs CEP is quite small and rather uncertain, the issue with the Higgs CEP is still far from its final resolution, from both theoretical and experimental point of view.

For the QCD-initiated CEP processes there is a serious problem of rather large theoretical uncertainties of the QCD diffraction mechanism in the framework of the Durham Model (see e.g. Refs. [99–101, 342, 343]). These uncertainties come from both the hard subprocess treatment (Sudakov form factor [346, 347], next-to-leading order QCD corrections [348]) and soft k_t-dependent parton densities as well as from a model-dependent gap survival probability factor (see e.g. Refs. [6, 104, 106, 177, 210, 347, 349, 350]). This situation forces the search for various possible ways to probe the underlying CEP QCD mechanism. In order to reduce theoretical uncertainties, new experimental data on various exclusive production channels are certainly required and expected to come soon from ongoing LHC measurements. In particular, a measurement of the exclusive dijets production at the LHC could largely reduce the theoretical uncertainty in the Higgs boson CEP [347]. Other exclusive measurements, e.g. heavy quarkonia [6, 104, 106, 177, 210, 350], $\gamma\gamma$ and W^+W^- pairs [11, 12], high-$p_\perp$ light mesons [105, 351], associated charged Higgs H^+W^- CEP [352], etc., can also be important in this context. Some of these results have been compared to experimental data from the Tevatron [180, 353–355], and a rough quantitative agreement between them has been achieved.

Besides the QCD-initiated CEP processes like the exclusive Higgs and dijet production, there are extra QED-initiated contributions coming from $\gamma\gamma \to X$ subprocesses. Normally, these

contributions are strongly suppressed by very small fine structure constant and therefore typically neglected compared to the QCD ones especially for not very large invariant masses of the X system, except for leading-order exclusive dilepton $X \equiv l^+l^-$ production. On the other hand, the exclusive reaction via the $\gamma\gamma$ fusion have significantly smaller theoretical uncertainties compared to the QCD-initiated Durham mechanism making it a very appealing option for New Physics searches for exotic resonances which are coupled to photons or SM gauge bosons only.

The final system X in the midrapidity region is predominantly produced in the $J_z = 0$ state as dictated by the well-known $J_z = 0$ selection rule [99–101, 342, 343]. However, corrections to this rule due to slightly off-forward protons can be important for lower (a few GeV) mass central systems and may lead to sizeable contributions in the observable signals, in particular, in the χ_c mesons [6, 104, 106, 177, 210, 350], $b\bar{b}$ [211, 344] and gg [345, 346] CEP. The emission of gluons from the "screening" gluon could also violate the $J_z = 0$ selection rule as has recently been emphasized in Ref. [346].

We focus on exclusive production of W^+W^- pairs in high-energy proton-proton collisions. It was found recently [356–359] that the reaction is an ideal case to probe experimentally the γW^+W^- and $\gamma\gamma W^+W^-$ anomalous couplings [1]. Here, we would like to focus on an extra interesting opportunity of making use of large rapidity gap processes at the LHC for probing new strongly-coupled dynamics. The $\gamma\gamma \to W^+W^-$ and $\gamma\gamma \to \gamma\gamma$ processes are interesting reactions to test the Standard Model and any other theory beyond the Standard Model, since that contribution dominates at high energies. The linear collider (ILC, CLIC) would be a good option to study the couplings of gauge bosons in the distant future. For instance in Refs. [360–362] the anomalous coupling in locally SU(2) $\times$ U(1) invariant effective Lagrangian was studied. Other models also lead to anomalous gauge boson coupling.

So far the photon-photon contribution for the purely exclusive production of W^+W^- was considered in the literature. The diffractive production and decay of Higgs boson into the W^+W^- pair was discussed in Ref. [363], and the corresponding cross section turned out to be significantly smaller than that for the $\gamma\gamma$-contribution. Provided this is the case, the W^+W^- pair production signal would be particularly sensitive to New Physics contributions in the $\gamma\gamma \to W^+W^-$ subprocess [356–359]. Similar analysis has been considered recently for $\gamma\gamma \to ZZ$ [364]. These previous analyses strongly motivate our present detailed study on a competitive diffractive contribution. The $pp \to pW^+W^-p$ process going through the diffractive QCD mechanism with the $gg \to W^+W^-$ subprocess naturally constitutes a background for the exclusive electromagnetic $pp \to p(\gamma\gamma \to W^+W^-)p$ process. We consider not only the mechanism with intermediate Higgs boson but also quark box contributions never estimated in exclusive processes. Both the Higgs and box contribution may interfere together. We discuss here the interference effects. Corresponding measurements will be possible to perform at the ATLAS detector with the help of very forward proton detectors [356, 357]. In order to quantify to what extent the QCD mechanism competes with the "signal" from the $\gamma\gamma$ fusion, we calculate both contributions and compare them differentially as a function of several relevant kinematical variables. Since the box contribution of exclusive diffractive $pp \to ppW^+W^-$ process is very similar to the $p\bar{p} \to p\bar{p}\gamma\gamma$ process which has been measured recently [355], we discuss the latter one and compare corresponding results with the recent CDF data.

5.1 Exclusive QCD mechanism

In this Section, the exclusive QCD diffractive mechanism for the diboson production (5.1) via off-shell gluon-gluon fusion is taken into consideration. A schematic diagram for central exclusive production of $W^\pm W^\mp$ pairs in proton-proton scattering with relevant kinematics notations is shown in Fig. 5.1. Similar mechanisms have been considered in inclusive production of W^+W^- pairs (see e.g. Refs. [365–370]). In what follows, we use the standard theoretical de-

[1] Some more subtle aspects of the beyond Standard Model anomalous couplings were discussed e.g. in [360].

scription of CEP processes developed by Khoze, Martin and Ryskin for the exclusive production of Higgs boson [99–101, 342, 343].

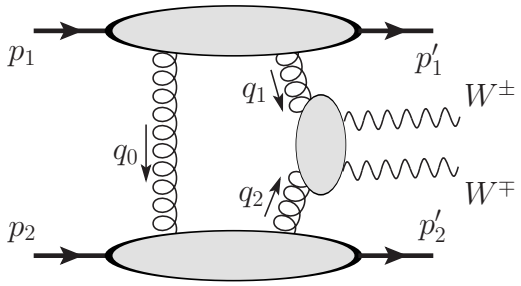

Figure 5.1: Generic diagram for the central exclusive WW pair production in pp collisions. Momenta of incident particles are shown explicitly; in the formulas below we have $p_1(p_a) + p_2(p_b) \to p_1'(p_1) + W^+(p_3)W^-(p_4) + p_2'(p_2)$.

The momenta of intermediate gluons are given by Sudakov decompositions into longitudinal and transverse parts in the high energy limit in the c.m.s. frame as follows

$$\begin{aligned} &q_1 = x_1 p_a + q_{1\perp}, \quad q_2 = x_2 p_b + q_{2\perp}, \quad 0 < x_{1,2} < 1, \\ &q_0 = x_1' p_a - x_2' p_b + q_{0\perp} \simeq q_{0\perp}, \quad x_1' \sim x_2' = x' \ll x_{1,2}, \end{aligned} \tag{5.2}$$

where $p_{a,b}$ are the incoming proton four-momenta, $q_{1,2\perp}$, $q_{0\perp}$, $x_{1,2}$ and $x_{1,2}'$ are the transverse four-momenta and the longitudinal momentum fractions for active (fusing) and color screening gluons, respectively. Making use of conservation laws

$$q_1 = p_a - p_1 - q_0, \quad q_2 = p_b - p_2 + q_0, \quad q_1 + q_2 = p_3 + p_4, \tag{5.3}$$

one can write

$$s\, x_1 x_2 = M_{VV}^2 + |\vec{k}_\perp|^2 \equiv M_{VV\perp}^2, \quad M_{VV}^2 = (p_3 + p_4)^2\,, \tag{5.4}$$

where M_{VV} is the invariant mass of the boson pairs.

For simplicity, in actual calculations we work in the forward proton scattering limit and we have

$$\begin{aligned} &t_{1,2} = (p_{a,b} - p_{1,2})^2 \simeq p_{1,2\perp}^2 \to 0\,, \\ &q_\perp \equiv q_{0\perp} \simeq -q_{1\perp} = q_{2\perp} \end{aligned} \tag{5.5}$$

and, hence, $\vec{p}_{3\perp} \simeq -\vec{p}_{4\perp}$. The QCD factorisation of the process at the hard scale μ_F is provided by

$$\mu_F^2 \equiv s\, x_1 x_2 \simeq M_{VV}^2\,. \tag{5.6}$$

It is convenient to introduce the Sudakov expansion for $V_{3,4}$ boson momenta

$$p_3 = x_1^+ p_a + x_2^+ p_b + p_{3\perp}, \quad p_4 = x_1^- p_a + x_2^- p_b + p_{4\perp} \tag{5.7}$$

leading to

$$x_{1,2} = x_{1,2}^+ + x_{1,2}^-, \quad x_{1,2}^+ = \frac{m_{3\perp}}{\sqrt{s}} e^{\pm y_3}, \quad x_{1,2}^- = \frac{m_{4\perp}}{\sqrt{s}} e^{\pm y_4}, \quad m_{3,4\perp} = \sqrt{m_{V_{3,4}}^2 + |\vec{p}_{3,4\perp}|^2}\,, \tag{5.8}$$

in terms of $V_{3,4}$ boson rapidities $y_{3,4}$ and transverse masses $m_{3,4\perp}$. For simplicity, in actual calculations we work in the forward limit given by Eq. (5.5).

We write the amplitude of the exclusive central-diffractive boson pairs production (5.1), which at high energy is dominated by its imaginary part, as

$$\mathcal{M}_{\lambda_3\lambda_4}(s,t_1,t_2) \;\simeq\; is\frac{\pi^2}{2}\int d^2\boldsymbol{q}_{0\perp}\, V_{\lambda_3\lambda_4}(q_1,q_2,p_3,p_4)\frac{f_g^{\rm off}(q_0,q_1;t_1)f_g^{\rm off}(q_0,q_2;t_2)}{\boldsymbol{q}_{0\perp}^2\,\boldsymbol{q}_{1\perp}^2\,\boldsymbol{q}_{2\perp}^2}\,, \tag{5.9}$$

where $\lambda_{3,4}$ are the polarisation states (helicities) of the produced bosons, $f_g^{\rm off}(r_1,r_2;t)$ is the off-diagonal unintegrated gluon distribution function (UGDF), which depends on the longitudinal and transverse components of both gluon momenta.

The off-shell gluon fusion (hard) subprocess $g^*g^* \to VV$ amplitude $V_{\lambda_3\lambda_4}(q_1,q_2,p_3,p_4)$ is given by the light cone projection

$$V_{\lambda_3\lambda_4} = n_\mu^+ n_\nu^- V_{\lambda_3\lambda_4,\mu\nu} = \frac{4}{s}\frac{q_{1\perp}^\mu}{x_1}\frac{q_{2\perp}^\nu}{x_2}V_{\lambda_3\lambda_4,\mu\nu}\,, \tag{5.10}$$

where $n_\mu^\pm = p_{a,b}^\mu/E_{p,cms}$ and the center-of-mass proton energy $E_{p,cms} = \sqrt{s}/2$. We adopt the definition of gluon transverse polarisation vectors proportional to the transverse gluon momenta $q_{1,2\perp}$, i.e. $\varepsilon_{1,2} \sim q_{1,2\perp}/x_{1,2}$.

The amplitude of fusion of two off-shell gluons $g^*g^* \to VV$ turns out to be explicitly gauge invariant. Indeed, by direct calculation it becomes clear that the gauge invariance over the first and second gluon line is satisfied, i.e.

$$q_1^\mu V_{\lambda_3\lambda_4,\mu\nu} = q_2^\nu V_{\lambda_3\lambda_4,\mu\nu} = 0\,. \tag{5.11}$$

The helicity matrix element in Eq.(5.10) reads

$$V^{\mu\nu}_{\lambda_3\lambda_4}(q_1,q_2,p_3,p_4) = \varepsilon^{*,\rho}(p_3,\lambda_3)\varepsilon^{*,\sigma}(p_4,\lambda_4)V^{\mu\nu}_{\rho\sigma}\,, \tag{5.12}$$

in terms of the Lorentz and gauge invariant $2 \to 2$ amplitude $V^{\mu\nu}_{\rho\sigma}$ and outgoing boson polarisation vectors $\varepsilon^*(p,\lambda)$ (4.57), where ϕ is the azimuthal angle of a produced boson. In the forward limit, provided by Eq. (5.5), the azimuthal angles of the V_3 and V_4 bosons are related as $\phi_3 = \phi_4 + \pi$. It can be checked that (4.57) satisfies the identities $\varepsilon^\mu(p,\lambda)\varepsilon^*_\mu(p,\lambda) = -1$ and $\varepsilon_\mu(p,\lambda)p^\mu = \varepsilon^*_\mu(p,\lambda)p^\mu = 0$.

The diffractive amplitude given by Eq. (5.9) is averaged over the color indices and over the two transverse polarizations of the incoming gluons. The relevant color factor which includes summing over colors of quarks in the loop (triangle or box) and averaging over fusing gluon colors (according to the definition of unintegrated gluon distribution function) is the same as in the previously studied Higgs CEP (for more details on derivation of the generic $pp \to pXp$ amplitude, see e.g. Ref. [128]). The matrix element V_{λ_3,λ_4} contains twice the strong coupling constant $g_s^2 = 4\pi\alpha_s$, where α_s is the "strong fine-structure constant". In our calculation here we take the running coupling constant $\alpha_s(\mu_{hard}^2 = M_{VV}^2)$ (see Eq. 5.6) which depends on the invariant mass of VV pair as a hard renormalisation scale of the process. The choice of the scale introduces roughly a factor of two model uncertainties when varying the hard scale μ_{hard} between $2M_{VV}$ and $M_{VV}/2$ values.

The bare amplitude above is subjected to absorption corrections that depend on the collision energy and typical outgoing proton transverse momenta. As was done in the original KMR calculations [99–101, 342, 343], the bare production cross section is usually multiplied by a gap survival factor which we take the same as for the Higgs boson and $b\bar{b}$ production to be $S_g = 0.03$ at the LHC energy (see e.g. Ref. [345]). This issue will be discussed shortly when presenting results. Absorption effects for exclusive Higgs boson production are discussed e.g. in Refs. [371, 372].

In actual calculations below, the outgoing $W^\pm$ bosons are assumed to be on-mass-shell, whereas particular contributions to the observables can then be estimated in the narrow-width

approximation. For example, in the leptonic channel we have the following observable cross section

$$\sigma_{l^+\nu l^-\nu} \simeq \sigma_{WW} \times \mathrm{BR}(W^+ \to l^+\nu)\,\mathrm{BR}(W^- \to l^-\nu)\,, \tag{5.13}$$

where $\mathrm{BR}(W^+ \to l^+\nu) = (10.80 \pm 0.09) \times 10^{-2}$ [96] for a given lepton flavor. Both electrons and muons can be used in practice [356, 357].

5.1.1 Hard subprocess matrix elements

$gg \to W^+W^-$

The typical contributions for the $gg \to W^+W^-(\lambda_1\lambda_2 \to \lambda_3\lambda_4)$ subprocess are shown in Fig. 5.2. The total number of topologically different loop diagrams amounts to two triangles, and six boxes. In the central exclusive W^+W^- production, triangle diagrams through the intermediate s-channel γ and Z bosons are suppressed due to the $J_z = \lambda_1 - \lambda_2 = 0$ and parity selection rule for the singlet gluon-gluon to (virtual) photon transition strictly valid in the on-shell limit of fusing gluons and the Landau-Yang theorem for the intermediate Z boson. Then the only non-zeroth contribution comes from the Higgs boson resonant diagram. However, this can only lead to a sizeable enhancement of the cross section close to its threshold $m_{h^0} \simeq M_{WW} \gtrsim 2m_W$ [363]. The Standard Model Higgs bosons with such large masses have been recently excluded by the Tevatron [373] and LHC [374, 375] measurements. For the values of Higgs mass $m_{h^0} \approx 125$ GeV, corresponding contribution to the W^+W^- channel is far from the Higgs boson resonance and turned out to be suppressed compared to box contributions at low invariant masses. However, due to interference effects at rather large invariant masses M_{WW} the resonant (triangles) contribution could become comparable to the non-resonant (boxes) one. Below, for comparison we have calculated box and triangle (through the s-channel SM Higgs boson exchange) contributions in different phase space regions [2] which could be interesting for future measurements with forward detectors at ATLAS or CMS.

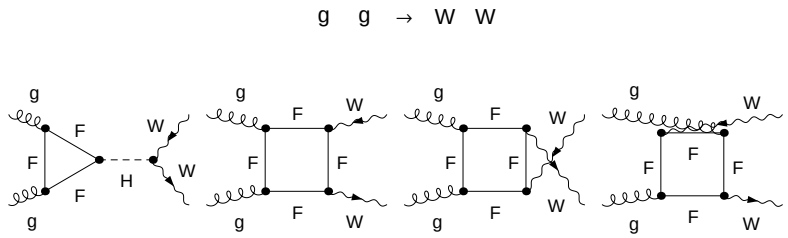

Figure 5.2: Representative diagrams of the hard subprocess $gg \to W^\pm W^\mp$, which contribute to the exclusive WW pair production.

The matrix element for the $gg \to h^0 \to W^+W^-$ transition with the intermediate s-channel Higgs boson exchange (see first diagram in Fig. 5.2) can be written in the narrow-width approximation as

$$V_{gg\to h^0\to W^+W^-}(q_1, q_2, p_3, p_4) = \delta^{(4)}(q_1 + q_2 - p_3 - p_4) \times$$
$$V_{gg\to h^0}(q_1, q_2, p_{h^0})\,\frac{i}{M^2_{WW} - m^2_{h^0} + iM_{WW}\Gamma^h_{\mathrm{tot}}}\,V_{h^0\to W^+W^-}(p_3, p_4, \lambda_3, \lambda_4)\,, \tag{5.14}$$

where the Higgs boson momentum is $p_{h^0} = q_1 + q_2$, and the δ-function reflects the momentum conservation in the process. In order to get a correct resonant invariant mass distribution, the standard Breit-Wigner Higgs propagator with the total Higgs decay width Γ^h_{tot}, which can be found e.g. in Ref. [378], is used.

[2] Close to the WW-threshold instability of W bosons [376, 377] should be included.

In Eq. (5.14), first the $gg \to h^0$ amplitude of the Higgs boson production through the top-quark triangle in the k_t-factorisation approach can be written as (see e.g. Refs. [379])

$$V_{gg\to h^0} \simeq \frac{i\delta^{ab}}{v}\,\frac{\alpha_s(\mu_F^2)}{\pi}\,(\boldsymbol{q}_{1\perp}\cdot\boldsymbol{q}_{2\perp})\,\frac{2}{3}\left(1+\frac{7}{120}\,\frac{M_{WW}^2}{m_{\rm top}^2}\right), \qquad v=\left(G_F\sqrt{2}\right)^{-1/2}. \tag{5.15}$$

The second tree-level $h^0 \to W^+W^-$ "decay" amplitude reads:

$$V_{h^0\to W^+W^-} \simeq i m_W\,\frac{e}{\sin\theta_W}\,\varepsilon^*(p_3,\lambda_3)\varepsilon^*(p_4,\lambda_4)\,, \tag{5.16}$$

where the polarisation vectors in the direction of motion of W^+ and W^- bosons in the proton-proton center-of-mass frame are used in practical calculations.

Potentially interesting contribution could come from the Higgs resonance if the Higgs mass was close to the WW production threshold. Similar resonance effects have been considered recently in inclusive [380] and exclusive associated [352] charged Higgs boson production, and large contributions beyond the Standard Model were found. However, the SM Higgs mass $\sim$ 160 GeV has been recently excluded in the inclusive searches by the CDF Collaboration at Tevatron [373] and by the ATLAS and CMS Collaborations at LHC [374, 375], so yet realistic SM Higgs boson mass $m_{h^0} \approx 125$ GeV leads to a suppressed triangles contribution to exclusive W^+W^- pair production. In the calculation presented here we take $m_{h^0} = 125$ GeV. Since the Higgs mass is certainly much smaller than the threshold value a precise value of the Higgs boson mass is not very important. A contribution from an extended Higgs sector beyond the Standard Model [380] could be interesting, but we postpone this issue for a later study.

We are primarily interested in estimation of dominant box contributions as well as in possible box-triangle interference effects within the Standard Model as potentially important irreducible background for the $\gamma\gamma \to W^+W^-$ signal relevant for a precision study of anomalous couplings. Thus, our numerical estimates provide minimal limit for the central exclusive WW production signal.

The box contributions to the $gg \to W^+W^-$ (or $gg \to ZZ$) parton level amplitude (see diagrams in Fig. 5.2) for on-shell fusing gluons were calculated analytically by using the Mathematica-based `FormCalc` (FC) [381–383] package. The complete matrix element was generated automatically by the FC tools in terms of one-loop Passarino-Veltman two-, three- and four-point functions [384] and other internally-defined functions (e.g. gluon and vector bosons polarisation vectors) and kinematical variables. In the next step, the Fortran code for the matrix element was generated, and then used as an external subroutine in our numerical calculations together with other FC routines setting up the Standard Model parameters, coupling constants and kinematics. Instead of built-in FC polarisation vectors we have used transverse gluon polarisation vectors which enter the projection in Eq. (5.10), and the standard $W^\pm$ polarisation vectors defined in Eq. (4.57), giving us an access to individual polarisation states of the W bosons. In accordance with the k_t-factorisation technique, the gauge invariance of the resulting amplitudes for the on-mass-shell initial gluons is ensured by a projection onto the gluon transverse polarisation vectors proportional to the transverse gluon momenta $q_{1,2\perp}$ according to Eq. (5.10).

For the evaluation of the scalar master tree- and four-point integrals in the gluon-gluon fusion subprocess we have used the `LoopTools` library [381–383]. The result is summed up over all possible quark flavors in loops and over distinct loop topologies. We have also checked that the sum of relevant diagrams is explicitly finite and obeys correct asymptotical properties and energy dependence. It is worth to mention that a large cancelation between separate box contributions in the total sum of diagrams takes place, which is expected from the general Standard Model symmetry principles.

As soon as the hard subprocess matrix element (5.10) has been defined as a function of relevant kinematical variables (four-momenta of incoming/outgoing particles), the loop integration over $q_{0\perp}$ in Eq. (5.9) was performed to obtain the diffractive amplitude, which then has been

used to calculate the differential distributions for (un)polarised W bosons in an external phase space integrator.

As we will demonstrate below, in the Standard Model the total box contribution is somewhat larger than the triangle one. We, however, keep both the triangle and box contributions and investigate a possible interference between them, which, in fact, is quite important, especially at rather large W^+W^--pair invariant masses, i.e. in the region we are interested in.

$gg \to \gamma\gamma$

Typical contributions to the leading order $gg \to \gamma\gamma$ subprocess are shown in Fig. 5.3. The total number of topologically different loop diagrams in the Standard Model amounts to twelve boxes. So the $\gamma\gamma$ does not exhibit resonant features, and can potentially serve as a probe for New Physics resonant contributions like the technipion signal under consideration in Section 5.5. The box contributions to the $gg \to \gamma\gamma$ parton level amplitude for on-shell fusing gluons were calculated analytically by using the Mathematica-based `FormCalc` (FC) [381–383] package.

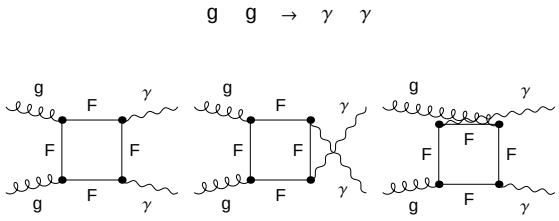

Figure 5.3: Representative quark loop diagrams of the hard subprocess $gg \to \gamma\gamma$, which contribute to the exclusive $\gamma\gamma$ pair production.

5.1.2 Gluon k_t-dependent densities in the forward limit

In the k_t-factorisation approach the density of gluons in the proton is described in terms of the off-diagonal unintegrated gluon distribution functions (UGDFs)

$$\begin{aligned} f_g^{\rm off}(q_0, q_{1,2}; t_{1,2}) &= f_g^{\rm off}(x', x_{1,2}, \boldsymbol{q}_{0\perp}^2, \boldsymbol{q}_{1/2\perp}^2, \mu_F^2; t_{1,2}) \\ &= f_g^{\rm off}(x', x_{1,2}, \boldsymbol{q}_{0\perp}^2, \boldsymbol{q}_{1/2\perp}^2, \mu_F^2) \exp(bt_{1,2}/2)\,, \end{aligned} \tag{5.17}$$

at the factorization scale $\mu_F \gg |\boldsymbol{q}_{0\perp}|$ and the diffractive slope is taken to be $b = 4$ GeV^{-2}. In the forward scattering (see Eq. (5.5)) and asymmetric limit of $x' \ll x_{1,2}$, the off-diagonal UGDF (5.18) is written as a skewedness factor $R_g(x')$ multiplied by the diagonal UGDF, which describes the coupling of gluons with longitudinal momentum fractions $x_{1,2}$ to the proton (see Refs. [190, 385] for details).

The skewedness parameter R_g is expected to be roughly constant at the LHC energies and gives only a small contribution to the overall normalization uncertainty. We take $R_g = 1.3$ in practical calculations. In the kinematics considered here ($x' << x_{1,2}$) the off-diagonal UGDFs can be written in terms of the conventional (integrated) gluon densities $xg(x, \boldsymbol{q}_\perp^2)$, see Fig. 5.4, as [190]

$$\begin{aligned} f_g^{\rm off}(x', x_{1,2}, \boldsymbol{q}_{0\perp}^2, \boldsymbol{q}_{1/2\perp}^2, \mu_F^2) &\simeq R_g(x') f_g(x_{1,2}, \boldsymbol{q}_\perp^2, \mu_F^2) = \\ & R_g(x') \frac{\partial}{\partial \ln \boldsymbol{q}_\perp^2} \left(x_{1,2}\, g(x_{1,2}, \boldsymbol{q}_\perp^2) \sqrt{T_g(\boldsymbol{q}_\perp^2, \mu_F^2)} \right), \end{aligned} \tag{5.18}$$

where T_g is the Sudakov form factor. The Sudakov factor $T_g(\boldsymbol{q}_\perp^2, \mu_F^2)$ is the survival probability that an active gluon with transverse momentum $q_\perp$ does not emit any partons in the evolution

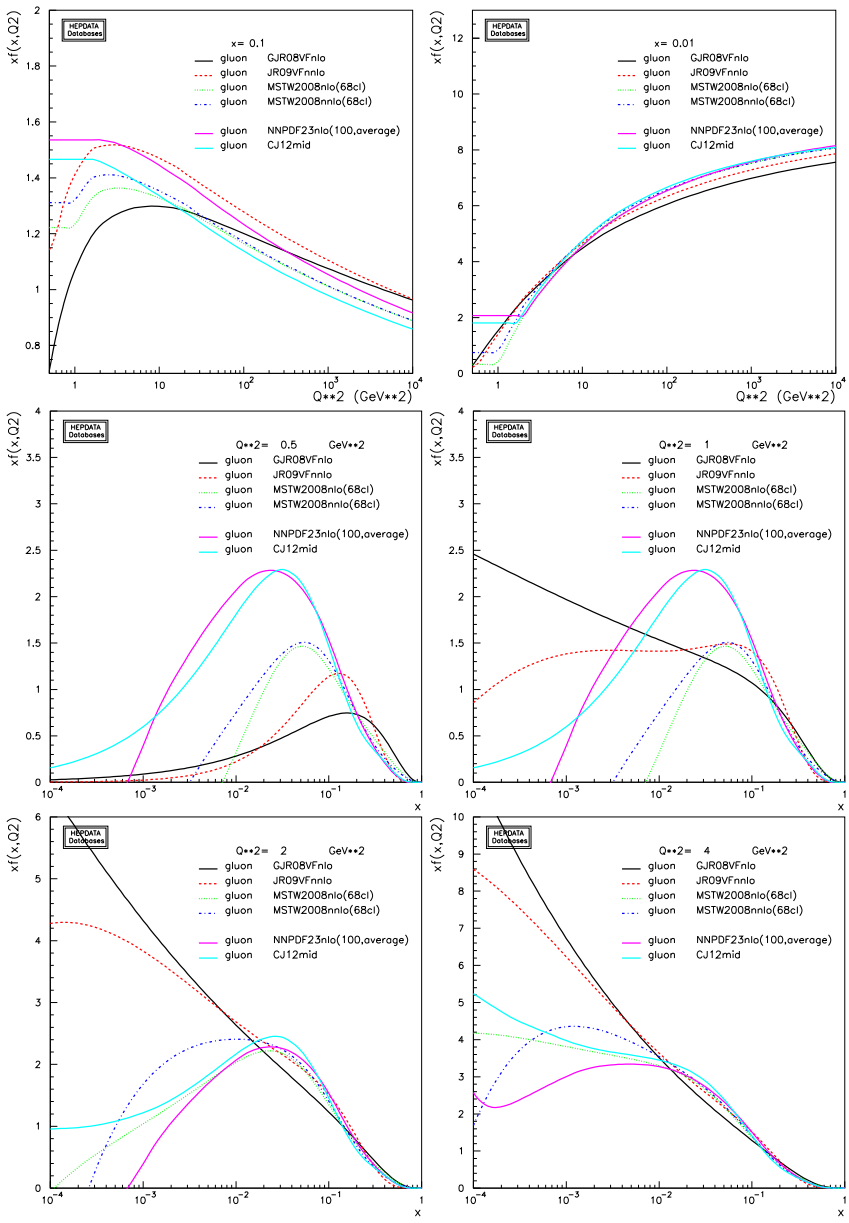

Figure 5.4: Gluon densities of $xf(x,Q^2)$ as a function of Q^2 at the longitudinal momentum fraction $x = 0.1$ and 0.01 (top panels) and as a function of x (bottom panels) for fixed values of the scales $Q^2 = 0.5, 1, 2$ and 4 GeV^2 given by the global parametrisations sets: GJR [191, 192], MSTW [386], NNPDF [387], and CTEQ [388, 389]. Access to the parton distribution code, on-line calculation with graphical display of the distributions is possible also at the Durham HepData Project [390].

up to the hard scale μ_F so that the rapidity gaps are not populated by gluons. It is given by [190]

$$T_g(\boldsymbol{q}_\perp^2, \mu_F^2) \;=\; \exp\left(-\int_{\boldsymbol{q}_\perp^2}^{\mu_F^2} \frac{d\boldsymbol{k}_\perp^2}{\boldsymbol{k}_\perp^2} \frac{\alpha_s(\boldsymbol{k}_\perp^2)}{2\pi} \int_0^{1-\Delta} \left[zP_{gg}(z) + \sum_q P_{qg}(z) \right] dz \right), \tag{5.19}$$

with Δ in the upper limit is taken to be [391]

$$\Delta = \frac{|\boldsymbol{k}_\perp|}{|\boldsymbol{k}_\perp| + \mu_F}. \tag{5.20}$$

Due to the presence of the Sudakov form factor in the KMR prescription only last gluon emission generates transverse momentum of incoming gluons. In our calculations we take $\mu_F^2 = M_{VV}^2$. The choice of the scale introduces uncertainties roughly of about factor two. Since in the present calculations we need values of $T_g(\boldsymbol{q}_\perp^2, \mu_F^2)$ for extremely large scales μ_F^2 the integration in Eq. (5.19) is

performed rather in $\log_{10}(k^2/k_0^2)$, where $k_0 = 1\,\text{GeV}$ was introduced for convenience; see Fig. 5.5.

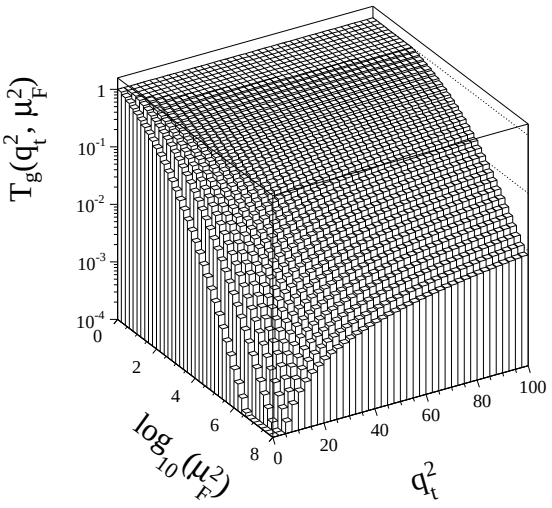

Figure 5.5: The two-dimensional map of the Sudakov form factor $T_g(\boldsymbol{q}_\perp^2, \mu_F^2)$.

5.1.3 Four-body phase space in the forward limit

The diffractive diboson CEP amplitude (5.9) described above is used now to calculate the corresponding cross section including realistic limitations on the phase space. The cross section can be obtained by integration over the four-body phase space given by

$$\sigma = \frac{(2\pi)^4}{2s} \int \overline{|\mathcal{M}|^2} \delta^4(p_a + p_b - p_1 - p_2 - k_3 - k_4) \frac{d^3p_1}{(2\pi)^3 2E_1} \frac{d^3p_2}{(2\pi)^3 2E_2} \frac{d^3k_3}{(2\pi)^3 2E_3} \frac{d^3k_4}{(2\pi)^3 2E_4}, \quad (5.21)$$

where $E_{1,2}$ and $E_{3,4}$ are the energies of the final-state protons and bosons, respectively, $\overline{|\mathcal{M}|^2} = \sum_{\lambda_3,\lambda_4} \mathcal{M}_{\lambda_3\lambda_4} \mathcal{M}^*_{\lambda_3\lambda_4}$ assuming, as usual, that the helicities of both protons are unchanged in the considered process. In order to calculate the total cross section one has to take the eight-dimensional integral numerically, see Eq. (A.35) in Appendix A.2. However, the evaluation of the corresponding hard subprocess amplitude $V_{\lambda_3\lambda_4}$, its subsequent convolution with the UGDFs in the diffractive amplitude (5.9) and the full phase space integration (5.21) is extremely time consuming. Clearly the calculation of diffractive mechanism must be simplified to be feasible. Such a simplification seems possible for the diffractive process considered here. We start from the choice of integration variables as in Ref. [3]. Then

$$d\sigma = \frac{1}{2s} \overline{|\mathcal{M}|^2} \frac{1}{2^4} \frac{1}{(2\pi)^8} \frac{1}{E_1 E_2} \frac{1}{4} dt_1 dt_2 d\phi_1 d\phi_2 \frac{p_{m\perp}}{4} \mathcal{J}^{-1} dy_3 dy_4 dp_{m\perp} d\phi_m \,, \quad (5.22)$$

where $p_{m\perp} = |\boldsymbol{k}_{3\perp} - \boldsymbol{k}_{4\perp}|$ is the difference between transverse momenta of V_3 and V_4, $\boldsymbol{k}_{3\perp}$ and $\boldsymbol{k}_{4\perp}$, respectively, and ϕ_m is the corresponding azimuthal angle. For the sake of simplicity, assuming an exponential slope of $t_{1,2}$-dependence of the UGDFs (see Eq. (5.18)), and as a consequence of the approximately exponential dependence of the cross section on t_1 and t_2 (proportional to $\exp(bt_1)$ and $\exp(bt_2)$), the four-body phase space can be calculated as

$$d\sigma \approx \frac{1}{2s} \overline{|\mathcal{M}|^2}\Big|_{t_{1,2}=0} \frac{1}{2^4} \frac{1}{(2\pi)^8} \frac{1}{E_1 E_2} \frac{1}{4} \frac{1}{b^2} (2\pi)^2 \frac{p_{m\perp}}{4} \mathcal{J}^{-1} dy_3 dy_4 dp_{m\perp} d\phi_m. \quad (5.23)$$

Since in this approximation we have assumed no correlations between outgoing protons (which is expected here and is practically true for the production of $b\bar{b}$ [211,344] or gg [345] dijets) there is

no dependence of the integrand in Eq. (5.23) on ϕ_m, which means that the phase space integration can be further reduced to three-dimensional one. The Jacobian $\mathcal{J}$ in Eq. (5.22) reads:

$$\mathcal{J} = \left| \frac{p_{1z}}{\sqrt{m_p^2 + p_{1z}^2}} - \frac{p_{2z}}{\sqrt{m_p^2 + p_{2z}^2}} \right| . \tag{5.24}$$

In actual calculations below we shall use the reduced form of the four-body phase space (5.23), and it is checked to give correct numerical results against the full phase space calculation for some simple reactions. Different representations of the phase space depending on a particular kinematical distributions needed can be found in Ref. [3].

5.2 Exclusive QED mechanism

We focus on the exclusive QED mechanism for the diboson production via off-shell photon-photon fusion. The $\gamma\gamma \to W^+W^-$ mechanism have already been discussed in the literature (see Refs. [356–359]). The relevant subprocess lowest-order diagrams are shown in Fig. 5.6.

In the Weizsäcker-Williams approximation the total cross section for the $pp \to pp(\gamma\gamma \to V_3V_4)$ can be written as in the parton model

$$\sigma = \int dx_1 dx_2 \, f_1^\gamma(x_1) \, f_2^\gamma(x_2) \, \hat{\sigma}_{\gamma\gamma\to VV}(\hat{s}) \, . \tag{5.25}$$

We take the Weizsäcker-Williams equivalent photon fluxes of protons from Ref. [273].

To calculate differential distributions the following parton-like formula can be conveniently used

$$\frac{d\sigma}{dy_3 dy_4 d^2p_{\perp,V}} = \frac{1}{16\pi^2 \hat{s}^2} \, x_1 f_1^\gamma(x_1) \, x_2 f_2^\gamma(x_2) \, \overline{|\mathcal{M}_{\gamma\gamma\to VV}(\hat{s},\hat{t},\hat{u})|^2} \, , \tag{5.26}$$

where the longitudinal momentum fractions of the fusing photons $x_{1,2}$ are defined as in Eq. (5.8).

In the same way as for QCD diffractive mechanism described above, the loop-induced helicity matrix elements for $\gamma\gamma \to VV$ subprocesses were calculated by using the `LoopTools` libraries [381–383].

$\gamma\gamma \to W^+W^-$

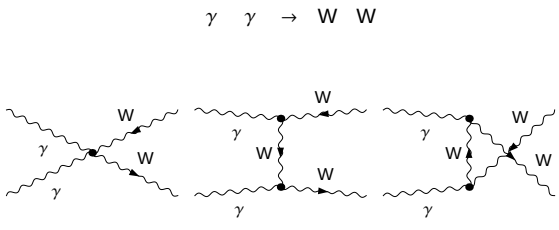

Figure 5.6: The Born diagrams for the $\gamma\gamma \to W^\pm W^\mp$ subprocess.

Several features of $\gamma\gamma \to W^+W^-$ have already been discussed in the literature. Most of the existing works concentrated on three-level predictions, in particular on the influence of anomalous gauge-couplings, e.g. [361, 362, 392]. The triple $WW\gamma$ and the quartic $WW\gamma\gamma$ couplings, which contribute to the $\gamma\gamma \to W^+W^-$ process in the leading order read

$$\mathcal{L}_{WW\gamma} = -ie(A_\mu W_\nu^- \overset{\leftrightarrow}{\partial_\mu} W^{+\nu} + W_\mu^- W_\nu^+ \overset{\leftrightarrow}{\partial_\mu} A^\nu + W_\mu^+ A_\nu \overset{\leftrightarrow}{\partial_\mu} W^{-\nu}) \, , \tag{5.27}$$

$$\mathcal{L}_{WW\gamma\gamma} = -e^2(W_\mu^- W^{+\mu} A_\nu A^\nu - W_\mu^- A^\mu W_\nu^+ A^\nu) \, , \tag{5.28}$$

where the asymmetric derivative has the form $X \overset{\leftrightarrow}{\partial_\mu} Y = X\partial^\mu Y - Y\partial^\mu X$.

Then within the Standard Model, the elementary tree-level cross section for the $\gamma\gamma \to W^+W^-$ subprocess can be written in the compact form in terms of the Mandelstam variables (see e.g. Ref. [370]) [3]

$$\frac{d\hat{\sigma}}{d\Omega} = \frac{3\alpha^2\beta}{2\hat{s}}\left(1 - \frac{2\hat{s}(2\hat{s}+3m_W^2)}{3(m_W^2-\hat{t})(m_W^2-\hat{u})} + \frac{2\hat{s}^2(\hat{s}^2+3m_W^4)}{3(m_W^2-\hat{t})^2(m_W^2-\hat{u})^2}\right), \tag{5.29}$$

where $\beta = \sqrt{1-4m_W^2/\hat{s}}$ is the velocity of the W bosons in their center-of-mass frame and the electromagnetic fine-structure constant $\alpha = e^2/(4\pi) \simeq 1/137.036$ for the on-shell photon. The total elementary cross section can be obtained by integration of the differential cross section above.

In Fig. 5.7 we show distribution in $\xi_1 = \log_{10}(x_1)$ and $\xi_2 = \log_{10}(x_2)$ at $\sqrt{s}$ = 14 TeV. We observe a maximum of the cross section at $\xi_1, \xi_2 \approx -2$ which means that corresponding longitudinal momentum fractions carried by photons are typically 10^{-2}.

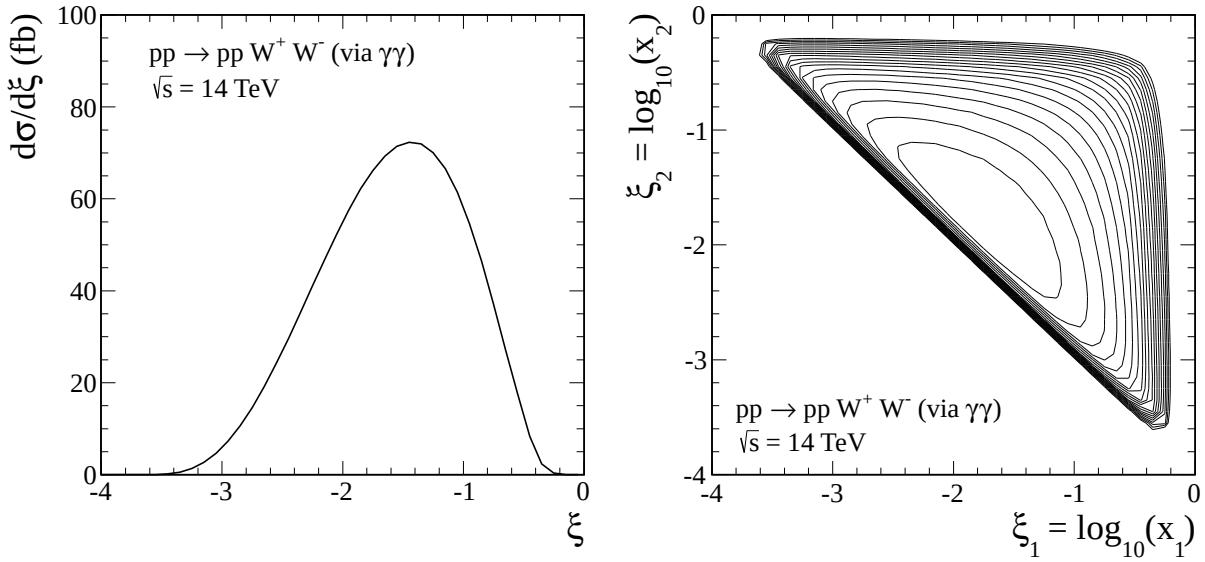

Figure 5.7: Summary of the $\gamma\gamma \to W^+W^-$ contribution. Here, $\xi_{1,2} = \log_{10}(x_{1,2})$, where $x_{1,2}$ are photon longitudinal fractions with respect to parent protons. The lines were calculated within Weizsäcker-Williams approximation (EPA) as described in the text with photon fluxes obtained in Ref. [273].

$\gamma\gamma \to \gamma\gamma$

The light-by-light scattering subprocess to the leading order was discussed earlier in the literature (see e.g. [393–397]). The relevant subprocess diagrams shown in Fig. 5.8 are similar in topology to those for $gg \to \gamma\gamma$ shown in Fig. 5.3 but contain extra contributions from leptonic and W bosons loops. The box contributions to the $\gamma\gamma \to \gamma\gamma$ subprocess for on-shell fusing photons were calculated analytically by using the Mathematica-based `FormCalc` (FC) [381–383] package. In Ref. [396] the authors considered both the QCD and QED corrections (the two-loop

[3] This formula does not include the process with virtual Higgs boson $\gamma\gamma \to H \to W^+W^-$. For heavy Higgs boson, this would lead to clear Higgs boson signal modifying the cross section (typical resonance plus background effect) [370], however, with the present Higgs boson mass [374, 375] only deeply off-shell Higgs boson contribution could be possible. Also, the diagram with an intermediate Higgs boson is, of course, of a higher order compared to the contributions considered here. This automatically means rather small effect on the measured cross section, in particular, on the W^+W^- invariant mass distribution in our case of the four-body $pp \to pW^+W^-p$ reaction. A potentially interesting Higgsless scenario of the WW-pair production has previously been discussed e.g. in Refs. [356–359].

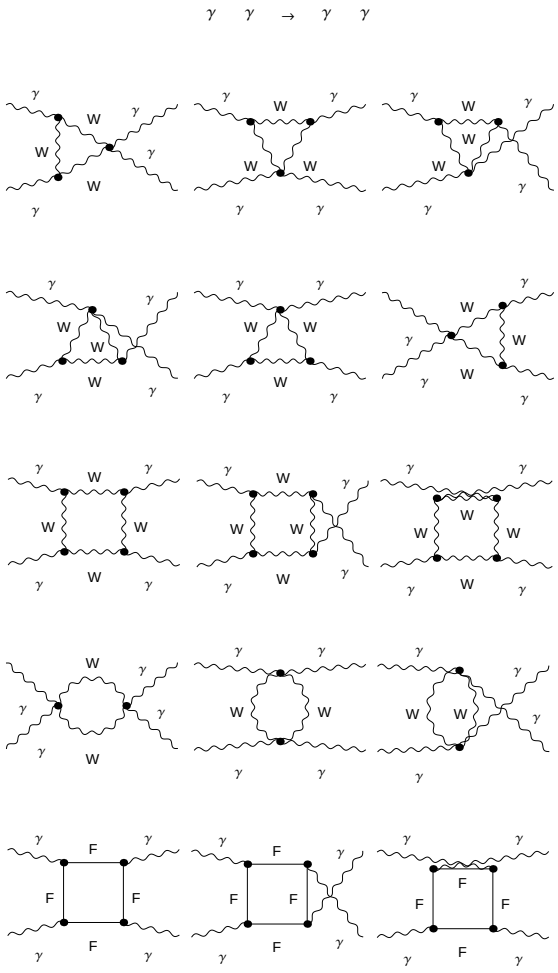

Figure 5.8: The Born diagrams for the $\gamma\gamma \to \gamma\gamma$ subprocess.

Feynman diagrams) to the one-loop fermionic contributions only in the $\gamma\gamma \to \gamma\gamma$ scattering. The corrections are quite small numerically, showing that the leading order computations considered by us are satisfactory.

5.3 Inclusive QCD mechanism

For a test and for a comparison we also consider a gluon-gluon contribution to the inclusive cross section. We are not interested in the quark-antiquark component which is well known and can be easily calculated [4].

In the lowest order of QCD the inclusive total cross section for the gluon-gluon fusion can be written as

$$\sigma^{gg}_{pp\to VVX} = \int dx_1 dx_2\, g(x_1,\mu_F^2)\, g(x_2,\mu_F^2)\, \hat{\sigma}_{gg\to VV}(\hat{s})\,. \tag{5.30}$$

and the differential cross section can be obtained as

$$\frac{d\sigma^{gg}}{dy_3 dy_4 d^2p_{V\perp}} = \frac{1}{16\pi^2\hat{s}^2} x_1 g(x_1,\mu_F^2) x_2 g(x_2,\mu_F^2) \overline{|\mathcal{M}_{gg\to VV}(\lambda_1,\lambda_2,\lambda_3,\lambda_4)|^2}\,. \tag{5.31}$$

The corresponding matrix elements have been discussed in the literature in detail [365, 366]. The distributions in rapidity of V_3 (y_3), rapidity of V_4 (y_4) and transverse momentum of one of them

[4] In the case of W^+W^- inclusive production we also omit $pp \to t\bar{t}X \to W^+W^-b\bar{b}X$ process very important at high energies.

$p_{V\perp}$ can be calculated in a straightforward way from Eq. (5.31). The distribution in invariant mass can be then obtained by an appropriate binning. Our inclusive $d\sigma/dM_{VV}$ distribution seems consistent with similar distributions presented in the past in the literature.

As discussed before, in the case of exclusive scattering the $J_z = \lambda_1 - \lambda_2 = 0$ contribution is the dominant one, where J_z is the total angular momentum along the z-axis. In the case of inclusive process the situation is slightly different. In Fig.5.9 we present the $J_z = 0$ and $|J_z| = 2$ components to angular distributions. The $J_z = 0$ contribution is generally larger than the $|J_z| = 2$ one. As in the exclusive case, at forward/backward scattering ($cos\,\theta = \pm 1$) we observe the dominance of the $J_z = 0$ contribution. At $\sqrt{\hat{s}} = 500$ GeV it happens very close to cos $\theta \approx \pm 1$.

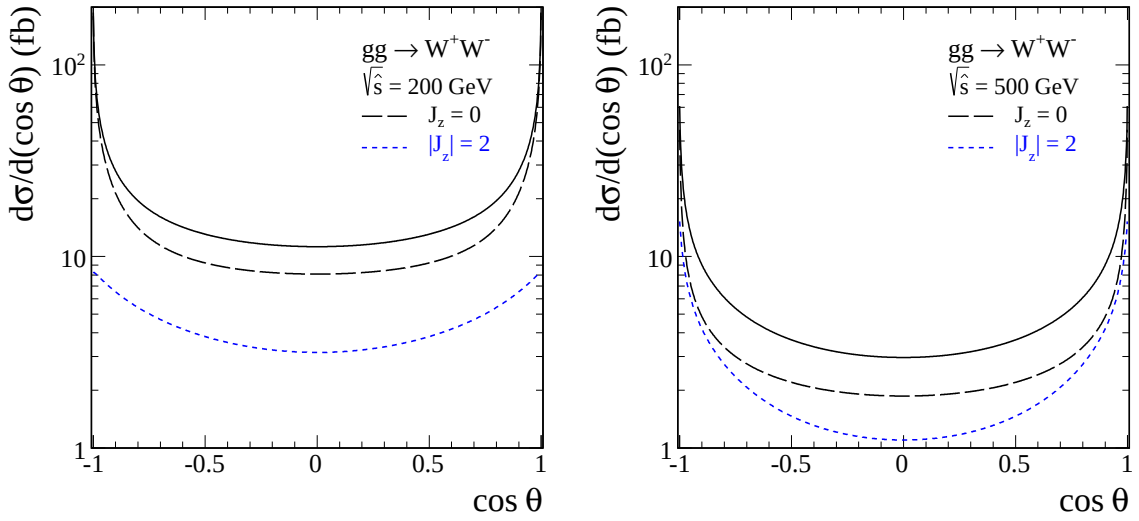

Figure 5.9: Centre-of-mass scattering angle dependence of the hard subprocess $gg \to W^+W^-(\lambda_1\lambda_2 \to \lambda_3\lambda_4)$ cross section averaged over incoming gluon polarizations at $\sqrt{\hat{s}} = 200$ GeV (left panel) and 500 GeV (right panel). The solid line represents the coherent sum of all contributions. The $J_z = \lambda_1 - \lambda_2 = 0$ (dashed line) and the $|J_z| = |\lambda_1 - \lambda_2| = 2$ (dotted line) contributions are shown separately.

For completeness in Fig.5.10 we show corresponding contributions to the rapidity distribution of one of W's in the $pp \to W^+W^-X$ process. Here the $J_z = 0$ contribution is larger in the whole range of rapidities.

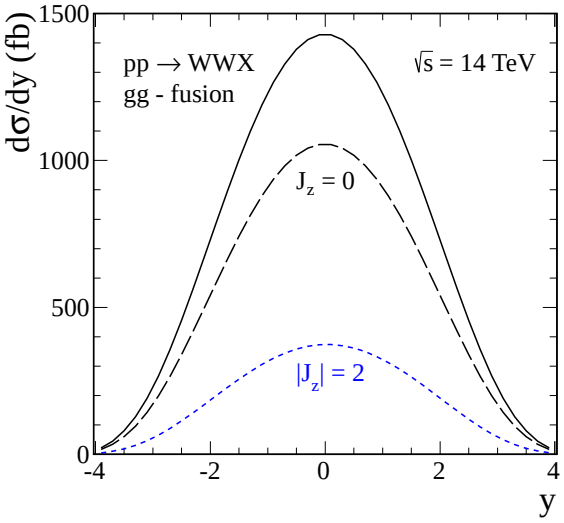

Figure 5.10: The $J_z = 0$ (dashed line) and $|J_z| = 2$ (dotted line) contributions to the inclusive $pp \to W^+W^-X$ rapidity distribution.

5.4 Results

5.4.1 $gg \to VV$ and $\gamma\gamma \to VV$ processes

Before we go to the presentation of our results for the $pp \to ppVV$ reaction let us concentrate for a while at the elementary bosonic processes (presented in Figs. 5.12 and 5.13)

$$V_1(k_1, \lambda_1) + V_2(k_2, \lambda_2) \to V_3(k_3, \lambda_3) + V_4(k_4, \lambda_4)\,, \tag{5.32}$$

where the helicities of the incoming photons or gluons are $\lambda_{1,2} = \pm 1$ and for the outgoing bosons are $\lambda_{3,4} = \pm 1$ (for photons) or $\lambda_{3,4} = 0, \pm 1$ (for Z and W pairs).

In Fig. 5.11 we present the total cross sections of the photon-photon and gluon-gluon scattering as well as separate contributions coming from charged fermion loops and W-boson loops. In the $gg \to \gamma\gamma$ case only quarks propagate in the box diagrams (see Fig. 5.3) and the amplitude is dominated by the light quarks. For the light-by-light scattering all the charged fermions (quarks, leptons) and W-bosons participate in the corresponding loop diagrams (see Fig. 5.8). As expected, below the W-boson threshold the fermion loop contribution is dominating, while boson loop dominates at the photon-photon collision energies $\sqrt{s} > 200$ GeV. For completeness, in the bottom panels we consider two cases for different helicities of the incoming photons and we show results with the restriction of the photon scattering angle $|cos(\theta)| < cos(30^o)$.

In Fig. 5.12(left panel) we present the total cross section for the $gg \to W^+W^-$ reaction as well as for box and triangle contributions separately. In this calculation we have assumed $m_{h^0} = 125$ GeV [398, 399]. We also show a vertical line at the $t\bar{t}$ threshold. The figure demonstrates a cancellation pattern between box and triangle contributions. We will discuss similar cancellation for the $pp \to ppW^+W^-$ reaction. In the right panel we show the cross section for the $gg \to W^+W^-, ZZ, \gamma\gamma$ reactions (the black, violet, blue lines, respectively) with cut on boson scattering angle $|cos(\theta)| < cos(30^o)$.

Fig. 5.13 shows comparison of the integrated elementary cross section for the considered reactions. We wish to notice that at high c.m. energies

$$\hat{\sigma}_{gg\to W^+W^-} \ll \hat{\sigma}_{\gamma\gamma\to W^+W^-} \xrightarrow{\sqrt{\hat{s}}\to\infty} \approx 10^2 \text{ pb}\,.$$

In principle, effects beyond the Standard Model possibly responsible for anomalous gauge-boson couplings could be important, see e.g. [361, 362]. This shows a potential role of photon-photon induced processes in proton-proton collisions at the LHC. The exception is the inclusive production of W^+W^- pairs in Ref. [400], where many new subleading processes have been considered.

We would like to mention some features of the differential production cross section in Figs. 5.14, 5.15 5.16, and 5.17. The labels $+$, $-$ represent right-handed and left-handed bosons, respectively. In Fig. 5.17 we consider the $\gamma\gamma \to W^+W^-$ reaction. Its angular dependence can be understood from the conservation of angular momentum in the $\gamma\gamma$ c.m. system (see e.g. [361]). Photons with opposite helicities lead to an initial state with z-component of angular momentum ± 2. Therefore one cannot produce W^- and W^+ bosons emitted along the z axis (in the forward and backward directions $\cos\theta = \pm 1$) with identical helicities, since this would be a state with z component of angular momentum zero. However, emission at an angle $0 < \theta < \pi$ is possible. Two photons with identical helicities can only produce W bosons with identical helicities. The lowest-order matrix element vanishes for the helicities $(\lambda_1, \lambda_2, \lambda_3, \lambda_4) = (\pm, \pm, \pm, \mp)$, $(\pm, \pm, \mp, \pm)$, $(\pm, \pm, 0, \pm)$, $(\pm, \pm, \pm, 0)$, $(\pm, \pm, 0, \mp)$, and $(\pm, \pm, \mp, 0)$. Furthermore, if the photons have identical helicities and the W bosons as well, the production of W bosons with helicity different to that of the photons is suppressed with rising energy. Moreover, it is apparent from Fig. 5.17 that the bulk of W bosons is transverse and is emitted at a small angle to the beam axis, i.e. $\cos\theta \approx \pm 1$. Bose symmetry implies that the amplitude M is invariant under the interchange

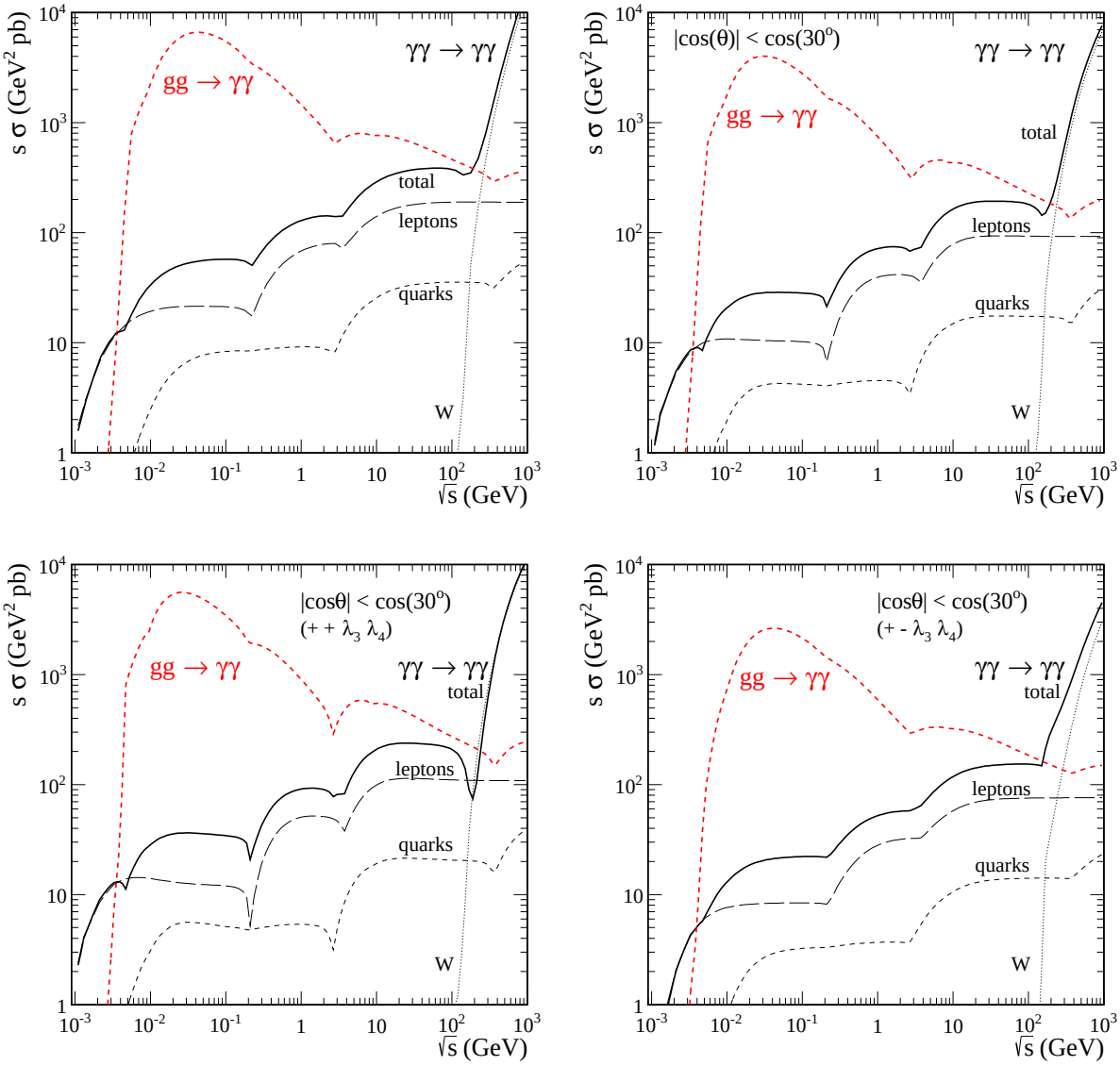

Figure 5.11: The integrated elementary cross section for the $gg \to \gamma\gamma$ (red lines) and $\gamma\gamma \to \gamma\gamma$ (black lines) reactions as a function of center-of-mass energy. We present the results without and with extra cut on photon scattering angle $|cos(\theta)| < cos(30^o)$. The cross section showing the fermion thresholds. For light-by-light scattering separate contributions coming from fermion and W-boson loop are shown. In the bottom panels the two choices of initial photon helicities $++$ (left panel) and $+-$ (right panel) are presented.

$(k_1, \varepsilon_1) \longleftrightarrow (k_2, \varepsilon_2)$. Besides Bose symmetry also CP is an exact symmetry and would be violated in the considered processes. The helicity amplitudes for fixed polarization configuration are related as follows:

$$\begin{aligned} M_{\lambda_1\lambda_2\lambda_3\lambda_4}(s,t,u) &= M_{\lambda_2\lambda_1\lambda_3\lambda_4}(s,u,t) \quad (Bose)\,, \\ M_{\lambda_1\lambda_2\lambda_3\lambda_4}(s,t,u) &= M_{-\lambda_1-\lambda_2-\lambda_4-\lambda_3}(s,u,t) \quad (CP)\,, \\ M_{\lambda_1\lambda_2\lambda_3\lambda_4}(s,t,u) &= M_{-\lambda_2-\lambda_1-\lambda_4-\lambda_3}(s,t,u) \quad (Bose + CP)\,. \end{aligned} \tag{5.33}$$

5.4.2 $pp \to pp\gamma\gamma$

Before we go to the presentation of results for the $pp \to ppW^+W^-$ reaction we wish to show similar results for the $p\bar{p} \to p\bar{p}\gamma\gamma$ reaction. The latter reaction was studied experimentally

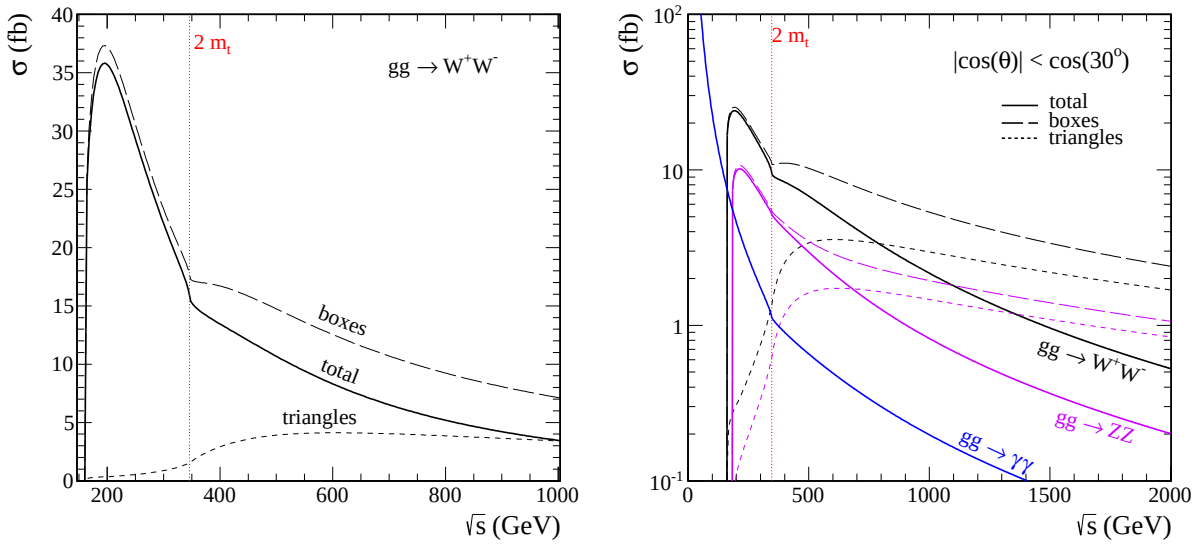

Figure 5.12: In the left panel we show the integrated elementary cross section for the $gg \to W^+W^-$ reaction. The solid line represents the coherent sum of all contributions. We show separate contributions of boxes (the dashed line) and triangles (dotted line). In the right panel we show the cross section for the $gg \to W^+W^-, ZZ, \gamma\gamma$ reactions (the black, violet, blue lines, respectively) with cut on boson scattering angle $|cos(\theta)| < cos(30^o)$.

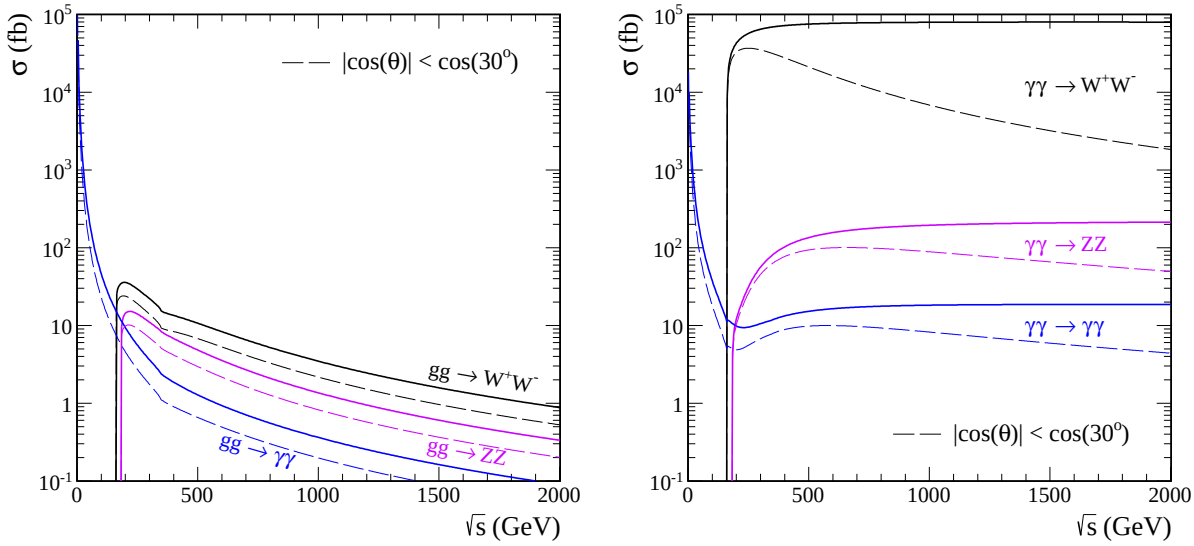

Figure 5.13: Comparison of the integrated elementary cross section for the $gg \to VV$ reactions (left panel) and the $\gamma\gamma \to VV$ reactions (right panel). The black, violet and blue lines correspond to the W^+W^-, ZZ and $\gamma\gamma$ processes, respectively. We present the results without (the solid lines) and with extra cut on boson scattering angle $|cos(\theta)| < cos(30^o)$ (the dashed lines).

in Ref. [355]. The CDF Collaboration has measured photons in the interval $|\eta(\gamma)| < 1$, $E_T > 2.5$ GeV and with the condition of no other particles detected in $-7.4 < \eta < 7.4$. They have obtained $\sigma_{\gamma\gamma}^{CDF} = 2.48$ pb with about quarter of relative uncertainty. We have used different choices of gluon PDFs at quite small values of gluon transverse momenta $q^2_{\perp,min} = 0.5$ GeV^2. We obtain $\sigma_{\gamma\gamma} = 2.99$ pb for the GJR NLO [191, 192], 2.46 pb for the MSTW08 NLO [386] and 2.1 pb for the CT12 NLO [388, 389]. Our results very well agree with the CDF experimental data [5]. In

[5]The $p\bar{p} \to p\bar{p}\gamma\gamma$ process was discussed recently in [175]. No differential distributions have been discussed there.

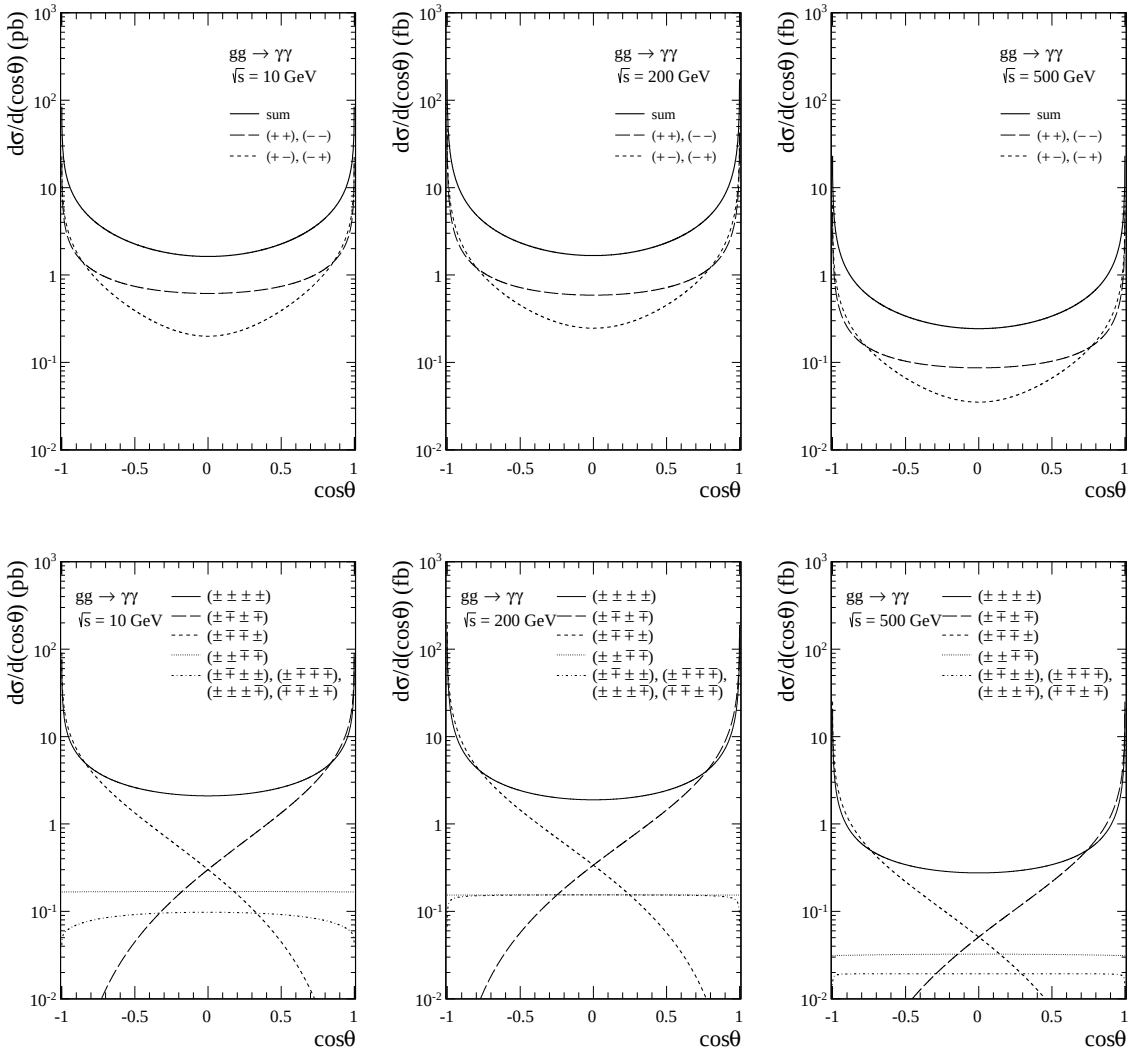

Figure 5.14: Differential cross section for the process $gg \to \gamma\gamma$ at gg c.m. energies $\sqrt{s} = 10$ GeV, 200 GeV and 500 GeV with unpolarised gluons for different helicities (λ_3, λ_4) of the photons (top panels) and for different helicities $(\lambda_1, \lambda_2, \lambda_3, \lambda_4)$ of the gluons and photons (bottom panels). For these curves where more than one helicity combination is indicated the curve corresponds to a single helicity combination, not the sum.

this calculation we have assumed averaged soft gap survival factor $S_g = 0.05$ and the scale of the Sudakov form factor was taken as $\mu^2 = M^2_{\gamma\gamma}$.

In Fig.5.18 (top panels) we show distribution of photon-photon invariant mass (left panel) and distribution in photon transverse momentum (right panel) with experimental CDF cuts. We show results for three different gluon distributions [191, 192, 386, 388, 389]. We obtain very good description of the CDF experimental data [355], both in shape and absolute normalization. In the bottom panels we show corresponding distribution in photon pseudorapidity, again for three different gluon distributions. In addition, we present decomposition into different pp center-of-mass photon helicity components. One can see the dominance of the $++ = --$ contributions over $+- = -+$ ones. Having shown that the results of the approach used here nicely describe the CDF experimental data [355] we can confidentially present our predictions for the $pp \to ppW^+W^-$ reaction.

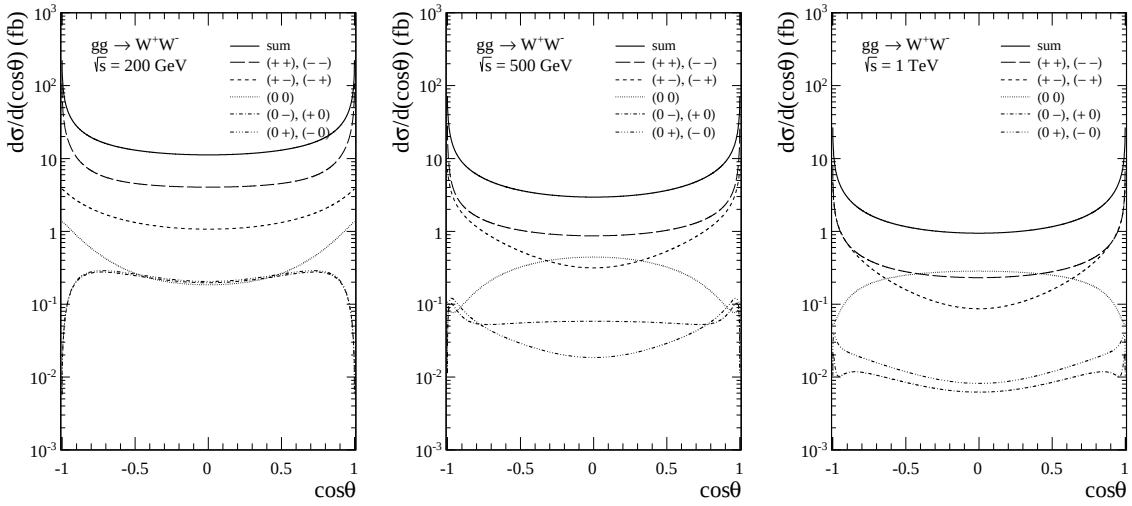

Figure 5.15: Differential cross section for the process $gg \to W^+W^-$ with unpolarised gluons at gg c.m. energies $\sqrt{s} = 200$ GeV, 500 GeV and 1 TeV for different helicities (λ_3, λ_4) of the W bosons. In this case, where more than one helicity combination is indicated, all the curve corresponds to a single helicity combination, not the sum.

5.4.3 $pp \to ppW^+W^-$

Let us present now our results for the central exclusive W^+W^- pair production at the nominal LHC energy $\sqrt{s} = 14$ TeV. In Fig. 5.19 (left panel) we compare rapidity distribution of W^+ (or W^-) for the electromagnetic $\gamma\gamma \to W^+W^-$ and diffractive $gg \to W^+W^-$ mechanisms. The two-photon induced contribution is almost three orders of magnitude larger than the diffractive contribution, in which all polarization components for W^+ and W^- have been included. For a reference, we show also inclusive cross section ($gg \to W^+W^-$ contribution only) which is roughly two more orders of magnitude bigger than the exclusive $\gamma\gamma \to W^+W^-$ contribution. We see, therefore, that the exclusive diffractive component is five orders of magnitude smaller for its inclusive counterpart. The diffractive contribution was calculated with the GJR NLO [191, 192] collinear gluon distribution to generate the off-diagonal UGDFs given by Eq. (5.18). This collinear PDF allows us to use quite small values of gluon transverse momenta ($q^2_{\perp,cut} = 0.5\,\mathrm{GeV}^2$).

A much smaller diffractive contribution compared to the two-photon one requires a special comment as it is rather exceptional. For example, it is completely opposite than for $pp \to ppH$ [211, 344], $pp \to ppM$ (e.g. light/heavy quarkonia production [6, 104, 106, 177, 210, 350]) or $pp \to pp Q\bar{Q}$ [211, 344, 401] CEP processes. The standard relative suppression, present also in the latter cases, is due to soft gap survival probability factor ($S_g \sim 0.03$ for diffractive contribution at the LHC energies versus $S_g \sim 1$ for two-photon contribution), and due to a suppression by the Sudakov form factor calculated at very large scales, here at $\mu_{hard} = M_{WW}$. The main difference compared to other cases is that in the diffractive case the leading contribution comes from loop diagrams (Fig. 5.2) while in the two-photon case already from tree-level diagrams (Fig. 5.6).

In Fig. 5.19 (right panel) we present, in addition, individual polarization components for the diffractive mechanism, along with the unpolarized cross section. The calculation of the helicity contributions is performed in the pp center-of-mass frame (in which all the experimental studies of the exclusive production processes are usually performed). As can be seen from the figure, where $\lambda_\pm$ are the helicities of $W^\pm$ bosons, the contribution of $(\lambda_+, \lambda_-) = (\pm 1, \mp 1)$ is bigger than other contributions and the contribution of $(\lambda_+, \lambda_-) = (\pm 1, \pm 1)$ concentrated mostly at midrapidities. Since the helicities are calculated in the proton-proton center-of-mass system there is no simple relation to the often used in a qualitative discussion $J_z = 0$ dominance rule. Discussion of the $J_z = 0$ rule would require complicated transformations between different

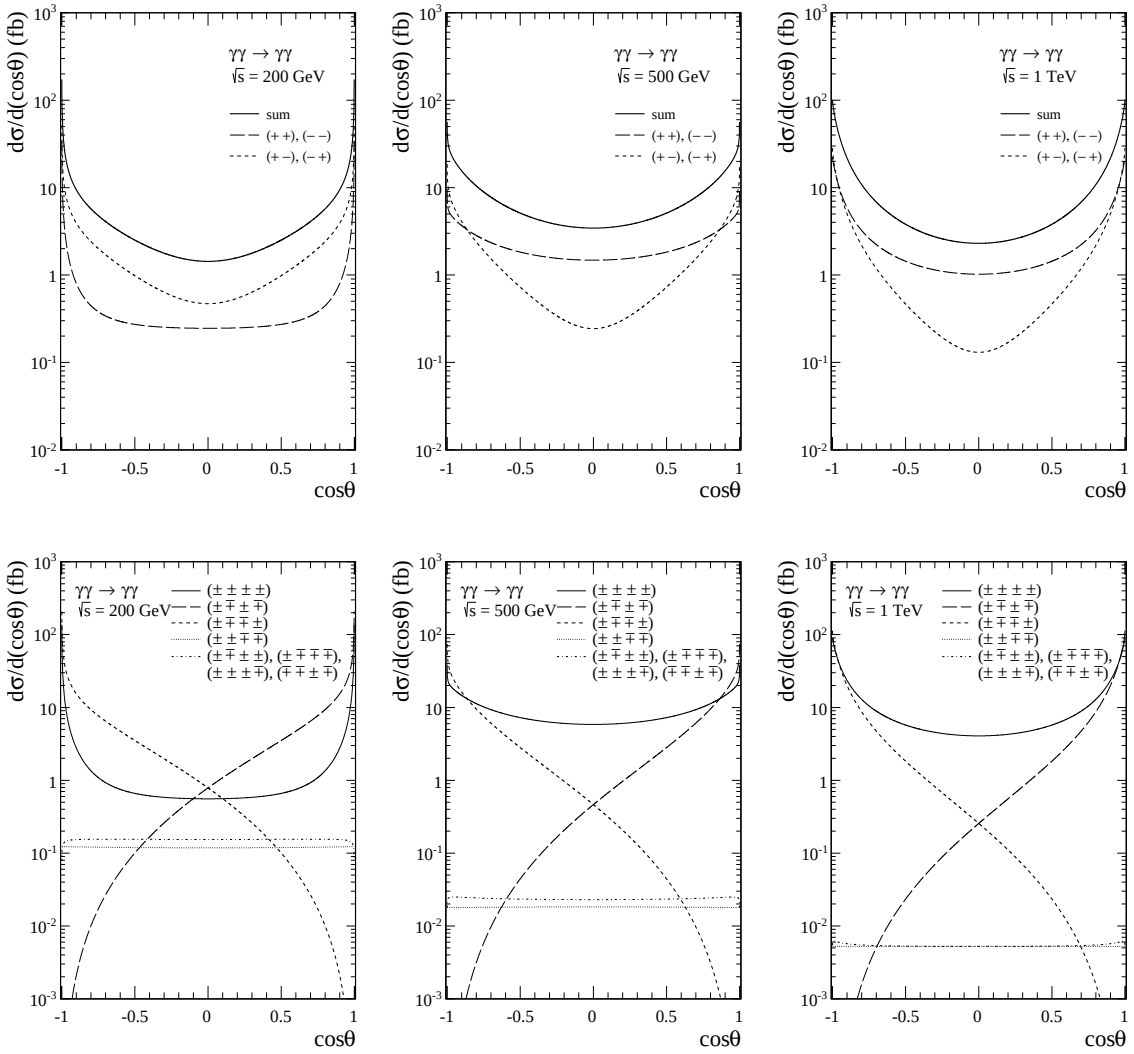

Figure 5.16: Differential cross section for the process $\gamma\gamma \to \gamma\gamma$ at $\gamma\gamma$ c.m. energies $\sqrt{s} = 200$ GeV, 500 GeV and 1 TeV with unpolarised ingoing photons for different helicities (λ_3, λ_4) of the outgoing photons (top panels) and for different helicities $(\lambda_1, \lambda_2, \lambda_3, \lambda_4)$ of all the photons (bottom panels). In this case, where more than one helicity combination is indicated, all the curve corresponds to a single helicity combination, not the sum.

reference frames and goes beyond approximations made here. In particular, we found that the helicity contributions obey the following relation

$$\frac{d\sigma_{\lambda_+\lambda_-}(y_+)}{dy_+} = \frac{d\sigma_{\lambda_-\lambda_+}(y_-)}{dy_-}\,, \tag{5.34}$$

where $y_\pm$ and $\lambda_\pm$ are rapidities and helicities of $W^\pm$ bosons, respectively. The unpolarized cross section does not show up any peculiarities in y-dependence and is symmetric with respect to $y = 0$ for both W^+ and W^- bosons.

In Fig. 5.20 (left panel) we show distribution in W^+ (W^-) transverse momentum. The distribution for exclusive diffractive production is much steeper than that for the electromagnetic contribution. A side remark is in order here. The diffractive contribution peaks at $p_{\perp,W} \sim 25$ GeV. This is somewhat smaller than for the $\gamma\gamma \to W^+W^-$ mechanism where the maximum is at $p_{\perp,W} \sim 40$ GeV. The exclusive cross section for photon-photon contribution is at large transverse momenta ~ 1 TeV smaller only by one order of magnitude than the inclusive $gg \to W^+W^-$ component. The situation could be even more favorable if New Physics would be

at the game [356, 357].

Fig. 5.20 (right panel) shows distribution in the W^+W^- invariant mass which is particularly important for the New Physics searches at the LHC [356, 357]. The distribution for the diffractive component drops quickly with the M_{WW} invariant mass. For reference and illustration, we show also distribution when the Sudakov form factor in Eq. (5.18) is set to one. As can be seen from the figure, the Sudakov form factor lowers the cross section by a large factor. The damping is M_{WW}-dependent as can be seen by comparison of the two curves. The larger M_{WW} the larger the damping. We show the full result with box and triangle (Higgs boson) contributions. At high invariant masses, the interference of boxes and triangles decreases the cross section. The distribution for the two-photon initiated component drops very slowly with W^+W^- invariant mass and at $M_{WW} > 1$ TeV the corresponding cross section is even bigger than the $gg \to W^+W^-$ component to inclusive production of W^+W^- pairs.

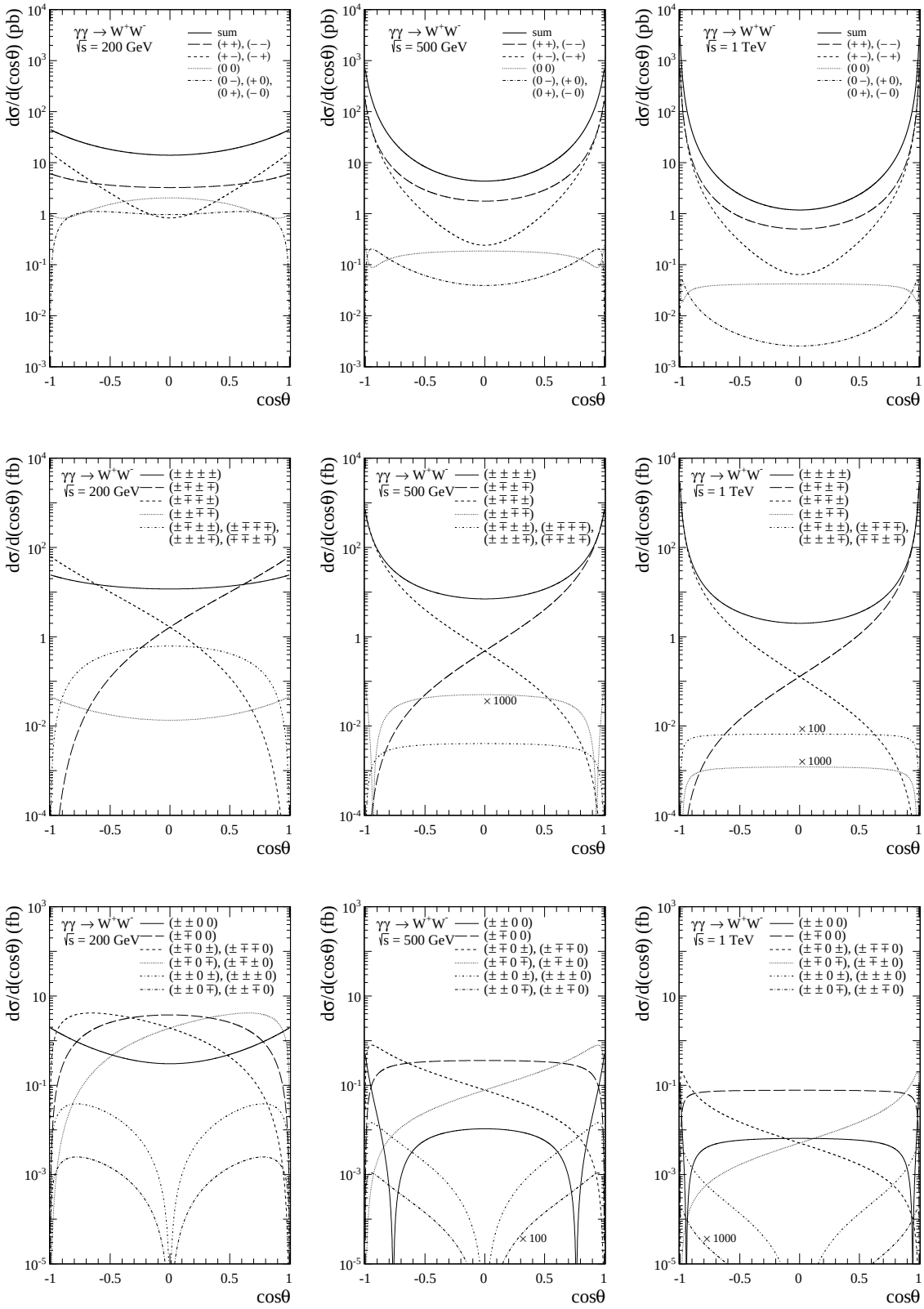

Figure 5.17: Differential cross section for the process $\gamma\gamma \to W^+W^-$ at $\gamma\gamma$ c.m. energies $\sqrt{s} = 200$ GeV, 500 GeV and 1 TeV with unpolarised incoming photons for different helicities (λ_3, λ_4) of the W bosons (top panels) as well as in the bottom panels for different helicities $(\lambda_1, \lambda_2, \lambda_3, \lambda_4)$ of the photons and W bosons. The upper part shows the cross section for purely transverse final states, whereas in the lower part one or both W's are longitudinal. In this case, where more than one helicity combination is indicated, all the curve corresponds to a single helicity combination, not the sum.

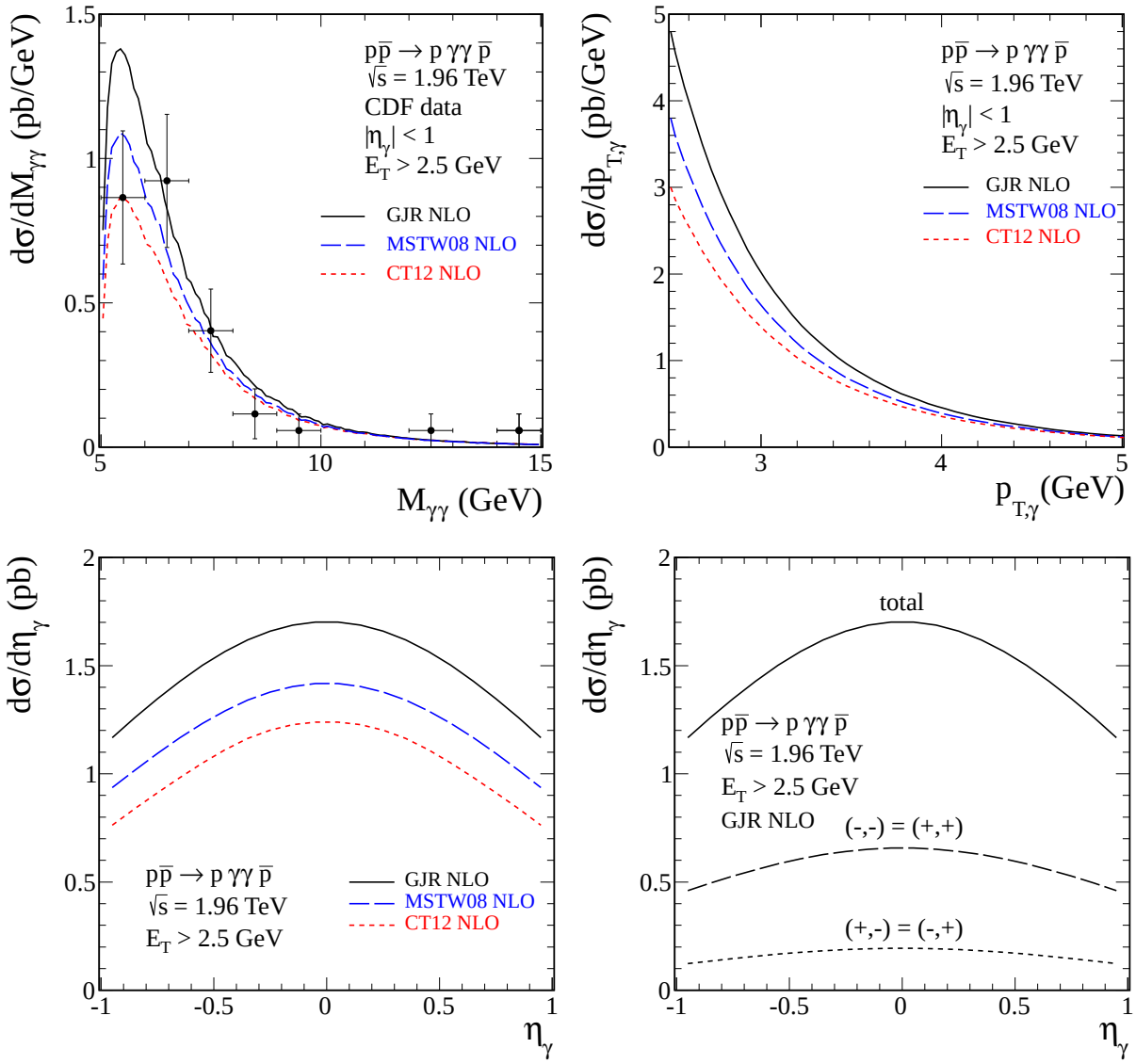

Figure 5.18: In the top panels we show distributions in photon-photon invariant mass (left panel) and distribution in photon transverse momentum (right panel). The experimental data are taken from Ref. [355]. We show results for three different gluon distributions specified in the figure. In the bottom panels we show distribution in photon pseudorapidity for three different gluon distributions (left panel) and the decomposition into different pp center-of-mass photon helicity components (right panel).

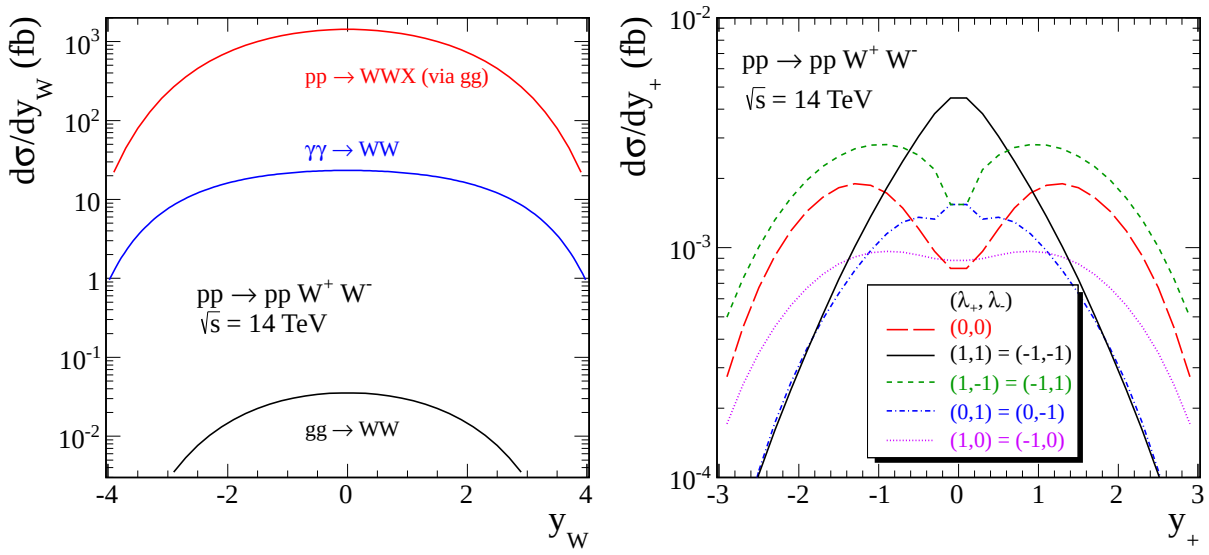

Figure 5.19: Rapidity distribution of W bosons. In the left panel the diffractive contribution is shown by the bottom black line, while the $\gamma\gamma \to W^+W^-$ contribution by the middle blue line. For comparison, we also show the cross section for the gg-fusion inclusive production case (upper red line). Right panel shows the W^+ rapidity distribution of separate polarisation components to the diffractive production. The individual contributions for different helicities (λ_+, λ_-) of the W bosons are marked in the figure.

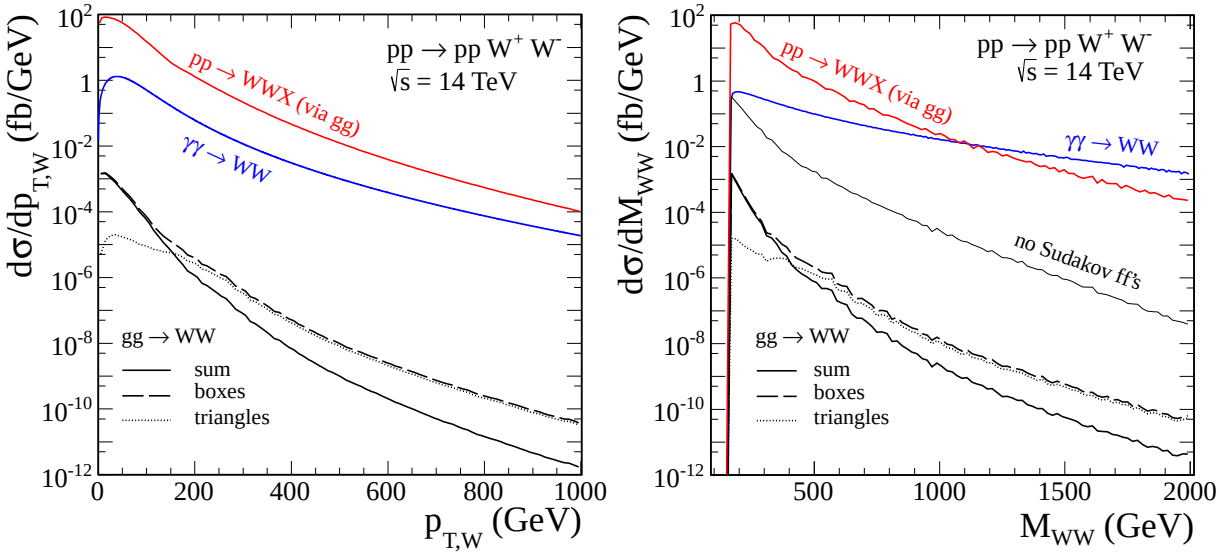

Figure 5.20: Distribution in transverse momentum of one of the W bosons (left panel) and in W^+W^- invariant mass (right panel). We show both the QCD diffractive contribution (the bottom black solid line) and the electromagnetic $\gamma\gamma \to W^+W^-$ contribution (the middle blue solid line). The most upper red solid line corresponds to the inclusive two-gluon initiated $pp \to W^+W^-X$ component. Separate contributions of boxes (dashed) and triangles (dotted) are shown in addition for illustrating the cancellation effect. The result when the Sudakov form factor is put to one is shown for illustrating its role.

5.5 Search for technipions in exclusive production of diphotons

In this section we focus on exclusive production of neutral technipion π_T^0 in pp collisions at the LHC, i.e. in the $pp \to pp\pi_T^0$ reaction. The dependence of the cross section on parameters of recently proposed vector-like Technicolor model is studied. Characteristic features of the differential distributions are discussed. For not too large technipion masses the diphoton decay channel has the dominant branching fraction. This is also the main reason for an enhanced production of neutral technipions in $\gamma\gamma$-fusion reaction. We discuss backgrounds of the QCD and QED origin to the $pp \to pp(\pi_T^0 \to \gamma\gamma)$ process at large invariant $\gamma\gamma$ masses. We conclude that compared to inclusive case the signal-to-background ratio in the considered exclusive reaction is very favourable which thereby could serve as a good probe for Technicolor dynamics searches at the LHC.

In general, there is a non-negligible possibility that potential, yet unknown, weaker resonances which decay mostly into two photons could be very difficult to identify in the inclusive measurements, at least, at current level of statistics. In such cases an exclusive measurement has the advantage that $\gamma\gamma$-resonance signals could be "enhanced" relative to the two-photon background offering important advantages compared to new $\gamma\gamma$-resonance searches in inclusive production reactions.

Noteworthy, the CMS Collaboration has indicated yet an unexplained resonant 2σ-signature in the $\gamma\gamma$ invariant mass spectrum around ~ 137 GeV [402, 403] while ATLAS studies do not reveal a similar signature. Yet poor statistical significance in both measurements does not allow to exclude completely the existence of extra weak resonances. So it is worth to consider alternative simple possibilities for an extra narrow neutral resonance decaying predominantly into the $\gamma\gamma$ pair. These exotic light physical states, in particular, pseudoscalar pseudo-Goldstone technipions, are naturally predicted by a high-scale strongly-coupled dynamics commonly referred to as Technicolor (TC) [404–407] (for a review, see also Refs. [408, 409]).

In original minimal Higgs-less TC models, the EW symmetry is broken by techniquark condensate $\langle Q_T \bar{Q}_T \rangle$ and there are no composite scalars left in the spectrum since pseudo-Goldstone technipions appearing due to the chiral symmetry breaking at a TeV energy scale are absorbed by the SM gauge bosons. Recently, however, the SM Higgs boson has been discovered [398, 399] leaving practically no room for minimal TC scenarios, and the search for consistent alternatives incorporating new strongly-coupled dynamics, dynamical EW symmetry breaking (EWSB) and the (elementary or composite) Higgs boson is on the way.

One of such promising low energy effective theories including both a Higgs doublet H and a new TC sector (e.g. technipions) is usually referred to as bosonic TC scenarios [410–412]. Most recent realization of the bosonic TC is based upon holographic ideas [413], and allows to explain the existence of recently discovered Higgs-like 125 GeV particle and its possible non-standard features [414]. In this approach, strongly coupled dynamics is defined using the AdS/CFT correspondence within the holographic approach allowing to avoid the EW precision constraints [415–417]. In contrast to conventional (Extended and Walking) TC models, in bosonic TC models the mechanism of the EWSB and generation of SM fermions masses is driven by the Higgs vacuum expectation value (vev) in the standard way, irrespectively of (elementary or composite) nature of the Higgs field itself. Due to linear source term in the Higgs potential the Higgs field H develops vev which in turn is induced by the technifermion condensate. This means the Higgs mechanism is not the primary source of the EWSB, but effectively induced by an unknown TC dynamics at high scales.

Many existing dynamical EWSB scenarios, including those with walking and topcolor dynamics, incorporate more than the minimal two flavors of techniquarks. Such scenarios feature pseudo-scalar technipion states that are remnants of the EWSB in models with more than one weak techniquark doublet. Discovery of such technipions is often considered as one the basic observational signatures of TC [418–420]. In extended TC scenarios with colorless (or colored) techniquarks the technipion can be produced via gluon-gluon and quark-antiquark fusion through a strong technipion coupling to heavy t, b quarks (or techniquark-gluon coupling). As

was shown in Ref. [421] (and in references therein) in such scenarios the relatively light technipions $m_{\pi_T} < 2m_t$ are excluded by the SM Higgs searches at the LHC. Do we still have a room for light ($m_{\pi_T} \sim 100 - 300$ GeV) technipions consistent with EW and LHC precision constraints?

We consider a further development of the bosonic TC and dynamical EWSB ideas – the so-called vector-like TC scenario recently proposed and discussed in detail in Refs. [422, 423]. This model is a successful alternative to the standard (Extended, Walking) TC implementations which is essentially the minimal TC extension of the SM with one (elementary or composite) Higgs doublet and extra strongly-coupled weak doublet of vector-like techniquarks (i.e. with two "techni-up" U and "techni-down" D flavors only).

The idea of vector-like (chiral-symmetric) ultraviolet completion which is fully consistent with precision EW constraints at the fundamental level has been realized in the framework of the gauged linear σ-model initially developed for QCD hadron physics [424–428]. In this phenomenological approach, the spontaneous *global* chiral symmetry breaking in the techiquark sector happens by means of technisigma vacuum expectation value (vev) in the chiral-symmetric (vector-like) way

$$SU(2)_{\rm L} \otimes SU(2)_{\rm R} \to SU(2)_{\rm V\equiv L+R}\,, \tag{5.35}$$

where the resulting unbroken chiral-symmetric subgroup $SU(2)_{\rm V\equiv L+R}$ is then *gauged* and therefore describes gauge interactions of the techniquark sector. The minimality of such a scenario which incorporates the SM Higgs sector is provided by the fact that one gauges *only* the vector part of the global chiral symmetry. In Ref. [422] it was argued that the vector-like gauge group $SU(2)_{\rm V}$ can, in principle, be *identified* with the weak isospin group $SU(2)_{\rm W}$ of the SM, i.e.

$$SU(2)_{\rm V\equiv L+R} \equiv SU(2)_{\rm W}\,, \tag{5.36}$$

in the techniquark sector. Such a dynamical realization of the chiral-gauge symmetry leads to specific properties of the techniquark sector w.r.t. weak interactions, which thereby make it to be very different from the chiral-nonsymmetric SM fermion sectors. It therefore means that after the chiral symmetry breaking in the techniquark sector the left and right components of the original Dirac techniquark fields can interact with the SM weak $SU(2)_{\rm W}$ gauge bosons with vector-like couplings, in contrast to ordinary SM fermions, which interact under $SU(2)_{\rm W}$ by means of their left-handed components only.

The resulting weak isospin symmetry $SU(2)_{\rm W}$ is broken by means of the effective SM Higgs mechanism which thereby gets *initiated* by the techniquark condensation providing the dynamical nature of the EWSB [422]. In this scenario, the additional Goldstone bosons arising from the Higgs weak doublet are absorbed by $Z, W^{\pm}$ bosons in the standard way while pseudo-Goldstone technipions from extra TC dynamics remain physical in a full analogy with QCD hadron physics. As we will see below these technipions can be rather light, in principle, as light as the W boson since they do not couple to ordinary quarks and gluons and could potentially be accessible to a standard Higgs boson searches e.g. in $\gamma\gamma$ and γZ decay channels. Since the diphoton channel appears to be the most favorable channel for such technipion searches at the LHC we wish to discuss in this Section also the diphoton backgrounds which turn out to be suppressed compared to the ${\pi_T}^0 \to \gamma\gamma$ signal in the exclusive production process.

Therefore, we consider the exclusive production of $\gamma\gamma$ pairs which is among one of the "golden channels" for both Higgs boson and light technipion searches at the LHC. The $pp \to p(\gamma\gamma)p$ process going through the diffractive QCD mechanism with the $gg \to \gamma\gamma$ subprocess naturally constitutes a background for the resonant technipion production. The photon-photon contribution for the purely exclusive production of low invariant mass of $\gamma\gamma$ was discussed very recently in Ref. [429]. There only lepton and quark loops have been considered. In the case of technipion production at the LHC we are rather interested in relatively large invariant diphoton masses $M_{\gamma\gamma} \gtrsim 100$ GeV relevant for the SM Higgs boson searches as well. We shall calculate both the QCD and QED contributions and compare them differentially as a function of diphoton invariant mass suggesting potentially measurable signature of vector-like Technicolor.

5.5.1 Technipion interactions from vector-like Technicolor

We start from vector-like TC model setup relevant for our purposes here. The local chiral vector-like subgroup $SU(2)_{\rm V\equiv L+R} = SU(2)_{\rm W}$ appearing due to the spontaneous global chiral symmetry breaking (5.35) acts on confined elementary techniquark sector [422], i.e.

$$Q_T = \left(\begin{array}{c} U \\ D \end{array} \right) , \tag{5.37}$$

which is thus in the fundamental representation of the SM gauge $SU(2)_{\rm W} \otimes U(1)_{\rm Y}$ group and $SU(3)_c$-neutral at the same time. As usual, in addition we have the initial scalar technisigma S field which is the SM singlet, and the triplet of initial (massless) technipion fields P_a, $a = 1, 2, 3$ which is the adjoint (vector) representation of $SU(2)_{\rm W}$ (with zeroth $U(1)_{\rm Y}$ hypercharge). The linear σ-model part of the Lagrangian responsible for the Yukawa-type interactions of the techniquarks (5.37) reads

$$\mathcal{L}_Y^{\rm TC} = -g_{\rm TC} \bar{Q}_T (S + i\gamma_5 \tau_a P_a) Q_T \, , \tag{5.38}$$

where τ_a, $a = 1, 2, 3$ are the Pauli matrices, and effective Yukawa coupling $g_{\rm TC} > 1$. After the chiral and EW symmetries breaking, the Yukawa terms (5.38) determine the strength of technipion interactions with techniquarks as well as (pseudo)scalar self-couplings [422].

Non-local effects in gauge boson couplings to technipions and constituent techniquarks, in general, can be incorporated via momentum-dependent form factors. In the case of a large techniconfinement scale $\Lambda_{\rm TC} \sim 0.1 - 1$ TeV, these effects are strongly suppressed by large constituent masses of techniquarks $M_{Q_T} \sim \Lambda_{\rm TC}$ and can be neglected to the first approximation. Thus the vector-like gauge interactions of Q_T and P_a fields with initial $U(1)_{\rm Y}$ and $SU(2)_{\rm W}$ gauge fields B_μ, W_μ^a, respectively, can be introduced in the local approximation via usual EW gauge couplings $g_{1,2}$ renormalized at the $\mu = 2M_{Q_T}$ scale, i.e.

$$\mathcal{L}_{\pi_T, Q_T} = \frac{1}{2} D_\mu P_a \, D^\mu P_a + i \bar{Q}_T \hat{D} Q_T \, , \tag{5.39}$$

where

$$D_\mu P_a = \partial_\mu P_a + g_2 \epsilon_{abc} W_\mu^b P_c \, , \tag{5.40}$$

$$\hat{D} Q_T = \gamma^\mu \left(\partial_\mu - \frac{i Y_{Q_T}}{2} g_1 B_\mu - \frac{i}{2} g_2 W_\mu^a \tau_a \right) Q_T \, , \tag{5.41}$$

besides that Q_T is also confined under a QCD-like $SU(N_{\rm TC})_{\rm TC}$ group. Here, we discuss a particular case with the number of technicolors $N_{\rm TC} = 3$.

After the EWSB, the physical Lagrangian of vector-like interactions of techniquarks and gauge bosons $V = Z^0$, $W^\pm$, γ reads

$$\begin{aligned} L_{\bar{Q}_T Q_T V} &= g_W^{Q_T} \, \bar{U} \gamma^\mu D \cdot W_\mu^+ + g_W^{Q_T} \, \bar{D} \gamma^\mu U \cdot W_\mu^- \\ &+ Z_\mu \sum_{Q_T = U, D} g_Z^{Q_T} \, \bar{f} \gamma^\mu f + \sum_{Q_T = U, D} g_\gamma^{Q_T} \, \bar{f} \gamma^\mu A_\mu f \, , \end{aligned} \tag{5.42}$$

where technifermion couplings to vector bosons $g_{V_{1,2}}^{Q_T}$ are

$$g_Z^{Q_T} = \frac{g}{c_W} \left(t_3^{Q_T} - q_{Q_T} s_W^2 \right) , \quad g_W^{Q_T} = \frac{g}{\sqrt{2}} , \quad g_\gamma^{Q_T} = e \, q_{Q_T} \, . \tag{5.43}$$

Here, $s_W = \sin\theta_W$, $c_W = \cos\theta_W$, and θ_W is the Weinberg angle, $e = g s_W$ is the electron charge, $t_3^{Q_T}$ is the weak isospin ($t_3^U = 1/2$, $t_3^D = -1/2$), $q_{Q_T} = Y_{Q_T}/2 + t_3^{Q_T}$ is the technifermion charge. Choosing the technifermion hypercharge to be the same as in the SM fermion sector $Y_{Q_T} = 1/3$,

we get $q_U = 2/3$ and $q_D = -1/3$. Also, the Yukawa-type interactions of constituent techniquarks with technipions are governed by

$$L_{\bar{Q}_T Q_T \pi_T} = -i\sqrt{2} g_{\rm TC}\, \pi_T^+ \bar{U}\gamma_5 D - i\sqrt{2} g_{\rm TC}\, \pi_T^- \bar{D}\gamma_5 U - i g_{\rm TC}\, \pi_T^0 (\bar{U}\gamma_5 U - \bar{D}\gamma_5 D)\,. \quad (5.44)$$

Since we are interested here in neutral technipion couplings in exclusive production processes, only the last two terms of the Yukawa Lagrangian (5.44) will be used. Finally, Born-level interactions of technipions with gauge bosons are defined as follows

$$\begin{aligned} L_{\pi_T \pi_T V} &= i g_2 W^{\mu +} \cdot (\pi_T^0 \pi_{T,\mu}^- - \pi_T^- \pi_{T,\mu}^0) + i g_2 W^{\mu -} \cdot (\pi_T^+ \pi_{T,\mu}^0 - \pi_T^0 \pi_{T,\mu}^+) \\ &+ i g_2 (c_W Z_\mu + s_W A_\mu) \cdot (\pi_T^- \pi_{T,\mu}^+ - \pi_T^+ \pi_{T,\mu}^-) \\ &+ g_2^2\, W_\mu^+ W^{\mu -} \cdot (\pi_T^0 \pi_T^0 + \pi_T^+ \pi_T^-) + g_2^2\, (c_W Z_\mu + s_W A_\mu)^2 \cdot \pi_T^+ \pi_T^- + \ldots\,, \end{aligned} \quad (5.45)$$

where $\pi_{T,\mu} \equiv \partial_\mu \pi_T$ notation is used for brevity. Other parts of the Lagrangian of the vector-like Technicolor model are not needed for present purposes and can be found in Refs. [422, 423].

It is worth to stress here that in distinction to extended TC scenarios, in the vector-like TC model the technipion interacts only with SM gauge bosons Z, γ and $W^\pm$ and with constituent $SU(3)_c$-singlet techniquarks. In practice, this makes the technipions rather difficult to produce and observe even in rather light ~ 100 GeV mass range.

5.5.2 Technipion production and decay: gauge boson channels

As it follows from Eq. (5.45), the pseudoscalar technipions can only be produced in pairs in gauge boson fusion reactions at Born level while single pion production is possible at one loop level only. For non-zeroth techniquark hypercharge $Y_{Q_T} \neq 0$, the effective one-loop technipion-vector bosons $\pi_T\, V_1\, V_2$ couplings are given by triangle diagrams shown in Fig. 5.21 (left). The latter is valid for the QCD-like TC scenario with $SU(3)_{\rm TC}$ group of confinement which is the subject of our analysis here.

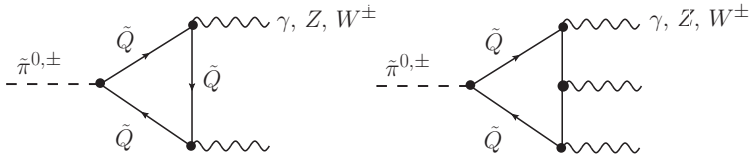

Figure 5.21: The loop-induced light technipion couplings to the gauge bosons through constituent techniquark loops. In the case of $Y_{Q_T} \neq 0$, the technipion is coupled to two gauge bosons to the lowest order $\pi_T V_1 V_2$ via techniquark triangle diagrams (left), while for the $Y_{Q_T} = 0$ case the technipion is coupled only to three gauge bosons $\pi_T V_1 V_2 V_3$ via a box diagram (right). The latter case is much more involved and will not be considered here.

The corresponding loop amplitude has the following form

$$i\mathcal{V}_{\pi_T V_1 V_2} = F_{V_1 V_2}(M_1^2, M_2^2, m_{\pi_T}^2; M_{Q_T}^2) \cdot \epsilon_{\mu\nu\rho\sigma} p_1^\mu p_2^\nu \varepsilon_1^{*\rho} \varepsilon_2^{*\sigma}\,, \quad (5.46)$$

$$F_{V_1 V_2} = \frac{N_{\rm TC}}{2\pi^2} \sum_{Q_T = U,D} g_{V_1}^{Q_T}\, g_{V_2}^{Q_T}\, g_{\pi_T}^{Q_T}\, M_{Q_T}\, C_0(M_1^2, M_2^2, m_{\pi_T}^2; M_{Q_T}^2)\,, \quad (5.47)$$

where $C_0(m_1^2, m_2^2, m_3^2; m^2) \equiv C_0(m_1^2, m_2^2, m_3^2; m^2, m^2, m^2)$ is the standard finite three-point function [384], $N_{\rm TC}$ is the number of technicolors in confined $SU(N_{\rm TC})$ group, $p_{1,2}$, $\varepsilon_{1,2}$ and $M_{1,2}$ are the 4-momenta, polarization vectors of the vector bosons $V_{1,2}$ and their on-shell masses, respectively, and neutral technipion couplings to U, D techniquarks are

$$g_{\pi_T^0}^U = g_{\rm TC}\,, \quad g_{\pi_T^0}^D = -g_{\rm TC}\,, \quad (5.48)$$

while gauge couplings of techniquarks $g_{V_{1,2}}^{Q_T}$ are defined in Eq. (5.43). We have assumed $M_U = M_D = M_{Q_T}$. We notice here that the $\pi_T^0 \to W^+ W^-$ decay mode is forbidden by symmetry [422].

Finally, the explicit expressions of the effective neutral technipion couplings $F_{V_1V_2}$ for on-shell $V_1V_2 = \gamma\gamma$, γZ and ZZ final states are

$$F_{\gamma\gamma} = \frac{4\alpha\, g_{\rm TC}}{\pi}\frac{M_{Q_T}}{m^2_{\pi_T}}\,\arcsin^2\Big(\frac{m_{\pi_T}}{2M_{Q_T}}\Big)\,, \qquad \frac{m_{\pi_T}}{2M_{Q_T}} < 1\,, \tag{5.49}$$

$$F_{\gamma Z} = \frac{4\alpha\, g_{\rm TC}}{\pi}\frac{M_{Q_T}}{m^2_{\pi_T}}\,\cot 2\theta_W\,\Big[\arcsin^2\Big(\frac{m_{\pi_T}}{2M_{Q_T}}\Big) - \arcsin^2\Big(\frac{M_Z}{2M_{Q_T}}\Big)\Big]\,, \tag{5.50}$$

$$F_{ZZ} = \frac{2\alpha\, g_{\rm TC}}{\pi} M_{Q_T}\, C_0(M_Z^2, M_Z^2, m^2_{\pi_T}; M^2_{Q_T})\,, \tag{5.51}$$

where $\alpha = e^2/4\pi$ is the fine structure constant.

Now the two-body technipion decay width in a vector boson channel can be represented in terms of the effective couplings (5.47) as follows:

$$\Gamma(\pi_T \to V_1\, V_2) = r_V \frac{m^3_{\pi_T}}{64\pi}\,\bar\lambda^3(M_1^2, M_2^2; m^2_{\pi_T})\,|F_{V_1V_2}|^2\,, \tag{5.52}$$

where $r_V = 1$ for identical bosons V_1 and V_2 and $r_V = 2$ for different ones, and $\bar\lambda$ is the normalized Källen function (triangle function) which is defined by

$$\bar\lambda(m_a, m_b; q) = \Big(1 - 2\frac{m_a^2 + m_b^2}{q^2} + \frac{(m_a^2 - m_b^2)^2}{q^4}\Big)^{1/2}. \tag{5.53}$$

In Fig. 5.21 (right) we show the leading-order contribution to single technipion-gauge bosons coupling for $Y_{Q_T} = 0$ (relevant in the case of an even $SU(N_{\rm TC})_{\rm TC}$ group of confinement, e.g. $SU(2)_{\rm TC}$ [423]). In the latter case, a single technipion can be produced in V_1V_2 fusion only in association with an extra gauge boson V_3 while produced technipion should further decay either into three gauge bosons $\pi_T \to V_1'V_2'V_3'$ or into a pair of Higgs bosons $\pi_T \to hh$. Such processes would be rather suppressed and difficult to study experimentally while they give rise to the only observable signatures of technipions in the case of $SU(2)_{\rm TC}$ group of confinement in the vector-like Technicolor scenario so will be studied elsewhere.

5.5.3 Exclusive technipion production

Since technipions do not couple directly to SM fermions and gluons, the only way to produce them is in the vector-boson ($\gamma\gamma$, γZ, ZZ) fusion channel. The VBF is typically considered as one of the key production modes of the Higgs boson at the LHC which allowed recently for a clear discrimination of the Higgs signal [398, 399]. While VBF Higgs studies were properly done elsewhere [422], here we focus on the VBF into a neutral technipion only. In the case of technipion production in partonic $2 \to 3$ hard subprocesses the gluon-gluon fusion channel is absent, only the loop-induced VBF is possible. There is a notable difference between the Higgs boson and technipion in the VBF as well: the Higgs boson VBF is dominated by $WW \to h$ and $ZZ \to h$ fusion channels at tree-level whereas the technipion VBF is given mostly by $\gamma\gamma \to \pi^0_T$ production channel via a techniquark loop diagram.

The loop-induced technipion VBF cross section is suppressed by roughly a factor of $\sim 10^{-3}$ or so (depending on TC model parameters) compared to the tree-level Higgs boson VBF cross section in the same mass range. Having in mind that inclusive sample for the Higgs boson production contains only 7.3% of VBF at $m_h = 125$ GeV, the net yield of the Higgs bosons dominates over technipion yield by a factor of 10^4 in the same mass range. On the other hand, having in mind very different branching ratios, $\mathrm{BR}(h \to \gamma\gamma) \sim 10^{-3}$ and $\mathrm{BR}(\pi^0_T \to \gamma\gamma) \sim 0.5 - 1$, one may argue that $\gamma\gamma$ yield from pseudoscalar technipions may be suppressed compared to that from the Higgs boson by roughly an order of magnitude in the same mass range, or even larger for large technipion masses, which introduces certain difficulties in the inclusive technipion observation, at least, at the current level of statistics.

In Fig. 5.22 we show characteristic diagrams for the inclusive (left) and central exclusive (right) technipion production processes in dominant $\gamma\gamma$ fusion and decay channel. Both, production and decay subprocesses are initiated by triangle loop of U, D techniquarks, where we assume $M_U = M_D$.

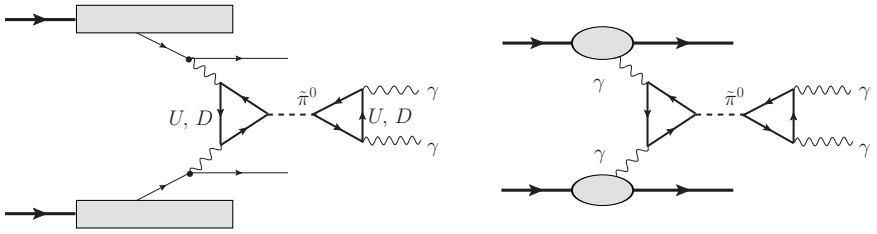

Figure 5.22: Hadron-level technipion production channels in VBF mechanism and the leading $\gamma\gamma$ decay channel: the inclusive $\pi_T^{0,\pm}$ production in association with two quark jets (left panel) and the central exclusive π_T^0 production in the $\gamma\gamma$ fusion (right panel).

The leading-order hard (parton level) VBF subprocess both in the inclusive h and π_T^0 production in the high energy pp scattering is quark-initiated one

$$q_i q_j' \to q_i q_j' (\gamma^*\gamma^* \to h,\, \pi_T^0)\,, \tag{5.54}$$

where q_i and q_j can be either a quark or an antiquark of various flavors from each of the colliding protons, and the virtual $\gamma\gamma$ fusion is concerned. So, the both VBF processes, the h and π_T^0 production may "compete". While $h \to \gamma\gamma$ branching ratio is very small $\sim 10^{-3}$, the corresponding $\pi_T^0 \to \gamma\gamma$ one is fairly large ~ 1. On the other hand, the Higgs boson has additional dominating production modes e.g. via gluon-gluon fusion mechanism and the Higgsstrahlung off gauge bosons and heavy flavor. In contrast to the Higgs boson production, one technipion can be produced only via heavy techniquark triangle loop in the VBF mechanism. Such observable signatures similar to those of the Higgs boson open an interesting and straightforward opportunity for technipion searches in standard Higgs boson studies at the LHC [6]. The calculation of inclusive production cross section in QCD based upon standard collinear factorization technique so we do not discuss it here. In numerical estimations of the cross section it is naturally assumed that the incoming quarks of (5.54) subprocess loose only a small fraction of their initial energy taken away by the intermediate vector bosons. In this kinematics, the final-state quarks are seen as forward-backward hard jets, and by measuring their momenta one accurately reconstructs the invariant mass of the produced state.

We consider the central exclusive $pp \to pp\pi_T^0$ process illustrated in Fig. 5.22 (right). Similarly to the inclusive case discussed above, this process is determined by the colorless VBF subprocess. The exclusive diffractive technipion production in the dominant $\gamma\gamma$ fusion and subsequent $\gamma\gamma$ decay channel [7] has advantages compared to the inclusive technipion production since this mode is not suppressed compared to the standard central exclusive Higgs boson production and the respective $\gamma\gamma$ backgrounds are suppressed at large $\gamma\gamma$ invariant masses. These advantages make the central exclusive technipion production favorable compared to the inclusive technipion production.

[6] As was advocated in Ref. [422], an overall one-technipion production rate is strongly suppressed compared to the Higgs boson production rate, which along with extremely narrow technipion resonance makes it rather hard to study experimentally. So, even light technipions down to W boson mass may be not excluded yet by LEP II and LHC studies, and the latter point is an interesting subject for further investigations.

[7] We take into account only dominating $\gamma\gamma \to \pi_T^0$ fusion reaction and omit $\gamma Z \to \pi_T^0$, $Z\gamma \to \pi_T^0$ and $ZZ \to \pi_T^0$ subprocesses which turn out to be numerically very small being suppressed by large masses in propagators. The gg-fusion is absent if the internal techni-fermions do not carry color, i.e. they are in a "color singlet" state.

The corresponding matrix element for the hadron-level $2 \to 3$ process can be written as:

$$\mathcal{M}^{pp\to pp\pi^0_T}_{\lambda_a\lambda_b\to\lambda_1\lambda_2} = V^{\mu_1}_{\lambda_a\to\lambda_1}\frac{(-ig_{\mu_1\nu_1})}{t_1}F_{\gamma\gamma}(M_{Q_T}, m_{\pi^0_T})\epsilon^{\nu_1\nu_2\alpha\beta}q_{1,\alpha}q_{2,\beta}\frac{(-ig_{\nu_2\mu_2})}{t_2}V^{\mu_2}_{\lambda_b\to\lambda_2}, \quad (5.55)$$

where the parton-level triangle amplitude $F_{\gamma\gamma}(M_{Q_T}, m_{\pi^0_T})$ is given by Eq. (5.49), and the vertex functions $V_{\mu_{1,2}}$ can be approximated in the spin conserving case relevant at high energies as follows

$$V^{\mu_1}_{\lambda_a\to\lambda_1} \simeq eF_1(t_1)\,\bar{u}(\lambda_1)i\gamma^{\mu_1}u(\lambda_a)\,, \quad V^{\mu_2}_{\lambda_b\to\lambda_2} \simeq eF_1(t_2)\,\bar{u}(\lambda_2)i\gamma^{\mu_2}u(\lambda_b)\,, \quad (5.56)$$

where $F_1(t)$ is the Dirac electromagnetic proton form factor (B.2). The natural limitation for a light pseudo-Goldstone technipion

$$\frac{m_{\pi^0_T}}{2M_{Q_T}} < 1 \quad (5.57)$$

is implied. In the exclusive case, the integration in proton transverse momenta requires a special care. Instead of integration over $p_{1\perp}$ and $p_{2\perp}$ we integrate over $\xi_1 = \log_{10}(p_{1\perp}/1\,\mathrm{GeV})$ and $\xi_2 = \log_{10}(p_{2\perp}/1\,\mathrm{GeV})$. The matrix element specified above is used in a three-body calculation precisely as for the usual exclusive neutral pion production in the $pp \to pp\pi^0$ process considered in Section 4.1.2, see Ref. [9].

5.5.4 Exclusive $\gamma\gamma$ background: QCD vs QED mechanisms

In order to estimate the feasibility of exclusive technipion production studies we need to analyse carefully the exclusive $\gamma\gamma$ background. There are two basic non-resonant leading order

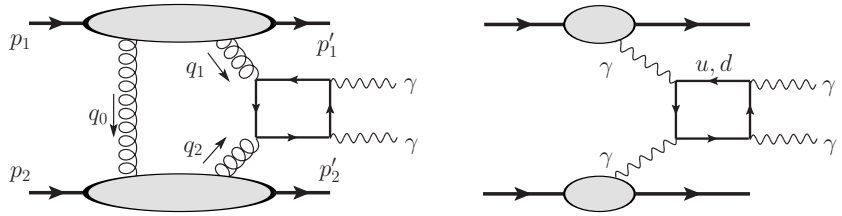

Figure 5.23: Irreducible non-resonant background processes for the central exclusive technipion $\pi^0_T \to \gamma\gamma$ production in pp collisions at the LHC: the QCD diffractive $\gamma\gamma$ pair production (left) and the QED-initiated $\gamma\gamma$ pair production (right). In the latter case, only a part of contributions corresponding to quark boxes is shown here for illustration while in actual calculations the full set of SM contributions from quark, lepton and W boson loops is included.

box-induced contributions – the QCD (Durham) diffractive mechanism via $gg \to \gamma\gamma$ shown in Fig. 5.23 (left) and the QED (light-by-light) scattering mechanism $\gamma\gamma \to \gamma\gamma$ shown in Fig. 5.23 (right). The details of the kinematics for the central exclusive production processes are discussed in Sections 5.1, 5.2, and 5.1.3.

In the case of light-by-light scattering in numerical calculations we include box diagrams with leptons, quarks as well as with W bosons. At high diphoton invariant masses the inclusion of diagrams with W bosons is crucial. In principle, effects beyond the Standard Model possibly responsible for anomalous gauge couplings could be important [393–395, 430–433], so the exclusive non-resonant $\gamma\gamma$ background at large invariant masses is very interesting by itself. In the present analysis we concentrate on the search for technipion so we ignore effects beyond the Standard Model as far as the background is considered. Two photons can annihilate into a neutral pion-like resonance via the anomaly coupling, just like $\gamma\gamma\pi^0$ in QCD. In some strongly interacting electroweak symmetry breaking models, e.g., technicolor type models, there often exist neutral pion-like resonances. There is a strong capability to discover such particles, because the Standard Model background in photon scattering goes through box diagrams and is therefore highly suppressed. Some previous studies of technimeson production at photon collisions can be found in Refs. [434, 435].

5.5.5 Results

Before discussing results for exclusive production of neutral technipion, we would like to summarize the inclusive π_T^0 production in association with two forward jets. In Fig. 5.24 we show the total inclusive cross section as a function of technipion (left) and techniquark (right) masses, m_{π_T} and M_{Q_T}, respectively, and integrated over the full phase space. The calculation

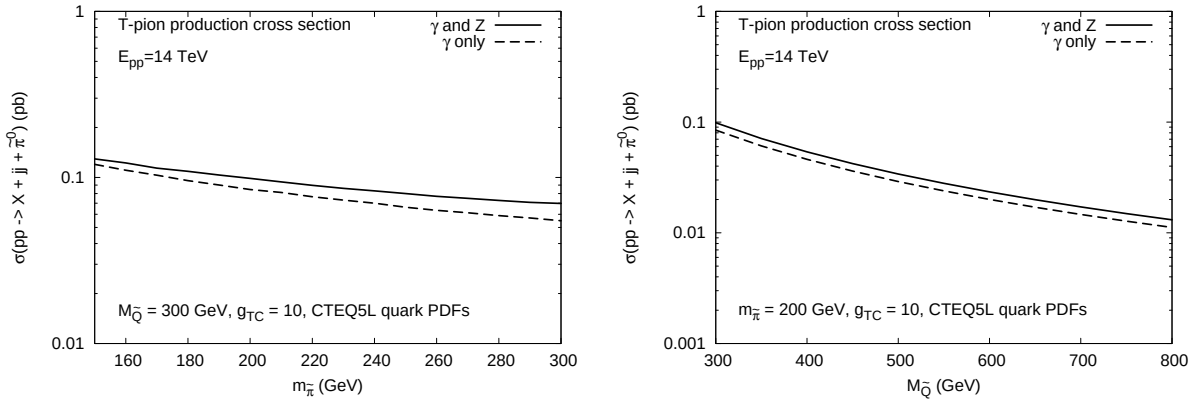

Figure 5.24: Inclusive π_T^0 production cross section in association with two forward jets as a function of technipion mass (left panel) and as a function of techniquark mass (right panel) for fixed values of the g_{TC} coupling constant at the nominal LHC energy $\sqrt{s} = 14$ TeV.

was performed in the collinear QCD factorization with hard (parton-level) $2 \to 3$ subprocess (5.54) including t-channel exchanges of γ and Z^0 bosons as illustrated in Fig. 5.22 (left) (for more details we refer to Ref. [422]). This calculation includes all the light quark and antiquark flavors in the initial state with respective quark PDFs. As can be seen from Fig. 5.24 the photon-photon $\gamma\gamma$ fusion mechanism dominates, while $Z\gamma$ and ZZ fusion contributions are always small (suppressed by a large mass of Z boson in propagators). The cross section for the vector-like TC model parameters and CTEQ5L quark PDFs [436] chosen as indicated in the figure is of the order of 100 fb. The larger the technipion mass or the techniquark mass the smaller the cross section.

Now let us look into the parameter dependence of the exclusive production cross section. This calculation is performed in the same way as the calculation for the exclusive production of usual neutral pion π^0 studied recently in Ref. [9], see Section 4.1.2.

In particular, Fig. 5.25 shows a two-dimensional map of the full phase space integrated cross section as a function of technipion and techniquark masses. A kinematical limit $m_{\pi_T^0} < 2M_{Q_T}$ is clearly visible. We obtain the cross section of the order of 1 fb for the same parameters as used in the calculation of the inclusive cross section. This is about two orders of magnitude less than in the inclusive case. The signal-to-background ratio, as will be discussed later, is more advantageous in the exclusive case than in the inclusive one.

In Fig. 5.26 we show one-dimensional dependencies on technipion (left) and techniquark (middle) masses. These dependencies can be compared to those in Fig. 5.24. Finally in Fig. 5.26 (right) we show dependence on technipion mass for fixed ratio of techniquark-to-technipion mass ratio. The latter dependence looks, however, steeper as an artifact of parameter correlations.

In order to demonstrate the importance the exclusive technipion signature compared to the VBF inclusive production mechanism one should compare results for the $pp \to jj + \pi_T^0 + X$ cross section in Fig. 5.24 (~ 0.1 pb) and technipion CEP cross section in Fig. 5.26 (~ 1 fb). Even though the VBF and CEP π_T^0 cross sections differ by two orders of magnitude, the $\gamma\gamma$ background for the technipion VBF is expected to be larger due to tree-level $WW \to \gamma\gamma$ contribution which is absent in $\gamma\gamma$ CEP case. The latter point leads to a larger S/B ratio for the technipion CEP than that for the technipion VBF.

In the exclusive case, the integration in proton transverse momenta requires a special

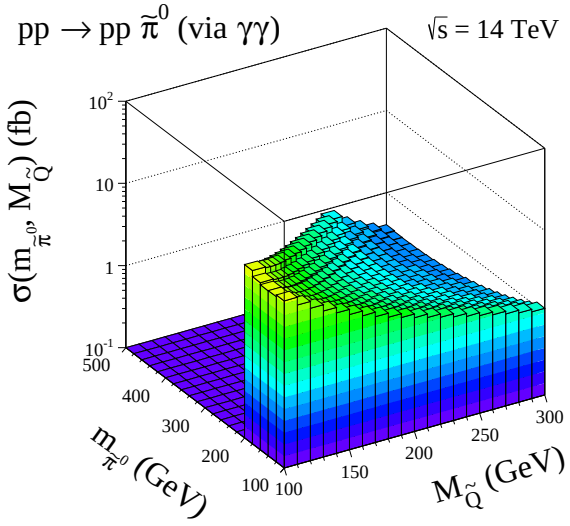

Figure 5.25: Exclusive cross section as a two-dimensional function of technipion mass ($m_{\pi_T^0}$) and techniquark mass (M_{Q_T}) for a fixed value of $g_{\rm TC} = 10$ at the nominal LHC energy $\sqrt{s} = 14$ TeV.

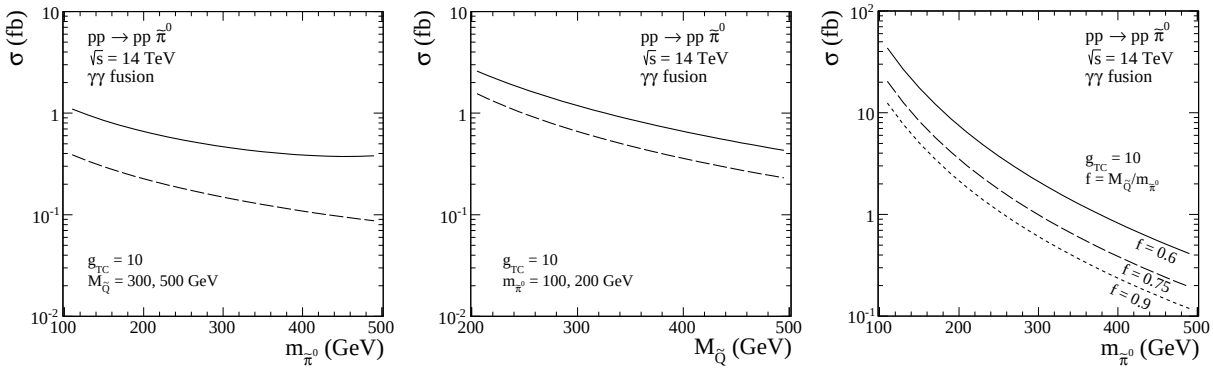

Figure 5.26: Integrated exclusive cross section as a function of technipion mass (left) and techniquark mass (middle) at $\sqrt{s} = 14$ TeV for fixed remaining model parameters as specified in the figure. In the right panel we show the cross section as a function of technipion mass for a few fixed ratios $f = M_{Q_T}/m_{\pi_T^0}$.

care. Instead of integration over $p_{1\perp}$ and $p_{2\perp}$ we integrate over: $\xi_1 = \log_{10}(p_{1\perp}/1\,\text{GeV})$ and $\xi_2 = \log_{10}(p_{2\perp}/1\,\text{GeV})$. The resulting cross section in the auxiliary quantities is shown in Fig. 5.27.

Now let us consider some important differential distributions. In Fig. 5.28 we show a distribution in technipion rapidity (left panel) and azimuthal angle between outgoing protons (right panel). The larger the technipion mass the smaller the cross section. The technipions are produced dominantly at midrapidities as expected. The fact that the signal dominates at $\phi_{12} = \pi/2$ can be further used to reduce QCD and QED background which is expected to dominate at $\phi_{12} \sim \pi$.

Up to now we have discussed cross sections and differential distributions for technipion production in exclusive pp scattering. In real experiment, an optimal decay channel must be chosen due to presumably low production cross sections, on the one hand, and to maximize the signal-to-background ratio, on the other hand. In Fig. 5.29 we show branching fractions for major real technipion ${\pi_T}^0$ decay channels. In a very broad range of technipion and techniquark masses the two-photon decay channel seems to be the most optimal one. In addition, this is one of the golden channels for Higgs boson searches and the LHC detectors are well suited for such studies.

Let us concentrate now on the exclusive diphoton background to the exclusive techni-

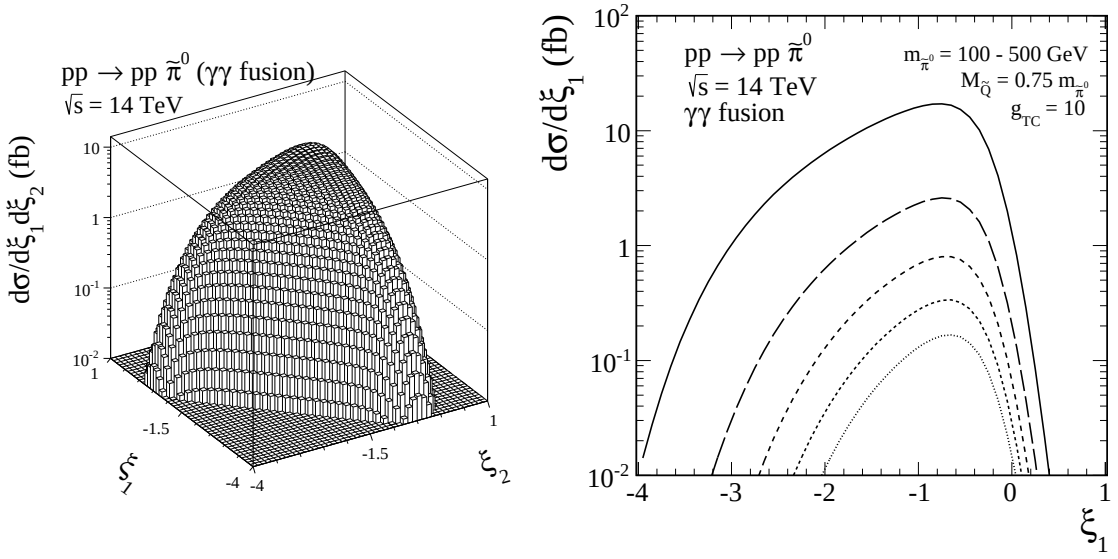

Figure 5.27: Two-dimensional distribution in the auxiliary quantities $\xi_1 = log_{10}(p_{1\perp}/1\text{GeV})$ and $\xi_2 = log_{10}(p_{2\perp}/1\text{GeV})$ (left panel) and the projection on one of the axes (right panel). Results for different masses of the technipion for $m_{\pi^0_T}$ = 100, 200, 300, 400, 500 GeV (from top to bottom) are shown. The techniquark mass is fixed to be $M_{Q_T} = 0.75\, m_{\pi^0_T}$.

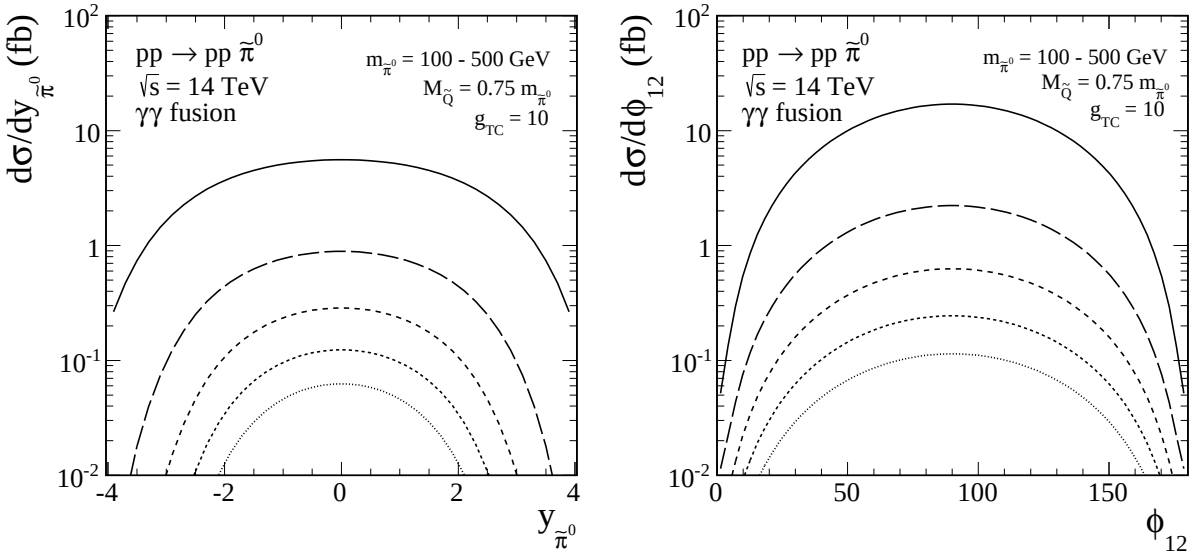

Figure 5.28: Differential distributions in technipion rapidity (left panel) and azimuthal angle between outgoing protons (right panel). Results for different masses of the technipion for $m_{\pi^0_T}$ = 100, 200, 300, 400, 500 GeV (from top to bottom) are shown. The techniquark mass is fixed to be $M_{Q_T} = 0.75\, m_{\pi^0_T}$.

pion production. In Fig. 5.30 we show the corresponding distribution in $M_{\gamma\gamma}$ invariant mass of the two outgoing photons (left panel) and distribution in the $p_{\gamma\perp}$ photon transverse momentum (right panel). We show contributions for the QCD (gg fusion) mechanism, the QED ($\gamma\gamma$ fusion) mechanism as well as contribution for the inclusive two-gluon initiated $pp \to \gamma\gamma X$ mechanism. In Fig. 5.31 we show corresponding two-dimensional distributions in $(p_{\gamma\perp}, M_{\gamma\gamma})$ for the two exclusive nonresonant background mechanisms. At relatively low masses, the QCD mechanism dominates. However, above $M_{\gamma\gamma} > 200$ GeV the photon-photon mechanism takes over. The later is therefore the most important potential background for the technipion signal if observed in the $\gamma\gamma$ decay channel. For the QCD background we have also shown a result without Su-

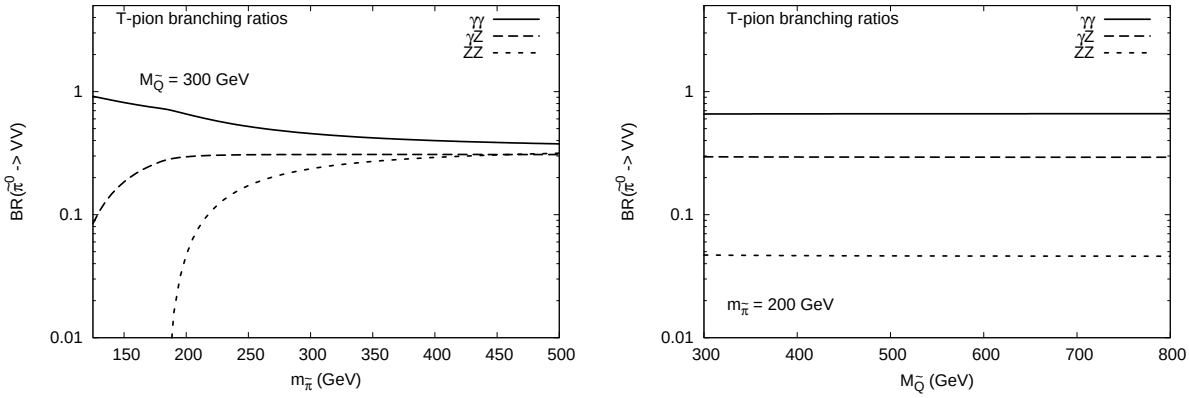

Figure 5.29: Branching fractions for technipion decays into $\gamma\gamma$, γZ and ZZ final states as a function of technipion mass $m_{\pi_T^0}$ for a fixed value of techniquark mass (left) and as a function of techniquark mass M_{Q_T} for a fixed value of technipion mass (right).

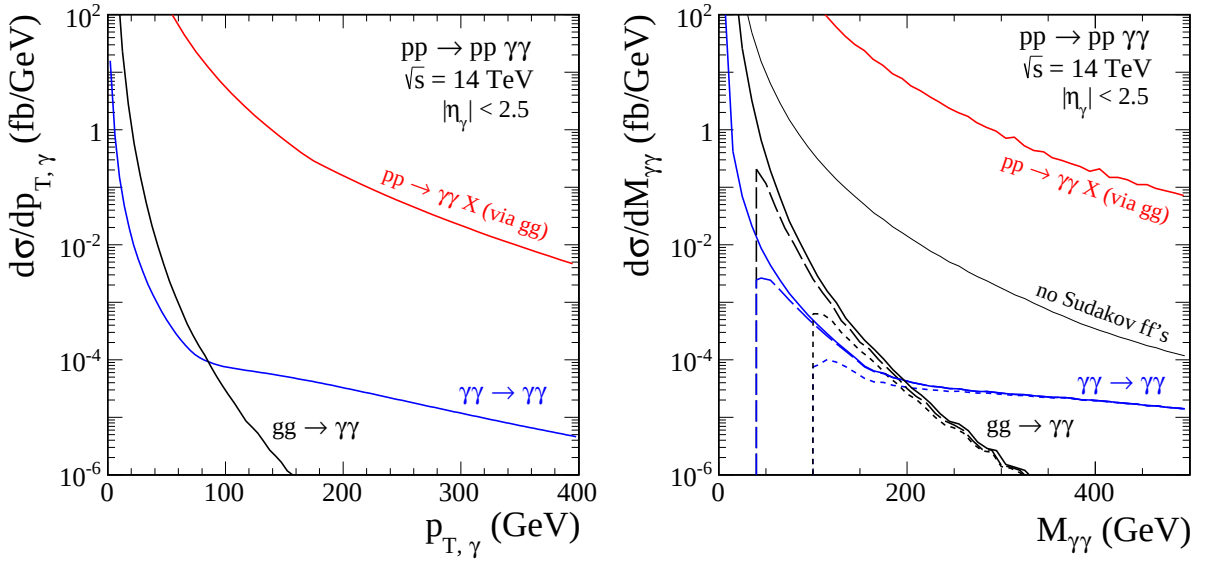

Figure 5.30: Distribution in the photon transverse momentum and in the invariant mass of the two-photon system for the QCD mechanism (black lines) and QED $\gamma\gamma$ fusion mechanism (blue lines) at $\sqrt{s} =$ 14 TeV. We present results without an extra cut (solid line) and with cut on transverse momenta of both outgoing photons $p_{\perp,\gamma} > 20, 50$ GeV (long dashed, dashed lines, respectively). For the QCD mechanism the result without the Sudakov form factors is shown for comparison. The most upper red solid line corresponds to the inclusive two-gluon initiated $pp \to \gamma\gamma X$ component.

dakov form factors. As can be seen from the figure, the Sudakov form factors strongly damp the cross section, especially at larger photon-photon invariant masses. Assuming the experimental resolution in the invariant $\gamma\gamma$ mass of about 5 GeV or so, the background turns out to be by two orders of magnitude smaller than the corresponding technipion signal for the whole range of vector-like TC model parameters considered here. To summarize, the signal-to-background ratio in exclusive technipion production process is by far better than that in inclusive technipion production [422]. The latter is clear from comparing the corresponding inclusive $\gamma\gamma$ background estimates which were done earlier in the Higgs boson $\gamma\gamma$ signal studies at the LHC [398,399,402] and typical inclusive technipion production cross sections shown e.g. in Fig. 5.24.

In Table 5.1 we list the total $pp \to pp\gamma\gamma$ exclusive cross sections at the LHC ($\sqrt{s} = 14$ TeV) for the QCD $gg \to \gamma\gamma$ and QED $\gamma\gamma \to \gamma\gamma$ mechanisms in separate 50 GeV - windows in diphoton $\gamma\gamma$ invariant mass $M_{\gamma\gamma}$ placed between 50 and 400 GeV of diphoton invariant mass. A

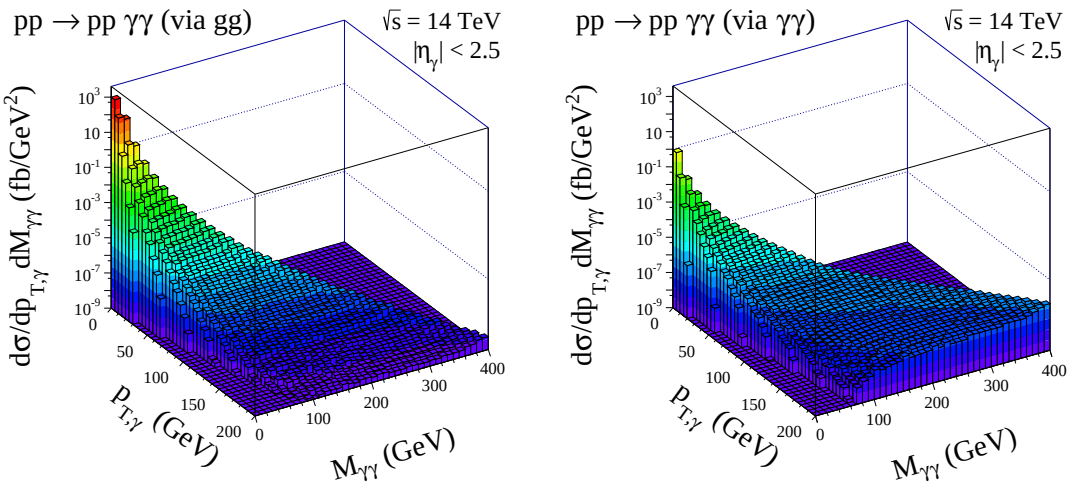

Figure 5.31: Two-dimensional distributions in $(p_{\gamma\perp}, M_{\gamma\gamma})$ for the diphoton production for the gg fusion (left panel) and the $\gamma\gamma$ fusion (right panel) in pp collisions at the nominal LHC energy $\sqrt{s} = 14$ TeV and $|\eta_\gamma| < 2.5$.

Table 5.1: The cross sections (in fb) for photon-pair central exclusive production at $\sqrt{s} = 14$ TeV in the photon pseudorapidity $|\eta_\gamma| < 2.5$ and with cuts in $p_{\perp,\gamma} > 50$ GeV on both outgoing photons. Different choices of gluon PDF [191, 192, 386] are used at quite small values of gluon transverse momenta $q^2_{\perp,min} = 0.5$ GeV^2.

$M_{\gamma\gamma}$	σ (fb) at $\sqrt{s} = 14$ TeV and $\|\eta_\gamma\| < 2.5$					
	$\gamma\gamma \to \gamma\gamma$		$gg \to \gamma\gamma$, GJR08VFNS NLO		$gg \to \gamma\gamma$, MSTW08 NLO	
	no cuts $p_{\perp,\gamma}$	$p_{\perp,\gamma} > 50$ GeV	no cuts $p_{\perp,\gamma}$	$p_{\perp,\gamma} > 50$ GeV	no cuts $p_{\perp,\gamma}$	$p_{\perp,\gamma} > 50$ GeV
50 – 100	97.01×10^{-3}	–	3.048	–	2.752	–
100 – 150	11.62×10^{-3}	4.10×10^{-3}	62.72×10^{-3}	22.55×10^{-3}	67.08×10^{-3}	23.20×10^{-3}
150 – 200	2.96×10^{-3}	2.01×10^{-3}	5.90×10^{-3}	4.21×10^{-3}	6.84×10^{-3}	4.74×10^{-3}
200 – 250	1.78×10^{-3}	1.51×10^{-3}	0.95×10^{-3}	0.79×10^{-3}	1.15×10^{-3}	0.94×10^{-3}
250 – 300	1.44×10^{-3}	1.34×10^{-3}	0.23×10^{-3}	0.21×10^{-3}	0.29×10^{-3}	0.25×10^{-3}
300 – 350	1.23×10^{-3}	1.19×10^{-3}	0.06×10^{-3}	0.05×10^{-3}	0.07×10^{-3}	0.07×10^{-3}
350 – 400	1.06×10^{-3}	1.05×10^{-3}	0.02×10^{-3}	0.02×10^{-3}	0.03×10^{-3}	0.02×10^{-3}

realistic cut on both photon pseudorapidities $|\eta_\gamma| < 2.5$ is imposed. For comparison, we show numerical results with an extra cut on transverse momenta of both outgoing photons $p_{\perp,\gamma} > 50$ GeV and without it, as well as for two different choices of the gluon PDFs [191, 192, 386] entering the calculation of UGDF in the Durham approach (c.f. Eq. (5.9)). As we have already observed in Fig. 5.30, the QCD component of the exclusive $\gamma\gamma$ background dominates only for smaller invariant masses $M_{\gamma\gamma} \lesssim 200$ GeV, while for larger ones the QED mechanism becomes important. Observation of much larger cross section in only one of the windows than those given in Table 5.1 would be then a probable signal of a new resonance (e.g. technipion). On the other hand, observation of much larger cross section in many windows simultaneously would be a signal of new particles appearing in loops.

5.6 Conclusions

We have calculated the QCD diffractive contribution to the exclusive $pp \to pW^+W^-p$ process with the full one-loop $gg \to W^+W^-$ matrix element. Two mechanisms have been considered. First mechanism is a virtual (highly off-shell) Higgs boson production and its subsequent transformation into real W^+W^- pair. Second mechanism relies on the formation of intermediate quark boxes, very much similar to ones in the exclusive two photon production mechanism.

We have calculated corresponding amplitudes using computer program package `FormCalc`. We have made a first estimate of the cross section using amplitudes in the forward limit "corrected" off-forward via a simple exponential (slope dependent) extrapolation.

In order to gain confidence to our calculations and the formalism used we have considered also the $p\bar{p} \to p\bar{p}\gamma\gamma$ process which was measured recently by the CDF Collaboration. Here the formalism of calculating quark box diagrams is essentially the same as for the exclusive production of W^+W^- pairs. We have obtained very nice agreement with experimental diphoton invariant mass distribution.

Having verified the formalism for diphoton production we have performed similar calculation for W^+W^- production. Differential distributions in the $W^\pm$ transverse momentum, rapidity and W^+W^- pair invariant mass have been calculated and compared with corresponding distributions for discussed in the literature $\gamma\gamma \to W^+W^-$ mechanism. The contribution of triangles with the intermediate Higgs boson turned out to be smaller than the contribution of boxes taking into account recent very stringent limitations on Higgs boson mass from Tevatron and LHC data. We have calculated several differential distributions and discussed their characteristic features. We have found that, in contrast to exclusive production of Higgs boson or dijets, the two-photon fusion dominates over the diffractive mechanism for small four-momentum transfers squared in the proton lines (t_1, t_2) as well as in a broad range of W^+W^--pair invariant masses, in particular, for large M_{WW}. Estimated theoretical uncertainties cannot disfavour this statement. The large M_{WW} region is damped in the diffractive model via scale dependence of the Sudakov form factor. From the experimental side, one could focus on the diffractive contribution by imposing lower cuts on t_1 and/or t_2 using very forward detectors on both sides of the interaction point at distances of 220 m and 420 m as planned for future studies at ATLAS and CMS. The corresponding cross section is, however, expected to be extremely low.

Compared to the previous studies in the effective field theory approach, in this work we have included complete one-loop (leading order) $gg \to W^+W^-$ matrix element, and have shown that extra box diagrams, even though they are larger than the resonant (s-channel Higgs) diagrams, constitute a negligibly small background for a precision study of anomalous couplings.

The unique situation of the dominance of the $\gamma\gamma \to W^+W^-$ contribution over the diffractive one opens a possibility of independent tests of the Standard Model as far as the triple-boson γWW and quartic-boson $\gamma\gamma WW$ coupling is considered. It allows also for stringent tests of some Higgsless models as discussed already in the literature (see e.g. Ref. [356, 357]).

We have made a first analysis of an interesting possibility to search for technipions mostly decaying into two photons in exclusive $pp \to pp\gamma\gamma$ process at the LHC. We have considered a particularly interesting case of light technipions which do not directly interact with gluons and quarks to the leading order, but can interact only with SM gauge bosons. A single technipion in this case can only be produced via a techniquark triangle loop in a vector boson fusion channel. The latter specific properties of physical technipions are predicted, in particular, by recently suggested phenomenologically consistent vector-like Technicolor (TC) model [422]. We have calculated the dependence of the $pp \to pp\pi_T^0$ cross section on the vector-like TC model parameters. With a natural choice of parameters obtained by a mere QCD rescaling the corresponding cross sections of the order of one to a few femtobarns could be expected. This means that the exclusive π_T^0 production cross section can be of the same order or even exceeds the traditional Higgs boson CEP cross section [99–101, 211, 342–344] making the considered proposal very important for the forward physics program at the LHC [128, 239].

The produced Higgs boson predominantly decays into $b\bar{b}$ pair which competes with irreducible $b\bar{b}$ background. As was shown in Refs. [211, 344] the major problem with central exclusive Higgs production is rather large irreducible $b\bar{b}$ background, and corresponding kinematical cuts maximizing S/B ratio strongly reduce the signal down to a few events per year. The considered technipion CEP, the largest (of the order of one) branching fraction is in the $\gamma\gamma$ decay channel. In order to study the competitiveness of the considered exclusive π_T^0 production we considered direct irreducible $\gamma\gamma$ production via QCD $gg \to \gamma\gamma$ and QED $\gamma\gamma \to \gamma\gamma$ subpro-

cesses. After inclusion of the ATLAS detector resolution, the S/B ratio for the technipion CEP is significantly better than that of the Higgs boson CEP. The latter is thus considered to be an attractive channel for New Physics searches in forward physics at the LHC.

We have demonstrated that for not too large technipion masses the photon-photon decay channel has the largest branching fraction. This shows that the exclusive reaction $pp \to pp\gamma\gamma$ is probably the best suited in searches for technipions at the LHC. The light-by-light rescattering subprocess contribution to the exclusive diphoton signal at the LHC in the region of large diphoton invariant masses is interesting in its own right as a good probe in searches for effects beyond the Standard Model (e.g. supersymmetry, Dirac monopoles, etc.). All this makes the $pp \to pp\gamma\gamma$ reaction particularly interesting for LHC phenomenology.

We have therefore studied expected Standard Model exclusive $\gamma\gamma$ backgrounds. We have considered two important sources of the non-resonant background: the Durham QCD mechanism (via $gg \to \gamma\gamma$ subprocess) and the QED mechanism (via $\gamma\gamma \to \gamma\gamma$ subprocess). In the later case we have included full set of box diagrams with lepton, quark and W boson loops thus focusing on the dominant Standard Model processes only. The photons are produced dominantly at midrapidities similarly for the exclusive technipion production as expected. The most interesting is the distribution in diphoton invariant mass. At lower invariant masses, the Durham QCD mechanism dominates. At larger invariant masses, the light-by-light rescattering occurs to be more relevant background in searches for technipions. We conclude that the signal-to-background ratio would be very favorable in the reaction under consideration.

In the present analysis we have considered purely exclusive processes, i.e. we have assumed that the both outgoing protons are detected. This is not yet possible at the LHC, but could be possible when forward proton detectors are installed by the ATLAS and/or CMS collaborations. We hope that this will be possible in a close future [239]. The particularly interesting ones are distributions in azimuthal angle between outgoing protons. The outgoing protons are scattered dominantly to perpendicular azimuthal directions. In principle, one could also allow semi-exclusive (e.g. single diffractive) processes when excited states of proton (proton resonances or continuum) are produced while the pile-up problem has to be solve in high luminosity runs.

Chapter 6

Summary and Outlook

The main goal of the studies presented in this thesis was to give a comprehensive description of several phenomena in the exclusive particle production in hadron-hadron interactions from low to high energies. Particular attention was devoted to the non-perturbative (soft) processes in the RHIC, Tevatron and LHC energy regime which constitute a valuable "laboratory" for studies of specific effects induced by strong and electromagnetic interactions. Starting from the general assumption about the form of production mechanism of exclusive processes, the predictions for the total cross sections of dihadron/diboson continuum together with the resonance/technipion signals have been performed and some observables typically measured in the experiment have been analysed. These processes may serve a valuable contribution for future experimental analyses. The aim of this thesis was to encourage experimentalists to perform such searches. Therefore, the study was done in the context of the different measurements performed from low (PANDA, COMPASS) to high (RHIC, Tevatron, LHC) energies.

Attempts at a partial synthesis of the presented results were made in each Chapter separately. Below, a set of more general remarks is presented, limited to the subjects which the author thinks are most interesting for consideration in view of future studies.

1. We have shown that very close to production threshold the pion-pion rescattering mechanism gives much smaller contribution than the excitation of the Roper resonance via σ-exchange and its subsequent decay $N^*(1440) \to N(\pi\pi)^{S-\text{wave}}_{I=0}$ and/or the double-Δ excitation and subsequent decays. At low energies all these mechanisms overlap and it is not possible to extract the pion-pion rescattering contributions and therefore not possible to study the $\pi^0\pi^0 \to \pi^+\pi^-$ process. Such exclusive production of pion pairs at sufficiently large energy could be measured e.g. by the PANDA experiment at the Facility for Antiproton and Ion Research in Darmstadt. Particularly interesting is the distribution in two-pion invariant mass, see Fig. 1.8, where one should observe bumps related to the famous scalar-isoscalar σ-meson and to tensor-isoscalar $f_2(1270)$ meson as well as a dip from the interference with $f_0(980)$ and σ mesons. We predict the dominance of the pion-pion contribution close to the threshold. Our calculation shows that the diffractive components (in fact its upper limit for the QCD mechanism) are by more than order of magnitude smaller than the pion-pion fusion component in the energy region of future PANDA experiment.

2. We have made detailed numerical predictions for several central exclusive scalar and pseudoscalar mesons in proton-proton collisions. A special attention was devoted to analysis within a new tensor model of soft pomeron. We wish to emphasize that the tensorial pomeron can, at least, equally well describe experimental WA102 data as the less theoretically justified vectorial pomeron frequently used in the literature. The existing low-energy experimental data do not allow to clearly distinguish between the two models as the presence of subleading reggeon exchanges is at low energies very probable for many reactions. This seems to be the case for the η meson production. In these cases we have included in our analysis also exchanges of subleading trajectories which significantly improve the

agreement with experimental data. Production of η' meson seems to be less affected by contributions from subleading exchanges. It would clearly be interesting to extend our study to central exclusive production of other mesons like the $f_2(1270)$ and go to higher energies, where the dominance of the pomeron exchange can be better justified. Future experimental data on central exclusive production of mesons at higher energies may provide a better information on the spin structure of the pomeron and its coupling to the nucleon and mesons. On the other hand the low energy data could help in understanding the role of subleading trajectories.

3a. We have provided a detailed description of a phenomenological model for the $pp \to pp\pi^+\pi^-$ (K^+K^-) reactions within the framework of Regge theory. Such a model compares well to the existing ISR data on exclusive $\pi^+\pi^-$ and K^+K^- production, but the new preliminary CDF data on pion pairs presented in [159–161], as well as the forthcoming data from RHIC [158], ATLAS, ALICE [162], CMS, and LHCb will be crucial to perform an extensive tests of this approach in a broad range of energy. We have demonstrated how different observables may be used to further test and constrain some its phenomenological ingredients (the off-shell meson form factor, the reggeization of exchanged meson, etc.). Furthermore, absorption effects are frequently taken into account by simply multiplying cross sections with a gap survival factor. We have shown that the distribution in azimuthal angle between the outgoing protons and the t distributions are highly sensitive to absorption effects. The deviation from "bare" distributions is more significant at high energies where the absorptive corrections are expected to be larger. In this way, measurements of exclusive meson pair production with tagged protons may be used as a novel probe of the models of hadronic interactions used to calculate the soft survival factors which are essential for understanding exclusive diffractive processes. Such measurements are possible at the LHC, with the ATLAS+ALFA [7] and CMS+TOTEM during special low luminosity runs, and already started at RHIC by the STAR Collaboration.

3b. This dimeson continuum production process also represents an irreducible background to the central exclusive production of resonant states (f_0, f_2, $\chi_{c(0,2)}$) via two-body decays to $M\bar{M}$ mesons. We find that the relative contribution of $\chi_{c(0)}$ resonant and dipion/dikaon continuum strongly depend on the cut on pion/kaon transverse momentum. The cuts play then a role of the $\pi\pi$ or KK resonance filter and may explain some different controversial observations by different experiments in the past. For the resonances decaying e.g. into the $\pi\pi$ channel an interference of the resonance signals with the two-pion continuum has to be included in addition. This requires a consistent model of the resonances and the non-resonant background. It would be very interesting to see if the exchange of tensorial pomerons may modify differential distributions for the $\pi^+\pi^-$ continuum compared to the existing calculations (e.g. [3, 6]). It concerns also the central exclusive production of the ρ^0 meson at high energies. Here the dominant mechanism is a photon-pomeron (pomeron-photon) fusion.

4a. The exclusive production processes with very forward neutral particles radiated off the initial and final state protons can significantly extend the physics programme at high-energy hadron colliders. Zero Degree Calorimeters (ZDC's) could be used for such studies. Such measurements can be an interesting and useful supplement to the central multipurpose LHC detectors (ATLAS, CMS) and the forward proton detectors (ALFA, TOTEM). It should be noted that for the exclusive π^0 meson production [9] the diffractive bremsstrahlung contributions dominate at large (forward, backward) rapidities and cross section of the order of mb is predicted, see Fig. 6.1 (left panel). Furthermore, we suggest a possibility of unique search for the odderon contribution at midrapidity and $p_{\perp,\pi^0} > 0.2$ GeV. Moreover, the precisely evaluated photoproduction mechanism in the $pp \to pp\omega$ process [5] constitutes a background for the odderon exchange searches. At small energies the photon-pomeron contribution described within the k_t-factorization approach is negligible compared to the

bremsstrahlung contributions (due to strong coupling of the ω meson to protons). It could be, however, identified at the LHC energies at the ω-meson midrapidity.

The integrated diffractive bremsstrahlung cross section for the exclusive $pp \to pp\gamma$ reaction [10] is only of the order of μb ($E_\gamma > 100$ GeV). We have considered different mechanisms for the first time in the literature, see Fig. 6.1 (right panel). Since this process was never studied at high energies it is worth to make efforts to obtain first experimental cross sections. Such non-diffractive exchanges represent a potential background in the analysis of diffraction at high energies. A good understanding of electromagnetic processes, as well as of Regge exchanges, is therefore mandatory. This would allow to test our understanding of the diffractive process and help in pinning down some hadronic and electromagnetic off-shell form factors, difficult to test otherwise.

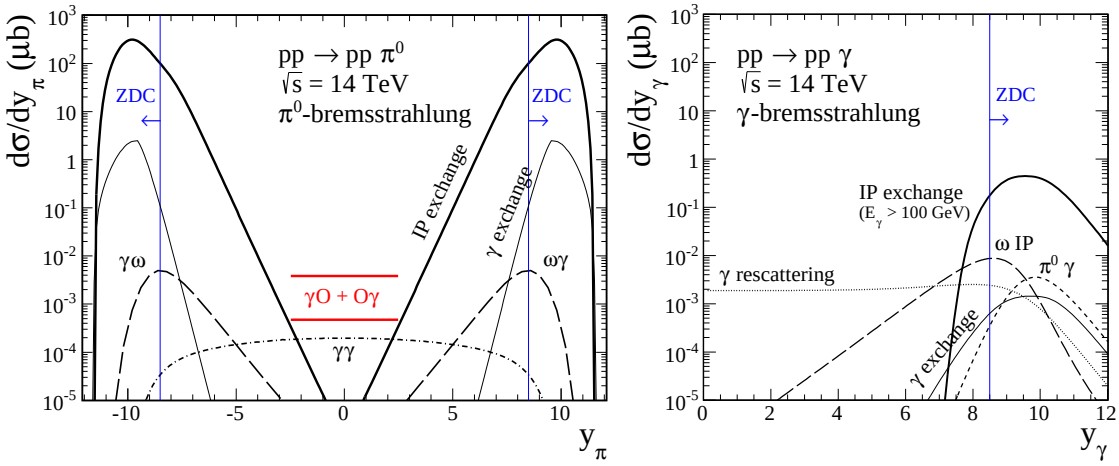

Figure 6.1: The rapidity distributions for $pp \to pp\pi^0$ (left panel) and $pp \to pp\gamma$ (right panel) at c.m. energy $\sqrt{s} = 14$ TeV. The π^0- and γ-bremsstrahlung mechanisms contribute at large forward and backward rapidity regions. The contributions from other mechanisms are also shown, e.g. the photon-odderon exchange ($\gamma O + O\gamma$) contributes at midrapidity of pion. The odderon-photon contribution is calculated for the HERA upper limit [270] (top red line) and for the Ewerz-Nachtmann estimate [271] (bottom red line). The lower limit for the CMS ZDC detectors is shown by the vertical lines.

4b. The $pp \to pp\pi^0$ process constitutes diffractive non-resonant background that contributes at small $\pi^0 p$ invariant mass and could be therefore misinterpreted as the Roper resonance. Issues such as the influence of baryon resonance production in view of diffractive processes also require further theoretical and experimental investigations. The bremsstrahlung mechanisms contribute also to the $pp \to p(n\pi^+)$ reaction. Both channels give a sizeable contribution to the low-mass single diffractive cross section and must be included in extrapolating the measured experimental single diffractive cross section. Furthermore, we have found very large cross section for the $pp \to nn\pi^+\pi^+$ reaction [4] due to interference of a few mechanisms what precludes extraction of the elastic $\pi^+\pi^+$ scattering cross section, but it is very interesting in the present context of low-mass double diffractive cross section. The hypothesis of low-mass excitations of nucleons in the large pseudorapidites region in hadron-hadron collisions calls for a detailed study and verification in view of future studies.

4c. A very interesting is also exclusive production of vector ρ^0 meson, ρ^0 excited states (e.g. $\rho(1450)$, $\rho(1700)$) and their subsequent decay into charged and/or neutral pions in proton-nucleus or nucleus-nucleus (pA or AA) collisions, which can be measured by the STAR experiment at the RHIC and in experiments at the LHC, e.g. by the ALICE Collaboration. The exclusive production of $\rho^0 \to \pi\pi$ meson (via the $\gamma I\!P$ and $I\!P\gamma$ mechanism) as well as the $\pi\pi$ continuum in pA or AA collisions are interesting by itself. It concerns also the

exclusive production of the $f_2(1270) \to \pi\pi$ via the $\gamma\gamma$-fusion [1]. The region of resonances can be measured already by the ALICE and STAR Collaborations with low statistics, while the measurements for large invariant masses, that is, the exclusive $\pi^+\pi^-$ production in the perturbative region, requires better statistics. Having the absolutely normalized cross sections is very important in this context. The $pA \to pA(X \to \pi\pi)$ process is naively enhanced only by the Z^2 factor [2] compared to the Z^4 factor for the $AA \to AA(\gamma\gamma \to \pi\pi)$ process discussed recently in [440]. A real comparison to future data will require inclusion of both mechanisms. This requires further development of diffractive processes and thus allow for a better understanding of nuclear effects in high energy photon-nucleus interactions.

5a. We have calculated the QCD diffractive contribution to the exclusive $pp \to pW^+W^-p$ and $pp \to pW^+W^-p$ processes with full one-loop $gg \to W^+W^-$ and $gg \to \gamma\gamma$ matrix elements. We have obtained very nice agreement with experimental diphoton invariant mass distribution obtained by the CDF Collaboration [355] for three different gluon distributions. The large diboson invariant mass region is damped in the diffractive model via scale dependence of the Sudakov form factor and soft gap survival factor. The unique situation of the dominance of the $\gamma\gamma \to W^+W^-$ contribution over the diffractive one opens a possibility of independent tests of the Standard Model as far as the triple-boson γWW and quartic-boson $\gamma\gamma WW$ gauge couplings are considered.

5b. We have made a first analysis of an interesting possibility to search for technipions mostly decaying into two photons in exclusive $pp \to pp\gamma\gamma$ process at the LHC. The current analysis discusses also important aspects of the exclusive two-photon production in general. We have considered two important sources of the non-resonant background: the QCD mechanism (via $gg \to \gamma\gamma$ subprocess) and the QED mechanism (via $\gamma\gamma \to \gamma\gamma$ subprocess). In the later case we have included full set of box diagrams with lepton, quark and W boson loops focusing on the dominant Standard Model processes only. At large $\gamma\gamma$ invariant masses the QED $\gamma\gamma \to \gamma\gamma$ process dominates over the QCD $gg \to \gamma\gamma$ process. This is interesting by itself and rather unique. Any deviation from the Standard Model production may be a signal of New Physics contributions. It would be wise to use the opportunity at the LHC.

We thus suggest to search for both continuum and $\gamma\gamma$-resonance signals of New Physics. In general, there is a non-negligible possibility that potential, yet unknown, weaker resonances which decay mostly into two photons could be very difficult to identify in the inclusive measurements, at least, at current level of statistics. In such cases an exclusive measurement has the advantage that $\gamma\gamma$-resonance signals could be "enhanced" relative to the two-photon background offering important advantages compared to new $\gamma\gamma$-resonance searches in inclusive production. Here we considered an important case of light exotic resonances, the pseudo-Goldstone technipions, commonly predicted by Technicolor extensions of the Standard Model. The exclusive technipion production in the dominant $\gamma\gamma \to \pi_T^0 \to \gamma\gamma$ mode has advantages compared to the inclusive technipion (VBF) production since (1) this mode is not suppressed compared to the standard central exclusive Higgs boson production [3] and (2) the respective $\gamma\gamma$ backgrounds are suppressed at large $M_{\gamma\gamma}$. These advantages make the central exclusive technipion production favorable compared to the inclusive technipion production. The QED process is therefore an attractive

[1] For a review of recent theoretical studies on exclusive J/Ψ and Y meson production in nucleus-nucleus collisions we refer readers to [437] as well as on the exclusive single and double ρ^0 meson production [438] and references therein. From experimental point of view, the single-ρ^0 exclusive cross section $AA \to AA\rho^0$ was measured by the STAR experiment at RHIC [439].

[2] The Z factor is the atomic number (also known as the proton number) and represents the number of protons found in the nucleus of an atom and therefore identical to the charge number of the nucleus.

[3] We conclude that the S/B ratio for the technipion CEP is significantly better than that of the Higgs boson CEP.

channel for New Physics searches (e.g. the hypothetical massless graviton with spin-2 or an electrically-charged supermassive magnetic monopoles) in forward physics at the LHC. This is also one of arguments for installation of forward tagging facility at ATLAS and CMS.

As a final remark, the author wishes to point at the interplay of different phenomena acting in the "soft" and "hard" kinematic regimes, where both diffractive and electromagnetic processes play an important role. For instance, the phenomenological Regge model although not firmly grounded in QCD, still presents an interesting and rich phenomenology, which at the beginning to be explored with new analyses from the Tevatron and forthcoming data from the LHC and RHIC. As the transverse momentum of meson increases, we would not expect to trust this approach, and so we must instead consider a pQCD formalism. Both approaches lead to many non-trivial predictions and displays several remarkable theoretical features. The central exclusive production of mesons therefore represents a process of much phenomenological interest, which can shed light on both perturbative and non-perturbative aspects of QCD. We may hope in the future to experimentally probe the transition between these two regimes, an issue which is still unclear. Moreover it is of particular experimental relevance, with a range of forthcoming and existing hadron collider data to be considered. In the author's personal opinion, this is exactly what makes exclusive processes so much exciting. The results presented in this thesis show the excellent potential for future measurements of exclusive processes. It is only to be hoped that the analysis presented in this thesis may be of some help in future phenomenological and experimental studies in this field.

Appendix A

Kinematics

In this section we give some kinematic relations needed for calculating the amplitudes for the reactions presented in this thesis.

A.1 Kinematic relations

The energy E and three-momentum $\vec{p}$ of particle form a four-vector $p = (E, \vec{p}\,)$ whose square $p^2 \equiv E^2 - |\vec{p}|^2 = m^2$. The scalar product of two four-momenta is invariant (frame independent). The following relations hold, cf. (3.2),

$$\begin{aligned} s_{13} &= (p_a + q_2)^2 = (s - 2m_p^2)\,\xi_2 + m_p^2 + t_2\,, \\ s_{23} &= (p_b + q_1)^2 = (s - 2m_p^2)\,\xi_1 + m_p^2 + t_1\,, \end{aligned} \tag{A.1}$$

where $\xi_1 = \dfrac{p_b \cdot q_1}{p_b \cdot p_a}$ and $\xi_2 = \dfrac{p_a \cdot q_2}{p_a \cdot p_b}$. We consider now the three-body reaction (3.1) in the overall c.m. system with the z axis along $\vec{p}_a$. We have then

$$\begin{aligned} p_a &= \begin{pmatrix} p_a^0 \\ 0 \\ 0 \\ |\vec{p}_a| \end{pmatrix}, \quad p_b = \begin{pmatrix} p_b^0 \\ 0 \\ 0 \\ -|\vec{p}_b| \end{pmatrix}, \\ p_a^0 &= p_b^0 = \frac{\sqrt{s}}{2}, \quad |\vec{p}_a| = |\vec{p}_b| = \frac{1}{2}\sqrt{s - 4m_p^2}\,. \end{aligned} \tag{A.2}$$

With $i = 1, 2$ we get

$$\begin{aligned} p_i &= \begin{pmatrix} p_i^0 \\ \vec{p}_{i\perp} \\ p_{iz} \end{pmatrix}, \quad q_i = \begin{pmatrix} q_i^0 \\ \vec{q}_{i\perp} \\ q_{iz} \end{pmatrix}, \\ \vec{p}_{i\perp} &= |\vec{p}_{i\perp}| \begin{pmatrix} \cos\phi_i \\ \sin\phi_i \end{pmatrix}, \quad \vec{q}_{i\perp} = -\vec{p}_{i\perp}\,. \end{aligned} \tag{A.3}$$

The azimuthal angle ϕ_{pp} between the two outgoing protons in (3.1) is given by

$$\phi_{pp} = \phi_{12} = \phi_1 - \phi_2\,. \tag{A.4}$$

The "glueball variable" [92] $dP_\perp = |d\vec{P}_\perp|$ is defined by the difference of the transverse momentum vectors

$$d\vec{P}_\perp = \vec{q}_{1\perp} - \vec{q}_{2\perp} = \vec{p}_{2\perp} - \vec{p}_{1\perp}\,. \tag{A.5}$$

Further relations are as follows (no summation over i in (A.7) for $\xi_i t_i$)

$$m_M^2 = k^2 = 2q_1q_2 + t_1 + t_2$$
$$= \frac{(s-2m_p^2)^3}{s(s-4m_p^2)}\xi_1\xi_2 + t_1 + t_2 - 2\vec{q}_{1\perp}\cdot\vec{q}_{2\perp} + \frac{(s-2m_p^2)}{s(s-4m_p^2)}\left[t_1t_2 - 2m_p^2(t_1\xi_2 + t_2\xi_1)\right], \quad (A.6)$$

$$t_i = -\vec{q}_{i\perp}^2 + \frac{1}{s(s-4m_p^2)}\left[(s-2m_p^2)^2(\xi_i t_i - \xi_i^2 m_p^2) - t_i^2 m_p^2\right], \quad (A.7)$$

$$p_i^0 = \frac{\sqrt{s}}{2}(1-\xi_i) + \frac{1}{2\sqrt{s}}(2m_p^2\xi_i - t_i), \quad (A.8)$$

$$\varepsilon_{\mu_1\mu_2\rho\sigma}(p_1+p_a)^{\mu_1}(p_2+p_b)^{\mu_2}(q_1-q_2)^{\rho}(q_1+q_2)^{\sigma} = -8\sqrt{s}\,\vec{p}_a\cdot(\vec{p}_{1\perp}\times\vec{p}_{2\perp})$$
$$= 8\sqrt{s}\,|\vec{p}_a||\vec{p}_{1\perp}||\vec{p}_{2\perp}|\sin\phi_{pp}. \quad (A.9)$$

In Fig.3.10 and 3.20 we have shown distributions in rapidity, y_M, and pseudorapidity, η_M, of the produced meson M in the overall c.m. system. We discuss here their kinematic relation. We have, with

$$k = \begin{pmatrix} k^0 \\ \vec{k}_\perp \\ k_z \end{pmatrix} \quad (A.10)$$

the four-momentum of meson M ($k^2 = m_M^2$)

$$y_M = \frac{1}{2}\ln\frac{k^0+k_z}{k^0-k_z} = \ln\frac{\sqrt{k_z^2+\vec{k}_\perp^2+m_M^2}+k_z}{\sqrt{\vec{k}_\perp^2+m_M^2}}, \quad (A.11)$$

$$\eta_M = \frac{1}{2}\ln\frac{|\vec{k}|+k_z}{|\vec{k}|-k_z} = \ln\frac{\sqrt{k_z^2+\vec{k}_\perp^2}+k_z}{\sqrt{\vec{k}_\perp^2}}. \quad (A.12)$$

Let us consider now the distributions of meson M in $(y_M, \vec{k}_\perp^2)$ and $(\eta_M, \vec{k}_\perp^2)$. We have

$$f(y_M,\vec{k}_\perp^2)dy_M d(\vec{k}_\perp^2) = \tilde{f}(\eta_M,\vec{k}_\perp^2)d\eta_M d(\vec{k}_\perp^2), \quad (A.13)$$

$$\tilde{f}(\eta_M,\vec{k}_\perp^2) = f(y_M,\vec{k}_\perp^2)\frac{\partial y_M/\partial k_z}{\partial\eta_M/\partial k_z}\,|_{\vec{k}_\perp^2\text{ fixed}}, \quad (A.14)$$

where

$$\frac{\partial y_M/\partial k_z}{\partial\eta_M/\partial k_z}\,|_{\vec{k}_\perp^2\text{ fixed}} = \frac{\sqrt{k_z^2+\vec{k}_\perp^2}}{\sqrt{k_z^2+\vec{k}_\perp^2+m_M^2}} \equiv w(k_z,\vec{k}_\perp^2). \quad (A.15)$$

Clearly, for large $|y_M|$ and correspondingly large $|\eta_M|$ we have $|k_z| \gg m_M$ and the transformation factor $w(k_z,\vec{k}_\perp^2) \to 1$. On the other hand, for $|y_M| \to 0$ corresponding to $|\eta_M| \to 0$ and $k_z \to 0$ we have $w(0,\vec{k}_\perp^2) < 1$. Thus, we conclude that, for fixed $\vec{k}_\perp^2 \neq 0$ a y_M distribution which is roughly constant for $|y_M| \to 0$ will give a dip in the η_M distribution for $|\eta_M| \to 0$. A dip in the y_M distribution for $|y_M| \to 0$ will be deepened in the η_M distribution. To get the y_M and η_M distributions of Fig.3.10 and 3.20 we still have to integrate in (A.13) over $\vec{k}_\perp^2$. We note, however, that integration over $\vec{k}_\perp^2$ at fixed y_M is, in general, not the same as integration at fixed η_M. Nevertheless, if the unintegrated distributions of (A.13) in $(y_M,\vec{k}_\perp^2)$, respectively $(\eta_M,\vec{k}_\perp^2)$, behave "reasonably" we should be able to replace $\vec{k}_\perp^2$ by some mean value $\langle\vec{k}_\perp^2\rangle$. Then the above

features will survive. That is, a y_M distribution being roughly constant for $|y_M| \to 0$ will give a dip for $|\eta_M| \to 0$, as observed in Fig.3.10. A dip in the y_M distribution for $|y_M| \to 0$ will be deepened in the η_M distribution, as observed in Fig.3.20.

Feynman's x (x_F) variable in the center-of-mass frame is given by

$$x_F = \frac{2p_z}{\sqrt{s}} = \frac{2m_\perp \sinh y}{\sqrt{s}}\,, \tag{A.16}$$

where $m_\perp$ is the transverse mass given by $m_\perp^2 = m^2 + p_x^2 + p_y^2$.

We consider now the high-energy small-angle limit where we require in reaction (3.1)

$$|t_1|, |t_2| \ll m_p^2\,, \quad m_M^2 \ll s\,, \quad \xi_1, \xi_2 = \mathcal{O}(m_M/\sqrt{s})\,. \tag{A.17}$$

In this limit ξ_1 and ξ_2 are the fractional energy losses of the protons with momenta p_a and p_b, respectively; and we have the simple relations

$$\xi_1 \cong \frac{s_{23}}{s}\,, \quad \xi_2 \cong \frac{s_{13}}{s}\,, \quad m_M^2 \cong s\xi_1\xi_2 \cong \frac{s_{13}s_{23}}{s}\,, \quad t_1 \cong -\vec{q}_{1\perp}^{\,2}\,, \quad t_2 \cong -\vec{q}_{2\perp}^{\,2}\,; \tag{A.18}$$

$$\bar{u}(p_1,\lambda_1)\gamma^\mu u(p_a,\lambda_a) \cong (p_1+p_a)^\mu \delta_{\lambda_1\lambda_a}\,,$$
$$\bar{u}(p_2,\lambda_2)\gamma^\mu u(p_b,\lambda_b) \cong (p_2+p_b)^\mu \delta_{\lambda_2\lambda_b}\,; \tag{A.19}$$

$$(p_1+p_a, p_2+p_b) \cong 2s\,; \tag{A.20}$$

$$(q_1, p_2+p_b)(q_2, p_1+p_a) - (q_1,q_2)(p_1+p_a, p_2+p_b) \cong 2s\,\vec{p}_{1\perp}\cdot\vec{p}_{2\perp} = 2s\,|\vec{p}_{1\perp}||\vec{p}_{2\perp}|\cos\phi_{pp}\,. \tag{A.21}$$

We see from (A.17) and (A.18) that in this limit both subenergies squared become large

$$s_{13}, s_{23} = \mathcal{O}(m_M\sqrt{s})\,. \tag{A.22}$$

A.2 Cross section and phase space

The cross section for the three-body reaction $pp \to ppM$ is calculated as

$$\sigma = \int \frac{1}{2\sqrt{s(s-4m_N^2)}}\,\overline{|\mathcal{M}|^2} d^3PS \tag{A.23}$$

by choosing convenient kinematical variables. The matrix element depends on the process and m_N is the mass of the nucleon. The three-body phase space volume element reads

$$d^3PS = \frac{d^3p_1}{2E_1(2\pi)^3}\frac{d^3p_2}{2E_2(2\pi)^3}\frac{d^3p_M}{2E_M(2\pi)^3}\,(2\pi)^4\delta^4(p_a+p_b-p_1-p_2-p_M)\,. \tag{A.24}$$

At high energies and small momentum transfers the phase space volume element can be written by

$$d^3PS \approx \frac{1}{2^8\pi^4} dt_1 dt_2 d\xi_1 d\xi_2 d\phi_{12}\;\delta\left(s(1-\xi_1)(1-\xi_2) - m_M^2\right)\,, \tag{A.25}$$

where ξ_1, ξ_2 are longitudinal momentum fractions carried by outgoing protons with respect to their parent protons and the relative angle between outgoing protons $\phi_{12} \in (0, 2\pi)$; see [216]. Changing the variables $(\xi_1, \xi_2) \to (x_F, M^2)$ one gets

$$d^3PS \approx \frac{1}{2^8\pi^4} dt_1 dt_2 \frac{dx_{F,M}}{s\sqrt{x_{F,M}^2 + 4(m_M^2 + |\mathbf{p}_{M\perp}|^2)/s}}\;d\phi_{12}\,. \tag{A.26}$$

The high-energy formulae (A.25) and (A.26) break close to the meson production threshold. Then exact phase space formula (A.24) must be taken and another choice of variables is more appropriate. We choose transverse momenta of the outgoing nucleons ($p_{1\perp}, p_{2\perp}$), azimuthal angle between outgoing nucleons (ϕ_{12}) and rapidity of the meson (y_M) as independent kinematically complete variables. Then the cross section can be calculated as:

$$d\sigma = \sum_k \mathcal{J}^{-1}(p_{1\perp}, p_{2\perp}, \phi_{12}, y_M)|_k \frac{\overline{|\mathcal{M}(p_{1\perp}, p_{2\perp}, \phi_{12}, y_M)|^2}}{2\sqrt{s(s-4m_N^2)}} \frac{2\pi}{(2\pi)^5} \frac{1}{2E_1} \frac{1}{2E_2} \frac{1}{2} \, p_{1\perp} p_{2\perp} dp_{1t} dp_{2t} d\phi_{12} dy_M \,, \tag{A.27}$$

where k denotes symbolically discrete solutions of the set of equations for p_{1z} and p_{2z}:

$$\begin{cases} \sqrt{s} - E_M &= \sqrt{m_{1\perp}^2 + p_{1z}^2} + \sqrt{m_{2\perp}^2 + p_{2z}^2} \,, \\ -p_{Mz} &= p_{1z} + p_{2z} \,, \end{cases} \tag{A.28}$$

where $m_{1\perp}$ and $m_{2\perp}$ are transverse masses of outgoing nucleons. The solutions of Eq.(A.28) depend on the values of integration variables:

$$\begin{aligned} p_{1z} &= p_{1z}(p_{1\perp}, p_{2\perp}, \phi_{12}, y_M) \,, \\ p_{2z} &= p_{2z}(p_{1\perp}, p_{2\perp}, \phi_{12}, y_M) \,. \end{aligned} \tag{A.29}$$

The extra Jacobian reads:

$$\mathcal{J}_k = \left| \frac{p_{1z}(k)}{\sqrt{m_{1\perp}^2 + p_{1z}(k)^2}} - \frac{p_{2z}(k)}{\sqrt{m_{2\perp}^2 + p_{2z}(k)^2}} \right| . \tag{A.30}$$

In the limit of high energies and central production, i.e. $p_{1z} \gg 0$ (very forward nucleon 1), $-p_{2z} \gg 0$ (very backward nucleon 2) the Jacobian (A.30) becomes a constant $\mathcal{J} \to \frac{1}{2}$.

The cross section for the $2 \to 4$ reaction, is obtained by integration over the four-body phase space

$$\sigma = \int \frac{1}{2s} \overline{|\mathcal{M}|^2} (2\pi)^4 \delta^4(p_a + p_b - p_1 - p_2 - p_3 - p_4) \frac{d^3p_1}{(2\pi)^3 2E_1} \frac{d^3p_2}{(2\pi)^3 2E_2} \frac{d^3p_3}{(2\pi)^3 2E_3} \frac{d^3p_4}{(2\pi)^3 2E_4} \,. \tag{A.31}$$

To calculate the total cross section one has to calculate the 8-dimensional integral numerically.

This can be written in a useful form of differential cross section:

$$\begin{aligned} d\sigma &= \frac{1}{2s} \overline{|\mathcal{M}|^2} \delta^4(p_a + p_b - p_1 - p_2 - p_3 - p_4) \frac{1}{(2\pi)^8} \frac{1}{2^4} \\ &\times (dy_1 p_{1\perp} dp_{1\perp} d\phi_1)(dy_2 p_{2\perp} dp_{2\perp} d\phi_2)(dy_3 d^2p_{3\perp})(dy_4 d^2p_{4\perp}) \,. \end{aligned} \tag{A.32}$$

This can be further simplified:

$$\begin{aligned} d\sigma &= \frac{1}{2s} \overline{|\mathcal{M}|^2} \delta(E_a + E_b - E_1 - E_2 - E_3 - E_4) \delta(p_{1z} + p_{2z} + p_{3z} + p_{4z}) \frac{1}{(2\pi)^8} \frac{1}{2^4} \\ &\times (dy_1 p_{1\perp} dp_{1\perp} d\phi_1)(dy_2 p_{2\perp} dp_{2\perp} d\phi_2) dy_3 dy_4 d^2p_{m\perp} \,. \end{aligned} \tag{A.33}$$

Above we have introduced an auxiliary quantity:

$$\mathbf{p}_{m\perp} = \mathbf{p}_{3\perp} - \mathbf{p}_{4\perp} \,. \tag{A.34}$$

We choose transverse momenta of the outgoing nucleons ($p_{1\perp}, p_{2\perp}$), the azimuthal angles of outgoing nucleons (ϕ_1, ϕ_2) and the rapidity of the pions (y_3, y_4) as independent kinematically complete variables. Then the cross section can be calculated as:

$$\begin{aligned} d\sigma &= \sum_k \mathcal{J}^{-1}(p_{1\perp}, \phi_1, p_{2\perp}, \phi_2, y_3, y_4, p_{m\perp}, \phi_m)|_k \frac{\overline{|\mathcal{M}(p_{1\perp}, \phi_1, p_{2\perp}, \phi_2, y_3, y_4, p_{m\perp}, \phi_m)|^2}}{2\sqrt{s(s-4m^2)}} \frac{1}{(2\pi)^8} \frac{1}{2^4} \\ &\times p_{1\perp} dp_{1\perp} d\phi_1 p_{2\perp} dp_{2\perp} d\phi_2 \frac{1}{4} dy_3 dy_4 d^2p_{m\perp} \,, \end{aligned} \tag{A.35}$$

where the δ functions have been totally eliminated and k denotes symbolically discrete solutions of the set of equations for energy and momentum conservation:

$$\begin{cases} \sqrt{s} - E_3 - E_4 &= \sqrt{m_{1\perp}^2 + p_{1z}^2} + \sqrt{m_{2\perp}^2 + p_{2z}^2}\,, \\ -p_{3z} - p_{4z} &= p_{1z} + p_{2z}\,. \end{cases} \tag{A.36}$$

The solutions of Eq.(A.36) depend on the values of integration variables:

$$\begin{aligned} p_{1z} &= p_{1z}(p_{1\perp}, p_{2\perp}, p_{3\perp}, p_{4\perp}, \phi_1, \phi_2, y_3, y_4)\,, \\ p_{2z} &= p_{2z}(p_{1\perp}, p_{2\perp}, p_{3\perp}, p_{4\perp}, \phi_1, \phi_2, y_3, y_4)\,. \end{aligned} \tag{A.37}$$

In Eq. (A.35) an extra Jacobian (A.30) of the transformation $(y_1, y_2) \to (p_{1z}, p_{2z})$ has appeared.

A.3 Lorentz transformations

The Lorentz transformation of pion three-momenta and energy from the pp center-of-mass to the $X = \pi\pi$ rest frame can be written (see formulae (4-3) in [441])

$$\begin{aligned} \vec{p}_\pi^{\,r.f.} &= \vec{p}_\pi + \vec{v}_X \gamma_X \left(\frac{\gamma_X}{\gamma_X + 1} \vec{v}_X \vec{p}_\pi - E_\pi \right)\,, \\ E_\pi^{r.f.} &= \gamma_X \left(E_\pi - \vec{v}_X \vec{p}_\pi \right)\,, \end{aligned} \tag{A.38}$$

where the relativistic γ_X factor is written as $\gamma_X \equiv 1/\sqrt{1 - v_X^2}$ and the velocity of two-pion system is $\vec{v}_X = \vec{p}_X / E_X$. [1] Explicitly, we have

$$v_X = |\vec{v}_X| = |\vec{p}_3 + \vec{p}_4| / (E_3 + E_4) = \sqrt{p_{x,X}^2 + p_{y,X}^2 + p_{z,X}^2} / (p_{30} + p_{40})\,, \tag{A.39}$$

where the x, y, and z components of $p_{i,X}$ are defined as $p_{i,X} = p_{3i} + p_{4i}$.

Then, we can calculate $\cos\theta_\pi^{r.f.} = p_{z,\pi}^{r.f.} / p_\pi^{r.f.}$ which fulfils $-1 < \cos\theta_\pi^{r.f.} < 1$. For example, if we denote the π^+ meson as particle 3 then we can write $\cos\theta_{\pi^+}^{r.f.} = p_{3z}^{r.f.} / |\vec{p}_3^{\,r.f.}|$. It was checked in our code that $\cos\theta_{\pi^+}^{r.f.} = -\cos\theta_{\pi^-}^{r.f.}$.

In a similar way, we carry out the transformation of 3-momenta and energy of pion from the $X = \pi\pi$ rest frame to the pp center-of-mass:

$$\begin{aligned} \vec{p}_\pi &= \vec{p}_\pi^{\,r.f.} + \vec{v}_X \gamma_X \left(\frac{\gamma_X}{\gamma_X + 1} \vec{v}_X \vec{p}_\pi^{\,r.f.} + E_\pi^{r.f.} \right)\,, \\ E_\pi &= \gamma_X \left(E_\pi^{r.f.} + \vec{v}_X \vec{p}_\pi^{\,r.f.} \right)\,. \end{aligned} \tag{A.40}$$

[1] In the following we shall use units where $c = 1$, where c is the speed of light. This is convenient in calculations characteristic for relativistic kinematics, because all expressions must then be homogeneous in energies, momenta and masses, and all have the same dimension. Then the particle velocities $\beta \equiv v/c$ are dimensionless and do not exceed 1.

Appendix B

Tensorial pomeron

For the case of the tensorial pomeron the $\boldsymbol{P}pp$ vertex reads as follows, see [203],

$$i\Gamma^{(\boldsymbol{P}pp)}_{\mu\nu}(p',p) = -i3\beta_{\boldsymbol{P}NN}F_1\big((p'-p)^2\big)\left\{\frac{1}{2}\left[\gamma_\mu(p'+p)_\nu+\gamma_\nu(p'+p)_\mu\right]-\frac{1}{4}g_{\mu\nu}(\not{p}'+\not{p})\right\}, \tag{B.1}$$

where $\beta_{\boldsymbol{P}NN} = 1.87\ \mathrm{GeV}^{-1}$ and $\not{p} = \gamma_\mu p^\mu$. The explicit factor 3 above counts the number of valence quarks in each proton. Following Donnachie and Landshoff [113] we use the proton's Dirac electromagnetic form factor $F_1(t)$ for describing the proton's extension. A good representation of this form factor is given by the dipole formula

$$F_1(t) = \frac{4m_p^2 - 2.79\,t}{(4m_p^2-t)(1-t/m_D^2)^2}, \tag{B.2}$$

where m_p is the proton mass and $m_D^2 = 0.71\ \mathrm{GeV}^2$ is the dipole mass squared.

The propagator of the tensor-pomeron exchange (see [203]) is given by

$$i\Delta^{(\boldsymbol{P})}_{\mu\nu,\kappa\lambda}(s,t) = \frac{1}{4s}\left(g_{\mu\kappa}g_{\nu\lambda}+g_{\mu\lambda}g_{\nu\kappa}-\frac{1}{2}g_{\mu\nu}g_{\kappa\lambda}\right)\left(-is\alpha'_{\boldsymbol{P}}\right)^{\alpha_{\boldsymbol{P}}(t)-1}. \tag{B.3}$$

Here the pomeron trajectory $\alpha_{\boldsymbol{P}}(t)$ is assumed to be of standard form (2.11), that is, linear in t and with intercept slightly above 1, see for instance [114].

The tensor-pomeron propagator fulfils the following relations

$$\begin{aligned}&\Delta^{(\boldsymbol{P})}_{\mu\nu,\kappa\lambda} = \Delta^{(\boldsymbol{P})}_{\nu\mu,\kappa\lambda} = \Delta^{(\boldsymbol{P})}_{\mu\nu,\lambda\kappa} = \Delta^{(\boldsymbol{P})}_{\kappa\lambda,\mu\nu},\\ &g^{\mu\nu}\Delta^{(\boldsymbol{P})}_{\mu\nu,\kappa\lambda} = 0, \quad g^{\kappa\lambda}\Delta^{(\boldsymbol{P})}_{\mu\nu,\kappa\lambda} = 0.\end{aligned} \tag{B.4}$$

Now we can calculate the pomeron contribution to the amplitude of pp elastic scattering

$$p(p_a,\lambda_a)+p(p_b,\lambda_b)\to p(p_1,\lambda_1)+p(p_2,\lambda_2). \tag{B.5}$$

With tensorial pomeron we get for the $\mathcal{T}$-matrix element

$$\begin{aligned}&\langle p(p_1,\lambda_1),p(p_2,\lambda_2)\,|\,\mathcal{T}\,|\,p(p_a,\lambda_a),p(p_b,\lambda_b)\rangle\,|_{\boldsymbol{P}} \equiv\\ &\mathcal{M}^{2\to2}_{\lambda_a\lambda_b\to\lambda_1\lambda_2}\,|_{\boldsymbol{P}} = (-i)\bar{u}(p_1,\lambda_1)i\Gamma^{(\boldsymbol{P}pp)}_{\mu_1\nu_1}(p_1,p_a)u(p_a,\lambda_a)\\ &\qquad\times i\Delta^{(\boldsymbol{P})\,\mu_1\nu_1,\mu_2\nu_2}(s,t)\\ &\qquad\times\bar{u}(p_2,\lambda_2)i\Gamma^{(\boldsymbol{P}pp)}_{\mu_2\nu_2}(p_2,p_b)u(p_b,\lambda_b),\end{aligned} \tag{B.6}$$

where

$$\begin{aligned}s &= (p_a+p_b)^2 = (p_1+p_2)^2,\\ t &= (p_1-p_a)^2 = (p_2-p_b)^2.\end{aligned} \tag{B.7}$$

Inserting in (B.6) the expressions for the $I\!Ppp$ vertex (B.1) and the $I\!P$ propagator (B.3) we get at high energies, $s \gg m_p^2$,

$$\mathcal{M}^{2\to 2}_{\lambda_a\lambda_b\to\lambda_1\lambda_2}\,|_{I\!P} \;\cong\; i\,2s\,\left[3\beta_{I\!PNN}\,F_1(t)\right]^2\,\left(-is\alpha'_{I\!P}\right)^{\alpha_{I\!P}(t)-1}\,\delta_{\lambda_1\lambda_a}\,\delta_{\lambda_2\lambda_b}\,. \tag{B.8}$$

This is exactly the same expression (using (2.11)) as obtained with the famous Donnachie-Landshoff-pomeron approach; see [113, 114], and Appendix C below. One advantage of the tensorial-pomeron ansatz is that it gives automatically, just using the rules of QFT, the same $I\!P$ contributions to the amplitudes of proton-proton and proton-antiproton scattering; see [203].

We turn now to the $I\!PI\!PM$ vertices which we want to construct in a field-theoretic manner, that is, using a meson field operator and two effective pomeron field operators $I\!P_{\mu\nu}(x)$. To get an overview of the possible couplings of this type we shall first consider a fictitious reaction: two "real pomeron particles" of spin 2 giving a meson M; see Fig.B.1. From this exercise we can then easily learn how to classify and write down covariant expressions for the $I\!PI\!PM$ vertices.

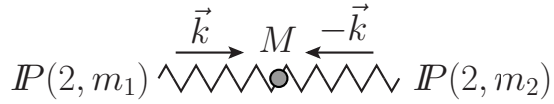

Figure B.1: The fictitious reaction of two "real spin 2 pomerons" of momenta $\vec{k}$ and $-\vec{k}$ annihilating to a meson M.

We consider, thus, the annihilation of two "pomeron particles" of spin 2 and z-components of spin m_1 and m_2 giving a meson of spin J and z-component J_z in the c.m. system, that is, the rest system of M:

$$\begin{aligned} &I\!P(\vec{k},2,m_1) + I\!P(-\vec{k},2,m_2) \to M(J,J_z)\,,\\ &m_{1,2} \in \{-2,\ldots,2\}\,,\quad J_z \in \{-J,\ldots,J\}\,. \end{aligned} \tag{B.9}$$

Note that we use here the Wigner basis for all particles; see [442], and for instance, chapter 16.2 of [443], and Appendix D. Clearly, in (B.9) M must have isospin and G parity $I^G = 0^+$ and charge conjugation $C = +1$. The question is: what are the possible values of spin J and parity P for meson M?

Let $a^\dagger_{2,m}(\vec{k})$, $a^\dagger_{2,m}(-\vec{k})$ be the creation operators for the "pomeron particles". We can first construct the states of the two "pomerons" with definite orbital angular momentum l, l_z and then those with given l, l_z and total spin S, S_z. We get with $\hat{k} = \vec{k}/|\vec{k}|$, $Y^{l_z}_l(\hat{k})$ the spherical harmonics, and the usual Clebsch-Gordan coefficients

$$|2,m_1;2,m_2;l,l_z\rangle = \int d\Omega_k\, Y^{l_z}_l(\hat{k})\, a^\dagger_{2,m_1}(\vec{k})\, a^\dagger_{2,m_2}(-\vec{k})\,|0\rangle\;, \tag{B.10}$$

$$|S,S_z;l,l_z\rangle = \sum_{m_1,m_2} \langle 2,m_1;2,m_2|S,S_z\rangle\,|2,m_1;2,m_2;l,l_z\rangle\;. \tag{B.11}$$

Here we have

$$\begin{aligned} l &= 0,1,2,\ldots,\\ -l &\leqslant l_z \leqslant l\,,\\ S &= 0,1,2,3,4\,,\\ -S &\leqslant S_z \leqslant S\,. \end{aligned} \tag{B.12}$$

From Bose symmetry of our "pomeron particles" we find that

$$|S,S_z;l,l_z\rangle = 0 \quad \text{for } l-S \text{ odd}\,. \tag{B.13}$$

Table B.1: The values, for orbital angular momentum l, of total spin S, total angular momentum J, and parity P, possible in the annihilation reaction (B.9). The continuation of the table for $l > 4$ is straightforward.

l	S	J	P
0	0	0	+
	2	2	
	4	4	
1	1	0, 1, 2	−
	3	2, 3, 4	
2	0	2	+
	2	0,1,2,3,4	
	4	2,3,4,5,6	
3	1	2,3,4	−
	3	0,1,2,3,4,5,6	
4	0	4	+
	2	2,3,4,5,6	
	4	0,1,2,3,4,5,6,7,8	

The parity transformation $U(P)$ gives

$$U(P)\,|S,S_z;l,l_z\rangle = (-1)^l\,|S,S_z;l,l_z\rangle\ . \tag{B.14}$$

It is straightforward to construct the two-pomeron states of definite total angular momentum J, J_z:

$$|l,S;J,J_z\rangle = \sum_{S_z,l_z} \langle S,S_z;l,l_z|J,J_z\rangle\,|S,S_z;l,l_z\rangle\ . \tag{B.15}$$

Clearly, J is then the spin of the produced meson in (B.9) and $P = (-1)^l$ its parity. In Table B.1 we list the values of J and P of mesons which can be produced in our fictitious reaction (B.9) where we restrict ourselves to $l \leqslant 4$.

It is clear that for each value of l, S, J, and P listed in Table B.1 we can construct a covariant Lagrangian density $\mathcal{L}'$ coupling the field operator for the meson M to the pomeron fields $I\!P_{\mu\nu}$. There, l is related to the number of derivatives in $\mathcal{L}'$, thus giving an indication of the angular momentum barrier in the production of M in (B.9). In Table B.2 we list interesting candidates for mesons M in central production and the corresponding minimal values of l and S which can lead to the meson states according to Table B.1.

The strategy is now to construct for a given meson M of Table B.2 a coupling Lagrangian $\mathcal{L}'_{I\!P I\!P M}$ corresponding to the l and S values listed there. We illustrate this here for the case of a $J^{PC} = 0^{++}$ meson M. The case of a pseudoscalar meson $\tilde{M}$ is treated in Section 3.1.2.

The Lagrangian $\mathcal{L}'_{I\!P I\!P M}$ for a scalar meson ($J^{PC} = 0^{++}$) corresponding to $l = S = 0$ reads

$$\mathcal{L}'_{I\!P I\!P M}(x) = M_0\, g'_{I\!P I\!P M}\, I\!P_{\mu\nu}(x)\, I\!P^{\mu\nu}(x)\, \chi(x)\,, \tag{B.16}$$

where $\chi(x)$ is the meson field operator, $M_0 \equiv 1$ GeV, and $g'_{I\!P I\!P M}$ is the dimensionless coupling constant. The "bare" vertex obtained from (B.16), see Fig.B.2 (a), reads

$$i\Gamma'^{(I\!P I\!P \to M)}_{\mu\nu,\kappa\lambda}\ |_{bare} = i\, g'_{I\!P I\!P M}\, M_0\, \left(g_{\mu\kappa}g_{\nu\lambda} + g_{\mu\lambda}g_{\nu\kappa} - \frac{1}{2} g_{\mu\nu}g_{\kappa\lambda} \right)\ . \tag{B.17}$$

Here we have made the vertex traceless since the $I\!P_{\mu\nu}$ are supposed to have trace zero.

In Appendix D we use (B.17) to calculate the T-matrix element for the fictitious reaction (B.9) with a scalar meson. We show there that in the Wigner basis we get from (B.16) an amplitude containing values of $(l,S) = (0,0)$, $(2,2)$, and $(4,4)$. But the higher terms are completely fixed by

Table B.2: Candidates for mesons producible in pomeron-pomeron annihilation. The values of the minimal orbital angular momentum l and of the corresponding total spin S for the reactions (B.9) and (C.4) with tensorial ($I\!P_T$) and vectorial ($I\!P_V$) "pomeron particles", respectively, are also indicated.

		$I\!P_T$		$I\!P_V$	
J^{PC}	meson M	l	S	l	S
0^{-+}	η $\eta'(958)$	1	1	1	1
0^{++}	$f_0(980)$ $f_0(1370)$ $f_0(1500)$	0	0	0	0
1^{++}	$f_1(1285)$ $f_1(1420)$	2	2	2	2
2^{++}	$f_2(1270)$ $f_2'(1525)$	0	2	0	2
4^{++}	$f_4(2050)$	0	4	2	2

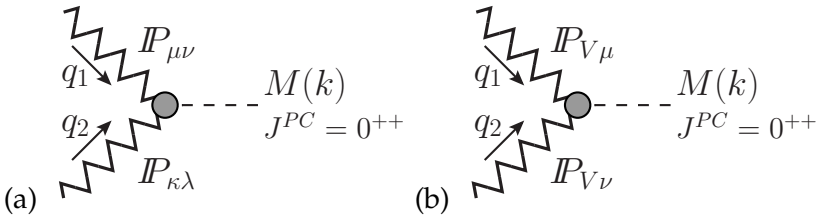

Figure B.2: A sketch of the pomeron-pomeron-scalar meson vertex for the tensorial (a) and vectorial (b) pomeron fusion.

the lowest term $(l,S)=(0,0)$. This justifies to call the coupling (B.16), the one corresponding to $(l,S)=(0,0)$.

The coupling Lagrangian $\mathcal{L}''_{I\!P I\!P M}$ and vertex $\Gamma''^{(I\!P I\!P\to M)}$ corresponding to $l=S=2$ read as follows:

$$\mathcal{L}''_{I\!P I\!P M}(x)=\frac{1}{2M_0}\,g''_{I\!P I\!P M}\,\left[\partial^\mu I\!P^{\nu\rho}(x)-\partial^\nu I\!P^{\mu\rho}(x)\right]\,\left[\partial_\mu I\!P_{\nu\rho}(x)-\partial_\nu I\!P_{\mu\rho}(x)\right]\,\chi(x)\,, \tag{B.18}$$

$$i\Gamma''^{(I\!P I\!P\to M)}_{\mu\nu,\kappa\lambda}(q_1,q_2)\;|_{bare}=\frac{i\,g''_{I\!P I\!P M}}{2M_0}$$
$$\times\left[q_{1\kappa}q_{2\mu}g_{\nu\lambda}+q_{1\kappa}q_{2\nu}g_{\mu\lambda}+q_{1\lambda}q_{2\mu}g_{\nu\kappa}+q_{1\lambda}q_{2\nu}g_{\mu\kappa}-2(q_1q_2)(g_{\mu\kappa}g_{\nu\lambda}+g_{\nu\kappa}g_{\mu\lambda})\right]\,, \tag{B.19}$$

where $g''_{I\!P I\!P M}$ is the dimensionless coupling constant. The vertex (B.19) must be added coherently to the vertex (B.17).

In the production reaction (3.1) we cannot take the "bare" vertices ((B.17) and (B.19)) directly. We have to take into account that hadrons are extended objects, that is, we shall have to introduce form factors. The actual vertex which is assumed in this paper reads then as follows

$$i\Gamma^{(I\!P I\!P\to M)}_{\mu\nu,\kappa\lambda}(q_1,q_2)=\left(i\Gamma'^{(I\!P I\!P\to M)}_{\mu\nu,\kappa\lambda}\;|_{bare}+i\Gamma''^{(I\!P I\!P\to M)}_{\mu\nu,\kappa\lambda}(q_1,q_2)\;|_{bare}\right)F_{I\!P I\!P M}(q_1^2,q_2^2)\,. \tag{B.20}$$

Unfortunately, the pomeron-pomeron-meson form factor is not well known as it is due to nonperturbative effects related to the internal structure of the respective meson. In practical calculations we take the factorized form with the following two approaches. Either we use

$$F^M_{I\!P I\!P M}(t_1,t_2)=F_M(t_1)F_M(t_2)\,, \tag{B.21}$$

with $F_M(t)$ the pion electromagnetic form factor in its simplest parametrisation, valid for $t<0$,

$$F_M(t)=F_\pi(t)=\frac{1}{1-t/\Lambda_0^2}\,, \tag{B.22}$$

where $\Lambda_0^2 = 0.5\,\mathrm{GeV}^2$; see e.g. (3.22) of [114]. Alternatively, we use the exponential form given as

$$F^E_{\boldsymbol{I\!P}PM}(t_1, t_2) = \exp\left(\frac{t_1 + t_2}{\Lambda_E^2}\right), \tag{B.23}$$

where $\Lambda_E^2 \approx 1\,\mathrm{GeV}^2$. This discussion of form factors applies also to the other pomeron-pomeron-meson vertices considered in this paper.

In the case of meson-exchange diagrams we use the monopole form factor which is normalized to unity at the on-shell point $t = m_M^2$

$$F(t) = \frac{\Lambda_M^2 - m_M^2}{\Lambda_M^2 - t}, \tag{B.24}$$

where $\Lambda_M > m_M$ and $t < 0$. Alternatively, we use the exponential form

$$F(t) = \exp\left(\frac{t - m_M^2}{\Lambda_E^2}\right). \tag{B.25}$$

The influence of the choice of the form-factor parameters is discussed in the results section.

Appendix C

Vectorial pomeron

In this section we perform the same analysis for the vectorial pomeron ansatz as is done for the tensorial pomeron in Appendix B.

In the vectorial approach, see [113, 114, 222–228], the pomeron is treated as a "$C = +1$ photon". Its coupling to the proton reads

$$i\Gamma_{\mu}^{(\mathbb{P}_V pp)}(p', p) = -i\, 3\beta_{\mathbb{P}NN}\, F_1\big((p'-p)^2\big)\, M_0\, \gamma_{\mu}\,, \tag{C.1}$$

where $\beta_{\mathbb{P}NN} = 1.87\ \mathrm{GeV}^{-1}$, $M_0 \equiv 1$ GeV; compare to (B.1). The effective $\mathbb{P}_V$ propagator is given by

$$i\Delta_{\mu\nu}^{(\mathbb{P}_V)}(s,t) = \frac{1}{M_0^2}\, g_{\mu\nu}\, \big(-is\alpha'_{\mathbb{P}}\big)^{\alpha_{\mathbb{P}}(t)-1}\,, \tag{C.2}$$

with $\alpha_{\mathbb{P}}(t)$ and $\alpha'_{\mathbb{P}}$ as in (2.11).

From (C.1) and (C.2) we get for proton-proton elastic scattering

$$\begin{aligned}
&\langle p(p_1,\lambda_1), p(p_2,\lambda_2)\,|\,\mathcal{T}\,|\,p(p_a,\lambda_a), p(p_b,\lambda_b)\rangle\ |_{\mathbb{P}_V} \equiv \\
&\mathcal{M}^{2\to 2}_{\lambda_a\lambda_b\to\lambda_1\lambda_2}\ |_{\mathbb{P}_V} = (-i)\bar{u}(p_1,\lambda_1) i\Gamma_{\mu}^{(\mathbb{P}_V pp)}(p_1,p_a) u(p_a,\lambda_a) \\
&\qquad\qquad \times i\Delta^{(\mathbb{P}_V)\,\mu\nu}(s,t) \\
&\qquad\qquad \times \bar{u}(p_2,\lambda_2) i\Gamma_{\nu}^{(\mathbb{P}_V pp)}(p_2,p_b) u(p_b,\lambda_b) \\
&\qquad\qquad \xrightarrow{s\gg m_p^2} i\,2s\ \big[3\beta_{\mathbb{P}NN}\, F_1(t)\big]^2\ \big(-is\alpha'_{\mathbb{P}}\big)^{\alpha_{\mathbb{P}}(t)-1}\ \delta_{\lambda_1\lambda_a}\,\delta_{\lambda_2\lambda_b}\,.
\end{aligned} \tag{C.3}$$

Comparing with (B.8) we see that for $s \gg m_p^2$, both, the tensorial and the vectorial pomeron give the same amplitude for pp elastic scattering.

In the next step we consider the annihilation of two "vector-pomeron particles" into a meson M

$$\begin{aligned}
&\mathbb{P}_V(\vec{k}, 1, m_1) + \mathbb{P}_V(-\vec{k}, 1, m_2) \to M(J, J_z)\,, \\
&m_{1,2} \in \{-1, 0, 1\}\,, \quad J_z \in \{-J, \ldots, J\}\,;
\end{aligned} \tag{C.4}$$

compare to (B.9). Here, again, we use the Wigner basis. The same analysis as done after (B.9) for the tensorial pomeron can now be performed for the vectorial one. The result is given in Table C.1 which is the analogue of Table B.1 for the tensorial pomeron.

As in Appendix B we illustrate the use of Table C.1 by discussing the coupling of two vectorial pomerons to a $J^{PC} = 0^{++}$ meson M. Let χ be the meson field, $\mathbb{P}_V^{\mu}$ the effective vector-pomeron field. The coupling corresponding to $(l, S) = (0, 0)$ reads

$$\mathcal{L}'_{\mathbb{P}_V\mathbb{P}_V M}(x) = M_0\, g'_{\mathbb{P}_V\mathbb{P}_V M}\, \mathbb{P}_{V\mu}(x)\, \mathbb{P}_V^{\mu}(x)\, \chi(x) \tag{C.5}$$

Table C.1: The values of l, S, J, and P, of orbital angular momentum, total spin of the two "vector-pomeron particles", total angular momentum, and parity of the state, respectively, possible in the vectorial pomeron annihilation reaction (C.4). We have $S \in \{0,1,2\}$, $P = (-1)^l$, $|l-S| \leqslant J \leqslant l+S$, and Bose symmetry requires $l-S$ to be even. The continuation of the table for $l > 4$ is straightforward.

l	S	J	P
0	0	0	+
	2	2	
1	1	0, 1, 2	−
2	0	2	+
	2	0,1,2,3,4	
3	1	2,3,4	−
4	0	4	+
	2	2,3,4,5,6	

with $M_0 \equiv 1$ GeV, and $g'_{\mathbb{P}_V\mathbb{P}_V M}$ the dimensionless coupling constant. From (C.5) we get the "bare" vertex, see Fig.B.2 (b),

$$i\Gamma'^{(\mathbb{P}_V\mathbb{P}_V\to M)}_{\mu\nu} \,|_{bare} = i\, g'_{\mathbb{P}_V\mathbb{P}_V M}\, M_0\, 2g_{\mu\nu}\,. \tag{C.6}$$

Using this vertex to calculate the amplitude for the fictitious reaction (C.4) we find, in the Wigner basis, contributions with $(l,S) = (0,0)$ and $(2,2)$ with the $(2,2)$ part completely fixed by the $(0,0)$ part; see Appendix D. Thus, we shall refer to the coupling (C.6) as the one corresponding to $(l,S) = (0,0)$.

For $l = S = 2$ the coupling Lagrangian and vertex read as follows:

$$\mathcal{L}''_{\mathbb{P}_V\mathbb{P}_V M}(x) = \frac{1}{2M_0}\, g''_{\mathbb{P}_V\mathbb{P}_V M}\, \left[\partial^\mu \mathbb{P}^\nu_V(x) - \partial^\nu \mathbb{P}^\mu_V(x)\right]\, \left[\partial_\mu \mathbb{P}_{V\nu}(x) - \partial_\nu \mathbb{P}_{V\mu}(x)\right]\, \chi(x)\,, \tag{C.7}$$

$$i\Gamma''^{(\mathbb{P}_V\mathbb{P}_V\to M)}_{\mu\nu}(q_1,q_2)\,|_{bare} = \frac{2i\, g''_{\mathbb{P}_V\mathbb{P}_V M}}{M_0}\, \left[q_{2\mu}q_{1\nu} - (q_1q_2)g_{\mu\nu}\right]\,, \tag{C.8}$$

where $g''_{\mathbb{P}_V\mathbb{P}_V M}$ is the dimensionless coupling constant.

The discussion of form factors for these vertices is identical to the one for the tensorial pomeron in Appendix B. Thus, for the full vertex for two vectorial pomerons giving a 0^{++} meson we add (C.6) and (C.8) and multiply the sum by a form factor

$$i\Gamma^{(\mathbb{P}_V\mathbb{P}_V\to M)}_{\mu\nu}(q_1,q_2) = \left(i\Gamma'^{(\mathbb{P}_V\mathbb{P}_V\to M)}_{\mu\nu}\,|_{bare} + i\Gamma''^{(\mathbb{P}_V\mathbb{P}_V\to M)}_{\mu\nu}(q_1,q_2)\,|_{bare}\right) F_{\mathbb{P}\mathbb{P}M}(q_1^2,q_2^2). \tag{C.9}$$

The coupling of two vectorial pomerons to a pseudoscalar mesons $\tilde{M}$ is given in Section 3.1.2; cf. (3.14) and (3.15).

Appendix D

Covariant $\mathbb{P}\mathbb{P}M$ couplings and the Wigner basis

In this appendix we discuss the relation of the covariant $\mathbb{P}\mathbb{P}M$ couplings to the classification of partial wave amplitudes in the Wigner basis as given in Table B.1 for the tensorial and in Table C.1 for the vectorial pomeron.

Let us consider as an example of the reaction (C.4) the annihilation of two fictitious "vectorial pomeron particles" of mass m giving a $J^{PC} = 0^{++}$ meson M:

$$\mathbb{P}_V(\vec{k}, \vec{\varepsilon}_1^{\,W}) + \mathbb{P}_V(-\vec{k}, \vec{\varepsilon}_2^{\,W}) \to M\,. \tag{D.1}$$

Here $\vec{\varepsilon}_{1,2}^{\,W}$ are the polarization vectors in the Wigner basis with

$$|\vec{\varepsilon}_1^{\,W}| = |\vec{\varepsilon}_2^{\,W}| = 1\,. \tag{D.2}$$

To transform to the covariant polarization vectors $\varepsilon_i{}^{\mu}$ $(i = 1, 2)$ we need the boost transformation $\Lambda_{\vec{k}}$:

$$(\Lambda_{\vec{k}}{}^{\mu}{}_{\nu}) = \begin{pmatrix} \dfrac{k^0}{m} & \dfrac{k^j}{m} \\ \\ \dfrac{k^i}{m} & \delta^{ij} + \hat{k}^i\hat{k}^j\Big(\dfrac{k^0}{m} - 1\Big) \end{pmatrix},$$
$$i, j \in \{1, 2, 3\}\,, \quad \hat{k} = \vec{k}/|\vec{k}|\,. \tag{D.3}$$

We have

$$(\varepsilon_1{}^{\mu}) = \Lambda_{\vec{k}} \begin{pmatrix} 0 \\ \vec{\varepsilon}_1^{\,W} \end{pmatrix},$$
$$(\varepsilon_2{}^{\mu}) = \Lambda_{-\vec{k}} \begin{pmatrix} 0 \\ \vec{\varepsilon}_2^{\,W} \end{pmatrix}. \tag{D.4}$$

From the vertex (C.6) we get the amplitude for reaction (D.1) as follows

$$\Big\langle M \,\Big|\, \mathcal{T} \,\Big|\, \mathbb{P}_V(\vec{k}, \vec{\varepsilon}_1^{\,W}), \mathbb{P}_V(-\vec{k}, \vec{\varepsilon}_2^{\,W}) \Big\rangle = \Gamma'^{(\mathbb{P}_V\mathbb{P}_V\to M)}_{\mu\nu}\varepsilon_1{}^{\mu}\varepsilon_2{}^{\nu} = -2\,M_0\,g'_{\mathbb{P}_V\mathbb{P}_V M}$$
$$\times\Big[\Big(1 + \frac{2}{3}\frac{\vec{k}^2}{m^2}\Big)\vec{\varepsilon}_1^{\,W}\cdot\vec{\varepsilon}_2^{\,W} + \frac{1}{m^2}\Big(k^ik^j - \frac{1}{3}\delta^{ij}\vec{k}^2\Big)\Big(\varepsilon_1^{W\,i}\varepsilon_2^{W\,j} + \varepsilon_2^{W\,i}\varepsilon_1^{W\,j} - \frac{2}{3}\delta^{ij}\vec{\varepsilon}_1^{\,W}\cdot\vec{\varepsilon}_2^{\,W}\Big)\Big]\,. \tag{D.5}$$

From the vertex (C.8) we get

$$\Big\langle M \,\Big|\, \mathcal{T} \,\Big|\, \mathbb{P}_V(\vec{k}, \vec{\varepsilon}_1^{\,W}), \mathbb{P}_V(-\vec{k}, \vec{\varepsilon}_2^{\,W}) \Big\rangle = \frac{2g''_{\mathbb{P}_V\mathbb{P}_V M}}{M_0}\Big[\Big(k_2\varepsilon_1\Big)\Big(k_1\varepsilon_2\Big) - \Big(k_1k_2\Big)\Big(\varepsilon_1\varepsilon_2\Big)\Big] = \frac{2g''_{\mathbb{P}_V\mathbb{P}_V M}}{M_0}$$
$$\times\Big[\Big(\frac{4}{3}\vec{k}^2 + m^2\Big)\vec{\varepsilon}_1^{\,W}\cdot\vec{\varepsilon}_2^{\,W} - \Big(k^ik^j - \frac{1}{3}\delta^{ij}\vec{k}^2\Big)\Big(\varepsilon_1^{W\,i}\varepsilon_2^{W\,j} + \varepsilon_2^{W\,i}\varepsilon_1^{W\,j} - \frac{2}{3}\delta^{ij}\vec{\varepsilon}_1^{\,W}\cdot\vec{\varepsilon}_2^{\,W}\Big)\Big]. \tag{D.6}$$

Thus, in the Wigner basis we get from both vertices, (C.6) and (C.8), partial wave amplitudes with $(l,S)=(0,0)$ and $(2,2)$. Multiplying the vertices (C.6) and (C.8) with suitable form factors and forming linear combinations of them it would be possible to construct vertices giving only $(l,S)=(0,0)$ or $(2,2)$ in the Wigner basis. But this would be a very cumbersome procedure. Therefore, we shall in this paper stick to the simple vertices as given above and label (C.6) with $(l,S)=(0,0)$ and (C.8) with $(l,S)=(2,2)$ since (C.6) has no momenta and (C.8) two momenta. But we keep in mind that the translation of the power of momenta in the covariant vertices to the angular momentum l in the Wigner basis is not one to one.

For the tensorial pomeron the situation is similar. We discuss the reaction (B.9) for a scalar meson M

$$\begin{aligned}&I\!P(\vec{k},\varepsilon_1^{W\,ij})+I\!P(-\vec{k},\varepsilon_2^{W\,hl})\to M\,,\\&i,j,h,l\in\{1,2,3\}\;.\end{aligned}\tag{D.7}$$

Here $\varepsilon_{1,2}^{W\,ij}$ are the polarization tensors of the fictitious "tensor-pomeron particle" of mass m in the Wigner basis. We have:

$$\begin{aligned}&\varepsilon_1^{W\,ij}=\varepsilon_1^{W\,ji},\quad \varepsilon_2^{W\,ij}=\varepsilon_2^{W\,ji},\\&\varepsilon_1^{W\,ij}\delta_{ij}=\varepsilon_2^{W\,ij}\delta_{ij}=0\,,\\&(\varepsilon_1^{W\,ij})^*(\varepsilon_1^{W\,ji})=1,\quad (\varepsilon_2^{W\,ij})^*(\varepsilon_2^{W\,ji})=1\,.\end{aligned}\tag{D.8}$$

The covariant polarization tensors are

$$\begin{aligned}\varepsilon_1{}^{\mu\nu}&=\Lambda_{\vec{k}}{}^{\mu}{}_{i}\,\Lambda_{\vec{k}}{}^{\nu}{}_{j}\,\varepsilon_1^{W\,ij}\,,\\\varepsilon_2{}^{\mu\nu}&=\Lambda_{-\vec{k}}{}^{\mu}{}_{i}\,\Lambda_{-\vec{k}}{}^{\nu}{}_{j}\,\varepsilon_2^{W\,ij}\,.\end{aligned}\tag{D.9}$$

With (D.9) we obtain the amplitude for (D.7) from the vertex (B.17) as follows:

$$\left\langle M\,\middle|\,\mathcal{T}\,\middle|\,I\!P(\vec{k},\varepsilon_1^{W\,ij}),I\!P(-\vec{k},\varepsilon_2^{W\,hl})\right\rangle=2\,M_0\,g'_{I\!P\!P\!M}\,\varepsilon_1{}^{\mu\nu}\varepsilon_{2\;\mu\nu}\,.\tag{D.10}$$

Inserting here the explicit expressions from (D.9) we see easily that the amplitude (D.10) has, in the Wigner basis, partial wave parts with $(l,S)=(0,0),(2,2)$, and $(4,4)$. Similarly, also the vertex (B.19) gives contributions with $(l,S)=(0,0),(2,2)$, and $(4,4)$. We label the vertex (B.17) with $(l,S)=(0,0)$ since it has no momenta, and (B.19) with $(l,S)=(2,2)$ since it is quadratic in the momenta.

The discussion of other pomeron-pomeron-meson couplings when going from the covariant forms to the partial wave amplitudes in the Wigner basis can be done in a completely analogous way.

Bibliography

[1] A. Szczurek and P. Lebiedowicz, *Exclusive scalar $f_0(1500)$ meson production for energy ranges available at the GSI Facility for Antiproton and Ion Research (GSI-FAIR) and at the Japan Proton Accelerator Research Complex (J-PARC),* Nucl.Phys. **A826** (2009) 101–130, arXiv:0906.0286 [nucl-th].

[2] P. Lebiedowicz, A. Szczurek, and R. Kamiński, *Low-energy pion-pion scattering in the $pp \to pp\pi^+\pi^-$ and $p\bar{p} \to p\bar{p}\pi^+\pi^-$ reactions,* Phys.Lett. **B680** (2009) 459–465, arXiv:0904.3872 [nucl-th].

[3] P. Lebiedowicz and A. Szczurek, *Exclusive $pp \to pp\pi^+\pi^-$ reaction: From the threshold to LHC,* Phys.Rev. **D81** (2010) 036003, arXiv:0912.0190 [hep-ph].

[4] P. Lebiedowicz and A. Szczurek, *Exclusive $pp \to nn\pi^+\pi^+$ reaction at LHC and RHIC,* Phys.Rev. **D83** (2011) 076002, arXiv:1005.2309 [hep-ph].

[5] A. Cisek, P. Lebiedowicz, W. Schäfer, and A. Szczurek, *Exclusive production of ω meson in proton-proton collisions at high energies,* Phys.Rev. **D83** (2011) 114004, arXiv:1101.4874 [hep-ph].

[6] P. Lebiedowicz, R. Pasechnik, and A. Szczurek, *Measurement of exclusive production of scalar χ_{c0} meson in proton-(anti)proton collisions via $\chi_{c0} \to \pi^+\pi^-$ decay,* Phys.Lett. **B701** (2011) 434–444, arXiv:1103.5642 [hep-ph].

[7] R. Staszewski, P. Lebiedowicz, M. Trzebiński, J. Chwastowski, and A. Szczurek, *Exclusive $\pi^+\pi^-$ Production at the LHC with Forward Proton Tagging,* Acta Phys.Polon. **B42** (2011) 1861–1870, arXiv:1104.3568 [hep-ex].

[8] P. Lebiedowicz and A. Szczurek, *$pp \to ppK^+K^-$ reaction at high energies,* Phys.Rev. **D85** (2012) 014026, arXiv:1110.4787 [hep-ph].

[9] P. Lebiedowicz and A. Szczurek, *Exclusive $pp \to pp\pi^0$ reaction at high energies,* Phys.Rev. **D87** (2013) 074037, arXiv:1303.2882 [hep-ph].

[10] P. Lebiedowicz and A. Szczurek, *Exclusive diffractive photon bremsstrahlung at the LHC,* Phys.Rev. **D87** (2013) 114013, arXiv:1302.4346 [hep-ph].

[11] P. Lebiedowicz, R. Pasechnik, and A. Szczurek, *QCD diffractive mechanism of exclusive W^+W^- pair production at high energies,* LU-TP-12-12, Nucl.Phys. **B867** (2013) 61, arXiv:1203.1832 [hep-ph].

[12] P. Lebiedowicz, R. Pasechnik, and A. Szczurek, *Search for technipions in exclusive production of diphotons with large invariant masses at the LHC,* Nucl.Phys. **B881** (2014) 288–308, arXiv:1309.7300 [hep-ph].

[13] P. Lebiedowicz, O. Nachtmann, and A. Szczurek, *Exclusive central diffractive production of scalar and pseudoscalar mesons tensorial vs. vectorial pomeron,* Annals Phys. **344** (2014) 301–339, arXiv:1309.3913 [hep-ph].

[14] P. Lebiedowicz and A. Szczurek, *Exclusive scalar $f_0(1500)$ meson production,* PoS **EPS-HEP2009** (2009) 457, arXiv:1206.2065 [hep-ph].

[15] P. Lebiedowicz and A. Szczurek, *Exclusive production of $\pi^+\pi^-$ pairs in proton-proton and proton-antiproton collisions,* Int.J.Mod.Phys. **A26** (2011) 748–750, arXiv:1008.4469 [hep-ph].

[16] P. Lebiedowicz, R. Pasechnik, and A. Szczurek, *Exclusive production of $\chi_c(0^+)$ meson and its measurement in the $\pi^+\pi^-$ channel,* Nucl.Phys.Proc.Suppl. **219-220** (2011) 284–287, arXiv:1108.2522 [hep-ph].

[17] P. Lebiedowicz, R. Pasechnik, and A. Szczurek, *Diffractive pQCD mechanism of exclusive production of W^+W^- pairs in proton-proton collisions,* PoS **QNP2012** (2012) 143, arXiv:1206.2754 [hep-ph].

[18] P. Lebiedowicz, *Exclusive Open Strangeness Production in the $pp \to ppK^+K^-$ Reaction at High Energies and a Measurement of Scalar χ_{c0} Meson,* Acta Phys.Polon.Supp. **5** (2012) 393–400, arXiv:1112.1022 [hep-ph].

[19] P. Lebiedowicz and A. Szczurek, *Exclusive meson pair production in proton-proton collisions,* EPJ Web Conf. **37** (2012) 06001, arXiv:1208.4288 [hep-ph].

[20] P. Lebiedowicz and A. Szczurek, *Exclusive production of meson pairs and resonances in proton-proton collisions,* AIP Conf.Proc. **1523** (2012) 132–136, arXiv:1212.0166 [hep-ph].

[21] P. Lebiedowicz and A. Szczurek, *Diffractive mechanisms in $pp \to pp\pi^0$ reaction at high energies,* PoS

DIS2013 (2013) 305, arXiv:1306.6823 [hep-ph].
[22] P. Lebiedowicz and A. Szczurek, *Exclusive diffractive photon bremsstrahlung at high energies,* PoS **DIS2013** (2013) 086, arXiv:1306.6819 [hep-ph].
[23] L. Alvarez Ruso, E. Oset, and E. Hernandez, *Theoretical study of the $NN \to NN\pi\pi$ reaction,* Nucl.Phys. **A633** (1998) 519–546, arXiv:nucl-th/9706046 [nucl-th].
[24] L. Alvarez Ruso, Ph.D. thesis, *Excitation of baryonic resonances induced by nucleons and leptons*, University of Valencia, 1999. `http://ific.uv.es/nucth/thesis_alvarezruso.ps`.
[25] X. Cao, B.-S. Zou, and H.-S. Xu, *Phenomenological analysis of the double pion production in nucleon-nucleon collisions up to 2.2 GeV,* Phys.Rev. **C81** (2010) 065201, arXiv:1004.0140 [nucl-th].
[26] X. Cao, B.-S. Zou, and H.-S. Xu, *Phenomenological study on the $\bar{p}N \to \bar{N}N\pi\pi$ reactions,* Nucl.Phys. **A861** (2011) 23–36, arXiv:1009.1060 [nucl-th].
[27] The PANDA Experiment Website. `http://www-panda.gsi.de/`.
[28] B. Ananthanarayan, G. Colangelo, J. Gasser, and H. Leutwyler, *Roy equation analysis of $\pi\pi$ scattering,* IISC-CTS-12-99, ZU-TH-10-00, BUTP-99-33, Phys.Rept. **353** (2001) 207–279, arXiv:hep-ph/0005297 [hep-ph].
[29] G. Colangelo, J. Gasser, and H. Leutwyler, *$\pi\pi$ scattering,* ZU-TH-3-01, BUTP-01-1, Nucl.Phys. **B603** (2001) 125–179, arXiv:hep-ph/0103088 [hep-ph].
[30] S. Descotes-Genon, N. Fuchs, L. Girlanda, and J. Stern, *Analysis and interpretation of new low-energy $\pi\pi$ scattering data,* SHEP-01-32, DFPD-01-TH-33, IPNO-DR-01-024, Eur.Phys.J. **C24** (2002) 469–483, arXiv:hep-ph/0112088 [hep-ph].
[31] I. Caprini, G. Colangelo, and H. Leutwyler, *Mass and width of the lowest resonance in QCD,* Phys.Rev.Lett. **96** (2006) 132001, arXiv:hep-ph/0512364 [hep-ph].
[32] J. Pelaez and F. Yndurain, *The Pion-pion scattering amplitude,* FTUAM-04-14, Phys.Rev. **D71** (2005) 074016, arXiv:hep-ph/0411334 [hep-ph].
[33] R. Kamiński, J. Pelaez, and F. Yndurain, *The Pion-pion scattering amplitude. III. Improving the analysis with forward dispersion relations and Roy equations,* FTUAM-07-11, Phys.Rev. **D77** (2008) 054015, arXiv:0710.1150 [hep-ph].
[34] R. Kamiński, R. Garcia-Martin, P. Grynkiewicz, and J. Pelaez, *Sigma pole position and errors of a once and twice subtracted dispersive analysis of $\pi - \pi$ scattering data,* Nucl.Phys.Proc.Suppl. **186** (2009) 318–321, arXiv:0811.4510 [hep-ph].
[35] R. Garcia-Martin, R. Kamiński, and J. Pelaez, *Precise dispersive data analysis of the $f_0(600)$ pole,* Int.J.Mod.Phys. **A24** (2009) 590–593, arXiv:0810.1134 [hep-ph].
[36] R. Kamiński, L. Leśniak, and B. Loiseau, *Elimination of ambiguities in $\pi\pi$ phase shifts using crossing symmetry,* Phys.Lett. **B551** (2003) 241–248, arXiv:hep-ph/0210334 [hep-ph].
[37] R. Garcia-Martin, R. Kamiński, J. Pelaez, J. Ruiz de Elvira, and F. Yndurain, *The Pion-pion scattering amplitude. IV: Improved analysis with once subtracted Roy-like equations up to 1100 MeV,* Phys.Rev. **D83** (2011) 074004, arXiv:1102.2183 [hep-ph].
[38] S. Godfrey and J. Napolitano, *Light meson spectroscopy,* Rev.Mod.Phys. **71** (1999) 1411–1462, arXiv:hep-ph/9811410 [hep-ph].
[39] E. Klempt and A. Zaitsev, *Glueballs, Hybrids, Multiquarks. Experimental facts versus QCD inspired concepts,* Phys.Rept. **454** (2007) 1–202, arXiv:0708.4016 [hep-ph].
[40] W. Ochs, *The Status of Glueballs,* MPP-2013-44, J.Phys. **G40** (2013) 043001, arXiv:1301.5183 [hep-ph].
[41] K. Au, D. Morgan, and M. Pennington, *Meson Dynamics Beyond the Quark Model: A Study of Final State Interactions,* RAL-86-076, DTP-86-9, Phys.Rev. **D35** (1987) 1633.
[42] J. Gunter *et al.*, (E852 Collaboration), *A Partial wave analysis of the $\pi^0\pi^0$ system produced in $\pi^- p$ charge exchange collisions,* Phys.Rev. **D64** (2001) 072003, arXiv:hep-ex/0001038 [hep-ex].
[43] D. Alde *et al.*, (GAMS Collaboration), *Study of the $\pi^0\pi^0$ system with the GAMS-4000 spectrometer at 100-GeV/c,* IHEP-98-23, IFVE-98-23, Eur.Phys.J. **A3** (1998) 361–371.
[44] R. Kamiński, L. Leśniak, and K. Rybicki, *A Joint analysis of the S wave in the $\pi^+\pi^-$ and $\pi^0\pi^0$ data,* IFJ-1897-PH-2002, Eur.Phys.J.direct **C4** (2002) 4, arXiv:hep-ph/0109268 [hep-ph].
[45] T. E. O. Ericson, B. Loiseau, and A. W. Thomas, *Determination of the pion nucleon coupling constant and scattering lengths,* CERN-TH-2000-166, TSL-ISV-2000-0232, LPNHE-LPTPE-2709-0011, ADP-00-36-T419, Phys.Rev. **C66** (2002) 014005, arXiv:hep-ph/0009312 [hep-ph].
[46] R. Machleidt, K. Holinde, and C. Elster, *The Bonn Meson Exchange Model for the Nucleon Nucleon Interaction,* Phys.Rept. **149** (1987) 1–89.
[47] D. Bugg and R. Machleidt, *πNN coupling constants from NN elastic data between 210 MeV and 800 MeV,* UI-NTH-9402, Phys.Rev. **C52** (1995) 1203–1211, arXiv:nucl-th/9404017 [nucl-th].
[48] A. Szczurek and J. Speth, *Role of meson degrees of freedom in deep inelastic lepton - nucleon scattering,* KFA-IKP-TH-1992-1, Nucl.Phys. **A555** (1993) 249–271.

[49] B. Pearce, J. Speth, and A. Szczurek, *Importance of the meson cloud to hadron structure,* KFA-IKP-TH-1992-30, Phys.Rept. **242** (1994) 193–232.
[50] J. Speth and A. W. Thomas, *Mesonic contributions to the spin and flavor structure of the nucleon,* PRINT-96-213 (CEBAF), Adv.Nucl.Phys. **24** (1997) 83–149.
[51] Z. Ouyang, J.-J. Xie, B.-S. Zou, and H.-S. Xu, *Role of the $N^*(1440)$ resonance in the $pp \to pn\pi^+$ reaction,* Nucl.Phys. **A821** (2009) 220–234, arXiv:0808.3257 [nucl-th].
[52] H. Clement, (PROMICE/WASA Collaboration), *Decay properties of the Roper resonance from $pp \to pp\pi^+\pi^-$,* arXiv:nucl-ex/0210006 [nucl-ex].
[53] S. Hirenzaki, P. Fernandez de Cordoba, and E. Oset, *Roper excitation in α - proton scattering,* Phys.Rev. **C53** (1996) 277–284, arXiv:nucl-th/9511036 [nucl-th].
[54] D. Cochran, P. Dean, P. Gram, E. Knapp, E. Martin, *et al.*, *Production of charged pions by 730 MeV protons from hydrogen and selected nuclei,* Phys.Rev. **D6** (1972) 3085–3116.
[55] F. Cverna, P. Bevington, M. Mcnaughton, H. Willard, N. King, *et al.*, *Single and double pion production from 800 MeV proton-proton collisions,* Phys.Rev. **C23** (1981) 1698–1705.
[56] F. Shimizu, Y. Kubota, H. Koiso, F. Sai, S. Sakamoto, *et al.*, *Measurement of the pp Cross-sections in the Momentum Range 0.9 GeV/c - 2.0 GeV/c,* Print-82-0243 (TOKYO), Nucl.Phys. **A386** (1982) 571.
[57] L. Dakhno, A. Kravtsov, E. Lobachev, M. Makarov, V. Medvedev, *et al.*, *Measurement Of Cross-sections Of Meson Pair Production In Nucleon Nucleon Collisions Below 1 GeV And Isospin Analysis,* Yad.Fiz. **37** (1983) 907–914.
[58] J. Pätzold, M. Bashkanov, R. Bilger, W. Brodowski, H. Calen, *et al.*, *Study of the $pp \to pp\pi^+\pi^-$ reaction in the low-energy tail of the Roper resonance,* Phys.Rev. **C67** (2003) 052202, arXiv:nucl-ex/0301019 [nucl-ex].
[59] J. Pätzold, Ph.D. thesis, *Exclusive Measurements of the $pp \to pp\pi^+\pi^-$ Reaction Close to Threshold*, University of Tübingen, 2002. `http://w210.ub.uni-tuebingen.de/dbt/volltexte/2002/550`.
[60] J. Johanson, R. Bilger, W. Brodowski, H. Calen, H. Clement, *et al.*, *Two-pion production in proton proton collisions near threshold,* Nucl.Phys. **A712** (2002) 75–94.
[61] W. Brodowski, R. Bilger, H. Calen, H. Clement, C. Ekstrom, *et al.*, *Exclusive measurement of the $pp \to pp\pi^+\pi^-$ reaction near threshold,* Phys.Rev.Lett. **88** (2002) 192301.
[62] S. Abd El-Bary *et al.*, (COSY-TOF Collaboration), *Two-Pion Production in Proton-Proton Collisions with Polarized Beam,* Eur.Phys.J. **A37** (2008) 267–277, arXiv:0806.3870 [nucl-ex].
[63] A. Buzzo *et al.*, (JETSET Collaboration), *Search for narrow anti-p p resonances in the reaction $\bar{p}p \to \bar{p}p\pi^+\pi^-$,* Z.Phys. **C76** (1997) 475–478, arXiv:hep-ex/9801015 [hep-ex].
[64] V. Baru, A. Gasparyan, J. Haidenbauer, C. Hanhart, A. E. Kudryavtsev, *et al.*, *Production of η mesons in nucleon-nucleon collisions,* FZJ-IKP-TH-2002-16, Phys.Rev. **C67** (2003) 024002, arXiv:nucl-th/0212014 [nucl-th].
[65] C. Hanhart and K. Nakayama, *On the treatment of NN interaction effects in meson production in NN collisions,* FZJ-IKP-TH-1998-20, Phys.Lett. **B454** (1999) 176–180, arXiv:nucl-th/9809059 [nucl-th].
[66] J. Haidenbauer, T. Hippchen, K. Holinde, B. Holzenkamp, V. Mull, *et al.*, *The Reaction $\bar{p}p \to \bar{\Lambda}\Lambda$ in the meson exchange picture,* KFA-IKP-TH-1991-31, Phys.Rev. **C45** (1992) 931–946.
[67] J. Haidenbauer, K. Holinde, V. Mull, and J. Speth, *Meson exchange and quark - gluon transitions in the $\bar{p}p \to \bar{\Lambda}\Lambda$ process,* KFA-IKP-TH-1992-24, Phys.Rev. **C46** (1992) 2158–2171.
[68] C. J. Morningstar and M. J. Peardon, *The Glueball spectrum from an anisotropic lattice study,* UCSD-PTH-98-36, HLRZ-1998-62, Phys.Rev. **D60** (1999) 034509, arXiv:hep-lat/9901004 [hep-lat].
[69] A. Vaccarino and D. Weingarten, *Glueball mass predictions of the valence approximation to lattice QCD,* IBMHET-99-1, Phys.Rev. **D60** (1999) 114501, arXiv:hep-lat/9910007 [hep-lat].
[70] Y. Chen, A. Alexandru, S. Dong, T. Draper, I. Horvath, *et al.*, *Glueball spectrum and matrix elements on anisotropic lattices,* UK-05-09, BIHEP-TH-05-15, JLAB-THY-05-456, Phys.Rev. **D73** (2006) 014516, arXiv:hep-lat/0510074 [hep-lat].
[71] A. Hart, C. McNeile, C. Michael, and J. Pickavance, (UKQCD Collaboration), *A Lattice study of the masses of singlet 0^{++} mesons,* EDINBURGH-PREPRINT-2006-18, Phys.Rev. **D74** (2006) 114504, arXiv:hep-lat/0608026 [hep-lat].
[72] A. H. Fariborz, *Isosinglet scalar mesons below 2 GeV and the scalar glueball mass,* Int.J.Mod.Phys. **A19** (2004) 2095–2112, arXiv:hep-ph/0302133 [hep-ph].
[73] A. H. Fariborz, *Mass Uncertainties of $f_0(600)$ and $f_0(1370)$ and their Effects on Determination of the Quark and Glueball Admixtures of the $I = 0$ Scalar Mesons,* Phys.Rev. **D74** (2006) 054030, arXiv:hep-ph/0607105 [hep-ph].
[74] M. Albaladejo and J. Oller, *Identification of a Scalar Glueball,* Phys.Rev.Lett. **101** (2008) 252002, arXiv:0801.4929 [hep-ph].
[75] S. Narison and G. Veneziano, *QCD Tests of $G(1.6)$ = Glueball,* CERN-TH-4987-88, PM-88-07,

Int.J.Mod.Phys. **A4** (1989) 2751.
[76] S. Narison, *Masses, decays and mixings of gluonia in QCD,* PM-96-37, Nucl.Phys. **B509** (1998) 312–356, arXiv:hep-ph/9612457 [hep-ph].
[77] S. Narison, *QCD tests of the puzzling scalar mesons,* HEP-MAD-2007-217.2, Phys.Rev. **D73** (2006) 114024, arXiv:hep-ph/0512256 [hep-ph].
[78] T. Huang, H.-Y. Jin, and A.-L. Zhang, *Determination of the scalar glueball mass in QCD sum rules,* Phys.Rev. **D59** (1999) 034026, arXiv:hep-ph/9807391 [hep-ph].
[79] L. Kisslinger, J. Gardner, and C. Vanderstraeten, *Mixed scalar glueballs and mesons,* Phys.Lett. **B410** (1997) 1–5.
[80] D. Harnett and T. G. Steele, *A Gaussian sum rules analysis of scalar glueballs,* Nucl.Phys. **A695** (2001) 205–236, arXiv:hep-ph/0011044 [hep-ph].
[81] G. Orlandini, T. G. Steele, and D. Harnett, *Gaussian sum rules and prediction of resonance properties,* Nucl.Phys. **A686** (2001) 261–289, arXiv:hep-ph/0007299 [hep-ph].
[82] T. G. Steele, D. Harnett, and G. Orlandini, *Gaussian sum rule analysis of scalar gluonium and quark mesons,* AIP Conf.Proc. **688** (2004) 128–141, arXiv:hep-ph/0308074 [hep-ph].
[83] D. Harnett, R. Kleiv, K. Moats, and T. Steele, *Near-Maximal Mixing of Scalar Gluonium and Quark Mesons: A Gaussian Sum-Rule Analysis,* Nucl.Phys. **A850** (2011) 110–135, arXiv:0804.2195 [hep-ph].
[84] C. Amsler and F. E. Close, *Is $f_0(1500)$ a scalar glueball?,* RAL-TR-95-003, Phys.Rev. **D53** (1996) 295–311, arXiv:hep-ph/9507326 [hep-ph].
[85] F. E. Close, *Glueballs: A Central mystery,* Acta Phys.Polon. **B31** (2000) 2557–2565, arXiv:hep-ph/0006288 [hep-ph].
[86] C. Amsler *et al.*, (Crystal Barrel Collaboration.), *Observation of a new $I^G(J^{PC}) = 1^-(0^{++})$ resonance at 1450 MeV,* Phys.Lett. **B333** (1994) 277–282.
[87] C. Amsler *et al.*, (Crystal Barrel Collaboration), *$\eta\eta'$ threshold enhancement in $\bar{p}p$ annihilations into $\pi^0\eta\eta'$ at rest,* Phys.Lett. **B340** (1994) 259–263.
[88] A. Abele *et al.*, (Crystal Barrel Collaboration), *Observation of $f_0(1500)$ decay into $K_L K_L$,* Phys.Lett. **B385** (1996) 425–432.
[89] V. Anisovich, *Resonance $f_0(1500)$: Is it a scalar glueball?,* Phys.Lett. **B364** (1995) 195–198, arXiv:hep-ph/9512206 [hep-ph].
[90] D. Barberis *et al.*, (WA102 Collaboration), *A Coupled channel analysis of the centrally produced K^+K^- and $\pi^+\pi^-$ final states in pp interactions at 450 GeV/c,* Phys.Lett. **B462** (1999) 462–470, arXiv:hep-ex/9907055 [hep-ex].
[91] D. Barberis *et al.*, (WA102 Collaboration), *A Study of the $f_0(1370)$, $f_0(1500)$, $f_0(2000)$ and $f_2(1950)$ observed in the centrally produced 4π final states,* Phys.Lett. **B474** (2000) 423–426, arXiv:hep-ex/0001017 [hep-ex].
[92] F. E. Close and A. Kirk, *A Glueball - $q\bar{q}$ filter in central hadron production,* RAL-96-101, BHAM-HEP-96-05, Phys.Lett. **B397** (1997) 333–338, arXiv:hep-ph/9701222 [hep-ph].
[93] F. E. Close, A. Kirk, and G. A. Schuler, *Dynamics of glueball and $q\bar{q}$ production in the central region of pp collisions,* Phys.Lett. **B477** (2000) 13–18, arXiv:hep-ph/0001158 [hep-ph].
[94] F. E. Close and G. A. Schuler, *Central production of mesons: Exotic states versus pomeron structure,* CERN-TH-99-28, Phys.Lett. **B458** (1999) 127–136, arXiv:hep-ph/9902243 [hep-ph].
[95] F. E. Close and G. A. Schuler, *Evidence that the pomeron transforms as a nonconserved vector current,* CERN-TH-99-131, Phys.Lett. **B464** (1999) 279–285, arXiv:hep-ph/9905305 [hep-ph].
[96] J. Beringer *et al.*, (Particle Data Group), *Review of Particle Physics (RPP),* Phys.Rev. **D86** (2012) 010001.
[97] T. Ericson and W. Weise, *Pions and Nuclei*. Oxford University Press, 1988.
[98] F. E. Close and Q. Zhao, *Production of $f_0(1710)$, $f_0(1500)$, and $f_0(1370)$ in J/ψ hadronic decays,* Phys.Rev. **D71** (2005) 094022, arXiv:hep-ph/0504043 [hep-ph].
[99] V. A. Khoze, A. D. Martin, and M. Ryskin, *The Rapidity gap Higgs signal at LHC,* DTP-97-12, Phys.Lett. **B401** (1997) 330–336, arXiv:hep-ph/9701419 [hep-ph].
[100] V. Khoze, A. Martin, and M. Ryskin, *Prospects for new physics observations in diffractive processes at the LHC and Tevatron,* IPPP-01-53, DCPT-01-106, Eur.Phys.J. **C23** (2002) 311–327, arXiv:hep-ph/0111078 [hep-ph].
[101] A. Kaidalov, V. Khoze, A. Martin, and M. Ryskin, *Extending the study of the Higgs sector at the LHC by proton tagging,* IPPP-03-51, DCPT-03-102, Eur.Phys.J. **C33** (2004) 261–271, arXiv:hep-ph/0311023 [hep-ph].
[102] A. Kaidalov, V. Khoze, A. Martin, and M. Ryskin, *Central exclusive diffractive production as a spin-parity analyser: From Hadrons to Higgs,* IPPP-03-35, DCPT-03-70, Eur.Phys.J. **C31** (2003) 387–396, arXiv:hep-ph/0307064 [hep-ph].

[103] V. Khoze, A. Martin, M. Ryskin, and W. Stirling, *Double diffractive χ meson production at the hadron colliders*, IPPP-04-13, DCPT-04-26, Eur.Phys.J. **C35** (2004) 211–220, arXiv:hep-ph/0403218 [hep-ph].
[104] R. Pasechnik, A. Szczurek, and O. Teryaev, *Central exclusive production of scalar χ_c meson at the Tevatron, RHIC and CERN LHC energies*, Phys.Rev. **D78** (2008) 014007, arXiv:0709.0857 [hep-ph].
[105] A. Szczurek, R. Pasechnik, and O. Teryaev, *$pp \to pp\eta'$ reaction at high energies*, Phys.Rev. **D75** (2007) 054021, arXiv:hep-ph/0608302 [hep-ph].
[106] R. Pasechnik, A. Szczurek, and O. Teryaev, *Elastic double diffractive production of axial-vector $\chi_c(1^{++})$ mesons and the Landau-Yang theorem*, Phys.Lett. **B680** (2009) 62–71, arXiv:0901.4187 [hep-ph].
[107] M. Łuszczak and A. Szczurek, *Gluon transverse momenta and charm quark-antiquark pair production in $p - \bar{p}$ collisions at Tevatron*, Phys.Rev. **D73** (2006) 054028, arXiv:hep-ph/0512120 [hep-ph].
[108] M. Glück, E. Reya, and A. Vogt, *Dynamical parton distributions of the proton and small x physics*, DO-TH-94-24, DESY-94-206, Z.Phys. **C67** (1995) 433–448.
[109] J. Gunion and D. E. Soper, *Quark Counting and Hadron Size Effects for Total Cross-Sections*, PRINT-76-0955 (UC,DAVIS), Phys.Rev. **D15** (1977) 2617–2621.
[110] E. Levin and M. Ryskin, *Born Approximation of QCD for Description of High-Energy Hadronic Interactions*, Sov.J.Nucl.Phys. **34** (1981) 619–623.
[111] A. Szczurek, N. N. Nikolaev, and J. Speth, *From soft to hard regime in elastic pion pion scattering above resonances*, Phys.Rev. **C66** (2002) 055206, arXiv:hep-ph/0112331 [hep-ph].
[112] D. Shirkov and I. Solovtsov, *Analytic model for the QCD running coupling with universal $\bar{\alpha}_s(0)$ value*, JINR-E2-97-133, Phys.Rev.Lett. **79** (1997) 1209–1212, arXiv:hep-ph/9704333 [hep-ph].
[113] A. Donnachie and P. Landshoff, *Total cross sections*, CERN-TH-6635-92, Phys.Lett. **B296** (1992) 227–232, arXiv:hep-ph/9209205 [hep-ph].
[114] A. Donnachie, H. G. Dosch, O. Nachtmann, and P. Landshoff, *Pomeron physics and QCD*. Cambridge University Press, 2002.
[115] A. Kirk, *Resonance production in central pp collisions at the CERN Omega spectrometer*, Phys.Lett. **B489** (2000) 29–37, arXiv:hep-ph/0008053 [hep-ph].
[116] A. Breakstone *et al.*, (Ames-Bologna-CERN-Dortmund-Heidelberg-Warsaw Collaboration), *Production of the f^0 Meson in the Double Pomeron Exchange Reaction $pp \to pp\pi^+\pi^-$ at $\sqrt{s} = 62$ GeV*, CERN-EP/86-11, Z.Phys. **C31** (1986) 185.
[117] M. Melis, F. Murgia, and J. Parisi, *Glueball production in radiative J/ψ, Υ decays*, Phys.Rev. **D70** (2004) 034021, arXiv:hep-ph/0404070 [hep-ph].
[118] A. Abele *et al.*, (Crystal Barrel Collaboration), *Study of f_0 decays into four neutral pions*, Eur.Phys.J. **C19** (2001) 667–675.
[119] A. Abele *et al.*, (Crystal Barrel Collaboration), *4π decays of scalar and vector mesons*, Eur.Phys.J. **C21** (2001) 261–269.
[120] D. Barberis *et al.*, (WA102 Collaboration), *A Spin analysis of the 4π channels produced in central pp interactions at 450-GeV/c*, Phys.Lett. **B471** (2000) 440–448, arXiv:hep-ex/9912005 [hep-ex].
[121] D. Barberis *et al.*, (WA102 Collaboration), *A Study of the $\eta\eta'$ and $\eta'\eta'$ channels produced in central pp interactions at 450-GeV/c*, Phys.Lett. **B471** (2000) 429–434, arXiv:hep-ex/9911041 [hep-ex].
[122] J. Pumplin and F. Henyey, *Double Pomeron Exchange in the Reaction $pp \to pp\pi^+\pi^-$*, Print-76-0635 (MICHIGAN STATE), Nucl.Phys. **B117** (1976) 377.
[123] J. Pelaez and F. Yndurain, *Regge analysis of pion pion (and pion kaon) scattering for energy $\sqrt{s} > 1.4$ GeV*, FTUAM-03-19, Phys.Rev. **D69** (2004) 114001, arXiv:hep-ph/0312187 [hep-ph].
[124] Data files and plots of cross-sections and related quantities. `http://pdg.lbl.gov/2013/hadronic-xsections/hadron.html`.
[125] A. Kaidalov, *Diffractive Production Mechanisms*, Phys.Rept. **50** (1979) 157–226.
[126] G. Alberi and G. Goggi, *Diffraction of Subnuclear Waves*, Phys.Rept. **74** (1981) 1–207.
[127] M. Good and W. Walker, *Diffraction disssociation of beam particles*, Phys.Rev. **120** (1960) 1857–1860.
[128] M. Albrow, T. Coughlin, and J. Forshaw, *Central exclusive particle production at high energy hadron colliders*, FERMILAB-PUB-10-193-E, Prog.Part.Nucl.Phys. **65** (2010) 149–184, arXiv:1006.1289 [hep-ph].
[129] D. Alde *et al.*, (GAMS Collaboration), *Study of the $\pi^0\pi^0$ system in pp central collisions at 450 GeV/c*, KEK-PREPRINT-96-174, Phys.Lett. **B397** (1997) 350–356.
[130] P. Collins, *An introduction to Regge theory and high energy physics*. Cambridge University Press, 1977.
[131] J. Forshaw and D. Ross, *Quantum Chromodynamics and the Pomeron*. Cambridge University Press, 1997.
[132] M. Froissart, *Asymptotic behavior and subtractions in the Mandelstam representation*, Phys.Rev. **123** (1961) 1053–1057.
[133] A. Martin, *Unitarity and high-energy behavior of scattering amplitudes*, Phys.Rev. **129** (1963) 1432–1436.

[134] G. Chew and S. C. Frautschi, *Regge Trajectories and the Principle of Maximum Strength for Strong Interactions,* Phys.Rev.Lett. **8** (1962) 41–44.
[135] A. Eide, P. Lehmann, A. Lundby, C. Baglin, P. Briandet, *et al.*, *Elastic scattering and two-body annihilations at 5 Gev/c,* Nucl.Phys. **B60** (1973) 173–220.
[136] I. Ambats, D. Ayres, R. Diebold, A. Greene, S. Kramer, *et al.*, *Systematic study of $\pi^{\pm}p$, $K^{\pm}p$, pp, and $\bar{p}p$ forward elastic scattering from 3 to 6 Gev/c,* Phys.Rev. **D9** (1974) 1179–1209.
[137] C. Akerlof, R. Kotthaus, R. Loveless, D. Meyer, I. Ambats, *et al.*, *Hadron-Proton Elastic Scattering at 50 GeV/c, 100 GeV/c and 200 GeV/c Momentum,* UM HE 76-6, Phys.Rev. **D14** (1976) 2864.
[138] D. Ayres *et al.*, (Fermilab Single Arm Spectrometer Group), *$\pi^{\pm}p$, $K^{\pm}p$, pp and $\bar{p}p$ Elastic Scattering from 50 GeV/c to 175 GeV/c,* FERMILAB-PUB-76-066-EXP, FERMILAB-PUB-76-066-E, MIT-LNS-99, ANL-HEP-PR-75-055, Phys.Rev. **D15** (1977) 3105.
[139] A. Schiz, L. Fajardo, R. Majka, J. Marx, P. Nemethy, *et al.*, *A High Statistics Study of π^+p, π^-p, and pp Elastic Scattering at 200-GeV/c,* FERMILAB-PUB-79-081-EXP, FERMILAB-PUB-79-081-E, Phys.Rev. **D24** (1981) 26.
[140] G. Antchev *et al.*, (TOTEM Collaboration), *Measurement of proton-proton elastic scattering and total cross-section at $\sqrt{s}$ = 7 TeV,* Europhys.Lett. **101** (2013) 21002.
[141] A. Donnachie and P. V. Landshoff, *pp and $\bar{p}p$ total cross sections and elastic scattering,* MAN-HEP-2013-19-DAMTP-2013-38, arXiv:1309.1292 [hep-ph].
[142] G. Antchev *et al.*, (TOTEM Collaboration), *Proton-proton elastic scattering at the LHC energy of $\sqrt{s}$ = 7 TeV,* CERN-PH-EP-2011-101, Europhys.Lett. **95** (2011) 41001, arXiv:1110.1385 [hep-ex].
[143] Y. I. Azimov, V. A. Khoze, E. Levin, and M. Ryskin, *Estimates of the Cross-Sections for Double-Reggeon Processes,* LENINGRAD-74-107, Sov.J.Nucl.Phys. **21** (1975) 215.
[144] M. Guidal, J. Laget, and M. Vanderhaeghen, *Pion and kaon photoproduction at high-energies: Forward and intermediate angles,* DAPNIA-SPHN-97-26, Nucl.Phys. **A627** (1997) 645–678.
[145] B. G. Yu, T. K. Choi, and W. Kim, *Regge phenomenology of pion photoproduction off the nucleon at forward angles,* Phys.Rev. **C83** (2011) 025208, arXiv:1103.1203 [nucl-th].
[146] L. Harland-Lang, V. Khoze, and M. Ryskin, *Modeling exclusive meson pair production at hadron colliders,* IPPP-13-102, DCPT-13-204, arXiv:1312.4553 [hep-ph].
[147] W. Schäfer and A. Szczurek, *Exclusive photoproduction of J/ψ in proton-proton and proton-antiproton scattering,* Phys.Rev. **D76** (2007) 094014, arXiv:0705.2887 [hep-ph].
[148] R. Schicker, L. Jenkovszky, and O. Kuprash, *Charge exchange reaction at high energies,* arXiv:1311.1103 [hep-ph].
[149] A. Dzyuba, M. Buscher, M. Hartmann, I. Keshelashvili, V. Koptev, *et al.*, *Coupled-channel effects in the $pp \to ppK^+K^-$ reaction,* Phys.Lett. **B668** (2008) 315–318, arXiv:0807.0524 [nucl-th].
[150] J.-J. Xie and C. Wilkin, *Associated strangeness production in the $pp \to pK^+K^-p$ and $pp \to pK^+\pi^0\Sigma^0$ reactions,* Phys.Rev. **C82** (2010) 025210, arXiv:1005.2957 [nucl-th].
[151] J. Laget, *Strangeness production in nucleon-nucleon collisions,* Phys.Lett. **B259** (1991) 24–28.
[152] T. Armstrong *et al.*, (WA76 Collaboration), *Study of the centrally produced $\pi\pi$ and $K\bar{K}$ systems at 85 GeV/c and 300 GeV/c,* CERN-PPE-91-40, Z.Phys. **C51** (1991) 351–364.
[153] F. Nerling, (COMPASS Collaboration), *Hadron Spectroscopy with COMPASS: Newest Results,* EPJ Web Conf. **37** (2012) 01016, arXiv:1208.0487 [hep-ex].
[154] A. Austregesilo and T. Schlueter, (COMPASS Collaboration), *Partial-Wave Analysis of the Centrally Produced $\pi^+\pi^-$ System in pp Reactions at COMPASS,* PoS **QNP2012** (2012) 098, arXiv:1207.0949 [hep-ex].
[155] A. Austregesilo, (COMPASS), *A Partial-Wave Analysis of Centrally Produced Two-Pseudoscalar Final States in pp Reactions at COMPASS,* PoS **Bormio2013** (2013) 014.
[156] T. Åkesson *et al.*, (AFS Collaboration), *A Search for Glueballs and a Study of Double Pomeron Exchange at the CERN Interacting Storage Rings,* CERN-EP-85-115, Nucl.Phys. **B264** (1986) 154.
[157] K. Ackermann *et al.*, (STAR Collaboration), *STAR detector overview,* Nucl.Instrum.Meth. **A499** (2003) 624–632.
[158] J. Turnau, (STAR Collaboration), *Measurement of the Central Exclusive Production of pion pairs using tagged forward protons at the STAR detector at RHIC,* EPJ Web Conf. **37** (2012) 06010.
[159] M. Albrow, A. Święch, and M. Żurek, (CDF Collaboration), *Exclusive central meson production in proton antiproton collisions at the Tevatron,* EPJ Web Conf. **37** (2012) 06011.
[160] M. Albrow, D. Lontkovskyi, I. Makarenko, A. Święch, and M. Żurek, (CDF Collaboration), *Central exclusive production of hadrons in CDF,* FERMILAB-CONF-12-797-PPD, AIP Conf.Proc. **1523** (2012) 294–297.
[161] M. Albrow, A. Święch, and M. Żurek, (CDF Collaboration), *Exclusive Central $\pi^+\pi^-$ production in CDF,* FERMILAB-CONF-13-467-PPD, EDSBLOIS-2013-37, arXiv:1310.3839 [hep-ex].

[162] R. Schicker, (ALICE Collaboration), *Central Diffraction in ALICE,* arXiv:1205.2588 [hep-ex].
[163] D. Denegri and et al., (French-Soviet Collaboration), *Double Pomeron Exchange and Diffractive Dissociation in the Reaction $pp \to pp\pi^+\pi^-$ at 69 GeV/c*, SACLAY-DPhPE 75-04, Nucl.Phys. **B98** (1975) 189.
[164] D. Brick, H. Rudnicka, A. Shapiro, M. Widgoff, R. Ansorge, *et al.*, *The reactions $pp \to pp\pi^+\pi^-$, $K^+p \to K^+p\pi^+\pi^-$, $\pi^+p \to \pi^+p\pi^+\pi^-$, $\pi^-p \to \pi^-p\pi^+\pi^-$ at 147 GeV/c,* FERMILAB-PUB-82-109-E, Z.Phys. **C19** (1983) 1–9.
[165] M. Derrick, B. Musgrave, P. Schreiner, and H. Yuta, *Double Pomeron Exchange Contribution to the Reaction $pp \to pp\pi^+\pi^-$ at 205 GeV/c.*, FERMILAB-PUB-74-170-E, ANL-HEP-7339, D74-01055, Phys.Rev.Lett. **32** (1974) 80–82.
[166] D. Chew, *Search for Experimental Evidence on Exclusive Double-Pomeron Exchange,* LBL-3009, Nucl.Phys. **B82** (1974) 422.
[167] L. Baksay, L. Baum, A. Bohm, A. Derevshchikov, H. Hilscher, *et al.*, *Evidence for Double Pomeron Exchange at the CERN ISR,* Print-75-1076 (CERN), Phys.Lett. **B61** (1976) 89.
[168] M. Della Negra *et al.*, (CERN-PARIS-HEIDELBERG-KARLSRUHE COLLABORATION), *Study of Double Pomeron Exchange in pp Collisions at $\sqrt{s} = 31$ GeV,* Phys.Lett. **B65** (1976) 394–396.
[169] H. de Kerret, N. Kwak, E. Nagy, R. Orr, M. Regler, *et al.*, *Experimental Evidence for Double-Pomeron Exchange at ISR Energies,* PRINT-77-0477 (CERN), Phys.Lett. **B68** (1977) 385.
[170] B. Oh, M. Pratap, G. Sionakides, G. Smith, J. Whitmore, *et al.*, *Evidence for Double Pomeron Exchange at Fermilab Energies,* FERMILAB-PUB-77-114-E, PRINT-77-0200 (MICHIGAN-STATE).
[171] D. Drijard *et al.*, (CCHK Collaboration), *Double Pomeron Exchange in the Reaction $pp \to pp\pi^+\pi^-$ at ISR Energies,* CERN-EP-PHYS-78-10, Nucl.Phys. **B143** (1978) 61.
[172] R. Waldi, K. Schubert, and K. Winter, *Search for glueballs in a pomeron pomeron scattering experiment,* Z.Phys. **C18** (1983) 301–306.
[173] A. Breakstone *et al.*, (ABCDHW Collaboration), *Inclusive Pomeron-Pomeron Interactions at the CERN ISR,* IS-J-3226, Z.Phys. **C42** (1989) 387.
[174] A. Breakstone *et al.*, (ABCDHW Collaboration), *The reaction Pomeron-Pomeron $\to \pi^+\pi^-$ and an unusual production mechanism for the $f_2(1270)$,* IS-J-4087, Z.Phys. **C48** (1990) 569–576.
[175] L. Harland-Lang, V. Khoze, M. Ryskin, and W. Stirling, *The Phenomenology of Central Exclusive Production at Hadron Colliders,* IPPP-12-12, DCPT-12-24, CAVENDISH-HEP-12-05, Eur.Phys.J. **C72** (2012) 2110, arXiv:1204.4803 [hep-ph].
[176] M. Albrow, J. Lewis, M. Żurek, A. Święch, D. Lontkovskyi, I. Makarenko, and J. S. Wilson, Measurement of Central Exclusive Hadron Pair Production in CDF. `http://www-cdf.fnal.gov/physics/new/qcd/GXG_12/`.
[177] R. Pasechnik, A. Szczurek, and O. Teryaev, *Nonperturbative and spin effects in the central exclusive production of tensor $\chi_c(2^+)$ meson,* Phys.Rev. **D81** (2010) 034024, arXiv:0912.4251 [hep-ph].
[178] L. Harland-Lang, V. Khoze, M. Ryskin, and W. Stirling, *Central exclusive χ_c meson production at the Tevatron revisited,* IPPP-09-70, DCPT-09-140, CAVENDISH-HEP-09-17, Eur.Phys.J. **C65** (2010) 433–448, arXiv:0909.4748 [hep-ph].
[179] L. Harland-Lang, V. Khoze, M. Ryskin, and W. Stirling, *Central exclusive quarkonium production with tagged forward protons at RHIC,* IPPP-10-87, DCPT-10-174, CAVENDISH-HEP-10-19, Eur.Phys.J. **C71** (2011) 1545, arXiv:1011.0680 [hep-ph].
[180] T. Aaltonen *et al.*, (CDF Collaboration), *Observation of Exclusive Charmonium Production and $\gamma\gamma \to \mu^+\mu^-$ in $p\bar{p}$ Collisions at $\sqrt{s} = 1.96$ TeV,* FERMILAB-PUB-09-037-E, Phys.Rev.Lett. **102** (2009) 242001, arXiv:0902.1271 [hep-ex].
[181] Q. He *et al.*, (CLEO Collaboration), *First Observation of Exclusive χ_{cJ} Decays to Two Charged and Two Neutral Hadrons,* CLNS-07-2007, CLEO-07-12, Phys.Rev. **D78** (2008) 092004, arXiv:0806.1227 [hep-ex].
[182] M. Ablikim *et al.*, (The BESIII Collaboration), *Branching fraction measurements of χ_{c0} and χ_{c2} to $\pi^0\pi^0$ and $\eta\eta$,* Phys.Rev. **D81** (2010) 052005, arXiv:1001.5360 [hep-ex].
[183] M. Ablikim *et al.*, (BESIII Collaboration), *First Observation of the Decays $\chi_{cJ} \to \pi^0\pi^0\pi^0\pi^0$,* Phys.Rev. **D83** (2011) 012006, arXiv:1011.6556 [hep-ex].
[184] M. Ablikim, (BESIII Collaboration), *Observation of χ_{cJ} decaying into the $p\bar{p}K^+K^-$ final state,* Phys.Rev. **D83** (2011) 112009, arXiv:1103.2661 [hep-ex].
[185] E. J. Eichten and C. Quigg, *Quarkonium wave functions at the origin,* FERMILAB-PUB-95-045-T, CLNS-95-1329, Phys.Rev. **D52** (1995) 1726–1728, arXiv:hep-ph/9503356 [hep-ph].
[186] R. Barbieri, M. Caffo, R. Gatto, and E. Remiddi, *QCD corrections to P wave quarkonium decays,* CERN-TH-3071, Nucl.Phys. **B192** (1981) 61.
[187] W. Kwong, P. B. Mackenzie, R. Rosenfeld, and J. L. Rosner, *Quarkonium Annihilation Rates,*

EFI-87-31-CHICAGO, FERMILAB-PUB-87-239-T, Phys.Rev. **D37** (1988) 3210.
[188] M. L. Mangano and A. Petrelli, *An update on χ_c decays: Perturbative QCD versus data,* CERN-TH-95-67, CERN-TH-95-067, Phys.Lett. **B352** (1995) 445–450, arXiv:hep-ph/9503465 [hep-ph].
[189] A. Shuvaev, K. J. Golec-Biernat, A. D. Martin, and M. Ryskin, *Off diagonal distributions fixed by diagonal partons at small x and ξ,* DTP-99-18, Phys.Rev. **D60** (1999) 014015, arXiv:hep-ph/9902410 [hep-ph].
[190] A. D. Martin and M. Ryskin, *Unintegrated generalized parton distributions,* IPPP-01-31, DCPT-01-62, Phys.Rev. **D64** (2001) 094017, arXiv:hep-ph/0107149 [hep-ph].
[191] M. Glück, P. Jimenez-Delgado, and E. Reya, *Dynamical parton distributions of the nucleon and very small-x physics,* DO-TH-07-06, Eur.Phys.J. **C53** (2008) 355–366, arXiv:0709.0614 [hep-ph].
[192] M. Glück, P. Jimenez-Delgado, E. Reya, and C. Schuck, *On the role of heavy flavor parton distributions at high energy colliders,* DO-TH-08-01, Phys.Lett. **B664** (2008) 133–138, arXiv:0801.3618 [hep-ph].
[193] V. Khoze, A. Martin, and M. Ryskin, *Physics with tagged forward protons at the LHC,* IPPP-02-18, DCPT-02-36, Eur.Phys.J. **C24** (2002) 581–587, arXiv:hep-ph/0203122 [hep-ph].
[194] A. Szczurek and J. Speth, *Perturbative QCD versus pion exchange and hadronic FSI effects in the $\gamma\gamma \to \pi^+\pi^-$ reaction,* Nucl.Phys. **A728** (2003) 182–202, arXiv:hep-ph/0207265 [hep-ph].
[195] O. Krehl, R. Rapp, and J. Speth, *Meson meson scattering: $K\bar{K}$ thresholds and $f_0(980) - a_0(980)$ mixing,* KFA-IKP-TH-1996-09, JLAB-THY-96-04, Phys.Lett. **B390** (1997) 23–28, arXiv:nucl-th/9609013 [nucl-th].
[196] A. Cisek, W. Schäfer, and A. Szczurek, *Exclusive photoproduction of ϕ meson in $\gamma p \to \phi p$ and $pp \to p\phi p$ reactions,* Phys.Lett. **B690** (2010) 168–174, arXiv:1004.0070 [hep-ph].
[197] G. Aad *et al.*, (ATLAS Collaboration), *The ATLAS Experiment at the CERN Large Hadron Collider,* JINST **3** (2008) S08003.
[198] (ATLAS Collaboration), *ATLAS Luminosity and Forward Physics Community:* ATLAS TDR 018, CERN/LHCC/2008-004.
[199] G. Anelli *et al.*, (TOTEM Collaboration), *The TOTEM experiment at the CERN Large Hadron Collider,* JINST **3** (2008) S08007.
[200] R. Staszewski and J. Chwastowski, *Transport Simulation and Diffractive Event Reconstruction at the LHC,* Nucl.Instrum.Meth. **A609** (2009) 136–141, arXiv:0906.2868 [physics.ins-det].
[201] G. Aad *et al.*, (ATLAS Collaboration), *Charged-particle multiplicities in pp interactions measured with the ATLAS detector at the LHC,* New J.Phys. **13** (2011) 053033, arXiv:1012.5104 [hep-ex].
[202] D. Gillberg, (ATLAS Liquid Argon Calorimeter Collaboration), *Performance of the ATLAS forward calorimeters in first LHC data,* J.Phys.Conf.Ser. **293** (2011) 012041.
[203] C. Ewerz, M. Maniatis, and O. Nachtmann, *A Model for Soft High-Energy Scattering: Tensor Pomeron and Vector Odderon,* Annals of Physics **342** (2014) 31–77, arXiv:1309.3478 [hep-ph].
[204] T. Arens, O. Nachtmann, M. Diehl, and P. Landshoff, *Some tests for the helicity structure of the pomeron in ep collisions,* HD-THEP-96-06, DAMTP-96-51, Z.Phys. **C74** (1997) 651–669, arXiv:hep-ph/9605376 [hep-ph].
[205] V. Petrov, R. Ryutin, A. Sobol, and J.-P. Guillaud, *Azimuthal angular distributions in EDDE as spin-parity analyser and glueball filter for LHC,* JHEP **0506** (2005) 007, arXiv:hep-ph/0409118 [hep-ph].
[206] J. R. Ellis and D. Kharzeev, *The Glueball filter in central production and broken scale invariance,* CERN-TH-98-349, arXiv:hep-ph/9811222 [hep-ph].
[207] N. Kochelev, *Unusual properties of the central production of glueballs and instantons,* arXiv:hep-ph/9902203 [hep-ph].
[208] D. Kharzeev and E. Levin, *Soft double diffractive Higgs production at hadron colliders,* FERMILAB-PUB-00-035-T, BNL-NT-00-14, TAUP-2636-2000, Phys.Rev. **D63** (2001) 073004, arXiv:hep-ph/0005311 [hep-ph].
[209] E. Shuryak and I. Zahed, *Semiclassical double pomeron production of glueballs and η',* Phys.Rev. **D68** (2003) 034001, arXiv:hep-ph/0302231 [hep-ph].
[210] R. Pasechnik, A. Szczurek, and O. Teryaev, *Polarisation effects in the central exclusive χ_c production and the J/ψ angular distributions,* Phys.Rev. **D83** (2011) 074017, arXiv:1008.4325 [hep-ph].
[211] R. Maciuła, R. Pasechnik, and A. Szczurek, *Central exclusive quark-antiquark dijet and Standard Model Higgs boson production in proton-(anti)proton collisions,* Phys.Rev. **D83** (2011) 114034, arXiv:1011.5842 [hep-ph].
[212] D. Barberis *et al.*, (WA102 Collaboration), *A Kinematical selection of glueball candidates in central production,* CERN-PPE-96-197, Phys.Lett. **B397** (1997) 339–344.
[213] D. Barberis *et al.*, (WA102 Collaboration), *A Study of pseudoscalar states produced centrally in pp interactions at 450 GeV/c,* Phys.Lett. **B427** (1998) 398–402, arXiv:hep-ex/9803029 [hep-ex].

[214] D. Barberis *et al.*, (WA102 Collaboration), *Experimental evidence for a vector like behavior of Pomeron exchange,* Phys.Lett. **B467** (1999) 165–170, arXiv:hep-ex/9909013 [hep-ex].
[215] S. Weinberg, *The Quantum Theory of Fields*, vol. II. Cambridge University Press, 1996.
[216] N. Kochelev, T. Morii, and A. Vinnikov, *Pomeron fusion and central η and η' meson production,* Phys.Lett. **B457** (1999) 202–206, arXiv:hep-ph/9903279 [hep-ph].
[217] L. Kaptari and B. Kämpfer, *η' Meson Production in Nucleon-Nucleon Collisions Near The Threshold,* Eur.Phys.J. **A37** (2008) 69–80, arXiv:0804.2019 [nucl-th].
[218] K. Nakayama, Y. Oh, and H. Haberzettl, *Combined analysis of η meson hadro- and photo-production off nucleons,* J.Korean Phys.Soc. **59** (2011) 224–246, arXiv:0803.3169 [hep-ph].
[219] K. Nakayama and H. Haberzettl, *Consistent analysis of the reaction $\gamma \to p\eta'$ and $pp \to pp\eta'$,* Phys.Rev. **C69** (2004) 065212, arXiv:nucl-th/0401030 [nucl-th].
[220] K. Nakayama, J. Speth, and T. Lee, *η meson production in NN collisions,* Phys.Rev. **C65** (2002) 045210, arXiv:nucl-th/0202012 [nucl-th].
[221] D. Barberis *et al.*, (WA91 Collaboration), *Observation of vertex factorization breaking in central pp interactions,* CERN-PPE-96-128, Phys.Lett. **B388** (1996) 853–858.
[222] A. Donnachie and P. Landshoff, *pp and $\bar{p}p$ Elastic Scattering*, M/C TH-83/13, DAMTP 83/9, Nucl.Phys. **B231** (1984) 189.
[223] A. Donnachie and P. Landshoff, *Elastic Scattering and Diffraction Dissociation,* DAMTP 84/6, M/C TH-84/8, Nucl.Phys. **B244** (1984) 322.
[224] A. Donnachie and P. Landshoff, *Dynamics of Elastic Scattering,* M/C-TH-85/14, DAMTP-85/26, Nucl.Phys. **B267** (1986) 690.
[225] A. Donnachie and P. Landshoff, *Diffractive Deep Inelastic Lepton Scattering*, DAMTP/87-2, M/C-TH-87/4, Phys.Lett. **B191** (1987) 309.
[226] P. Landshoff and O. Nachtmann, *Vacuum Structure and Diffraction Scattering,* HD-THEP-86-23, DAMTP-86/27, Z.Phys. **C35** (1987) 405.
[227] A. Donnachie and P. Landshoff, *Exclusive ρ Production in Deep Inelastic Scattering,* M/C TH-86/26, DAMTP-86/25, Phys.Lett. **B185** (1987) 403.
[228] A. Donnachie and P. Landshoff, *Hard Diffraction: Production of High p_T Jets, W or Z, and Drell-Yan Pairs,* M/C-TH-87/05, DAMTP-87/16, Nucl.Phys. **B303** (1988) 634.
[229] F. E. Close and A. Kirk, *Isospin breaking exposed in $f_0(980) - a_0(980)$ mixing,* Phys.Lett. **B489** (2000) 24–28, arXiv:hep-ph/0008066 [hep-ph].
[230] C. Di Donato, G. Ricciardi, and I. Bigi, *$\eta - \eta'$ Mixing - From electromagnetic transitions to weak decays of charm and beauty hadrons,* UND-HEP-11-BIG, DSF-6-2011, Phys.Rev. **D85** (2012) 013016, arXiv:1105.3557 [hep-ph].
[231] P. Kroll and K. Passek-Kumericki, *Two gluon components of the η and η' mesons to leading-twist accuracy,* WU-B-02-02, Phys.Rev. **D67** (2003) 054017, arXiv:hep-ph/0210045 [hep-ph].
[232] N. Kochelev, T. Morii, B. Reznik, and A. Vinnikov, *The Role of secondary Reggeons in central meson production,* Eur.Phys.J. **A8** (2000) 405–408, arXiv:hep-ph/0005088 [hep-ph].
[233] P. Castoldi, R. Escribano, and J. Frere, *Central pseudoscalar production in pp scattering and the gluon contribution to the proton spin,* ULB-TH-97-21, Phys.Lett. **B425** (1998) 359–364, arXiv:hep-ph/9712387 [hep-ph].
[234] W. Kilian and O. Nachtmann, *Single pseudoscalar meson production in diffractive ep scattering*, HD-THEP-97-57, Eur.Phys.J. **C5** (1998) 317–326, arXiv:hep-ph/9712371 [hep-ph].
[235] P. Jenni, M. Nordberg, M. Nessi, and K. Jon-And, (ATLAS Collaboration), *ATLAS Forward Detectors for Measurement of Elastic Scattering and Luminosity,* CERN-LHCC-2008-004, ATLAS-TDR-18.
[236] O. Grachov *et al.*, (CMS Collaboration), *Performance of the combined zero degree calorimeter for CMS,* CMS-CR-2008-038, J.Phys.Conf.Ser. **160** (2009) 012059, arXiv:0807.0785 [nucl-ex].
[237] P. Jenni, M. Nessi, and M. Nordberg, (ATLAS Collaboration), *Zero degree calorimeters for ATLAS,* CERN-LHCC-2007-001, LHCC-I-016.
[238] Y. Itow, H. Menjo, G. Mitsuka, T. Sako, K. Kasahara, *et al.*, *Letter of intent; Precise measurements of very forward particle production at RHIC,* arXiv:1401.1004 [physics.ins-det].
[239] M. Albrow *et al.*, (FP420 R&D Collaboration), *The FP420 R&D Project: Higgs and New Physics with forward protons at the LHC,* FERMILAB-FN-0825-E, JINST **4** (2009) T10001, arXiv:0806.0302 [hep-ex].
[240] M. Albrow *et al.*, (CMS Collaboration), *Forward Physics with Rapidity Gaps at the LHC,* JINST **4** (2009) P10001, arXiv:0811.0120 [hep-ex].
[241] H. Meyer, M. Ross, R. Pollock, A. Berdoz, F. Dohrmann, *et al.*, *Total cross-section for $p + p \to p + p + \pi^0$ near threshold measured with the Indiana cooler,* Phys.Rev.Lett. **65** (1990) 2846–2849.
[242] H. Meyer, C. Horowitz, H. Nann, P. Pancella, S. Pate, *et al.*, *Total cross-section for $p + p \to p + p + \pi^0$*

close to threshold, Nucl.Phys. **A539** (1992) 633–661.
[243] A. Bondar, H. Calen, S. Carius, C. Ekstrom, K. Fransson, *et al.*, *The $pp \to pp\pi^0$ reaction near the kinematical threshold,* Phys.Lett. **B356** (1995) 8–12.
[244] R. Bilger, W. Brodowski, H. Calen, H. Clement, J. Dyring, *et al.*, *Cross sections of the $pp \to pp\pi^0$ reaction between 310-MeV and 425-MeV,* Nucl.Phys. **A693** (2001) 633–662.
[245] P. Thörngren Engblom, S. Negasi Keleta, F. Cappellaro, B. Hoistad, M. Jacewicz, *et al.*, *Anisotropy in the pion angular distribution of the reaction $pp \to pp\pi^0$ at 400-MeV,* Phys.Rev. **C76** (2007) 011602, arXiv:nucl-ex/0609003 [nucl-ex].
[246] S. Abd El-Samad *et al.*, (COSY-TOF), *Single-Pion Production in pp Collisions at 0.95-GeV/c. II.,* Eur.Phys.J. **A39** (2009) 281–289, arXiv:0807.1189 [nucl-ex].
[247] C. Hanhart, J. Haidenbauer, A. Reuber, C. Schutz, and J. Speth, *The Reaction $pp \to pp\pi^0$ near threshold,* KFA-IKP-TH-1995-9, Phys.Lett. **B358** (1995) 21–26, arXiv:nucl-th/9508005 [nucl-th].
[248] C. Hanhart, J. Haidenbauer, M. Hoffmann, U.-G. Meissner, and J. Speth, *The Reactions $pp \to pp\pi^0$ and $pp \to d\pi^+$ at threshold: The Role of the isoscalar πN scattering amplitude,* KFA-IKP-TH-1997-14, Phys.Lett. **B424** (1998) 8–14, arXiv:nucl-th/9707029 [nucl-th].
[249] C. Hanhart, *Meson production in nucleon-nucleon collisions close to the threshold,* FZJ-IKP-TH-2003-16, Phys.Rept. **397** (2004) 155–256, arXiv:hep-ph/0311341 [hep-ph].
[250] P. Moskal, M. Wolke, A. Khoukaz, and W. Oelert, *Close-to-threshold meson production in hadronic interactions,* Prog.Part.Nucl.Phys. **49** (2002) 1, arXiv:hep-ph/0208002 [hep-ph].
[251] E. Dahl-Jensen and et al., (Scandinavian Bubble Chamber Collaboration), *Exchange Mechanisms and Energy Dependence of Isospin Amplitudes for the Reaction $p + n \to n + n + \pi$ in the Energy Range 5 GeV - 1480 GeV,* Print-74-1635 (STOCKHOLM), Nucl.Phys. **B87** (1975) 426.
[252] S. Humble, *The Peripheral Impact Parameter Description of Inelastic Diffraction Dissociation at Very High-Energies,* CERN/D.Ph.II/PHYS 74-34, CERN-TH-1920, Nucl.Phys. **B86** (1975) 285.
[253] H. de Kerret, E. Nagy, M. Regler, W. Schmidt-Parzefall, K. R. Schubert, *et al.*, *Experimental Results on Diffractive One Pion Production at the CERN ISR,* PRINT-76-0612 (CERN), Phys.Lett. **B63** (1976) 477.
[254] G. Mantovani, M. Cavalli-Sforza, C. Conta, M. Fraternali, G. Goggi, *et al.*, *First Results on Diffraction Dissociation of Neutrons at the ISR,* PRINT-76-0888 (CERN), Phys.Lett. **B64** (1976) 471–474.
[255] A. Babaev, E. Brachman, G. Eliseev, A. Ermilov, I. Galaktionov, *et al.*, *Diffraction Dissociation of Neutrons Into $(p\pi^-)$ on Protons in the Momentum Range 35-GeV/c to 65-GeV/c,* PRINT-76-0760 (CERN), Nucl.Phys. **B116** (1976) 28.
[256] J. Biel, E. Bleser, D. Duke, T. Ferbel, D. Freytag, *et al.*, *Structure in Momentum Transfer for $(p\pi^-)$ Systems Produced in Diffractive Dissociation of Neutrons on Protons,* UR-597, COO-3065-155, FERMILAB-PUB-76-076-EXP, NU-EXP-4, FERMILAB-PUB-76-076-E, Phys.Lett. **B65** (1976) 291.
[257] J. Biel, T. Ferbel, P. Slattery, D. Underwood, B. Gobbi, *et al.*, *Study of the Dissociation Reaction $np \to (p\pi^-)p$ for Incident Neutron Momenta Between 50 GeV/c and 300 GeV/c,* UR-656, COO-3065-200, Phys.Rev. **D18** (1978) 3079.
[258] S. Drell and K. Hiida, *Quasi-Elastic Peak in High-Energy Nucleon-Nucleon Scattering,* Phys.Rev.Lett. **7** (1961) 199–202.
[259] R. T. Deck, *Kinematical interpretation of the first $\pi - \rho$ resonance,* Phys.Rev.Lett. **13** (1964) 169–173.
[260] E. R. Berger, A. Donnachie, H. G. Dosch, W. Kilian, O. Nachtmann, and M. Rüeter, *Odderon and photon exchange in electroproduction of pseudoscalar mesons,* HD-THEP-99-3, TAUP-2548-99, Eur.Phys.J. **C9** (1999) 491–501, arXiv:hep-ph/9901376 [hep-ph].
[261] E. R. Berger, A. Donnachie, H. G. Dosch, and O. Nachtmann, *Observing the odderon: Tensor meson photoproduction,* HD-THEP-99-53, M-C-TH-99-19, LPT-ORSAY-99-106, Eur.Phys.J. **C14** (2000) 673–682, arXiv:hep-ph/0001270 [hep-ph].
[262] E. R. Berger and O. Nachtmann, *Odderon and photon exchange in pseudoscalar meson production,* Nucl.Phys.Proc.Suppl. **79** (1999) 352–354.
[263] Y.-s. Oh, A. I. Titov, and T. Lee, *Nucleon resonances in ω photoproduction,* Phys.Rev. **C63** (2001) 025201, arXiv:nucl-th/0006057 [nucl-th].
[264] E. L. Berger and P. Pirilä, *Absorptive Effects in Exclusive Diffraction Dissociation,* ANL-HEP-PR-75-27, Phys.Rev. **D12** (1975) 3448.
[265] G. L. Kane and A. Seidl, *An Interpretation of Two-Body Hadron Reactions,* UM-HE-75-18, Rev.Mod.Phys. **48** (1976) 309.
[266] L. Tarasiuk, *Absorptive effects in nucleon diffraction dissociation,* Acta Phys.Polon. **B10** (1979) 901–910.
[267] V. Tsarev, *Nucleon Diffractive Dissociation. 1. Peripheral Model with Absorption,* Phys.Rev. **D11** (1975) 1864.
[268] S. Uehara *et al.*, (Belle Collaboration), *Measurement of $\gamma\gamma^* \to \pi^0$ transition form factor at Belle,* BELLE-PREPRINT-2012-16, KEK-PREPRINT-2012-8, Phys.Rev. **D86** (2012) 092007,

arXiv:1205.3249 [hep-ex].
[269] H. G. Dosch, C. Ewerz, and V. Schatz, *The Odderon in high-energy elastic pp scattering*, HD-THEP-01-45, Eur.Phys.J. **C24** (2002) 561–571, arXiv:hep-ph/0201294 [hep-ph].
[270] C. Adloff *et al.*, (H1 Collaboration), *Search for odderon induced contributions to exclusive π^0 photoproduction at HERA*, DESY-02-087, Phys.Lett. **B544** (2002) 35–43, arXiv:hep-ex/0206073 [hep-ex].
[271] C. Ewerz and O. Nachtmann, *Chiral Symmetry and Diffractive Neutral Pion Photo- and Electroproduction*, ECT*-06-10, HD-THEP-06-16, Eur.Phys.J. **C49** (2007) 685–696, arXiv:hep-ph/0608082 [hep-ph].
[272] A. Donnachie, H. G. Dosch, and O. Nachtmann, *The Missing odderon*, HD-THEP-05-14, Eur.Phys.J. **C45** (2006) 771–776, arXiv:hep-ph/0508196 [hep-ph].
[273] M. Drees and D. Zeppenfeld, *Production of Supersymmetric Particles in Elastic ep Collisions*, MAD/PH/443, Phys.Rev. **D39** (1989) 2536.
[274] A. Rybarska, W. Schäfer, and A. Szczurek, *Exclusive photoproduction of* Υ*: From HERA to Tevatron*, Phys.Lett. **B668** (2008) 126–132, arXiv:0805.0717 [hep-ph].
[275] L. Jenkovszky, O. Kuprash, R. Orava, and A. Salii, *Low missing mass, single- and double diffraction dissociation at the LHC*, arXiv:1211.5841 [hep-ph].
[276] L. Jenkovszky, O. Kuprash, J. Lämsä, V. Magas, and R. Orava, *Dual-Regge Approach to High-Energy, Low-Mass Diffraction Dissociation*, Phys.Rev. **D83** (2011) 056014, arXiv:1011.0664 [hep-ph].
[277] K. A. Goulianos, *Diffractive Interactions of Hadrons at High-Energies*, DOE-ER-40033-24, RU-81-A-23, Phys.Rept. **101** (1983) 169.
[278] V. Tsarev, *Nucleon Diffractive Dissociation. 2. Energy Dependence of the Low Missing Mass Cross-Section and Constraints on Triple Regge Couplings*, Phys.Rev. **D11** (1975) 1875.
[279] O. Adriani *et al.*, (LHCf Collaboration), *Measurement of forward neutral pion transverse momentum spectra for $\sqrt{s}$ = 7TeV proton-proton collisions at LHC*, Phys.Rev. **D86** (2012) 092001, arXiv:1205.4578 [hep-ex].
[280] G. Antchev, P. Aspell, I. Atanassov, V. Avati, J. Baechler, *et al.*, *First measurement of the total proton-proton cross section at the LHC energy of $\sqrt{s} = 7$ TeV*, CERN-PH-EP-2011-158, 24-SEPTEMBER-2011, Europhys.Lett. **96** (2011) 21002, arXiv:1110.1395 [hep-ex].
[281] I. Ivanov, N. Nikolaev, and A. Savin, *Diffractive vector meson production at HERA: From soft to hard QCD*, DESY-04-243, Phys.Part.Nucl. **37** (2006) 1–85, arXiv:hep-ph/0501034 [hep-ph].
[282] C. Marquet, R. B. Peschanski, and G. Soyez, *Exclusive vector meson production at HERA from QCD with saturation*, Phys.Rev. **D76** (2007) 034011, arXiv:hep-ph/0702171 [HEP-PH].
[283] R. Fiore, L. Jenkovszky, V. Magas, S. Melis, and A. Prokudin, *Exclusive J/ψ electroproduction in a dual model*, Phys.Rev. **D80** (2009) 116001, arXiv:0911.2094 [hep-ph].
[284] I. Anikin, D. Y. Ivanov, B. Pire, L. Szymanowski, and S. Wallon, *QCD factorization of exclusive processes beyond leading twist: $\gamma_T^* \to \rho_T$ impact factor with twist three accuracy*, LPT-09-75, Nucl.Phys. **B828** (2010) 1–68, arXiv:0909.4090 [hep-ph].
[285] S. R. Klein and J. Nystrand, *Photoproduction of quarkonium in proton proton and nucleus nucleus collisions*, Phys.Rev.Lett. **92** (2004) 142003, arXiv:hep-ph/0311164 [hep-ph].
[286] A. Cisek, Ph.D. thesis, *Exclusive processes with large rapidity gaps in the formalism of unintegrated gluon distributions*, IFJ PAN, 2012. `http://www.ifj.edu.pl/msd/index.php?menu=rozprawy`.
[287] V. Rebyakova, M. Strikman, and M. Zhalov, *The LHC potential for study of the small x gluon physics in ultraperipheral collisions of 3.5 TeV protons*, Phys.Rev. **D81** (2010) 031501, arXiv:0911.5169 [hep-ph].
[288] V. Goncalves and W. Sauter, *Diffractive vector meson production at large-t in coherent hadronic interactions at CERN LHC*, Eur.Phys.J. **A47** (2011) 117, arXiv:1004.1952 [hep-ph].
[289] R. Enberg, J. R. Forshaw, L. Motyka, and G. Poludniowski, *Vector meson photoproduction from the BFKL equation. 1. Theory*, TSL-ISV-2003-0269, JHEP **0309** (2003) 008, arXiv:hep-ph/0306232 [hep-ph].
[290] G. Poludniowski, R. Enberg, J. R. Forshaw, and L. Motyka, *Vector meson photoproduction from the BFKL equation. 2. Phenomenology*, JHEP **0312** (2003) 002, arXiv:hep-ph/0311017 [hep-ph].
[291] A. Sibirtsev, *Heavy-meson production cross sections from proton-proton collisions*, Nucl.Phys. **A604** (1996) 455–465.
[292] K. Nakayama, A. Szczurek, C. Hanhart, J. Haidenbauer, and J. Speth, *Production of ω mesons in proton-proton collisions*, FZJ-IKP-TH-1998-02, Phys.Rev. **C57** (1998) 1580–1587, arXiv:nucl-th/9802013 [nucl-th].
[293] K. Tsushima and K. Nakayama, *Near threshold ω and ϕ meson productions in pp collisions*, Phys.Rev. **C68** (2003) 034612, arXiv:nucl-th/0304017 [nucl-th].
[294] N. Kaiser, *Chiral corrections to the isovector double scattering term for the pion deuteron scattering length*, Phys.Rev. **C65** (2002) 057001, arXiv:nucl-th/0203001 [nucl-th].

[295] L. Kaptari and B. Kämpfer, *Combined analysis of near-threshold production of ω and ϕ mesons in nucleon-nucleon collisions within an effective meson-nucleon model*, Eur.Phys.J. **A23** (2005) 291–304, arXiv:nucl-th/0406077 [nucl-th].
[296] K. Nakayama, Y. Oh, J. Haidenbauer, and T.-S. Lee, *On the sign of the $\pi - \rho - \omega$ coupling constant*, Phys.Lett. **B648** (2007) 351–356, arXiv:nucl-th/0611101 [nucl-th].
[297] M. Abdel-Bary *et al.*, (TOF Collaboration), *Systematic study of the $pp \to pp\omega$ reaction*, Eur.Phys.J. **A44** (2010) 7–22, arXiv:1001.3043 [nucl-ex].
[298] R. Machleidt, *The Meson theory of nuclear forces and nuclear structure*, Adv.Nucl.Phys. **19** (1989) 189–376.
[299] A. Schäfer, L. Mankiewicz, and O. Nachtmann, *Double-diffractive J/ψ and ϕ production as a probe for the odderon*, PRINT-91-0476 (HEIDELBERG), Phys.Lett. **B272** (1991) 419–424.
[300] A. Bzdak, L. Motyka, L. Szymanowski, and J.-R. Cudell, *Exclusive J/ψ and Υ hadroproduction and the QCD odderon*, DESY-07-015, Phys.Rev. **D75** (2007) 094023, arXiv:hep-ph/0702134 [hep-ph].
[301] J. Czyzewski, J. Kwiecinski, L. Motyka, and M. Sadzikowski, *Exclusive η_c photoproduction and electroproduction at HERA as a possible probe of the odderon singularity in QCD*, TPJU-23-96, Phys.Lett. **B398** (1997) 400–406, arXiv:hep-ph/9611225 [hep-ph].
[302] I. Ivanov, N. N. Nikolaev, and I. Ginzburg, *Possible odderon discovery at HERA via charge asymmetry in the diffractive $\pi^+\pi^-$ production*, arXiv:hep-ph/0110181 [hep-ph].
[303] I. Ginzburg, I. Ivanov, and N. Nikolaev, *Possible odderon discovery via observation of charge asymmetry in the diffractive $\pi^+\pi^-$ production at HERA*, Eur.Phys.J.direct **C5** (2003) 02, arXiv:hep-ph/0207345 [hep-ph].
[304] P. Hägler, B. Pire, L. Szymanowski, and O. Teryaev, *Hunting the QCD odderon in hard diffractive electroproduction of two pions*, CPHT-S-001-01-02, Phys.Lett. **B535** (2002) 117–126, arXiv:hep-ph/0202231 [hep-ph].
[305] M. Derrick *et al.*, (ZEUS Collaboration), *Measurement of elastic omega photoproduction at HERA*, DESY-96-159, Z.Phys. **C73** (1996) 73–84, arXiv:hep-ex/9608010 [hep-ex].
[306] J. Breitweg *et al.*, (ZEUS Collaboration), *Measurement of the proton structure function F_2 at very low Q^2 at HERA*, DESY-00-071, Phys.Lett. **B487** (2000) 53–73, arXiv:hep-ex/0005018 [hep-ex].
[307] I. Ivanov and N. Nikolaev, *Anatomy of the differential gluon structure function of the proton from the experimental data on $F_{2p}(x, Q^2)$*, FZJ-IKP-TH-2000-08, Phys.Rev. **D65** (2002) 054004, arXiv:hep-ph/0004206 [hep-ph].
[308] A. Aktas *et al.*, (H1 Collaboration), *Elastic J/ψ production at HERA*, DESY-05-161, Eur.Phys.J. **C46** (2006) 585–603, arXiv:hep-ex/0510016 [hep-ex].
[309] M. Derrick *et al.*, (ZEUS Collaboration), *Measurement of total and partial photon proton cross-sections at 180 GeV center of mass energy*, DESY-94-032, Z.Phys. **C63** (1994) 391–408.
[310] M. Derrick *et al.*, (ZEUS Collaboration), *Measurement of elastic ρ^0 photoproduction at HERA*, DESY-95-143, Z.Phys. **C69** (1995) 39–54, arXiv:hep-ex/9507011 [hep-ex].
[311] S. Aid *et al.*, (H1 Collaboration), *Elastic photoproduction of ρ^0 mesons at HERA*, DESY-95-251, Nucl.Phys. **B463** (1996) 3–32, arXiv:hep-ex/9601004 [hep-ex].
[312] J. Breitweg *et al.*, (ZEUS Collaboration), *Elastic and proton dissociative ρ^0 photoproduction at HERA*, DESY-97-237, Eur.Phys.J. **C2** (1998) 247–267, arXiv:hep-ex/9712020 [hep-ex].
[313] B. Friman and M. Soyeur, *Photoproduction of vector mesons off nucleons near threshold*, GSI-PREPRINT-95-68, Nucl.Phys. **A600** (1996) 477–490, arXiv:nucl-th/9601028 [nucl-th].
[314] G. Mennessier, S. Narison, and X.-G. Wang, *σ and $f_0(980)$ substructures from $\gamma\gamma \to \pi\pi$, J/ψ, ϕ radiative and D_s semi-leptonic decays*, Phys.Lett. **B696** (2011) 40–50, arXiv:1009.2773 [hep-ph].
[315] J. Laget, *Photoproduction of vector mesons at large transfer*, DAPNIA-SPHN-00-15, Phys.Lett. **B489** (2000) 313–318, arXiv:hep-ph/0003213 [hep-ph].
[316] M. Williams *et al.*, (CLAS Collaboration), *Differential cross sections and spin density matrix elements for the reaction $\gamma p \to p\omega$*, JLAB-PHY-09-1049, Phys.Rev. **C80** (2009) 065208, arXiv:0908.2910 [nucl-ex].
[317] F. Abe *et al.*, (CDF Collaboration), *Measurement of small angle $\bar{p}p$ elastic scattering at $\sqrt{s} = 546$ GeV and 1800 GeV*, FERMILAB-PUB-93-232-E, Phys.Rev. **D50** (1994) 5518–5534.
[318] H. Holtmann, A. Szczurek, and J. Speth, *Flavor and spin of the proton and the meson cloud*, KFA-IKP-TH-94-25, Nucl.Phys. **A596** (1996) 631–669, arXiv:hep-ph/9601388 [hep-ph].
[319] Z. Dziembowski, H. Holtmann, A. Szczurek, and J. Speth, *Pionic corrections to nucleon electromagnetic properties in a light cone framework*, Annals Phys. **258** (1997) 1–36.
[320] N. N. Nikolaev, W. Schafer, A. Szczurek, and J. Speth, *Do the E866 Drell-Yan data change our picture of the chiral structure of the nucleon?*, Phys.Rev. **D60** (1999) 014004, arXiv:hep-ph/9812266 [hep-ph].
[321] J. Storrow, *Baryon Exchange Processes*, M/C TH-83/21, Phys.Rept. **103** (1984) 317.
[322] K. Nakayama and H. Haberzettl, *On the interaction current in $pp \to pp\gamma$*,

Phys.Rev. **C80** (2009) 051001, arXiv:0910.0469 [nucl-th].
[323] H. Haberzettl and K. Nakayama, *Gauge-invariant formulation of $NN \to NN\gamma$*, Phys.Rev. **C85** (2012) 064001, arXiv:1011.1927 [nucl-th].
[324] K. Nakayama and F. Huang, *Model-independent analysis of $p + p \to pp(^1S_0) + gamma$*, Phys.Rev. **C82** (2010) 065201, arXiv:1008.0943 [nucl-th].
[325] A. Johansson, H. Haberzettl, K. Nakayama, and C. Wilkin, *Measurement and analysis of the $pp \to pp\gamma$ reaction at 310 MeV*, Phys.Rev. **C83** (2011) 054001, arXiv:1101.5557 [nucl-ex].
[326] S. Kondratyuk, G. Martinus, and O. Scholten, *On electromagnetic off-shell effects in proton proton Bremsstrahlung*, Phys.Lett. **B418** (1998) 20–26, arXiv:nucl-th/9708019 [nucl-th].
[327] M. Cozma, G. Martinus, O. Scholten, R. Timmermans, and J. Tjon, *Covariant model for proton proton bremsstrahlung: Comparison with high precision data*, KVI-1552, Phys.Rev. **C65** (2002) 024001, arXiv:nucl-th/0111039 [nucl-th].
[328] M. Mahjour-Shafiei, J. Bacelar, M. Cozma, M. van Goethem, M. Harakeh, *et al.*, *High-precision proton-proton bremsstrahlung measurements at 190 MeV*, Phys.Rev. **C70** (2004) 024004.
[329] V. Khoze, J. Lämsä, R. Orava, and M. Ryskin, *Forward Physics at the LHC, Detecting Elastic pp Scattering by Radiative Photons*, IPPP-10-40, DCPT-10-80, JINST **6** (2011) P01005, arXiv:1007.3721 [hep-ph].
[330] H. Grönqvist, V. Khoze, J. Lämsä, M. Murray, and R. Orava, *Detecting Elastic pp Scattering by Radiative Photons in CMS at the LHC*, IPPP-10-96, DCPT-10-192, arXiv:1011.6141 [hep-ex].
[331] M. Diehl, *The Donnachie-Landshoff pomeron and gauge invariance*, DAPNIA-SPHN-98-16, Eur.Phys.J. **C6** (1999) 503–510, arXiv:hep-ph/9803296 [hep-ph].
[332] A. Szczurek and V. Uleshchenko, *Nonpartonic components in the nucleon structure functions at small Q^2 in the broad range of x*, Eur.Phys.J. **C12** (2000) 663–671, arXiv:hep-ph/9904288 [hep-ph].
[333] V. Petrov, R. Ryutin, and A. Sobol, *LHC as πp and $\pi\pi$ Collider*, Eur.Phys.J. **C65** (2010) 637–647, arXiv:0906.5309 [hep-ph].
[334] A. Grau, G. Pancheri, O. Shekhovtsova, and Y. N. Srivastava, *Modeling pion and proton total cross-sections at LHC*, Phys.Lett. **B693** (2010) 456–461, arXiv:1008.4119 [hep-ph].
[335] A. Sobol, R. Ryutin, V. Petrov, and M. Murray, *Elastic $\pi^+ p$ and $\pi^+\pi^+$ scattering at LHC*, Eur.Phys.J. **C69** (2010) 641–655, arXiv:1005.2984 [hep-ph].
[336] H. Holtmann, N. N. Nikolaev, A. Szczurek, J. Speth, and B. Zakharov, *On the determination of double diffraction dissociation cross-section at HERA*, KFA-IKP-TH-06-1995, Z.Phys. **C69** (1996) 297–304, arXiv:hep-ph/9503441 [hep-ph].
[337] Z. Ouyang, J.-J. Xie, B.-S. Zou, and H.-S. Xu, *Theoretical study on $pp \to pn\pi^+$ reaction at medium energies*, Int.J.Mod.Phys. **E18** (2009) 281–292, arXiv:0902.1818 [nucl-th].
[338] A. Irving and R. Worden, *Regge Phenomenology*, Phys.Rept. **34** (1977) 117–231.
[339] C. Adler, A. Denisov, E. Garcia, M. J. Murray, H. Strobele, *et al.*, *The RHIC zero degree calorimeter*, Nucl.Instrum.Meth. **A470** (2001) 488–499, arXiv:nucl-ex/0008005 [nucl-ex].
[340] B. Abelev *et al.*, (ALICE Collaboration), *Neutral pion and η meson production in proton-proton collisions at $\sqrt{s} = 0.9$ TeV and $\sqrt{s} = 7$ TeV*, CERN-PH-EP-2012-001, Phys.Lett. **B717** (2012) 162–172, arXiv:1205.5724 [hep-ex].
[341] M. Albrow and A. Rostovtsev, *Searching for the Higgs at hadron colliders using the missing mass method*, FERMILAB-PUB-00-173, arXiv:hep-ph/0009336 [hep-ph].
[342] V. A. Khoze, A. D. Martin, and M. Ryskin, *Can the Higgs be seen in rapidity gap events at the Tevatron or the LHC?*, DTP-00-08, Eur.Phys.J. **C14** (2000) 525–534, arXiv:hep-ph/0002072 [hep-ph].
[343] V. A. Khoze, A. D. Martin, and M. Ryskin, *Double diffractive processes in high resolution missing mass experiments at the Tevatron*, IPPP-00-10, DTP-00-74, Eur.Phys.J. **C19** (2001) 477–483, arXiv:hep-ph/0011393 [hep-ph].
[344] R. Maciuła, R. Pasechnik, and A. Szczurek, *Exclusive $b\bar{b}$ pair production and irreducible background to the exclusive Higgs boson production*, Phys.Rev. **D82** (2010) 114011, arXiv:1006.3007 [hep-ph].
[345] R. Maciuła, R. Pasechnik, and A. Szczurek, *New contributions to central exclusive production of dijets in proton-(anti)proton collisions*, LU-TP-11-30, Phys.Rev. **D84** (2011) 114014, arXiv:1109.5517 [hep-ph].
[346] J. Cudell, A. Dechambre, O. Hernandez, and I. Ivanov, *Central exclusive production of dijets at hadronic colliders*, Eur.Phys.J. **C61** (2009) 369–390, arXiv:0807.0600 [hep-ph].
[347] A. Dechambre, O. Kepka, C. Royon, and R. Staszewski, *Uncertainties on exclusive diffractive Higgs and jets production at the LHC*, Phys.Rev. **D83** (2011) 054013, arXiv:1101.1439 [hep-ph].
[348] V. Khoze, M. Ryskin, and W. Stirling, *On radiative QCD backgrounds to exclusive $H \to b\bar{b}$ production at the LHC and a photon collider*, IPPP-06-45, DCPT-06-90, Eur.Phys.J. **C48** (2006) 477–488, arXiv:hep-ph/0607134 [hep-ph].
[349] M. Ryskin, A. Martin, and V. Khoze, *Soft processes at the LHC. II. Soft-hard factorization breaking and*

gap survival, IPPP-08-93, DCPT-08-186, Eur.Phys.J. **C60** (2009) 265–272, arXiv:0812.2413 [hep-ph].
[350] L. Harland-Lang, V. Khoze, M. Ryskin, and W. Stirling, *Standard candle central exclusive processes at the Tevatron and LHC,* IPPP-10-32, DCPT-10-64, CAVENDISH-HEP-10-08, Eur.Phys.J. **C69** (2010) 179–199, arXiv:1005.0695 [hep-ph].
[351] L. Harland-Lang, V. Khoze, M. Ryskin, and W. Stirling, *Central exclusive meson pair production in the perturbative regime at hadron colliders,* IPPP-11-19, DCPT-11-38, CAVENDISH-HEP-11-06, Eur.Phys.J. **C71** (2011) 1714, arXiv:1105.1626 [hep-ph].
[352] R. Enberg and R. Pasechnik, *Associated central exclusive production of charged Higgs bosons,* Phys.Rev. **D83** (2011) 095020, arXiv:1104.0889 [hep-ph].
[353] T. Aaltonen *et al.*, (CDF Collaboration), *Search for exclusive $\gamma\gamma$ production in hadron-hadron collisions,* FERMILAB-PUB-07-384-E, Phys.Rev.Lett. **99** (2007) 242002, arXiv:0707.2374 [hep-ex].
[354] T. Aaltonen *et al.*, (CDF Collaboration), *Observation of Exclusive Dijet Production at the Fermilab Tevatron $p\bar{p}$ Collider,* FERMILAB-PUB-07-647-E, Phys.Rev. **D77** (2008) 052004, arXiv:0712.0604 [hep-ex].
[355] T. Aaltonen *et al.*, (CDF Collaboration), *Observation of Exclusive Gamma Gamma Production in $p\bar{p}$ Collisions at $\sqrt{s} = 1.96$ TeV,* FERMILAB-PUB-11-643-PPD, Phys.Rev.Lett. **108** (2012) 081801, arXiv:1112.0858 [hep-ex].
[356] O. Kepka and C. Royon, *Anomalous $WW\gamma$ coupling in photon-induced processes using forward detectors at the LHC,* Phys.Rev. **D78** (2008) 073005, arXiv:0808.0322 [hep-ph].
[357] E. Chapon, C. Royon, and O. Kepka, *Anomalous quartic $WW\gamma\gamma$, $ZZ\gamma\gamma$, and trilinear $WW\gamma$ couplings in two-photon processes at high luminosity at the LHC,* Phys.Rev. **D81** (2010) 074003, arXiv:0912.5161 [hep-ph].
[358] J. de Favereau de Jeneret, V. Lemaitre, Y. Liu, S. Ovyn, T. Pierzchala, *et al.*, *High energy photon interactions at the LHC,* CP3-09-37, arXiv:0908.2020 [hep-ph].
[359] S. Chatrchyan *et al.*, (CMS Collaboration), *Study of exclusive two-photon production of W^+W^- in pp collisions at $\sqrt{s} = 7$ TeV and constraints on anomalous quartic gauge couplings,* CMS-FSQ-12-010, CERN-PH-EP-2013-084, JHEP **1307** (2013) 116, arXiv:1305.5596 [hep-ex].
[360] M. Maniatis, A. von Manteuffel, and O. Nachtmann, *Anomalous couplings in $\gamma\gamma \to W^+W^-$ at LHC and ILC,* Nucl.Phys.Proc.Suppl. **179-180** (2008) 104–108.
[361] O. Nachtmann, F. Nagel, M. Pospischil, and A. Utermann, *Effective-Lagrangian approach to $\gamma\gamma \to WW$. I. Couplings and amplitudes,* HD-THEP-05-18, Eur.Phys.J. **C45** (2006) 679–691, arXiv:hep-ph/0508132 [hep-ph].
[362] O. Nachtmann, F. Nagel, M. Pospischil, and A. Utermann, *Effective-Lagrangian approach to $\gamma\gamma \to WW$. II. Results and comparison with $e^+e^- \to WW$,* HD-THEP-05-19, Eur.Phys.J. **C46** (2006) 93–105, arXiv:hep-ph/0508133 [hep-ph].
[363] B. Cox, A. De Roeck, V. Khoze, T. Pierzchala, M. Ryskin, *et al.*, *Detecting the standard model Higgs boson in the WW decay channel using forward proton tagging at the LHC,* IPPP-05-20, DCPT-05-40, MAN-HEP-2005-2, Eur.Phys.J. **C45** (2006) 401–407, arXiv:hep-ph/0505240 [hep-ph].
[364] R. S. Gupta, *Probing Quartic Neutral Gauge Boson Couplings using diffractive photon fusion at the LHC,* CERN-PH-TH-2011-284, MCTP-11-40, Phys.Rev. **D85** (2012) 014006, arXiv:1111.3354 [hep-ph].
[365] E. N. Glover and J. van der Bij, *Vector boson pair production via gluon fusion,* CERN-TH-5247/88, Phys.Lett. **B219** (1989) 488.
[366] C. Kao and D. A. Dicus, *Production of W^+W^- from gluon fusion,* DOE-ER40200-232, Phys.Rev. **D43** (1991) 1555–1559.
[367] S. Choi and F. Schrempp, *Constraints on anomalous $WW\gamma$ and $WW\gamma\gamma$ couplings at 500 GeV linear e^+e^- collider,* DESY-91-086, Phys.Lett. **B272** (1991) 149–157.
[368] E. Yehudai, *Probing $W\gamma$ couplings using $\gamma\gamma \to W^+W^-$,* SLAC-PUB-5495, Phys.Rev. **D44** (1991) 3434–3444.
[369] G. Belanger and F. Boudjema, *$\gamma\gamma \to W^+W^-$ and $\gamma\gamma \to ZZ$ as tests of novel quartic couplings,* ENSLAPP-A-364-92, UDEM-LPN-TH-80, Phys.Lett. **B288** (1992) 210–220.
[370] A. Denner, S. Dittmaier, and R. Schuster, *Radiative corrections to $\gamma\gamma \to W^+W^-$ in the electroweak standard model,* WUE-ITP-95-01, BI-TP-95-04, Nucl.Phys. **B452** (1995) 80–108, arXiv:hep-ph/9503442 [hep-ph].
[371] V. A. Khoze, A. D. Martin, and M. Ryskin, *Soft diffraction and the elastic slope at Tevatron and LHC energies: A MultiPomeron approach,* DTP-00-48, Eur.Phys.J. **C18** (2000) 167–179, arXiv:hep-ph/0007359 [hep-ph].
[372] U. Maor, *The Interplay between Data and Theory in Recent Unitarity Models,* AIP Conf.Proc. **1105** (2009) 248–251, arXiv:0811.2636 [hep-ph].
[373] D. Benjamin, (CDF Collaboration, D0 Collaboration, TEVNPH Working Group (Tevatron New

Phenomena and Higgs Working Group)), *Combined CDF and D0 upper limits on $gg \to H \to W^+W^-$ and constraints on the Higgs boson mass in fourth-generation fermion models with up to 8.2 fb^{-1} of data*, FERMILAB-CONF-11-372-E, CDF-NOTE-10608, D0-NOTE-6230, arXiv:1108.3331 [hep-ex].

[374] G. Aad *et al.*, (ATLAS Collaboration), *Search for the Higgs Boson in the $H \to WW^{(*)} \to l^+\nu l^-\bar{\nu}$ Decay Channel in pp Collisions at $\sqrt{s} = 7$ TeV with the ATLAS Detector*, CERN-PH-EP-2011-190, Phys.Rev.Lett. **108** (2012) 111802, arXiv:1112.2577 [hep-ex].

[375] S. Chatrchyan *et al.*, (CMS Collaboration), *Search for the standard model Higgs boson decaying to a W pair in the fully leptonic final state in pp collisions at $\sqrt{s} = 7$ TeV*, CMS-HIG-11-024, CERN-PH-EP-2012-018, Phys.Lett. **B710** (2012) 91–113, arXiv:1202.1489 [hep-ex].

[376] V. Kuksa and R. Pasechnik, *Near-threshold W-pair production in the model of unstable particles with smeared mass,* Int.J.Mod.Phys. **A24** (2009) 5765–5777, arXiv:0902.2857 [hep-ph].

[377] R. S. Pasechnik and V. I. Kuksa, *Finite-width effects in the near-threshold ZZZ and ZWW production at ILC,* Mod.Phys.Lett. **A26** (2011) 1075–1093, arXiv:1011.4202 [hep-ph].

[378] G. Passarino, *Standard Higgs boson searches at LEP-2,* Nucl.Phys. **B488** (1997) 3–38, arXiv:hep-ph/9611248 [hep-ph].

[379] R. Pasechnik, O. Teryaev, and A. Szczurek, *Scalar Higgs boson production in a fusion of two off-shell gluons,* Eur.Phys.J. **C47** (2006) 429–435, arXiv:hep-ph/0603258 [hep-ph].

[380] R. Enberg, R. Pasechnik, and O. Stal, *Enhancement of associated $H^{\pm}W^{\mp}$ production in the NMSSM,* DESY-11-247, LU-TP-11-47, Phys.Rev. **D85** (2012) 075016, arXiv:1112.4699 [hep-ph].

[381] T. Hahn, *Generating Feynman diagrams and amplitudes with FeynArts 3,* KA-TP-23-2000, Comput.Phys.Commun. **140** (2001) 418–431, arXiv:hep-ph/0012260 [hep-ph].

[382] T. Hahn and M. Perez-Victoria, *Automatized one loop calculations in four-dimensions and D-dimensions,* UG-FT-87-98, KA-TP-7-1998, Comput.Phys.Commun. **118** (1999) 153–165, arXiv:hep-ph/9807565 [hep-ph].

[383] T. Hahn, *A Mathematica interface for FormCalc-generated code,* MPP-2006-159, Comput.Phys.Commun. **178** (2008) 217–221, arXiv:hep-ph/0611273 [hep-ph].

[384] G. Passarino and M. Veltman, *One Loop Corrections for e^+e^- Annihilation Into $\mu^+\mu^-$ in the Weinberg Model,* Print-79-0284 (UTRECHT), Nucl.Phys. **B160** (1979) 151.

[385] M. Kimber, A. D. Martin, and M. Ryskin, *Unintegrated parton distributions,* IPPP-01-05, DCPT-01-10, Phys.Rev. **D63** (2001) 114027, arXiv:hep-ph/0101348 [hep-ph].

[386] A. Martin, W. Stirling, R. Thorne, and G. Watt, *Parton distributions for the LHC,* IPPP-08-95, DCPT-08-190, CAVENDISH-HEP-08-16, Eur.Phys.J. **C63** (2009) 189–285, arXiv:0901.0002 [hep-ph].

[387] R. D. Ball, V. Bertone, S. Carrazza, C. S. Deans, L. Del Debbio, *et al.*, *Parton distributions with LHC data*, CERN-PH-TH-2012-037, Nucl.Phys. **B867** (2013) 244–289, arXiv:1207.1303 [hep-ph].

[388] P. M. Nadolsky, H.-L. Lai, Q.-H. Cao, J. Huston, J. Pumplin, *et al.*, *Implications of CTEQ global analysis for collider observables,* MSUHEP-080125, UCRHEP-T447, Phys.Rev. **D78** (2008) 013004, arXiv:0802.0007 [hep-ph].

[389] H.-L. Lai, J. Huston, Z. Li, P. Nadolsky, J. Pumplin, *et al.*, *Uncertainty induced by QCD coupling in the CTEQ global analysis of parton distributions,* MSUHEP-100421, SMU-HEP-10-07, Phys.Rev. **D82** (2010) 054021, arXiv:1004.4624 [hep-ph].

[390] The Durham HepData Project. On-line Unpolarized Parton Distribution Calculator with Graphical Display. `http://hepdata.cedar.ac.uk/pdfs`.

[391] T. Coughlin and J. Forshaw, *Central Exclusive Production in QCD,* MAN-HEP-2009-46, JHEP **1001** (2010) 121, arXiv:0912.3280 [hep-ph].

[392] J. Aranda, F. Ramirez-Zavaleta, F. Tlachino, J. Toscano, and E. Tututi, *Lorentz-violating effects on pair production of W bosons in photon collisions,* arXiv:1308.4664 [hep-ph].

[393] G. Jikia and A. Tkabladze, *Photon-photon scattering at the photon linear collider,* IFVE-93-89, Phys.Lett. **B323** (1994) 453–458, arXiv:hep-ph/9312228 [hep-ph].

[394] G. Gounaris, P. Porfyriadis, and F. Renard, *The $\gamma\gamma \to \gamma\gamma$ process in the standard and SUSY models at high-energies,* PM-99-04, THES-TP-99-01, Eur.Phys.J. **C9** (1999) 673–686, arXiv:hep-ph/9902230 [hep-ph].

[395] G. Gounaris, P. Porfyriadis, and F. Renard, *Light by light scattering at high-energy: A Tool to reveal new particles,* PM-98-41, THES-TP-98-09, Phys.Lett. **B452** (1999) 76–82, arXiv:hep-ph/9812378 [hep-ph].

[396] Z. Bern, A. De Freitas, L. J. Dixon, A. Ghinculov, and H. Wong, *QCD and QED corrections to light by light scattering,* SLAC-PUB-8974, UCLA-01-TEP-18, JHEP **0111** (2001) 031, arXiv:hep-ph/0109079 [hep-ph].

[397] D. Bardin, L. Kalinovskaya, and E. Uglov, *Standard Model light-by-light scattering in SANC: analytic and numeric evaluation,* Phys.Atom.Nucl. **73** (2010) 1878–1888, arXiv:0911.5634 [hep-ph].

[398] G. Aad *et al.*, (ATLAS Collaboration), *Observation of a new particle in the search for the Standard Model*

Higgs boson with the ATLAS detector at the LHC, CERN-PH-EP-2012-218, Phys.Lett. **B716** (2012) 1–29, arXiv:1207.7214 [hep-ex].
[399] S. Chatrchyan *et al.*, (CMS Collaboration), *Observation of a new boson at a mass of 125 GeV with the CMS experiment at the LHC,* CMS-HIG-12-028, CERN-PH-EP-2012-220, Phys.Lett. **B716** (2012) 30–61, arXiv:1207.7235 [hep-ex].
[400] M. Łuszczak and A. Szczurek, *Subleading processes in production of W^+W^- pairs in proton-proton collisions,* arXiv:1309.7201 [hep-ph].
[401] R. Maciuła, R. Pasechnik, and A. Szczurek, *Exclusive double-diffractive production of open charm in proton-proton and proton-antiproton collisions,* Phys.Lett. **B685** (2010) 165–169, arXiv:0912.4345 [hep-ph].
[402] S. Chatrchyan *et al.*, (CMS Collaboration), *Search for the standard model Higgs boson decaying into two photons in pp collisions at $\sqrt{s} = 7$ TeV,* CMS-HIG-11-033, CERN-PH-EP-2012-024, Phys.Lett. **B710** (2012) 403–425, arXiv:1202.1487 [hep-ex].
[403] C. Collaboration, (CMS Collaboration), *Properties of the observed Higgs-like resonance using the diphoton channel,* CMS-PAS-HIG-13-016.
[404] S. Weinberg, *Implications of Dynamical Symmetry Breaking,* PRINT-75-0804 (HARVARD), Phys.Rev. **D13** (1976) 974–996.
[405] L. Susskind, *Dynamics of Spontaneous Symmetry Breaking in the Weinberg-Salam Theory,* SLAC-PUB-2142, Phys.Rev. **D20** (1979) 2619–2625.
[406] S. Dimopoulos and L. Susskind, *Mass Without Scalars,* CU-TP-147, ITP-626-STANFORD, Nucl.Phys. **B155** (1979) 237–252.
[407] E. Eichten and K. D. Lane, *Dynamical Breaking of Weak Interaction Symmetries,* HUTP-79-A062, Phys.Lett. **B90** (1980) 125–130.
[408] C. T. Hill and E. H. Simmons, *Strong dynamics and electroweak symmetry breaking,* FERMILAB-PUB-02-045-T, BUHEP-01-09, Phys.Rept. **381** (2003) 235–402, arXiv:hep-ph/0203079 [hep-ph].
[409] F. Sannino, *Conformal Dynamics for TeV Physics and Cosmology,* CP3-ORIGINS:2009-20, Acta Phys.Polon. **B40** (2009) 3533–3743, arXiv:0911.0931 [hep-ph].
[410] E. H. Simmons, *Phenomenology of a Technicolor Model With Heavy Scalar Doublet,* HUTP-88/A005, Nucl.Phys. **B312** (1989) 253.
[411] S. Samuel, *Bosonic Technicolor,* CCNY-HEP-90-1, Nucl.Phys. **B347** (1990) 625–650.
[412] A. Kagan and S. Samuel, *Renormalization group aspects of bosonic technicolor,* CCNY-HEP-91-8, Phys.Lett. **B270** (1991) 37–44.
[413] C. D. Carone, J. Erlich, and J. A. Tan, *Holographic Bosonic Technicolor,* WM-06-113, Phys.Rev. **D75** (2007) 075005, arXiv:hep-ph/0612242 [hep-ph].
[414] C. D. Carone, *Technicolor with a 125 GeV Higgs Boson,* Phys.Rev. **D86** (2012) 055011, arXiv:1206.4324 [hep-ph].
[415] K. Agashe, R. Contino, and A. Pomarol, *The Minimal composite Higgs model,* UAB-FT-567, Nucl.Phys. **B719** (2005) 165–187, arXiv:hep-ph/0412089 [hep-ph].
[416] J. Hirn and V. Sanz, *A Negative S parameter from holographic technicolor,* FTUV-06-0608, UG-FT-206-06, CAFPE-76-06, Phys.Rev.Lett. **97** (2006) 121803, arXiv:hep-ph/0606086 [hep-ph].
[417] D. K. Hong and H.-U. Yee, *Holographic estimate of oblique corrections for technicolor,* PNUTP-06-A01, KIAS-P06002, Phys.Rev. **D74** (2006) 015011, arXiv:hep-ph/0602177 [hep-ph].
[418] J. Jia, S. Matsuzaki, and K. Yamawaki, *Walking techni-pions at LHC,* MISC-2012-11, Phys.Rev. **D87** (2013) 016006, arXiv:1207.0735 [hep-ph].
[419] M. T. Frandsen and F. Sannino, *Discovering a Light Scalar or Pseudoscalar at The Large Hadron Collider,* CP3-ORIGINS-2012-005, DIAS-2012-06, arXiv:1203.3988 [hep-ph].
[420] T. Hapola, F. Mescia, M. Nardecchia, and F. Sannino, *Pseudo Goldstone Bosons Phenomenology in Minimal Walking Technicolor,* Eur.Phys.J. **C72** (2012) 2063, arXiv:1202.3024 [hep-ph].
[421] R. S. Chivukula, P. Ittisamai, E. H. Simmons, and J. Ren, *Technipion Limits from LHC Higgs Searches,* MSUHEP-111013, Phys.Rev. **D84** (2011) 115025, arXiv:1110.3688 [hep-ph].
[422] R. Pasechnik, V. Beylin, V. Kuksa, and G. Vereshkov, *Chiral-Symmetric Technicolor with Standard Model Higgs boson,* arXiv:1304.2081 [hep-ph].
[423] R. Pasechnik, V. Beylin, V. Kuksa, and G. Vereshkov, *Vector-like technineutron Dark Matter: is a QCD-type Technicolor ruled out by XENON100?,* arXiv:1308.6625 [hep-ph].
[424] B. W. Lee and H. Nieh, *Phenomenological Lagrangian for field algebra, hard pions, and radiative corrections,* Phys.Rev. **166** (1968) 1507–1515.
[425] S. Gasiorowicz and D. Geffen, *Effective Lagrangians and field algebras with chiral symmetry,* Rev.Mod.Phys. **41** (1969) 531–573.

[426] P. Ko and S. Rudaz, *Phenomenology of scalar and vector mesons in the linear sigma model,* UMN-TH-1154-93, TPI-MINN-93-27-T, Phys.Rev. **D50** (1994) 6877–6894.
[427] M. Urban, M. Buballa, and J. Wambach, *Vector and axial vector correlators in a chirally symmetric model,* Nucl.Phys. **A697** (2002) 338–371, arXiv:hep-ph/0102260 [hep-ph].
[428] B. Serot and J. Walecka, *Chiral QHD with vector mesons,* Acta Phys.Polon. **B23** (1992) 655–679.
[429] D. d'Enterria and G. G. da Silveira, *Observing light-by-light scattering at the Large Hadron Collider,* Phys.Rev.Lett. **111** (2013) 080405, arXiv:1305.7142 [hep-ph].
[430] J. Ohnemus, T. Walsh, and P. Zerwas, *$\gamma\gamma$ production of nonstrongly interacting SUSY particles at hadron colliders,* DESY-93-173, UCD-93-39, Phys.Lett. **B328** (1994) 369–373, arXiv:hep-ph/9402302 [hep-ph].
[431] I. Ginzburg and A. Schiller, *Visible effect of a very heavy magnetic monopole at colliders,* UL-NTZ-09-99, Phys.Rev. **D60** (1999) 075016, arXiv:hep-ph/9903314 [hep-ph].
[432] H. Davoudiasl, *$\gamma\gamma \to \gamma\gamma$ as a test of weak scale quantum gravity at the NLC,* SLAC-PUB-8121, Phys.Rev. **D60** (1999) 084022, arXiv:hep-ph/9904425 [hep-ph].
[433] K.-m. Cheung, *Diphoton signals for low scale gravity in extra dimensions,* UCD-HEP-99-8, Phys.Rev. **D61** (2000) 015005, arXiv:hep-ph/9904266 [hep-ph].
[434] J. Tandean, *Observing the technieta at a photon linear collider,* UMHEP-418, Phys.Rev. **D52** (1995) 1398–1403, arXiv:hep-ph/9505256 [hep-ph].
[435] K. Cheung and H.-W. Tseng, *Neutral pion-like resonances at photon colliders,* Phys.Rev. **D71** (2005) 037501, arXiv:hep-ph/0410231 [hep-ph].
[436] H. Lai *et al.*, (CTEQ Collaboration), *Global QCD analysis of parton structure of the nucleon: CTEQ5 parton distributions,* MSUHEP-903100, FERMILAB-PUB-00-266-E, Eur.Phys.J. **C12** (2000) 375–392, arXiv:hep-ph/9903282 [hep-ph].
[437] A. Cisek, W. Schafer, and A. Szczurek, *Exclusive coherent production of heavy vector mesons in nucleus-nucleus collisions at LHC,* Phys.Rev. **C86** (2012) 014905, arXiv:1204.5381 [hep-ph].
[438] M. Klusek-Gawenda and A. Szczurek, *Double-scattering mechanism in exclusive $AA \to AA\rho^0\rho^0$ reaction at ultrarelativistic collisions,* arXiv:1309.2463 [nucl-th].
[439] B. Grube, (STAR Collaboration), *Photoproduction in Ultra-Peripheral Heavy Ion Collisions at STAR,* Nucl.Phys.Proc.Suppl. **179** (2008) 117–124, arXiv:0808.3991 [nucl-ex].
[440] M. Klusek-Gawenda and A. Szczurek, *Exclusive production of large invariant mass pion pairs in ultraperipheral ultrarelativistic heavy ion collisions,* Phys.Lett. **B700** (2011) 322–330, arXiv:1104.0571 [nucl-th].
[441] R. Hagedorn, *Relativistic Kinematics: A guide to the kinematic problems of high-energy physics*. W.A. Benjamin, New York, Amsterdam, 1964.
[442] E. Wigner, *On Unitary Representations of the Inhomogeneous Lorentz Group,* Ann. Math. **40** (1939) 149.
[443] O. Nachtmann, *Elementary Particle Physics*. Springer-Verlag, Berlin, Heidelberg, 1990.